Defence Research
Establishment Pacific

DREP REPORT 93-1

WORKSHOP PROCEEDINGS

RESEARCH AND DEVELOPMENT ON ALUMINUM-LITHIUM ALLOYS

6-7 APRIL 1993

UNLIMITED

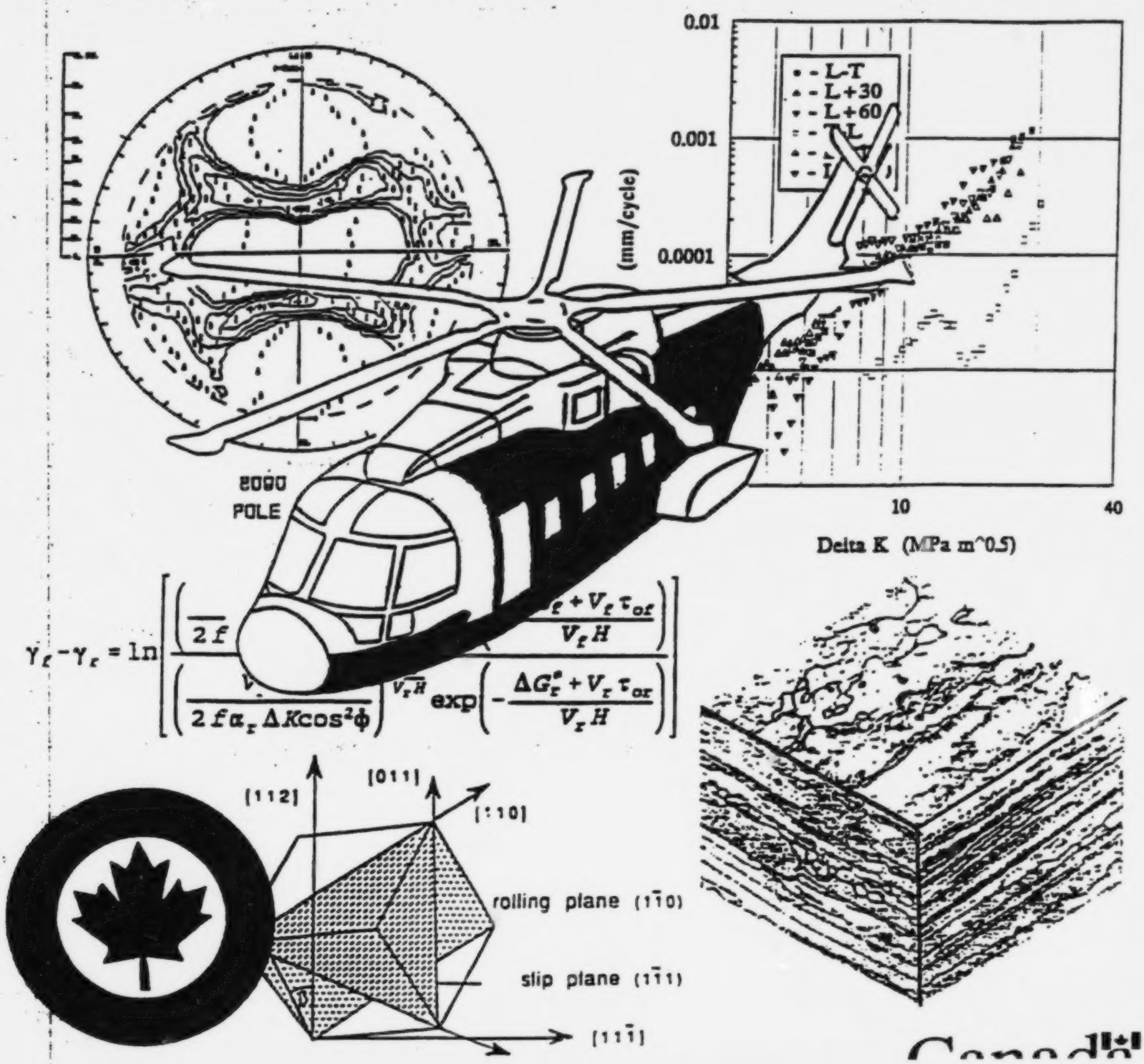
8090
POLE
0.01
0.001
0.0001
(mm/cycle)
- L-T
- L+30
- L+60
10
40
Delta K (MPa m^0.5)
[112]
[011]
[110]
rolling plane (1$\bar{1}$0)
slip plane (1$\bar{1}\bar{1}$)
[11$\bar{1}$]
$\gamma_t - \gamma_r = \ln$
$2 f \alpha_r \Delta K \cos^2\phi$
$\exp\left(-\frac{\Delta G_r^{\circ} + V_r \tau_{or}}{V_r H}\right)$

DREP REPORT 93-1

PROCEEDINGS OF A WORKSHOP ON "RESEARCH AND DEVELOPMENT ON ALUMINUM-LITHIUM ALLOYS"

Defence Research Establishment Pacific
Forces Mail Office
Victoria, BC, Canada
V0S 1B0

6-7 April 1993

Prepared by J. Morrison

November 1993

DREP Report 93-1

PROCEEDINGS OF THE WORKSHOP ON "RESEARCH AND DEVELOPMENT ON ALUMINUM-LITHIUM ALLOYS"

Abstract

The high stiffness and low density of lithium-containing aluminum alloys makes them prime candidates for a number of commercial and defence aircraft applications. It is well recognized that the strong crystallographic texture developed during the processing of these alloys, and the complex precipitation resulting from their heat treatment yields a material with some unusual properties. For several years Canadian government laboratories have had programs on aluminum-lithium alloysdealing with both long term research and development to characterize these materials, and the quality assurance issues and life cycle management implications arising from their exploitation in defence systems. This workshop was intended to provide a review of the activities undertaken to date, and to foster an increasing coordination of the overall effort to maximize the technical support provided to the Canadian Forces.

Résumé

La haute rigidité et la densité faible d'alliages d'aluminium contenant du lithium les apprêtent aux applications pour des aéronefs commerciaux et de défense. La forte texture cristallographique qui se produit au cours du traitement de ces alliages ainsi que la précipitation complexe résultant du traitement thermique de ceux-ci produit un matériau aux propriétés peu communes. Depuis quelques années les laboratoires du gouvernement canadien ont des programmes qui portent sur les alliages aluminium-lithium : la recherche à long terme aussi bien que le développement pour caractériser ces matériaux, ainsi que les questions d'assurance de qualité et les implications de gestion de cycle de vie provenant de l'exploitation de ces matériaux dans les systèmes de défense. Le but de cet atelier fut de résumer les activités initiées à date et d'encourager la coordination croissante de l'effort global de maximiser les soutiens techniques fournis aux Forces canadiennes.

CONTENTS

		Page
INTRODUCTION		1
LIST OF ATTENDEES		2
ACKNOWLEDGEMENTS		2
SESSION A. Keynote Presentations		3
1. "The New Shipborne Aircraft and the New Search and Rescue Helicopter Project Overview"	Capt. D. Lamanque, PMO NSA/NSH NDHQ, Ottawa	5
2. "Alcan's 8090 Products and Properties"	R. Grimes, M.A. Reynolds and A.J. Morris, Alcan International Ltd., Banbury, UK	27
3 "An Overview of the Use of Aluminium-Lithium Alloys on the EH101"	A.F. Smith, Westland Helicopters Ltd. Yeovil, UK	43
SESSION B. Mechanical Properties, Fracture and Fatigue I		73
4. "Fracture Toughness and Corrosion Fatigue Behaviour of 8090 Al-Li and 7XXX Aluminum Alloys".	A. Douchant and M. Yanishevsky, QETE, Hull, P.Q.	75
5. "Tensile and Fatigue Properties of an Aluminum-Lithium Alloy at Low Temperatures"	T. Bui-Quoc and M. Bernard, Ecole Polytechnique, Montreal, P.Q.	115
6. "The Effect of Shot Peening on the Fatigue Fracture Behaviour of Advanced Airframe Alloys"	M. Ferahi and S.A. Meguid, University of Toronto	131
7. "Effect of Anodizing on the Fatigue Properties of 8090C Alloy Sheet"	A. Douchant and A.M. Abdel-Latif, QETE, Hull, P.Q.	139
8. "A Comparison of Fatigue and Fracture Toughness Properties of Al-Li 8090 and 7050 Plate in Low Strength Directions"	Capt. K. Lemke and S.D. Antolovich, Georgia Institute of Technology, USA	151

CONTENTS (Contd.)

		Page
SESSION C. Corrosion and Corrosion Fatigue		172
9. "Electrochemical Characterization of the Resistance of Al-Li Alloy Sheet to Seawater Corrosion"	P.R. Roberge and E. Halliop, Royal Military College, Kingston, Ont., D. Lenard, and J.G.M. Moores, DREP, Victoria, B.C.	173
10. "Comparison of the Response of a Variety of Aluminum-Lithium Alloys During Accelerated Laboratory Corrosion Tests"	M. Roth, QETE, Hull, P.Q.	187
SESSION D. Mechanical Properties, Fracture and Fatigue II		213
11. "The Fatigue and fracture Behaviour of Aluminium-Lithium Plate - UK Study"	M.W. Squibb and R.N. Wilson, Defence Research Agency Farnborough, UK.	215
12 "The Effects of Orientation on Fatigue Crack Growth and Fracture in 8090 Aluminum-Lithium Plate"	X. Wu, W. Wallace, M.D. Raizenne, and A.K. Koul, IAR/NRC, Ottawa, Ont.	241
13. "Directionality of Strength and Toughness in Aluminum-Lithium Plate"	J. Morrison and Z. Zhai, DREP, Victoria, B.C., K.J. KarisAllen, . DREA, Halifax, N.S.	287
14. "Constant Amplitude Fatigue Crack Growth in Aluminum-Lithium"	Z. Zhai and J. Morrison, DREP. Victoria, B.C.	305
15. "A Fractographic Study of Selected Aluminum -Lithium Alloys"	D. A. Hull, Engineering Material Research, Downsview, Ont.	323
16. "Fatigue Crack Investigation of 2090 and 8090 Aluminum-Lithium Alloys"	D.A. Hull, Engineering Materials Research, Toronto, M.D. Raizenne, IAR / NRC, Ottawa, Ont.	349

Distribution List

PROCEEDINGS OF THE WORKSHOP ON "RESEARCH AND DEVELOPMENT ON ALUMINUM-LITHIUM ALLOYS"

Defence Research Establishment Pacific

Victoria, BC, April 1993

INTRODUCTION

The high stiffness and low density of lithium-containing aluminum alloys makes them prime candidates for a number of commercial and defence aircraft applications. It is well recognized that the strong crystallographic texture developed during the processing of these alloys, and the complex precipitation resulting from their heat treatment yields a material with some unusual properties. There has been increasing commercial interest in these materials over the past decade, and for several years laboratories within the Canadian Department of National Defence, notably the Defence Research Establishment Pacific (DREP) and the Quality Engineering Test Establishment (QETE), and also the National Research Council's Institute for Aerospace Research (IAR), have had programs on aluminum-lithium alloys. This work has included both long term research and development to characterize these materials as they become commercially available, and has also addressed the quality assurance issues and life cycle management implications arising from their potential exploitation in defence systems. Although these efforts involved some loose coordination and an awareness of each others objectives and technical activities, and the exchange of materials as they became available, there was no attempt at this stage to formalize the overall program. DREP and, to a certain extent, IAR were engaged in an extensive international collaborative effort under the Technical Cooperation Program (TTCP), while QETE was responding to NDHQ procurement and life cycle management concerns.

Prior to its recent cancellation, Canada's intention to purchase the EH101 helicopter under the New Shipborne Aircraft and New Search and Rescue Helicopter projects also added considerable impetus to aluminum-lithium studies within the Department of National Defence. The development of this helicopter featured the most extensive application seen to date of these new light alloys. DREP, QETE, and IAR agreed to sponsor a workshop to provide a review of the activities undertaken to date, and to foster an increasing coordination of the overall effort to maximize the technical support provided to the Canadian Forces. In addition to the inputs from the government laboratories, and their contractors, the workshop included a keynote seesion on both the development of aluminum-lithium alloys, and also on the EH101 project. The scope of the workshop was also broadened to include inputs from interested Canadian universites, and also from foreign laboratories involved in the international collaboratiive programs.

The two day workshop was held at DREP in April 1993, and a total of 16 papers were presented. The invited audience of about 35 included DND personnel from government laboratories and agencies, DND contractors, plus interested industrial engineers and university researchers. This proceedings includes the contributions from all sixteen presentations. In addition to the Keynote presentations, the program included two sessions on mechanical properties, fatigue, and fracture, and one session on corrosion. It is intended that this proceedings will provide a useful basis for the assessment of the future research and development needs of the Canadian Forces in aluminum-lithium alloy technology.

LIST OF ATTENDEES

Name	**Representing**
A.M. Abdel-Latif	QETE
S.D. Antolovich	University of Washington
Major P. Ayotte	PMO NSA/NSA
Major P. Beaudet	DGAEM/DAS Eng 6
M. Bernard	Ecole Polytechnique
Captain T.I. Bocz	AMDU/MPO 4
M. Bright	QETE
Captain M. Castonguay	DGAEM/DAS Eng 6
N.G. Cerullo	DGAEM/DAS Eng 3
M. Chadwick	DREP
T. Croft	Pyrotek Inc.
S. Cowley	Canadian Aircraft Products
M. Ferahi	University of Toronto
Captain J.S. Ferguson	DREP
R. Grimes	Alcan International Ltd.
D.A. Hull	Engineering Material Research
G.R. Labbé	DGMEM/DSE
Captain D. Lamanque	PMO NSA/NSH
Captain K. Lemke	Georgia Tech.
D. Lenard	DREP
W.L. MacMillan	CRAD/DRDA
B. Martin	Canadian Aircraft Products
S.A. Meguid	University of Toronto
J. Morrison	DREP
M. Paré	AMDU/MPO 4
B.F. Peters	DREP
J. W. Provan	University of Victoria
D. Raizenne	NRC/IAR
P.R. Roberge	RMC
M. Roth	QETE
A. Smith	Westlend Helicopters Ltd.
M. Squibb	DRA (Farnborough)
R. Thompson	CRAD/DRDA
W. Wallace	NRC/TIAR
W. Williams	Canadian Aircraft Products
X. Wu	NRC/IAR
M. Yanishevsky	QETE
Z. Zhai	DREP

ACKNOWLEDGEMENTS

The assistance of Martin Roth of the Quality Engineering Test Establishment and Don Raizenne of the NRC Institute for Aerospace Research in developing this workshop is gratefully acknowledged. Paul Martin of the Defence Research Establishment provided extensive support in arranging DREP facilities and CFB Esquimalt support.

SESSION A

KEYNOTE PRESENTATIONS

141633

NEW SHIPBORNE AIRCRAFT
NSA

NSH
NEW SAR HELICOPTER

1.

"The New Shipborne Aircraft and the New Search and Rescue Helicopter Project Overview"

Capt. D. Lamanque

PMO NSA/NSH
NDHQ, Ottawa

THE NEW SHIPBORNE AIRCRAFT AND THE NEW SEARCH & RESCUE HELICOPTER PROJECT OVERVIEW

BY

CAPTAIN DENIS LAMANQUE

SEM 2-3

PMO NSA/NSH

GOOD MORNING LADIES AND GENTLEMEN. IT IS AN HONOUR TO BE ONE OF THE KEYNOTE SPEAKER AT THIS WORKSHOP... (BRIEF PERSONAL INTRODUCTION). THE USE OF ALUMINIUM-LITHIUM ON THE NSA/NSH HAS CERTAINLY BEEN CONTROVERSIAL IN THE CANADIAN SCIENTIFIC COMMUNITY SINCE EH INDUSTRIES TOOK THE DECISION TO MAKE USE OF THIS ALLOY ON THE EH101.

AS THE FIRST SPEAKER THIS MORNING, AND AS THE ONLY SPEAKER FROM THE PROJECT OFFICE, I THOUGHT IT WAS APPROPRIATE THAT MY PRESENTATION PROVIDE YOU WITH A BRIEF INSIGHT INTO HOW CANADA CAME TO BUYING THE EH101, AND HOW THE ACQUISITION WILL BE MANAGED, WITH SOME EMPHASIS ON THE EH101 STRUCTURE AND ON THE USE OF ALUMINIUM-LITHIUM. THEREFORE, MY PRESENTATION THIS MORNING WILL WILL HAVE THE FOLLOWING CONTENT:

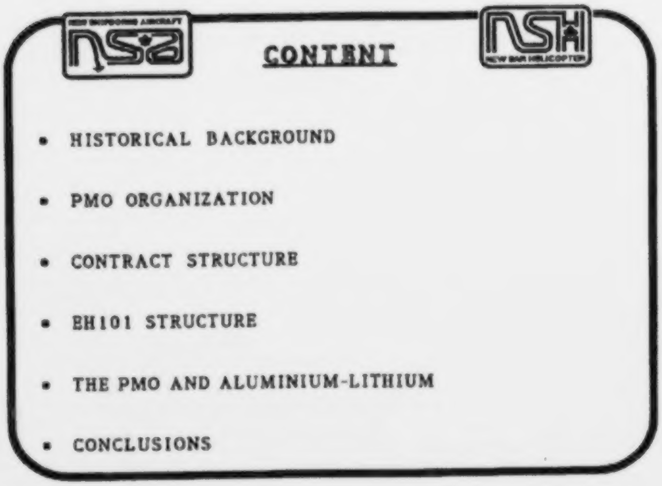

CONTENT

- HISTORICAL BACKGROUND
- PMO ORGANIZATION
- CONTRACT STRUCTURE
- EH101 STRUCTURE
- THE PMO AND ALUMINIUM-LITHIUM
- CONCLUSIONS

A SHORT HISTORICAL BACKGROUND.

THE PMO ORGANIZATION.

THE CONTRACT STRUCTURE.

AN OVERVIEW OF THE EH101 STRUCTURE.

THE PMO'S POSITION WITH RESPECT TO AL-LI

AND I WILL TERMINATE WITH SOME CONCLUDING REMARKS REMARKS BEFORE ENTERTAINING YOUR QUESTIONS.

I WILL NOT PROVIDE MUCH DETAILS ON THE USE OF AL-LI ON THE EH101 BECAUSE WE ARE FORTUNATE TO HAVE DR ALAN SMITH FROM WESTLAND AS OUR NEXT SPEAKER WHO WILL COVER THIS ISSUE IN DETAILS.

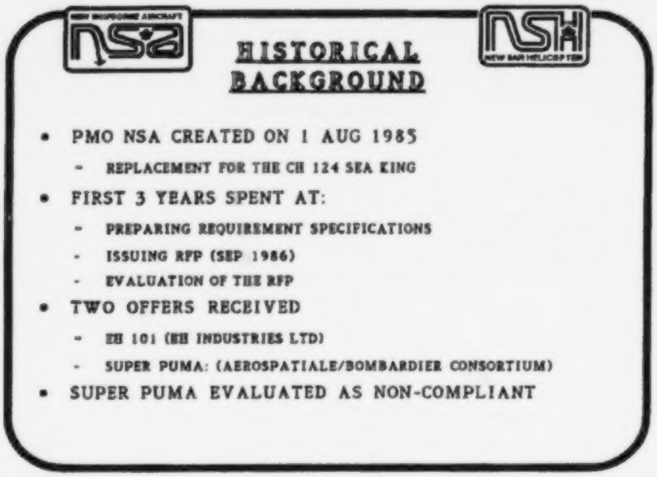

HISTORICAL BACKGROUND

- PMO NSA CREATED ON 1 AUG 1985
  - REPLACEMENT FOR THE CH 124 SEA KING
- FIRST 3 YEARS SPENT AT:
  - PREPARING REQUIREMENT SPECIFICATIONS
  - ISSUING RFP (SEP 1986)
  - EVALUATION OF THE RFP
- TWO OFFERS RECEIVED
  - EH 101 (EH INDUSTRIES LTD)
  - SUPER PUMA: (AEROSPATIALE/BOMBARDIER CONSORTIUM)
- SUPER PUMA EVALUATED AS NON-COMPLIANT

The Project Management Office for the New Shipborne Aircraft was created on 1 Aug 85. The objective of PMO NSA was to manage the Project Definition Phase for the replacement of the existing Sikorsky CH 124A Sea King helicopter fleet.

THE FIRST 2 YEARS OF THE PROJECT WERE SPENT AT PREPARING THE OPERATIONAL AND PRIME VEHICLE REQUIREMENT SPECIFICATIONS SUCH THAT A REQUEST FOR PROPOSAL COULD BE ISSUED. THE LATTER WAS ISSUED IN SEP 86 AND REPLIES WERE RECEIVED IN FEB 87 FROM EH INDUSTRIES WITH THE EH101 AND FROM AN AEROSPATIALE AND BOMBARDIER CONSORTIUM WITH THE SUPER PUMA.

AFTER A CAREFUL EVALUATION OF BOTH PROPOSALS, THE AEROSPATIALE/BOMBARDIER OFFER WAS DETERMINED TO BE NON-COMPLIANT WITH THE REQUIREMENT SPECIFICATIONS AND ACQUIRING THE EH101 REMAINED THE ONLY OPTION AVAILABLE.

HISTORICAL BACKGROUND (Cont'd)

- CASE MADE TO TREASURY BOARD FOR SOLE SOURCING THE EH101 AIRFRAME
- COMPETITIVE PROCESS FOR ENGINES AND ALL SUB-SYSTEMS INSTALLED ON THE AIRCRAFT
- OFFER MADE TO GOVERNMENT OF CANADA TO PARTICIPATE IN THE DEVELOPMENT OF THE EH101
  - OFFER DECLINED
  - NO POWER IN INFLUENCING THE AIRCRAFT DESIGN
  - AIRCRAFT BOUGHT ON A COMMERCIAL BASIS

THE CASE WAS MADE WITH TREASURY BOARD FOR SOLE SOURCING THE EH101 AIRFRAME AS IT WAS THE ONLY AIRFRAME AVAILABLE THAT COULD FULFILL THE NAVAL OPERATION REQUIREMENTS. TO RENDER THE PROCESS COMPETITIVE, ALL THE SUB-SYSTEMS, SUCH AS THE ENGINES AND THE MISSION SYSTEM EQUIPMENT, WERE TO BE ACQUIRED UNDER THE COMPETITIVE PROCESS.

IT SHOULD BE NOTED THAT EARLY IN THE DEFINITION PROGRAM, AN OFFER WAS MADE TO THE GOVERNMENT OF CANADA TO PARTICIPATE, WITH UK AND ITALY, IN THE DEVELOPMENT OF EH101. WITH THE REFUSAL OF THIS OFFER, CANADA RELEGATED ANY INFLUENCE IN THE DESIGN OF THE AIRCRAFT AND BASICALLY ACCEPTED TO PURCHASE THE AIRCRAFT ON A COMMERCIAL BASIS.

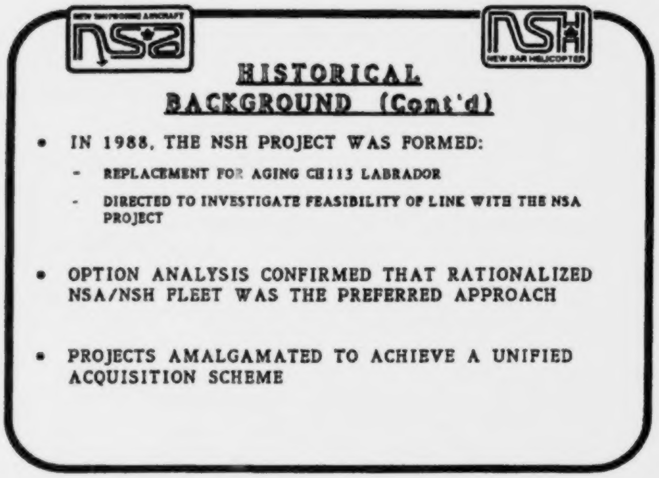
NEW SAR HELICOPTER

HISTORICAL BACKGROUND (Cont'd)

- IN 1988, THE NSH PROJECT WAS FORMED:
  - REPLACEMENT FOR AGING CH113 LABRADOR
  - DIRECTED TO INVESTIGATE FEASIBILITY OF LINK WITH THE NSA PROJECT
- OPTION ANALYSIS CONFIRMED THAT RATIONALIZED NSA/NSH FLEET WAS THE PREFERRED APPROACH
- PROJECTS AMALGAMATED TO ACHIEVE A UNIFIED ACQUISITION SCHEME

In 1988, the New Search and Rescue Aircraft (NSH) project, TO REPLACE OUR AGING CH 113 LABRADOR HELICOPTER, was directed to investigate the feasibility of a link with the NSA project. An Options Analysis confirmed that a rationalized NSA/NSH fleet was the preferred approach.

The projects team were therefore amalgamated, using common expertise and resources, to achieve a unified acquisition scheme.

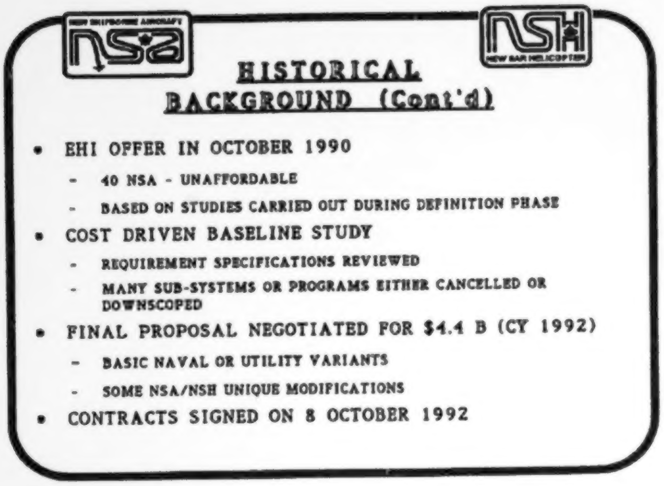

HISTORICAL BACKGROUND (Cont'd)

- EHI OFFER IN OCTOBER 1990
  - 40 NSA - UNAFFORDABLE
  - BASED ON STUDIES CARRIED OUT DURING DEFINITION PHASE
- COST DRIVEN BASELINE STUDY
  - REQUIREMENT SPECIFICATIONS REVIEWED
  - MANY SUB-SYSTEMS OR PROGRAMS EITHER CANCELLED OR DOWNSCOPED
- FINAL PROPOSAL NEGOTIATED FOR $4.4 B (CY 1992)
  - BASIC NAVAL OR UTILITY VARIANTS
  - SOME NSA/NSH UNIQUE MODIFICATIONS
- CONTRACTS SIGNED ON 8 OCTOBER 1992

BASED ON THE VEHICLE REQUIREMENTS AND ON THE ENGINEERING STUDIES CARRIED OUT BY EHI DURING DEFINITION, AN UNFFORDABLE OFFER WAS MADE IN OCTOBER 1990 FOR THE ACQUISITION OF 40 NSA. BECAUSE THE COST OF THE PROPOSAL WAS WELL BEYOND THE AFFORDABLE LIMIT, A COST DRIVEN BASELINE STUDY WAS UNDERTAKEN TO RATIONALIZE THE OPTIONS. AS A RESULT OF THIS STUDY, MANY OF THE MISSION SYSTEMS, SUCH AS THE MAGNETIC ANOMALY DETECTOR, WERE DELETED FROM THE REQUIREMENTS. WITH RESPECT TO THE BASIC VEHICLE ACQUISITION, A SERIES OF PROGRAMS SUCH AS A DEDICATED CANADIAN CORROSION CONTROL PROGRAM, A 20 FT/SEC CAPABLE LANDING GEAR AND THE AIRCRAFT STRUCTURAL INTEGRITY PROGRAM WERE EITHER DOWNSCOPED OR CANCELLED. THE MANAGEMENT AND CONTRACTOR STRUCTURE THAT I WILL DISCUSS IN A MOMENT WAS ADOPTED TO RATIONALIZE COSTS.

THE IMPLEMENTATION CONTRACTS WITH PARAMAX AND EH INDUSTRIES WERE SIGNED ON THE EIGHT OF OCTOBER 1992. CANADA IS ACQUIRING THE BASIC NAVAL AND UTILITY VARIANTS OF THE EH101WITH SOME CANADIAN UNIQUE MODIFICATIONS.

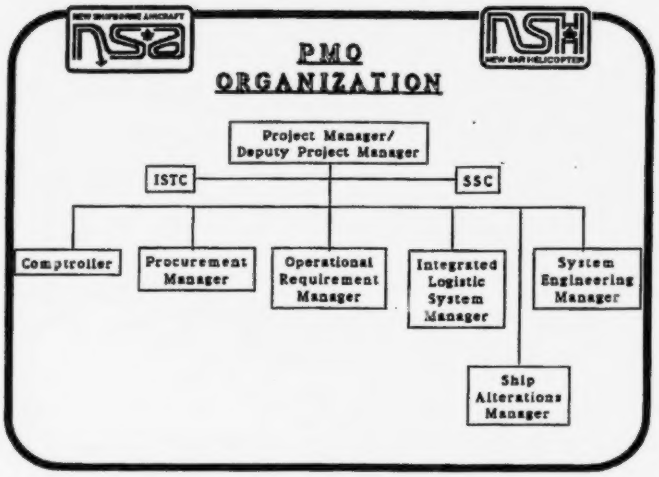
PMO
ORGANIZATION
Project Manager/ Deputy Project Manager
ISTC
SSC
Comptroller
Procurement Manager
Operational Requirement Manager
Integrated Logistic System Manager
System Engineering Manager
Ship Alterations Manager

THE ORGANIZATION CHART REPRESENTS THE TOP LEVEL PMO STRUCTURE. SIX SUB-SECTIONS REPORT TO THE PROJECT AND DEPUTY PROJECT MANAGERS.

THE COMPTROLLER AND PROCUREMENT MANAGERS ARE RESPONSIBLE FOR THE ADMINISTRATION OF THE FINANCE AND THE VARIOUS CONTRACTS ISSUED FOR THE PROJECT.

THE OPERATIONAL REQUIREMENT MANAGER IS ULTIMATELY THE AIR COMMAND REPRESENTATIVE IN THE PMO TO ENSURE THAT THE AIRCRAFT OPERATIONAL REQUIREMENTS ARE RESPECTED.

THE INTEGRATED LOGISTIC SYSTEM MANAGER IS RESPONSIBLE FOR ALL ASPECTS OF THE AIRCRAFT SUPPORT WHILE IN SERVICE SUCH AS: SPARE ACQUISITION, FACILITIES INFRASTRUCTURE, SIMULATOR ACQUISITION, TRAINING ETC.

THE SYSTEM ENGINEERING MANAGER IS RESPONSIBLE FOR THE ACQUISITION OF THE VEHICLE FROM THE CONTRACTORS. THIS ENTAILS ALL ASPECTS OF CERTIFICATION, QUALIFICATION AND DAY-TO-DAY TECHNICAL MANAGEMENT OF THE CONTRACT AS WELL AS MANAGING THE INTERFACE BETWEEN THE CONTRACTORS.

THE SHIP ALTERATION MANAGER IS RESPONSIBLE FOR THE SHIP MODIFICATIONS THAT WILL BE REQUIRED ON THE THREE TYPES OF SHIPS FROM WHICH THE EH101 WILL OPERATE.

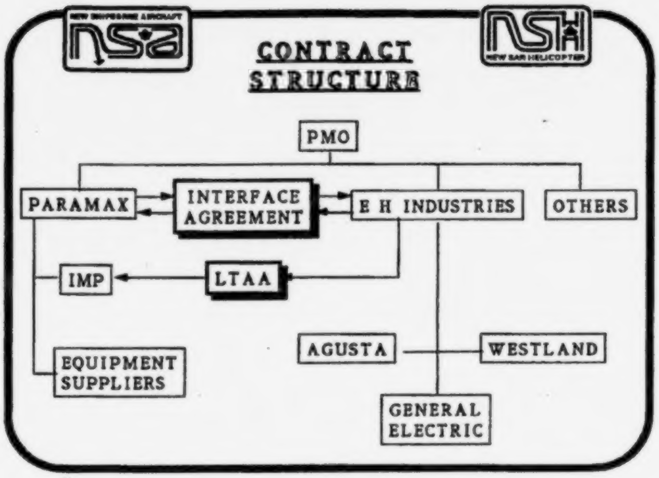

NEW SHIPBORNE AIRCRAFT

NEW SAR HELICOPTER

CONTRACT STRUCTURE

PMO

PARAMAX

INTERFACE AGREEMENT

E H INDUSTRIES

OTHERS

IMP

LTAA

EQUIPMENT SUPPLIERS

AGUSTA

WESTLAND

GENERAL ELECTRIC

THE OVERALL CONTRACT MANAGEMENT STRUCTURE IS DEPICTED ON THE PRESENT SLIDE. FROM THE PMO OFFICE, THROUGH SUPPLY AND SERVICES CANADA, STEM TWO MAJOR CONTRACTS THAT HAVE BEEN ISSUED FOR THE ACQUISITION OF THE NSA/NSH. WE ARE ACQUIRING THE BASIC VEHICLE FROM EH INDUSTRIES, THAT IS THE AIRFRAME, THE ENGINES AND THE COCKPIT AVIONICS. THE 15 NSH FINAL ASSEMBLY WILL TAKE PLACE IN WESTLAND WHEREAS THE 35 NSA FINAL ASSEMBLY WILL TAKE PLACE IN AGUSTA. THE AIRCRAFT ARE THEN TURNED OVER TO PARAMAX FOR THE INTEGRATION AND INSTALLATION OF THE MISSION AVIONIC EQUIPMENT THAT WILL FORM THE PRIME MISSION VEHICLE.

AN INTERFACE AGREEMENT WAS NEGOTIATED AS PART OF THE CONTRACTS TO ENSURE COORDINATION BETWEEN THE CONTRACTORS. FURTHERMORE A LICENSE AND TECHNICAL ASSISTANCE AGREEMENT WAS NEGOTIATED BETWEEN EHI AND IMP AND IS NOW IN PLACE.

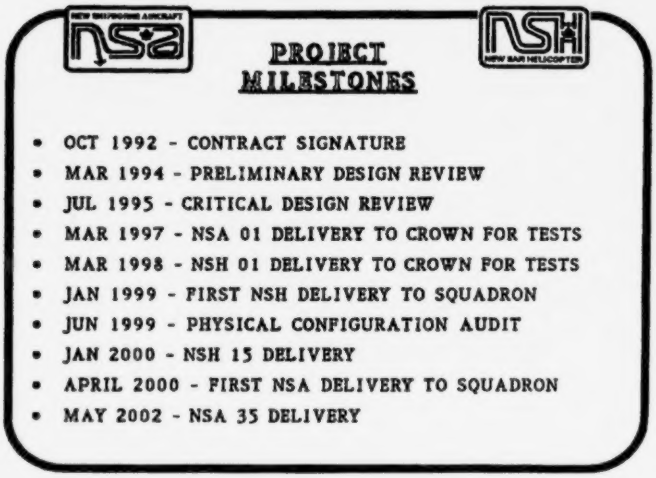

PROJECT MILESTONES

- OCT 1992 - CONTRACT SIGNATURE
- MAR 1994 - PRELIMINARY DESIGN REVIEW
- JUL 1995 - CRITICAL DESIGN REVIEW
- MAR 1997 - NSA 01 DELIVERY TO CROWN FOR TESTS
- MAR 1998 - NSH 01 DELIVERY TO CROWN FOR TESTS
- JAN 1999 - FIRST NSH DELIVERY TO SQUADRON
- JUN 1999 - PHYSICAL CONFIGURATION AUDIT
- JAN 2000 - NSH 15 DELIVERY
- APRIL 2000 - FIRST NSA DELIVERY TO SQUADRON
- MAY 2002 - NSA 35 DELIVERY

THE PRESENT SLIDE PROVIDES SOME MAJOR MILESTONES ON THE PROJECT. AS YOU CAN SEE, THIS IS VERY MUCH A LONG TERM ACQUISITION PROGRAM.

NSA01 DELIVERY IS ONE OF THE FIRST TEN ON THE EHI PRODUCTION LINE, THIS NUMBER IS STILL FLUID AT THIS TIME. THIS AIRCRAFT WILL BE USED FOR THE MISSION AVIONIC INTEGRATION BY PARAMAX. THE SECOND NSA WILL MAINLY BE USED FOR SHIP/HELO CAT II TRIALS BEFORE BEING TURNED OVER FOR SERVICE. THE DELIVERY SCHEDULE OF THE NSA WAS PUSHED FURTHER TO THE RIGHT TO ACCOMMODATE AN EARLIER DELIVERY OF THE NSH AS THE LABRADOR LIFE WILL BE AT THE CRITICAL STAGE BY THEN.

THE PHYSICAL CONFIGURATION AUDIT IS THE POINT AT WHICH THE DESIGN IS FROZEN. ANY MODIFICATION TO THE DESIGN BEFORE PCA WILL BE RETROFITTED ON THE FLEET AT THE CONTRACTOR'S COST.

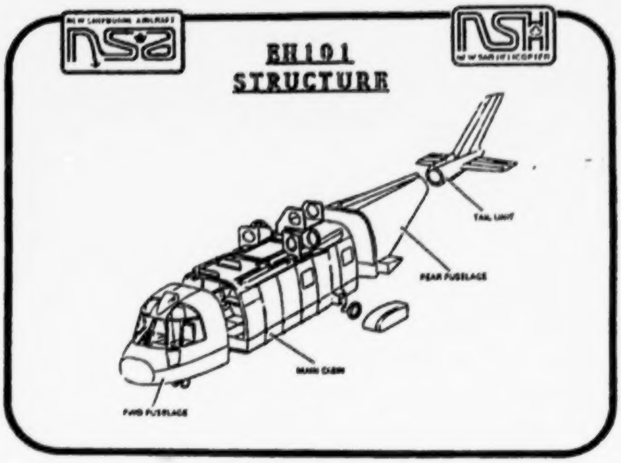

EH101
STRUCTURE

THE EH101 IS BUILT BY MODULE. AS PART OF THE WORKSHARE AGREEMENT BETWEEN WESTLAND AND AGUSTA, THE FORWARD FUSELAGE AND THE MAIN CABIN STRUCTURES ARE BUILT BY WESTLAND. THE TAIL REAR FUSELAGE (OR THE TAIL/RAMP SECTION FOR THE CASE OF THE NSH) AND THE TAIL UNIT ARE PRODUCED BY AGUSTA. AGUSTA ALSO HAS THE RESPONSIBILITY FOR THE DESIGN AND INTEGRATION OF THE ENGINE AND THE DYNAMIC SYSTEMS. ALL THE OTHER SYSTEMS ON THE AIRCRAFT HAVE BEEN DIVIDED AS SUCH. FOR INSTANCE, THE BLADES ARE WESTLAND RESPONSIBILITY WHEREAS THE ROTOR HEAD IS AGUSTA'S. LET ME ALSO ADD THAT THE LEAD DESIGN COMPANY IN A PARTICULAR AREA ALSO HAS THE RESPONSIBILITY FOR QUALIFYING, AND ULTIMATELY CERTIFYING THEIR DESIGN.

NEW SHIPBORNE AIRCRAFT

NEW SAR HELICOPTER

FORWARD
FUSELAGE STRUCTURE

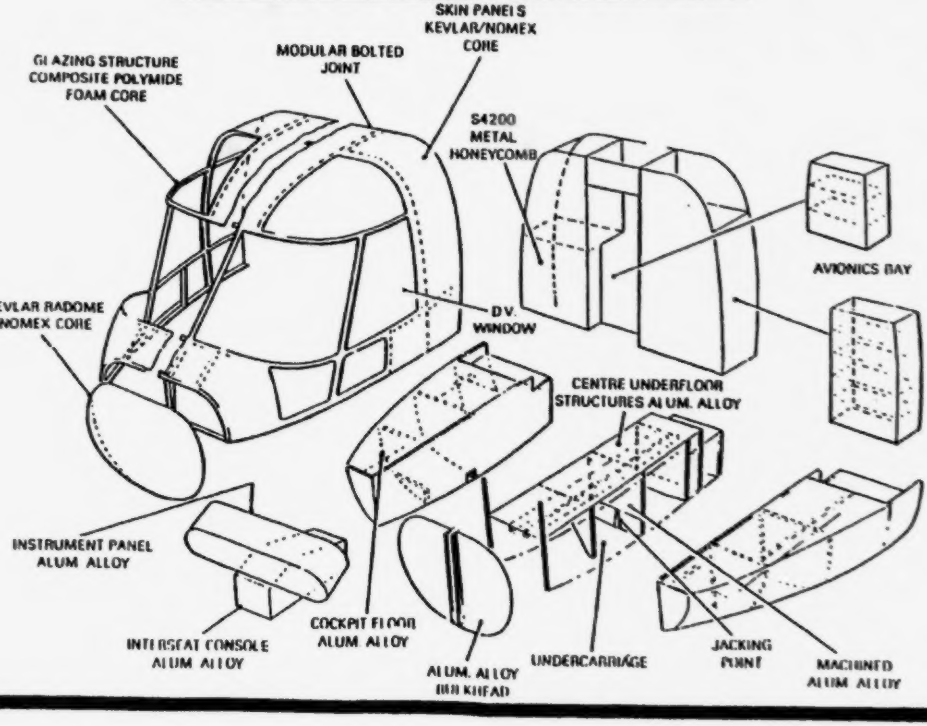
SKIN PANELS KEVLAR/NOMEX CORE
GLAZING STRUCTURE COMPOSITE POLYMIDE FOAM CORE
MODULAR BOLTED JOINT
S4200 METAL HONEYCOMB
AVIONICS BAY
KEVLAR RADOME NOMEX CORE
DV. WINDOW
CENTRE UNDERFLOOR STRUCTURES ALUM. ALLOY
INSTRUMENT PANEL ALUM ALLOY
INTERSEAT CONSOLE ALUM ALLOY
COCKPIT FLOOR ALUM ALLOY
ALUM. ALLOY BULKHEAD
UNDERCARRIAGE
JACKING POINT
MACHINED ALUM ALLOY

NEW SHIPBORNE AIRCRAFT

NEW SAR HELICOPTER

MAIN CABIN STRUCTURE

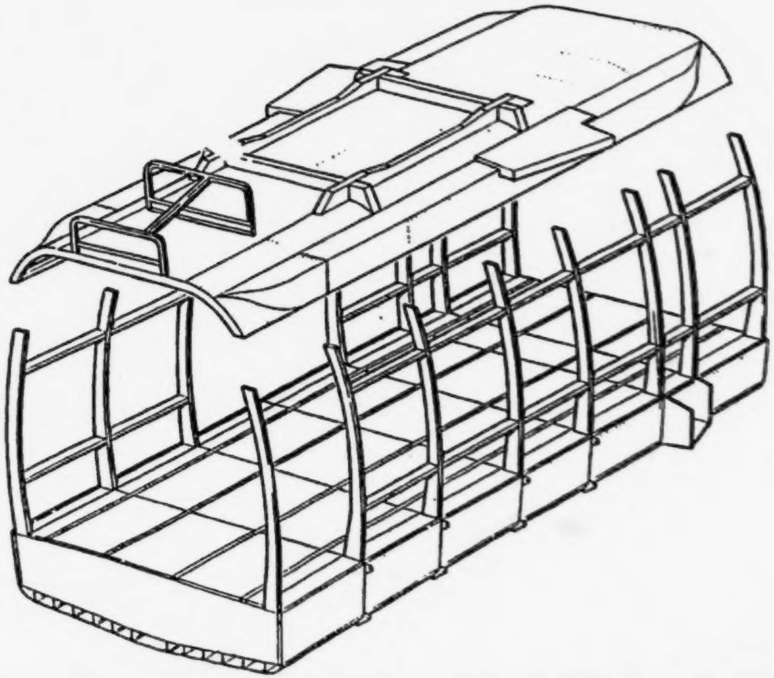

NEW SHIPBORNE AIRCRAFT

NEW SAR HELICOPTER

MAIN CABIN STRUCTURE (Cont'd)

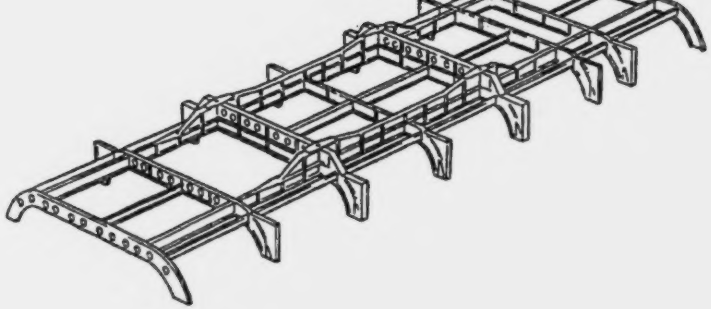

NEW SHIPBORNE AIRCRAFT

NEW SAR HELICOPTER

TRANSMISSION MOUNTING

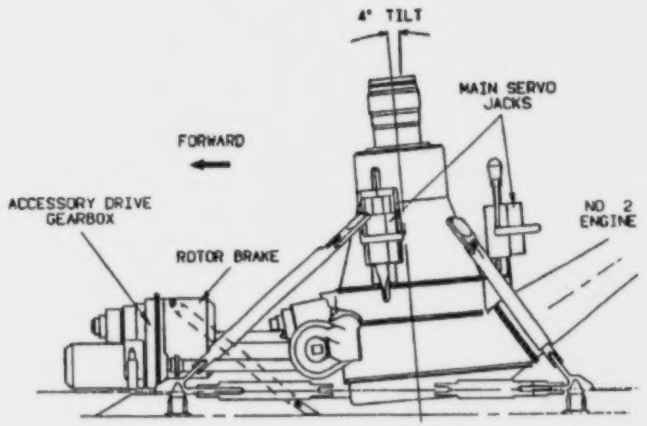
4° TILT
MAIN SERVO JACKS
FORWARD
ACCESSORY DRIVE GEARBOX
ROTOR BRAKE
NO 2 ENGINE

NEW SHIPBORNE AIRCRAFT

NEW SAR HELICOPTER

MAIN CABIN STRUCTURE (Cont'd)

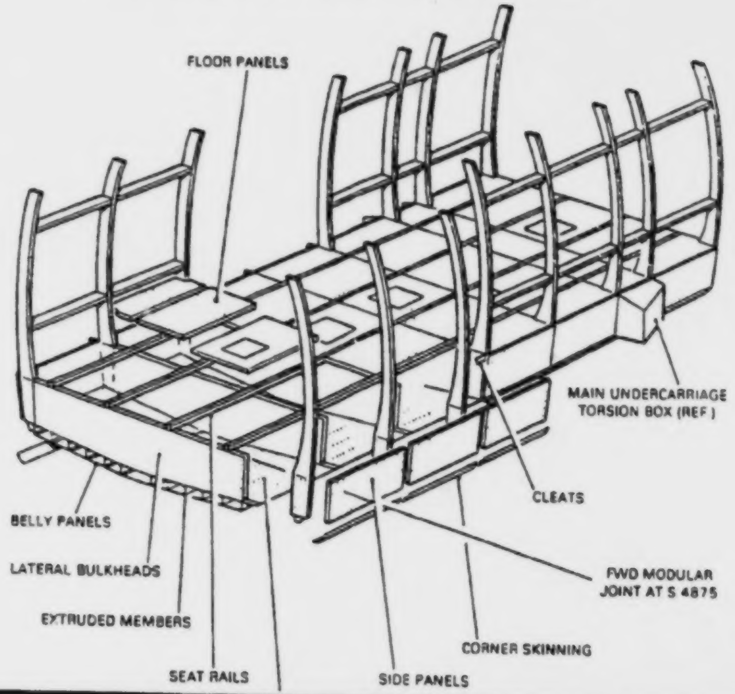
FLOOR PANELS
MAIN UNDERCARRIAGE TORSION BOX (REF)
CLEATS
BELLY PANELS
LATERAL BULKHEADS
EXTRUDED MEMBERS
FWD MODULAR JOINT AT S 4875
CORNER SKINNING
SEAT RAILS
SIDE PANELS

NEW SHIPBORNE AIRCRAFT
NSA

NEW SAR HELICOPTER
NSH

TAIL CONE STRUCTURE

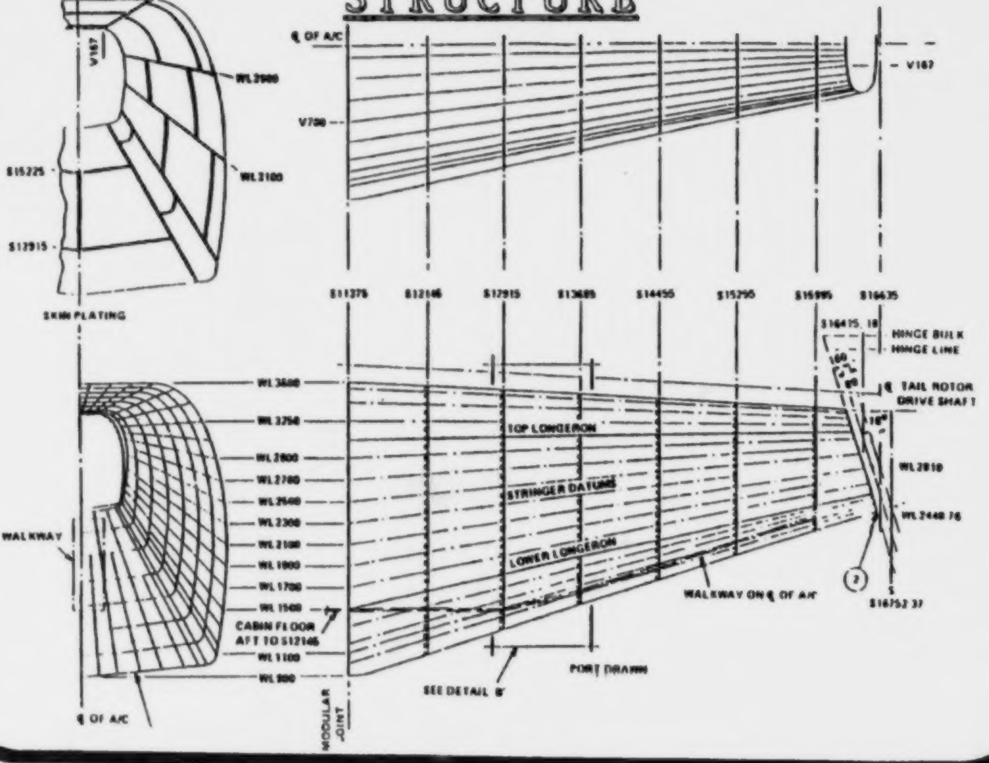
V167
WL2900
WL3100
S15225
S12915
SKIN PLATING
℄ OF A/C
V700
V167
S11375
S12146
S12915
S13685
S14455
S15295
S15995
S16635
S16475. 18
HINGE BULK
HINGE LINE
℄ TAIL ROTOR DRIVE SHAFT
18°
WL2810
WL2448 76
S16752 37
2
WL 3600
WL 3250
WL 2900
WL 2700
WL 2500
WL 2300
WL 2100
WL 1900
WL 1700
WL 1500
CABIN FLOOR AFT TO S12146
WL 1100
WL 900
WALKWAY
℄ OF A/C
MODULAR JOINT
TOP LONGERON
STRINGER DATUMS
LOWER LONGERON
WALKWAY ON ℄ OF A/C
SEE DETAIL 'B'
PORT DRAWN

NEW SHIPBORNE AIRCRAFT

NEW SAR HELICOPTER

COMPOSITES ON THE EH101

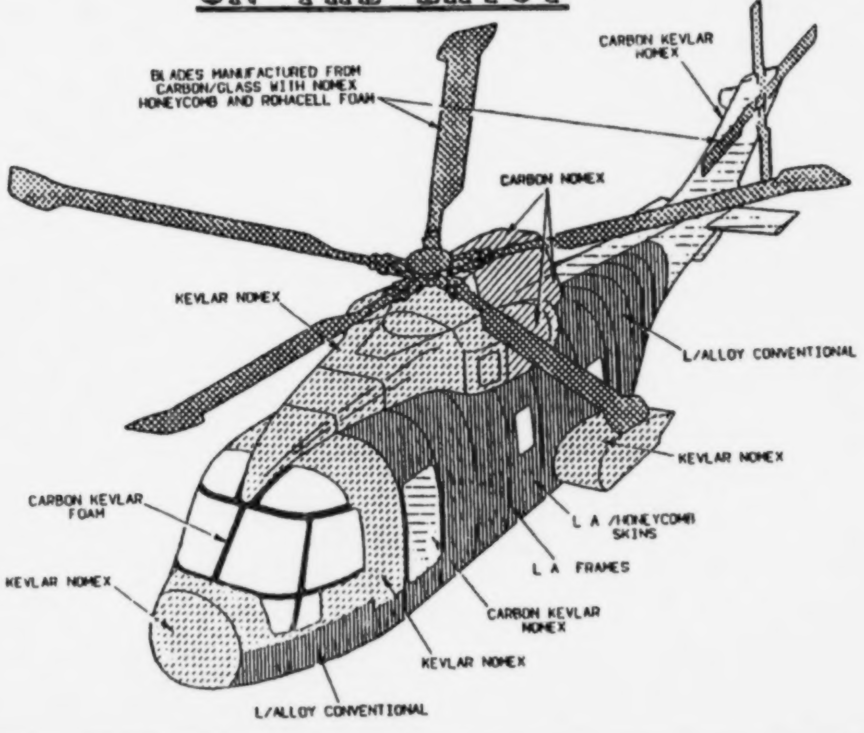
BLADES MANUFACTURED FROM CARBON/GLASS WITH NOMEX HONEYCOMB AND ROHACELL FOAM
CARBON KEVLAR NOMEX
CARBON NOMEX
KEVLAR NOMEX
L/ALLOY CONVENTIONAL
KEVLAR NOMEX
CARBON KEVLAR FOAM
L A /HONEYCOMB SKINS
L A FRAMES
KEVLAR NOMEX
CARBON KEVLAR NOMEX
KEVLAR NOMEX
L/ALLOY CONVENTIONAL

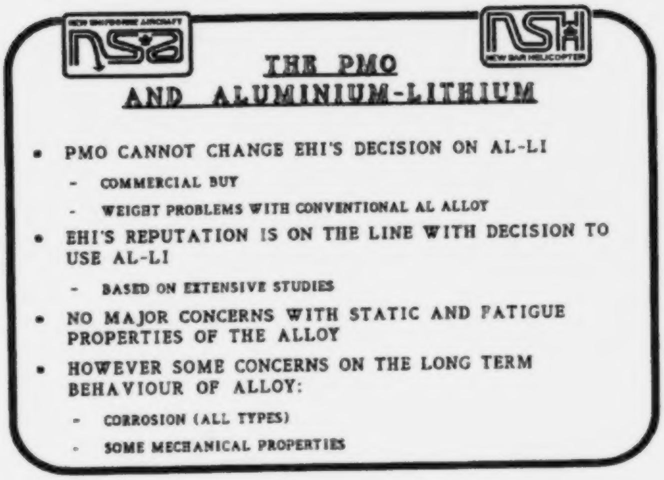

THE PMO
AND ALUMINIUM-LITHIUM

- PMO CANNOT CHANGE EHI'S DECISION ON AL-LI
  - COMMERCIAL BUY
  - WEIGHT PROBLEMS WITH CONVENTIONAL AL ALLOY
- EHI'S REPUTATION IS ON THE LINE WITH DECISION TO USE AL-LI
  - BASED ON EXTENSIVE STUDIES
- NO MAJOR CONCERNS WITH STATIC AND FATIGUE PROPERTIES OF THE ALLOY
- HOWEVER SOME CONCERNS ON THE LONG TERM BEHAVIOUR OF ALLOY:
  - CORROSION (ALL TYPES)
  - SOME MECHANICAL PROPERTIES

BY ACCEPTING THE ACQUISITION OF THE EH101, THE PMO ALSO HAD TO ACCEPT HAVING AL-LI AS PART OF ITS AIRFRAME. MOREOVER, USING CONVENTIONAL AL ALOY, THE EH101 WOULD WEIGHT CONSIDERABLY MORE AND THAT WOULD PRECLUDE IT FROM MEETING ALL IF ITS OPERATIONAL REQUIREMENTS.

ONE ALSO HAS TO ADMIT THAT BY USING AL-LI, EHI, AND ITS MAIN SUB-CONTRACTORS (WHL AND AG), HAVE PUT THEIR REPUTATION ON THE LINE AS AIRCRAFT MANUFACTURERS AND HAVE CERTAINLY NOT TAKEN THIS DECISION WITHOUT THE MAXIMUM AVAILABLE DATA. ON THE OTHER HAND THE LONG TERM IN-SERVICE PROPERTIES OF AL-LI ALLOYS HAVE NOT BEEN PROVEN YET, AND THAT REMAINS A CONCERN AT THE PMO AND AN ELEMENT OF RISK FOR THE ACQUISITION.

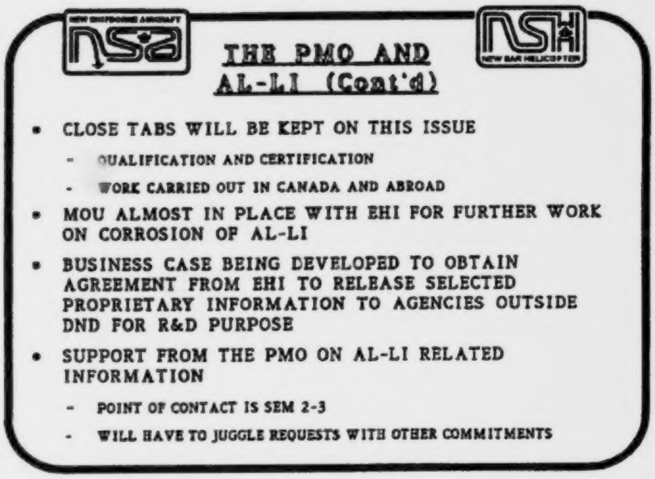

THE PMO AND AL-LI (Cont'd)

- CLOSE TABS WILL BE KEPT ON THIS ISSUE
  - QUALIFICATION AND CERTIFICATION
  - WORK CARRIED OUT IN CANADA AND ABROAD
- MOU ALMOST IN PLACE WITH EHI FOR FURTHER WORK ON CORROSION OF AL-LI
- BUSINESS CASE BEING DEVELOPED TO OBTAIN AGREEMENT FROM EHI TO RELEASE SELECTED PROPRIETARY INFORMATION TO AGENCIES OUTSIDE DND FOR R&D PURPOSE
- SUPPORT FROM THE PMO ON AL-LI RELATED INFORMATION
  - POINT OF CONTACT IS SEM 2-3
  - WILL HAVE TO JUGGLE REQUESTS WITH OTHER COMMITMENTS

IN THE MEANTIME, THE PMO WILL KEEP ABREAST OF THE DEVELOPMENTS THAT ARE ACHEIVED IN THE AL-LI FIELD. ANY ELEMENTS OF QUALIFICATION AND CERTIFICATION ASSOCIATED WITH MATERIALS WILL BE CLOSELY SCRUTINIZED.

TO ENHANCE OUR KNOWLEDGE OF THIS NEW MATERIAL THAT WILL SOON ENTER SERVICE FOR DND, AN AGREEMENT IS ABOUT TO BE SIGNED BETWEEN EHI AND THE PMO FOR AN EXCHANGE OF DATA RELATED TO THE CORROSION PROPERTIES OF AL-LI. QETE AND DREP WILL BE THE LEAD FOR THESE ACTIVITIES. FURTHERMORE, AGREEMENT IS BEING SOUGHT FROM EHI FOR THE RELEASE OF SOME AL-LI PROPRIETARY INFORMATION TO SELECTED AGENCIES OUTSIDE OF DND.

INFORMATION CAN BE SOUGHT FROM MYSELF AT THE PMO. I WILL DO MY BEST TO OBTAIN THE REQUESTED INFORMATION WITHIN THE CONTRACTUAL LIMITS AND THE OTHER COMMITMENTS ASSOCIATED WITH MY POSITION.

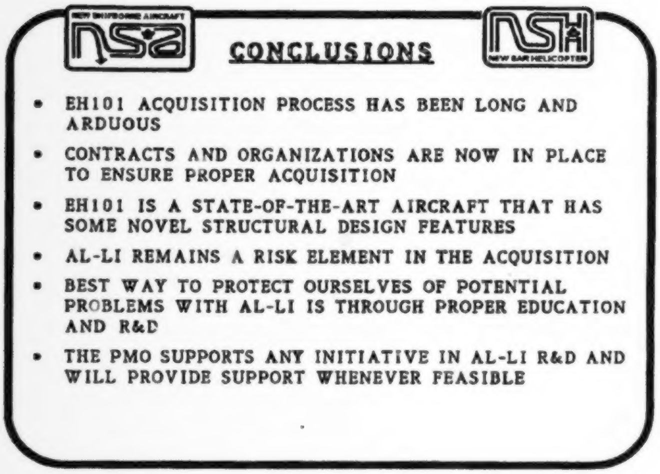

CONCLUSIONS

- EH101 ACQUISITION PROCESS HAS BEEN LONG AND ARDUOUS
- CONTRACTS AND ORGANIZATIONS ARE NOW IN PLACE TO ENSURE PROPER ACQUISITION
- EH101 IS A STATE-OF-THE-ART AIRCRAFT THAT HAS SOME NOVEL STRUCTURAL DESIGN FEATURES
- AL-LI REMAINS A RISK ELEMENT IN THE ACQUISITION
- BEST WAY TO PROTECT OURSELVES OF POTENTIAL PROBLEMS WITH AL-LI IS THROUGH PROPER EDUCATION AND R&D
- THE PMO SUPPORTS ANY INITIATIVE IN AL-LI R&D AND WILL PROVIDE SUPPORT WHENEVER FEASIBLE

ALTHOUGH THE ROAD WAS LONG AND WINDING TO ACHIEVE THE IMPLEMENTATION PHASE OF THIS PROJECT, IT IS BELIEVED THAT THE EH101 SOLUTION WILL PROVIDE US WITH AN AIRCRAFT THAT WILL MEET OUR DEMAND FOR MANY YEARS TO COME.

AL-LI REMAINS AN ELEMENT OF RISK IN THE ACQUISITION OF THE EH101. UNFORTUNATELY, SERVICE USE WILL BE THE ONLY TRUE TEST FOR THIS ALLOY. HOWEVER, KNOWLEDGE AND R&D ARE THE ONLY TOOL THAT WE HAVE AT OUR DISPOSITION TO ENSURE THAT WE ARE READY TO MEET THE CHALLENGE OF SUPPORTING THE EH101 STRUCTURE IN THE SEVERE ENVIRONMENT THAT IT HAS TO OPERATE IN.

THE PMO SUPPORTS ANY INITIATIVE IN AL-LI R&D AND WILL PROVIDE SUPPORT WHENEVER IT IS POSSIBLE.

THIS, LADIES AND GENTLEMEN, CONCLUDES MY PRESENTATION, I WILL GLADLY ENTERTAIN ANY QUESTIONS THAT YOU MY HAVE ON THE EH101 OR ON THE PROJECT.

141634

2.

"Alcan's 8090 Products and Properties"

R. Grimes, M.A. Reynolds, and A.J. Morris

Alcan International Ltd.,
Banbury, UK

Alcan's 8090 Products and Properties

Introduction

4) Alcans involvement in the development of aluminium-lithium based alloys began, at a very low level of activity, in approximately 1977. The early work was performed under contract to the UK Ministry of Defence and for the first several years was centred upon alloys within the Al-Mg-Li system. These alloys proved difficult to cast and difficult to fabricate and did not possess a particularly attractive combination of properties. However, in 1981 the Defence Research Agency (Aerospace) (then the Royal Aircraft Establishment, Farnborough) demonstrated that the Al-Li-Cu-Mg-Zr system was capable of producing material with a considerably improved strength/toughness relationship compared with the earlier Al-Li based alloys. The optimised alloy, from this activity, registered as 8090, also proved to be considerably easier to cast and to fabricate and subsequently the great majority of Alcans Al-Li development activity has been concerned with optimisation/characterisation of 8090 in its various product forms and tempers.

The 8090 alloy is now commercially available as plate, extrusion, sheet, tube and forgestock and the purpose of this paper is to give a summary of the currently available products and properties together with an indication of continuing Alcan development activity.

Current Products

Table 1 (a) gives composition, density and modulus for 8090 while physical capabilities for the various product forms are indicated in Table 1 (b).

Sheet This product was originally developed for application as a 2024 T3 replacement for use in applications, such as the pressure cabins of large passenger aircraft, where damage tolerance is of the highest importance. The commercial decision by British Alcan to cease manufacture of any aircraft sheet in their major rolling mills has reduced the available size range to those available from the British Alcan small speciality rolling mill, Aluminium Corporation at Dolgarrog in north Wales.

The early, straight rolled 8090 sheet possessed an unrecrystallised microstructure which resulted in an unacceptable level of anisotropy. It also became clear (Figure 1) that, at damage tolerant strength levels, the strength/toughness relationship was superior for fine grained recrystallised sheet and this has become the standard product for applications requiring high damage tolerance.

However, where a component is very complex and requires re-heat treatment during manufacture an unrecrystallised miscrostructure is still preferred and anisotropy is controlled in the current product by use of cross rolling. Properties for both unrecrystallised and recrystallised products are given in Table 2.

Plate In the earlier stages of the Al-Li development most effort was devoted to a peak aged variant of 8090 plate intended as substitute for 2014 T651. This T8771 variant has been employed in significant quantities in space applications (Figure 2) and has been made in gauges up to 150 mm.

More recently work has concentrated upon developing the damage tolerant (T8651) variant as a substitute for 2024 T351 particularly for use in lower wing structures. For this reason all recent work has been on relatively thin gauges (up to about 30 mm). However, it is believed that comparable properties can be achieved in significantly thicker plate.

Plate properties are summarised in Table 3 (a) for the damage tolerant temper and Table 3 (b) for the medium strength variant.

Extrusion Thin extrusions do not, generally, have high requirements for damage tolerance and hence are supplied in a near to peak aged condition. Ageing at a relatively high temperature produces S' precipitation which blocks planar slip and gives the extrudate better L direction ductility than can be achieved with lower ageing temperatures.

Thicker section extrusions have been developed in a damage tolerant temper to complement the damage tolerant 8090 plate for use in lower wing structures. In terms of strength, toughness and fatigue performance the properties of a typical wing stringer section are, at least, as good as those for the same section in 2024 T3 although the ductility of the 8090 extrusion is usually lower than that of the 2024.

Properties of thin extrusions are summarised in Table 4 while the strength and toughness attainable in thick damage tolerant extrusions are compared with those for 2024 T351 in Figure 3. The corresponding fracture toughness values for the L-T and S-L orientations after 12 hours at 150° C would be > 60 MPa √m and 25 MPa √m respectively.

Tube Apart from some limited space application, there has been little demand for 8090 tube. Nevertheless, manufacturing routes have been established both for thick wall extruded tube and for cold drawn tube with wall thicknesses down to 0.8 mm.

Indicative properties are given in Table 5.

Continuing Development

1993 development targets include:

- **definition of a strip rolling route for 8090 sheet in the thin gauges required for the EH 101 helicopter.**

  Pending development of a more cost effective strip rolling route, a pack rolling technique has been developed at Aluminium Corporation allowing production of sheet down to 0.6 mm. Initially, the physical dimensions were achieved but the recrystallised grain size was too coarse resulting in low properties (Fig 4 (a)) but subsequent modification to the starting condition resulted in refinement of the grain structure (Figure 4 (b)) and the EH 101 specification targets are achieved (Figure 5).

- **development of stronger 8090 sheet to match the specific properties of 7475.**

  The property targets for this activity were defined by our customer and are shown in Table 6 while the composition used in the processing trials (selected from the rich end of the 8090 specification) is shown in Table 7. Both recrystallised and unrecrystallised sheets have been examined in T8 and T62 tempers but, at present, the recrystallised variant appears more promising. Strength levels are shown in Figure 6 and fatigue performance compared with 7475 in Figure 7. Fracture toughness testing is continuing but the indications are that difficulty may be encountered in achieving the target value in the L-T orientation.

- **improvement in the minimum short transverse fracture toughness of 8090 T8771 plate to ≥ 18 MPa √m.**

  Figure 8, showing all Alcan S-L fracture toughness data for 8090 T8771 plate demonstrates that the material is certainly capable of achieving the required combination of strength and toughness but also that about half the plate made falls beneath the required minimum toughness level. The current development programme has examined the influence of homogenisation treatments, rolling conditions, ageing conditions and cast grain size. Of these, cast grain size appears to exert the greatest influence upon S-L fracture toughness. (Table 8).

CONCLUDING SUMMARY

The 8090 alloy has now been developed to the stage where it is commercially available and characterised for use in damage tolerant or medium strength applications in the form of plate, extrusions and sheet. This paper has made no mention of 8090 forgings because Alcan has simply acted in the role of forgestock supplier for this product but various European forgemasters have developed the manufacturing techniques for both hand forgings and cold compressed die forgings.

While evolutionary improvements in the 8090 products should continue, new Al-Li product developments in which Alcan is involved are centred upon a high strength alloy and a high temperature alloy suitable for use in supersonic transport aircraft.

Table 1 (a) : Alcan Aluminium-Lithium Alloy Lital 8090

The alloy has the following composition (in weight percent):

	Min	Max
Lithium	2.2	2.7
Copper	1.0	1.6
Magnesium	0.6	1.3
Zirconium	0.04	0.16
Iron	-	0.3
Silicon	-	0.2
Zinc	-	0.25
Titanium	-	0.1
Manganese	-	0.1
Chromium	-	0.1
Others: Each	-	0.05
TOTAL	-	0.15

The density, typically 2.54 gm/ml, (maximum 2.56 gm/ml) is about 10% less than that of conventional aircraft alloys and stiffness, ≥ 78 GPa, about 10% greater.

Table 1 (b) : 8090 Products : Physical Capabilities

Plate	● Up to 1.25 tonnes plate weight ● Gauge >6 - 100 mm ● Width up to 2.5 m ● Length up to 15 m	
Sheet	● Gauge 1.2 mm - 6.0 mm ● Width 25 mm - 1250 mm ● Length 100 mm - 2500 mm ● Process developments to allow manufacture of gauges down to 0.5 mm and increase in length are well advanced. ● Available in two microstructural variants	
Extrusion	● Heavy	- Must lie within 330 mm circumscribing circle - Maximum heat treated length 17 m
	● Light	- Must lie within 100 mm circumscribing circle - Minimum wall thickness 1.0 mm - Maximum length 12 m
Tube	● Extruded wall thickness down to 3 mm. ● Manufacturing route for drawn tube proved to 0.8 mm wall thickness ● Length up to 6 m.	

Table 2 : **Alcan Lital 8090 Sheet**

1. **Unrecrystallised**

For superplastic forming or cold forming complex parts requiring re-solution treatment (up to three times).

Manufacturing route involves cross rolling to control anisotropy.

Properties (any orientation) after ageing to T6 (32h at 170° C)

Minima:	0.2% PS	310 MPa	UTS 410 MPa	EL 4%
Typical	0.2% PS	325 MPa	UTS 425 MPa	EL 5%

2. **Recrystallised**

Available T3 with excellent cold forming characteristics and capable of ageing to damage tolerant or medium strength tempers. Retains good forming behaviour for, at least, 2 years after solution treatment and stretching (without refrigeration).

Typical properties T3 : 0.2% PS 180 MPa UTS 270 MPa EL 15%

After ageing for 24 h at 150° C for damage tolerance.

Minima:	0.2% PS	280 MPa	UTS 410 MPa	EL9%
Typical:	0.2% PS	300 MPa	UTS 420 MPa	EL 10%

After ageing to medium strength (32h at 170° C):

Typical:	0.2% PS	390 MPa	UTS 480	EL9%

Table 3 (a) : Alcan Lital 8090 Plate : Damage Tolerant Temper (T 8651)

Material is currently supplied against a specification (AECMA pr EN6007) with the following minima for plate in the gauge range 9 to 40 mm.

	6 < a < 25 mm			25 < a < 40 mm			
	L	LT	45°	L	LT	ST	45°
0.2% PS (MPa)	350	330	280	350	320	265	280
UTS (MPa)	440	440	430	420	420	370	430
EL %	5.0	5.0	8.0	5.0	5.0	2.5	8.0

	Kc	Kq	
Fracture Toughness	L-T	L-T	T-L
(MPa √m)	110	35	30

Typical tensile properties achieved are:

	L			LT			45°		
	0.2% PS (MPa)	UTS (MPa)	EL (%)	0.2% PS (MPa)	UTS (MPa)	EL (%)	0.2% PS (MPa)	UTS (MPa)	EL (%)
9 mm	397	470	3.8	343	466	7.9	306	435	11.3
12 mm	423	490	2.8	373	488	8.0	316	442	8.9
25-30 mm	420	474	6.4	373	470	9.1	303	430	9.7

Fracture toughness values comfortably exceed the minimum requirements and for 12 mm plate Kq values in both the directions exceed 60 MPa √m.

Table 3 (b) : Alcan Lital 8090 Plate : Medium Strength (T 8771)

The specification tensile properties to which plate has been made are shown below.

	L			T			S		
	0.2% PS (MPa)	UTS (MPa)	EL (%)	0.2% PS (MPa)	UTS (MPa)	EL (%)	0.2% PS (MPa)	UTS (MPa)	EL (%)
25-50 mm	366	452	4	366	445	4	338	421	1.5
50-150 mm	345	435	3	345	435	3	331	414	1.5

Typical properties of this temper are:

	L			T			S		
	0.2% PS (MPa)	UTS (MPa)	EL (%)	0.2% PS (MPa)	UTS (MPa)	EL (%)	0.2% PS (MPa)	UTS (MPa)	EL (%)
45 mm	438	493	6.8	382	475	7.8	370	470	2.8
90 mm	430	490	5.5	385	470	6.0	355	450	2.5

Fracture Toughness (MPa √m)	L-T	T-L	S-L
45 mm	31	27	15.0
90 mm	34	25	17.0

Table 4 : **Properties of medium strength, thin 8090 extrusions**

These are supplied to meet the following specification properties (AECMA pr EN 6014).

Gauge (mm)	0.2% PS (MPa)	UTS (MPa)	EL (%)
1.2 ≤2.0	400	450	4
>2.0 ≤20.0	420	480	4

The use of high ageing temperatures ensures that the necessary combination of strength and ductility can be obtained.

Typical properties of a 1.6 mm section aged at 210° C are 415 MPa PS 475 MPa UTS and 6.0% Elongation

Table 5 : **8090 Tube : Indicative Properties**

	Wall Thickness (mm)	0.2% PS (MPa)	UTS (MPa)	EL (%)
Customer Specification (T8)	1.27 - 12.7	393	462	3.0
Typical (T3)	{63.5 mm OD x 3.2 mm wall}	290	315	9.0
(T8)		463	528	6.5

Table 6: **Target Property Combination for High Strength 8090 Sheet**

Tensile Strength	450 MPa
Proof Stress	320 MPa
Elongation	3%
Kc_{ao} (160 mm wide panels)	65 MPa√m
Density	<2.6 g/ml

Table 7: **Composition of Ingot Used to Manufacture High Strength Variant of 8090 Sheet**

Li	Cu	Mg	Zr	Fe	Si
2.36	1.30	0.83	0.13	0.07	0.06

Table 8: **Variation in Short Transverse Properties of 8090 T8771 Plate with Ingot Structure and Ageing Treatment**

T8771 Plate						
	96 h/150° C		64 h/60° C		32 h/170° C	
	0.2% PS (MPa)	S-L F/T (MPa√m)	0.2% PS (MPa)	S-L F/T (MPa√m)	0.2% PS (MPa)	S-L F/T (MPa√m)
Coarse grain -High Fe	351	17.2	357	16.5	377	19.2
Coarse grain - Normal Fe (Low ZR)	322	17.6	338	16.9	339	18.6
Fine grain - High Fe	350	11.2	366	12.2	367	12.1
Fine grain - Normal Fe	348	15.5	364	13.5	365	14.0

Figure 1: **Fracture Toughness of Lital 8090 Sheet with Different Microstructures**

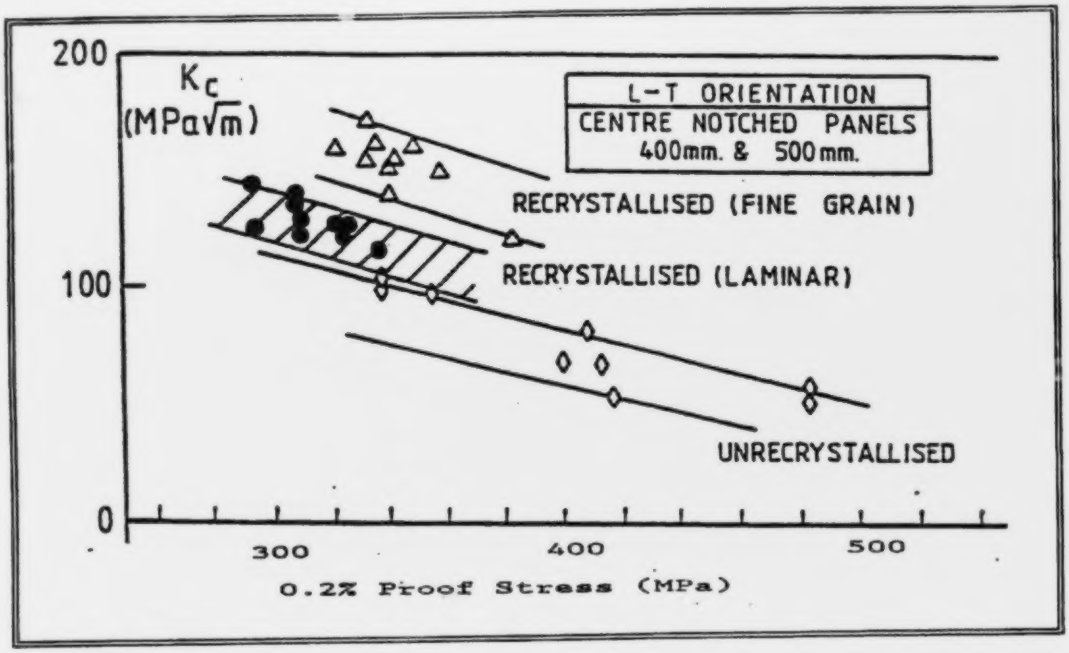

Figure 2: **Titan IV Payload Adaptor : Fabricated from 8090 T8771 Plate. Use of Al-Li Saved ~ 400 lbs per structure.**

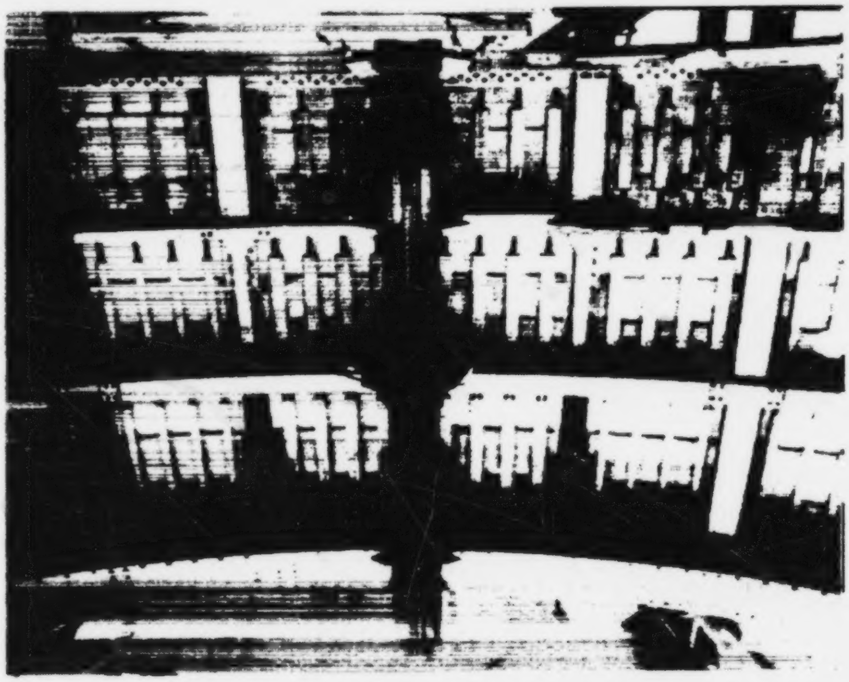

Figure 3 : **Longitudinal Tensile properties and Fracture Toughness of a Large Airbus Extrusion Aged for Various Times at 150° C compared to 2024 T351.**

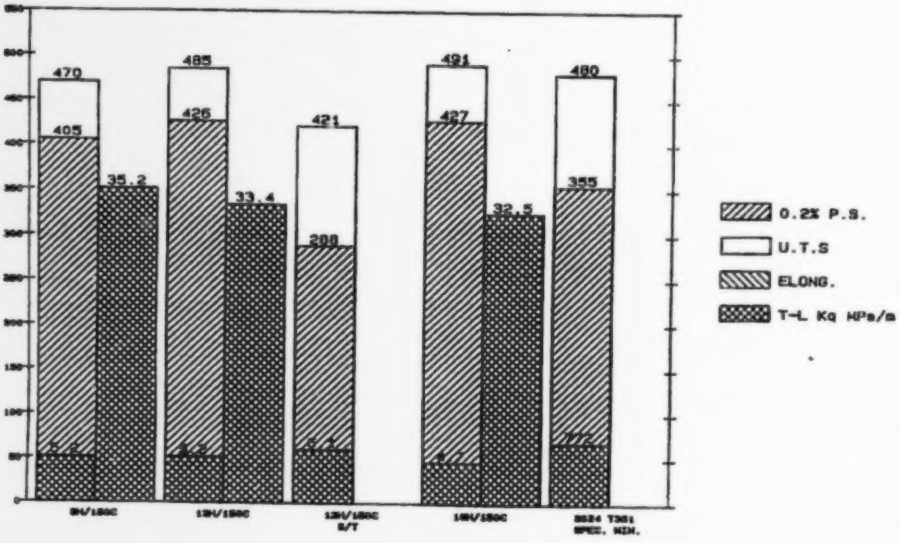

Figure 4. Grain Structures of Pack Rolled 0.7 mm 8090 Sheet

Magnification 100X

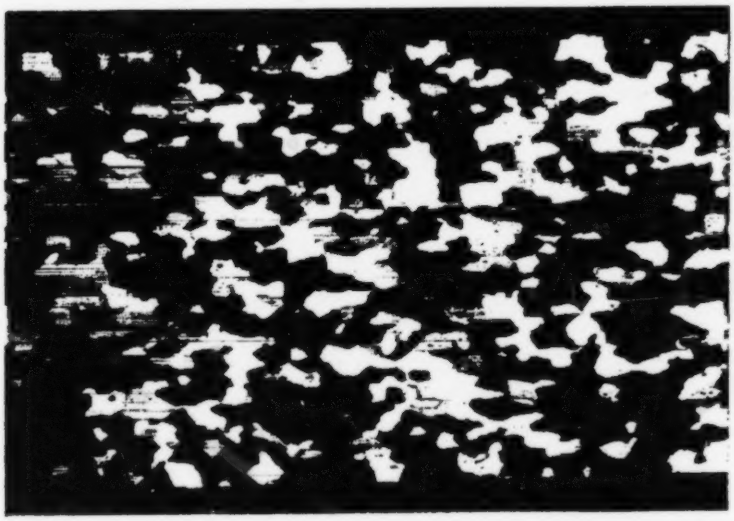

a. Initial Rolling Trial - Microstructure Too Coarse

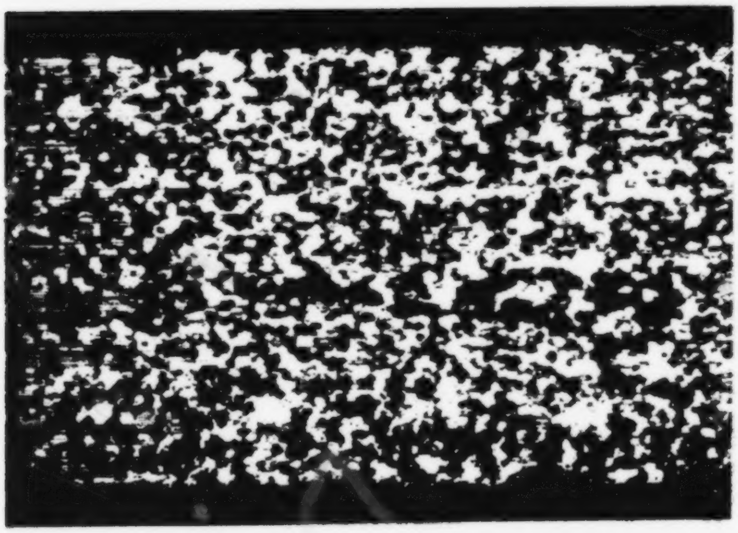

b. Optimised Starting Material Resulting in Refined Microstructure

Figure 5: Tensile Properties of 8090 T8 - 45 Hrs at 175° C Manufactured at ACL Dolgarrog

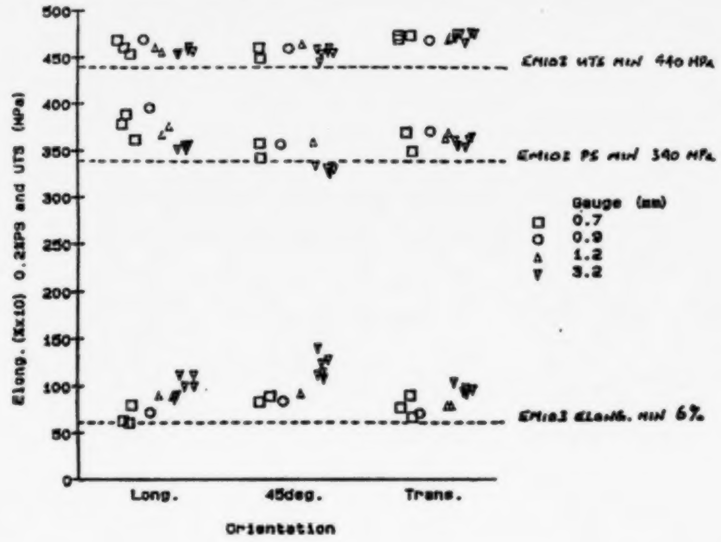

Figure 6: Tensile Properties of 1.6 mm Sheet Aged 72 Hours at 160° C.

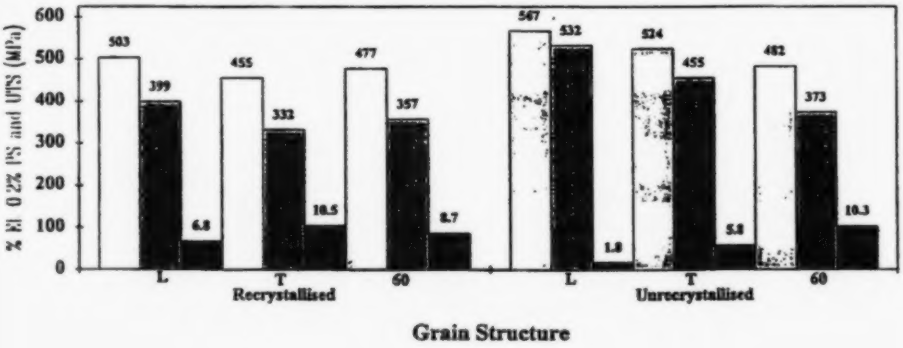

Figure 7: **Fatigue Crack Growth Data**
3.2 mm 8090 CCT, R = 0.1

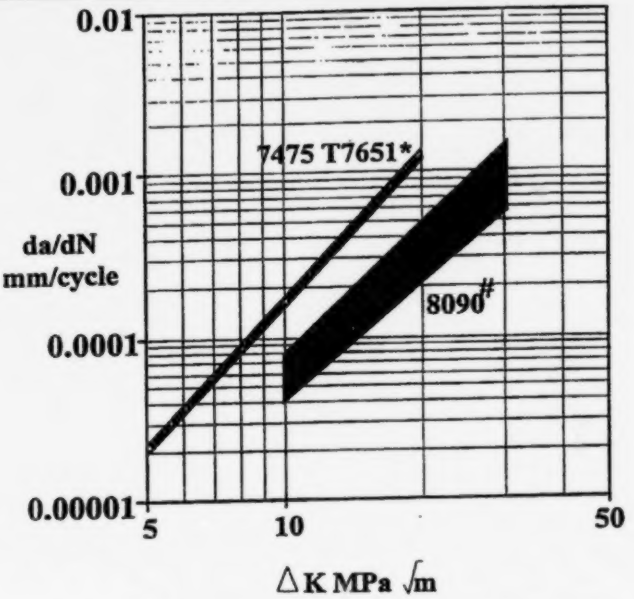

* Data from Damage Tolerant Handbook
# Range of experimental values

Figure 8: **Distribution of S-L Fracture Toughness in 8090 T8771 Plate**

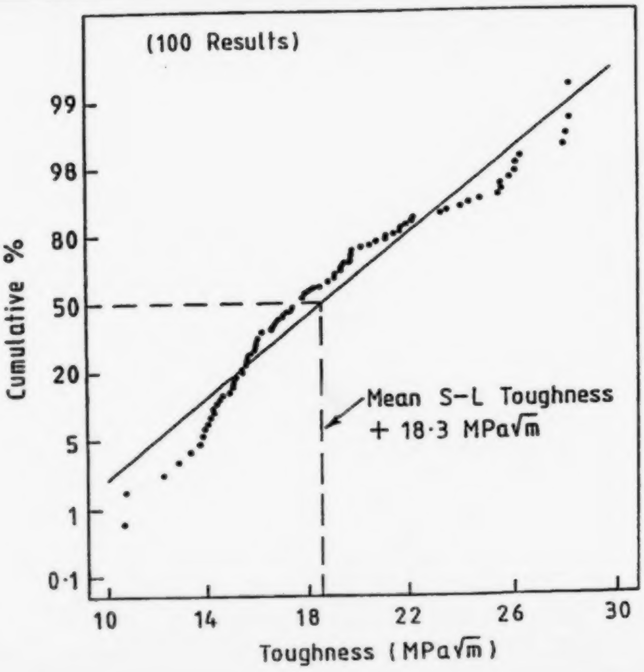

141635

3.

"An Overview of the Use of Aluminium-Lithium Alloys on the EH101"

A.F. Smith

Westland Helicopters
Ltd., Yeovil, UK

WORKSHOP - "REVIEW OF RESEARCH AND DEVELOPMENT ON ALUMINIUM-LITHIUM ALLOYS"

DEFENCE RESEARCH ESTABLISHMENT PACIFIC (DREP), VICTORIA, BC, CANADA

6th and 7th April 1993

An Overview of the Use of Aluminium-Lithium Alloys on the EH101

by

A. F. Smith
Westland Helicopters Ltd
Yeovil, Somerset, England
BA20 2YB

ABSTRACT

Significant contributions to an extensive structural weight saving programme on the EH101 helicopter are being provided by the use of the recently commercialised aluminium-lithium alloys registered as 8090, 2091, 2090 and 5091. Following in-depth studies during the past 10 years, the overall final choice of alloys and product forms has now been made for production aircraft build which has now commenced. This paper provides an overview of the use of these alloys specifically on the EH101 and concentrates upon topics such as the choice of particular aluminium-lithium alloy/product form as substitutes for originally used 'conventional' aluminium alloys in the prototype aircraft, Westland-Agusta aluminium lithium specifications, specific details of sheet, extrusion and die forging use on the aircraft and concludes with some detailed discussion of the overall positive and negative aspects associated with the use of these new alloys. Relatively little attention is paid in this paper to the properties, characteristics and metallurgy of these alloys as these have been covered in previous publications and elsewhere in this workshop.

1. INTRODUCTION

In the preceding paper Capt. D Lamanque explained that the EH101 is a large (14t class), three engined helicopter available in military/utility/SAR and civil variants whose development, construction and marketing is carried out by Westland Helicopters Ltd (England) and Agusta S.p.A. (Italy) via their jointly controlled company, EH Industries Ltd, which was formed specifically for this purpose. As with all modern aircraft, both rotary and fixed wing, significant effort is devoted to minimising structural weight and it is in the respect that aluminium-lithium based alloys, together with other advanced aerospace materials, have an important role to play on the EH101. Whilst this is primarily through exploitation of the approximately 10% density reduction compared to established, non-lithium containing aluminium alloys (shown schematically in VIEWGRAPH No. 1), the concomitant 10% increase in Youngs Modulus and superiority of other properties, to be discussed later in this paper, are also advantageous.

Following extensive studies into the properties and characteristics of a number of previously developmental aluminium-lithium based alloys during the past 10 years, the commercialisation of 4 of these (shown in VIEWGRAPH No. 2) has lead to definition of various alloy/tempers/product forms for specific applications on the aircraft (listed in VIEWGRAPH No. 3) now that EH101 productionisation has commenced. It will be noted that whilst sheet, extrusions and die forgings are now specified, corresponding plate is excluded due to the combination of high material cost and the relatively low utilisation rate of plate (typically only 5 - 10% of the starting material) resulting in a prohibitively low fly:buy ratio. Consequently, much of the originally specified 'conventional' aluminium alloy plate will be replaced by aluminium-lithium forgings which have a significantly higher fly:buy ratio.

This paper provides an overview of the use of aluminium-lithium alloys on the EH101 and concentrates upon those issues of direct relevance to the manufacture of components in these alloys and the associated practical implications in their use, rather than discussion of properties and metallurgical characteristics of the metal itself which have been published previously and which are also addressed by other papers in this Workshop.

2. ALUMINIUM-LITHIUM SPECIFICATIONS

Although 2 aluminium-lithium specifications have been published to date, (AMS 4251 for unclad 2090-T83 sheet and AMS 4332 for 5091 forgings) and a number of prEN drafts prepared under the auspices of, and for eventual issue by AECMA (Association Europeenne Des Constructeurs De Materiel Aerospatial), all aluminium-lithium alloys/product forms for the EH101 will be ordered and manufactured in the foreseeable future against joint Westland-Agusta EM XXX 'in-house' specifications: VIEWGRAPH No. 4 shows the full list of these. It should be noted that many of these specifications represent the final product form and temper and as such, the relevant specification number appears on the drawing for a given part. However, there are 5 'procurement' specifications which represent only the material as it is ordered from the metal manufacturer but which undergoes further treatment to produce the final part, and as such, the 5 procurement specification numbers should not appear on any drawing of the finished part. This is discussed further in the next section.

3. TRANSFORMATION ROUTES FROM PROCUREMENT TO FINAL USE SPECIFICATIONS

The routes for transformation of material covered by the above procurement specifications to the final use specifications are discussed below:

(a) EM 221 to EM 121 (VIEWGRAPH No. 5)

It was deemed prudent that a specific procurement specification was prepared for 5091 extruded bar for forging in view of the fact that this material is non-heat treatable and as such, any deficiencies in ability of the starting stock to achieve properties in the final forging cannot be overcome by subsequent heat treatment. By requiring properties to be measured from the starting stock, it is hoped that any inferior ingot could be identified and thus prevented from being fabricated into forgings, which would eventually be rejectable due to unsatisfactory property levels.

(b) EM 141 to EM 140 (VIEWGRAPH No. 6)

EM 141 is 8090 sheet but specifically processed by the sheet manufacturer (Alcan Aluminium) to exhibit enhanced superplastic characteristics. This sheet will be subsequently superplastically formed to produce the final component, which, after the appropriate ageing treatment, would exhibit property levels satisfying the final use condition, EM 140. It should be noted that 8090 is advantageous compared to its 'conventional' SUPRAL 150 counterpart in that the relatively low quench sensitivity of the former allows precipitation strengthening to occur by directly artificially ageing the component after forming. This would be largely ineffective in SUPRAL 150 unless an intermediate solution treatment were employed which in many cases would be impractical due to loss or severe distortion of the superplastically formed shape. The result is that higher strength levels can be achieved in superplastically formed 8090.

(c) EM 201 to EM 101, EM 103, EM 106 (VIEWGRAPH No. 7)
EM 202 to EM 102, EM 104, EM 107 (VIEWGRAPH No. 8)

Alloys 8090 and 2091, both nominally in the recrystallised condition, are specified since their final properties may be regarded as equivalent, therefore addressing the issue of dual sourcing, since there is currently only one supply source for each of these alloys in sheet form. Each alloy is procured in the T3 temper and subsequently used to produce a number of final conditions, thus providing commercial benefits in buying a common starting alloy and temper. Particularly in the case of 8090-T3 (EM 201), the lack of any appreciable natural age hardening effects, together with inherently good formability, enables the great majority of sheet components to be formed from this temper (both press and stretch forming) and with no need to solution treat just prior to forming, as is the case with 2024 and 2014. Indeed, bend tests using sheet in the 0.6 mm to 2.3 mm thickness range have consistently indicated comparable or superior formability of 8090-T3 relative to freshly solution treated 2024 (i.e. W condition). Furthermore, trial components have been satisfactorily made from 2.3 mm gauge 8090-T3 sheet while the same article could not be made without cracking in freshly solution treated 2024 sheet. Selection of the appropriate artificial ageing parameters subsequently leads to either the "damage tolerant" or "medium strength" final use conditions. On the rare occasions where even greater 8090/2091 sheet formability is required, re-solution treatment would be necessary and although the "damage tolerant" category can be achieved by artificially ageing to produce the δ'-Al_3Li phase, the removal of the cold-work-induced dislocation networks (inherent in producing the T3 temper) prevents attaining "medium strength" levels which are dependent upon co-precipitation of the dislocation-nucleated S-Al_2CuMg phase.

As well as providing 2014 and 2024 lightweight replacements, 8090 and 2091 will also be used as lightweight substitutes for the relatively small number of parts made from "low strength" 6082 alloy (≡ BS L113) sheet since the aluminium-lithium alloys are similarly amenable to TIG welding.

(d) EM 203 to EM 204 (VIEWGRAPH No. 9)

As with 8090 and 2091 in the "medium strength" conditions, the "high strength" of 2090 requires the presence of the cold work-induced dislocation networks as nucleation sites for the prerequisite strengthening phase (T_1-Al_2CuLi in the case of 2090) to co-precipitate with δ'-Al_3Li during artificial ageing. Accordingly, all forming of 2090 will be carried out directly from the T3 temper (EM 203) to give components satisfying the final use condition of EM 204.

4. APPROVED SUPPLIERS OF ALUMINIUM-LITHIUM FOR EH101

Due to the very limited number of manufacturers of aluminium-lithium ingot, the choice of supplier of starting stock for further fabrication is pre-determined. (Although Reynolds Aluminium of Richmond, Va, USA also manufacture aluminium-lithium, this is currently limited to the ultra-high strength 2095/2195 Al-Cu-Li-Mg-Zr-Ag alloy which is not used on the EH101). The same situation pertains with regard to sheet as this is currently made only by Alcan and Alcoa (in alloys 8090 and 2091 respectively) from their own ingot. However, these 2 companies, together with Inco (with alloy 5091) also sell ingot to other fabricators for conversion to forgings and extrusions, as appropriate. The full list of aluminium-lithium ingot, sheet, extrusion and forging suppliers for the EH101 is shown in VIEWGRAPH No .10. Because the EH101 will represent one of the first extensive applications of alloys 8090, 2091, 2090 and 5091, very strict control will be kept on all aspects of supply of this material in the following ways:

i) All suppliers of aluminium-lithium (ingot and subsequent fabricated forms) will be subject to separate approval status for these alloys, irrespective of whether they already hold this for 'conventional' aluminium alloys.

ii) Technical and quality audits will be carried out annually until such time that sufficient knowledge/confidence exists to reduce this to bi-annual visits.

iii) Sampling of all product forms from each manufacturer will be required on a more frequent basis than with current 'conventional' aluminium alloys.

iv) Sub-Contract companies involved with construction of the EH101 airframe will be allowed to procure material only from the WHL-approved sources shown in VIEWGRAPH No. 10.

5. AREAS OF APPLICATION OF ALUMINIUM-LITHIUM ON THE EH101 - SHEET AND EXTRUSIONS

VIEWGRAPH No. 11 shows the general areas of application of aluminium-lithium alloys on the EH101. VIEWGRAPH No. 12 lists in more detail the use of sheet and extrusions.

6. THE USE OF ALUMINIUM-LITHIUM FORGINGS ON THE EH101

The choice of alloy for fabrication into forgings has been determined primarily by the size/configuration of the component. As mentioned earlier, alloys 8090, 2091 and 2090 require post-solution treatment cold working in order to achieve 'medium'/'high' strength static property levels. This can be achieved in the case of forgings by use of cold compression, but is only effective if the section is of shape and thickness to enable sufficient metal to be sheared, in order to introduce into the metal the pre-requisite dislocation networks upon which the S-Al_2CuMg (8090 and 2091) or T1-Al_2CuLi (2090) strengthening phases can nucleate. The size and shape of die forgings for the cabin frame enables effective cold compression to be achieved, and consequently, alloy 8090 is specified for these applications. However, in the cases of smaller, 'bulkier' components, the metal in the interior of the forgings would be constrained by the adjacent material, thus limiting the effectiveness of cold compression and therefore preventing the required property levels to be achieved upon artificial ageing. It is for these applications that 5091 is specified, this alloy being made by the mechanical alloying process and is strengthened by oxide and carbide dispersoids during metal manufacture, therefore requiring no heat treatment and thus eliminating the need for cold compression. Furthermore, since quenching stresses are absent, this alloy shows extremely good dimensional stability during machining, whilst the very fine, uniform microstructure and lack of copper or zinc in the composition impart an exceptionally high resistance to corrosion to the alloy. VIEWGRAPH No. 13 summarises the areas of the aircraft to be constructed from forgings in alloys 8090 and 5091 and VIEWGRAPH No. 14 shows schematically the main cabin frame which will be made from components machined from 8090 cold compressed die forgings.

7. SUMMARY OF POSITIVE AND NEGATIVE ASPECTS OF THE USE OF ALUMINIUM-LITHIUM ALLOYS ON THE EH101

The positive aspects are shown in VIEWGRAPH No. 15, which refers to superior corrosion properties of 8090 (VIEWGRAPH No. 16) and slower fatigue crack growth rate (VIEWGRAPH No. 17). VIEWGRAPH No. 18 shows the electrical conductivity of aluminium-lithium alloys to be approximately half that of 'conventional' aluminium alloys, thus providing a ready means of identifying them. Work at WHL has indicated that these characteristics have little effect on the overall electrical characteristics of the aircraft. The perceived 'negative' aspects of these alloys are listed in VIEWGRAPH NO. 19 although proponents of these alloys would perhaps feel that 'negative' is too strong a word for most of these features and could perhaps be better described as 'less-positive'.

8. CONCLUSIONS

The main conclusions to be drawn from this presentation are shown in VIEWGRAPH No .20.

DENSITIES OF 'CONVENTIONAL' ALUMINIUM AND ALUMINIUM-LITHIUM ALLOYS

E8167-02

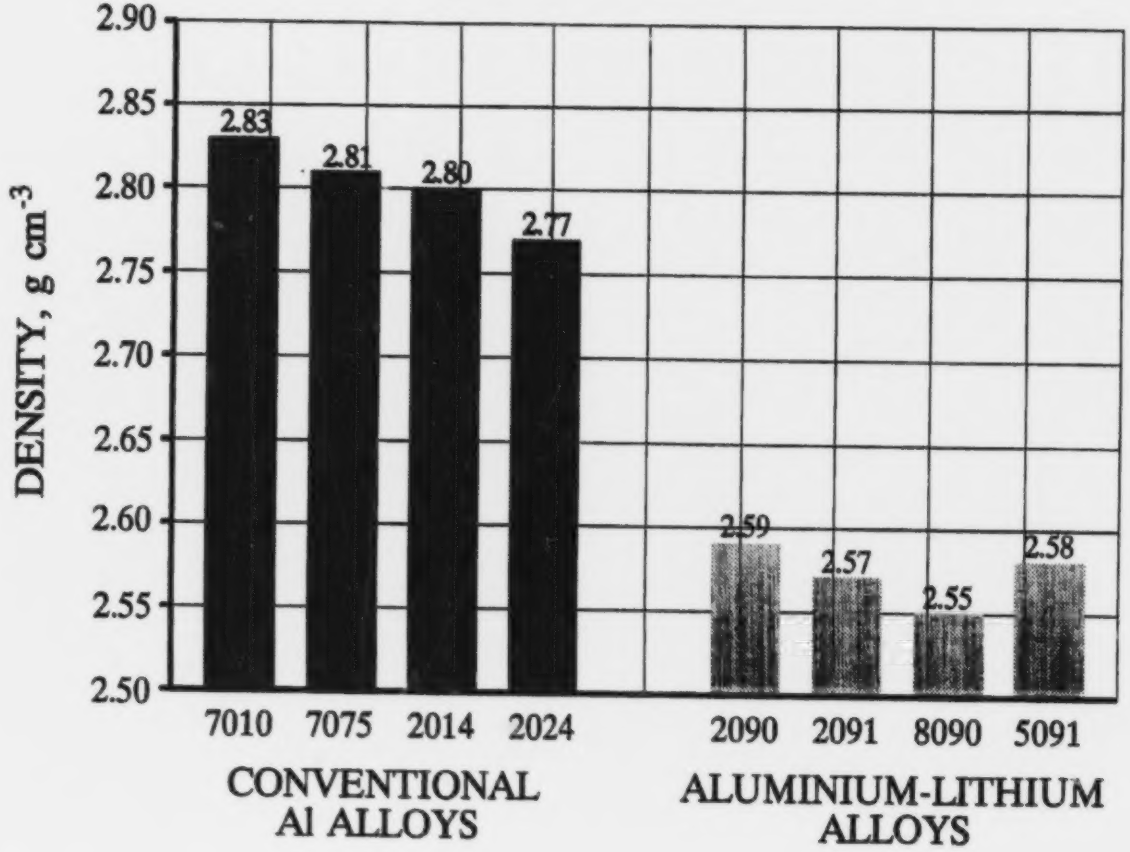

VIEWGRAPH No. 1

COMMERCIALLY AVAILABLE ALUMINIUM-LITHIUM ALLOYS USED ON EH101

E8187-03

Alloy	Chemical Composition Range (wt%)					Ingot Manufacturer
	Li	Cu	Mg	Zr	Al	
8090	2.2 to 2.7	1.0 to 1.6	0.6 to 1.3	0.04 to 0.16	Base	ALCAN (UK) ALCOA (USA)
2091	1.7 to 2.3	1.8 to 2.5	1.1 to 1.9	0.04 to 0.16	Base	ALCOA (USA)
2090	1.9 to 2.6	2.4 to 3.0	--	0.08 to 0.15	Base	ALCOA (USA)
5091*	1.2 to 1.4	--	3.8 to 4.2	--	Base	INCO (USA)

* Produced by mechanical alloying. Composition also contains 0.2 - 0.7% O as oxides and 1.1 - 1.3% C as carbides

VIEWGRAPH No. 2

ALUMINIUM-LITHIUM ALLOYS/PRODUCT FORMS ON THE EH101 - SHEET

E8157-04

Product Details	Aluminium-Lithium Alloy	Substitute for :-
Sheet ('Low strength')	8090-T81 or 2091-T84 (8090-T621* or 2091-T621*)	6082-T6 (BS L113) and 6061-T6 (QQA 250/11)
Sheet ('Damage tolerant')	8090-T81 or 2091-T84	Unclad 2024-T3 (QQA 250/4) Clad 2024-T3 (BS L109 & QQA 250/5) Unclad 2024-T42 (QQA 250/4) Clad 2024-T42 (BS L110 & QQA 250/5)
	8090-T621* or 2091-T621*	Unclad 2024-T42 (QQA 250/4) and Clad 2024-T42 (BS L110 & QQA 250/5)
Sheet ('Medium strength')	8090-T8 or 2091-T8	Clad 2014A-T6 (BS L165)
Sheet ('Superplastic')	8090-T5 (Superplastic grade)	'Supral' 150 and 2024/2014 fabrications
Sheet ('High strength')	2090-T83	Clad 7475-T76 (AMS 4100)

*** Re-solution treated for greater formability**

VIEWGRAPH No. 3

COMMERCIALLY AVAILABLE ALUMINIUM-LITHIUM ALLOYS USED ON EH101

E8157-03

Alloy	Chemical Composition Range (wt%)					Ingot Manufacturer
	Li	Cu	Mg	Zr	Al	
8090	2.2 to 2.7	1.0 to 1.6	0.6 to 1.3	0.04 to 0.16	Base	ALCAN (UK) ALCOA (USA)
2091	1.7 to 2.3	1.8 to 2.5	1.1 to 1.9	0.04 to 0.16	Base	ALCOA (USA)
2090	1.9 to 2.6	2.4 to 3.0	--	0.08 to 0.15	Base	ALCOA (USA)
5091*	1.2 to 1.4	--	3.8 to 4.2	--	Base	INCO (USA)

* Produced by mechanical alloying. Composition also contains 0.2 - 0.7% O as oxides and 1.1 - 1.3% C as carbides

VIEWGRAPH No. 2

ALUMINIUM-LITHIUM ALLOYS/PRODUCT FORMS ON THE EH101 - SHEET

E8167-04

Product Details	Aluminium-Lithium Alloy	Substitute for :-
Sheet ('Low strength')	8090-T81 or 2091-T84 (8090-T621* or 2091-T621*)	6082-T6 (BS L113) and 6061-T6 (QQA 250/11)
Sheet ('Damage tolerant')	8090-T81 or 2091-T84	Unclad 2024-T3 (QQA 250/4) Clad 2024-T3 (BS L109 & QQA 250/5) Unclad 2024-T42 (QQA 250/4) Clad 2024-T42 (BS L110 & QQA 250/5)
	8090-T621* or 2091-T621*	Unclad 2024-T42 (QQA 250/4) and Clad 2024-T42 (BS L110 & QQA 250/5)
Sheet ('Medium strength')	8090-T8 or 2091-T8	Clad 2014A-T6 (BS L165)
Sheet ('Superplastic')	8090-T5 (Superplastic grade)	'Supral' 150 and 2024/2014 fabrications
Sheet ('High strength')	2090-T83	Clad 7475-T76 (AMS 4100)

* Re-solution treated for greater formability

VIEWGRAPH No. 3

ALUMINIUM-LITHIUM ALLOYS/PRODUCT FORMS ON THE EH101 - EXTRUSIONS & FORGINGS

E8157-05

Product Details	Aluminium-Lithium Alloy	Substitute for :-
Cold Compressed Die Forgings	8090-T852	7010-T7451 plate (DTD 5130A)
Non-cold Compressed Die Forgings	5091-H112	7010-T7451 plate (DTD 5130A) and 7010-T74 forgings (DTD 5636) and 7075-T73 forgings (BS L161 or QQA 367)
Extruded Bar and Sections	8090-T8511	7075-T7351 (BS L160) and 7075-T73510/T73511 (QQA 200/11)

VIEWGRAPH No. 3 (Continued)

ALUMINIUM-LITHIUM ALLOYS/PRODUCT FORMS ON THE EH101 - EXTRUSIONS & FORGINGS

E8157-05

Product Details	Aluminium-Lithium Alloy	Substitute for :-
Cold Compressed Die Forgings	8090-T852	7010-T7451 plate (DTD 5130A)
Non-cold Compressed Die Forgings	5091-H112	7010-T7451 plate (DTD 5130A) and 7010-T74 forgings (DTD 5636) and 7075-T73 forgings (BS L161 or QQA 367)
Extruded Bar and Sections	8090-T8511	7075-T7351 (BS L160) and 7075-T73510/T73511 (QQA 200/11)

VIEWGRAPH No. 3 (Continued)

—WHL/AGUSTA Al-Li SPECIFICATIONS

E8157-09

EM101	8090-T81	'Damage Tolerant' sheet and strip
EM102	2091-T84	'Damage Tolerant' sheet and strip
EM103	8090-T8	'Medium Strength' sheet and strip
EM104	2091-T8	'Medium Strength' sheet and strip
EM105	8090-T8511	'Medium Strength' extruded bar and sections
EM106	8090-T621	'Damage Tolerant' sheet and strip, re-solution treated for enhanced formability
EM107	2091-T621	'Damage Tolerant' sheet and strip, re-solution treated for enhanced formability
EM120	8090-T852	'Medium Strength' cold compressed die forgings
EM121	5091-H112	'Medium/High Strength', non-cold compressed die forgings

VIEWGRAPH No. 4

—WHL/AGUSTA Al-Li SPECIFICATIONS

E8157-9A

EM140	**8090-T5**	**Formings made from superplastic sheet**
EM141	8090-02	Superplastic sheet
EM201	8090-T3	Procurement specification for sheet for forming/heat treatment by the user
EM202	2091-T3	Procurement specification for sheet for forming/heat treatment by the user
EM221	5091-H112	Procurement specification for extruded ingot for subsequent die forging
EM203	2090-T3	Procurement specification for sheet for forming/heat treatment by the user
EM204	**2090-T83**	**'High Strength' sheet and strip**

VIEWGRAPH No. 4 (Continued)

—Al-Li ALLOY 5091 FORGING ROUTE

E8157-13

5091 Extruded Bar
(EM 221)

↓ Die Forging

5091 Die Forging
EM 121
(≡ DTD 5130A
DTD 5636)

VIEWGRAPH No. 5

AI-Li ALLOY 8090 (SPF GRADE) SHEET FORMING ROUTE

E8157-14

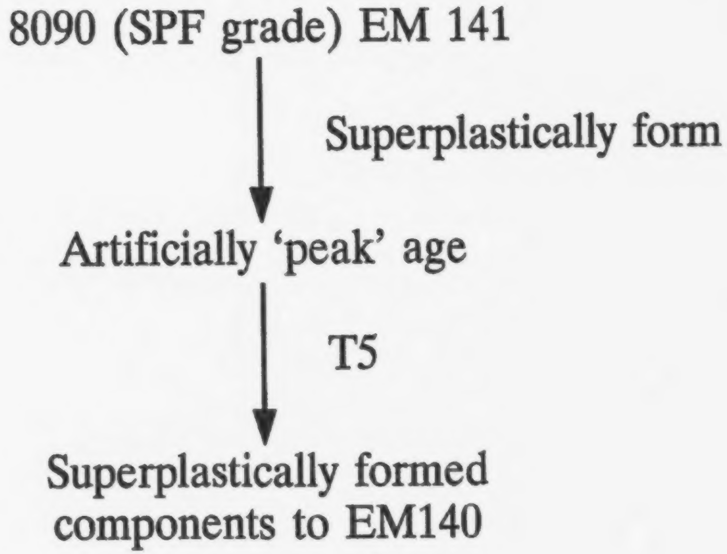

8090 (SPF grade) EM 141

Superplastically form

Artificially ‘peak’ age

T5

Superplastically formed
components to EM140

VIEWGRAPH No. 6

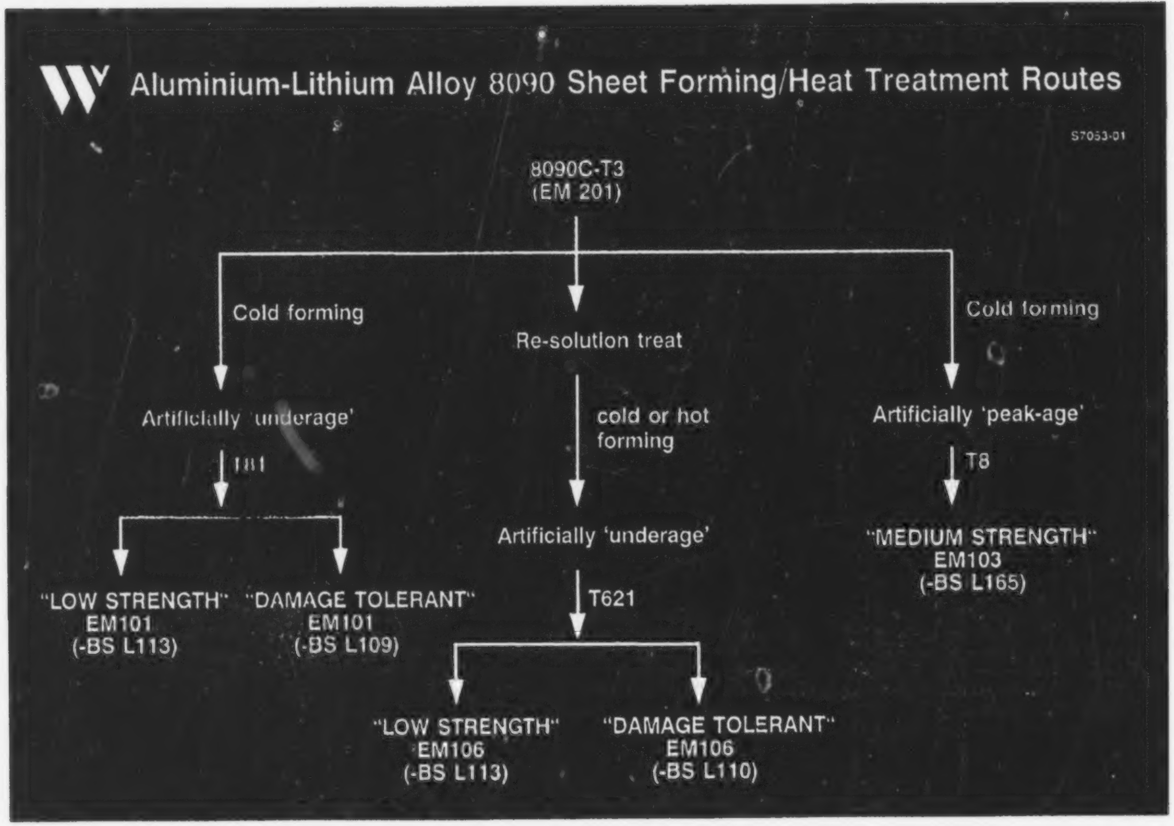

Aluminium-Lithium Alloy 8090 Sheet Forming/Heat Treatment Routes

S7053-01

8090C-T3
(EM 201)

Cold forming

Re-solution treat

Cold forming

Artificially 'underage'

cold or hot
forming

Artificially 'peak-age'

T81

T8

Artificially 'underage'

"MEDIUM STRENGTH"
EM103
(-BS L165)

"LOW STRENGTH"
EM101
(-BS L113)

"DAMAGE TOLERANT"
EM101
(-BS L109)

T621

"LOW STRENGTH"
EM106
(-BS L113)

"DAMAGE TOLERANT"
EM106
(-BS L110)

VIEWGRAPH No. 7

Aluminium-Lithium Alloy 8090 Sheet Forming/Heat Treatment Routes

S7053-01

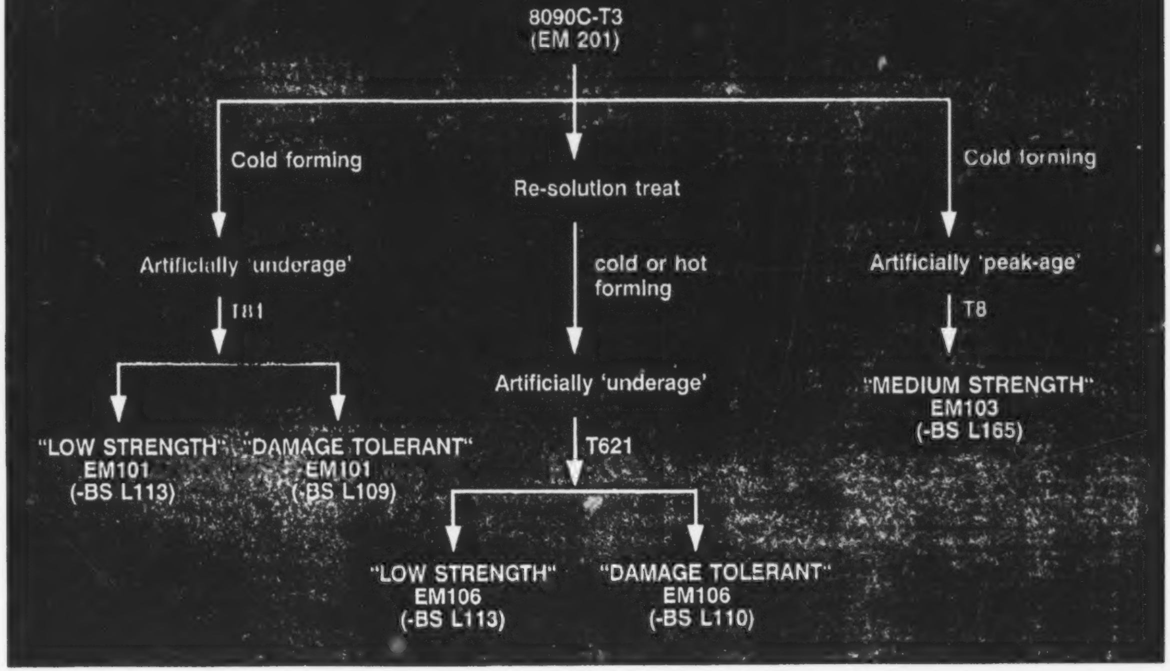

8090C-T3
(EM 201)

Cold forming

Re-solution treat

Cold forming

Artificially 'underage'

T81

cold or hot
forming

Artificially 'peak-age'

T8

Artificially 'underage'

"MEDIUM STRENGTH"
EM103
(-BS L165)

"LOW STRENGTH"
EM101
(-BS L113)

"DAMAGE TOLERANT"
EM101
(-BS L109)

T621

"LOW STRENGTH"
EM106
(-BS L113)

"DAMAGE TOLERANT"
EM106
(-BS L110)

VIEWGRAPH No. 7

Al-Li ALLOY 2091 SHEET FORMING/HEAT TREATMENT ROUTE

E8157-16

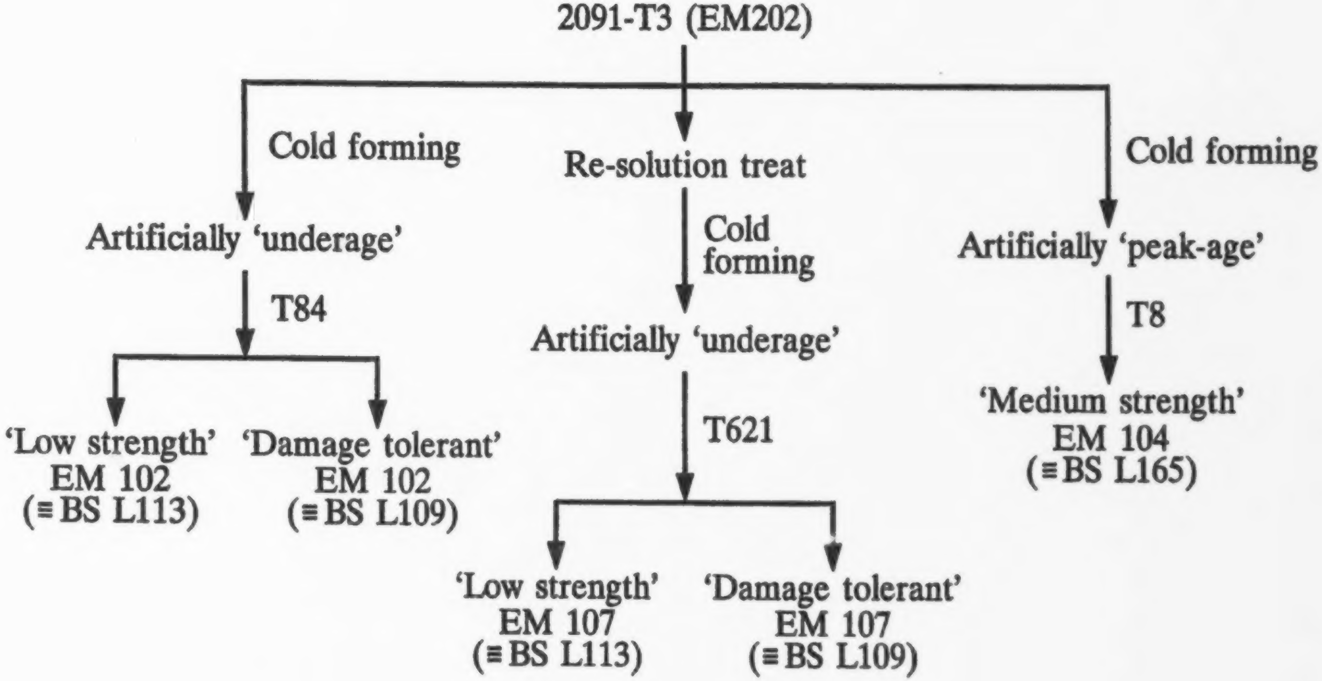

2091-T3 (EM202)

Cold forming

Artificially 'underage'

T84

'Low strength'
EM 102
(≡BS L113)

'Damage tolerant'
EM 102
(≡BS L109)

Re-solution treat

Cold forming

Artificially 'underage'

T621

'Low strength'
EM 107
(≡BS L113)

'Damage tolerant'
EM 107
(≡BS L109)

Cold forming

Artificially 'peak-age'

T8

'Medium strength'
EM 104
(≡BS L165)

VIEWGRAPH No. 8

Al-Li ALLOY 2090 SHEET FORMING/HEAT TREATMENT ROUTE

E8157-15

2090-T3
(EM203)

↓ Cold form

Artificially 'peak age'

↓ T83

'High strength'
EM204 (≡AMS 4100)

VIEWGRAPH No. 9

—APPROVED Al-Li PRODUCT SUPPLIERS FOR EH101—

E8187-06

- **Sheet**
  - 8090 recrystallised sheet - ALCAN, Dolgarrog, N. Wales
  - 2091 recrystallised sheet - ALCOA, Davenport, IA, USA
  - 2090 unrecrystallised sheet - ALCOA, Davenport, IA, USA

- **Extrusions**
  - 8090 unrecrystallised sections
    - Otto Fuchs Metallwerke, Meinerzhagen, Germany
  - 8090 unrecrystallised sections
    - VAW, Hannover, Germany
  - 8090 unrecrystallised sections
    - ALCAN Speciality Extrusions, Workington, Cumbria, UK

- **Die Forgings**
  - 8090 cold compressed forgings
    - Otto Fuchs Metallwerke, Meinerzhagen, Germany
  - 5091 non-cold compressed die forgings
    - Otto Fuchs Metallwerke, Meinerzhagen, Germany
  - 5091 non-cold compressed die forgings
    - Aerospace Forgings Ltd, Oldbury, UK
  - 5091 non-cold compressed die forgings
    - H.D.A. Forgings Ltd, Redditch, UK

VIEWGRAPH No. 10

—APPROVED Al-Li PRODUCT SUPPLIERS FOR EH101—

E8157-8A

Superplastic Formings	Supreform Metals Ltd, Worcester, UK made from SPF grade 8090 from ALCAN, Dolgarrog
Ingot	8090 for extrusions and forgings - ALCAN Plate Ltd, Kitts Green, UK 8090 for extrusions and forgings - ALCOA, Pittsburgh, PA, USA 5091 for forgings - INCO Alloys International, Pittsboro, NC, USA

VIEWGRAPH No. 10 (Continued)

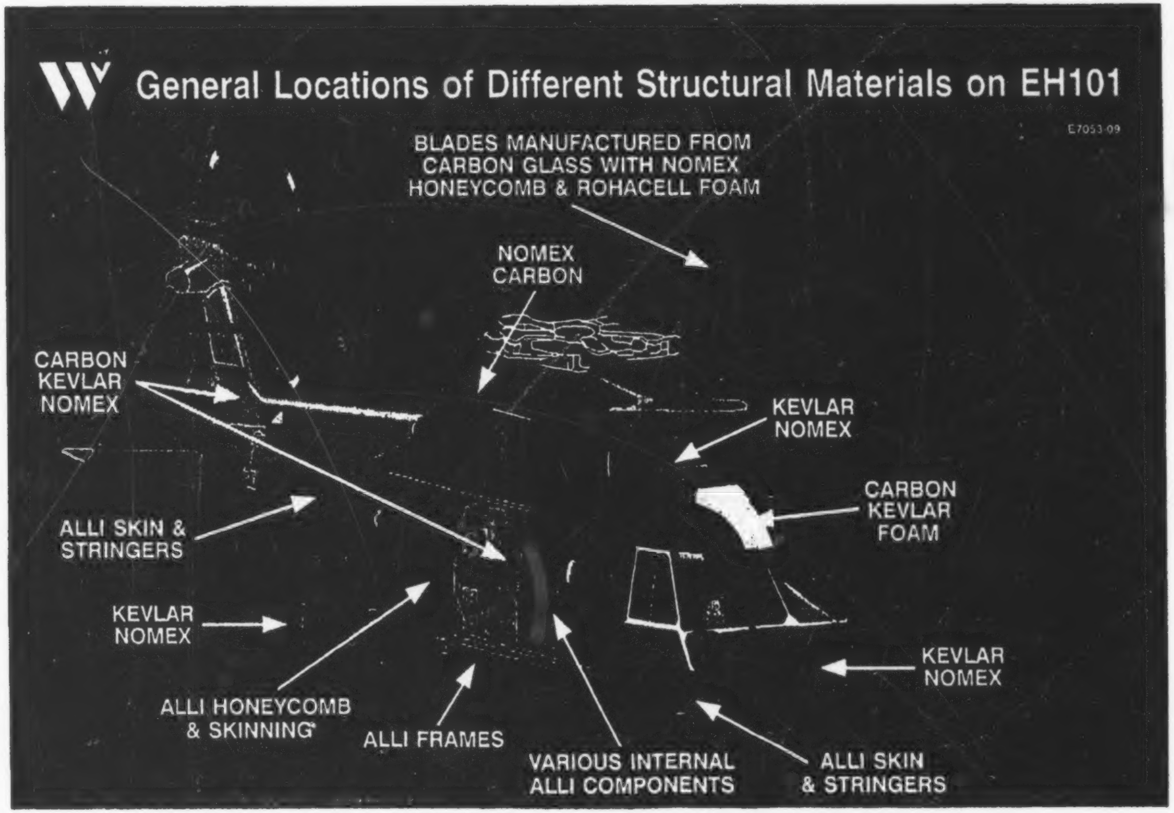

General Locations of Different Structural Materials on EH101

E7053-09

BLADES MANUFACTURED FROM CARBON GLASS WITH NOMEX HONEYCOMB & ROHACELL FOAM
NOMEX CARBON
CARBON KEVLAR NOMEX
KEVLAR NOMEX
CARBON KEVLAR FOAM
ALLI SKIN & STRINGERS
KEVLAR NOMEX
KEVLAR NOMEX
ALLI HONEYCOMB & SKINNING
ALLI FRAMES
VARIOUS INTERNAL ALLI COMPONENTS
ALLI SKIN & STRINGERS

VIEWGRAPH No. 11

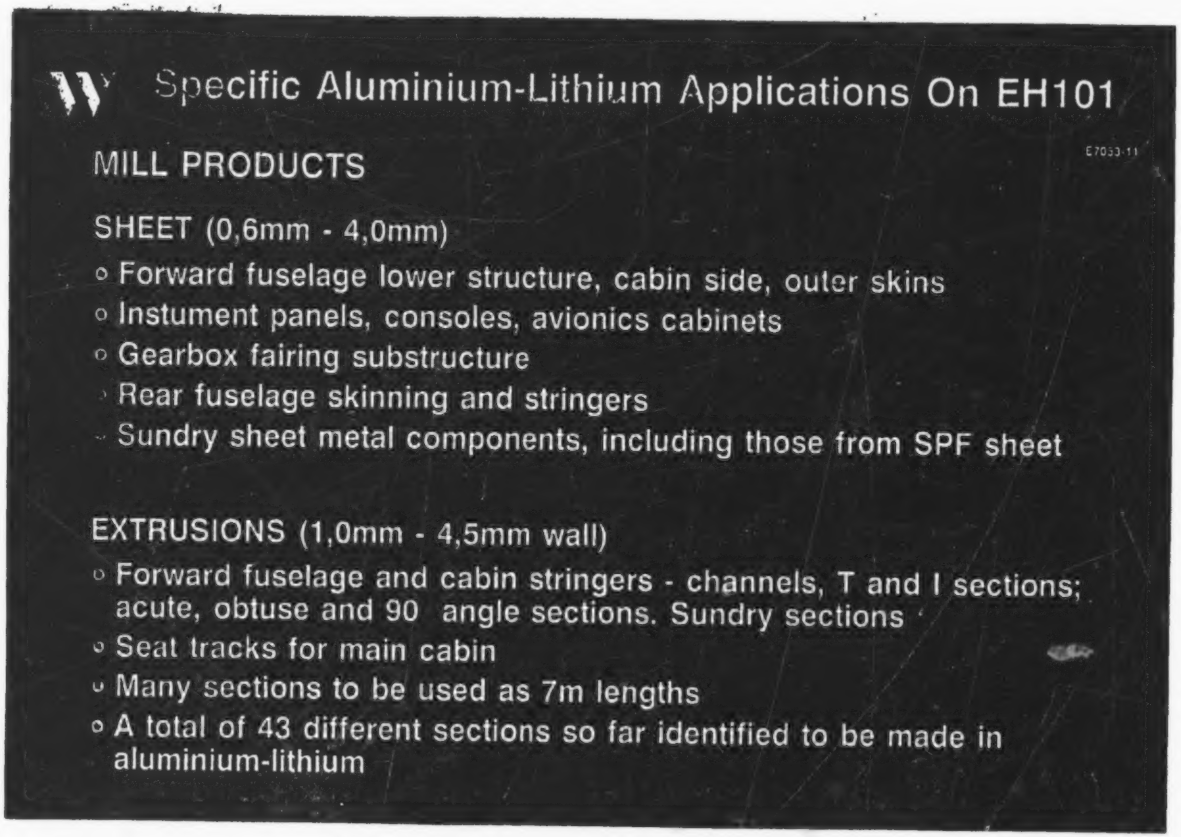

Specific Aluminium-Lithium Applications On EH101

E7053-11

MILL PRODUCTS

SHEET (0,6mm - 4,0mm)

- Forward fuselage lower structure, cabin side, outer skins
- Instument panels, consoles, avionics cabinets
- Gearbox fairing substructure
- Rear fuselage skinning and stringers
- Sundry sheet metal components, including those from SPF sheet

EXTRUSIONS (1,0mm - 4,5mm wall)

- Forward fuselage and cabin stringers - channels, T and I sections; acute, obtuse and 90 angle sections. Sundry sections
- Seat tracks for main cabin
- Many sections to be used as 7m lengths
- A total of 43 different sections so far identified to be made in aluminium-lithium

VIEWGRAPH No. 12

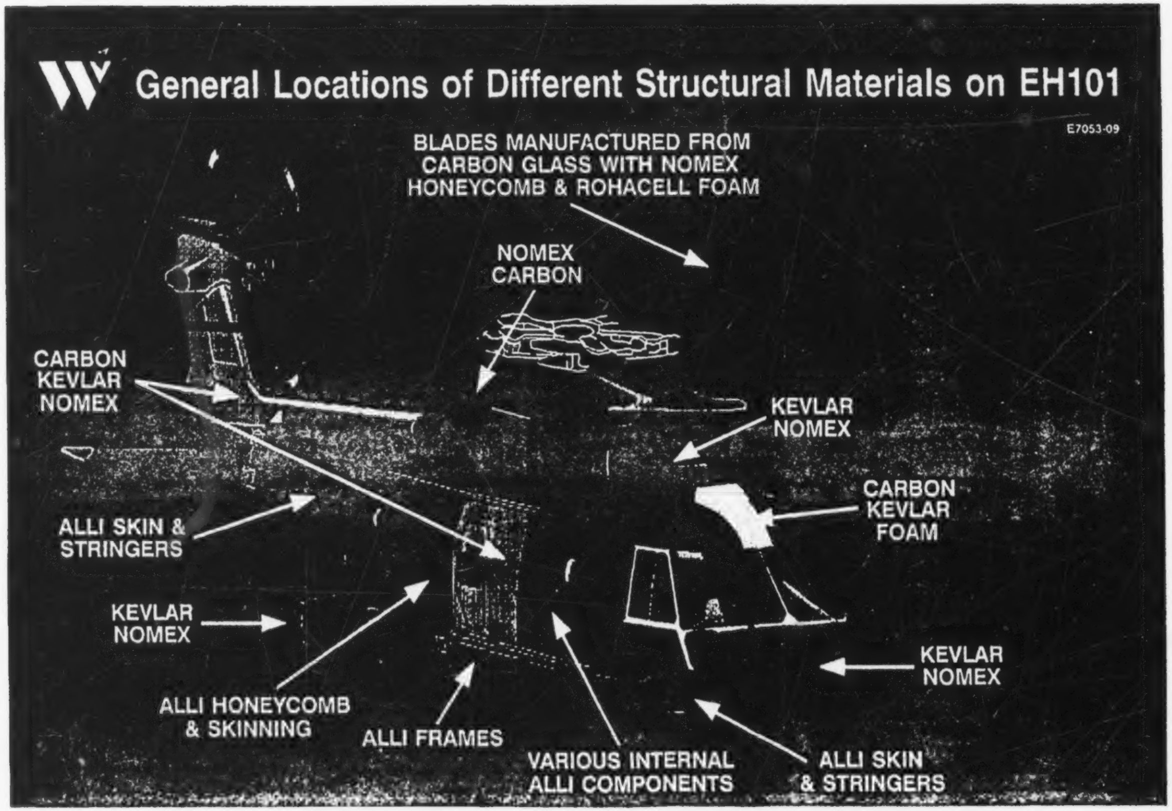

General Locations of Different Structural Materials on EH101

E7053-09

BLADES MANUFACTURED FROM
CARBON GLASS WITH NOMEX
HONEYCOMB & ROHACELL FOAM
NOMEX
CARBON
CARBON
KEVLAR
NOMEX
KEVLAR
NOMEX
CARBON
KEVLAR
FOAM
ALLI SKIN &
STRINGERS
KEVLAR
NOMEX
KEVLAR
NOMEX
ALLI HONEYCOMB
& SKINNING
ALLI FRAMES
VARIOUS INTERNAL
ALLI COMPONENTS
ALLI SKIN
& STRINGERS

VIEWGRAPH No. 11

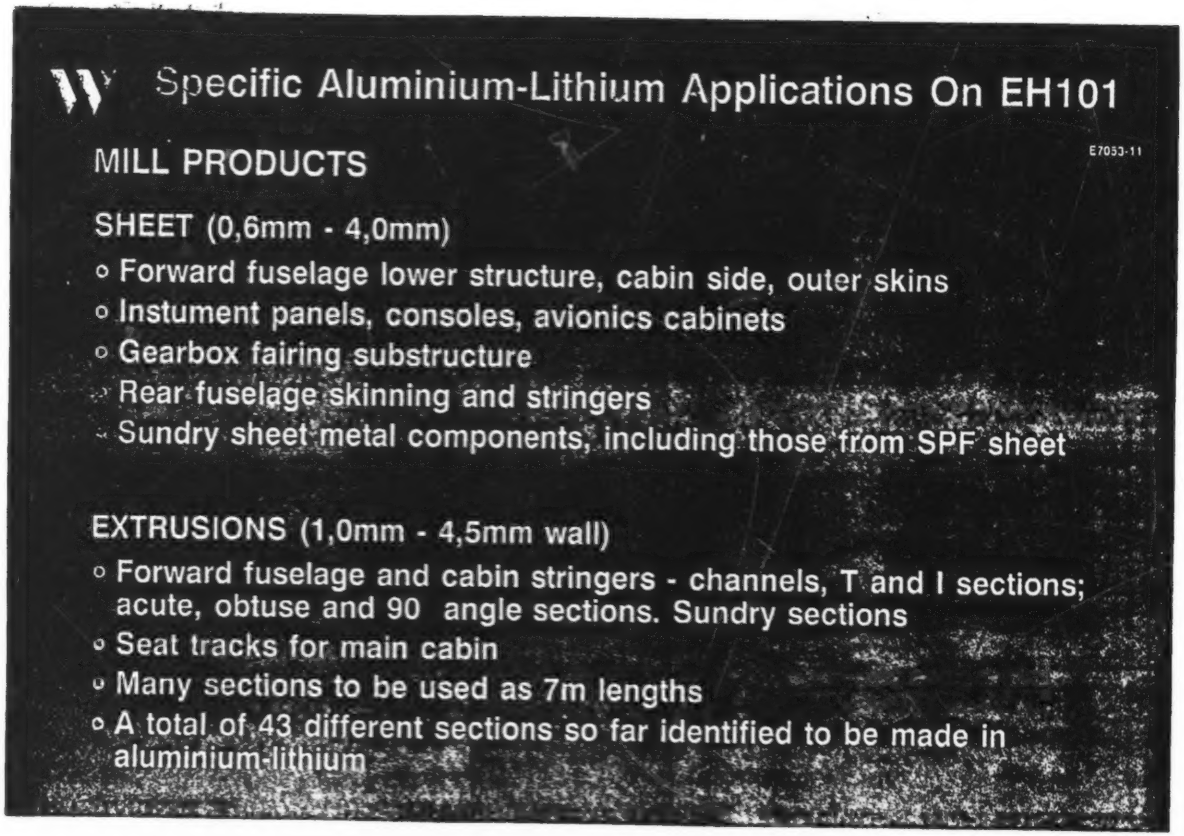

Specific Aluminium-Lithium Applications On EH101

E7053-11

MILL PRODUCTS

SHEET (0,6mm - 4,0mm)

- Forward fuselage lower structure, cabin side, outer skins
- Instument panels, consoles, avionics cabinets
- Gearbox fairing substructure
- Rear fuselage skinning and stringers
- Sundry sheet metal components, including those from SPF sheet

EXTRUSIONS (1,0mm - 4,5mm wall)

- Forward fuselage and cabin stringers - channels, T and I sections; acute, obtuse and 90 angle sections. Sundry sections
- Seat tracks for main cabin
- Many sections to be used as 7m lengths
- A total of 43 different sections so far identified to be made in aluminium-lithium

VIEWGRAPH No. 12

—SPECIFIC Al-Li APPLICATIONS ON EH101

E8187-10

- Cold Compressed Die Forgings (8090)
  - Construction of main cabin lift frame.
  - 38 different components will be machined from a total of 16 different forging configurations.

- Non-cold Compressed Die Forgings (5091)
  - Undercarriage components - torque links, castor housing, cross beam. Nose and main landing gear cylinders may convert to 5091 from 7010 (DTD 5636) at a later date.
  - Other applications where cold compression of forgings would be largely ineffective eg. flotation fitting, engine mounting brackets, hoist brackets, tail section folding hinge.

VIEWGRAPH No. 13

EH101 MAIN CABIN FRAME

E7053-12

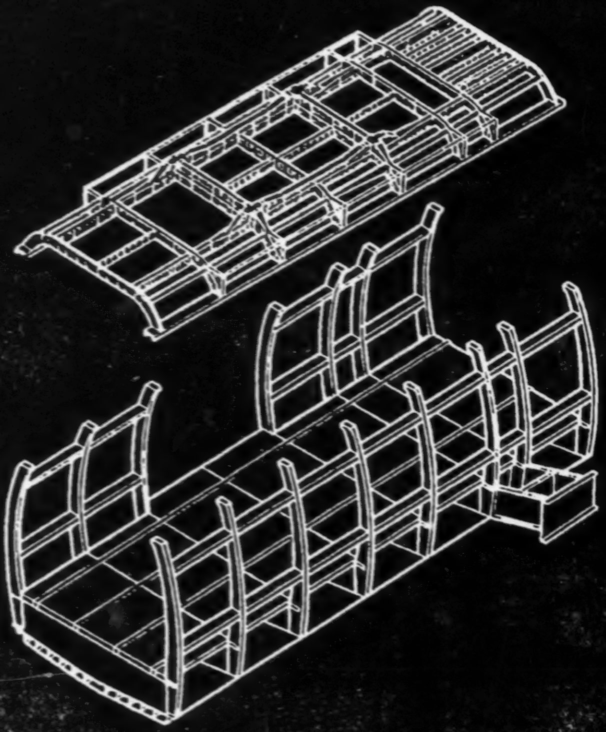

VIEWGRAPH No. 14

POSITIVE ASPECTS OF *Al-Li* ALLOYS COMPARED TO 'CONVENTIONAL' *Al* ALLOYS

E9157-11

- Approximately 10% lighter and 10% stiffer.
- Generally superior corrosion resistance - all Al-Li sheet on EH101 will be unclad.
- Fatigue crack growth rate for IM Al-Li alloys significantly slower.
- Significantly reduced degree/absence of natural ageing in 8090 - forming possible in T3 temper.
- Enhanced extrudability of 8090 - ability to make hollow seat track extrusions.
- Reduced quench sensitivity of Al-Li alloy 8090.
- Can be superplastically formed (IM Al-Li alloys).
- Heat treatment not required for alloy 5091 - very stable dimensionally.

VIEWGRAPH No. 15

POSITIVE ASPECTS OF *Al-Li* ALLOYS COMPARED TO 'CONVENTIONAL' *Al* ALLOYS

E8187-11A

- For 8090 and 2091 sheet, a single starting condition (T3) can be used for 'low strength', 'damage tolerant' and 'medium strength' categories, thus providing commercial benefits.
- IM Al-Li alloys can be TIG, spot and resistance welded.
- May be readily identified if mixed with 'conventional' Al alloys by electrical conductivity measurements. (Al-Li is typically 17 - 20% IACS c.f. 30 - 40% IACS for 2xxx and 7xxx alloys).
- Al-Li alloys amenable to most fabrication/manufacturing/processing methods and often are superior to their 'conventional' counterparts.

VIEWGRAPH No. 15 (Continued)

Comparison of Corrosion Properties of 8090C-T8 & L157

E6808-04

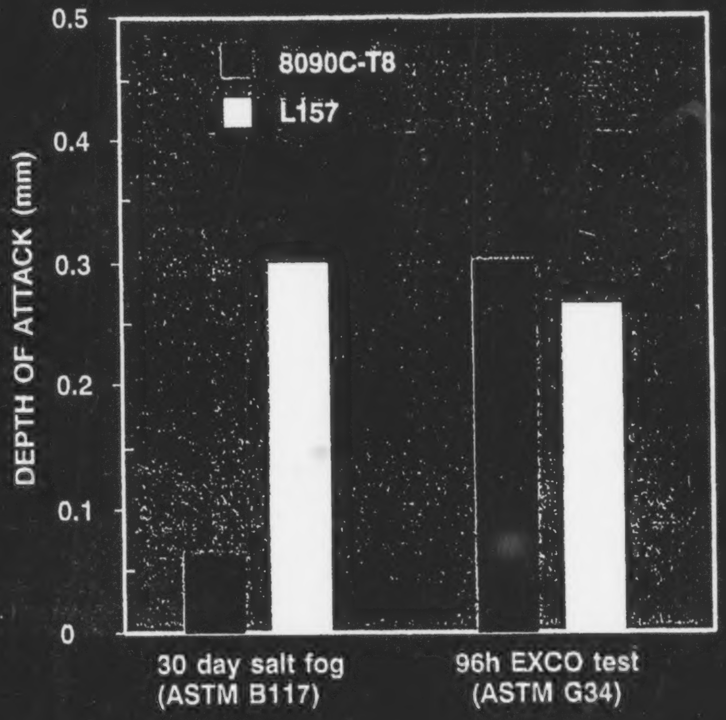

VIEWGRAPH No. 16

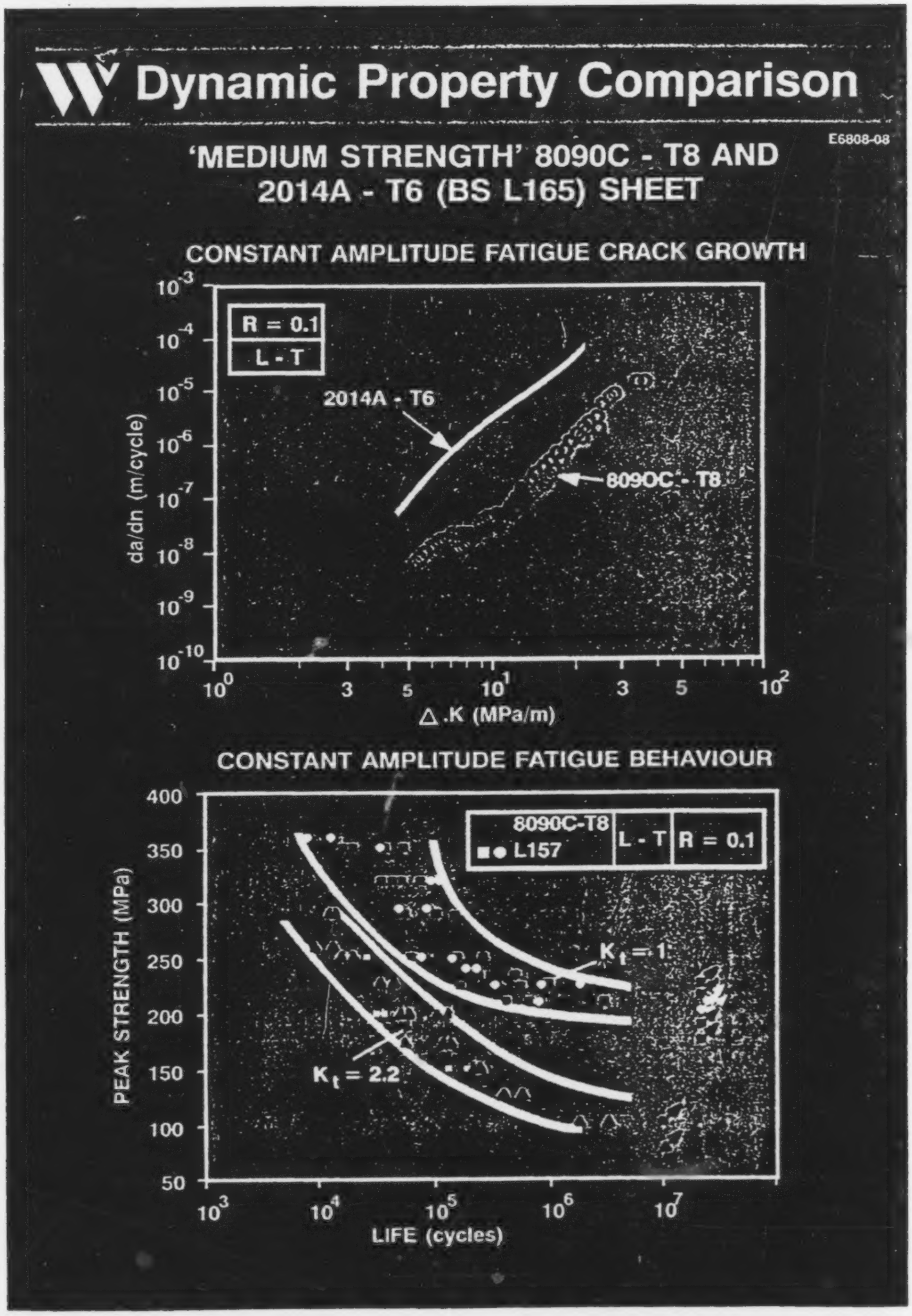

Dynamic Property Comparison

E6808-08

'MEDIUM STRENGTH' 8090C - T8 AND 2014A - T6 (BS L165) SHEET

CONSTANT AMPLITUDE FATIGUE CRACK GROWTH

CONSTANT AMPLITUDE FATIGUE BEHAVIOUR

VIEWGRAPH No. 17

Comparison of Corrosion Properties of 8090C-T8 & L157

E6808-04

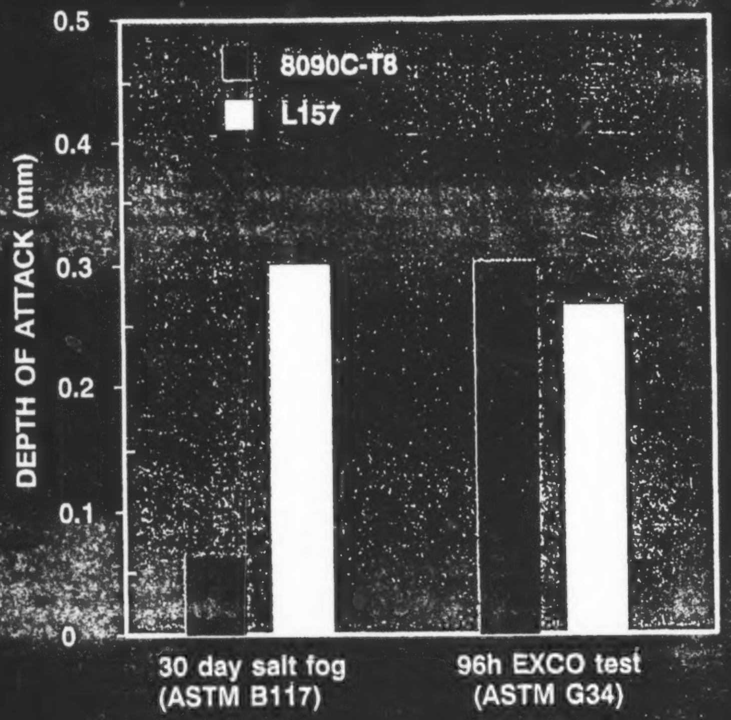

VIEWGRAPH No. 16

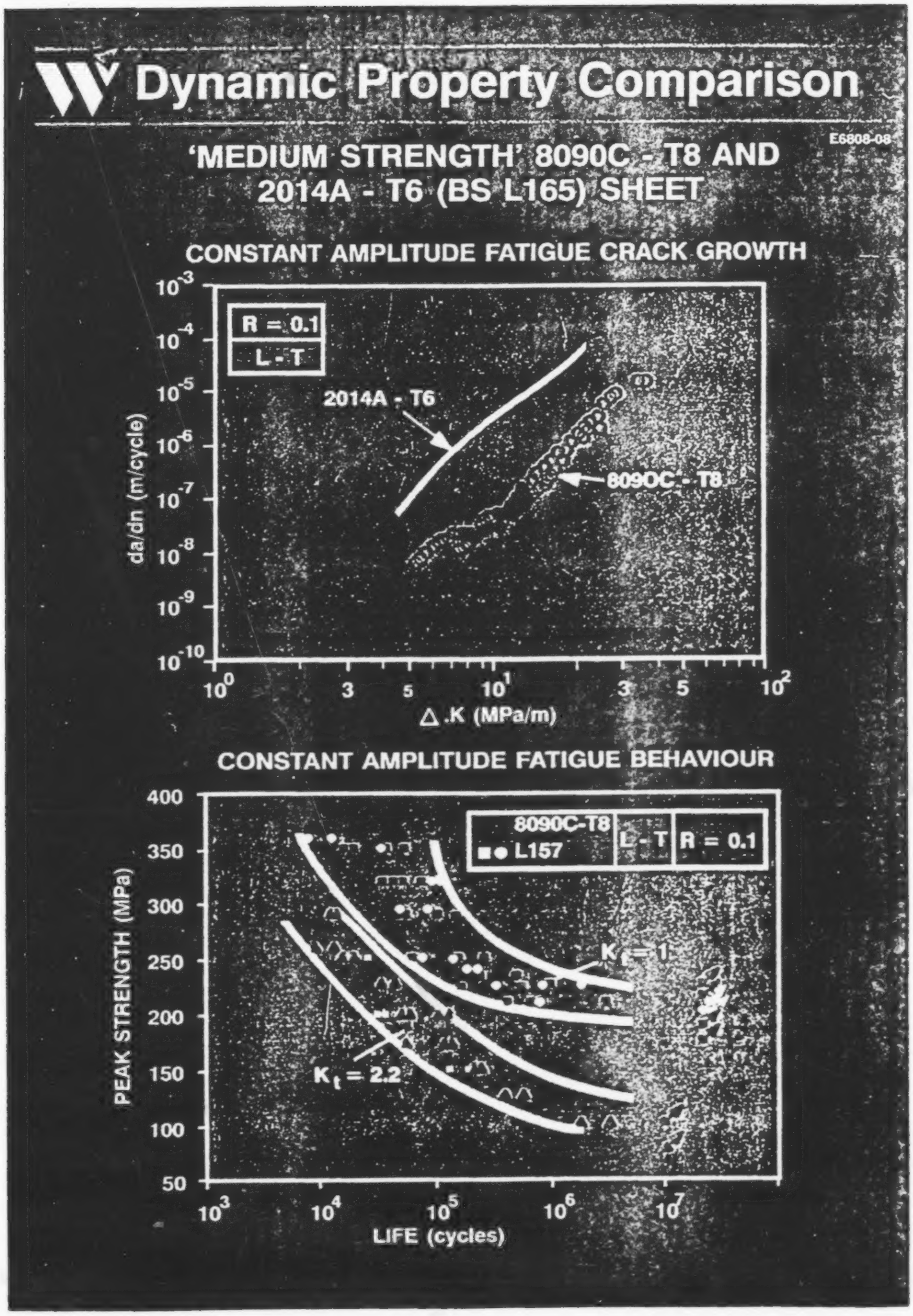

Dynamic Property Comparison

E6808-08

'MEDIUM STRENGTH' 8090C - T8 AND 2014A - T6 (BS L165) SHEET

CONSTANT AMPLITUDE FATIGUE CRACK GROWTH

CONSTANT AMPLITUDE FATIGUE BEHAVIOUR

VIEWGRAPH No. 17

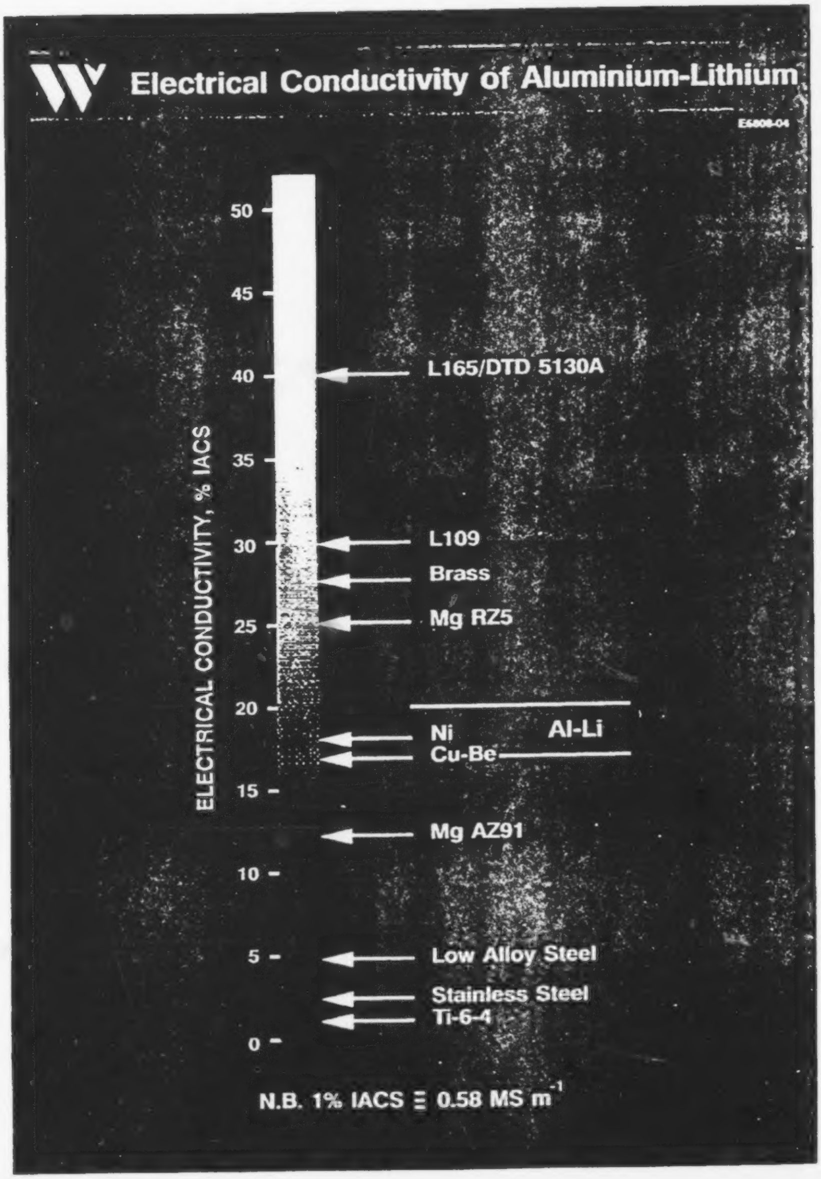

Electrical Conductivity of Aluminium-Lithium

E6808-04

N.B. 1% IACS ≡ 0.58 MS m^{-1}

VIEWGRAPH No. 18

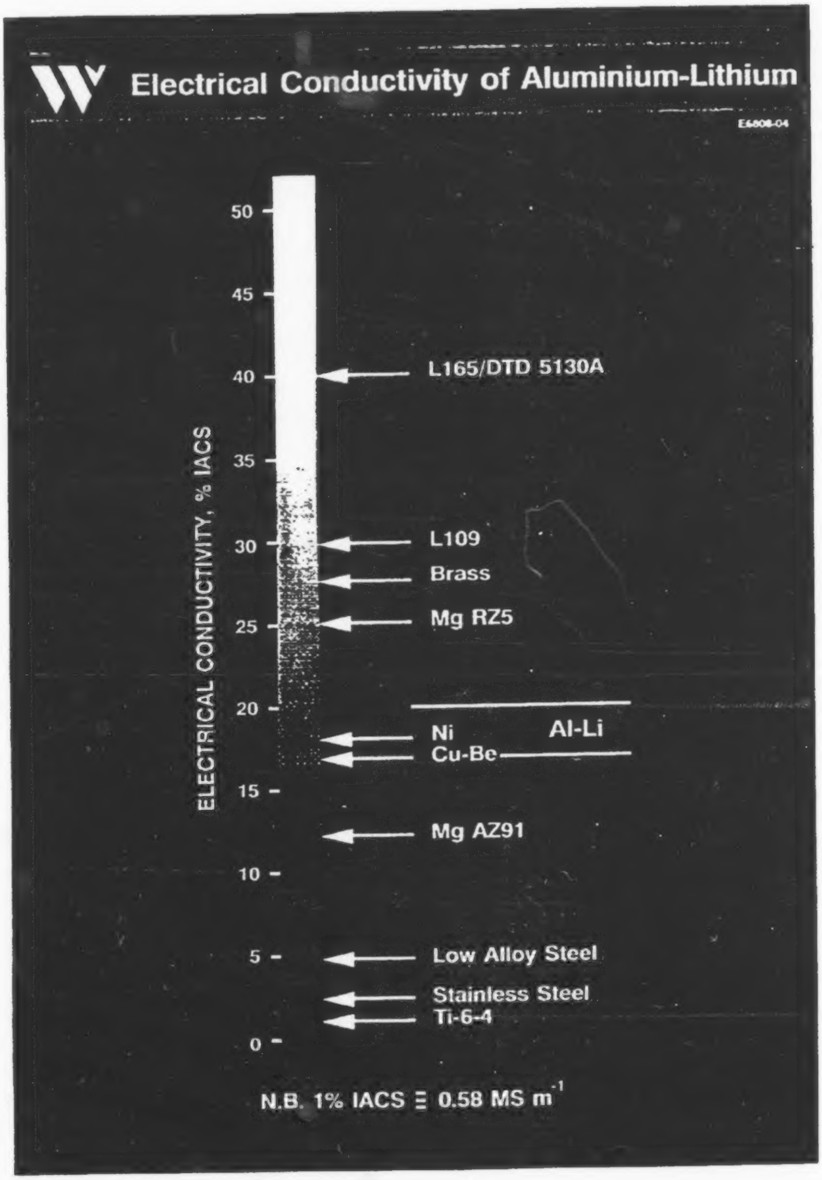

Electrical Conductivity of Aluminium-Lithium

E6808-04

N.B. 1% IACS ≡ 0.58 MS m^{-1}

VIEWGRAPH No. 18

NEGATIVE ASPECTS OF *Al-Li* ALLOYS COMPARED TO 'CONVENTIONAL' Al ALLOYS

E8157-12

- Higher cost.
- Post-solution treatment cold work necessary for medium/high strength in IM Al-Li alloys.
- Greater texture effects, particularly in unrecrystallised variants, results in high levels of anisotropy in static strength in IM Al-Li alloys.
- Scrap segregation necessary for commercial considerations.
- Fracture toughness levels generally lower than 2xxx/7xxx alloys, except possibly in damage tolerant sheet/thin plate.

VIEWGRAPH No. 19

—CONCLUSIONS

E8157-07

- Extensive use of Al-Li alloys 8090, 2091, 2090, 5091 will be made on the EH101 in the form of sheet, extrusions and die forgings. Plate will not be used.
- Approximately 10% density reduction and 10% Youngs Modulus increase are primary reasons for use of Al-Li alloys, but enhanced corrosion resistance and fatigue crack growth rate also advantageous.
- Compared to 'conventional' aluminium alloys, Al-Li alloy 8090 in particular is advantageous with regard to component manufacture due to:
    i) enhanced formability of sheet in T3 temper
    ii) reduced quench sensitivity
    ii) superior extrudability
- Compared to 'conventional' aluminium forging alloys, Al-Li alloy 5091 does not require heat treatment and is therefore extremely stable upon machining. The corrosion resistance of this alloy is also exceptionally high.
- To ensure strict control over manufacture of Al-Li alloys/product forms for EH101, all suppliers will be subject to separate approval status for Al-Li. Quality/technical audits will be carried out annually for the foreseeable future.

VIEWGRAPH No. 20

SESSION B

Mechanical Properties, Fracture and Fatigue I

14163 6

4.

"Fracture Toughness and Corrosion Fatigue Behaviour of 8090 Al-Li and 7XXX Aluminum Alloys"

A. Douchant and M. Yanishevsky

QETE, Hull, P.Q.

FRACTURE TOUGHNESS AND CORROSION FATIGUE BEHAVIOUR OF 8090 Al - Li AND 7XXX ALUMINIUM ALLOYS

by

Alain Douchant and Marko Yanishevsky
Quality Engineering Test Establishment
Department of National Defence
Ottawa, Canada
K1A 0K2

INTRODUCTION

This paper describes the fracture toughness behaviour and the laboratory air and 3.5% NaCl solution fatigue crack growth characteristics of 8090 aluminium alloy forgings and plate, in comparison to 7000 series aluminium alloys. Prototype 8090 cabin frame forgings were assessed, as well as 8090 plate material that was supplied by the Canadian TTCP (The Technical Cooperation Programme) representative.

DESCRIPTION OF THE MATERIALS

The 8090 cabin frame forging was prototype material cast by Pechiney (France) and forged by Otto Fuchs (Germany). The full forging was approximately 2.2 metres long and weighed approximately 47 kg. After forging, the part was solution treated, cold water quenched, cold compressed and then artificially aged. The additional cold compression of a few percent was applied to enhance the formation of uniformly distributed precipitates during the age hardening heat treatment cycle.

The 8090 plate was manufactured by Alcan (UK) in the T8771 condition and submitted to TTCP for research and development purposes. A portion of this plate was provided to QETE by the Canadian TTCP delegate, Dr. Jack Morrison, for complementary testing.

7075-T651 plate material, used for baseline comparison purposes in the fatigue crack growth studies, was standard aircraft quality production from Alcoa.

CHEMICAL COMPOSITION

The general chemical composition specification for 8090 is provided in Table 1. The main alloying elements are: Cu, Mg and Li. Zr is added primarily to help control grain growth. The prototype Pechiney material was higher in Mg and Cu than the prototype Alcan material previously investigated by Westland. The 8090 Alcan plate from TTCP was similar in composition to the prototype Alcan material.

METALLOGRAPHY

The grain flow in the forgings was found to be typical of conventional aluminium alloy forgings. In the Pechiney material (Figure 1), the unrecrystallized grains had a flattened shape, with the flattening most severe along the forging flashline in the thinnest sections of the forgings. The microstructure was quite clean and free of stringers and intermetallic particles. Most of the grains were decorated with precipitates. The Alcan forging material (Figure 2) was quite similar to the Pechiney forging. The 8090 Alcan plate (Figures 3) was also clean of intermetallic stringers; however, the grains were only partially recrystallized with less uniform grain sizes.

TENSILE PROPERTIES

The tensile properties of the materials investigated are provided in Table 2. The 8090 Alcan forging results were generated by Westland. The Alcan plate results were generated by TTCP members. Typical 7075-T651 plate properties data were taken from MIL-Handbook 5F. The 8090 Pechiney forging results are the average properties as generated collectively by Westland and QETE. Good correlation was found to exist between these two data sets. The Pechiney forging represented a 5 - 10% improvement in yield and ultimate strength properties over the prototype Alcan forging. In comparison, the Alcan plate from TTCP represented an increase of about 25% in yield strength and 10% in ultimate strength over the prototype Alcan forging. However, ductility was limited in both the Pechiney forging and the Alcan plate. Note that all three Al-Li alloys exhibited significant anisotropy in comparison to the behaviour of the conventional aluminium alloy, 7075-T651.

FRACTURE TOUGHNESS

The fracture toughness test results are provided in Table 3. The tests were conducted employing compact tension specimens with a width of 40 mm and thickness of 20 mm and straight through starter notches. In this table, the results for 7010 plate, 8090 Alcan and Pechiney forgings were provided courtesy of Westland; QETE generated complementary results on 8090 Pechiney forging material. The results for 8090 Alcan plate were obtained courtesy of TTCP.

In the case of the Pechiney forging, both QETE and Westland tested samples from the same forging; the results agreed favourably in all orientations. The highest fracture toughness results were obtained for the L-T and L-S orientations. The S-L orientation results were quite low, approximately 3 times lower than the L-T values. The Alcan forging results were slightly lower than the Pechiney forging in the L-T orientation; however, the other orientations compared favourably. In the case of the Alcan plate from TTCP, the L-T and T-L orientation results were significantly higher than the forging values. The Alcan plate properties were not available in the S-L or S-T orientation for comparison with the 8090 forgings. The 7010 results were superior in all orientations. (Note that the quoted values for fracture toughness in this table are K_q not K_{IC}.)

Figure 4 shows some examples of the unusual fatigue precrack and final overload behavioural nuances encountered when testing aluminium lithium forgings, which were responsible for the test results not meeting the validity requirements of ASTM test method E399 for plane strain fracture toughness testing [1]. These peculiar features do not occur in conventional 7000 series alloys. In the L-T orientation, the 8090 Pechiney forging occasionally exhibited excessive crack tunnelling. In one case, the fatigue precrack was over 5 mm deep without having become apparent at the front and back surfaces of the specimen. This behaviour has implications for visual and dye penetrant surface inspection techniques for thick sections. As well, reverse crack tunnelling was experienced, where the crack grew faster on the outside surfaces than on the inside. In this case, the fretting debris impeding crack growth was readily apparent on the fatigue surface. Lack of crack symmetry from side to side was also prevalent during fatigue precracking. In some orientations the crack path was very tortuous making it very difficult to fatigue precrack the samples (this is a highly desirable characteristic to resist fatigue crack growth). On many of the samples of L-T and L-S orientation, the final overload was out of plane. On one occasion, the overload failure had completely bifurcated. The S-L orientation exhibited a highly smooth failure surface indicative of poor crack resistance.

FATIGUE CRACK GROWTH

Fatigue crack propagation tests were conducted on compact tension specimens with thicknesses of 5 and 10 mm, and width of 40 mm machined with chevron-type starter notches. A clip-gauge extensometer was mounted at the front face of the specimen to monitor crack growth using the compliance technique [2].

General Fatigue Crack Growth Behaviour of 8090 in Laboratory Air Compared to 7075-T651

These tests were conducted under ΔK increasing conditions in laboratory air, under sinusoidal loading conditions at R ratio of 0.1 and frequency of 20 Hz. The data presented here are for the L-T orientation.

8090 Pechiney forging versus 7075-T651 plate

In these da/dN versus ΔK nominal graphs, a crossover in the data was found at ΔK = 10 MPa√m. At low values of ΔK, the Pechiney forging crack propagation rate was approximately 5 times higher than for 7075-T651 plate material (Figure 5). At high values of ΔK, the fatigue crack growth rate in 7075-T651 was approximately 3 to 4 times higher than in the 8090 Pechiney forging material.

8090 Alcan forging versus 7075-T6 plate

In this case, the fatigue crack growth behaviour was very similar to that exhibited by the Pechiney forging. Crossover in the crack propagation rate occurred at 10 MPa√m with the 7075-T651 plate exhibiting superior behaviour at low ΔK values and the Alcan forging exhibiting superior crack growth characteristics at high ΔK values (Figure 6).

8090 Alcan plate (TTCP) versus 7075-T6 plate

For Alcan plate (Figure 7), the crossover occurred at ΔK values between 9 and 10 MPa√m. At low ΔK values, the Alcan plate exhibited a crack propagation rate about 3 to 4 times higher than in 7075-T651 plate; at high ΔK levels, crack propagation in 7075-T651 plate was approximately 2 to 3 times higher than in the Alcan plate.

R Ratio Effects

In an attempt to simulate the vibratory loads that occur on helicopter structural components, a series of tests were conducted at R ratio, R=0.7. These tests were performed under ΔK increasing conditions in laboratory air, using compact tension specimens with a thickness of 10 mm and width of 40 mm, under sinusoidal loading at a frequency of 20 Hz. The results generated at R ratio, R=0.7, were compared to R=0.1 data.

7075-T651 plate (L-T orientation)

At low values of ΔK, there was approximately a 10 times increase in crack propagation rate for R=0.7 (Figure 8); in the mid range the data generated at R=0.7 was 2 to 3 times more aggressive than R=0.1 data.

8090 Pechiney forging (L-T orientation)

For the Pechiney forging material, the fatigue crack growth rate was approximately 6 to 10 times more aggressive at R=0.7 (Figure 9).

8090 Pechiney forging (T-L orientation)

The T-L orientation exhibited essentially the same effect as L-T for the Pechiney forging. The fatigue crack growth rate was approximately 5 to 10 times greater at R=0.7 (Figure 10).

Orientation Effects (L-T versus T-L) in 8090 Pechiney Forging and Alcan Plate (TTCP)

These tests were conducted under ΔK increasing conditions in laboratory air, under sinusoidal loading at R=0.1 and frequency of 20 Hz. The Pechiney forging (Figure 11) exhibited a 2 to 3 times higher crack growth rate in the T-L orientation than in the L-T orientation. On the other hand, the Alcan plate (Figure 12) exhibited similar stable fatigue crack propagation behaviour at ΔK levels below 7 MPa√m in both the L-T and T-L orientations. At ΔK levels between 7 and 15 MPa√m, the Alcan plate T-L orientation exhibited a plateau in its fatigue crack growth, with the crack propagation rate being approximately 3 times slower than for the L-T orientation under the same stress intensity range conditions. Beyond 15 MPa√m, the T-L orientation crack growth rapidly increased to the same levels experienced by the L-T orientation. In the case of the Alcan plate T-L specimen, the crack had started to deflect from the normal cracking plane at a ΔK value of 12 MPa√m, along a path of lesser resistance, whereupon the crack growth rate rapidly approached that of the L-T orientation.

Effect of Environment on Fatigue Crack Growth (Laboratory Air versus 3.5% NaCl)

A series of ΔK increasing tests were conducted under sinusoidal loading conditions at R=0.1, a loading frequency of 20 Hz, and exposed to 3.5% (by weight) NaCl solution for comparison with laboratory air data. The environment was introduced by squirting 3.5% NaCl solution into the machined notch and fatigue cracked surfaces of the specimens, and its presence was maintained at the crack tip at regular 10 minute intervals.

7075-T651 plate

At low values of ΔK, the crack growth rate in 7075-T651 plate (Figure 13) was found to be approximately 6 times more aggressive in the 3.5% NaCl environment than in laboratory air, about 2 times higher in the mid range, and there was little effect noted in the upper tertiary (unstable) portion of the da/dN versus ΔK curve.

8090 Alcan forging

In the case of the Alcan forging exposed to the 3.5% NaCl solution (Figure 14), the crack growth rate was approximately 3 to 4 times more rapid than in laboratory air throughout the full range of crack growth rates investigated.

8090 Alcan plate (TTCP)

For the Alcan plate tested in 3.5% NaCl solution (Figure 15), at low ΔK levels, the crack growth rate was approximately twice that observed in laboratory air; in the mid range crack growth increased by about 6 to 10 times. At high ΔK levels near final failure there was very little environmental effect noted.

ΔK Constant Fatigue Crack Growth Tests - Exposure to Both Lab Air and 3.5% NaCl

There was some concern raised during the first series of corrosion fatigue crack growth tests that the environmental effects may have been influenced by the microstructural variability in each specimen due to their different locations in the Pechiney forging. Consequently, it was not possible to establish that the variable response was exclusively due to the presence of the 3.5% NaCl environment. To overcome these nuisance variables, a second series of tests was conducted which consisted of testing one half of each specimen in one environment, with the other half being tested in the other environment.

Again, all these tests were conducted under sinusoidal loading conditions at R=0.1 and a loading frequency of 20 Hz. However, to better isolate the effect of environment, these tests were conducted under constant ΔK levels of 7 MPa√m (maintained by automated load shedding), which had a corresponding crack growth rate of approximately 1×10^{-8} m/cycle in the 8090 alloys during ΔK increasing laboratory air tests.

In the ensuing six figures, two sets of data are plotted. The top graph contains ΔK nominal and ΔK effective versus crack length data. The bottom graph describes the corresponding fatigue crack growth rate behaviour as a function of crack length. In the first four sets of data, the first half portions of the specimens were used to generate laboratory air data; the latter half portions of the specimens were used to generate the 3.5% NaCl environment data. Two final sets of data were also generated with the order of environments reversed.

Laboratory air followed by 3.5% NaCl

8090 Pechiney forging

Under the initial laboratory air conditions, the crack closure exhibited by the Pechiney forging was substantial, between 40 to 50 % (Figure 16). The fatigue crack growth rate was stable at approximately 1×10^{-8} m/cycle. Once the 3.5% NaCl environment was squirted into the machined notch and fatigue cracked portion of the specimen, the crack closure rapidly diminished to a level of approximately 10%. A corresponding rapid increase in crack growth rate of about 5 to 6 times occurred during testing in the 3.5% NaCl environment.

8090 Alcan forging

In the case of the Alcan forging (Figure 17), the crack closure remained effectively the same at about 25% in both the laboratory air and 3.5% NaCl environments. Once exposed to the 3.5% NaCl, the crack growth rate rapidly increased by a factor of 6 to 9 times the laboratory air rate.

8090 Alcan plate (TTCP)

For the Alcan plate, once exposed to the 3.5% NaCl environment, the crack closure decreased from the 35% experienced in laboratory air to about 15% (Figure 18). The crack growth rate did not increase rapidly once the 3.5% NaCl environment was introduced as in the two previous cases. In fact it took considerable time to achieve the higher crack growth rates of up to 6 times those in laboratory air. This phenomenon may partially explain why some laboratories conducting ΔK increasing tests with this plate material have noticed little or no increase in crack growth rate in 3.5% NaCl solution over laboratory air. It appears that there is a much longer incubation period required in the 3.5% NaCl environment for the Alcan plate material to achieve the full interaction of material, loading and environment.

7075-T651 plate

During the testing of 7075-T651 plate specimens, there was a slight increase in crack closure from about 10% to 15% when the 3.5% NaCl environment was applied, contrary to the behaviour in all the 8090 alloys (Figure 19). The crack propagation rate increased by 2 to 3 times when 7075-T651 plate specimens were exposed to the 3.5% NaCl environment, as reported in [3].

3.5% NaCl followed by laboratory air

In order to investigate whether the order of exposure to environment was a significant concern, tests with exposure to 3.5% NaCl environment first, followed by laboratory air were conducted.

8090 Pechiney forging

Under the 3.5% NaCl environmental conditions, the crack closure was approximately 5% (Figure 20). The crack was kept open under the mean load condition, and a blow dryer was used to attempt to dry out the 3.5% NaCl environment. Apparently this was not done effectively, as shown by the relatively slow reduction in crack growth rate as the crack advanced further in laboratory air. However, this data does show that at longer crack lengths, when the crack surfaces were free of the 3.5% NaCl solution, crack closure increased to a maximum of about 50% in laboratory air. As well, the corresponding crack growth rate decreased by a factor of 6 to 7 times to effectively the same crack propagation rates observed in the previous test, where the order of the environments was reversed.

8090 Alcan plate (TTCP)

In the case of the Alcan (TTCP) plate (Figure 21), while exposed to the 3.5% NaCl environment, the crack closure was approximately 20%. In this test, the procedure to remove the environment consisted of wiping the specimen dry with no load on the sample, followed by drying with a blow dryer while the cracked specimen was loaded at the mean test load. In this case, the increase in both crack closure (to about 50%) and corresponding crack growth rate occurred immediately upon resumption of the test. The fatigue crack growth rate decreased by a factor of between 2 to 4.

FRACTOGRAPHIC FEATURES OF THE CORROSION FATIGUE CRACK GROWTH TESTS

Optical and scanning electron microscopy were employed to fractographically discern any differences in the fatigue crack growth mechanisms. The corresponding figures show an optical micrograph at a magnification of 200X, taken of the test coupon cross section in the direction of crack propagation, and 200X and 1000X fractographs. The laboratory air and 3.5% NaCl environment pictures are provided together for ease of comparison. In all cases, the direction of crack propagation is up the page.

7075-T651 plate

For the portion of the sample tested in laboratory air, the 200X magnification photo of the polished 7075-T651 sample with the cross-section cut in the direction of crack propagation, the surface was found to be relatively smooth with primarily transgranular crack growth (Figure 22). The fatigue surface at the 200X magnification indicated typical fatigue features: facets, furrows and terraces. At 1000X magnification, typical fan shaped fatigue features were evident.

The optical micrograph of the fatigue surface cross section of the portion of the 7075-T651 sample exposed to 3.5% NaCl environment was slightly smoother; the crack propagation was still transgranular. The fatigue surface features at 200X and 1000X were essentially the same as in the case of laboratory air.

8090 Pechiney Forging

The optical micrograph of the portion of the Pechiney sample tested in laboratory air conditions indicated that the fatigue was primarily transgranular (Figure 23). The fractograph at 200X showed fatigue features that were somewhat elongated, i.e., longer than the typical grain size. As well, there were large peaks and valleys, indicative of crack path tortuosity. At 1000X, mixed-mode fatigue features were evident. There were quasi-cleavage and fan-like fatigue features in the grains with the grain boundaries showing plasticity, which impedes crack propagation.

The portion of the Pechiney sample tested in the 3.5% NaCl environment revealed that the crack growth was mixed intergranular / transgranular. The fractograph at 200X indicated that the fatigue features were smaller, about the same size as the grains, and there was a significant decrease in crack path tortuosity. At 1000X it was evident that the grain boundaries did not exhibit plasticity. In addition to being generally transgranular, there were distinct islands of fracture present where preferred crystallographic planes were evident, as well as regions of intergranular failure.

8090 Alcan Forging

The Alcan forging exhibited micrographic and fractographic features very similar to the Pechiney forging material (Figure 24). Again, the portion of the sample tested in laboratory air revealed that the fatigue was primarily transgranular with significant crack path tortuosity. At 1000X magnification, quasi-cleavage fatigue features were evident, and there was significant plasticity at the grain boundaries.

In the 3.5% NaCl environment, the Alcan forging sample revealed that the crack propagation was primarily intergranular with some transgranular features. Finer fatigue features were evident with less crack path tortuosity. At 1000X, the crack growth was found to be intergranular.

8090 Alcan Plate (TTCP)

For the portion of the sample tested under laboratory air conditions, the micrograph taken at 200X along the direction of crack propagation (the LT plane) revealed a relatively smooth surface (Figure 25). The micrograph taken perpendicular to the direction of crack propagation (the ST direction) revealed large peaks and valleys, a high degree of crack path tortuosity. The portion tested in 3.5% NaCl solution revealed an smoother surface with substantially smaller peaks and valleys, i.e., a smaller degree of crack path tortuosity. In both the laboratory air and 3.5% NaCl environments, the cracks had propagated in a transgranular fashion.

The 200X and 1000X fractographs taken of the portion of the coupon tested in laboratory air indicated significant peaks and valleys along the crack front and that the fatigue features were somewhat elongated (Figure 26). There was also some limited plasticity evident at the grain boundaries. The fractographs taken of the specimen portion tested in 3.5% NaCl environment revealed that the peaks and valleys were not as severe as in laboratory air. There were some large peaks and valleys; however, there were several small peaks and valleys in between. Some delamination was also evident on the fatigue surface. At 1000X the fatigue features were highly crystallographic. There was no evidence of plasticity at the grain boundaries and the primary fatigue mechanism was intergranular. Similar observations of the fatigue surfaces on 8090 Alcan plate were reported in [4].

DISCUSSION

Designers of components/structures using 8090 aluminium lithium alloys are faced with a number of challenges when using this highly directional and anisotropic class of materials [5]. Though their residual strength in the presence of cracks may be highly favourable in the majority of orientations, the S-L (and presumably also S-T) loading/cracking modes have been found to be quite poor, typically about a factor of 3 lower than for the L-T orientation.

Significant differences in the behaviour between plate and forged materials were found. During the conduct of these experiments, it was revealed that in the case of forgings, crack deflection occurred in the L-T orientation. However, in the case of the Alcan plate material from TTCP, crack deflection occurred in the T-L orientation, indicating that the designer will not be able to assume plate characteristics to necessarily be reflected in forged materials. As well, the designer will be significantly challenged to ensure that local forging characteristics account for the end use modes of loading.

Crack tunnelling observed in thick sections in the L-T orientation (which presumably will be the most highly loaded orientation) could have severe implications on inspection, particularly for surface NDT techniques, such as visual and fluorescent dye penetrant inspections.

In general, the fatigue crack growth behaviour of 8090 alloys was found to be inferior to that of 7075-T651 plate at ΔK values below 10 MPa√m. Above 10 MPa√m, 8090 crack propagation behaviour was found to be superior to that of 7075-T651 plate.

8090 alloys benefit from crack path tortuosity, crack shielding and subsequent crack closure to achieve their crack growth resistance [6]. High mean loads, such as under R=0.7 loading conditions, were found to significantly influence the behaviour of 8090 forging material, increasing the crack growth rates by 5 to 10 times. The corresponding effect on a conventional aluminium alloy, 7075-T651 plate, was found to be an increase in fatigue crack growth rate of only 2 to 3 times. The introduction of environment, such as 3.5% NaCl solution, also had a very significant effect on fatigue crack growth; crack path tortuosity was significantly reduced with a corresponding reduction in crack closure. In laboratory air, the fatigue surfaces for all the 8090 materials tested were faceted with typical fan-shaped and quasi-cleavage fatigue features; in 3.5% NaCl solution the features were less resistant intergranular / crystallographic in nature. During the course of experimentation it was also observed that once the 3.5% NaCl environment was applied to a crack, removal of the environment was very difficult and as such had an irreversible effect on overall specimen fatigue life. When exposed to 3.5% NaCl environment, the increase in fatigue crack growth rate in 8090 Alcan plate was observed to be comparable to that in 7075-T651, an increase of 2 to 4 times. Similar results for 8090 Alcan plate were found by Kemp et al [4]. However, in the cases of the 8090 Pechiney and Alcan forging materials, the crack growth rate increased by 6 to 9 times in the 3.5% NaCl environment. At high levels of ΔK in the tertiary crack growth regime, the presence of 3.5% NaCl environment did not increase the fatigue crack growth rates above those obtained in laboratory air tests.

CONCLUSIONS

Aluminium lithium 8090 alloys have significant differences in fracture toughness and fatigue crack growth properties as compared to a conventional 7075-T651 aluminium alloy. This study has found significant variability in damage tolerance properties between two different forging manufactures and also 8090 plate. These differences in the behaviour emphasize the need for conducting the right engineering / design detail tests on relevant materials of manufacturing quality, and heat treatment typical of that which will be ultimately used in production.

As well, for damage tolerant structural designs using 8090 alloy forgings and plate, the effect of loading modes, service load spectra and service environment must be characterized on representative design detail to assure safety and structural integrity.

REFERENCES

1. ASTM Standard Test Method for Plane-Strain Fracture Toughness (K_{IC}) of Metallic Materials, E399-90, Annual Book of ASTM Standards, vol. 03.01.

2. ASTM Standard Test Method for Measurement of Fatigue Crack Growth Rates, E647-91, Annual Book of ASTM Standards, vol. 03.01.

3. P.S. Pao, M.A. Imam, L.A. Cooley and G.R. Yoder, "Comparison of Corrosion-Fatigue Cracking of Al-Li AA 2090-T8E41 and Alloy AA 7075-T651 in Salt Water", Corrosion, National Association of Corrosion Engineers, July 1989, pp 530-535.

4. R.M.J Kemp, R.N. Wilson, Farnborough (UK) and P.J. Gregson, Southhampton (UK), "Effect of Environment on Fatigue Crack Growth in Aluminium Alloy 8090 Plate", Aluminium - Lithium, M. Peters and P.J. Winkler, editors, 1992, pp 575-580.

5. J.F.P. Beaudet, A.M. Abdel-latif, I. Fraser, M. Roth, A.A. Steffen and M. Yanishevsky, "A Review of the Properties of Aluminium - Lithium (Al-Li) Alloy Systems, QETE Internal QETE Report for Project A012588, November 1988.

6. K.T. Venkateswara, R.S. Piascik, R.P. Gangloff and R.O. Ritchie, "Fatigue Crack Propagation in Aluminium-Lithium Alloys, Aluminium Lithium Alloys volume 2, Proceedings of the 5th International Aluminium-Lithium Conference, Williamsburg, Virginia, T.H. Sanders and E.A. Starke, editors, pp 955 - 971.

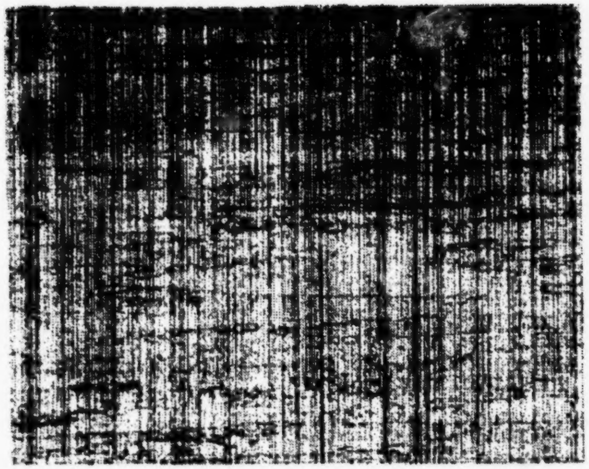

L↔ T↕

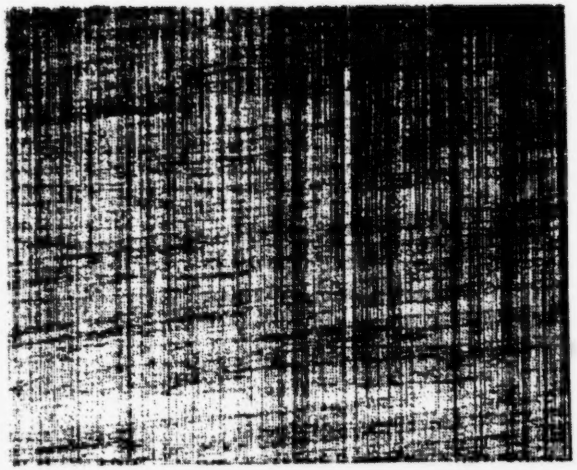

L↔ S↕

8090
PECHINEY FORGING
(MAG X100)

FIGURE 1

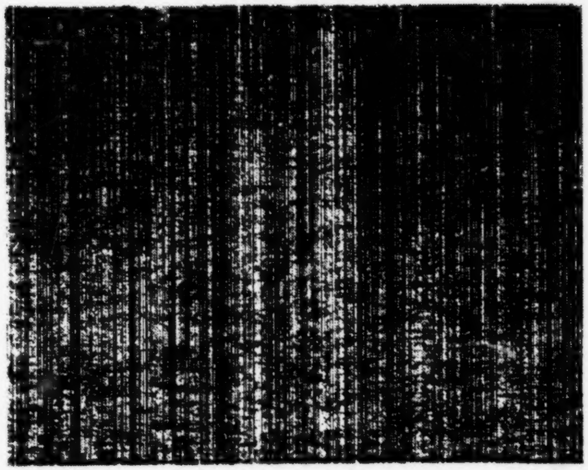

T↔ S↕

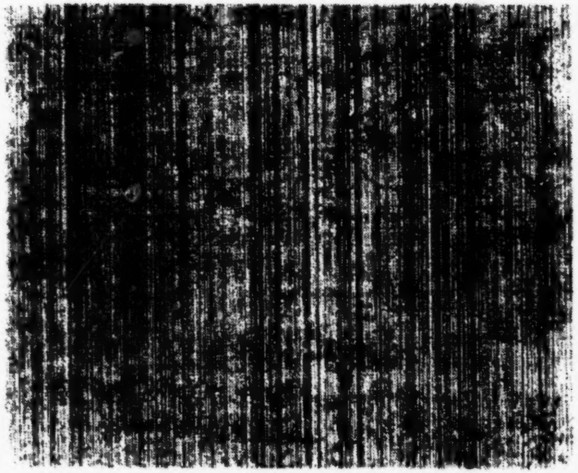

L↔ T↕

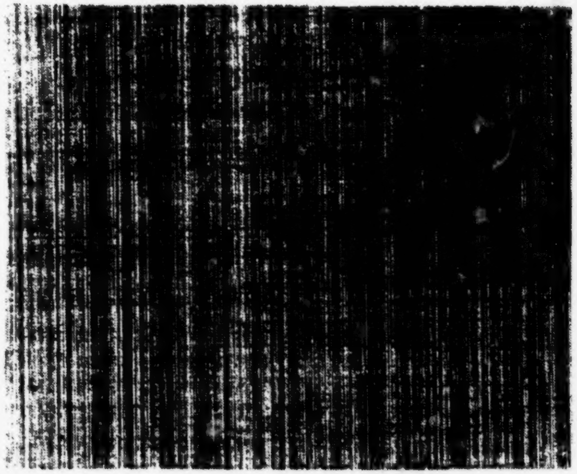

L↔ S↕

8090
ALCAN FORGING
(MAG X100)

FIGURE 2

T↔ S↕

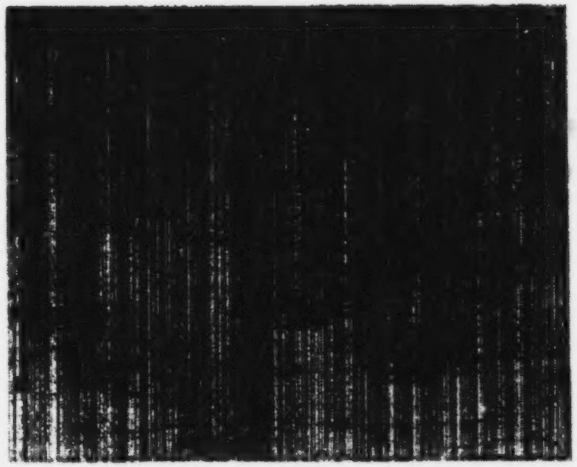

L↔ T↕

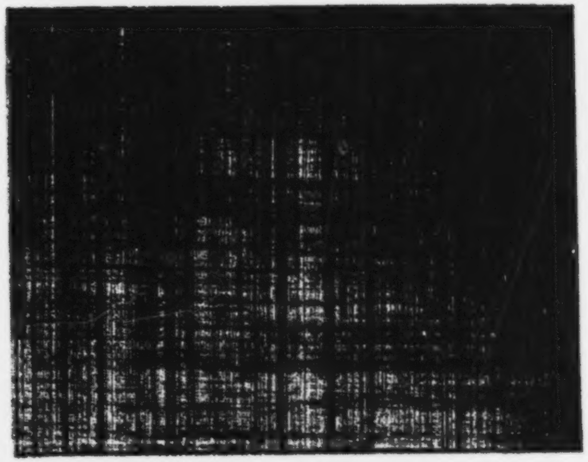

L↔ S↕

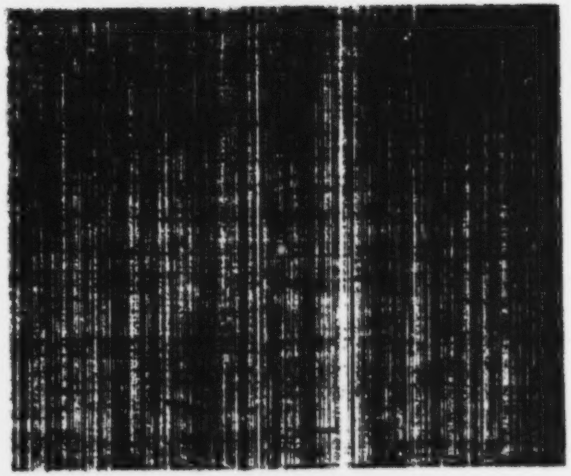

T↔ S↕

8090
ALCAN PLATE (TTCP)
(MAG X100)

FIGURE 3

8090 PECHINEY FORGING

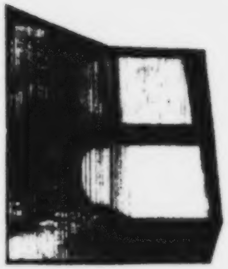

CRACK TUNNELING
L-T

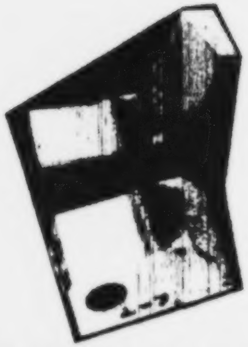

REVERSE TUNNELING
AND FRETTING DEBRIS
L-T

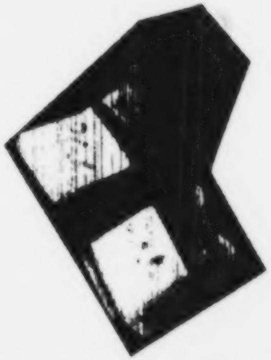

CRACK TORTUOSITY
L-S

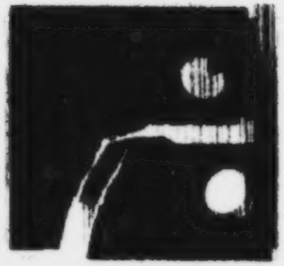

CRACK DEFLECTION
L-T

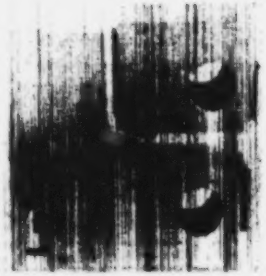

CRACK BIFURCATION
L-S

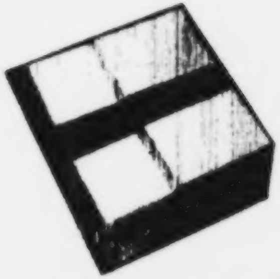

LACK OF CRACK
RESISTANCE
S-L

FIGURE 4

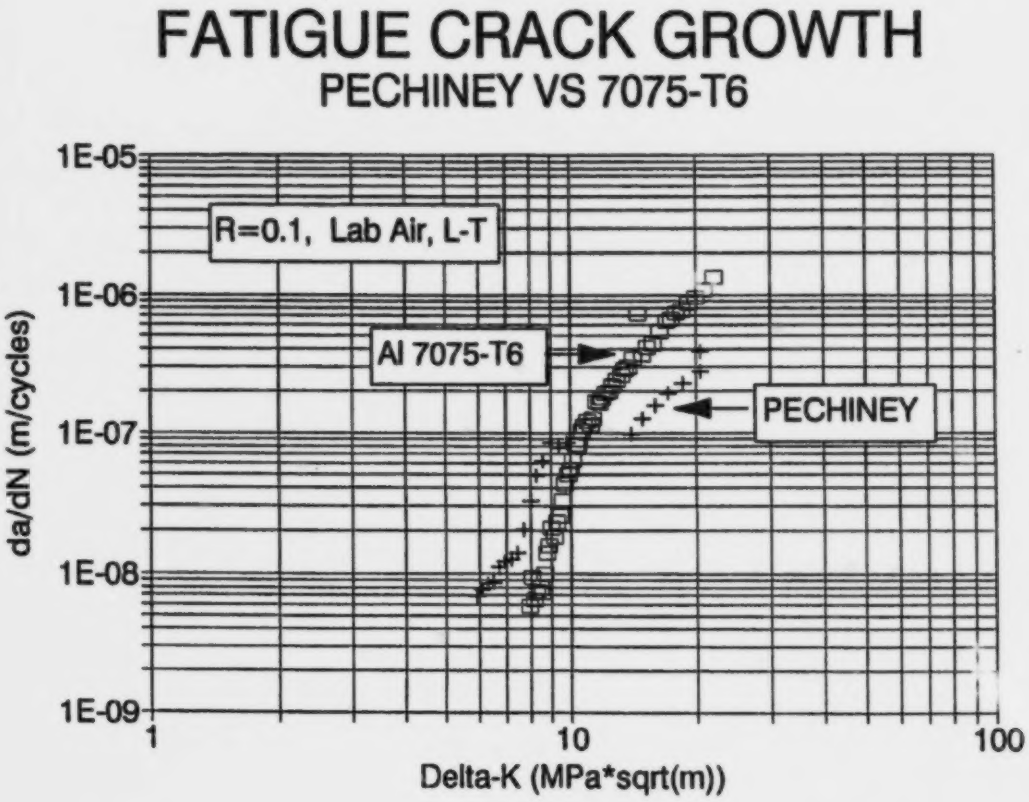

FATIGUE CRACK GROWTH
PECHINEY VS 7075-T6

FIGURE 5

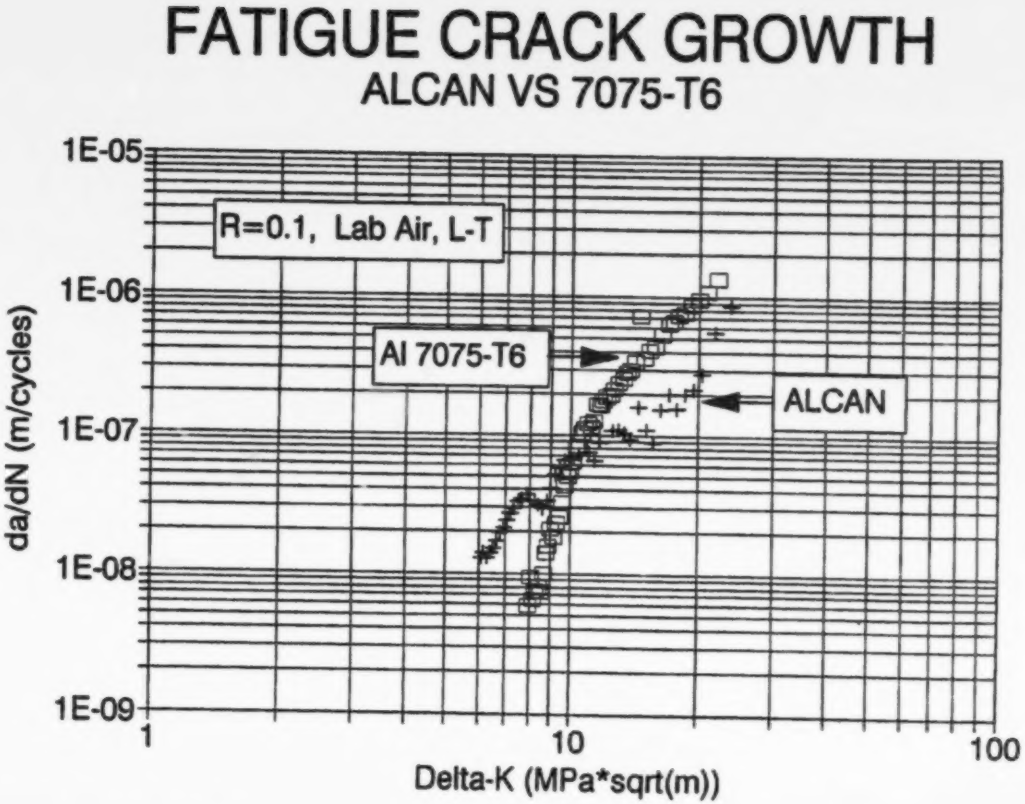
FATIGUE CRACK GROWTH
ALCAN VS 7075-T6
R=0.1, Lab Air, L-T
Al 7075-T6
ALCAN
da/dN (m/cycles)
1E-05
1E-06
1E-07
1E-08
1E-09
1
10
100
Delta-K (MPa*sqrt(m))

FIGURE 6

FATIGUE CRACK GROWTH
TTCP VS 7075-T6

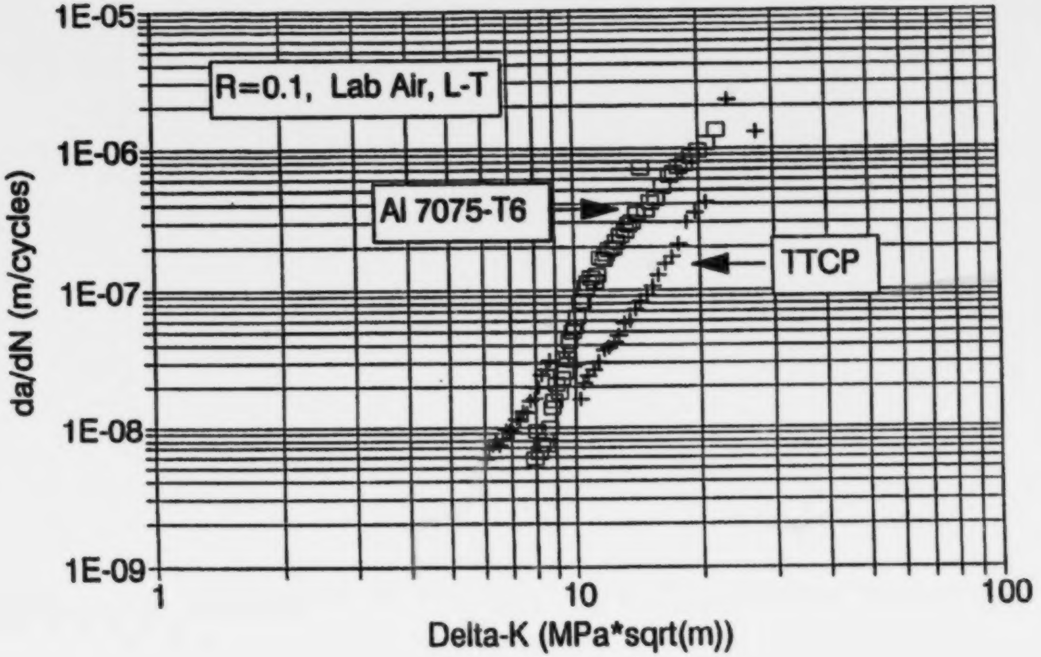

FIGURE 7

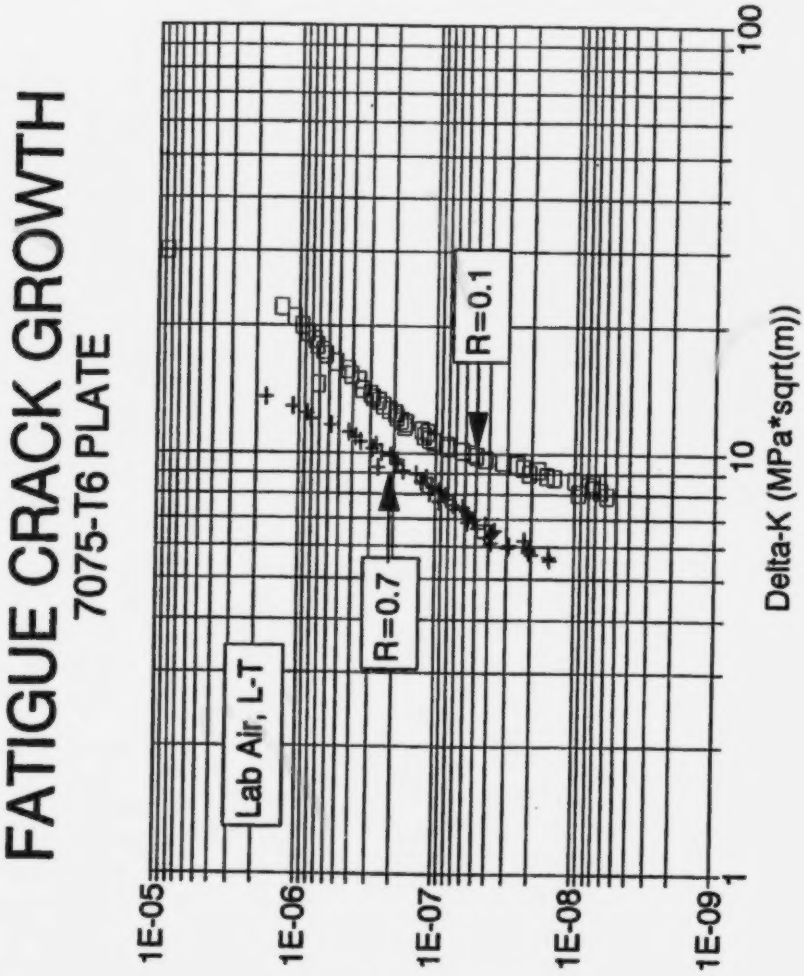
FATIGUE CRACK GROWTH
7075-T6 PLATE
Lab Air, L-T
R=0.7
R=0.1
da/dN (m/cycles)
1E-05
1E-06
1E-07
1E-08
1E-09
Delta-K (MPa*sqrt(m))
1
10
100

FIGURE 8

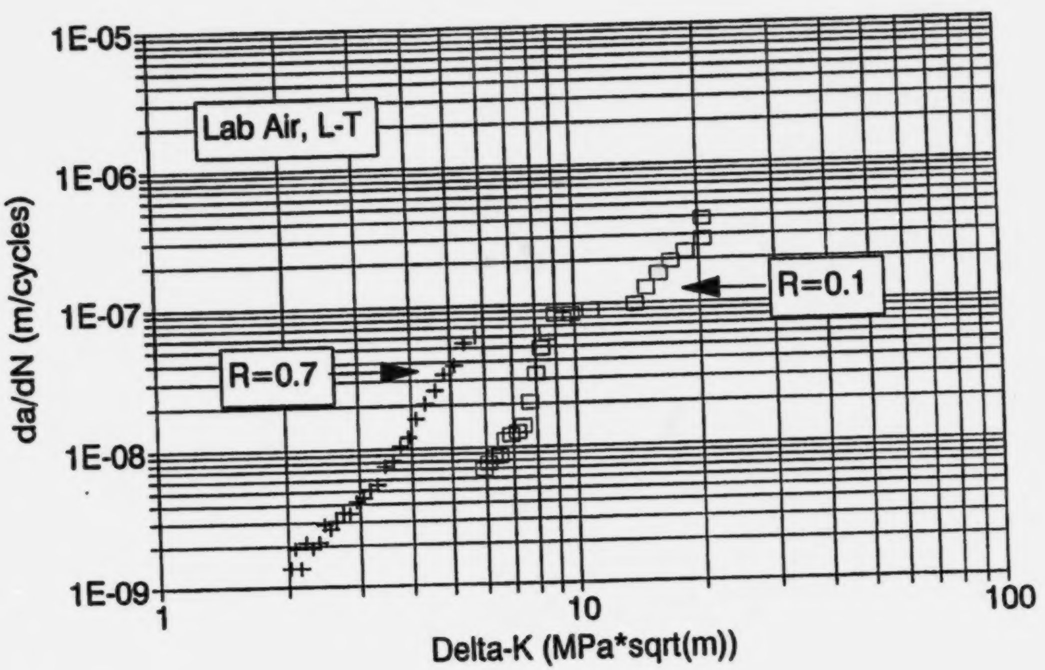

FATIGUE CRACK GROWTH
PECHINEY FORGING

FIGURE 9

FATIGUE CRACK GROWTH
PECHINEY FORGING

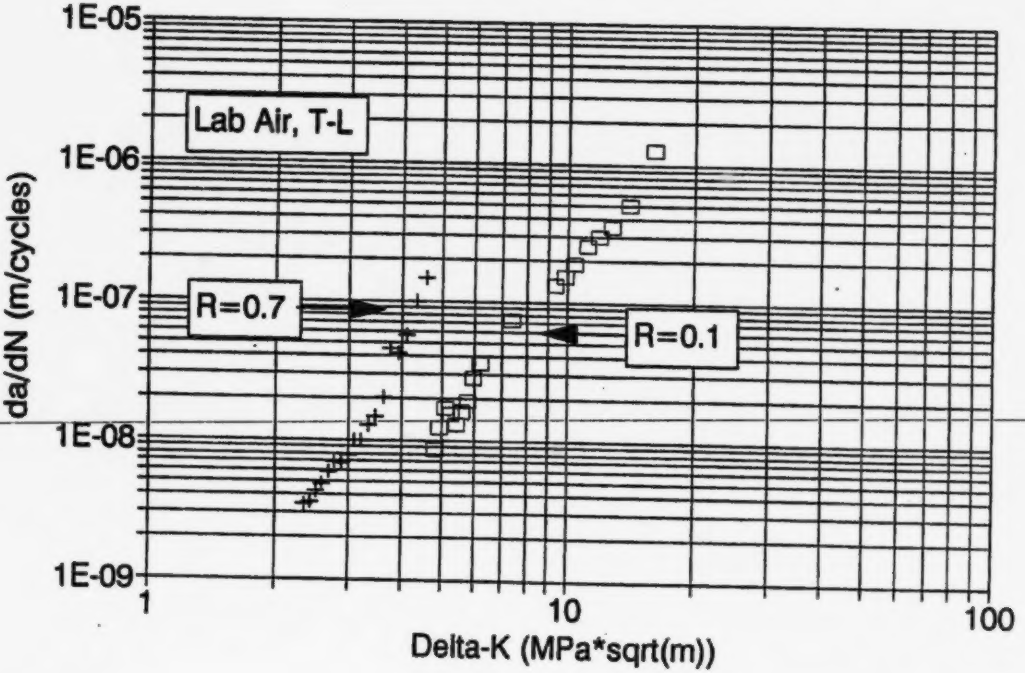

FIGURE 10

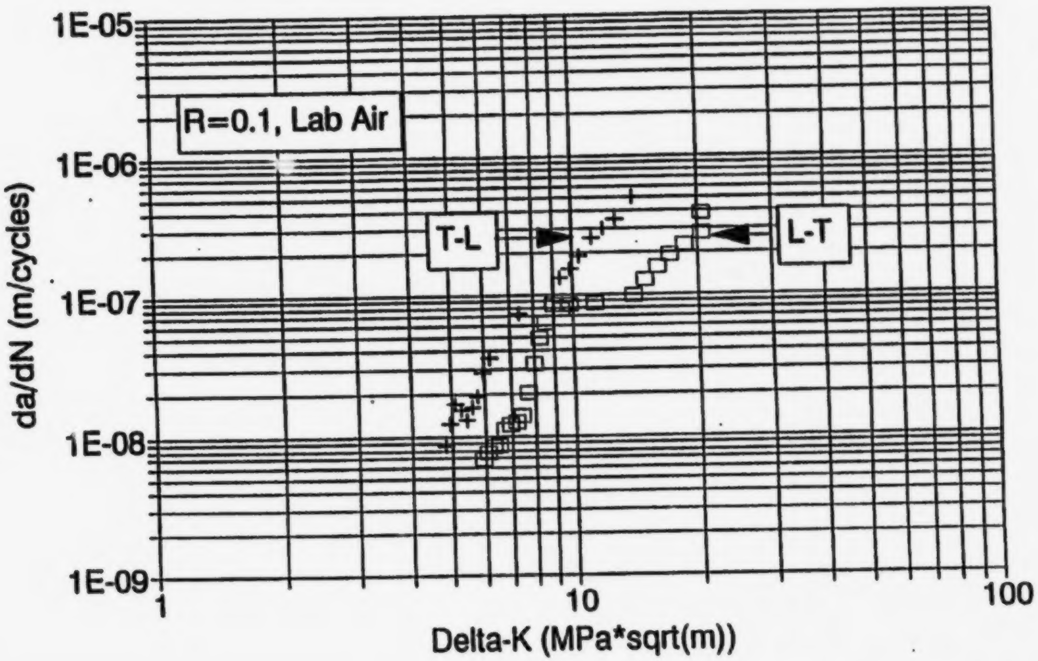
FATIGUE CRACK GROWTH

Al-Li 8090 PECHINEY

FIGURE 11

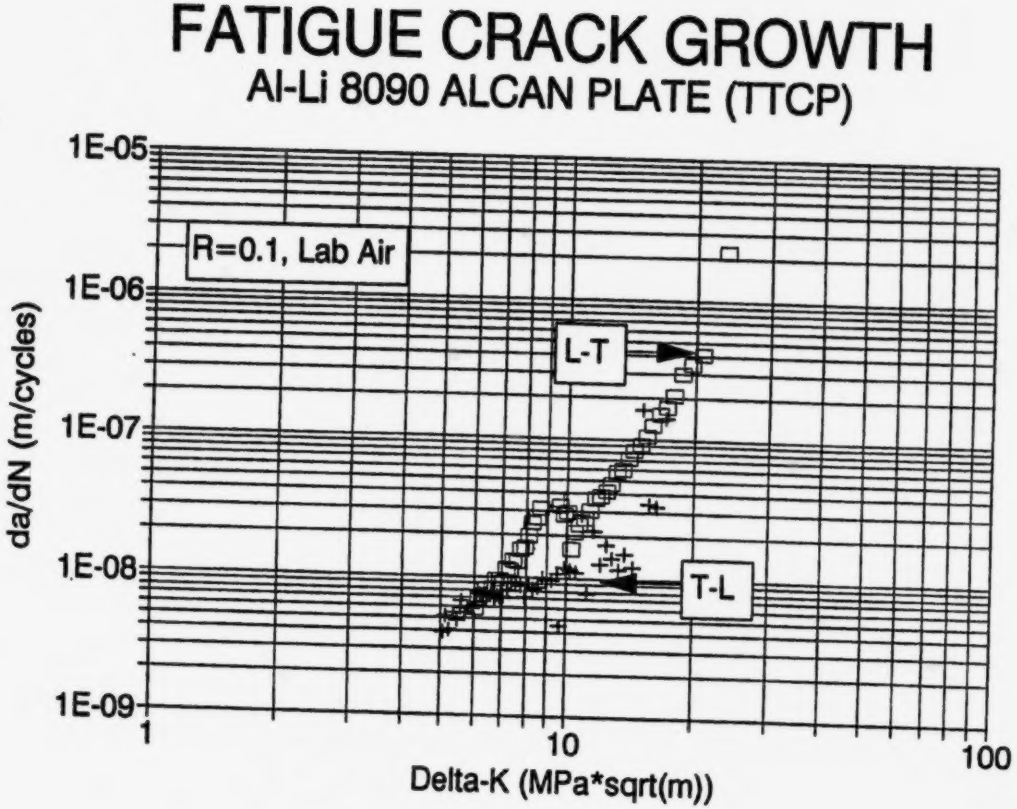
FATIGUE CRACK GROWTH
Al-Li 8090 ALCAN PLATE (TTCP)
R=0.1, Lab Air
L-T
T-L
1E-05
1E-06
1E-07
1E-08
1E-09
da/dN (m/cycles)
1
10
100
Delta-K (MPa*sqrt(m))

FIGURE 12

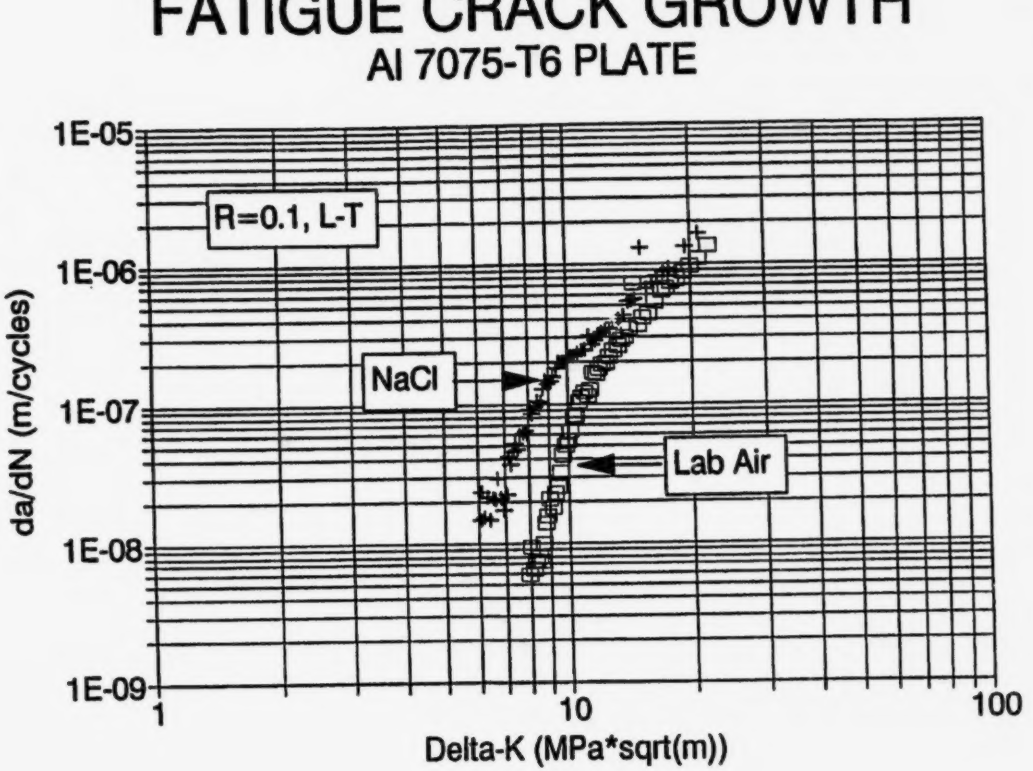
FATIGUE CRACK GROWTH
Al 7075-T6 PLATE
R=0.1, L-T
NaCl
Lab Air
da/dN (m/cycles)
1E-05
1E-06
1E-07
1E-08
1E-09
1
10
100
Delta-K (MPa*sqrt(m))

FIGURE 13

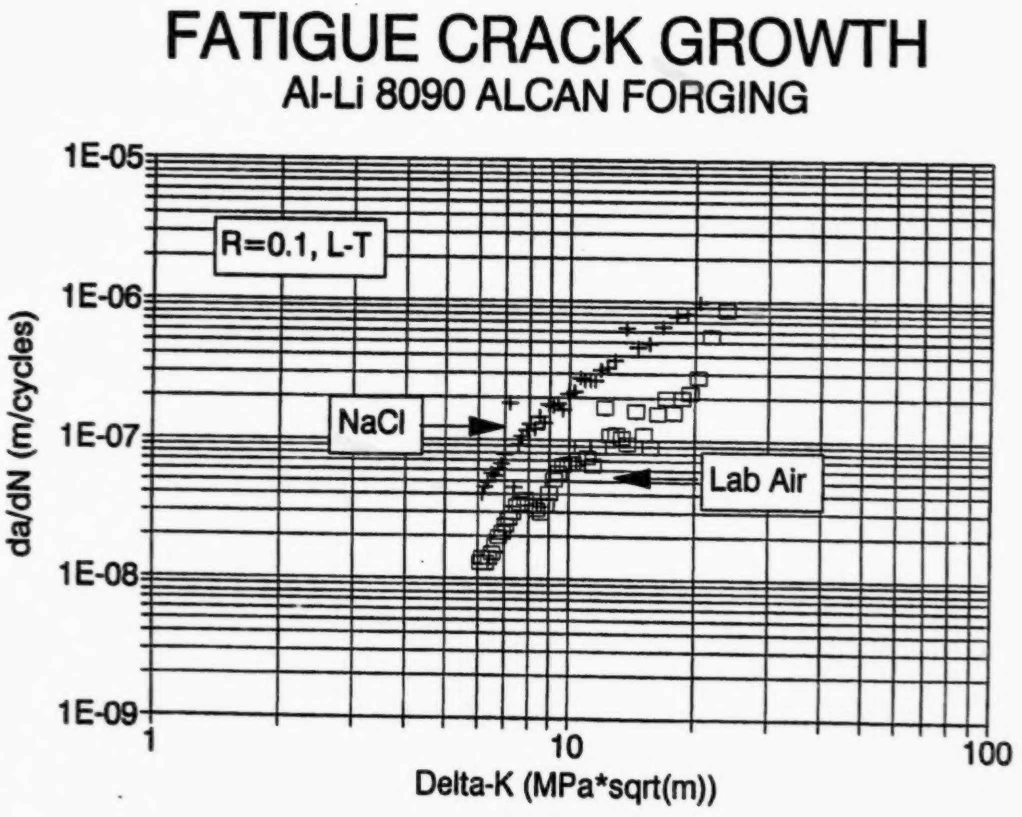

FATIGUE CRACK GROWTH
Al-Li 8090 ALCAN FORGING

FIGURE 14

FATIGUE CRACK GROWTH
Al-Li 8090 ALCAN PLATE (TTCP)

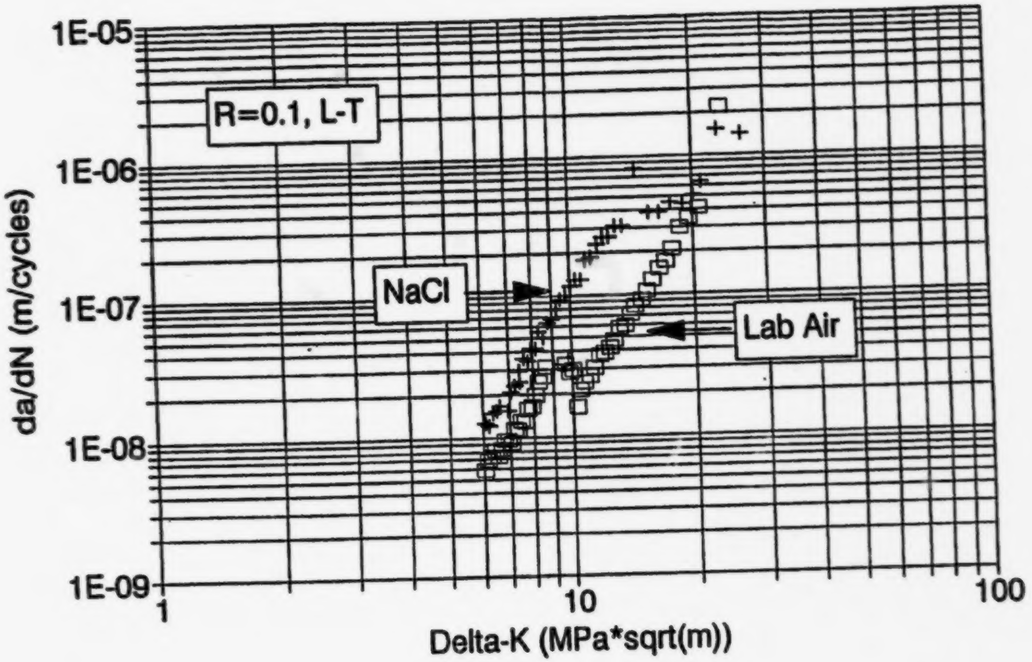

FIGURE 15

Specimen I.D.: B12588.005
Material: Al-Li Pechiney Forging
Orientation: L-T
Environment: First half, Lab Air; second half 3.5% NaCl
R-ratio: 0.1
Test Procedure: Constant Delta K (7.0 MPa*sqrt(m))

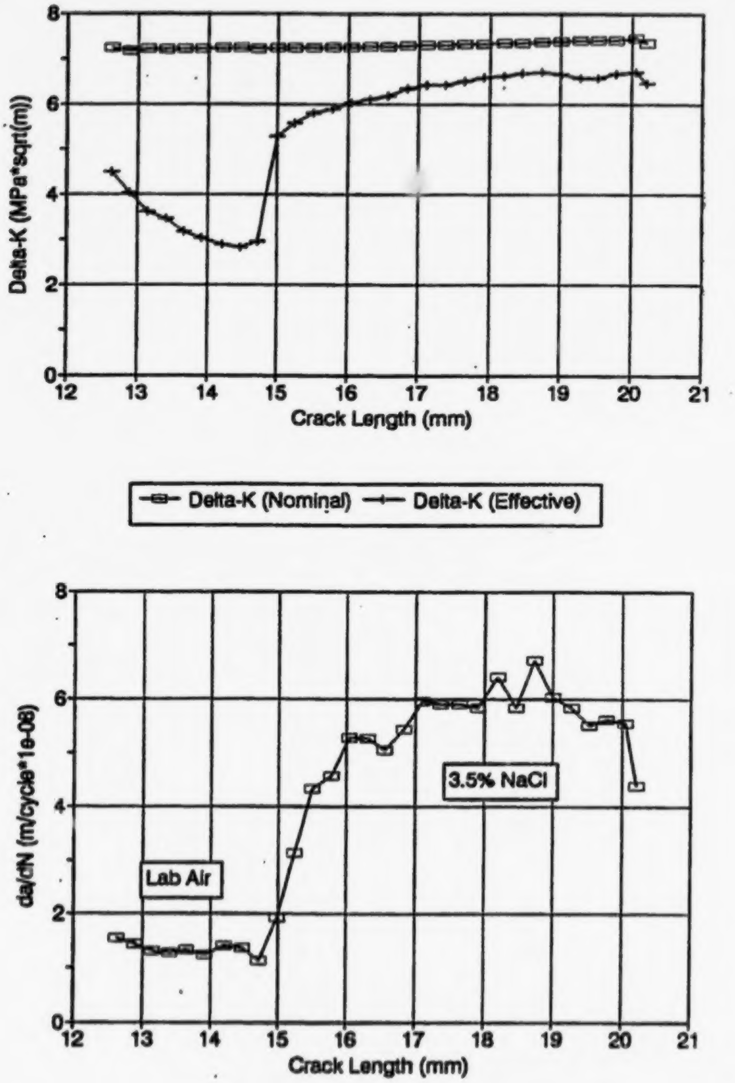

FIGURE 16

Specimen I.D.: B12588.020
Material: Al-Li Alcan Forging
Orientation: L-T
Environment: First half, Lab Air; second half 3.5% NaCl
R-ratio: 0.1
Test Procedure: Constant Delta K (7.0 MPa*sqrt(m))

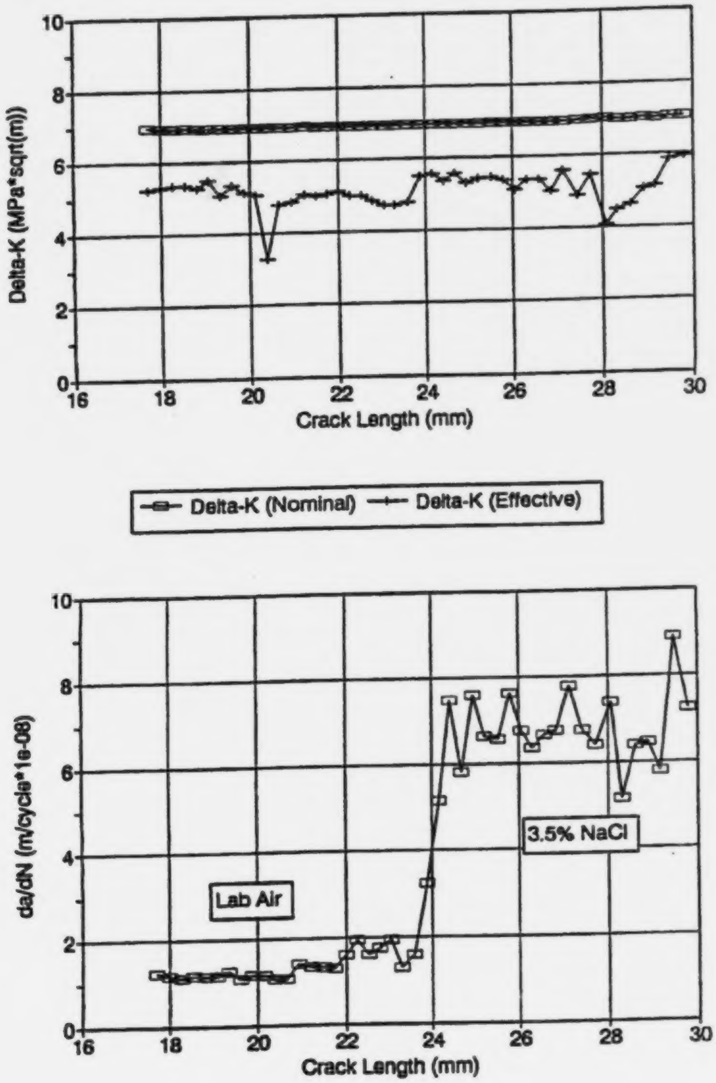

FIGURE 17

Specimen I.D.: B12588.028
Material: Al-Li Alcan Plate (TTCP)
Orientation: L-T
Environment: First half, Lab Air; second half 3.5% NaCl
R-ratio: 0.1
Test Procedure: Constant Delta K (7.0 MPa*sqrt(m))

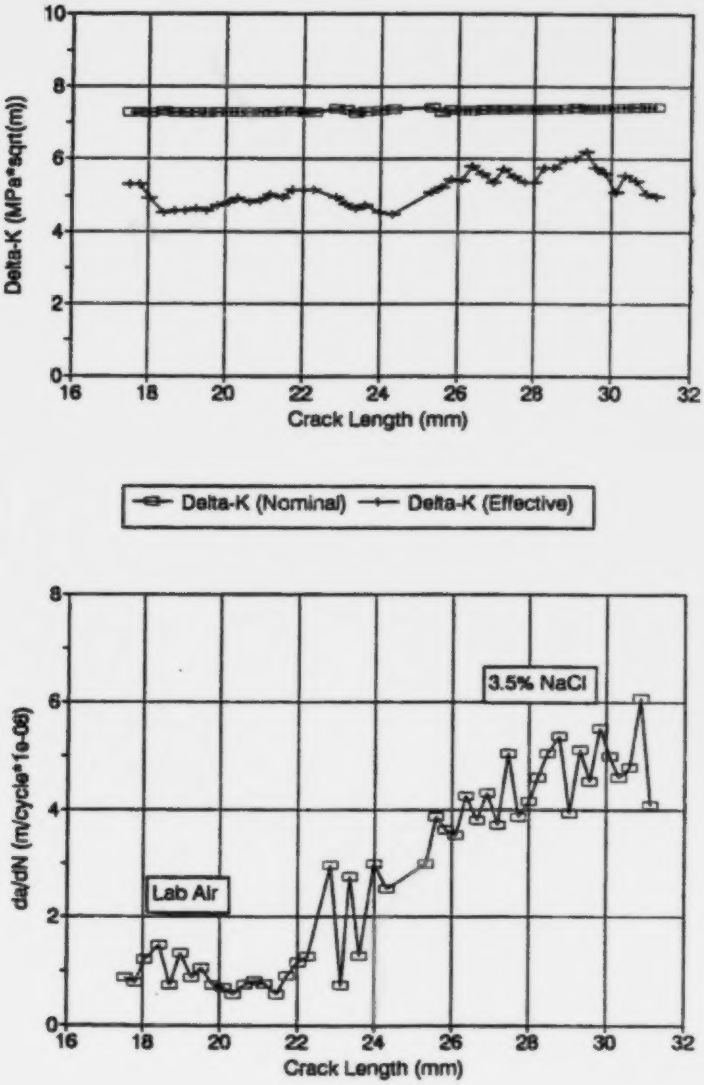

FIGURE 18

Specimen I.D.: B09289.011
Material: Al 7075-T6
Orientation: L-T
Environment: First half, Lab Air; second half 3.5% NaCl
R-ratio: 0.1
Test Procedure: Constant Delta K (7.0 MPa*sqrt(m))

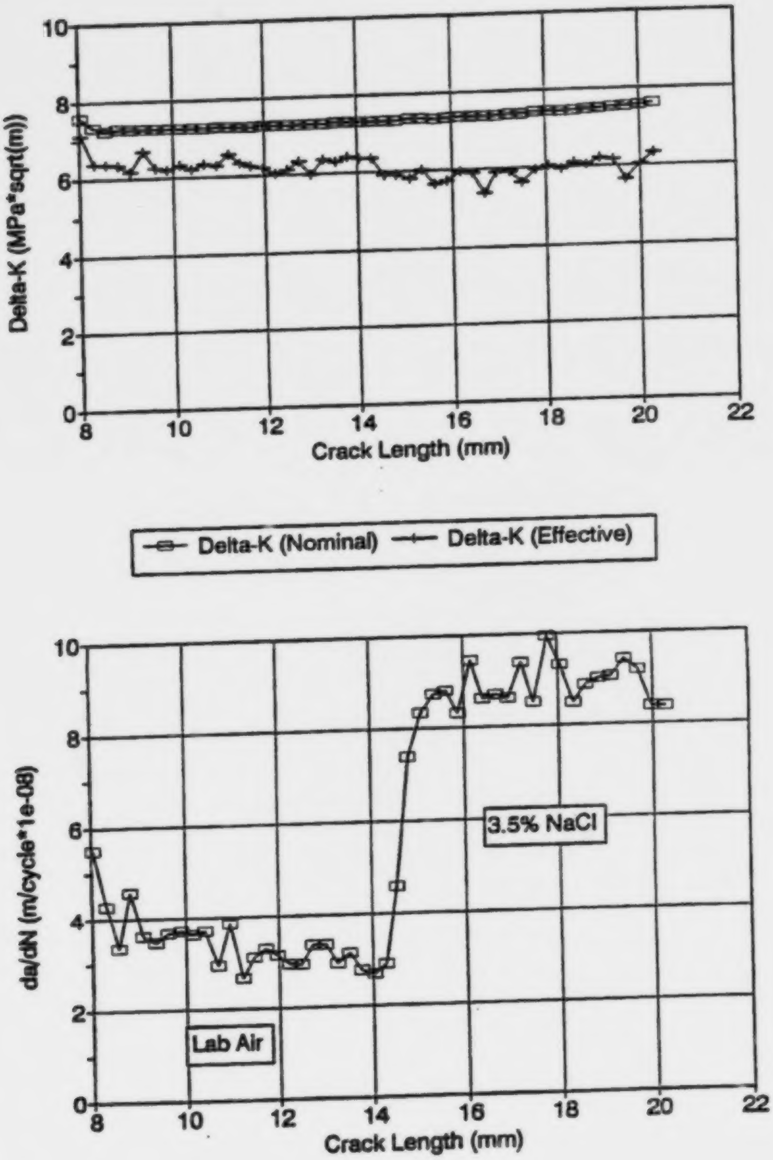

FIGURE 19

Specimen I.D.: B12588.006
Material: Al-Li Pechiney Forging
Orientation:L-T
Environment: First half, 3.5% NaCl; second half Lab Air
R-ratio: 0.1
Test Procedure: Constant Delta K (7.0 MPa*sqrt(m))

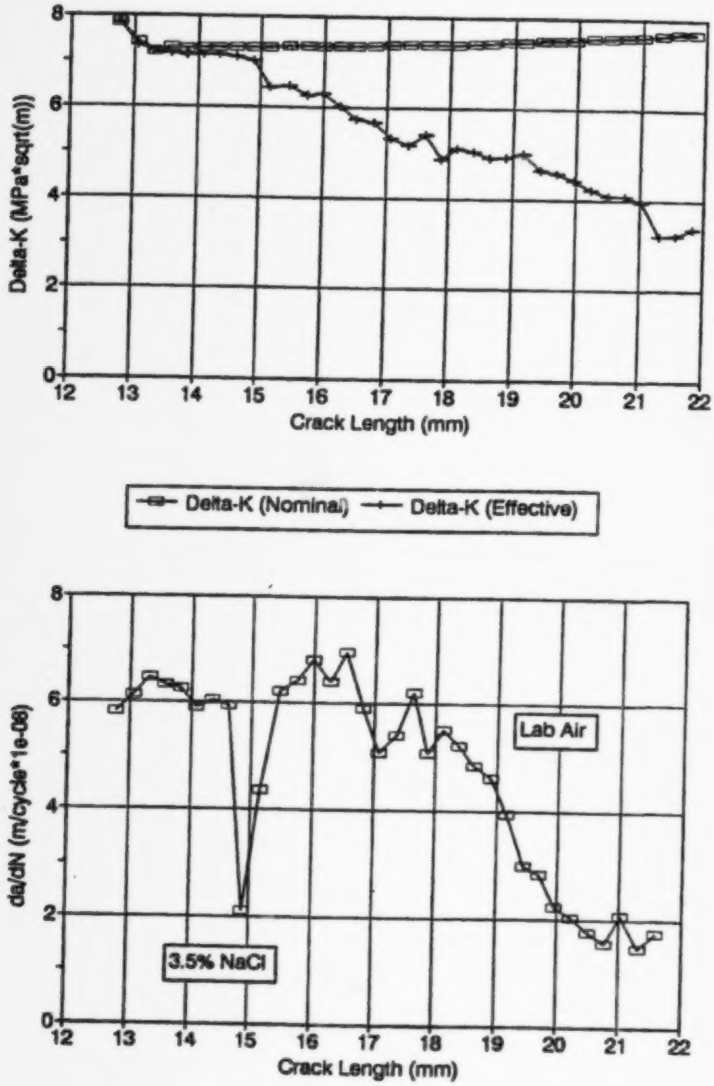

FIGURE 20

Specimen I.D.: B12588.029
Material: Al-Li Alcan Plate (TTCP)
Orientation:L-T
Environment: First half, 3.5% NaCl; second half Lab Air
R-ratio: 0.1
Test Procedure: Constant Delta K (7.0 MPa*sqrt(m))

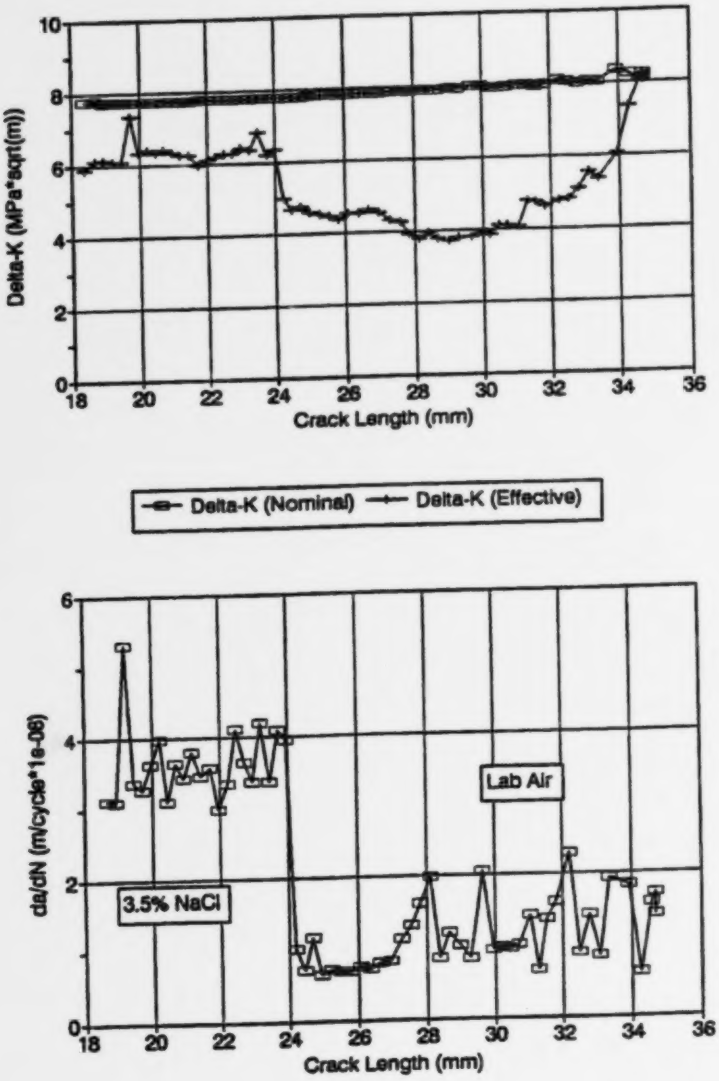

FIGURE 21

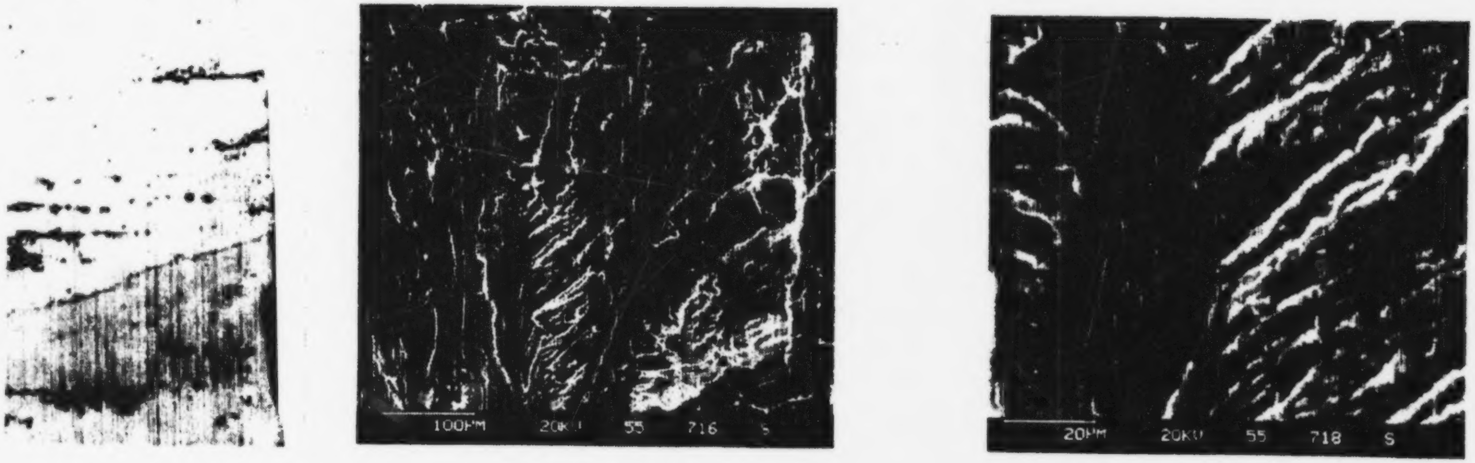
100PM 20KU 55 716 S
20PM 20KU 55 718 S

LAB AIR 7075-T6 PLATE L-T, R=0.1, ΔK=7 MPa√m, 20Hz

100PM 20KU 55 720 S
20PM 20KU 55 723 S

3.5% NaCl 7075-T6 PLATE L-T, R=0.1, ΔK=7 MPa√m, 20Hz

FIGURE 22

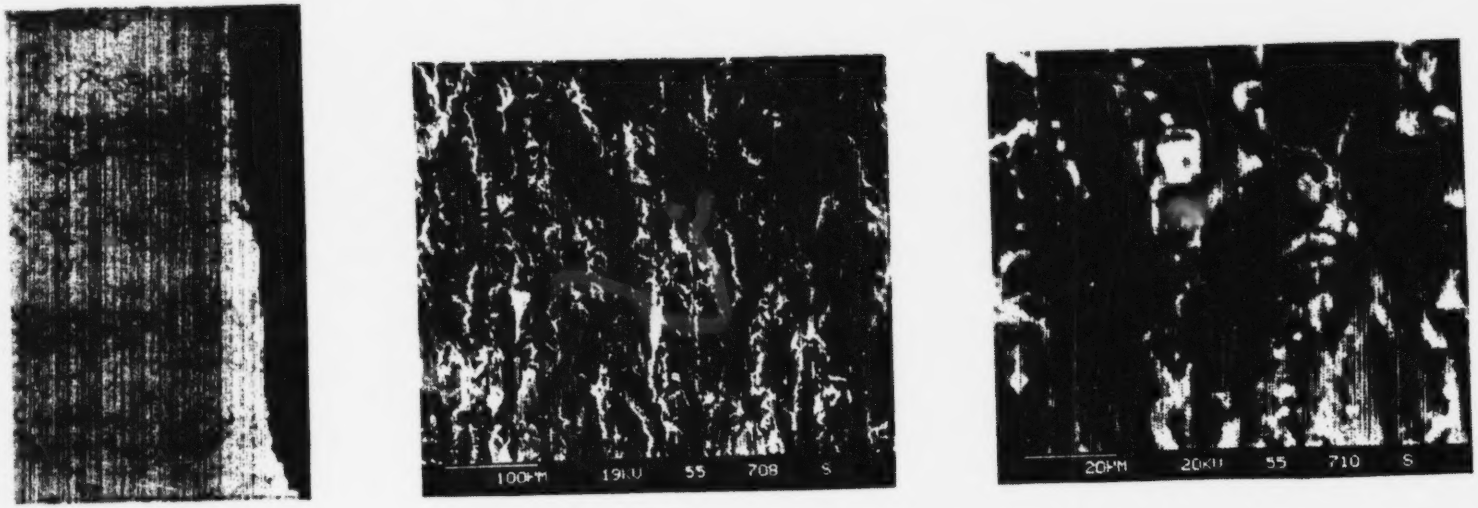
100μm 19KV 55 708 S
20μm 20KV 55 710 S

LAB AIR **PECHINEY FORGING** **L-T, R=0.1, ΔK=7 MPa√m, 20Hz**

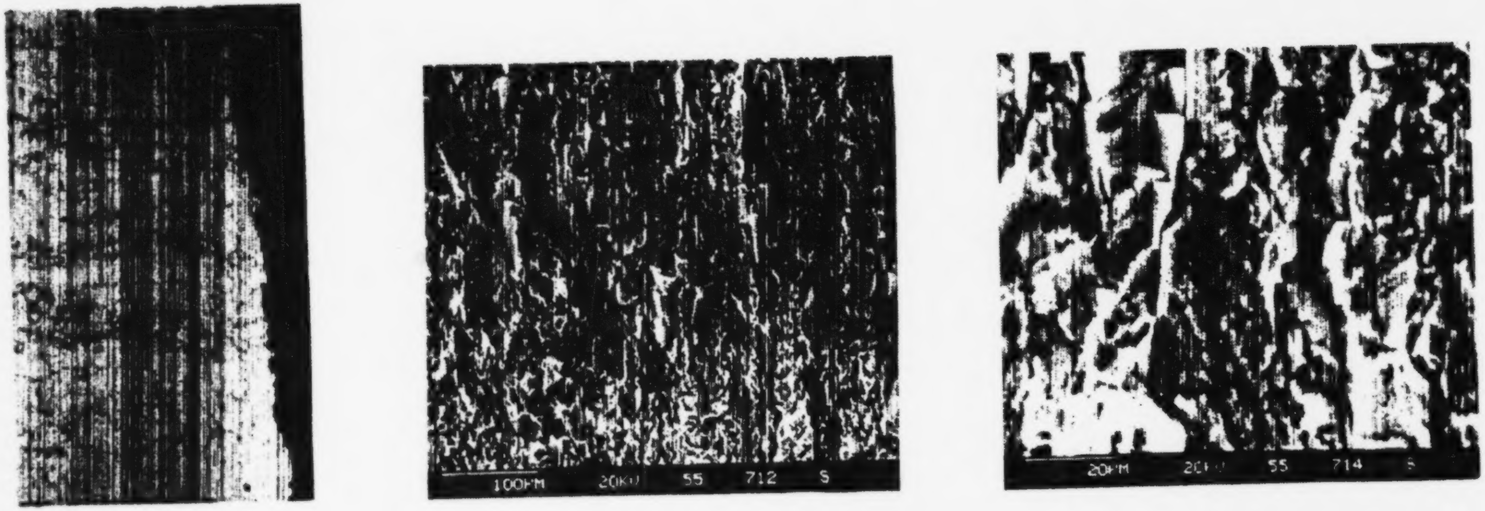
100μm 20KV 55 712 S
20μm 20KV 55 714 S

3.5% NaCl **PECHINEY FORGING** **L-T, R=0.1, ΔK=7 MPa√m, 20Hz**

FIGURE 23

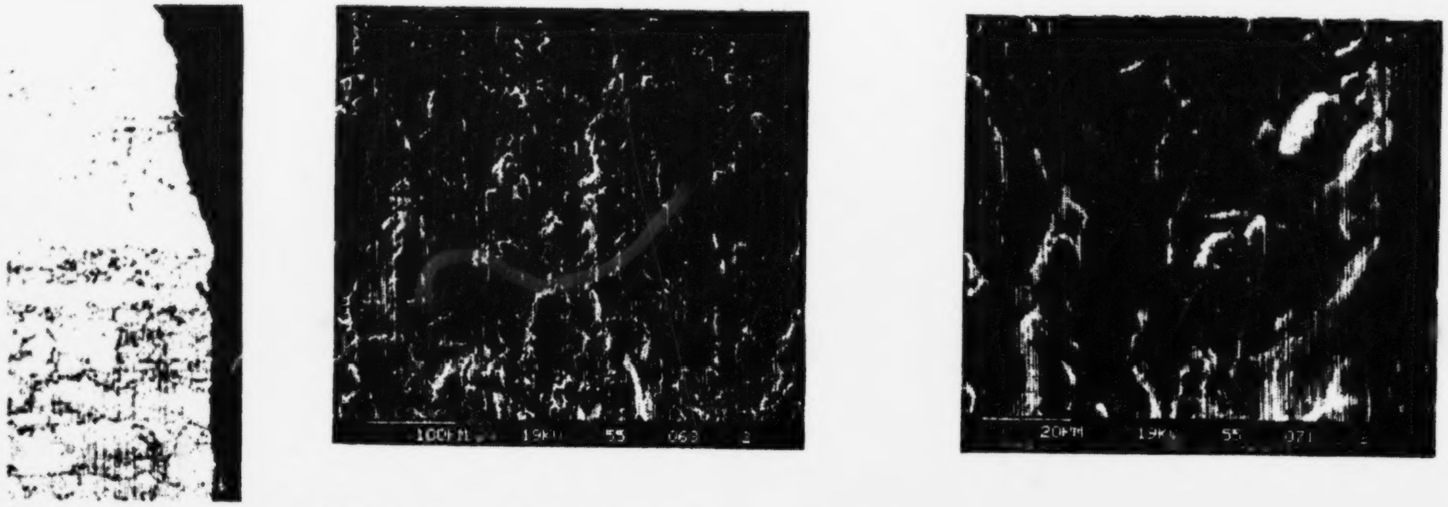
100µm 19KV 55 063 2
20µm 19KV 55 071 2

LAB AIR ALCAN FORGING L-T, R=0.1, ΔK=7 MPa√m, 20Hz

100µm 19KV 55 073 2
20µm 20KV 55 075 2

3.5% NaCl ALCAN FORGING L-T, R=0.1, ΔK=7 MPa√m, 20Hz

FIGURE 24

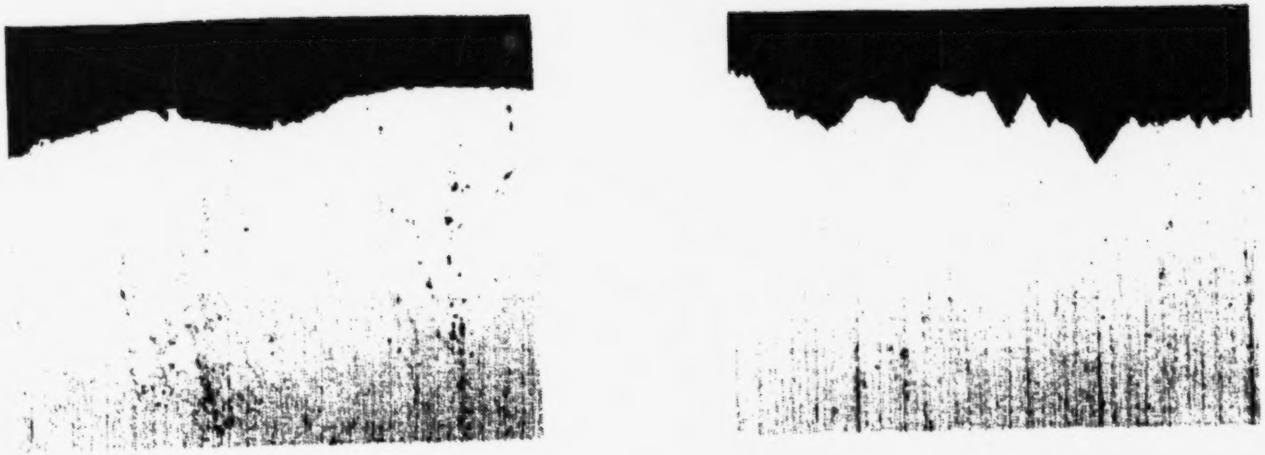

⊥ TO CRACK FRONT LAB AIR ALCAN PLATE (TTCP) ∥ TO CRACK FRONT

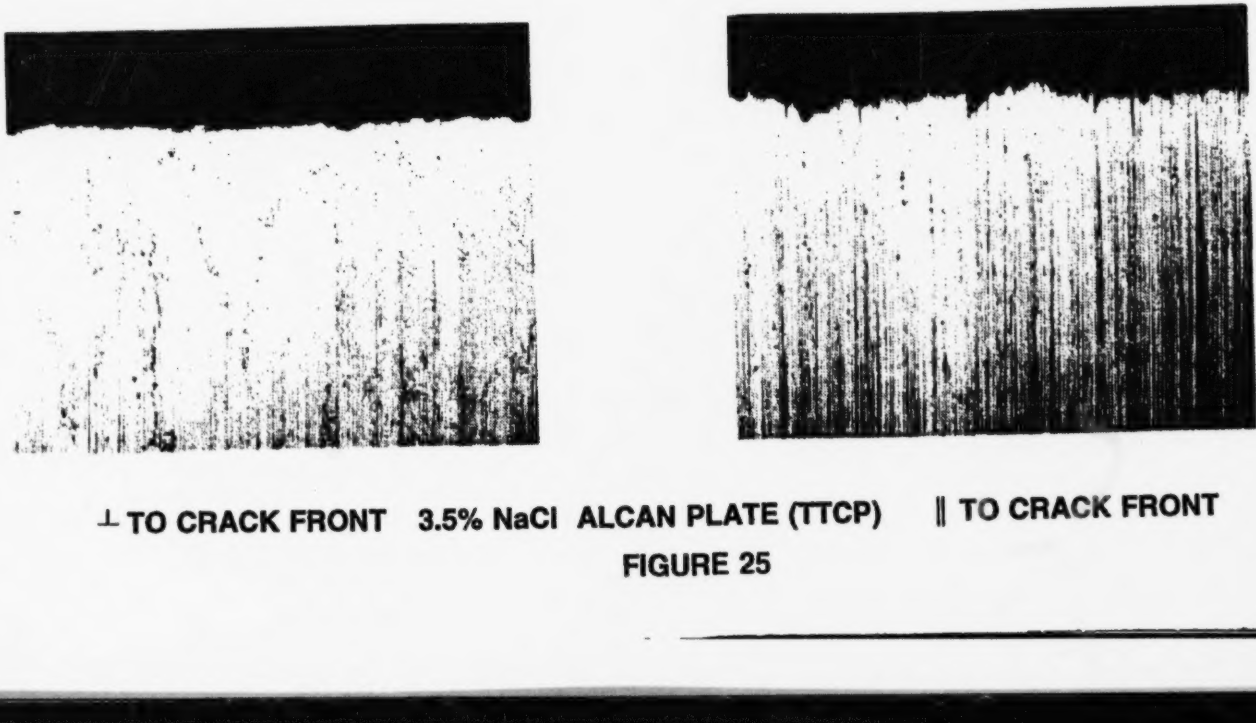

⊥ TO CRACK FRONT 3.5% NaCl ALCAN PLATE (TTCP) ∥ TO CRACK FRONT

FIGURE 25

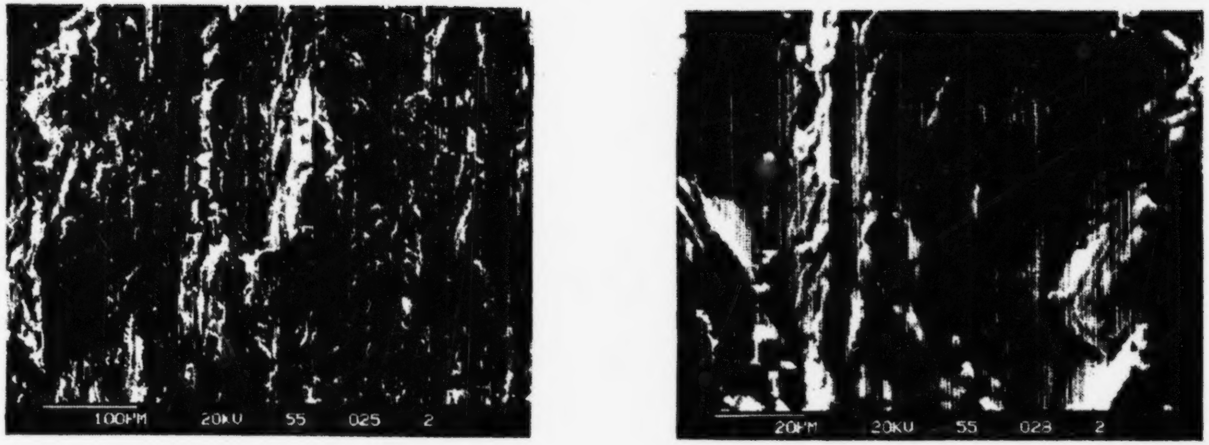
100ΡΜ 20KU 55 025 2
20ΡΜ 20KU 55 028 2

LAB AIR ALCAN PLATE (TTCP) L-T, R=0.1, ΔK=7 MPa√m, 20Hz

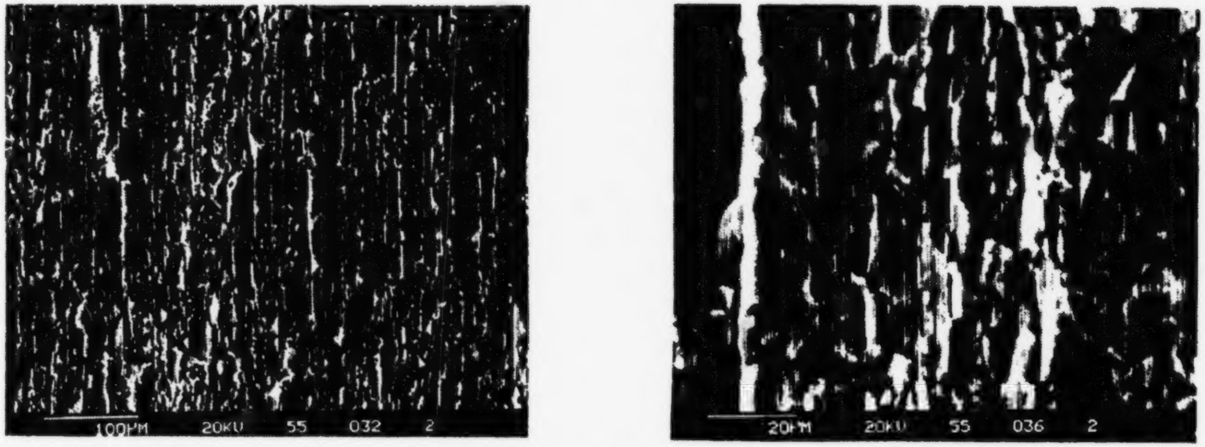
100ΡΜ 20KU 55 032 2
20ΡΜ 20KU 55 036 2

3.5% NaCl ALCAN PLATE (TTCP) L-T, R=0.1, ΔK=7 MPa√m, 20Hz

FIGURE 26

141637

5.

"Tensile and Fatigue Properties of an Aluminum-Lithium Alloy at Low Temperatures"

T. Bui-Quoc and M. Bernard

Ecole Polytechnique, Montreal, P.Q.

TENSILE AND FATIGUE PROPERTIES OF AN ALUMINIUM-LITHIUM ALLOY AT LOW TEMPERATURES

by:

Thang BUI-QUOC, professor, eng.
and Marie BERNARD, professor, eng.
Dept. of Mechanical Engineering
École Polytechnique de Montréal

---

1. INTRODUCTION

Al-Li Alloys have an excellent potential for use as aircraft structure materials because they offer significant weight saving as compared with other structural aluminium alloys [1]. The outstanding potential of these alloys has given rise to many studies in the past [2-4].

The effort has mostly been focused on the development of the microstructure of Al-Li Alloys for improving their mechanical properties which depend upon many parameters such as chemical composition, methods of fabrication, heat treatment, temperature, etc. Due to a wide range of potential variations of these parameters, it is not possible to study their combined effect. Therefore, the usual approach is to have individual presentations.

Considering the actual knowledge on the fatigue performance of relatively high strength Al-Li Alloys, the objective of this project is to investigate the tensile and fatigue properties of a potentially high strength alloy with a particular heat treatment condition, in order to establish the effect of the following parameters:

- Orientation of specimen axis; the effect of the specimen orientation on the tensile and fatigue properties at room temperature will be examined. Two extreme orientations, longitudinal (rolling) and transverse, will be considered.

- Low temperature; the effect of low temperature (-20 and -56°C) on tensile and fatigue properties will be investigated in relation with those obtained at room temperature. The lowest temperature (-56°C) represents the atmosphere temperature at 40 000 ft in altitude.

- Microstructure; a microstructure examination on the rupture surface will be made in order to obtain pertinent information concerning the mechanisms involved in the rupture process for both tensile and fatigue loadings.

2. EXPERIMENTAL PROCEDURE

2.1 Material

The Al-Li Alloy investigated in this project is of the type 2090 in a sheet form of 0.063 in. in thickness. The chemical analysis has been made and its composition is reported in Table 1. The specified heat treatment is to be T8E50 (now designated as T84) to obtain a higher toughness than that with T8E41 (now designated as T83) treatment; the 2090 T8E41 Al-Li Alloy was intended for replacement of the 7075-T6 Aluminium Alloy. According to the most recent phase diagram [5], this Al-Li Alloy is composed of two phases $(\alpha + \delta')$; the microstructure, illustrated in Figure 1, shows a strong texture in the rolling direction. The hardness varies in the range of 82 to 85 R_B (Rockwell Hardness, Scale B).

2.2 Specimens

The specimen geometry with a uniform gage length is shown in Figure 2. The specimen axis is oriented along the rolling direction (hereafter identified as orientation L). In addition, a series of specimens with the axis oriented along the transverse direction (orientation T) has also been considered in order to establish the anisotropy effect on material properties. The surface of the sheet, in the as-received condition, presented many small scratches. The lateral surfaces of the specimen have not been polished in order to respect faithfully the actual situation of the component in service.

2.3 Testing machine and environmental chamber

Tests were performed on a MTS closed loop servo-hydraulic testing machine with a maximum capacity of 55 000 lb. A calibrated 10% scale (maximum load of 5 500 lb) was used.

For low temperature testing conditions, the specimen was cooled inside an environmental chamber. Cooling is accomplished by a direct injection of liquid nitrogen behind the air baffles in the chamber interior. The air baffles provide diffused air flow achieved by a circulation fan. During the temperature calibration phase, the specimen temperature measured by three thermocouples simply in contact with the specimen along the gage length were compared with those obtained from three other thermocouples embedded in the specimen through just-fit holes at the same locations. The temperature gradient along the central portion of the specimen was less than 3°C.

During a test, the chamber temperature was monitored by a thermocouple in contact with the specimen and the temperature at the central portion of the test sample was maintained within 2°C. The test temperature was reached after a cooling period of 3/4 hour for -20°C and of 1 1/4 hour for -56°C; during an additional half hour, the specimen was then maintained at zero stress for material stabilization before starting the test. The experimental facilities and the testing procedure have been described in detail in [6, 7].

2.4 Testing conditions

Short-term tensile tests were carried out on specimens cut in the longitudinal direction at room temperature, -20°C and -56°C. In addition, tests were performed at room temperature on specimens cut in the transverse direction. For each selected testing condition (temperature and specimen orientation) two tests have been performed.

Fatigue behaviour was investigated at room temperature, -20° and -56°C for longitudinal direction and at room temperature for transverse direction. During the cyclic tests, the maximum and minimum values (5% of the maximum load) of the load were controlled. The driving signal was a sinusoidal waveform with a frequency of 10 Hz. For each selected testing condition (temperature and stress level), tests were repeated six times. The fatigue life corresponds to the complete rupture of the specimen; for some cases in the low stress region, tests were stopped when the applied cycles significantly exceeded the planned number of cycles at failure.

3. EXPERIMENTAL RESULTS AND ANALYSIS

3.1 Tensile test results

3.1.1 Effect of specimen orientation

Data obtained at room temperature for longitudinal and transverse directions are presented in table 2. The effect of the specimen orientation on the main static tensile properties at room temperature is quite significant. In fact, with respect to the values associated with the L-oriented specimen, the yield stress and ultimate tensile strength of the T-oriented specimens are reduced by about 8%; however, the elongation and the reduction of area increase by 14 and 80%, respectively. On the other hand, the elastic modulus and the true stress at fracture remain essentially unchanged. The reduction of area is very sensitive to specimen orientation; this may be explained by the preferential orientation of the grains, as already shown in Fig. 1.

3.1.2 Effect of temperature

The effect of the temperature on the main static tensile properties is shown in Figures 3a and 3b. It appears that the true stress at fracture, the yield stress and the ultimate tensile strength slightly increase with a decrease of the temperature. For example, with respect to the values obtained at room temperature, these properties increase by a percentage smaller than 2.5%. In particular, the material seems to be more resistant against the flow condition at -20°C (see Figure 3a). This characteristic is closely related to the variation of the elongation and the reduction of area with the temperature, as illustrated in Figure 3b. The situation will be discussed in relation with the microstructure examination in section 4.

3.2 Fatigue test results

3.2.1 Effect of specimen orientation

The results obtained at room temperature for longitudinal and transverse orientations are plotted in Figure 4. It appears that, for a given stress level, the fatigue resistance of the T-oriented specimens is smaller than that of the L-oriented specimens. The ratio in lives is almost constant and close to 1.8.

This characteristic is closely related to the microstructure composed of layers parallel to the rolling direction. In addition, the voids observed in the microstructure along the interface of the layers are more sensitive to the loading direction; it is, therefore, expected that the material strength is lower under transverse loading than under longitudinal loading.

3.2.2 Effect of temperature

The fatigue curves, based on the average lives at 20°, -20° and -56°C are plotted together in Figure 5 for comparison purposes. It is seen that, for a given stress, the 2090-T8E50 offers the weakest fatigue strength at -20°C, whereas it becomes the strongest at -56°C (for the three temperatures considered). Furthermore, it is expected that the fatigue limit at -20°C would be levelled at the lowest stress.

The effect of the temperature on the fatigue resistance of the Al-Li Alloy investigated is clearly shown in Figure 6 with the applied stress level as a parameter. For example for 50 ksi, in comparison to the fatigue life at room temperature, the life at -20°C is reduced by a factor of 1.33 whereas the life at -56°C increases by a factor of 1.70. These factors depend upon the stress level.

4. MICROSTRUCTURE EXAMINATION

The morphological analysis of the fracture profiles and the fracture surfaces of the specimens failed under static or fatigue loading has been made by means of a scanning electron microscope. The examination of these surfaces has permitted to identify the failure modes involved in the fracture process under different loading conditions.

4.1 Static tensile rupture

The fracture surfaces of the specimen under tensile loading were essentially of transgranular nature with an increased tendency of intergranular decohesion at the grain boundaries during the crack propagation phase.

At room temperature, many crack onset points on both surfaces of the specimen were observed; the presence of dimples on the grain surfaces indicated significant plastic deformations at the grain boundaries. In addition, delamination was noted at the mid-thickness. At -56°C, it appeared that the two fracture mechanisms, transgranular and intergranular cracking, were activated simultaneously with an increase of the intergranular fracture mode.

4.2 Fatigue rupture

4.2.1 Tests at room temperature

At room temperature, with a low stress loading (40 ksi) the fracture profiles showed many crack initiation points on both lateral surfaces of the specimen. The crack was transgranular and propagated along two different planes. During the propagation phase, extended striation zones with dimples were noted with the presence of numerous secondary cracks oriented parallel to the propagation front; these cracks followed the grain boundaries where the secondary phase particles were located. At the mid-thickness, intergranular decohesion was observed (Figure 7).

As the stress increased, the fracture surface became more fibrous. The crack onset points on the lateral surfaces were more numerous with important plastic deformations at the grain boundaries. No striations were observed on the fracture surface. On the other hand, the morphology of the crack surface was less crystallographic than that for the low stress cases; however, the fracture profiles showed an increase of intergranular decohesion.

4.2.2 Tests at -20°C

For tests at a low stress (40 ksi), the presence of many onset points indicated that the crack initiation sites were multiple. However, the number of elliptic zones was much smaller than that at room temperature. On the propagation surface, many cleavage-like zones were noted. Dimpling became less evident and grain boundary separation took place. This situation suggested that the material exhibits a tendency for brittle fracture. No striations were observed. The crack surface corresponding to the initiation period was of transgranular nature with an increasing tendency for intergranular decohesion during the propagation phase.

At a high stress (70 ksi), there were numerous non-coplanar crack onset points extending in small elliptic zones. The fracture surfaces were more fibrous. As in case of 20°C with high stress loading, the extent of the region of intergranular decohesion and delamination was relatively large (about 80% of the total ruptured surface) with a particular characteristic due to the presence of cleavage-like zones. The dimples on the grain surface were observed only at the last phase of the propagation period.

4.2.3 Tests at -56°C

The fracture surfaces of the specimens subjected to a low stress (40 ksi) presented essentially a smooth and transgranular fracture with indication of small intergranular decohesion during the propagation period. At the mid-thickness, the delamination became extensive. The elliptic zones appearance on the fracture surfaces were similar to those already observed for tests at the two other temperatures. However, there is no evidence concerning the cleavage-like morphology characterizing brittle fracture. No striations were observed.

At a higher stress (70 ksi), the number of crack onset points was larger than that in the previous case and there was an increase of the tendency for intergranular cracking; the striations became more evident in extended zones. Fracture profiles showed that intergranular cracking occurred early in the initiation phase.

4.2.4 Discussion

In summary, the fracture surfaces of the material subjected to fatigue at the three temperatures considered showed mainly transgranular crack initiation with a presence of dimples on the grain surfaces corresponding to the propagation zone. In particular, relatively few dimples were noted for specimens failed at -20°C; this is a characteristic associated to a brittle failure. In general, the effect of the temperature on the cracking mode seems to be very small and the intergranular cracking nature increases with the stress level. The strongest evidence of the predominance of this cracking mode was noted for tests with a high stress at -56°C. On the basis of fracture surface observations, the fatigue crack seems to propagate with the fastest rate at -20°C. Further investigations should be carried out to explore the crack growth behaviour under different stress and temperature conditions. The experimental results may then be combined with the observations performed on the fracture surfaces by means of an advanced technique (e.g. TEM) to obtain pertinent information concerning the fatigue characteristics of the material studied at -20°C with respect to those obtained at the other two temperatures.

5. CONCLUSION AND RECOMMENDATIONS

Experimental investigations on the tensile properties and the fatigue behaviour of 2090-T8E50 Al-Li Alloy at 20, -20 and -56°C have been carried out. In addition, the effect of the specimen orientation has also been examined. The main conclusions are as follows.

1) The temperature effect on the static tensile properties is relatively small. At low temperature, the yield and ultimate tensile strengths are larger by about 2.5%; however, the alloy becomes more brittle.

2) The specimen orientation has a significant effect on the static tensile properties at room temperature. In fact, the yield and ultimate tensile strengths of the transversally-

oriented specimens are reduced by about 8% with respect to those of the rolling-oriented specimens.

3) The experimental curves in the fatigue diagram (σ - N diagram) have the common characteristics of the fatigue behaviour of aluminium alloys. For a given stress, the material offers the weakest strength at -20°C and the strongest strength at -56°C. The average life range for the three temperatures considered varies within a factor of 3.

4) The effect of the specimen orientation on the fatigue resistance is quite significant at room temperature. For a given stress, the transversally-oriented specimen has a life smaller than that of the rolling-oriented specimen; the ratio between the two lives is close to 1/1.8.

5) The fracture surfaces of the material failed under fatigue loading with a low stress indicate, for the three temperatures considered, a transgranular crack initiation mode with the presence of dimples on the grain surfaces for the subsequent phases. However, relatively few dimples are noted for tests at -20°C in comparison with the cases of the other two temperatures; this is a result of a relatively brittle fracture. When the stress increases, the intergranular cracking mode becomes more important with the highest crack growth rate in tests at -20°C.

6) Further investigations on the material behaviour are recommended to determine the crack growth characteristics under different stress and temperature conditions. The results will be combined with an examination using transmission electron microscope in order to identify the mechanisms involved in the crack nucleation and propagation.

6. REFERENCES

1. KAR, R.J., AGRAWAL, S.P. and QUIST, W.E., (Eds), "Aluminium-Lithium Alloys: Design, Development and Application Update," ASM Int., 1988, part III.
2. SANDERS, T.H. Jr. and STARKE, E.A., Jr., (Eds), "Aluminium-Lithium Alloys II", Proc. 2nd Int. Al-Li Conf., April 12-14, 1983, The Metallurgical Society of AIME.
3. BAKER, C., GREGSON, P.J., HARRIS, S.J. and PEEl, C.J., (Eds), "Aluminium-Lithium Alloys III", Inst. of Metals, Oxford, UK, 1986.
4. CHAMPIER, G., DUBOST, B., MIANNAY, D. and SABETAY, L., (Eds), Colloque no. 3, Jl de Physique, Proc. 4th Int. Al-Li Conf., June 10-12, 1987, Les Éditions de Physique, les Ulis Cedex, France.
5. WILLIAM, D.B., "Microstructural Characteristics of Al-Li Alloys," Al-Li Alloys, Metallurgical Society of AIME, 1980, pp. 90-100.
6. BUI-QUOC, T., GOMUC, R., BIRON, A., NGUYEN, H.L. and TADROS, R.N., "Cyclic Stress Strain Behavior and Low-Cycle Fatigue of Ti 6242," Jl of Testing and Evaluation, Vol. 18, 1990, pp. 160-171.
7. BUI-QUOC, T. and BERNARD, M., "Residual Toughness Due to Crack Extension", proc. Sixth Int. Conf. on Mech. Behavior of Mat., Kyoto, Japan, July 1991.

TABLE 1

CHEMICAL COMPOSITION OF 2090 Al-Li ALLOY USED IN THE PRESENT PROGRAM.

Element	Al	Li	Cu	Fe	Cr	Na	Mn	Mg
Wt(%)	95.69	1.51	2.70	0.066	0.004	0.019	0.004	0.003

TABLE 2

STATIC TENSILE PROPERTIES OF 2090 T8E50 (or T84) AT 20°C

SPECIMENS PROPERTIES	LONGITUDINAL DIRECTION	TRANSVERSE DIRECTION
Elastic Modulus (10^3 ksi)	11.0	10.7
Yield Stress (ksi)	70.9	64.9
Ultimate Tensile Strength (ksi)	76.7	70.8
Elongation on 1/2" (%)	10.6	12.1
Reduction of Area (%)	14.1	25.5
True stress at fracture (Ksi)	86.4	86.4

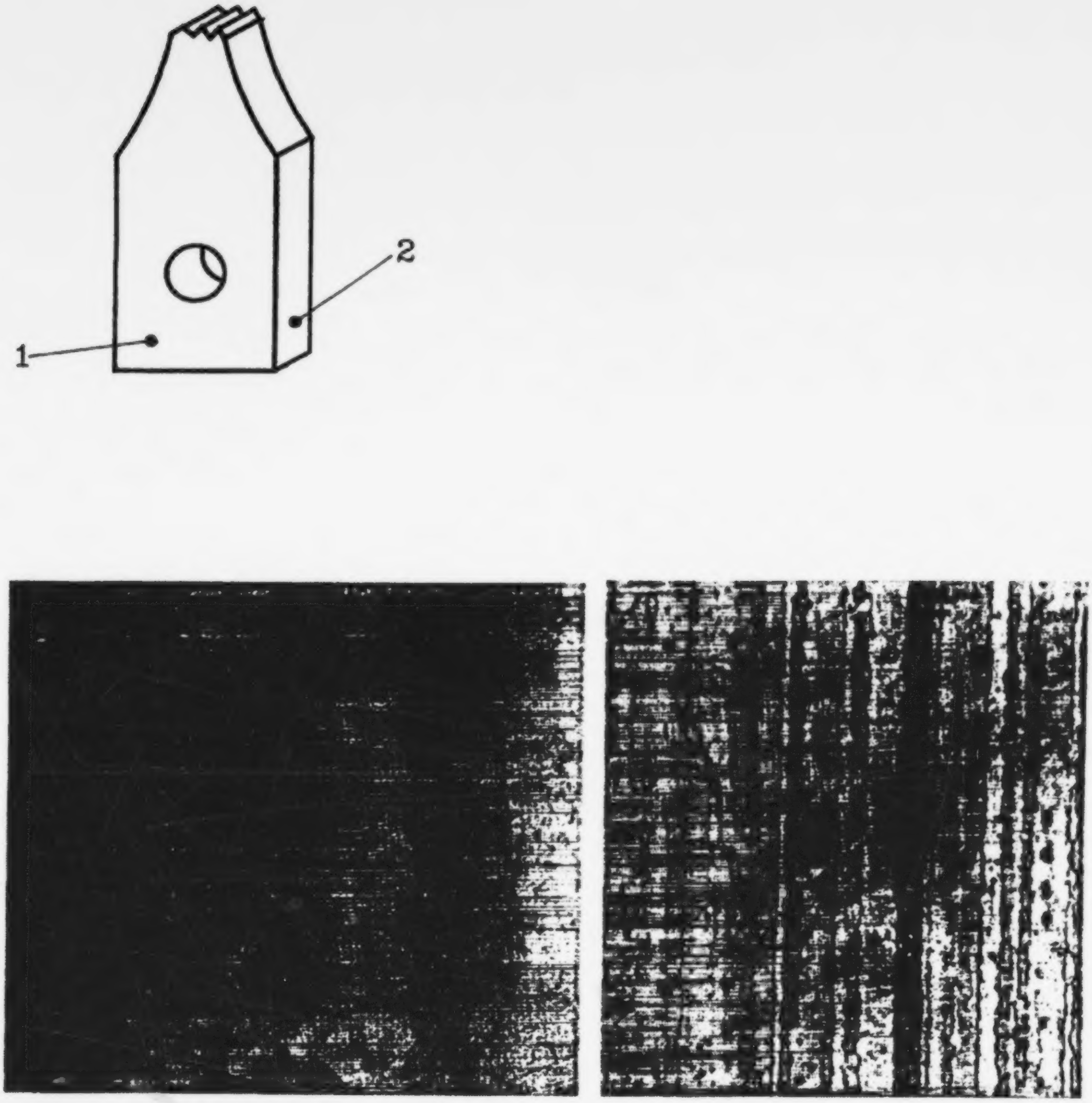

FIGURE 1: Microstructure of 2090 T8E50 Al-Li Alloy along the rolling direction.

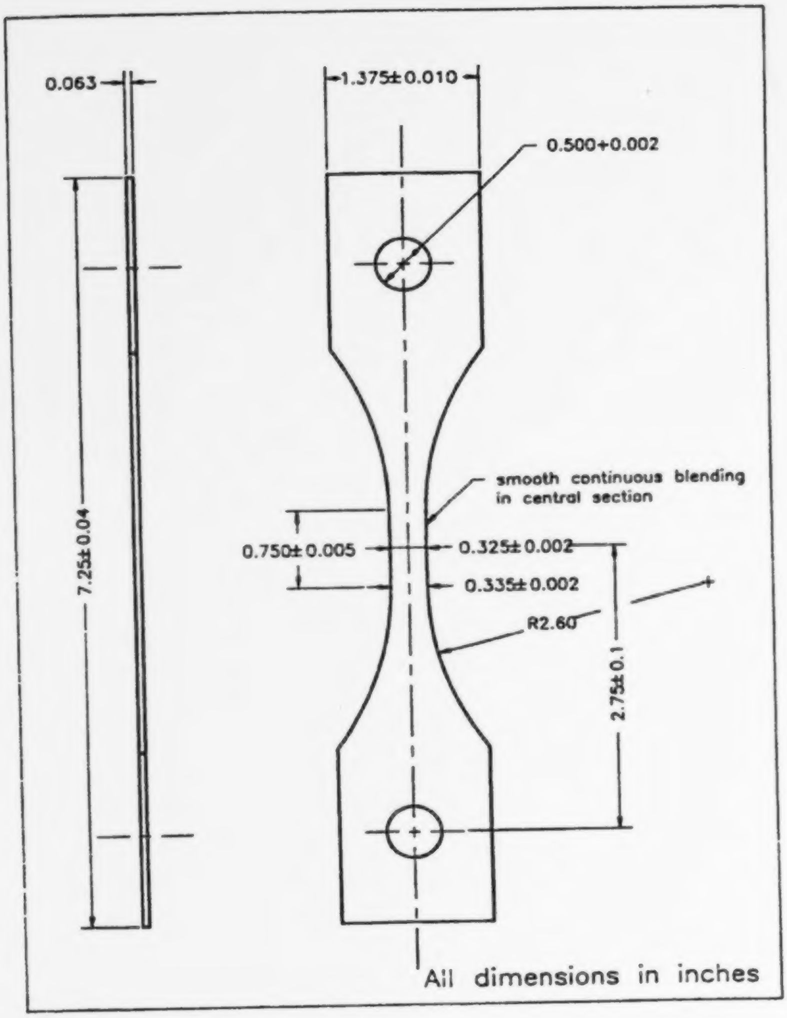
0.063
1.375±0.010
0.500+0.002
7.25±0.04
smooth continuous blending
in central section
0.750±0.005
0.325±0.002
0.335±0.002
R2.60
2.75±0.1
All dimensions in inches

FIGURE 2: Specimen geometry

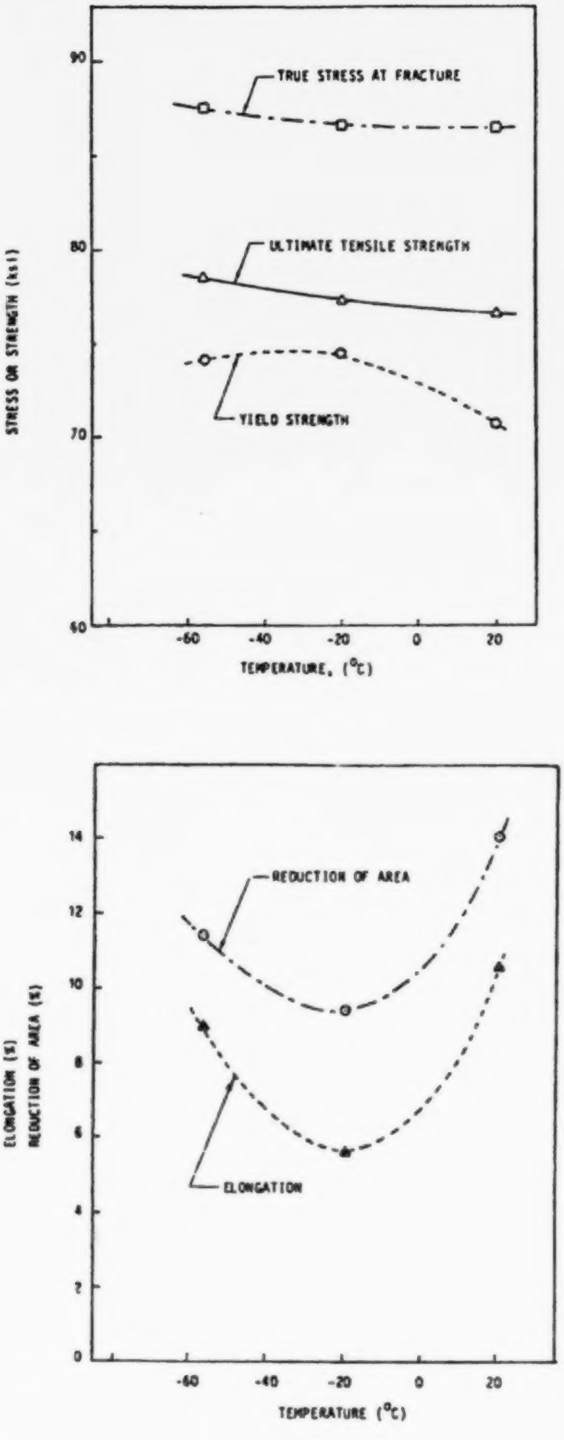

FIGURE 3: Effect of temperature: a) on the yield and ultimate tensile strengths and on the true stress at fracture; b) on the elongation and on the reduction of area.

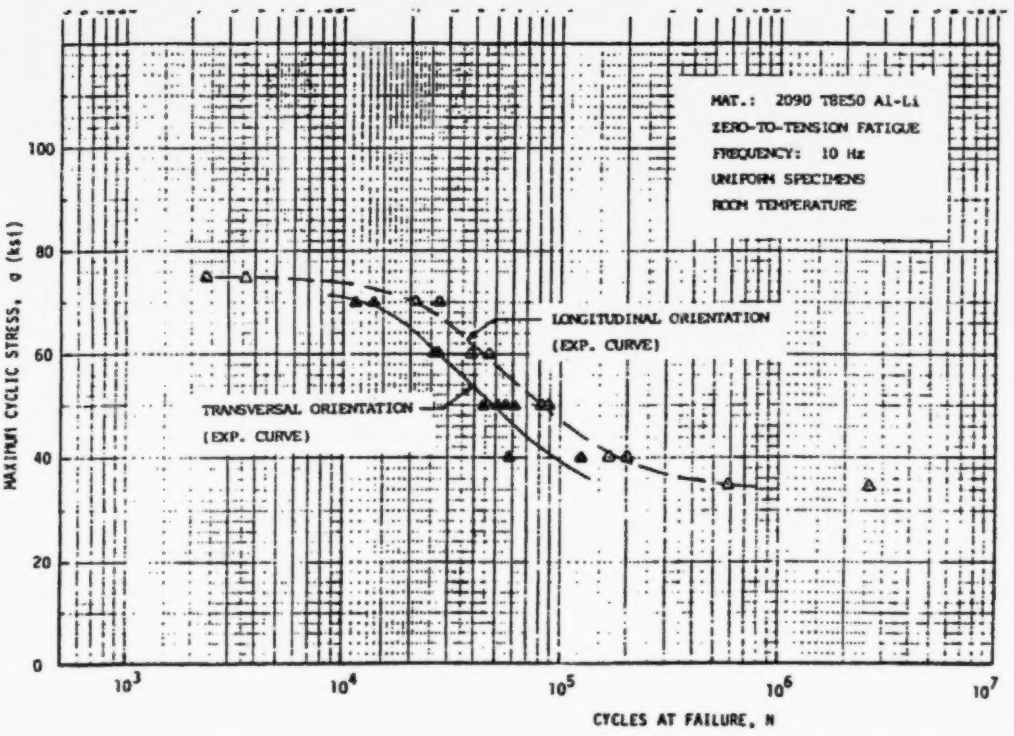

FIGURE 4: Effect of specimen orientation on fatigue properties at 20°C.

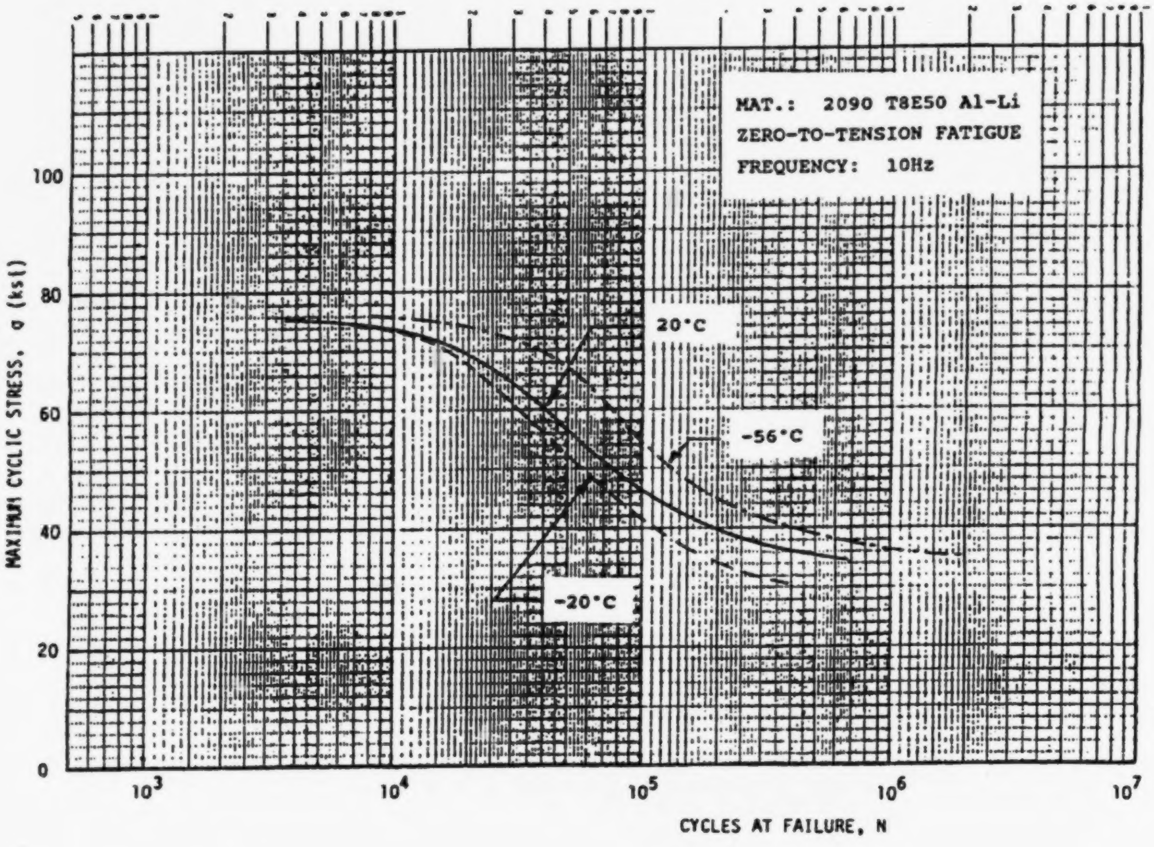

FIGURE 5: Fatigue life of 2090 T8E50 Al-li alloy at room temperature, -20° and -56°C.

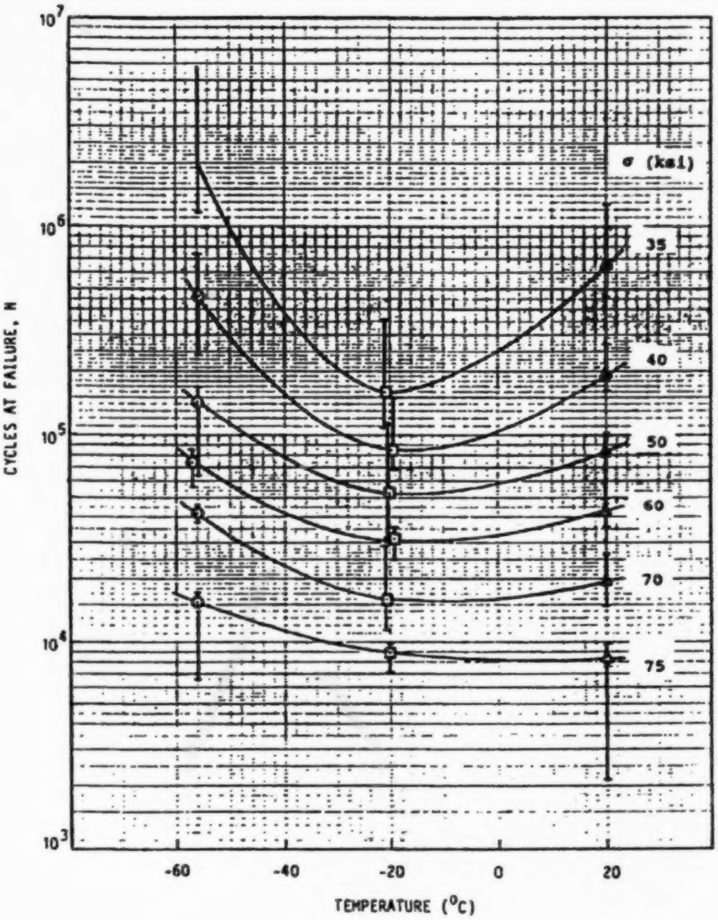

FIGURE 6: Temperature effect on fatigue properties with maximum cyclic stress as a parameter.

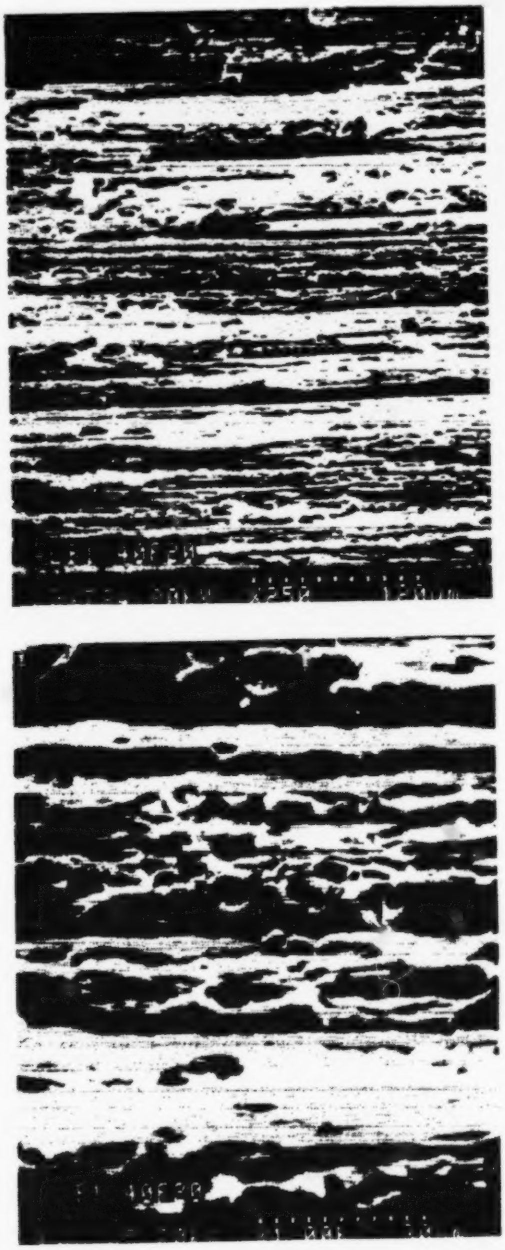

FIGURE 7: Intergranular decohesion at mid-thickness of a specimen under a fatigue test with a low stress at room temperature.

141638

6.

"The Effect of Shot Peening on the Fatigue Fracture Behaviour of Advanced Airframe Alloys"

M. Ferahi and S.A. Meguid

University of Toronto

THE EFFECT OF SHOT-PEENING ON THE FATIGUE FRACTURE BEHAVIOR OF ADVANCED AIRFRAME ALLOYS

M. Ferahi* and S. A. Meguid*

The present work examines the effect of shot-peening residual stresses upon fatigue crack initiation and propagation behavior of Aluminum-Lithium 2090-T81. Accordingly, uniaxial fatigue tests were conducted on specimens containing a high stress concentration notch. The residual stress field was evaluated using the incremental hole drilling technique. The presence of high compressive residual stress in the vicinity of the surface resulted in slower growth of physically short (100-500 μm.) and relatively long (500-2000 μm.) corner cracks emanating from the notch. The results also reveal that the crack morphology is influenced by the presence of the residual stress field.

INTRODUCTION

Shot-peening is employed as one of the most effective surface treatments for improving the fatigue properties of engineering components. The method is used to enhance fatigue strength, reduce fatigue crack growth rate, and retard stress corrosion cracking. Earlier studies showed that the fatigue performance of high strength 7000 Al alloys can be significantly improved by shot-peening (Hammond and Meguid (1), Oshida and Daly(2) and Mutoh et al (3)). This improvement in fatigue life is due mainly to the high surface compressive residual stresses introduced by the peening treatment.

It must be recognized, however, that surface compressive residual stresses are not permanent. They fade-out (relax) with cyclic loading (James (4)). The time dependent relaxation of these residual stresses strongly influence the fatigue fracture behavior of the treated components. The rate at which the residual stress field relaxes is governed by: (i) the applied load and its history, (ii) the mechanical properties and (iii) the microstructure of the treated components.

The effect of compressive residual stresses upon the fatigue fracture performance of high strength Al-Li 2090-T81 have not been investigated. In view of their

*Engineering Mechanics and Design Laboratory, Department of Mechanical Engineering, University of Toronto.

significant reduction in density, increase in elastic modulus, and compatibility with existing metal forming techniques, Al-Li alloys are currently being considered as replacement for conventional 7000 aluminum series in various applications in the aircraft industry. In this study, attention is devoted to the characterization of the induced shot-peening residual stresses, evaluate their effects on fatigue initiation and propagation of cracks emanating from high stress concentration features, and the interaction of these effects with the cyclic load level.

METHOD

Rolled Al-Li alloy 2090-T8 was received in a 12.7 mm thick plate form from ALCOA. The chemical composition is given in Table 1. The T8 temper corresponds to solution treatment at 549 °C, 6% stretch and aging at 163 °C for 18 hours. The material exhibits a highly anisotropic microstructure, with an average grain size of 50μm, 500μm and 3 mm in the short transverse (ST), the long transverse (LT) and the longitudinal (L) orientations, respectively. The L orientation being the rolling direction. The measured mechanical properties are given in Table 2.

TABLE 1 - Chemical Composition of Al-Li 2090 alloy (wt%)

Cu	Li	Zr	Fe	Si	Mg	Mn	Ti	Zn	Cr
2.4-3.0	1.9-2.6	0.08-0.15	0.12	0.1	0.25	0.05	0.15	0.1	0.05

TABLE 2 - Mechanical Properties of Al-Li 2090-T81 alloy (wt%)

Orientation	Yield Stress (MPa)	Tensile Stress (MPa)	Elongation (%)
L	552	586	8.2
LT	548	586	6.5

A digitally controlled electro-hydraulic servo-controlled fatigue test equipment was used to conduct uniaxial fatigue tests of specimens containing a semi-circular notch through the thickness with a stress concentration factor of 3.26. The uniaxial loading was applied parallel to the rolling orientation. The tests were carried out under load control with a sinusoidal waveform at a frequency of 20 Hz. All tests were conducted at room temperature at a stress ratio R = 0.1.

The notch surface was shot-peened to an Almen intensity of 12-14 A, with S330 shots and a coverage of 100%. The peening parameters were selected in compliance with the Military Specifications 13165C for conventional Al alloys of comparable strength to Al-Li.

The resulting residual stress field was measured using the incremental hole-drilling technique (ASTM (5)). The method was modified to accommodate the non-uniformity of shot-peening residual stresses. The modified approach, which is based on the integral method of Schajer (6), adopts the finite element to evaluate the calibration constants associated with a non-uniform stress distribution, and takes into account the unequal contributions to the measured surface strain from stresses at different depths. The calibration constants were calculated for two commercial strain gage rosettes, and their accuracy was checked by measuring bending stresses in beams. A discrepancy of about 10% from the theoretical bending stresses was observed.

Crack initiation and growth was monitored by examining cellulose acetate replicas of lightly polished surfaces in a light optical microscope. Both the surface of the notch as well as the side surfaces ahead of the notch root were replicated. This allowed the monitoring of the length of the corner crack (c) in the direction of the thickness (ST orientation), and the crack depth (a) in the long transverse orientation (LT). The replicas were taken at a load equal to 80% of the maximum load. A number of tests were interrupted and the specimens were broken and observed in a scanning electron microscope (SEM) to study the crack morphology.

RESULTS AND DISCUSSIONS

Despite the anisotropic and inhomogeneous nature of the material, the measured strains revealed an equal biaxial residual stress field. The residual stress distribution in the peened specimen is shown in Figure 1. The distribution showed a compressive layer of 600μm, with the maximum occurring at a depth of 200μm below the peened surface. The residual stress in the machined specimens was relatively negligible compared to the applied fatigue loads and the peening residual stresses.

Figure 2 shows the total life of the unpeened and peened specimens as a function of the alternating stress σ_a. The fatigue life of the treated specimens is generally higher than the unpeened specimens. The improvement due to peening is more evident for stress levels approaching the fatigue limit. In both specimens, and for most load levels, the fatigue process began with a corner crack at the root of the notch. Unlike long cracks where significant crack deflection and branching were encountered, the small cracks were initiated and grown perpendicular to the loading axis with little deflection. The initiation life in both unpeened and peened specimens was relatively small compared to the propagation life. This is due in part to the high stress level arising from the high stress concentration factor and the poor fatigue strength associated with the ST orientation in this alloy. Fatigue crack initiation mechanisms are currently being investigated.

The improvement in the fatigue life due to peening resulted from the slower propagation of short and relatively long cracks (150-2000 μm) which grew through the compressive layer of the residual stress field. The crack propagation rates da/dN in both specimens are compared in Figure 3 as a function of crack depth (a). The crack growth rates in the peened specimen are reduced for crack depths beyond the compressive layer. At a crack depth a=1300-1500 μm the propagation rate in both specimens became comparable. The difference in the growth rates is maximum at a depth of 350μm which does not correspond to the location of the maximum compressive residual stress.

Two dimensional finite element approximations of the applied and residual stress intensity factors K^{app} and K^{res} distributions along the crack path for a through-thickness crack is shown in Figure 4. Assuming that the trend of the distributions is similar to that of a corner crack, it is found that the maximum retardation in the peened specimen corresponds to the maximum absolute value of K^{res}. The results show that K^{app} is reduced even in the region of tensile residual stress, which accounts in part for the crack growth retardation in that region.

Another reason for the slower crack advance in the region beyond the compressive layer is the crack shape difference in the peened and unpeened specimens.

Figure 5 shows the crack aspect ratios (c/a) in both specimens as a function of the crack length c. Cracks in the unpeened specimen initiated with an aspect ratio $c/a < 1$ and increased with increasing crack length c. This is due to the fact that as the crack size increases, it becomes more sensitive to microstructure effects (Venkateswara et al (7)), and since the short transverse (ST) orientation had lower crack growth resistance, the crack length c grows faster than the crack depth a advancing in the LT orientation which exhibits higher resistance to crack propagation. In the case of the shot-peened specimens, the aspect ratio remained relatively smaller resulting in a lower crack driving force for the same value of crack depth a. The lower crack aspect ratio in the peened specimen is a consequence of the high compressive residual stress at the notch base where the crack length c is growing. Scanning electron micrographs of the fractured surface of partially fatigued specimens revealed a quarter elliptical morphology of the crack, with a smooth crack front in the unpeened specimens and a relatively tortuous front in the peened ones. The intense fretting between the rough surfaces of the crack during the fatigue fracture process made the crack profile clearly visible in the SEM.

Crack propagation rates in peened and unpeened specimens were investigated for three different load levels. The results presented in Figures 3,4 and 5 were obtained at a maximum alternating stress of σ_a=135 MPa with a stress ratio of R=0.1. Similar results were observed for σ_a= 160 MPa (R=0.1). However, the crack depth at which the rate of growth in peened specimens approached that of the unpeened samples was reduced to a=600-700 μm compared to $a = 1300 - 1500\mu$m for σ_a=135 MPa. This may be due to the residual stress relaxation resulting from the increase in the alternating load. The fatigue data of Figure 3 showed that the total fatigue life for these stresses is of the order of 10^5 cycles. This fatigue regime is between the extremes of low cycle fatigue (LCF) where residual stresses may relax rapidly, and high cycle fatigue (HCF) where the relaxation may not be significant. At a test stress of σ_a=190 MPa (R=0.1), for which the total life corresponds to LCF regime, the propagation rates in both specimens were comparable. Finite element calculation of the stress distribution for this load level resulted in a localized plastic zone ahead of the notch root, which caused the residual stress field to redistribute in the early stage of the fatigue process, resulting in little or no account of peening.

CONCLUSIONS

Fatigue life of notched specimens made of Al-Li 2090-T81 can be improved by shot-peening. Although the fatigue life of the peened specimens is consistently higher, it must be appreciated, however, that due to the scatter in fatigue data, further tests are needed. It is believed that this improvement in life is due to the slower crack propagation of short and relatively long cracks (0.1-2 mm.). The presence of the peening compressive residual stresses in the vicinity of the exposed surface layers reduces the crack aspect ratio c/a, which in turn reduces the crack driving force, resulting in crack growth retardation beyond the compressive layer. The intense fretting between the fractured surfaces is an indication of the roughness induced crack closure present in this alloy. The effect of residual stresses upon the crack closure behavior is currently being investigated. The relaxation of residual stresses at load levels high enough to introduce local plasticity resulted in comparable fatigue crack propagation rates in unpeened and peened specimens. Further studies relating to the optimization of the peening parameters for Al-Li alloys, as well as the relaxation of residual stresses are currently being conducted.

ACKNOWLEDGMENTS

The financial support of the Manufacturing Research Corporation of Ontario and the Natural Sciences and Engineering Research Council of Canada is gratefully acknowledged. Thanks are also due to Ms. S. Verzasconi of ALCOA (Pitsburgh) for provision of the material, and to Mr. B. Billings and the staff of the Metal Improvement Company of Canada for performing the peening treatment.

REFERENCES

(1) D.W. Hammond and S.A. Meguid: Engineering Fracture Mechanics, 1990, Vol. 37, 373-387.

(2) Y. Mutoh, G.H. Fair, B. Noble and R.B. Waterhouse: Fatigue of Engineering Materials, 1987, Vol. 10, 261-272.

(3) Y. Oshida and J. Daly: Surface Engineering, ed. by S. A. Meguid, Elsevier Appl. Sci. Publ., London, 1990, pp.404-416.

(4) M.R. James: Residual Stress and Stress Relaxation, ed. by E. Kula and V. Weiss, 1982, N.Y., 297-314.

(5) ASTM Standards: Standard test method for determining residual stresses by the hole drilling strain gage method, ASTM E-837, 1985.

(6) G. S. Schajer: ASME J. Engineering Materials and Technology, 1988, Vol.110, pp.338-343.

(7) K.T. Venkateswara Rao, W. Yu, and R.O. Ritchie: Metallurgical Transactions , Vol.19, 1988, pp.549-569.

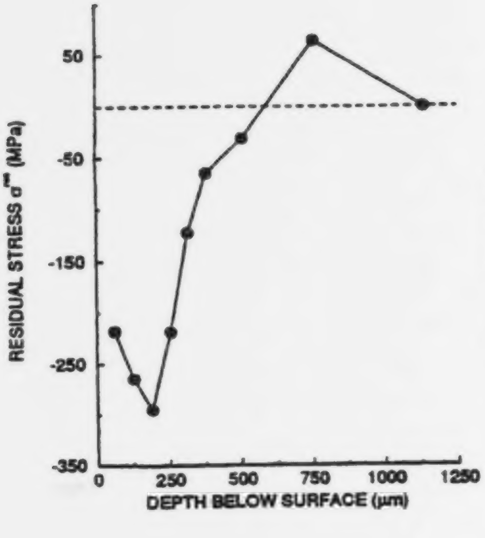

Fig. 1: Residual stress distribution resulting from shot-peening

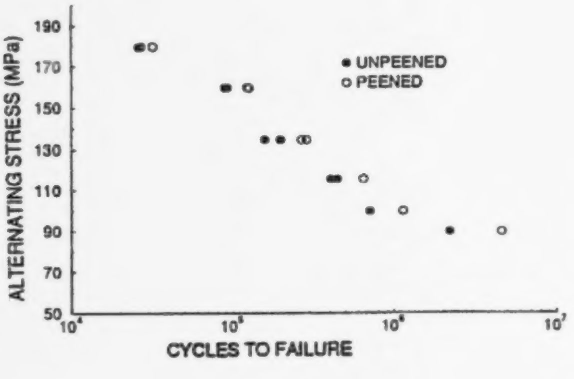

Fig. 2: S–N curves for peened and unpeened specimens

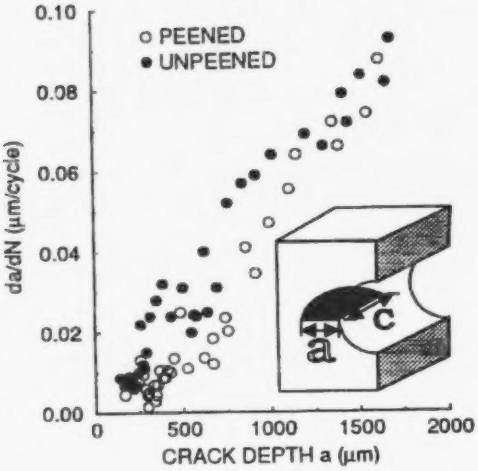

Fig. 3: Comparison of crack growth rates in peened and unpeened specimens

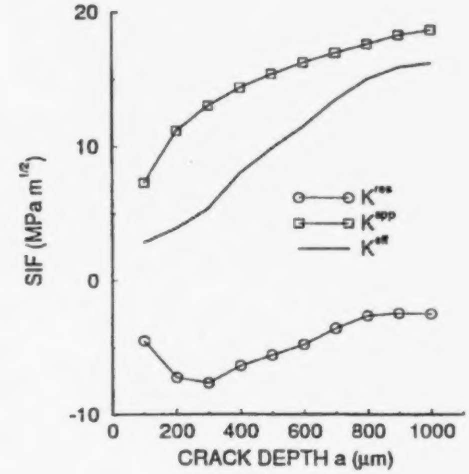

Fig. 4: 2-D. FE of SIF for residual, applied and the effective stresses

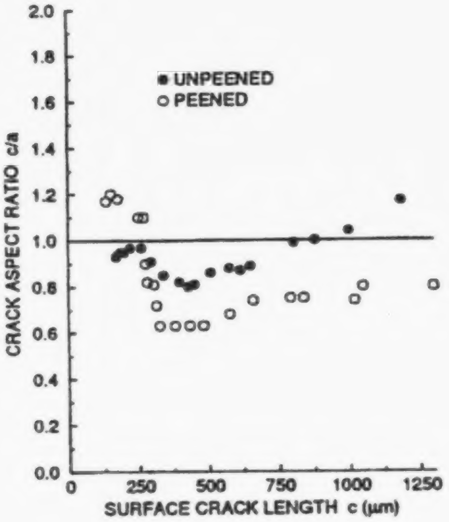

Fig. 5: Crack aspect ratio variation in peened and unpeened specimens

141639

7.

“Effect of Anodizing on the Fatigue Properties of 8090C Alloy Sheet”

A. Douchant and A.M. Abdel-Latif

QETE, Hull, P.Q.

EFFECT OF ANODIZING ON THE FATIGUE PROPERTIES OF 8090C ALLOY SHEET

by

A. Douchant and A. M. Abdel-Latif
Quality Engineering Test Establishment
Department of National Defence
Ottawa, Canada
K1A 0K2

INTRODUCTION

Aluminium -lithium alloys are promising structural materials for aerospace application which require weight-savings with increased stiffness and toughness. Based on the premise that they are similar in all engineering respects to conventional 2xxx and 7xxx aluminium alloys series, they are proposed for direct substitution in existing aircraft designs. One of the main applications of Al-Li 8090 alloy sheet is in the outer skin of the fuselage. Conventionally, the outer skin material are anodized for corrosion protection, adhesive bonding and painting.

It is well established that the fatigue performance of conventional aluminium alloys is deleteriously affected by the sulphuric acid anodizing process. Similar effects have been reported for chromic acid anodizing. Recent research work on chromic acid anodized 8090 Al-Li alloys suggested that the fatigue performance is unaffected by chromic acid anodizing which caused substantial reduction in fatigue life 2014-T651 alloy plate [1]. The objective of the present work was to determine the effects of chromic acid anodizing on fatigue performance of 8090C-T8 alloy and 2024-T3 sheet.

MATERIALS AND EXPERIMENTAL PROCEDURE

8090C-T3 alloy sheets (EM 103) were provided by Westland and were subsequently tempered to the T8 condition at QETE. Aircraft quality 2024-T3 sheet (QQ-A-250) were obtained locally. The chemical composition of both alloys is given in Table 1. Tensile specimens were machined with a central hole (k_t=2.2) to simulate a fastener hole. A batch of fatigue specimens were chromic acid anodized in accordance with Westland procedure. The anodized coatings were then evaluated using radial sectioning, metallography and salt spray testing.

S-N fatigue data were generated from bare and anodized specimens at ambient temperature in lab air at a frequency of 80 Hz and an R ratio of 0.1. The maximum applied stress ranged from 100 to 300 MPa. The effect of orientation on the fatigue performane was investigated using specimens machined in the L and T loading directions. S-N fatigue data were generated for the following conditions:

i) Unanodized 8090-T8 in the L and T and limited 45° loading direction.

ii) Unanodized 2024-T3 in the L and T loading direction,

iii) Anodized 8090-T8 in the L loading direction, and

iv) Anodized 2024-T3 in the T loading direction.

Data were statistically analyzed based upon ASTM E 739 standard where S-N relationships are fitted by a straight line for a specific interval of stress.

RESULTS AND DISCUSSIONS

Effect of Anodizing

The anodized coating was examined visually and using scanning electron microscopic techniques. The thickness of the coatings, shown in Figures 1a and 1b, was determined using a radial sectioning technique. The thickness of the anodic coating on both alloys measured 2 microns. Examination of the coatings indicated that they were uniformly applied with no apparent surface discontinuities or cracks. Detailed SEM analysis revealed the presence of circular pit-like features in the 8090C-T8 anodic coating as shown in Figure 2a. Additionally, elongated indentations were detected in the 2024-T3 anodic coating as shown in Figure 2b. It is believed that these indentations and pit-like features were caused by the pickling process whereby intermetallic particles/phases formed during the tempering process were preferentially attacked. These indentations were not detected in 8090-T8 due to the limited presence of intermetallic particles in the microstructure. The results suggest that 8090C-T8 is not significantly attacked by the pickling process, resulting in a uniformally applied coating. It would be expected that the fatigue life of the substrate metal would not be reduced by the chromic acid anodizing of 8090C-T8 due the absence of sharp stress risers in the coating.

Data shown in Figure 3 suggests that the fatigue life is independent of the orientation regardless at high stress levels. A marginal difference in the fatigue life was observed below 150 MPa. Data generated at 45° orientation were not incorporated in the analysis due to insufficient number of tests. The results shown in Figure 4 and 5 implied that the fatigue performance of 2024-T3 is noticeably better than 8090C-T8 in both L [1] and T orientations at all stress levels. The fatigue data in Figure 6 indicates that chromic acid anodizing has caused a marginal reduction in the fatigue life of 8090C-T8 at low stress levels approaching the endurance limit. Figure 7 indicates that the fatigue life 2024-T3 is insensitive to chromic acid anodizing. Reported research data showed a trend towards a reduction in fatigue life of anodized specimens manufactured from 2014-T6 plate[3]. In the present case, the inherent variations among the specimens containing central holes, which simulated fastener holes, and the associated scatter in the fatigue data may have effectively masked the influence of the thin chromic anodized layer.

CONCLUSIONS

Both 8090C-T8 and 2024-T3 responded well to the chromic acid anodizing process with no defects/cracks in the coating. The fatigue performance of 8090-T8 in the bare condition is unaffected in the L and T orientation however 2024-T3 is marginally better that 8090-T8 in the same orientations. Chromic acid anodizing marginally reduces the fatigue performance of 8090-T8 at low stress levels only but has no effect on and 2024-T3 sheet alloy.

REFERENCES

1. L. Shra and W.G.J. 't Hart, Residual strength and fatigue crack growth properties of of Al-Li-Cu-Mg-Zr sheet materials, National Aerospace Laboratory NLR Technical Report 88079 L, Amsterdam, The Netherlands, May 1988

2. ASTM E 739, Standard Practice for Statistical Anlysis of Linear or Linearized Stress-Life (S-N) and Strain-Life (ε-N) Fatigue Data, (1991)

3. V. J. Bolam, P.J. Gregson and A. Gray, Effect of pretreatment and anodising on the fatigue properties of 8090 alloy plate, Proceedings 6th International Aluminium-Lithium Conference, Editors M. Peters and P.-J. Winkler, Verlag, (1991) 609

TABLE 1- Nominal composition (wt. %) of Al-Li 8090C and Al 2024

Alloy	Li	Cu	Mg	Mn	Zr	Si	Fe	Zn	Al
8090C	2.2 2.7	1.0 1.6	0.6 1.3	0.0 0.1	0.04 0.16	0.0 0.2	0.0 0.3		Bal
2024-T3		3.9 5.0	1.2	0.3		0.5	0.5	0.25	Bal

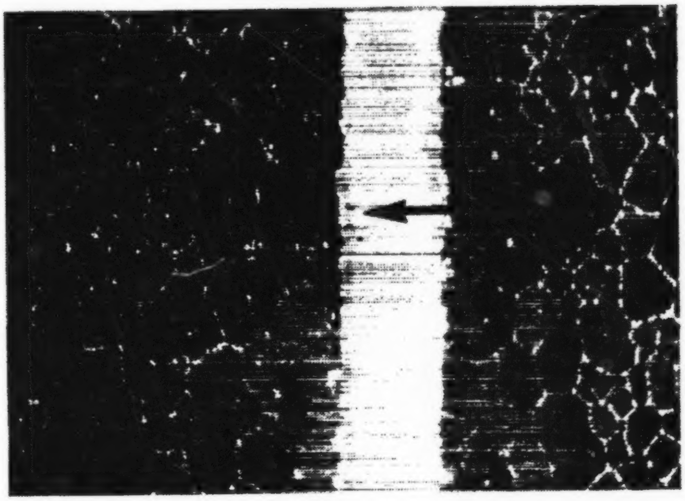

(a)

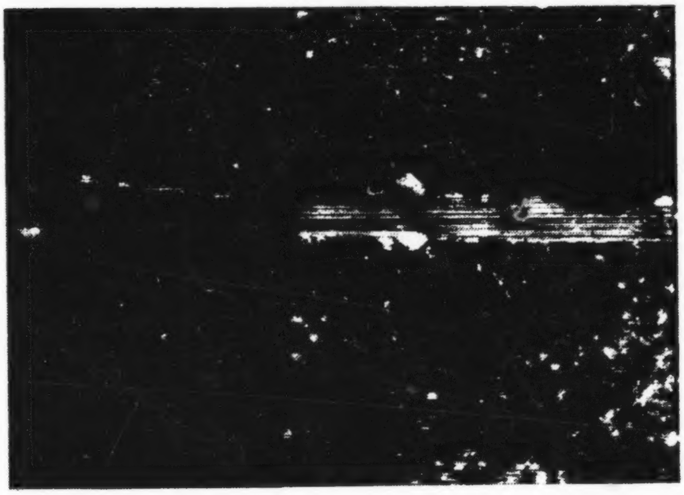

(b)

Figure 1. Chromic acide anodized coating on (a) 8090-T8 and (b) 2024-T3

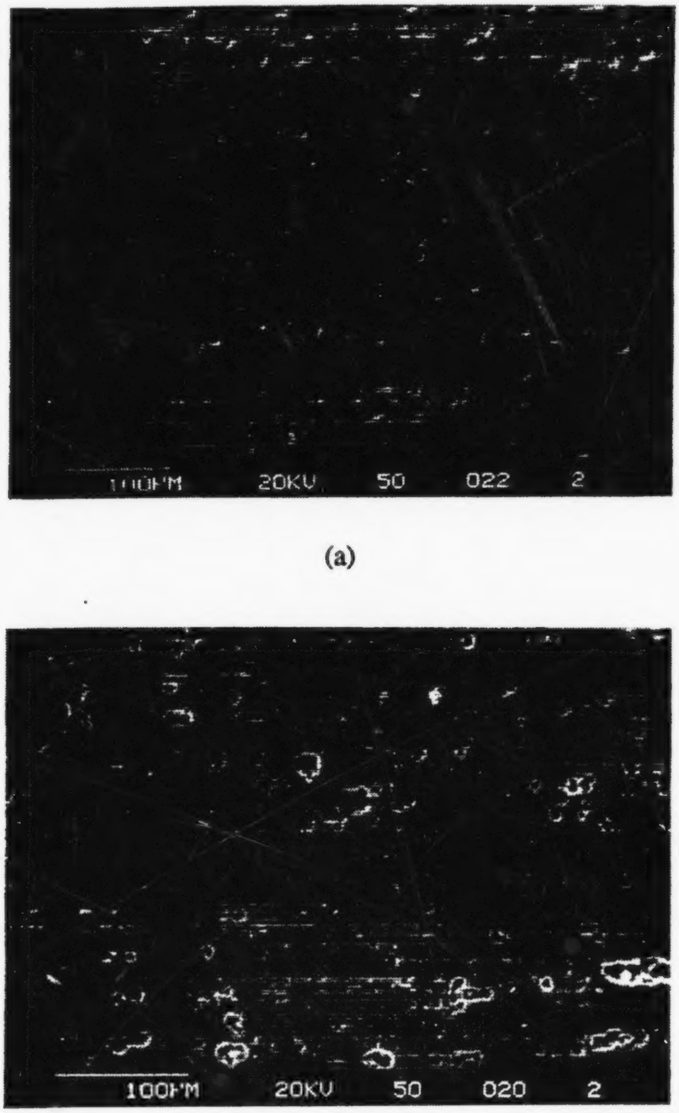
100µM 20KV 50 022 2
100µM 20KV 50 020 2

(a)

(b)

Figure 2. SEM micrographs showing the features of the anodic coating (a) 8090-T8 and (b) 2024-T3.

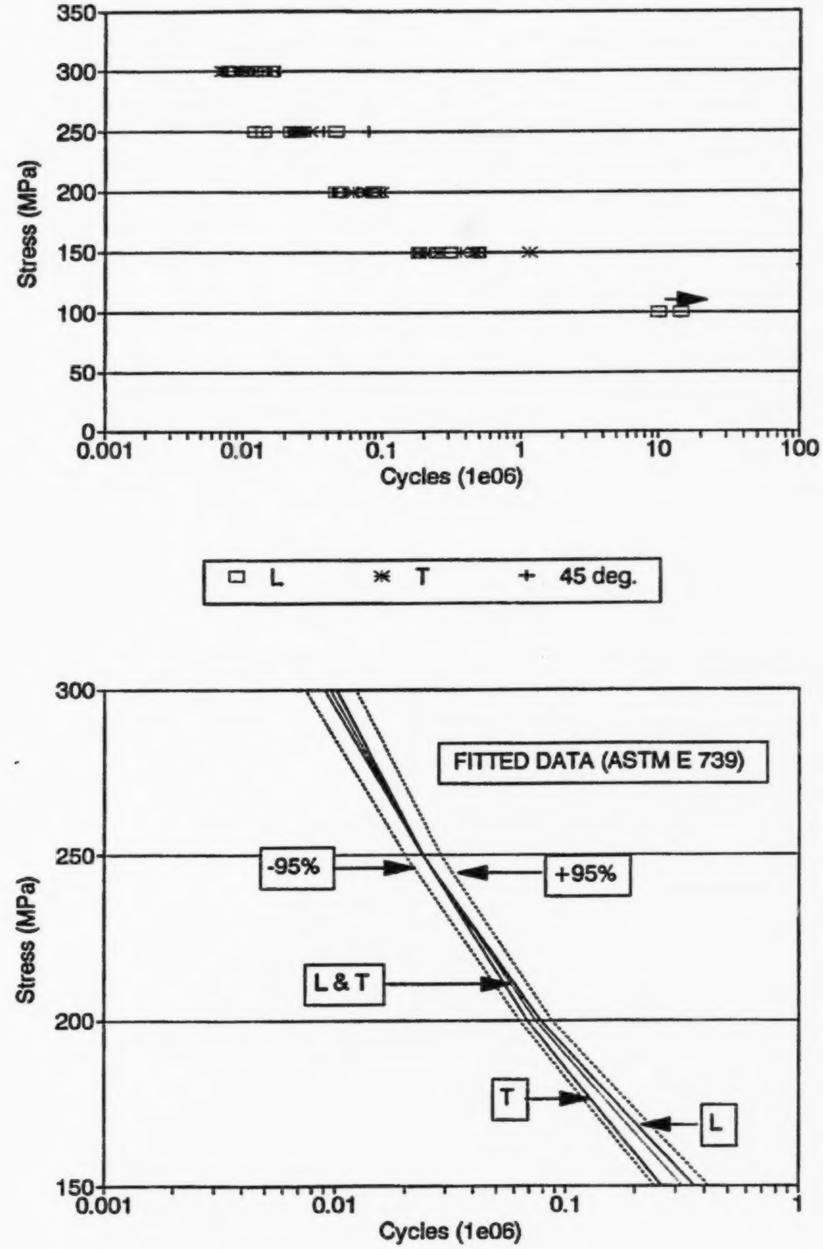

Figure 3. 8090-T8 bare in the L, T and 45° orientation.

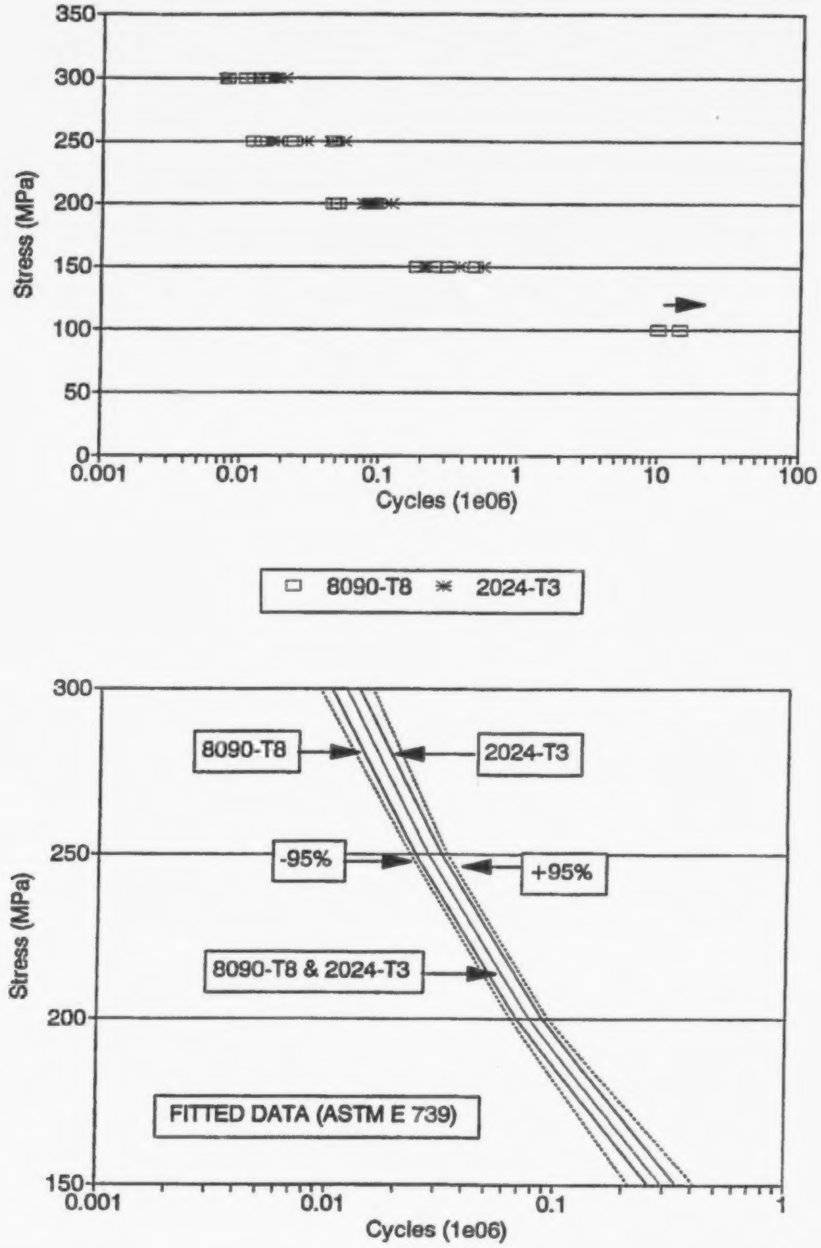

Figure 4. 8090-T8 and 2024-T3 bare in the L orientation.

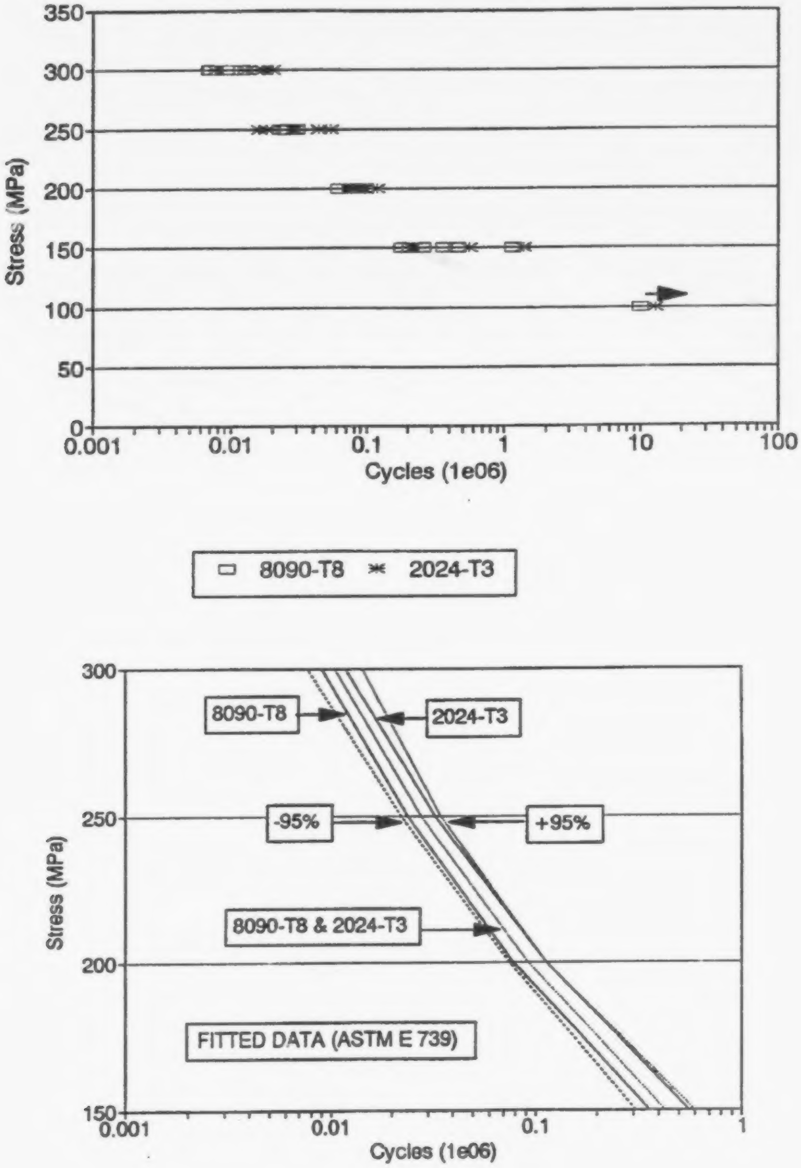

Figure 5. 8090-T8 and 2024-T3 bare in the T orientation.

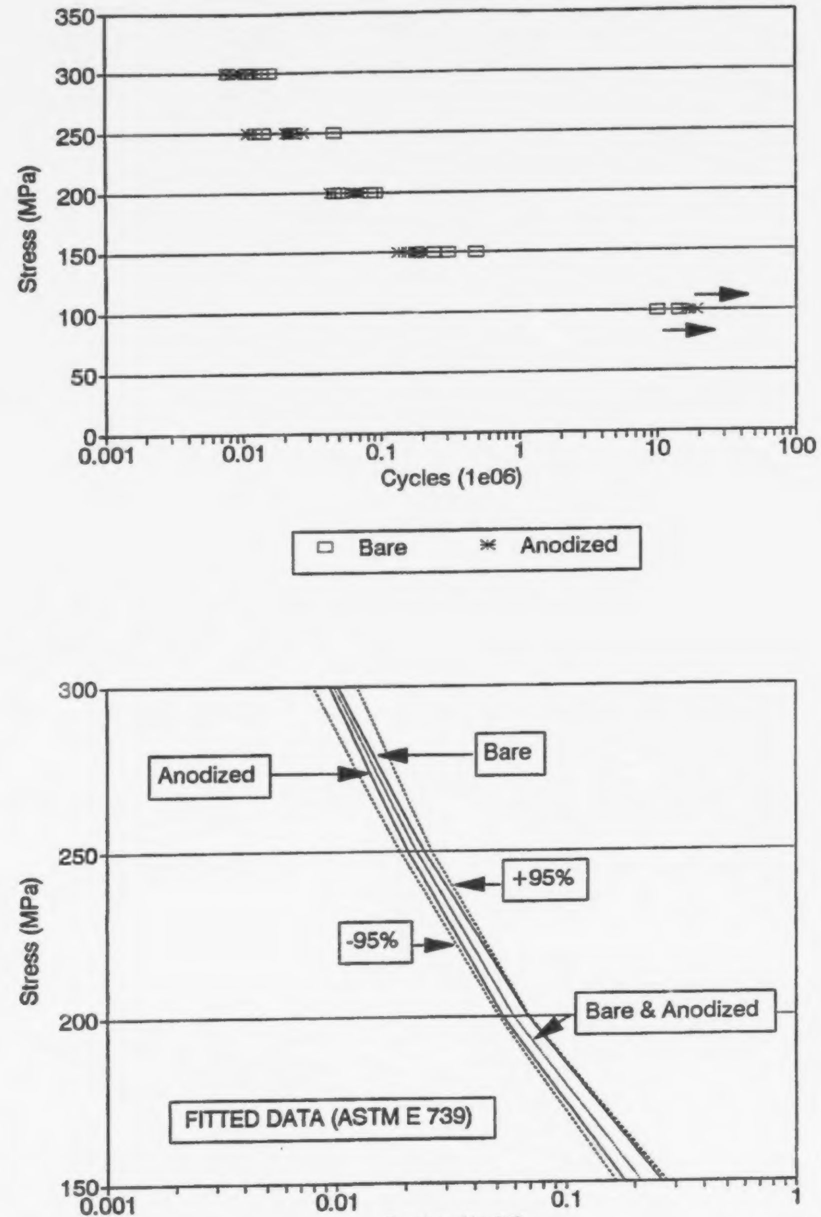

Figure 6. 8090-T8 bare and anodized in the L orientation

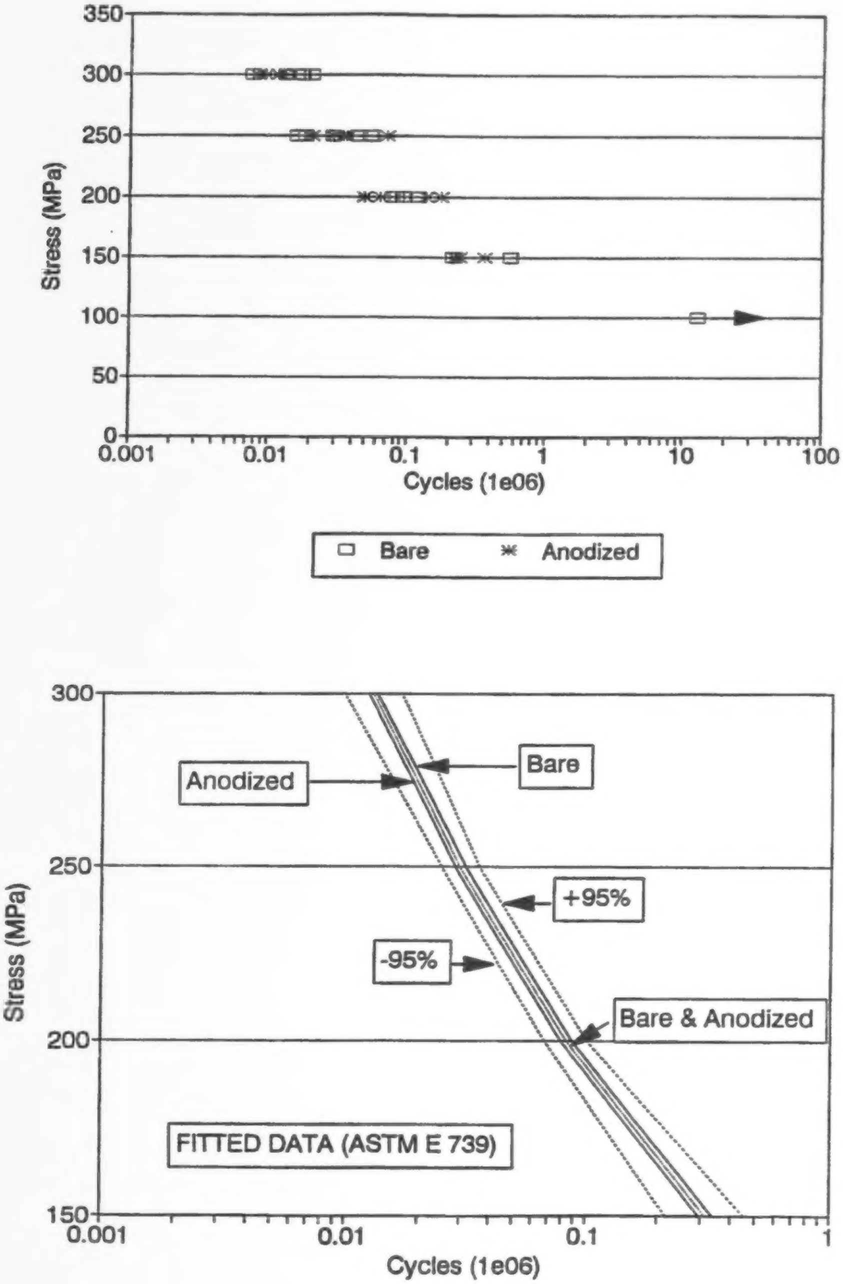

Figure 7. 2024-T3 bare and anodized in the T orientation.

141640

8.

"A Comparison of Fatigue and Fracture Toughness Properties of Al-Li 8090 and 7050 Plate in Low Strength Directions"

Capt. K. Lemke and S.D. Antolovich

Georgia Institute of Technology, USA

A COMPARISON OF FATIGUE AND FRACTURE TOUGHNESS PROPERTIES OF Al-Li 8090 AND 7050 PLATE IN LOW STRENGTH ORIENTATIONS

KEVIN L. LEMKE and STEPHEN D. ANTOLOVICH

The greatest area of concern in replacing aerospace components fabricated from traditional aluminum alloys with Al-Li alloys is the low strength of the Al-Li alloys in the short transverse direction. In this investigation the mechanical properties 8090 in these weak orientations is compared with 7050 alloy. Fracture toughness tests and fatigue crack growth test at low and high R ratios were conducted for the S-L and S-T orientations. Results indicate that the 8090 has a significantly lower fracture toughness but superior fatigue crack propogation properties at low R ratios and comparable fatigue properties at high R ratios.

INTRODUCTION

Low density lithium-containing aluminum alloys are of considerable interest to the aerospace industry because they offer a lower density/higher modulus material with mechanical properties similar to traditional alloys. Of the several lithium containing aluminum alloys currently being developed the most commercially advanced is the alloy designated 8090. This alloy has been selected for several commercial applications including in the main cabin frame of the Westland Helicopters EH101. In this application, 8090 forgings and extrusions will be used to directly replace components originally fabricated from 7010 plate.

Materials tests conducted by Westland and others have demonstrated that 8090 meets or exceeds the design specifications for most mechanical properties. The one exception is the low fracture toughness for cracks growing in the short transverse plane, due to the highly textured grain structure of the 8090 components. In this report the fracture toughness and fatigue crack growth (FCG) properies in this orientation are further investigated and compared with a traditional aluminum alloy.

MATERIALS AND EXPERIMENTAL PROCEDURE

The 8090 alloy used in this research was provided by Westland Helicopters. The test specimens where machined from production-run forgings from the EH101 main cabin roof. The location of the forgings and specimens machined from the forgings are shown in slide #1. The highlighted specimens indicated the location of single K_{IC} or two FCG specimens which have been tested to date. The comparison tests where conducted on specimens machined from 7050 forged plate provided by McDonnell Douglas. The 7050 alloy was selected because of its similarities to 7010 which was unavailable. The location of 7050 specimens machined and tested to date are shown in slide #2. As shown in these slides, specimens were obtained in both the S-L and S-T orientations. The chemical composition and heat treatment of the two alloys are shown in slide #3.

Standard metallographic procedures were used to examine the grain texture of the alloys, shown in slide #4. Both alloys displayed grains that were highly elongated in the longitudinal direction. The grain texture of the 7050 was quite consistent throughout the plate while the 8090 showed some variations at different forging locations.

Mechanical tests conducted to date include fracture toughness tests and FCG tests at both a low R ratio (R=0.1) and a higher R ratio (R=0.6). All tests have been done on both orientations (S-L and S-T) of both materials. The higher R ratio value was selected to provide test results for a reasonable range of ΔK values while ensuring the failure mechanisms were indicative of high mean stress loading conditions. This type of loading condition is comparable to that experienced by a component which has vibrational loads superimposed on a structural load. All tests were conducted in accordance with the applicable ASTM standard. Test details are given in slide #5. The specimens used were standard C-T specimens with a width of W=40mm and a thickness of B=20mm for K_{IC} tests and B=10mm for FCG tests. At least three K_{IC} tests and two FCG tests have been completed for each test condition. In addition to standard ASTM tests, the FCG tests were stopped prior to failure and loaded at a constant rate to rupture. This data was used to calculate a provisional K_Q which was not a technically valid K_{IC} value but which is nonetheless indicative of failure for high ΔK tests. Following failure all fracture sufaces were analyzed using SEM. Stereo pairs were used to view the fracture surface in thre dimensions.

RESULTS AND DISCUSSION

The test results for the fracture toughness tests are shown in slide #6. This includes the results of the valid K_{IC} tests and the provisional K_Q results obtained following the FCG tests. The results showed a maximum variability of ±3.5% for the K_{IC} tests and ±5.0% for the K_Q tests. As can been seen from the slide the fracture toughness of the 8090 is low when compared with the 7050 and both materials exhibit a slight increase in fracture toughness in the S-T orientation. The K_Q values are quite close to the K_{IC} values although the 8090 material exhibits slightly higher K_Q values, particularly for the S-L orientation. Examination of the fracture surfaces shown in slide #7 provides insight into the reasons for the differences between the materials. As can be seen in the slide, the 8090 fracture surfaces were almost entirely intergranular with fine ductile dimples visible on the grain boundaries. The 7050 on the other hand displayed considerable normal rupture along bands of what are most likely intermetallic particles. This normal rupture mode vice the intergranular mode displayed by the 8090 alloy would account for the higher fracture toughness of the 7050. It is proposed that the higher value of K_Q for the 8090 can be explained by the fact that the material exhibits a completely different fracture mechanism during fatigue (as will be seen later) and for the K_Q tests has a larger plastic zone size ahead of the crack tip through which the crack must extend before the intergranular rupture can begin. In essence, the crack tip is significantly blunted in the grain interiors and must be extended to the grain boundaries before intergranular failure can begin, requiring higher loads than a sharper crack tip.

The results of the FCG tests are shown in slides #8 and #9. The test repeatability graphs show examples of two tests for the same material under identical conditions. The 8090 tests all displayed excellent reproducability particularly considering that the test samples were from a forging. The 7050 samples showed somewhat more scatter, the most extreme example being shown, although this scatter was generally within the factor of two considered acceptable in the ASTM standard. The results are also shown for each material, orientation and R ratio. For the low R ratio tests the FCG rate for the 7050 is similar to the 8090 at low values of ΔK but increases more rapidly,ultimately being 3-4X higher. Both materials exhibited a signifigantly slower FCG rate for the S-T orientation, 2-4X for the 7050 and 4-6X for the 8090. At the higher R ratio the FCG rate increased substantially for all tests. The 8090 FCG rates displayed convergence for the two orientations and the advantage of the 8090 over the 7050 disappeared . The 7050 S-T orientation, however, maintained a lower FCG rate than the S-L orientation.

Some examples of the fracture surfaces observed for the FCG tests are shown in slides #10 and #11. The 8090 samples displayed primarily transgranular failure with some intergranular regions at low loading levels. The S-L samples had relatively large areas which exhibited considerable secondary cracking along crystallographically oriented slip bands. The S-T orientation showed somewhat less secondary cracking but had a very microscopically rough surface resulting from many small plates sheared on crystallographic planes of different orientation. This would indicate that the lower FCG rate of the S-T orientation can be in part attributed to roughness induced closure , an observation supported by the disappearance of this advantage for the high R ratio tests. Examination of the 8090 fracture surfaces for the high R ratio tests showed very similar fracture surfaces.

The 7050 fracture surfaces clearly showed failure by shear of similarly oriented crystallographic planes at low R ratios. At higher loads there was also evidence of normal rupture along the bands of intermetallic particles. These features were oriented perpendicular to the direction of crack growth in the S-L samples and parallel in the S-T samples. These orientation differences likely would increase the resistance of the S-T samples to crack propagation. At the higher R ratios much more normal rupture was evident in both orientations. This would account for the increased FCG rate and suggests that closure effects are less apparent in the 7050, explaining the difference between S-L and S-T orientations at high R values.

To help evaluate the engineering significance of these results some simple calculations were conducted using the experimentally determined results. The calculations determined the critical crack size and fatigue life for an edge cracked plate subjected to a given load level. The initial flaw sizes were selected to be representative of flaw detection capabilities and the load levels choosen to produce stress intensities in the range of the experimental data. The development of the equations is given in slide #12 and some sample results for both materials in the S-L orientation at R=0.1 are given in slide #13. These calculations show that the low fracture toughness of the 8090 means that the 7050 material can withstand a crack of nearly three times the length of the 8090 before failing at the same load rate. Using this critical crack length, the life of the plate was calculated at the same load level for a range of initial flaw sizes from 1-10 mm. The graph shows despite the lower fracture toughness the 8090 material would have a life very comparable to the 7050 because of its superior FCG properties.

SUMMARY AND CONCLUDING REMARKS

A summary of the testing results and observations is given in slide #14. The results show that the 8090 alloy fracture toughness values in the short transverse orientations are signifigantly less than for alloys such as 7050, a cause for concern. If these fracture toughness values do in fact meet the design criteria the fatigue life of 8090 components should not be signifigantly less than for 7050 alloys for low mean stress loading conditions because of the 8090s superior FCG resistance. Further studies of these materials are planned to confirm these results, to examine more closely closure effects, and to examine the effect of corrosion fatigue.

ACKNOWLEDGEMENTS

The authors would like to thank Westland Helicopters, McDonnell Douglas and the Quality Engineering Test Establishment for their support of this research. Also the contributions and assistance of Dr. Tom Sanders and Dr. Graham Webb of Georgia Tech is highly appreciated.

7050 SPECIMEN LOCATIONS

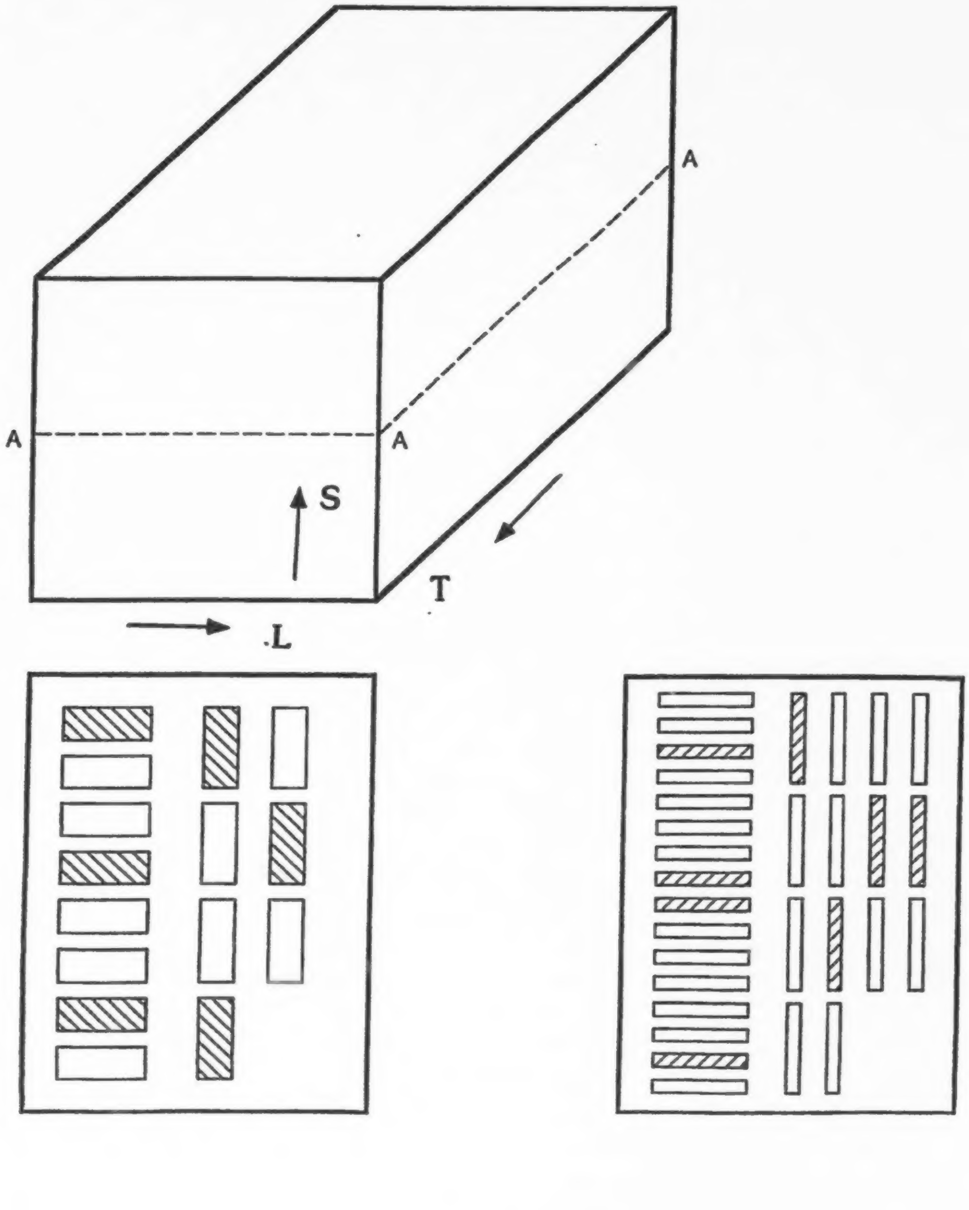

8090 SPECIMEN LOCATIONS

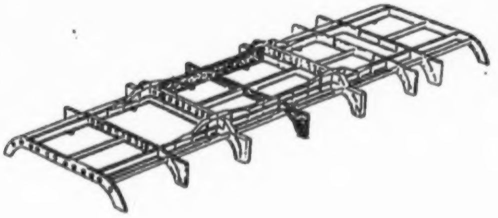

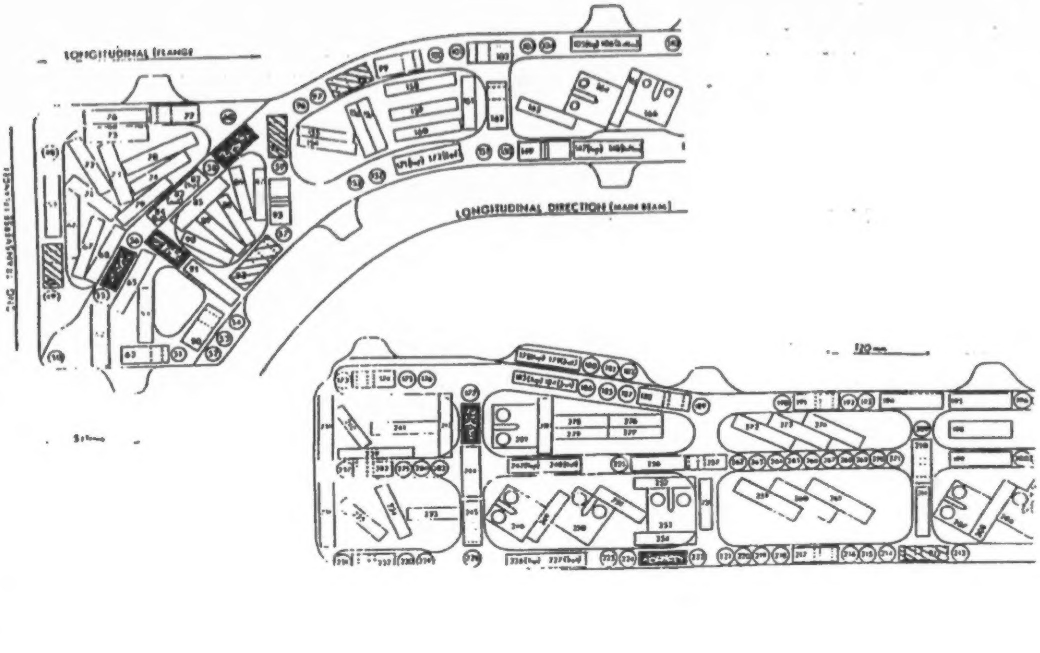
LONGITUDINAL (FLANGE
LONG TRANSVERSE (FLANGE)
LONGITUDINAL DIRECTION (MAIN BEAM)
120mm
51mm

EXPERIMENTAL MATERIALS

Chemical Compositions (wt%)

Alloy\Element	Zn	Li	Cu	Mg	Zr	Al
Alcan 8090	0	2.45	1.17	0.66	0.12	Bal.
ALCOA 7050	6.2	0	2.3	2.25	0.12	Bal.

Heat treatment

8090 – T852

- Component forged from casting
- Solutionized at 540°C, cold quenched
- Cold compressed
- aged 24 hrs at 175°C

7050 – T7452

- Forged plate
- Solutionized at 477° C
- Aged 3 hrs at 121° C
- Aged 24 hrs at 165° C

MICROSTRUCTURES

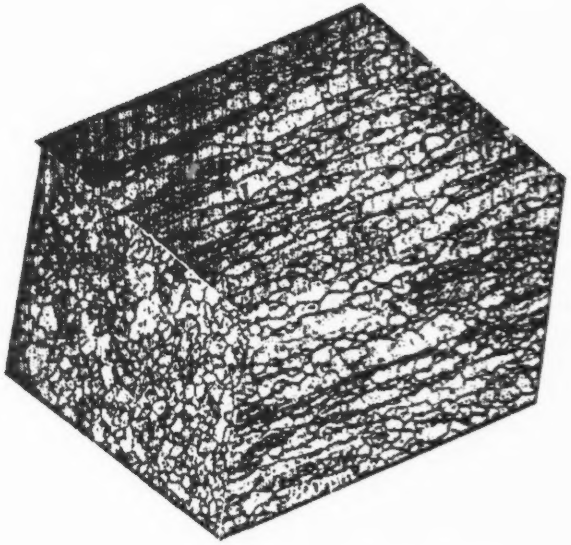

8090

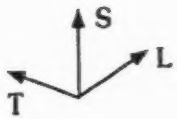

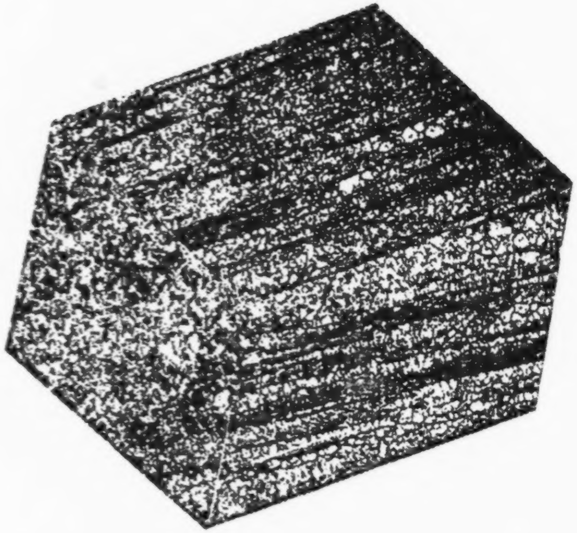

7050

EXPERIMENTAL PROCEDURES

K_{IC} testing

- Conducted IAW ASTM E399.
- Precracking at 10 Hz, sinusoidal waveform, $R = 0.1$.
- Tests conducted on Instron screw driven machine.
- Loading rate 50 lbf/sec $\Delta K = 0.8$ MPa(m)$^{1/2}$/sec.

FCP TESTING

- Conducted IAW ASTM E647
- Tests conducted using MTS servohydraulic machine.
- Constant load increasing ΔK.
- Test frequency of 10 Hz.
- R ratio of 0.1 and 0.6.
- Triangular waveform.
- Crack length monitored by DC current electropotential drop method.

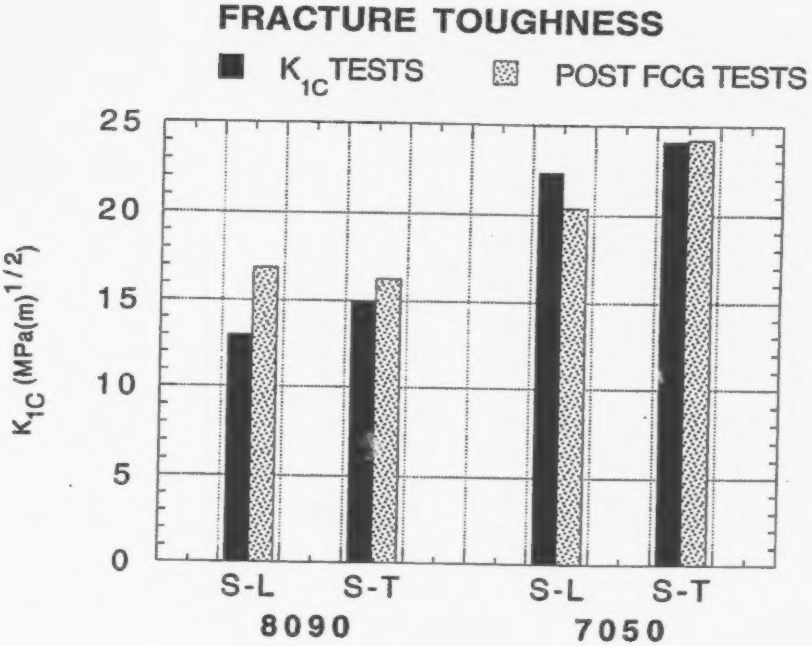
FRACTURE TOUGHNESS
K_{1C} TESTS
POST FCG TESTS
K_{1C} (MPa(m)$^{1/2}$)
0
5
10
15
20
25
S-L
S-T
8090
S-L
S-T
7050

K_{IC} FRACTURE SURFACES

7050

S-L

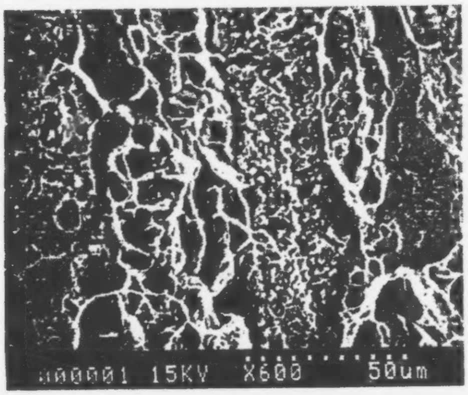
000001 15KV X600 50um

S-T

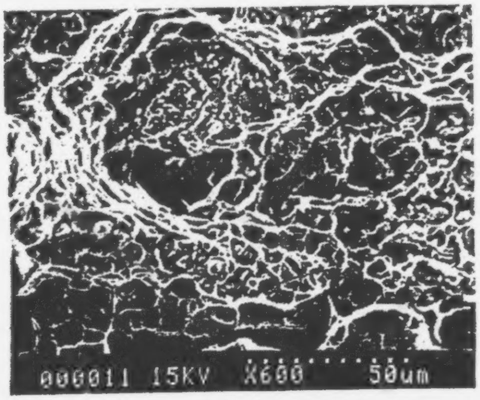
000011 15KV X600 50um

8090

S-L

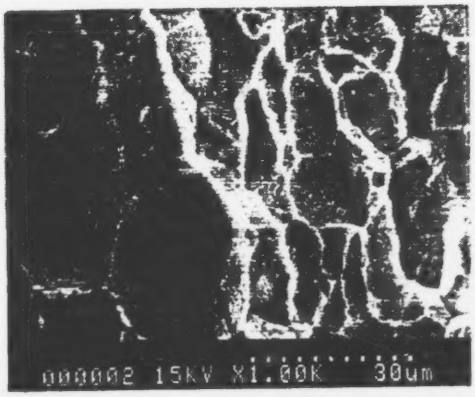
000002 15KV X1.00K 30um

S-T

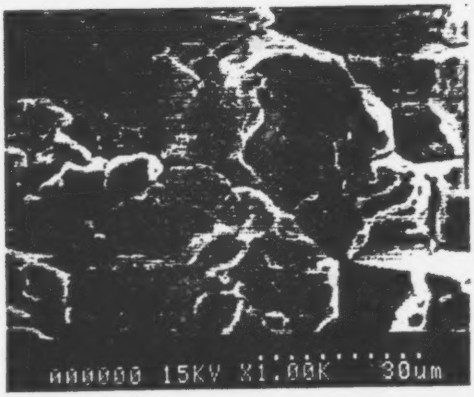
000000 15KV X1.00K 30um

8090 S-T R=0.1

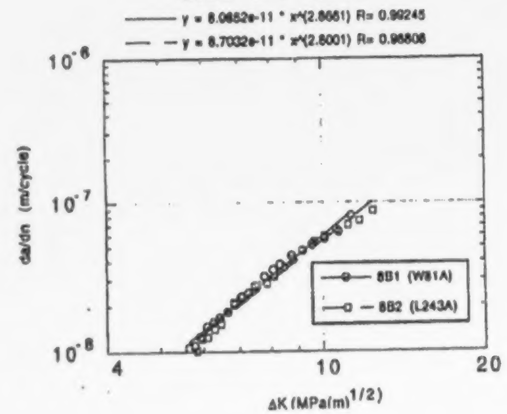

7050 S-T R=0.6

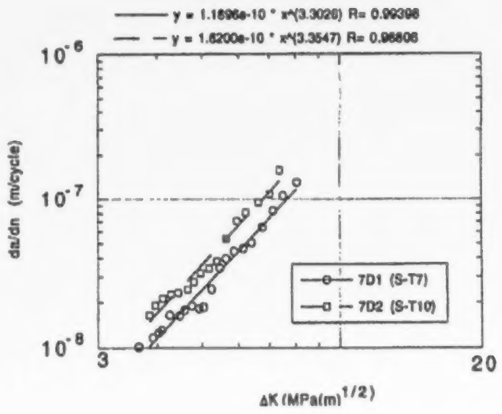

Al-Li 8090

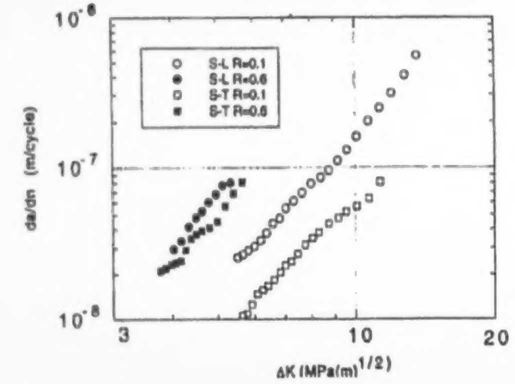

Al 7050

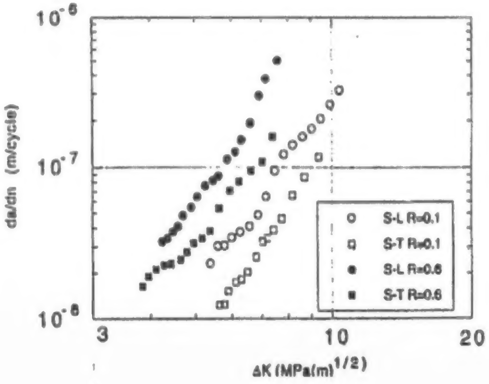

S-L ORIENTATION

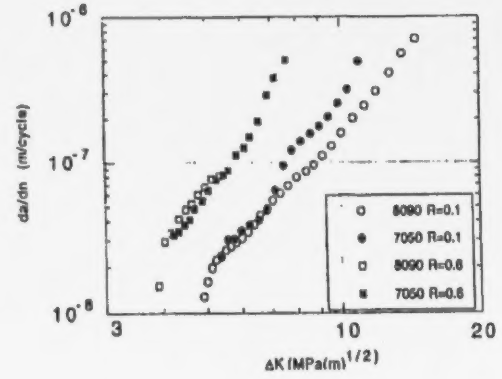

S-T ORIENTATION

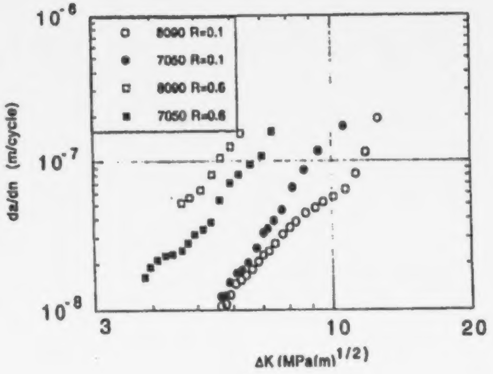

LOW R RATIO

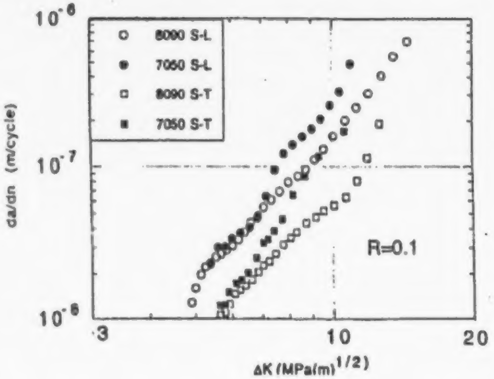

HIGH R RATIO

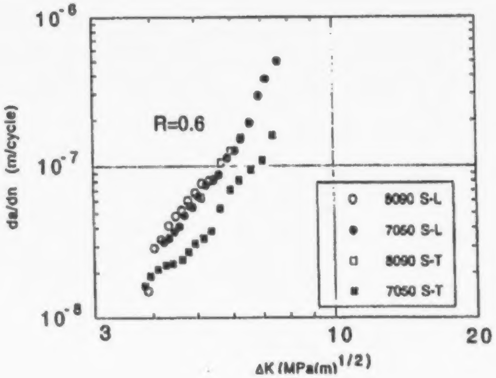

8090 FCG SPECIMEN, R = 0.1

S-L

Slow FCG

c.g.

Fast FCG

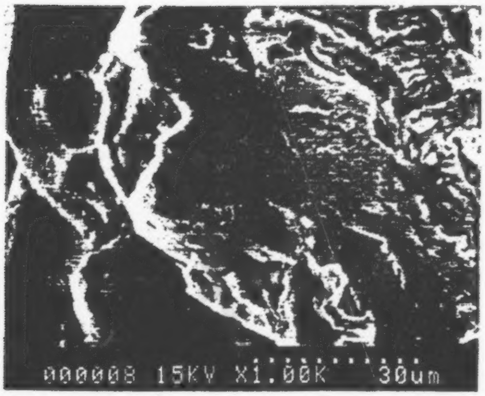
000008 15KV X1.00K 30um

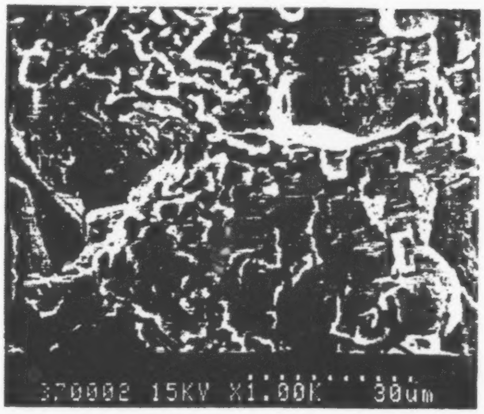
370002 15KV X1.00K 30um

S-T

Slow FCG

c.g.

Fast FCG

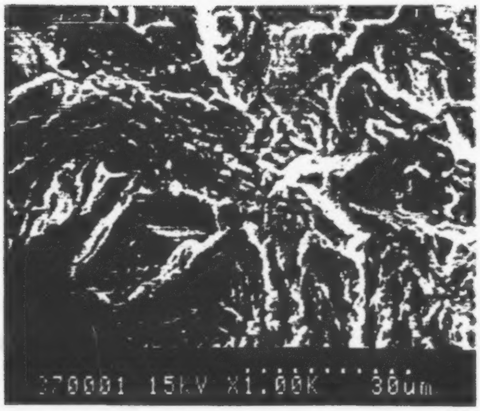
370001 15KV X1.00K 30um

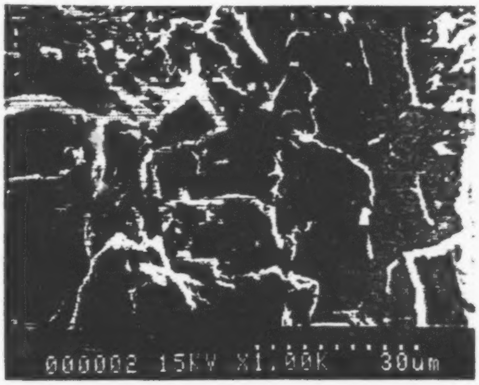
000002 15KV X1.00K 30um

7050 FCG SPECIMEN, R = 0.1

S-L

Slow FCG

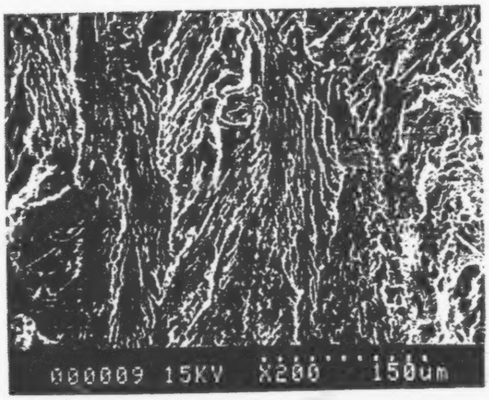
000009 15KV X200 150um

c.g.

Fast FCG

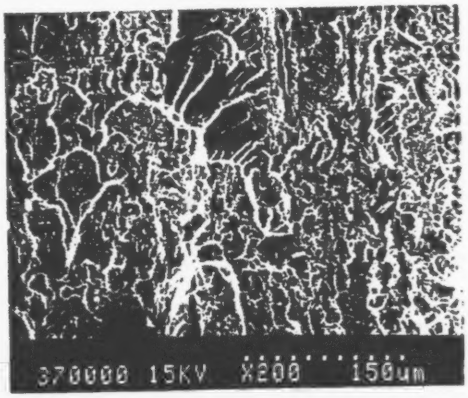
370000 15KV X200 150um

S-T

Slow FCG

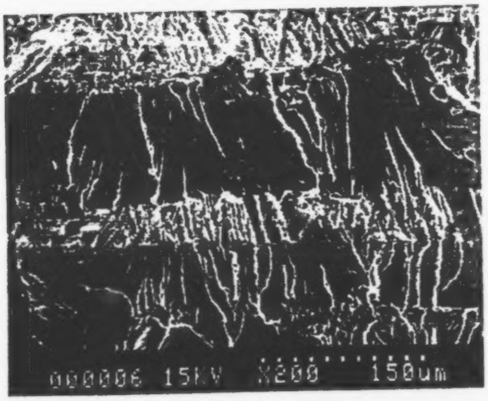
000006 15KV X200 150um

c.g.

Fast FCG

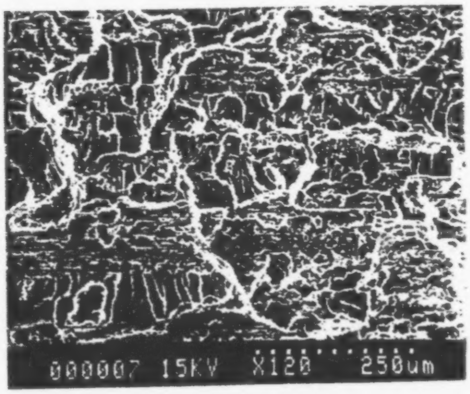
000007 15KV X120 250um

LIFE CALCULATIONS

TO DEMONSTRATE AND COMPARE THE EFFECT OF EXPERIMENTALLY DETERMINED K_{IC} VALUES AND PARIS LAW (FCG) CONSTANTS FOR THE TWO MATERIALS

EQUATION DEVELOPMENT

CRITICAL CRACK LENGTH

$$K=\sigma(\pi*a)^{1/2}*f(g)$$

$$a_f=(1/f(g)^2*\pi)*(K_{IC}/\sigma)^2$$

FOR A WIDE EDGE CRACKED PLATE

$$f(g)=1.12$$

$$a_f=(1/1.25\pi)\cdot(K_{IC}/\sigma)^2$$

FATIGUE LIFE

PARIS LAW FOR CRACK GROWTH

$$da/dN=C(\Delta K)^m$$

$$\Delta K=1.12\Delta\sigma(\pi*a)^{1/2}$$

Therefore

$$da/dN=C(1.12\Delta\sigma(\pi*a)^{1/2})^m$$

$$dN=(1/C(1.12\sigma\Delta*\pi^{1/2})^m)*da/a^{m/2}$$

Integrating gives:

$$N_f=B*\left[\,(1/(-m/2+1)a_i^{m/2+1})\right.$$
$$\left.-(1/(-m/2+1)a_f^{m/2+1})\right]$$

Where $B=(1/C\cdot 1.12^m\cdot\Delta\sigma^m\cdot\pi^{m/2})$

SAMPLE CALCULATIONS

CRITICAL CRACK LENGTH

$$a_f=(1/1.25\cdot\pi)\cdot(K_{IC}/\sigma)^2$$
Let σ=50MPa

8090 S-L	7050 S-L
K_{IC}=13MPa$(m)^{1/2}$	K_{IC}=22MPa$(m)^{1/2}$
$a_f=0.255(13/50)^2$	$a_f=0.255(22/50)^2$
a_f=0.0172m	a_f=0.0494m

FATIGUE LIFE

$$N_f=B*\Big[(1/(-m/2+1)a_i^{-m/2+1})-(1/(-m/2+1)a_f^{-m/2+1})\Big]$$

$$B=(1/C\cdot 1.12^m\cdot\Delta\sigma^m\cdot\pi^{m/2})$$

Let a_i=1mm
For R=0.1 $\Delta\sigma=0.9\sigma_{max}$=45 MPa

8090 S-L	7050 S-L
a_f=0.0172	a_f=0.0494
C=8.1298e-11	C=2.3474e-11
m=3.3108	m=4.06575
N_f= 5.10e5	N_f= 5.84e5

FATIGUE LIFE R-0.1

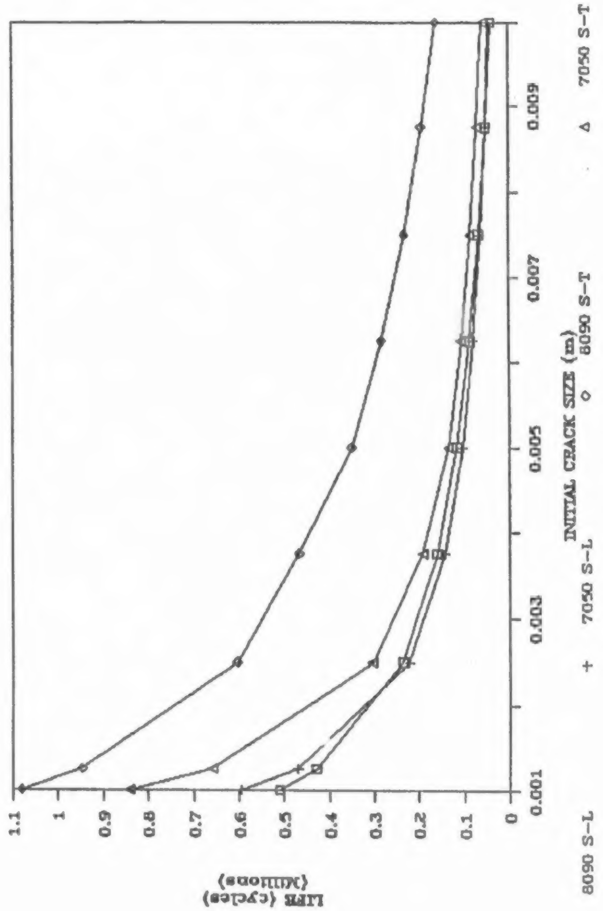

SUMMARY

TEST	ORIENT	8090	7050
K_{IC}	S-L	-LOW FRACTURE TOUGHNESS -INTERGRANULAR FAILURE -FINE DUCTILE DIMPLES ON GBs	-TOUGHNESS > 60% HIGHER THAN 8090 -LESS INTERGRANULAR FAILURE -NORMAL RUPTURE ALONG PRECIPS AND INTERMETALLICS
	S-T	-K_{IC} SLIGHTLY HIGHER -SIMILAR FRACTURE SURFACE	-K_{IC} ALSO SLIGHTLY HIGHER THAN S-L -FRACTURE SURFACE SAME EXCEPT FOR PRECIP. ORIENT.
FCP R=0.1	S-L	-TRANSGRANULAR FRACTURE WITH SOME INTERGRANULAR -SECONDARY CRACKING ALONG SLIP BANDS -MICROSCOPICALLY ROUGH	-FCG RATE INCREASES MORE QUICKLY THAN 8090 -TRANSGRANULAR FAILURE ON CRYSTALLOGRAPHIC PLANES -NORMAL RUPTURE ALONG PRECIP BANDS PARALLEL TO CRACK GROWTH DIR'N AT HIGHER ΔK
	S-T	-FCG RATE SIGNIFIGANTLY SLOWER THAN S-L -SIMILAR FRACTURE SURFACE BUT LESS SECONDARY CRACKING - APPEARS ROUGHER	-AGAIN FCG RATE INCREASES MORE QUICKLY THAN 8090 -SIMILAR FRACTURE SURFACE TO S-L WITH PRECIP BANDS ⊥TO CRACK GROWTH DIR'N
FCP R=0.6	S-L	-FCG RATE 6-8X HIGHER THAN R=0.1 -FRACTURE MECHANISM SIMILAR TO R=0.1 SUGGESTING LESS CLOSURE	-FCG RATE SIMILAR TO 8090 -LESS CRYSTALOGRAPHIC FRACTURE, MORE NORMAL RUPTURE R=0.1
	S-T	-LARGER INCREASE IN FCG RATE THAN S-L -AGAIN SIMILAR FRACTURE SURFACE TO R=0.1 SUGGESTING LESS CLOSURE	-LOWER FCG RATE INCREASE THAN 8090, SIMILAR TO S-L -AGAIN MORE NORMAL RUPTURE THAN R=0.1

SESSION C.

Corrosion and Corrosion Fatigue

141641

9.

"Electrochemical Characterization of the Resistance of Al-Li Alloy Sheet to Seawater Corrosion"

P.R. Roberge, E. Halliop

Royal Military College, Kingston, Ont.

D. Lenard, and J.G.M. Moores

DREP, Victoria, B.C.

Electrochemical Characterization of the Resistance of Al-Li Alloy Sheet to Seawater Corrosion

P.R. Roberge and E. Halliop
Department of Chemistry and Chem. Eng., Royal Military College
Kingston, Ontario, K7K 5L0 (Canada)

D.R. Lenard and J.G.M. Moores
Materials Technology Section, Defence Research Establishment Pacific
FMO Victoria, B.C., V0S 1B0 (Canada)

Abstract

The electrochemical measurements obtained with the three orthogonal faces of commercial aluminum and aluminum-lithium sheet material were compared to the results obtained during the long term exposure of the same alloys to real sea water. The results obtained during this extensive study indicated that short term EIS measurements can help to predict the general and localized corrosion behavior of this material when exposed to sea water. A systematic analysis of 610 fifteen minute noise records with the stochastic pattern detector technique has demonstrated that the exponential decay model describes very well the potential fluctuations observed during these experiments, thereby confirming the random nature of the corrosion processes in progress. The parameters revealed during the noise analysis were additionally related to the features calculated from EIS measurements or observed after long term exposure of the same alloys in a flowing sea water tank.

Introduction

The development of a special group of aluminum alloys containing lithium as one of the primary alloying elements was described as the single largest R&D effort in the history of aluminum metallurgy[1]. The main advantage of alloying lithium to aluminum used in aerospace vehicles comes from the increased modulus of elasticity and strength, which are paralleled by a unique reduction of density of the alloys. The aluminum-lithium alloys can offer substantial (≈10%) weight savings over conventional aerospace aluminum alloys such as the 2000 and 7000 series. In addition, fatigue properties and corrosion resistance of aluminum alloys are said to improve by alloying them with lithium[2]. But past experience indicates that gains in mechanical properties are often taxed by a simultaneous increase of the susceptibility to catastrophic forms of corrosion. For example, the T6 temper of Aluminum Alloy (AA) 7075 was readily adopted by aircraft designers because of its high modulus and strength. It was subsequently discovered to be highly susceptible to stress corrosion and exfoliation in the marine environment[3], at great cost to aircraft operators. As a result of this history and because elemental lithium is extremely reactive, there has been considerable interest in the corrosion susceptibility of aluminum-lithium alloys.

A variety of accelerated corrosion tests[4-8] and standard electrochemical techniques[8-11] have been used to study the corrosion behavior of Al-Li. The resistance of aluminum alloys to stress corrosion cracking (SCC) has also been extensively studied in many laboratories around the world[4,10,12-18]. But the multitude of heat treatments which are possible, added to the variability of alloy compositions which have been studied, have resulted in an uncomfortable degree of uncertainty concerning the factors that control the initiation of localized corrosion on aluminum-lithium alloys. In order to acquire first hand experience with the behavior of these alloys in the marine environment, the Defence Research Establishment Pacific (DREP) subjected panels made from (AA)2090 and 8090 sheet, along with 2024 and 7075 sheet, to several tests involving exposure to sea water fog and full or part immersion in sea water[8]. The results of these tests were then compared with results obtained at the Royal Military College of Canada during the analysis of EIS and electrochemical noise measurements made with the same alloys exposed to synthetic sea water (3% NaCl).

Electrochemical Techniques

Electrochemical impedance spectroscopy (EIS)

Electrochemical Impedance Spectroscopy (EIS) has been successfully applied to the study of corrosion systems for almost twenty-five years. Since the early work published by Epelboin and co-workers[19] EIS has gained tremendous momentum and popularity in corrosion laboratories around the world. An important advantage of EIS over other laboratory techniques is the possibility of using very small amplitude signals without disturbing the properties being measured. EIS has also recently found its way into practical field applications[20-22] where its capability of working in difficult and changing hydrodynamic conditions can become a serious advantage once the complications of analyzing EIS results are overcome.

EIS has been shown to be a rapid, powerful and accurate method for measuring corrosion rates. But in order to access the charge transfer conductance, which is proportional to the corrosion rate at the monitored interface, the EIS results have to be understood with the help of a model of the interface. The simplest model representing such an interface must also include a capacitance which describes the capacitive charge acceptance of any metallic surface exposed to an electrolyte. The validation of this simple RC equivalent circuit model can be achieved by permuting the three data points selected to project the center of a circle in a Nyquist representation. The application of this principle to the study of various alloys exposed to aqueous environments has revealed that the non-adherence of the EIS measurements to a perfect RC model is a rich source of information[23] concerning the types of corrosion processes occurring on a metallic surface.

One omnipresent characteristic of the EIS spectra that must be addressed properly, in terms of its significance in corrosion studies, is the constant phase element (CPE) which is commonly introduced as an empirical factor in fitting procedures to describe the angle of tilt often visible in Nyquist plots. The empirical factor would then appear as an exponent β with a value between 0 and 1, which would be added to the imaginary component of an impedance frequency (ω) response $Z(\omega)$ (Eq. 1).

$$Z(\omega) = R_s + \frac{R_p}{1+(j\omega R_p C_{dl})^{\beta}} \qquad (1)$$

A traditional explanation for the CPE has been surface dispersion effects[24-26] which, in the case of a corroding metal, have themselves been attributed to microscopic roughening of the surface[27-29] and more recently to typical defects produced by localized corrosion such as encountered when carbon steel[30-32] or aluminum alloys[33,34] are exposed to mildly corrosive environments.

Electrochemical noise (EN)

The most accepted technique to analyze noise data has been to transform time records in the frequency domain in order to obtain power spectra. Since noise signals can be produced by either deterministic or stochastic processes and often consist of a complex combination of these processes, a practical approach has been to correlate predominant frequencies and deconvolute unwanted signals in an iterative manner using well established mathematical functions[35].

The approach used in the present study for the analysis of voltage fluctuations has been extensively described elsewhere[36,37]. With this technique the voltage fluctuations are first transformed into individual voltage peaks as basic events. The rise time of the basic events (dV/dt) is then computed since this parameter is thought to be an important characteristic of the electrochemical systems being studied. During a second process of data transformation the probability distribution of the basic events is compared with a typical Poisson probability distribution of stochastic point processes. A measure of the goodness-of-fit is then evaluated by comparing the ideal exponential distribution to the experimental distributions observed and corresponding to individual λ_t calculated with Eq. 2 and subsequently averaged. The goodness-of-fit itself would be an expression of the difference between this average and the ideal value λ (Eq. 3).

$$\lambda_t = \frac{f(t)}{e^{-\lambda t}} \qquad (2)$$

$$\text{Goodness-of fit}(\%) = \quad \left(1-\left|1-\frac{\bar{\lambda}}{\lambda}\right|\right)\cdot 100\,\% \qquad (3)$$

Experimental

Sea water exposure

The 76 x 76 mm panels used in the exposure tests were sheared from sheets made of Aluminum Alloys 2024-T3, 2090-T8, 7075-T6 and 8090-T851.The nominal composition of the alloys are shown in Table 1. Both surfaces of each panel were sanded with 120 grit silicon carbide abrasive paper and each panel was then fitted with two ceramic multiple-crevice washers (designed according to ASTM G78) that were held in place with a #12 stainless steel nut and bolt assembly that passed through a 6.3 mm central hole. Each bolt was fitted through plastic tubing to prevent contact with the aluminum panel. Each washer provided twelve separate sites for initiation of crevice corrosion. Each panel was suspended by way of a plastic-coated wire that was passed through a 3 mm hole that had been drilled in one corner of the specimen.

SF850 Corrosive Fog Exposure System. The exposure was conducted according to ASTM B117 with the exception that natural sea water was used to generate the fog instead of the standard sodium chloride solution.

Partial and total immersion. The remaining specimens were suspended in sea water that was drawn from the Strait of Juan de Fuca and directed through a tank measuring 16 X 62 x 177 cm. The sea water flowed past any specimen immersed in it at a rate of 1 cm/sec and was then returned to the Strait 40 m from the intake. The water temperature in this location was within the range 7-11^{o}C. One set was suspended in a single row perpendicular to the direction of flow so that one half of the specimen was under water. A second set was suspended in a single row 1 m downstream from the first so that the entire specimen was immersed.

All specimens were removed after an exposure time of four months. After the specimens were dismantled, the aluminum panels were cleaned by immersion in concentrated nitric acid. They were then rinsed with distilled water and allowed to dry after a final rinse with ethanol. Sections were cut from the panels and set in epoxy according to standard metallographic techniques in an effort to determine the depth of corrosion that had been initiated at the edges of the specimens.

Electrochemical tests

The aluminum specimens were cut to appropriate sizes for mounting in epoxy according to metallographic techniques. The samples were mounted in a manner that would expose only one face of each of three orthogonal planes that were related to the rolling direction of the sheet (the rolled surface, the long transverse edge and the short transverse edge). Prior to mounting, provisions were made for electrical connection to the unexposed part of the samples, and the edges were coated with an aluminum-vinyl anti corrosive paint to prevent crevice corrosion between the epoxy mount and the aluminum electrodes. After mounting, the specimens were polished (using 240, 400 and finally 600 grit papers) and cleaned with acetone and dichloromethane.

For each experiment, a pair of identical aluminum specimens (same alloy and same exposed face) was immersed in a 2 l beaker containing a solution of 3% sodium chloride. Each cell was equipped with an air purge and a saturated calomel reference electrode brought into close proximity with one electrode by a Luggin probe. The mounted specimens were separated by 2.5 mm and kept in a stable parallel position with plastic holders. EIS measurements were performed with a commercial frequency response analyzer (Solartron Model 1255) at the corrosion potential. A potentiostat was not used in these measurements. The alternating current was applied between the two aluminum electrodes and kept at a value which would not cause more than 10 mV difference (peak to peak) across the cell.

The reference electrode served to measure the corrosion potential and its fluctuations which were monitored with a sensitive multimeter (HP model 3457) through a high pass filter (1 MΩ resistor in parallel to a 1 μF capacitor) which served to increase the sensitivity even further by nulling the DC voltage component. A custom-made multiplexer controlled by a laboratory computer directed the inputs from each technique to a storage device. At the completion of these experiments, which lasted approximately two weeks, the specimens were removed and examined with both optical and scanning electron microscopy to observe any differences in corrosion morphologies.

Results and Discussion

The EIS data analysis technique mentioned earlier was used to calculate polarization resistance (R_p) values for each impedance plot gathered. These values were then converted into corrosion currents by multiplying them with a proportionality constant (B)[38] according to the Tafel extrapolation technique for measurement of corrosion kinetic parameters introduced by Stern[39] and Stern and Geary[40]. The corrosion current was itself converted into penetration rates using Faraday's law. The global equation is expressed in Eq. 4 where the corrosion rate is in mm/y when R_p is in $\Omega{\cdot}cm^2$. B is a proportionality constant for aluminum in chlorides (24 mV)[38], E.W. is the equivalent weight (9g) of aluminum (g/equiv.) and d its density (2.7g/cm^3).

$$\text{Corrosion rate} = \frac{3.3 \cdot B \cdot E.W.}{R_p \cdot d} \qquad (4)$$

According to the EIS polarization resistance data, which are summarized in Table 2, the 8090 alloy showed roughly equal corrosion rates for all three faces. Except for the rolled face, the corrosion rate of the 8090 alloy was substantially lower than the corresponding faces of the 2024 alloy. With the assumption that the CPE, which is directly proportional to (1-β), increases in some manner with increased pitting, the EIS data indicated that the rolled surface of the 8090 had the lowest susceptibility to pitting, followed by the long transverse edge and the short transverse edge, which had the highest rate (Table 2). Examination of these surfaces with optical and scanning electron microscopy suggested that the correlation between the CPE and pitting rate involved the number of pits formed in any given area (pit density) rather than the pit depth. The low pitting rate suggested by EIS for the rolled surface was consistent with visual observation of the long term exposure panels. However, the approximate equivalence for all three faces was not. If the interpretation of EIS data is correct, the corrosion of the rolled surface must occur initially at this high rate, but then would fall to a much lower value over the longer term. The R_p values for the 2024-T3 alloy showed a pronounced difference in overall corrosion rate between its rolled surface and its edges, with the edges having consistently higher rates. After about 50 hours, a similar trend was observed for the CPE. These results are consistent with observations made on the long term exposure panels, which were characterized by a higher density of localized corrosion sites on the edges.

On the basis of the EIS data the conclusion would be reached that the edges of the 8090-T8 alloy had lower overall corrosion rates and were less prone to pitting than their 2024-T3 counterparts. The edges of the 8090 long term exposure panels had substantial areas where no visible corrosion had occurred. This could be consistent with the lower overall corrosion rates and lower pitting density suggested by EIS results in comparison with 2024. However, the depth of attack within each pit (Fig. 1) was as large or larger than a corresponding pit on 2024. Thus the rate of corrosion within a pit was at least as severe for 8090 as for 2024.

As was the case for the 8090 alloy, the corrosion rate determined with EIS for the rolled surface of the 7075 was approximately equal to that measured for the edges. This was not consistent with the appearance of the long term panels, which suffered more metal loss along the edges than the rolled surface. The CPE values obtained for these experiments indicated that the rolled surface of the 7075 alloy had the lowest pitting density while the long and short edges had higher rates. The higher rates reached similar and essentially constant values after 200 hours. These results did correlate very well with the long term exposure tests, in which the edges did indeed suffer much worse localized attack.

According to the EIS results the rolled surface of the 2090 alloy had a consistently lower general corrosion rate than the same surface of the 7075. This did not appear to be consistent with the long term exposure tests, in which corrosion damage seemed to be more extensive on the surface of the 2090 alloy. On the other hand the EIS data suggested that the edges of the 2090 were only slightly more corrosion resistant than the 7075 edges. Once again this did not appear to be consistent with visual observation of the long term exposure panels. In this case the edges of the 2090 panels suffered noticeably less corrosion than their 7075 counterparts. The CPE data indicated that the pit density should be lower on the rolled surface of the 2090 than the 7075 and that the pit density should be much lower on the edges of the 2090 than the 7075. These results are completely consistent with the appearance of the long term exposure panels.

In an effort to correlate the parameters calculated by the exponential decay model, 610 records of fifteen-minute data gathered during the laboratory testing of the aluminum sheet material were compared to the results obtained on the same specimens with EIS or during the long term exposure to sea water. While the agreement between the noise patterns and the model seemed to be excellent (average Goodness-of-fit = 97.2% (Eq. 3)), no simple correlation could be found between any of the calculated parameters and the general corrosion rates evaluated with EIS. Such a conclusion would confirm what others[41,42] had found previously, i.e. the degree of potential fluctuations at the corrosion potential is a relatively insensitive indication of general corrosion rates.

Fig. 2 illustrates the global behavior of the average rising time measured on all three faces of 8090-T8 sheet material for each of the noise data record gathered during the experiments, when plotted as a function of corrosion potential. These two parameters were chosen for this global representation of the results because they were thought to reflect the fundamental behavior of the equilibria being established during the continuous corrosion of aluminum specimens. It was observed that the four alloys tested behave quite differently during these two week experiments.

The predominance of the high rise time values in the anodic fraction of these plots seems to be related to the good performance of an alloy and is probably associated with the control of the corrosion processes by passivation (anodic potentials). An electrical analogy would be an open circuit situation with fast unbuffered switching of the potential. The relative fraction of slow transients was quantified (everything that is not in the left uppermost corner of Fig. 2) and these fractions were compared (Fig. 3) to the average corrosion rates measured with EIS (Table 2).

While the correlation coefficient between the two variables presented in Fig. 3 seems to be excellent ($r = 0.99$) the relation itself has to be interpreted with some caution since the time of exposure, which is not represented in these comparisons, would have a strong influence on the absolute values estimated for the predominance of fast transients which were always more prevalent during the first few days of each experiment and tapered off as exposure time progressed.

Conclusion

The long term exposure tests indicated that the rolled surfaces of the 8090-T851 sheet were more resistant to corrosion than the conventional 2024-T3 sheet. Except for some pits which developed at an air/water interface, these surfaces suffered only minor corrosion. The same tests indicated that the rolled surfaces of the 2090-T8 sheet suffered as much or even more corrosion damage than their counterparts on the 7075-T6 sheet. Some fairly deep pits occurred on the rolled surfaces of the 2090, even during the exposure to sea water fog.

The results obtained during the electrochemical testing of various faces of aluminum sheet material indicated that short term EIS measurements can help to predict the general and localized corrosion behavior of this material when exposed to sea water. In fact the prediction of the localized corrosion behavior with the CPE calculated from the EIS data seemed to agree more closely to the long term tests results than the general corrosion estimation. A systematic analysis of 610 fifteen minute noise records with the stochastic pattern detector technique has also demonstrated that the exponential decay model describes almost perfectly the potential fluctuations observed during these experiments, thereby confirming the random nature of the corrosion processes in progress. The parameters revealed during the noise analysis could additionally be globally related to the features calculated from EIS measurements.

References

1. W. E. Quist and G. H. Narayanan, "Aluminum-Lithium Alloys," in A. K. Vasudevan and R. D. Doherty, Eds., Treatise on Materials Science and Technology, Academic Press, New York, 31 (1989), p. 219.
2. D.B. Williams and P.R. Howell, "The Microsstructure of Aluminum-Lithium Base Alloys," in A. K. Vasudevan and R. D. Doherty, Eds., Treatise on Materials Science and Technology, Academic Press, New York, 31 (1989), p. 364.
3. S.J. Ketcham and J.J. de Luccia, Aircraft Corrosion, AGARD Conference Proceedings No. 315 (1981).
4. C.J.E. Smith et al., "New Light Alloys," AGARD Conference Proceedings No. 444, Mierlo, Netherlands, 3-5 October 1988, p. 7-1.
5. T.S. Srivatsan, "Microstructure Compatibility of an Al-Li-Cu-Mg-Zr Alloy Exposed to Corrosive Environmenst," Report AD-A215 540, Naval Surface Weapons Center, White Oak, MD, USA (1987).
6. J. Kozol et al., "In-Service Evaluation of 2090 Aluminum-Lithium Alloy on F/A-18 Aircraft," Report AD-A248 472, Naval Air Systems Command, Washington, DC, USA (1991).
7. J.P. Moran et al., Corrosion, 43 6 (1987): p. 374.

8. D.R. Lenard, J.G. Moores. P.R. Roberge and E. Halliop, Marine Corrosion of Aluminum-Lithium Aloy Sheet, TTCP-P-TP1 Report, Defence Research Establishment Pacific, Victoria, Canada (1991).
9. R.G. Buchheit Jr., J.P. Moran and G.E. Stoner, Corrosion, 46 8 (1990): p. 610.
10. M. Habashi, Corrosion Science, in press.
11. A. Roth and H. Kaesche, "Electrochemical Investigation of Technical Aluminum-Lithium Alloys," Proceedings of Aluminum-Lithium Alloys, Williamsburg, VA, USA (1989), p. 1196.
12. R.C. Dorward, Materials Science and Engineering, 84 (1986): p. 89.
13. R.C. Dorward and K.R. Hasse, Corrosion, 44 12 (1988): p. 932.
14. B. Bavarian et al., "Localized Corrosion of 2090 and 2091 Al-Li Alloys," Proceedings of Aluminum-Lithium Alloys, Williamsburg, VA, USA (1989), p. 1227.
15. A. Buis and J. Schijve, Corrosion, 48 11 (1992): p. 898.
16. E.S.C. Chin et al., "Evaluation of 2090-T8E48 Aluminum-Lithium Plates," Report AD-A217 262, U.S. Army Materials Technology Laboratory, Watertown, MA, USA (1989).
17. C. Kumai et al., Corrosion, 45 4 (1989): p. 294.
18. T. Sheppard and N.C. Parson, Materials Science and Technology, 3 (May 1987): p. 345.
19. I. Epelboin, M. Keddam and H. Takenouti, Journal of Applied Electrochemistry, 2 (1972): p. 71.
20. V.S. Sastri and P.R. Roberge, "Monitoring Corrosion in Sour Media," Materials Performance: Sulphur and Energy, P.R. Roberge et al., Eds., The Canadian Institute of Mining, Metallurgy and Petroleum, Montreal, 1992, pp. 57-69.
21. P.R. Roberge and V.S. Sastri, CORROSION 93, Paper No. 396, (National Association of Corrosion Engineers; Houston, TX, 1992).
22. P.R. Roberge and V.S. Sastri, Corrosion Science, in press.
23. P.R. Roberge, "Analyzing Simulated Electrochemical Impedance Spectroscopy Results by the Systematic Permutation of Data Points," Electrochemical Impedance Analysis and Interpretation, D.C. Silverman and J.R. Scully, Eds., ASTM STP 1188, American Society for Testing of Materials, in press.
24. K.S. Cole and R.H. Cole, Journal of Chemical Physics, 9 4 (1941): p. 341.
25. B.W. Davidson and R.H. Cole, J. Chemical Physics, 19 12 (1951): p. 1484.
26. A.K Jonscher, Dielectric Relaxation in Solids, (Chelsea Dielectrics Press, London, U.K., 1983).
27. R. De Levie, Electrochimica Acta,, 10 (1965): p. 113.
28. P.H. Bottelbergs and G.H.J. Broers, Journal of Electroanalytical Chemistry, 72 (1976): p. 257.
29. J.B. Bates, J.C. Wang and Y.T. Chu, Solid State Ionics, 18&19 (1986): p. 1045.
30. P.R. Roberge, E Halliop, M. Asplund and V.S. Sastri, Journal of Applied Electrochemistry, 20 (1990): p. 1004.
31. P.R. Roberge, "Analyzing Electrochemical Impedance Corrosion Measurements by the Systematic Permutation of Data Points," Computer Modeling in Corrosion,

R.S. Munn, Ed., ASTM STP 1154, (American Society for Testing of Materials 1992), p. 197.

32. P.R. Roberge, E. Halliop and V.S. Sastri, Corrosion, 48 6 (1992): p. 447.
33. P.R. Roberge, E. Halliop, D. Lenard and J. Moores, Corrosion Science, in press.
34. P.R. Roberge, E. Halliop, D. Lenard and J.G. Moores, "Marine Corrosion Behavior of Al-Li Alloy Sheet," 3rd. Int. SAMPE Metals and Metals Processing Conf., Toronto, October 20-22, 1992, p. M51.
35. J.S. Bendat and A.G. Piersol, Random Data: Analysis and Measurement Procedures, 2nd Ed, (John Wiley & Sons, New York, 1986).
36. P.R. Roberge, M. Farahani and K. Tomanstchger, Journal of Power Sources, 41 3 (1993): p. 321.
37. P.R. Roberge, Journal of Applied Electrochemistry, in press.
38. R. Grauer, P.J. Moreland and G. Pini, A literature review of polarisation resistance constant (B) values for the measurement of corrosion rate, (National Association of Corrosion Engineers, Houston, TX, 1982).
39. M. Stern, Corrosion, 14 (1958): p. 440.
40. M. Stern and A.L. Geary, Journal of the Electrochemical Society, 104 (1957): p. 56.
41. Lumsden, M.W. Kendig and S. Jeanjaquet, Corrosion92, Paper No. 224, (National Association of Corrrosion Engineers, Houston, TX, 1992).
42. Eden, K. Hladky and D.G. John, Corrosion86, Paper No. 274, (National Association of Corrosion Engineers, Houston, TX, 1986).

Table 1 Nominal composition of alloys tested (wt %).

Alloy	Li	Cu	Mg	Si	Fe	Mn	Zn	Zr
2024	-	3.8-4.9	1.2-1.8	0.5	0.5	0.3-0.9	0.25	-
2090	1.9-2.6	2.4-3.0	0.25	0.1	0.12	0.05	0.1	0.08-0.15
7075	-	1.2-2.0	2.1-2.9	0.4	0.5	0.3	5.1-6.1	-
8090[a]	2.35	1.23	0.67	0.02	0.03	0.001	0.02	0.11

Note a: Actual heat analysis for the specimens supplied by ALCAN

Table 2 Analyzed EIS results obtained with aluminum alloys.

Alloy	Thickness (mm)	Face	Corrosion Rate (mm/y)	β -
2024-T3	1.0	Rolled	0.05	0.81
		Long	0.16	0.77
		Short	0.22	0.75
2090-T3	1.2	Rolled	0.06	0.89
		Long	0.08	0.82
		Short	0.09	0.79
7075-T6	1.0	Rolled	0.14	0.87
		Long	0.11	0.63
		Short	0.12	0.68
8090-T8	1.5	Rolled	0.05	0.93
		Long	0.04	0.87
		Short	0.03	0.81

Table 3 Results of sea water exposure.

Alloy	Fog		Immersion		
			Partial		Total
	general	crevice	general	interface	
2024-T3	pitting	6 sites	severe pitting	severe pitting	severe pitting
2090-T3	few deep pits	none	"poultice"	severe	scattered pits
7075-T6	pitting	1 site	"poultice"	severe	scattered pits
8090-T8	minor	1 site	minor	few deep pits[a]	minor

[a] Figures 1a and 1b.

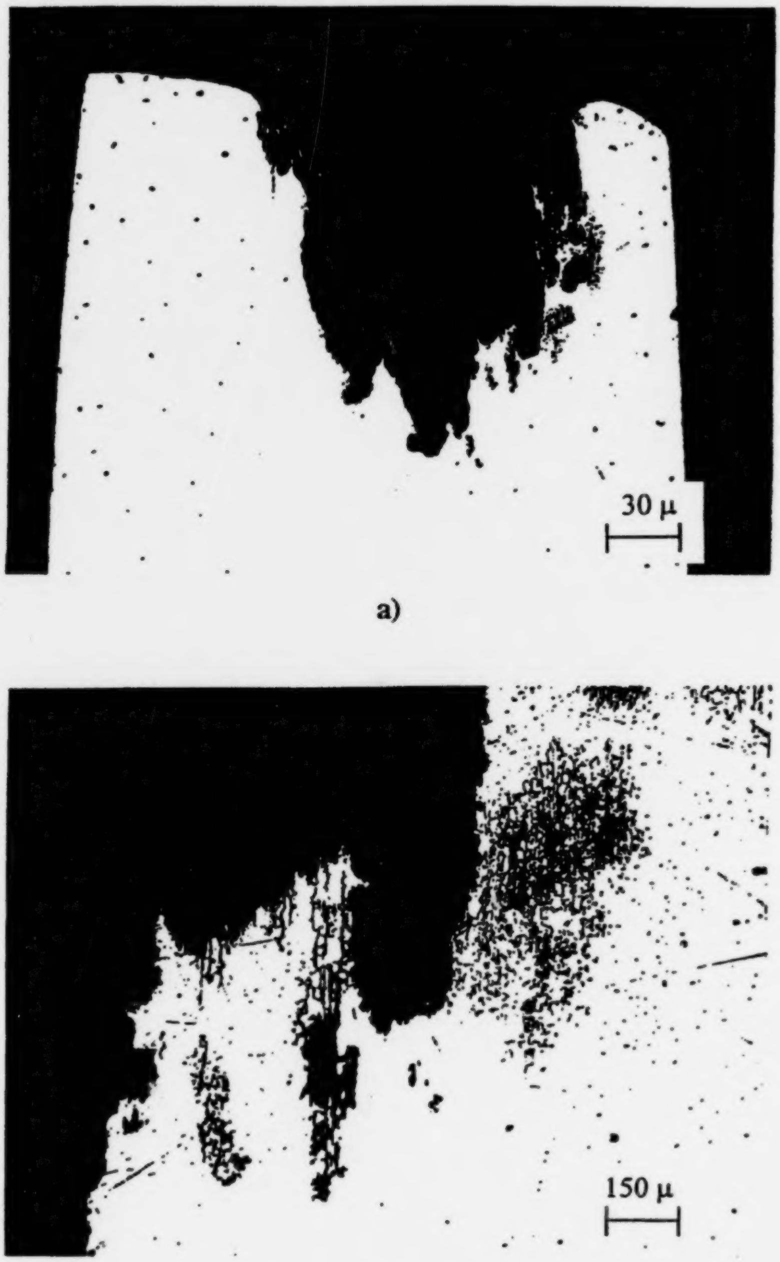

a)

b)

Fig. 1 Metallograph of a section through an edge of the 8090 panel immersed in sea wate during four months; a) at 64x and b) at 320x to illustrate the intergranular nature of th corrosion attack.

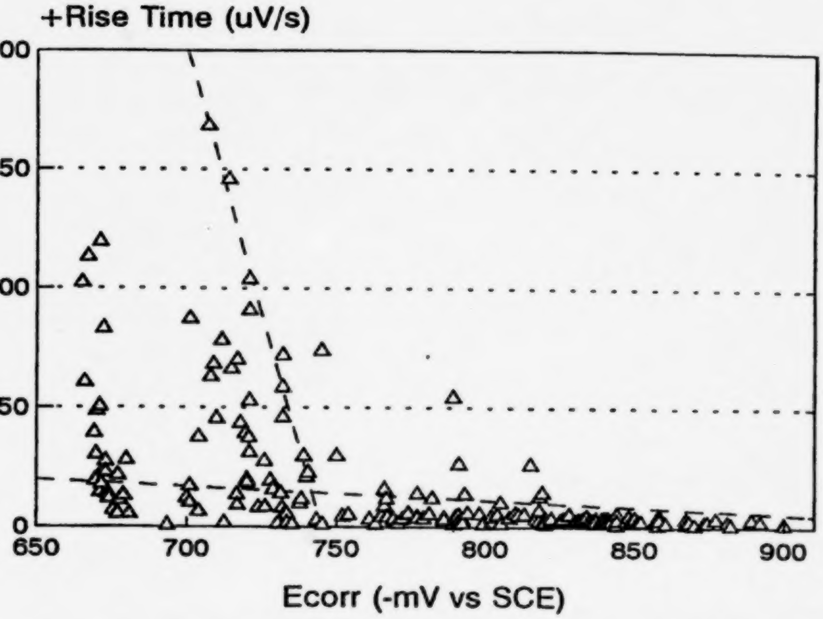

Fig. 2 Positive rise time calculated for each of 128 noise records gathered during the laboratory testing of 2090-T3 sheet material as a function of the corrosion potential.

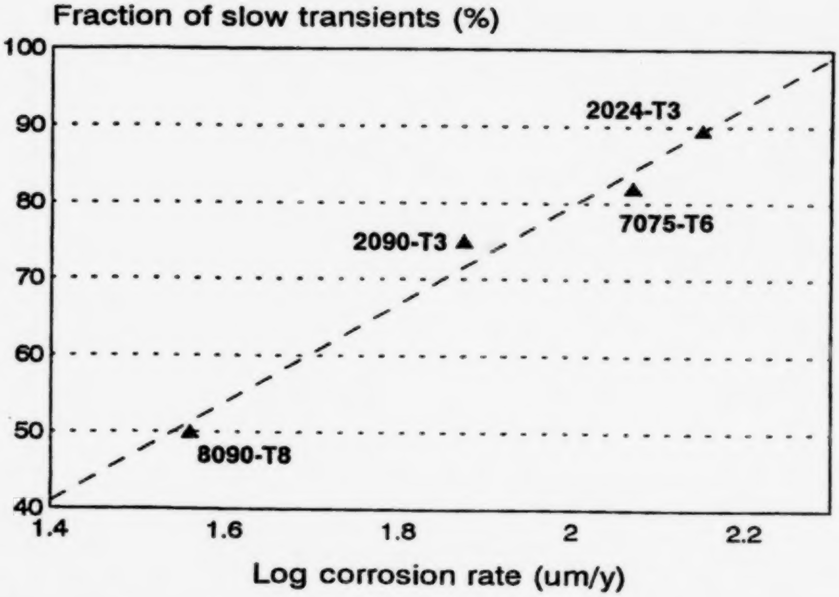

Fig. 3 Fraction of slow potential transients as a function of average corrosion rates.

141642

10.

"Comparison of the Response of a Variety of Aluminum-Lithium Alloys During Accelerated Laboratory Corrosion Tests"

M. Roth

QETE, Hull, P.Q.

EVALUATION OF THE CORROSION RESISTANCE OF ALUMINIUM-LITHIUM ALLOYS

Martin Roth
Quality Engineering Test Establishment
Department of National Defence
Ottawa, Canada
K1A 0K2

INTRODUCTION

The long term resistance and serviceability of an aircraft structure to its in-service environment is addressed at the design stage by the selection of materials with intrinsic corrosion resistance and by the use of appropriate protection schemes (i.e. anodizing, plating, sealing, painting...). However, it is well known that most heat treatable high strength aluminum alloys for aerospace applications are, to some degree, susceptible to localized forms of corrosion, such as pitting, exfoliation and stress corrosion cracking (SCC) [1].

The intrinsic corrosion resistance of Al-Li alloys in a relatively aggressive maritime environment is still relatively poorly understood. There is a scarcity of data on the long term corrosion behaviour of current Al-Li alloys which can be directly applied to the alloys selected for the EH101. Extensive corrosion resistance data have been generated in laboratories using accelerated corrosion tests. These results have to be interpreted with caution for two main reasons. Firstly, the early investigations were performed on developmental and no longer relevant alloys with compositions, processing routes, microstructure and tempers which do not necessarily correspond to those currently selected. Secondly, there is an increasing body of evidence indicating that some of the conventional accelerated corrosion tests rate Al-Li alloys unreliably or might not apply unmodified to these alloys. Furthermore the topic of the correlation of laboratory data with real life behaviour is still being debated.

D// QETE has embarked on an evaluation of the corrosion behaviour of Al-Li alloys using current production materials and tempers plus a few other Al-Li and conventional alloys for comparison purposes. ~~Table 1 lists the materials investigated. While bare and anodized panels are being exposed to a seacoast environment at DREP,~~ QETE has performed/is performing a number of laboratory investigation to:

- verify that the corrosion resistance criteria set in the specifications are met,
- obtain a relative ranking of all alloys evaluated,
- broaden the data base for correlation with the outdoor exposure panels,
- identify potential problem areas. //

Most Al-Li materials specifications call for the evaluation of resistance to intergranular corrosion (IGC), exfoliation and, for forgings, SCC. QETE performed the specified IGC and exfoliation tests. The pitting behaviour of the same materials was evaluated using the ASTM B117 salt spray and the ASTM G 44 alternate immersion in 3.5 % NaCl. In addition specimens were half immersed in sea water. Some exploratory investigation of SCC of forged material has been performed.

MIL-H-6088 INTERGRANULAR CORROSION TEST

The evaluation of IGC is one of the quality assurance provisions of the specification MIL-H-6088 "Heat Treatment of Aluminum Alloys" (paragraphs 4.4.3 and 4.5.3). It was introduced in the mid forties when exfoliation and SCC were identified with IGC and blame was often laid on faulty heat treatment, particularly the quality of the quench following solution heat treatment [2]. When applied to the conventional Al alloys of the 2xxx and 7xxx series, serviceability can only be predicted for thin sections of the naturally aged Al-Cu alloys and the peak aged Al-Cu-Zn-Mg alloys. Despite these limitations this IGC test is still considered relevant as it has just been incorporated in ASTM G110-92 "Standard Practice for Evaluating Intergranular Corrosion Resistance of Heat Treatable Aluminum Alloys by Immersion in Sodium Chloride + Hydrogen Peroxide Solution".

The MIL-H-6088 or the AECMA (Association Européennnes des Constructeurs de Matériel Aérospatial) EN 2716 intergranular corrosion tests have been called for in a number of prEN specifications for Al-Li alloys. For most materials and forms a limit of attack of 125 microns has been set, but in some cases the limit is 150 or 200 microns. However the rationale behind the selection of these limits is not known. MIL-H-6088F does not specify what an acceptable limit is for IGC. In the section on limits of acceptability, paragraph 4.5.3 (Intergranular Corrosion and Alclad Diffusion) states: "There shall be no evidence of excessive intergranular corrosion or Alclad diffusion. Consideration should be given to size and thickness of the material in deciding whether intergranular corrosion is excessive."

QETE performed this specified test following the procedure outlined in para 4.4.3 of MIL-H-6088F to establish trends within the families of Al-Li alloys from changes in microstructure, composition or heat treatment. The choice of surface to be evaluated was unclear: some specifications indicate that the surface at mid-thickness (T/2) should be tested, others mention T/10 and the remaining do not specify any surface (see Table 2). As the location of the tested surface is believed to be less significant in thin products which will not undergo surface machining, the original surface was evaluated. Care was exercised in preparing the edges of the specimens so that IGC, if any, of the exposed end grains could also be investigated. The specimens were examined metallographically to determine the depth of the attack.

In many cases, examination of the specimens revealed a combination of surface pitting and IGC. QETE's results are summarized in Table 2 where the depth of pitting is listed alongside the maximum depth of intergranular corrosion measured from the initial sample surface.

The behaviour of the 8090C Al-Li sheets is of prime interest as their extensive use is forecast. The sheets of recrystallised 8090C are received in the formable T3 temper and will be used in the heat treated T81, T621 and predominantly T8 tempers. The T3 temper did not show any IGC; only superficial pitting was observed. The other tempers showed localized areas of IGC, the depth of attack increasing from 100 to 150 microns going from the T81 to the T8 to the T621 temper (Figure 1). Often the width of the intergranular zone was about the same or slightly larger than its depth. The locations of the IGC zones were random except for the T621 temper where the attack was localized in areas of small grains between large surface grains which resulted from grain growth during heat treatment (Figure 1). Another noticeable feature was the quite extensive and relatively uniform attack of the end grains in the heat treated sheets. The depth of the surface and end grain IGC were similar. The other recrystallized sheet material investigated, 2091-T8, showed a maximum depth of attack of about 200 microns, and severe and uniform end grain IGC.

In the case of the unrecrystallized 2090 sheets, the IGC was more severe in the heat treated sheets than in the as received sheets with either the T3 (T3E28) or T31 (T3E27) temper. The as-received T3 sheet was slightly less attacked than the as received T31 material. The same ranking was observed after heat treatment, for the T84 and T8x temper respectively. The zones of attack were much wider than they were deep (Figure 1). The maximum depth of attack was at most 100 microns. The attack of the end grains was not very extensive and usually restricted to the mid-planes.

The IGC of the surface of the unrecrystallized 8090A-T851 extrusion was dependent on the local microstructure. The maximum depth of attack of 60 microns occurred in areas with small grains, otherwise only pitting was observed. The depth of attack was more significant when the internal grain structure was exposed (Figure 2). The unrecrystallized 8090A sheet, in the as-received T351 temper, was only slightly pitted.

In the case of forged materials, 5091 (905XL) did not show any signs of pitting or IGC. The localized IGC of the two heat treated 8090 forgings showed directionality and depended on the orientation of the recrystallized grains (Figure 2). The depth of attack was around 100 microns.

The conventional 7050 and 7075 alloys in the overaged T73xx temper, providing improved stress corrosion resistance, did not undergo IGC but instead showed severe pitting up to 180 microns for 7050 and 150 microns for 7075.

To summarize the results of the IGC tests:
- the depth and severity of the attack was dependent on grain structure and heat treatment,
- as received materials in the T3 tempers showed little or no IGC,
- heat treated materials, especially those with a recrystallized grain structure, were more severely attacked in this test,
- recrystallized sheets showed fairly uniform end grain attack,
- the localized grain flow in extrusions and forgings affected the depth of attack,
- the depth of attack was in general within the specified limits.

EXFOLIATION CORROSION

Exfoliation is a form of localized corrosion where attack propagates along preferential paths parallel to the material surface. Corrosion products create a wedging action which separates layers of metal leading to severe delamination; heat treatable Al alloy sheet, plate and extrusion products are particularly prone to exfoliation, since they often have highly directional grain structures which can be susceptible to intergranular modes of attack [3].

Over the years a number of accelerated exfoliation corrosion tests have been developed. Reference [4] discusses the selection of ASTM test methods, the round-robin qualification tests, the known alloy applicability of the standard methods, and their appropriateness when testing new alloys or tempers.

The ASTM G 34 EXCO immersion test has gained wide acceptance for 2xxx and 7xxx aerospace alloys, with immersion periods of 96 hours prescribed for the 2xxx alloys and 48 hours for the 7xxx alloys [5]. The panels are then visually rated using the reference photos in ASTM G 34.

The EXCO test has been used to evaluate Al-Li alloys, but it has been reported that the 96 hour immersion is too severe and not representative of outdoor performance for a variety of Al-Li alloys [6, 7]. A number of investigators have shown that there is a better correlation between the ASTM Practice G 85 Annex A2 cyclic acidified salt fog testing also known as MASTMAASIS (Modified ASTM Acetic Acid Salt Intermittent Spray) test and outdoor exposure for some Al-Li alloys [8]. However this longer test requires a special chamber and exact definition of the test conditions (i.e. wet or dry bottom) [3, 7].

Because of its simplicity and reproducibility, the EXCO test still has appeal as a qualification test. This is why some material specifications call for a 48 hour EXCO test with a rating not worse than EB. Another approach, proposed by Alcoa, was to modify the EXCO solution by increasing its pH and adding $AlCl_3$ to eliminate the dissolution of the alloys which could be quite severe in the early stages of immersion in the standard solution [6].

QETE has evaluated Al-Li and conventional Al alloys using the standard EXCO solution with immersion times of 48 and 96 hours at room temperature and the Alcoa modified EXCO solution for 48 hours at 52°C for Al-Li and 2xxx alloys, and 96 hours at room temperature for 7xxx alloys.

Visual evaluation of the 8090C panels in the T3, T81 ,T8 and T621 tempers revealed a similar relative ranking under these three exposure conditions (Figure 3). The material in the as-received T3 temper showed the least exfoliation. The heat treated samples were more severely attacked especially 8090C-T8 where heavy layers of material lifted from the surface in the standard EXCO solution. The exfoliated products were usually much finer in the modified solution. Evaluation of the 2090 panels in the T3, T31, T84 and T8x tempers also revealed a similar ranking in the EXCO and modified EXCO solutions. In the standard EXCO solution there was a marked difference between the very limited exfoliation in the as-received T3 and T31 tempers and the more severe attack in the aged T84 and T8x tempers, while in the modified solution all panels were exfoliated (Figure 3).

The other product which showed severe exfoliation in these tests was the 8090A-T851 extrusion. Some severe delamination can be seen in Figure 4. It will be important to establish more accurately the exfoliation susceptibility of this material as well as 8090C-T8, because the laboratory tests to date have shown both to severely exfoliate.

The panels exposed at DREP will provide a more realistic rating of the alloys as seacoast exposure is considered to be more representative of the most extreme conditions parts can encounter in service. As well comparison between the outdoor exposure trials and accelerated laboratory testing will establish the appropriateness of the latter tests. However, at least two years exposure is needed at a seacoast site to be considered a significant length of exposure [4]. Materials with marked susceptibility to exfoliation normally begin to show some evidence of attack within 6 to 24 months.

ASTM B 117 SALT FOG EXPOSURE 1000 HOURS
ALTERNATE IMMERSION IN 3.5% NaCl (ASTM G 44) 1000 HOURS

The specimens of Al-Li and conventional alloys have been exposed to the ASTM B117 salt spray for 1000 hours and to alternate immersion in 3.5% NaCl as outlined in ASTM G 44 also for 1000 hours [9]. After removal from the chambers, the specimens were cleaned using concentrated nitric acid. Visual examination of the specimens revealed that pitting was the main form of corrosion induced. The density of pitting was dependent on the material and heat treatment. In general pitting was more severe in materials exposed to the alternate immersion test cycle.

Radiographs of the sheet specimens provided a qualitative assessment of the density and severity of pitting (Figures 5 and 6). Overall evidence from the radiographs tends to indicate a significantly higher density of pits in the recrystallized 8090C and 2091 alloys in the peak aged T8 temper than in the other tempers (Figure 5). In the case of the 2090 alloy, the pit density was relatively high in both the as-received and aged tempers (Figure 6). The conventional 2024-T3 alloy in the same alternate immersion test was very severely pitted. It is proposed to further evaluate the specimens by metallography for pit density and depth.

HALF IMMERSION IN SEAWATER

Partial immersion in flowing seawater was selected to represent a very severe marine environment for the Al-Li and conventional Al alloys. The sheet, extrusion and forging samples with machined or ground edges were cleaned using a chromic-sulphuric acid pickle, a common pretreatment prior to anodizing Al alloys. Teflon or ceramic crevice washers were installed on both sides at the centre of some panels using stainless steel nuts and bolts insulated with a plastic sleeve. The specimens were suspended in the flowing seawater tank at DREP in such a way that only the bottom half of the samples was immersed. The 7 to 11°C water flowed past the specimens with a velocity of 1 cm/sec [10]. The specimens were removed after 1000 hours. Once photographed, they were cleaned using concentrated nitric acid.

Visual examination of the specimens revealed, to varying degrees, many forms of corrosion: pitting in the immersed half and less so in air, water line general corrosion and pitting, edge attack, and crevice corrosion. Visual evaluation of the severity of the corrosion was made difficult by the appearance of the specimens where the immersed half had turned quite dark. Radiographs of the sheet specimens proved to be easier to interpret as the local change in density of the radiographic film was directly related to the thickness of the material or depth of corrosion (Figures 7 and 8).

All the specimens showed extensive corrosion at or slightly above the water line. A previous investigation had shown that this is an area where the corrosion is expected to be severe because of the possibility of differential aeration cells resulting from changes in oxygen concentration in the water as a function of distance from the interface or formation of porous corrosion products [10]. The latter situation seemed to predominate. The water line corrosion ranged from a high density of small pits to scattered relatively deep areas of localized corrosion. The severity of the attack was difficult to quantify, but 2024-T3 was considered the worst material for this type of attack.

Attack of the immersed edge ranged from negligible to quite severe. In this case, by examining the radiographs, a clear distinction could be made between the sheets with a recrystallized grain structure and those with unrecrystallized grains, the latter showing either no attack or very limited attack. As far as 8090C was concerned the attack was fairly uniform in the T8 and T81 tempers, and more localized and deeper in the T3 and T621 tempers.

The radiographic observations were confirmed by metallographic observation of a number of specimens.

STRESS CORROSION CRACKING EVALUATION BY ALTERNATE IMMERSION IN 3.5% NaCl (ASTM G 44) USING THE BREAKING LOAD METHOD

The SCC resistance of Al alloys has often been measured in the laboratory using preloaded specimens (i.e. smooth axial, C-ring or bend type) in a corrosive environment. With enough specimens, a time to failure versus exposure stress curve can be obtained. This allows for the determination of a threshold stress below which failure is not expected to occur in that environment. The ASTM G 44 practice is often followed [9]. As a qualification test, a pass-fail criterion is often set: the specimens must withstand a specified stress for a given length of time in a corrosive environment, typically the one defined in ASTM G 44. This approach to SCC testing provides little information on the process of SCC (i.e. initiation, crack growth, and final failure) or the factors affecting each of these stages.

The breaking load method was developed at the Alcoa laboratories to overcome some of these shortcomings. The method involves the measurement of the residual strength of tensile bar specimens which have been exposed to different stress levels for increasing lengths of time in a corrosive environment. The residual strength provides an indication of the corrosion damage, such as pitting and SCC, sustained by the specimens in the corrosive environment. Two approaches have been followed in analyzing the results of the breaking load method. The statistical one allows the determination of a statistical threshold stress. This analysis is described in more detail in Reference [11]. In the other approach the data is analyzed in fracture mechanics terms to correlate the residual strength with depth of corrosion or SCC [12].

QETE has evaluated the SCC of 8090 Pechiney material from a prototype forging using the breaking load method to determine the potential of this approach for evaluating current materials.

Tensile specimens with a diameter of 0.125 inches were machined so that their axis of revolution were parallel to the short transverse (ST) direction of the forging. The specimens were preloaded using fixtures and a loading frame illustrated in Figure 3 of Reference [13]. The exposure stresses selected were 10 and 20 ksi. The preloading stress was measured using an extensometer. The preloaded specimens, as well as unstressed ones, were exposed to the standard ASTM G 44 alternate immersion environment (Figure 9). That is, the specimens were immersed for 10 minutes in a 3.5% NaCl solution, then allowed to dry for 50 minutes at 27±1°C at a relative humidity of 45±6%, and the cycle repeated. Triplicate specimens were removed after 2, 5, 7, and 9 days. They were tensile tested within two hours of being removed from the chamber to determine their residual strengths.

The average breaking stresses are listed as a function of exposure time in Figure 9. Those results are also plotted in Figure 10 alongside corresponding data for 7075-T651 obtained from the literature [12]. In the unstressed specimens, a gradual decrease in strength is observed as a function of time as the result of pitting and general corrosion. The drop is more pronounced for the specimens prestressed at 10 ksi and especially 20 ksi. Care has to be taken interpreting the 20 ksi data for 7 and 9 days because a number of the specimens had broken in the chamber prior to their removal; in this case the corresponding breaking stress was taken to be the exposure stress, 20 ksi. The behaviour of 7075-T651 and 8090 is fairly similar. In comparison a very stress corrosion resistant material, such as 7075-T73, will only show a small decrease in breaking stress even at significantly higher loads [12].

The breaking load data can be interpreted in fracture mechanics terms [12]. Three different stages can be considered (Figure 11). At small flaw sizes, the breaking load can be correlated using a net section strength/limit load analysis where the reduced strength is proportional to the reduced cross sectional area. For deeper cracks, the residual strength can be analyzed in terms of linear elastic fracture mechanics (LEFM). The curve for 7075-T651 was obtained using an equivalent semi-elliptical flaw geometry of depth a and major axis 2.5a [12]. The middle range corresponds to the elastic-plastic transition between the limit load range for small crack depths and the LEFM range for longer cracks. The corresponding curves for 8090 were obtained from those for 7075-T651 by scaling the data in relation to their relative ultimate tensile strengths and toughnesses.

The fracture surfaces of the broken specimens were examined under a stereomicroscope and the maximum crack depth estimated. The experimental points were plotted in relation to the theoretical breaking stress versus flaw depth curve for 8090. There is a good correlation in most cases. The two exceptions resulted from multiple cracking in one case and a nearly triangular crack in the other.

This method of analysis can then be used to determine the evolution of the depth of cracking as a function of exposure time as shown in Figure 12 for 7075-T651 and 8090. Such plots provide a better comparison of the SCC behaviour of materials because only cracking is compared, unaffected by differences in tensile strength and fracture toughness of the alloys. Again the behaviour of 7075-T651 and this 8090 forging are similar; however the performance of these two alloys is inferior to that of 7xxx Al alloys in the T73 temper [12].

OUTDOOR SEACOAST EXPOSURE

In order to validate the laboratory evaluation of the corrosion resistance of Al-Li alloys, 4"x 6" panels of the same sheet materials have been exposed to a seacoast atmosphere at DREP since November 1992.

Three sets of panels were prepared. The first one was pickled in a chromic-sulphuric acid solution. The two other batches were given the same pretreatment and then chromic acid anodized following standard practice and sealed in distilled hot water. One batch of the anodized panels was scratched to simulate damage to the anodizing.

CONCLUSIONS

The accelerated laboratory corrosion tests revealed that the resistance of Al-Li alloys to these corrosive environments was strongly dependent on microstructure and heat treatment. In general materials in the as-received tempers were less susceptible to attack than those in the peak aged tempers; however the relative ranking of the alloys was test dependent.

The MIL-H-6088 IGC test revealed that the as-received materials in the T3 tempers were much less susceptible to IGC than the heat treated materials. The sheets with a recrystallized grain structure showed fairly uniform end grain attack. In forgings and extrusions the severity of the attack was dependent on the microstructure. The depth of IGC attack was usually within the limits specified.

The severity of the exfoliation depended on the test environment and the heat treatment of the materials. The 8090C-T8 sheet and the 8090A-T851 extrusion were the most susceptible. The behaviour of these two materials will have to be closely monitored during the seacoast exposure test which is considered to be more representative of the most extreme conditions parts can encounter in service.

The salt fog exposure and the alternate immersion in 3.5% NaCl solution tests mainly induced pitting. The latter test was more severe. In 8090C the density of pits was the highest in the T8 temper material, while in 2090 pitting was observed in all tempers investigated.

The specimens half-immersed in sea water showed many forms of corrosion: pitting in the immersed half and less so in air, water line general corrosion and pitting, edge attack, and crevice corrosion. The recrystallized Al-Li alloys showed more severe attack of the end grains. This potential greater susceptibility of the end grains deserve further evaluation.

In all the corrosion tests performed to date, 5091 (905XL) did not show signs of corrosion.

The accelerated laboratory corrosion tests only provided a relative ranking for the different alloys/heat treatment combinations. These results will be validated after evaluation of the panels which have been exposed to a seacoast atmosphere.

The breaking load approach to the evaluation of SCC appears quite promising in that each factor affecting SCC can be separated.

REFERENCES

[1] Wallace, W., Hoepner, D.W., and Kandachar, P.V., AGARD Corrosion Handbook Volume 1, Aircraft Corrosion: Causes and Case Histories, AGARDograph No.278.

[2] Lifka, B.W. and Sprowls, D.O., "Significance of Intergranular Corrosion in High-Strength Aluminum Alloy Products," Localized Corrosion-Cause of Metal Failure, ASTM STP 516, American Society for Testing and Materials, 1972, pp. 120-144.

[3] Colvin, E.L. and Murtha, S.J., "Exfoliation Corrosion Testing of Al-Li Alloys 2090 and 2091", Aluminum-Lithium Alloys: Proceedings of the Fifth International Aluminum-Lithium Conference, Sanders, T.J. and Starke, E.A. Eds, Materials and Component Engineering Publications, Birmingham, England, 1989, pp. 1251-1260.

[4] ASTM G 112 - 92 "Guide for Conducting Exfoliation Corrosion Tests in Aluminum Alloys", Annual Book of ASTM Standards, Vol 03.02.

[5] ASTM G 34 - 86 "Standard Test Method for Exfoliation Susceptibility in 2xxx and 7xxx Series Aluminum Alloys (EXCO Test)", Annual Book of ASTM Standards, Vol 03.02.

[6] Lee, S. and Lifka, W., "Modification of the EXCO Test Method for Exfoliation Corrosion Susceptibility in 7xxx, 2xxx and Aluminum-Lithium Alloys", New Methods for Corrosion Testing of Aluminum Alloys, ASTM STP 1134, American Society for Testing and Materials, 1992, pp. 1-19.

[7] Schra, L., 't Hart, W.G.J., and Boogers, J.A.M., "Outdoor Corrosion Testing of Aluminium-Lithium Alloys", National Aerospace Laboratory Report NLR TP 90272 U, Amsterdam, The Netherlands.

[8] Smith, C.J.E., et al., "Corrosion and Stress Corrosion of Aluminium-Lithium Alloys", New Light Alloys, AGARD Conference Proceedings No.444.

[9] ASTM G 44 - 88, "Standard Practice for Evaluating Stress Corrosion Resistance of Metals and Alloys by Alternate Immersion in 3.5% Sodium Chloride Solution", Annual Book of ASTM Standards, Vol 03.02.

[10] Roberge, P.R., et al., "Marine Corrosion Behaviour of Al/Li Sheet", 3rd International SAMPE Metals Conference, October 20-22, 1992, pp. M51-M62.

[11] Colvin, E.L. and Emptage, M.R., "The Breaking Load Method: Results and Statistical Modification from the ASTM Interlaboratory Test Program", New Methods for Corrosion Testing of Aluminum Alloys, ASTM STP 1134, American Society for Testing and Materials, 1992, pp. 82-100.

[12] Lukasak, D.A. et al., "Damage-Based Assessment of Stress Corrosion Performances Among Aluminum Alloys", New Methods for Corrosion Testing of Aluminum Alloys, ASTM STP 1134, American Society for Testing and Materials, 1992, pp. 101-116.

[13] ASTM G 49 - 85 " Standard Practice and Use of Direct Tension Stress-Corrosion Test Specimens", Annual Book of ASTM Standards, Vol 03.02.

MATERIALS

SHEETS	Recrystallized	
	8090C-T3	
	8090C-T81	T3 + 24 hours at 150°C
	8090C-T8	T3 + 45 hours at 175°C
	8090C-T621	T3 + 20 min at 520°C, cold water quench, 24 hours at 150°C
	2091-T8	
	Unrecrystallized	
	8090A-T351	
	2090-T31 (T3E27)	
	2090-T8X	T31 + 24 hours at 152°C
	2090-T3 (T3E28)	
	2090-T84 (T8E40)	T3 + 24 hours at 152°C
EXTRUSIONS		
	8090A-T851	
	8090 (Pechiney)	
	8090 HT (Pechiney)	
FORGINGS		
	8090-T8xx (Pechiney)	
	8090-T852 (Alcan)	
	5091 (905XL)	

Table 1

TEST	MIL-H-6088 INTERGRANULAR CORROSION (IGC)		
MATERIAL	SPECIFICATION	PITTING	IGC
8090C-T3		20-30 µm	
8090C-T81	PrEn 6001 Ed 3 125 µm T/2	20 µm	100 µm
8090C-T8		20 µm	120 µm
8090C-T621	PrEN 6002 Ed 3 125 µm T/2	20-30 µm 50 µm max	150 µm
8090A-T351		10 µm 30 µm max	
2090-T31 (T3E27)		20-50 µm	50 µm av. 100 µm max
2090-T8x		50 µm	100 µm
2090-T3 (T3E28)		30 µm	
2090-T84	PrEN 6011 Ed 1 125 µm T	30 µm	40-50 µm 70 µm max
2091-T8		20-30 µm	200 µm
8090A-T851 SEAT TRACK	PrEN 6014/5 100 m T/2		60 µm
8090 ANGLE (P)		20 µm	0 µm
8090 HT ANGLE (P)		20 µm	70 µm max
8090-T8xx FORGING (P)			100 µm
8090-T852 FORGING (A)			120 µm
5091 (905XL)			0 µm
7050-T73		150 µm max	
7075-T7351 SEAT TRACK		180 µm max	

Table 2

INTERGRANULAR CORROSION RESULTS

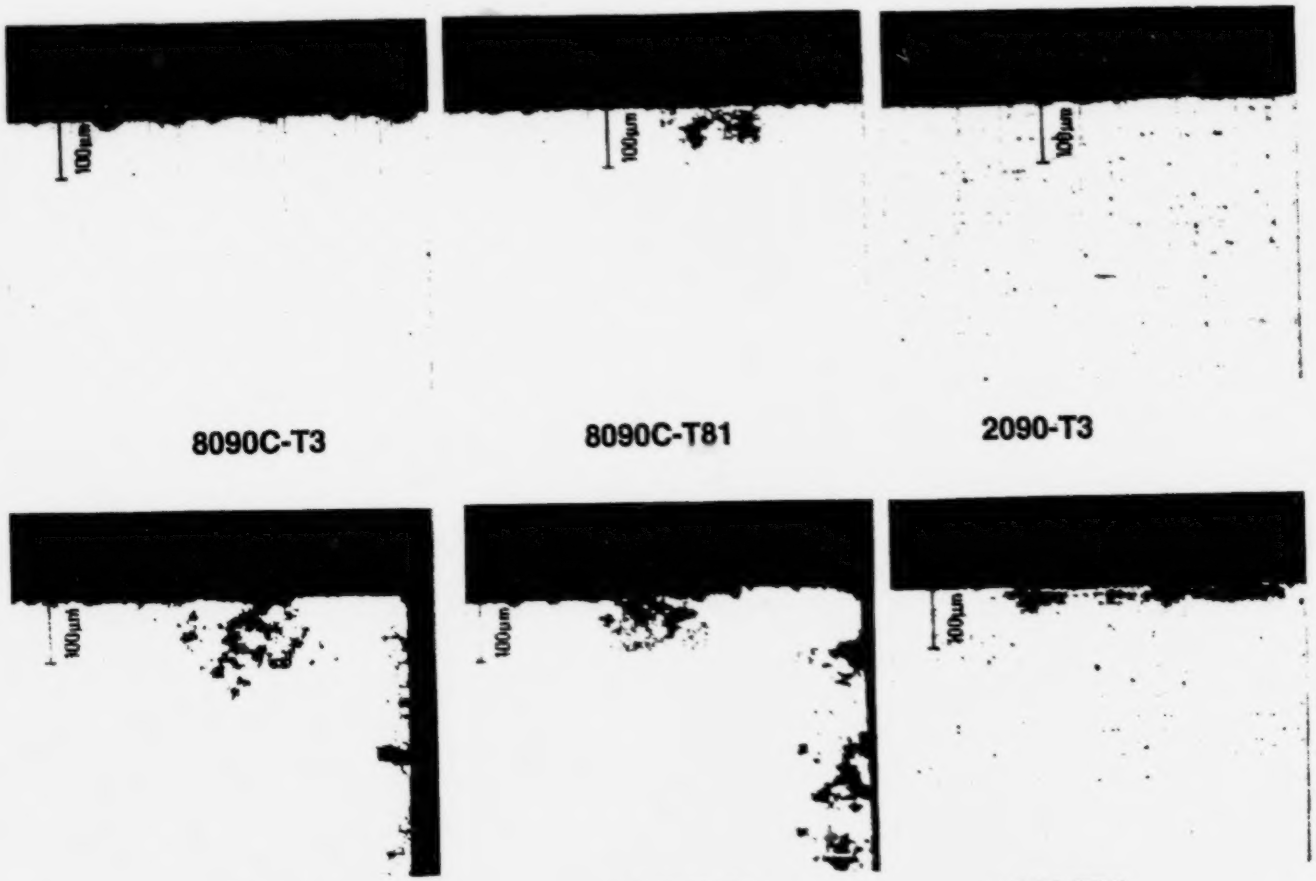
100µm
100µm
100µm
100µm
100µm
100µm

8090C-T3 8090C-T81 2090-T3

8090C-T8 8090C-T621 2090-T84

Figure 1

INTERGRANULAR CORROSION RESULTS

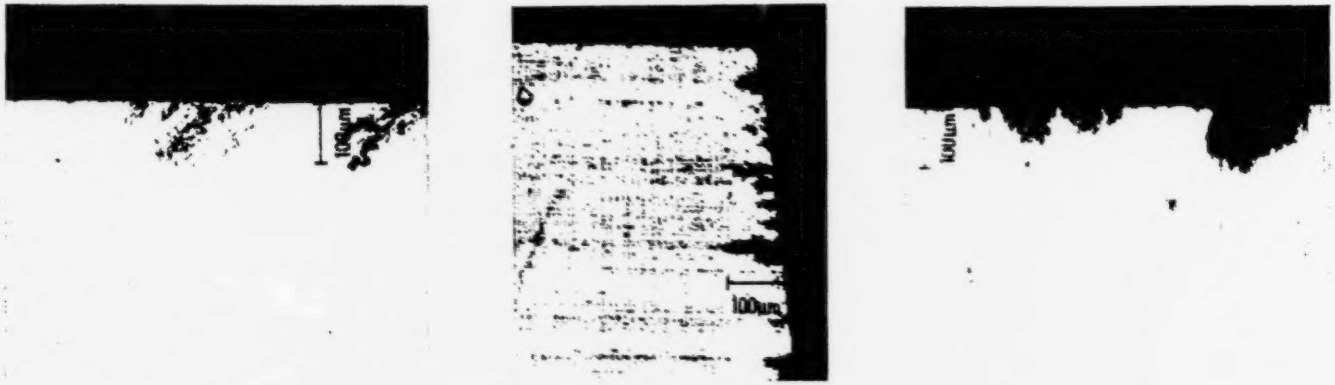

8090-T852 8090A-T851 7075-T7351

CONCLUSIONS:

- HEAT TREATMENT DEPENDENCE
- MICROSTRUCTURE DEPENDENCE (RECRYSTALLIZED VS UNRECRYSTALLIZED, GRAIN FLOW)
- SOME MATERIALS SHOW PITTING RATHER THAN IGC ATTACK USUALLY LESS THAN 150 MICRONS
- EDGE ATTACK

Figure 2

EXFOLIATION EVALUATION RESULTS

THE RELATIVE RANKING OF THE ALLOYS IS ABOUT THE SAME IN THE THREE TESTS, EXCO FOR 48 AND 96 HOURS, AND MODIFIED EXCO FOR 8090C AND 2090 SHEETS IN DIFFERENT TEMPERS.

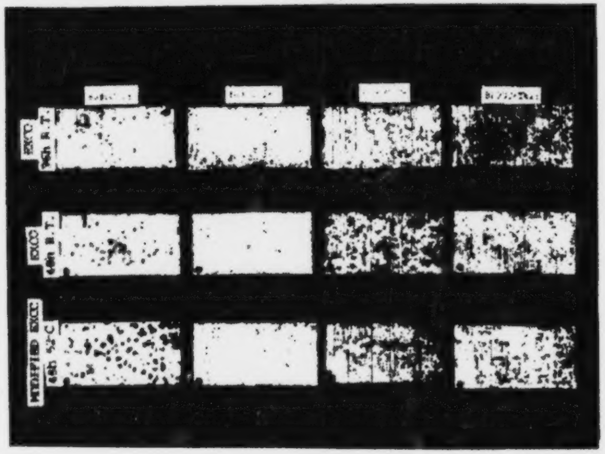
EXCO 96h R.T.
EXCO 48h R.T.
MODIFIED EXCO 48h 52°C

FOR RECRYSTALLIZED 8090C SHEETS:
- T3 RELATIVELY IMMUNE
- T81 FAIRLY IMMUNE
- T8 MOST SUSCEPTIBLE
- T621 FAIRLY IMMUNE

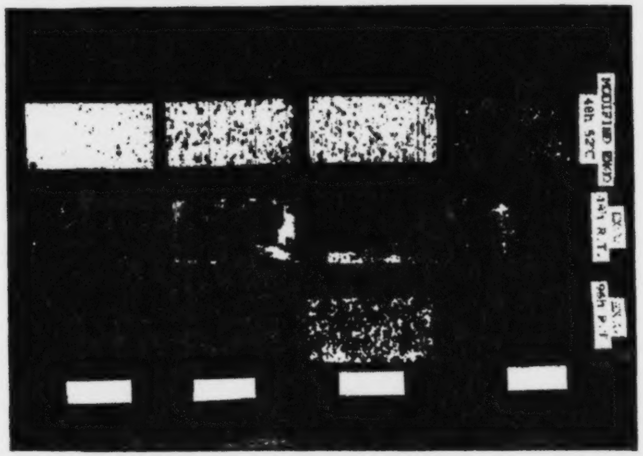
MODIFIED EXCO 48h 52°C
96h R.T.

FOR UNRECRYSTALLIZED 2090 SHEETS:
- T3 LESS SUSCEPTIBLE
- T84 MORE SUSCEPTIBLE
- T31 LESS SUSCEPTIBLE
- T8X MORE SUSCEPTIBLE

Figure 3

EXFOLIATION EVALUATION RESULTS

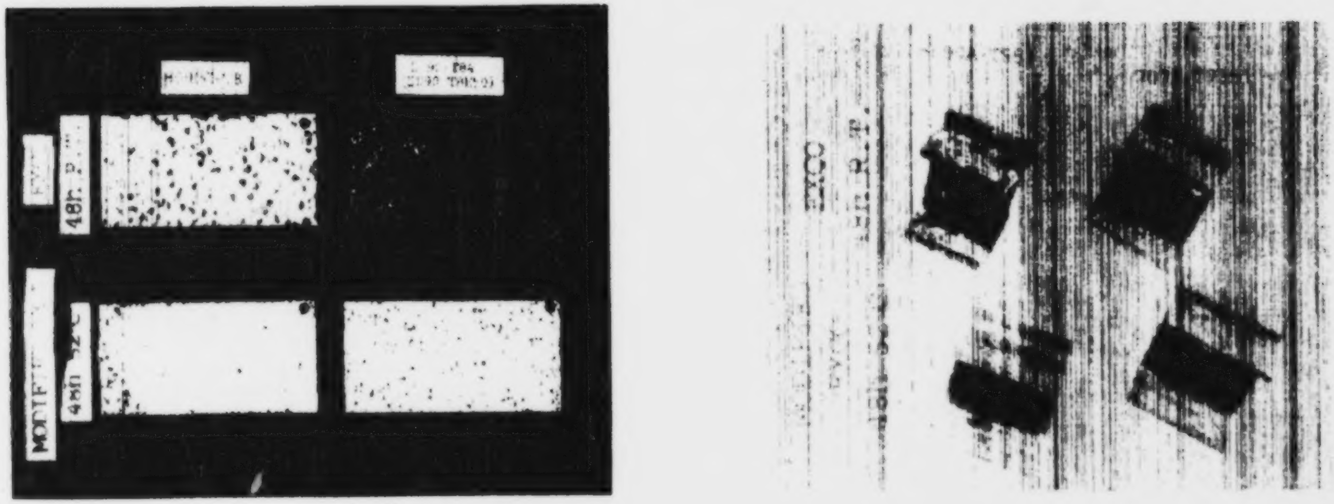

CONCLUSIONS:

- THESE EXFOLIATION TESTS ONLY PROVIDE, TO DATE, A RELATIVE RANKING OF MATERIALS
- HEAT TREATED MATERIALS ARE MORE SUSCEPTIBLE THAN AS RECEIVED ONES
- 8090C-T8 SHEET AND 8090A-T851 EXTRUSION SHOWED THE MOST SEVERE EXFOLIATION IN THESE TESTS EXCO 48 HOURS RATING EB-EC
- SEACOAST EXPOSURE OF THESE TWO MATERIALS WILL HAVE TO BE CLOSELY MONITORED

Figure 4

ALTERNATE IMMERSION IN 3.5%NaCl FOR 1000 HOURS

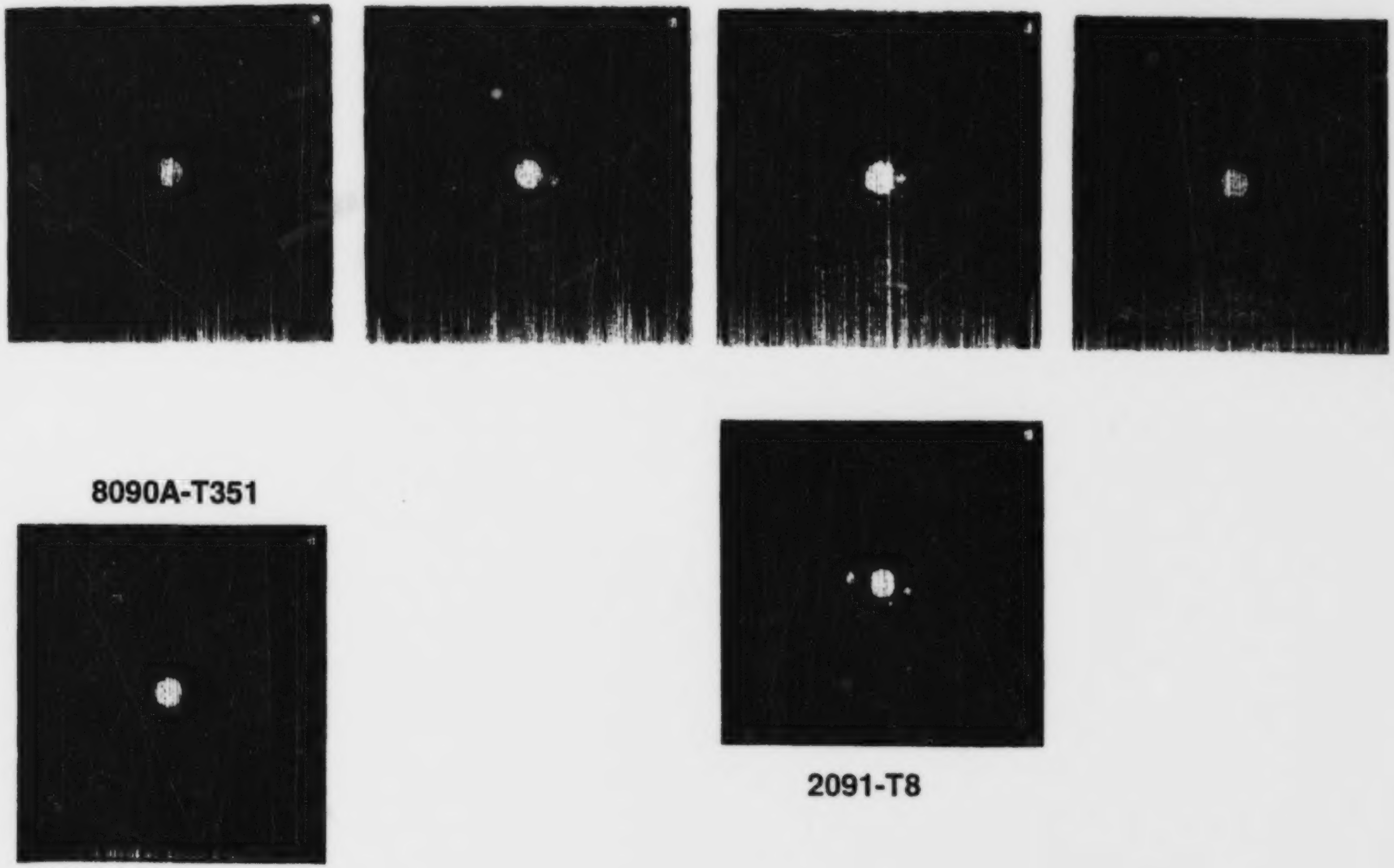

8090C-T3

8090C-T81

8090C-T8

8090C-T621

8090A-T351

2091-T8

Figure 5

ALTERNATE IMMERSION IN 3.5%NaCl FOR 1000 HOURS

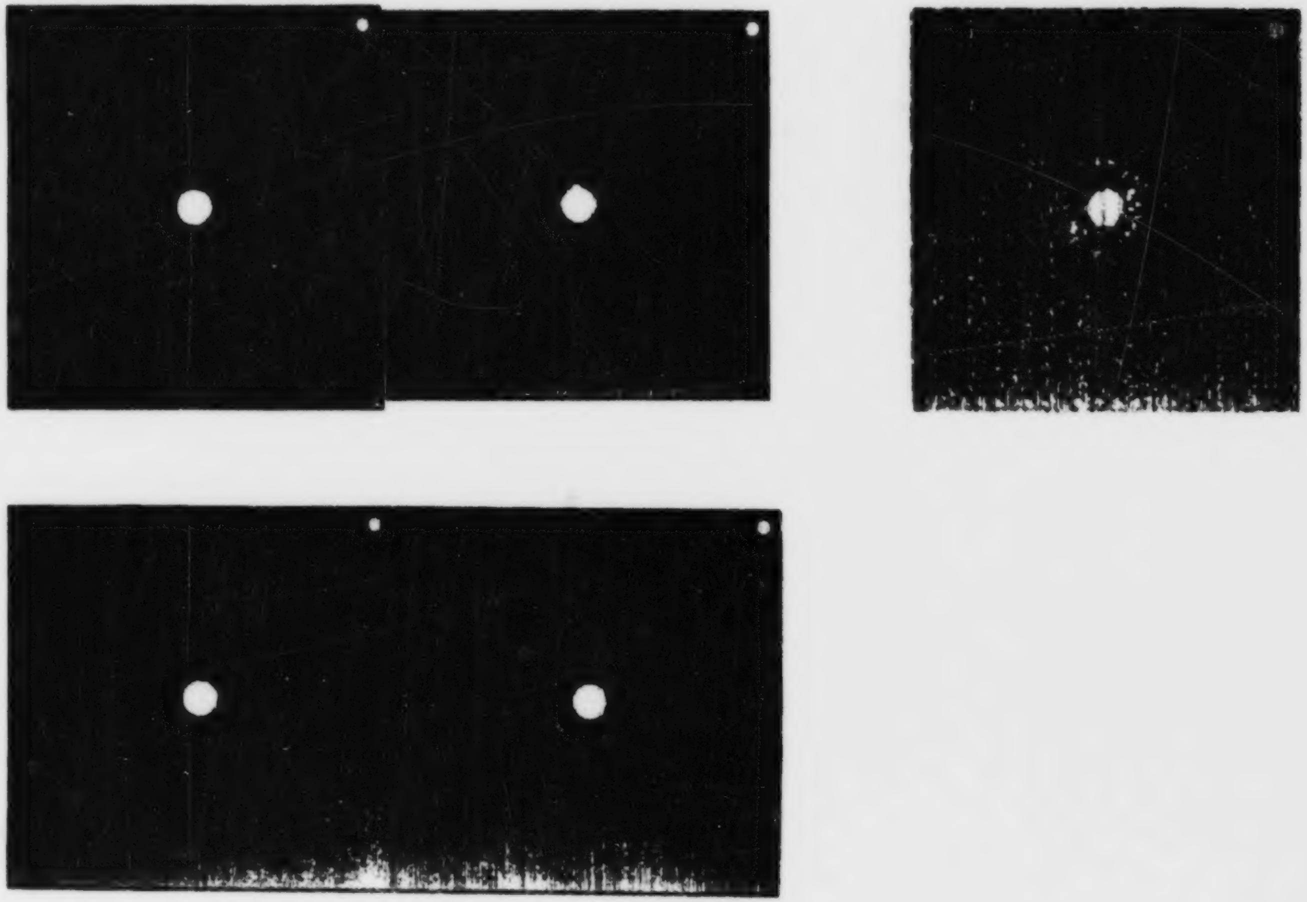

2090-T31

2090-T3

2024-T3

2090-T8X

2090-T84

Figure 6

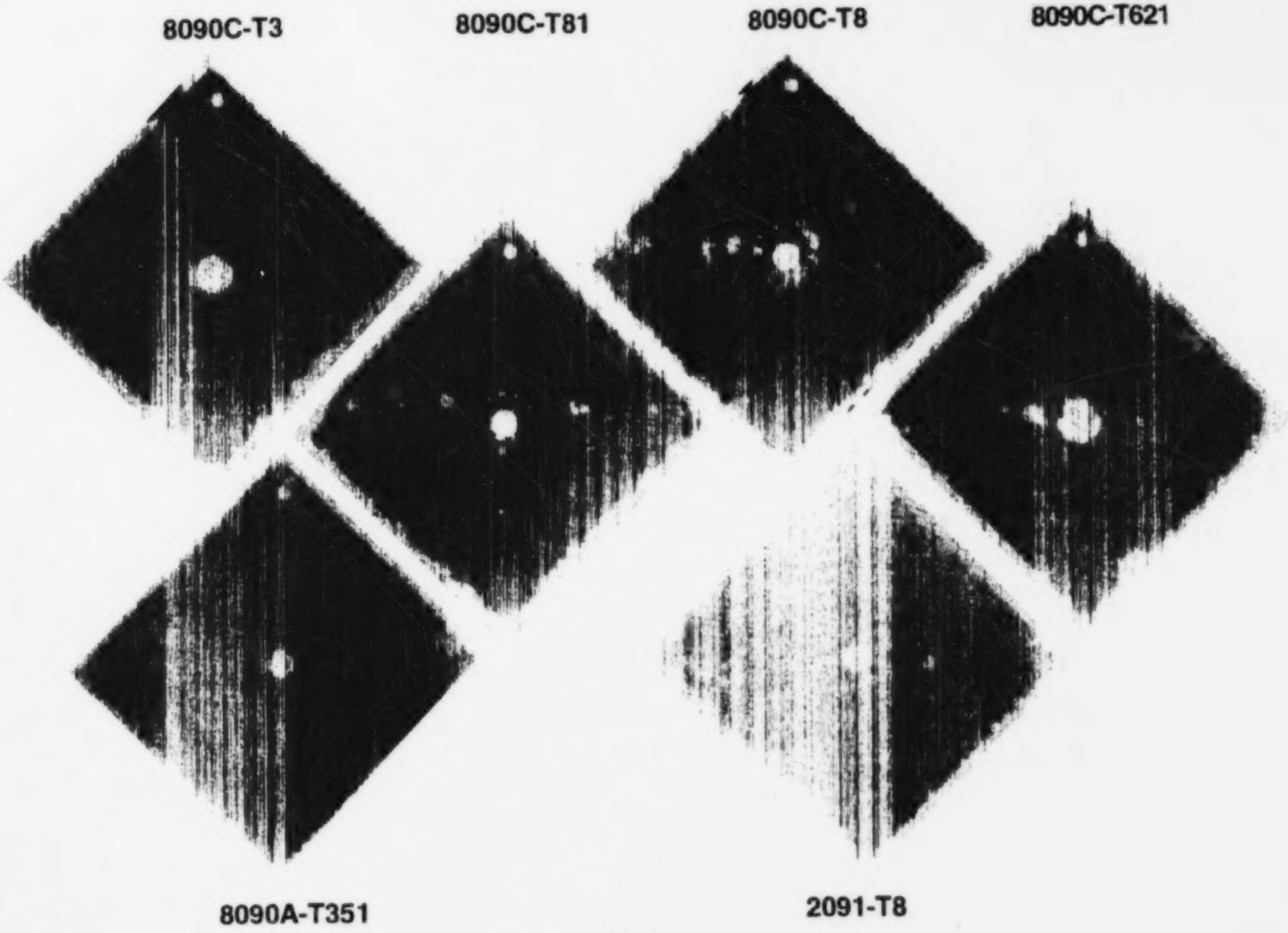

8090C-T3
8090C-T81
8090C-T8
8090C-T621
8090A-T351
2091-T8

HALF IMMERSION IN SEA WATER

Figure 7

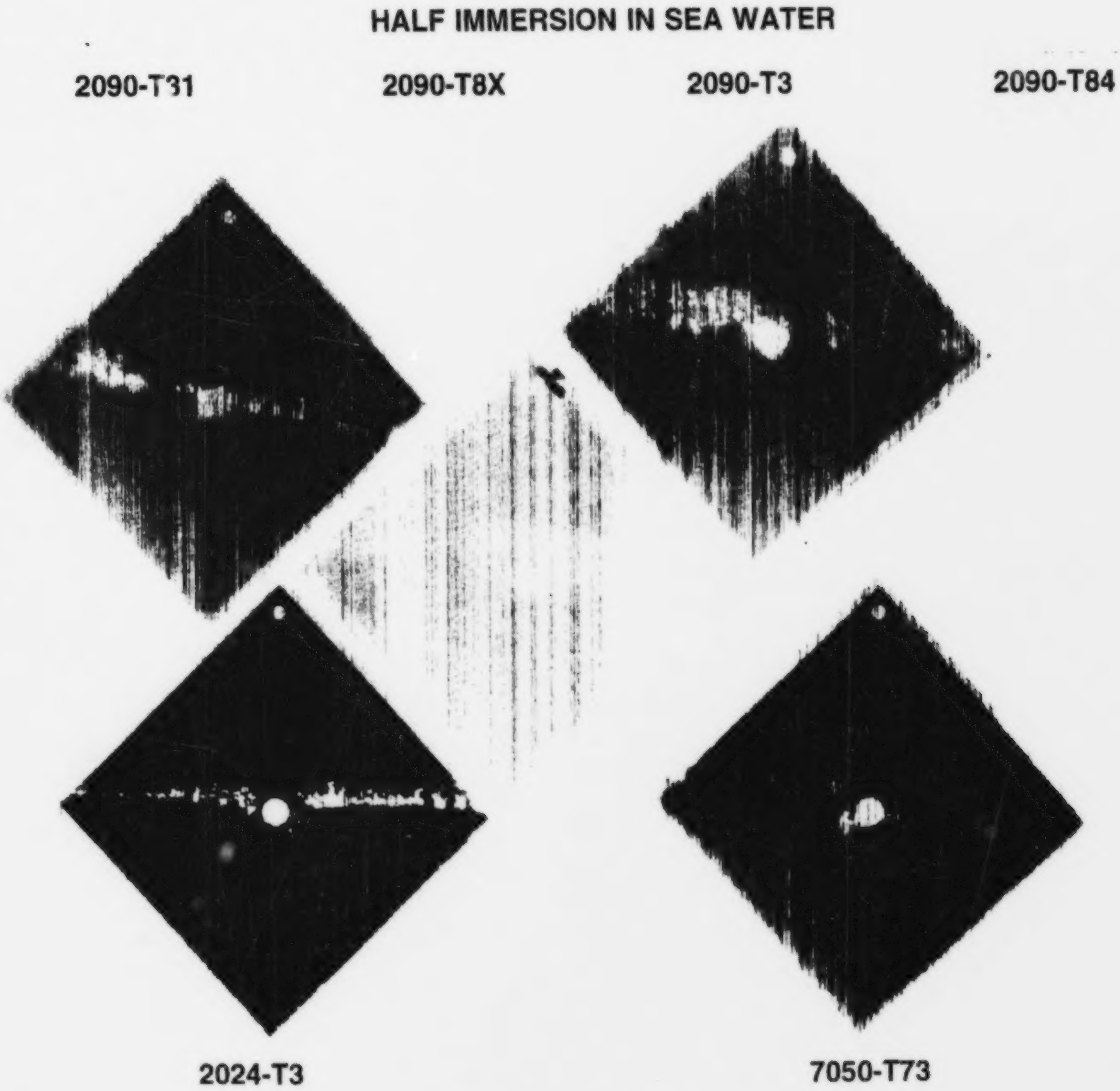
HALF IMMERSION IN SEA WATER
2090-T31
2090-T8X
2090-T3
2090-T84
2024-T3
7050-T73

Figure 8

SCC BREAKING LOAD METHOD

- MATERIAL 8090 FORGING (PECHINEY)
- SMOOTH AXIAL 0.125" SPECIMENS IN ST ORIENTATION
- STRESSES 0, 10 AND 20 ksi
- ALTERNATE IMMERSION IN 3.5% NaCl

  2, 5, 7 AND 9 DAYS

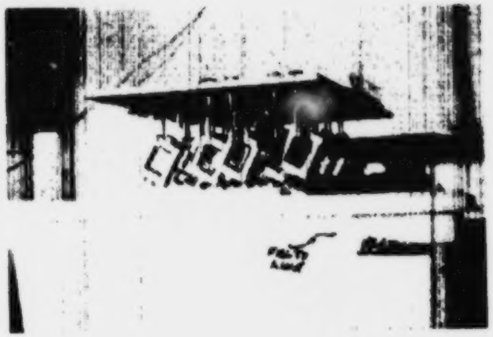

- RESIDUAL STRENGTH MEASURED

-	0 DAYS	2 DAYS	5 DAYS	7 DAYS	9 DAYS
0 ksi	67.9ksi		63.3ksi		61.8ksi
10 ksi		60.2ksi	58.1ksi	59.4ksi	50.4ksi
20 ksi		38.1ksi	30.4ksi	30.4ksi	

Figure 9

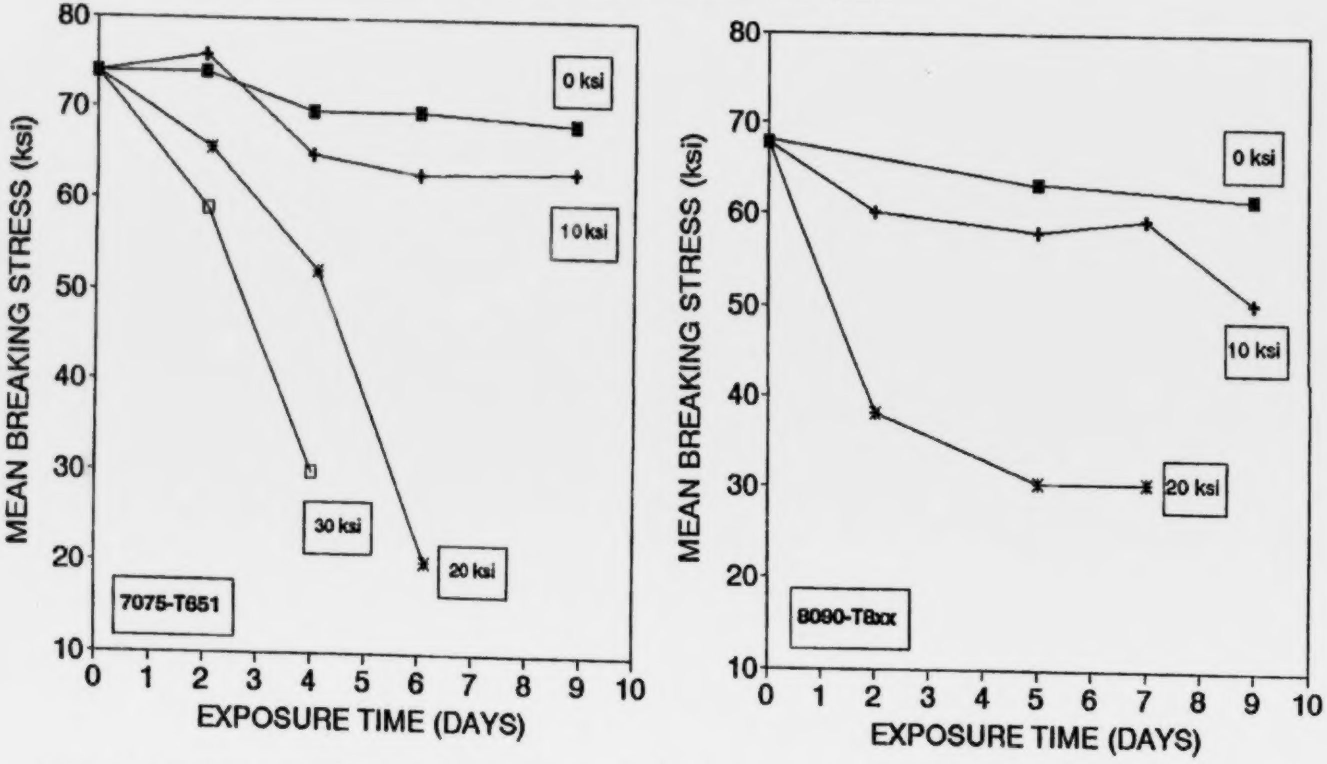

SCC BREAKING LOAD METHOD

MEAN BREAKING STRESS VERSUS EXPOSURE TIME FOR SHORT TRANSVERSE TENSION SPECIMENS EXPOSED TO 3.5% NaCl BY ALTERNATE IMMERSION (ASTM G44) AT VARIOUS EXPOSURE STRESS LEVELS FOR 7075-T651 (ALCOA DATA) AND A 8090-T8XX FORGING.

Figure 10

SCC BREAKING LOAD METHOD

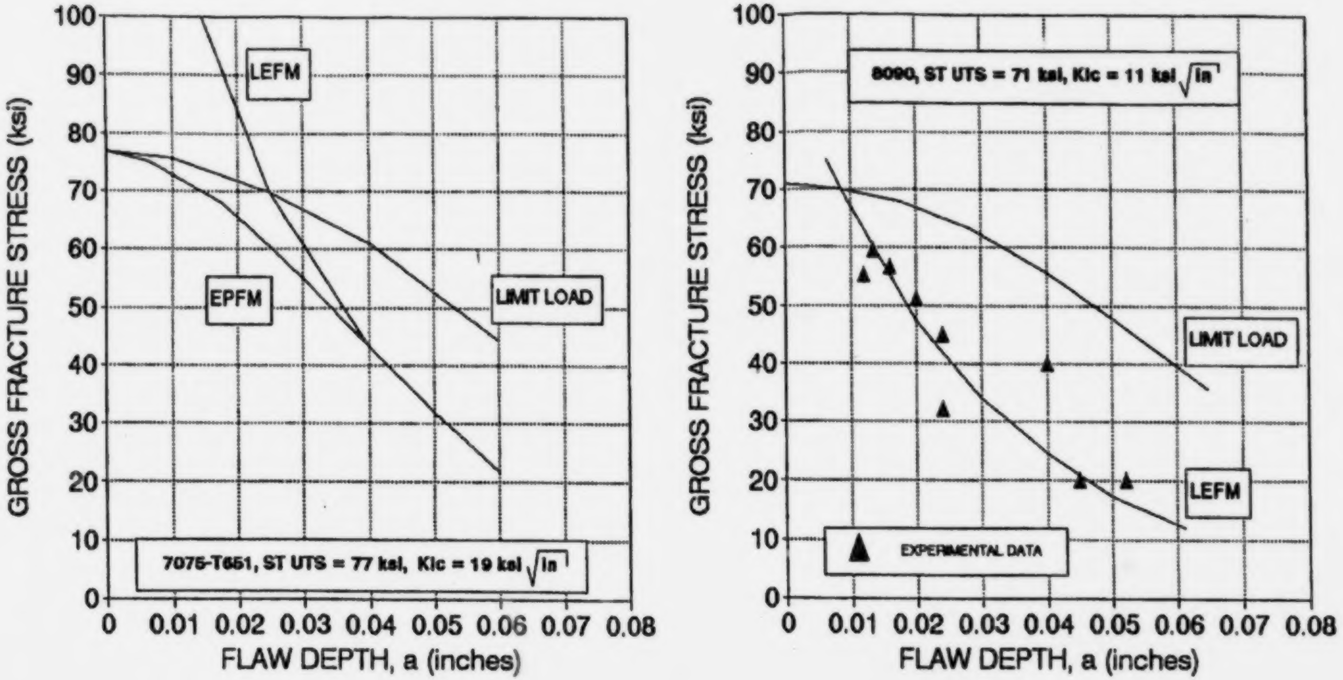

LEFM: LINEAR ELASTIC FRACTURE MECHANICS
EPFM: ELASTIC PLASTIC FRACTURE MECHANICS

ANALYTICAL APPROACH USED TO RELATE RESIDUAL STRENGTH AND FLAW SIZE FOR THE BREAKING LOAD SPECIMEN CONFIGURATION

Figure 11

SCC BREAKING LOAD METHOD

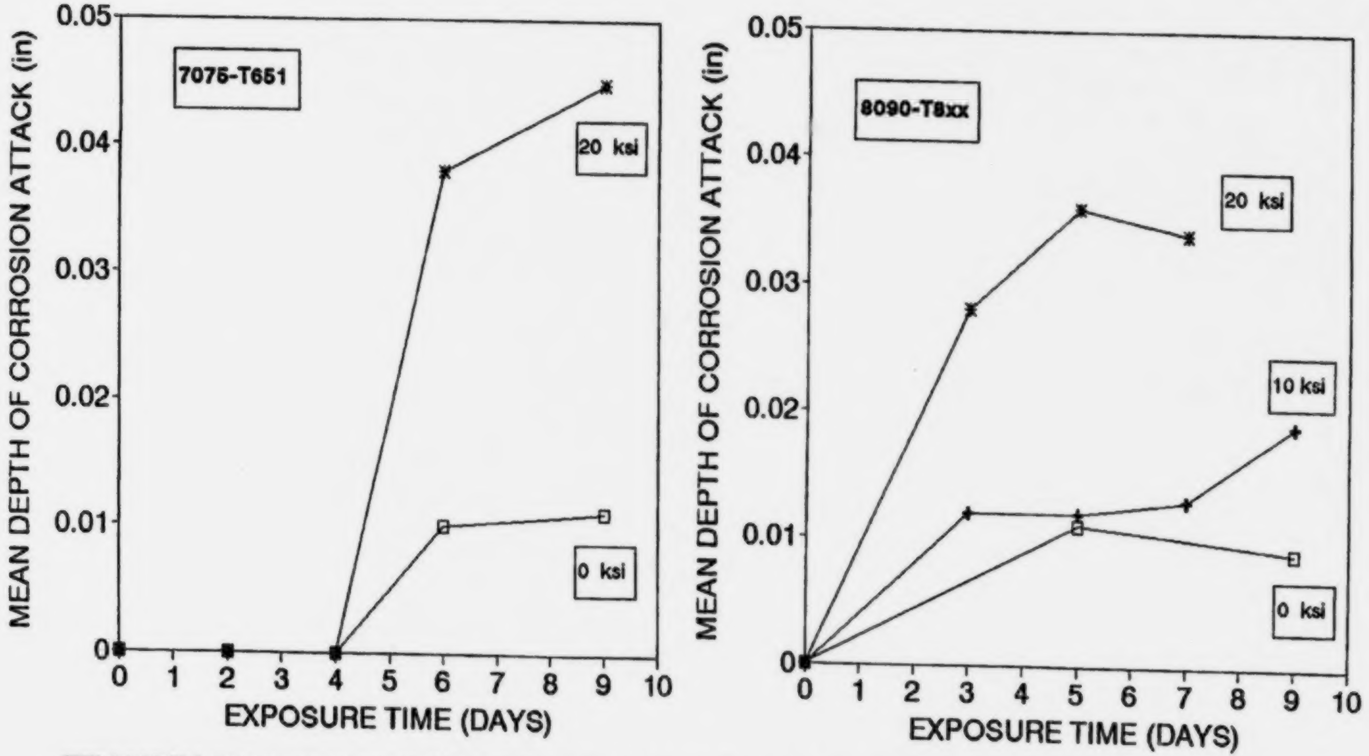

TRANSFORMATION OF THE BREAKING LOAD TEST DATA TO PROVIDE MEAN DEPTH OF ATTACK AS A FUNCTION OF EXPOSURE TIME FOR 7075-T651 AND A 8090-T8XX FORGING

Figure 12

SESSION D

Mechanical Properties, Fracture and Fatigue II

11.

"The Fatigue and fracture Behaviour of Aluminium-Lithium Plate - UK Study"

M.W. Squibb and R.N. Wilson

Defence Research Agency Farnborough, UK.

141643

THE FATIGUE AND FRACTURE BEHAVIOUR OF ALUMINIUM-LITHIUM ALLOY PLATE -U.K. STUDY-

M. W. SQUIBB & R.N. WILSON

This report summarises work carried out at the Defence Research Establishment (Farnborough) U.K. on the fatigue and fracture properties of some aluminium-lithium alloy plates of various thickness, compositions and tempers. The work forms part of the U.K. contribution to the TTCP Operating Assignment P-TP1-11.

Materials

Two compositions of plate were included in the study, namely the quaternary Al-Li-Cu-Mg-Zr alloy 8090, and the tertiary Al-Li-Cu-Zr alloy 2090. The 8090 was supplied as plate, produced via ingot metallurgy routes, in three nominal thicknesses, 12.5, 25, and 37.5mm and in the T8771 temper. The 2090 was supplied as 12.5mm plate in the T8E41 temper. All plates were light grey in colour and were free from surface defects. The 8090 plates had been ultrasonically inspected by the manufacturer so as to ensure that the plates were free from internal defects.

Composition

The compositions of each of the alloys was determined using ICP spectroscopy. The quantities of the major additions, in wt%, are shown in Table 1, together with the specification ranges for the alloys. Each element, (with the exception of Li in the 37.5mm 8090 alloy), was within its specified range. The Zr addition to the 2090 alloy was found to be at the lower limit.

Heat Treatment

The thermomechanical treatment procedures are shown in Table 2. The T8771 temper consists of solution treatment at 530°C, a 7% stretch, and artificial ageing at 170° for 32 hours. This temper condition was introduced by the manufacturer in order to improve the short transverse toughness. Improvements in S-T toughness from 12 MPa√m for the T651 temper to 19 MPa√m for the T8771 temper have been previously reported(1). The T8E41 temper is an experimental temper condition consisting of solution treatment at 549°C followed by a water quench, a 6% stretch, and artificial ageing at 163°C for 24 hours.

Microstructure

Microsections were taken from each of the plates, polished, and etched using Kellers reagent. The composite microstructures for 8090-T8771 and 2090-T8E41 are shown in Figure 1. The 8090 plates showed an unrecrystallised microstructure, consisting of flat grains which were elongated in the direction of rolling. The grain dimensions are shown in Table 3. The average grain size, measured at ½t (where t=plate thickness), was smallest in the thinnest plate, i.e 12.5mm thick, and increased with plate thickness. Sections taken from the 37.5mm plate from near the surface and at the centre showed that the grain size varied through the plate, being coarser at the centre position. In each of the 8090 plates, the grain boundaries were decorated with precipitates. The 2090 plate also showed a banded microstructure consisting of large unrecrystallised pancake shaped grains elongated in the longitudinal orientation sandwiched between layers of finer grains. As with the 8090 alloy, the grain boundaries were decorated with precipitates.

Also shown in table 3, are the main texture components for ½t and ¼t, determined from (111), (200), and (220) pole figures. The main texture component in all cases was {110}<112>, and this was found to be stronger at half plate thickness. The variation of texture through the plate was greater in the 25 and 37.5mm plates and in the 2090 alloy, with the 12.5mm 8090 alloy showing similar intensity of texture at the ½ and ¼ positions.

Tensile Properties

The tensile properties of the 12.5mm thick 8090 and 2090 alloys as a function of angle of the tensile axis to the rolling direction are shown in Tables 4 & 5. The 2090 alloy exhibited the greater 0.2% proof stress and tensile stress in both the L and the T orientations by 48MPa and 17MPa and 66MPa and 34MPa respectively. The 0.2% proof stress and the tensile stress were found to vary by approximately 100MPa as the tensile axis was rotated through 90° for both alloys, reaching a minimum at ~55° to the rolling direction. This feature has been observed in unrecrystallised rolled sheet(2), and has been attributed to the strong {110}<112> texture developed in the rolled product. The elongation values show a maximum at 55° to the rolling direction, the 8090 alloy showing the greater ductility. The Young's Modulus values for both alloys was ~75GPa.

For the 25mm 8090 plate, tensile test pieces were machined such that the centre of the tensile axis was at ¼, ½, and ¾ of the plate thickness. The tensile results are shown in Table 6. The 0.2% proof stress and the tensile strength showed an increase of ~60 MPa and 40 MPa respectively at the centre of the plate compared to the ¼ and ¾ positions for the L orientation, and 100 MPa and 50 MPa respectively for the T orientation. A difference of ~20MPa was observed in the L tensile properties at the ¼ and ¾ positions. The strengths were ~80MPa lower than the 12.5mm 8090 plate in both the L and T orientations for the ¼ and ¾ positions, but compareable at ½ plate thickness.

For the 37.5mm 8090 plate, tensile test pieces were machined such that the centre of the tensile axis was at $^{1}/_{6}$, ½ and $^{5}/_{6}$ of the plate thickness, and from the S orientation. The results are shown in Table 7. Tensile strengths at the $^{1}/_{6}$ and $^{5}/_{6}$ positions were similar to the 25mm plate for both the L and T orientations. The 0.2% proof stress at ½ plate thickness showed an increase of ~70MPa and 110MPa in the L and T orientations respectively, and the tensile strength and increase of ~50MPa and 70MPa. This is a somewhat surprising feature since the average grain size at ½ plate thickness was greater than at ¼ plate thickness. Therefore from the Hall-Petch law, the proof stress should be less at ½ plate thickness. However it has been shown that the variation in tensile properties at the centre of the plate arise predominantly from the development of the {110}<112>

texture(3). The strengths and ductilities at ½ plate thickness were comparable in both orientations to those of the 12.5mm 8090 plate. The 0.2% proof stress and tensile strength of specimens from the short direction was 378 and 509 MPa respectively with an elongation of 2.7%.

Fracture Toughness

The plane strain fracture toughness tests were carried out in accordance with BS5447 (1977) using compact tension specimens of full plate thickness in both the L-T, T-L and, in the thickest plate, the S-L orientations. The specimens were pre-cracked in fatigue at a frequency of 5Hz, with R=0.1 and at a constant ΔK. It was found to be necessary to keep the ΔK below a critical value in order to maintain a reasonably straight crack front. Nevertheless it was still found that in a number of cases crack front curvature invalidated the test and only a K_Q could be obtained. The results obtained at ambient temperature are shown in Table 8.

Toughness values obtained for the 12.5mm 8090 plate in the L-T direction were above the specified minima required for medium strength Lital A material and fell slightly short of the toughness that might be typically expected(4). For the T-L direction however, the toughness was found to be ~4 MPa√m lower than the specified minimum and 10 MPa√m below that typically expected. However it should be noted that target properties are for material in the T651 heat treatment condition in which the tensile and proof stresses are 60-70MPa lower than the T8771 condition. When compared to the 2090-T8E41 alloy the 8090-T8771 alloy showed superior L-T toughness, ~33.5 MPa√m compared to ~30 MPa√m, but inferior T-L toughness ~22.5 MPa√m compared to ~28 MPa√m.

The 25mm plate exhibited toughness values similar to the 12.5mm plate in the L-T direction, and slightly improved values in the T-L direction, approaching the specified minima value. The similarity in toughness with the 12.5mm plate reflects the similar strengths at ½ plate thickness.

Problems were encountered in obtaining representative fracture toughness values for the 37.5mm 8090 plate. A typical load/displacement fracture toughness curve for a full thickness specimen in the L-T direction is shown in Figure 2. As expected, the displacement varied linearly with increasing load, but rather than experiencing a sudden unstable fast fracture mode, the crack grew in a relatively stable manner reaching a peak load of 32.7kN. This was certainly unexpected since due to the thickness of the specimen plane strain conditions should have existed. The P_Q load obtained from the 5% secant line was measured at 27.38kN, giving a P_{max}/P_Q ratio 1.195 which is above the limit given in BS 5447. Examination of the fracture surface showed two distinct areas of fracture as shown in Figure 3. The first area at the centre of the plate consisted of a band ~12mm wide of transgranular fracture normal to the applied load. Either side of this band were ridges of shear fracture in which the shear plane on one side of the ridge was at 45° to the applied load and the other was parallel to the applied load. Such a variation in fracture mode across the specimen width may well be the result of the through thickness variations of strength and crystallographic texture. Similar fracture behaviour was also observed in the T-L orientation. K_Q values obtained for full thickness specimens showed a reduced toughness in the L-T direction compared to both the 12.5 and 25mm plate, and an increase in toughness for the T-L orientation. In order to obtain valid K_{1C} values for the plate, it was decided to reduce the thickness of the test piece by machining equal amounts from both sides of the plate. This was done for the L-T orientation, reducing the specimen thickness to 25 and 12.5mm. Fracture toughness tests performed on these specimens yielded valid K_{1C} values of 28.3 and 26.1 MPa $\sqrt{m}$ respectively. These results fall some way short of the specified minimum for the L-T orientation however it should be remembered that the specimens were taken from the region of plate that showed the highest tensile properties.

S-L fracture toughness values were determined from 12.5mm thick compact tension test pieces (W=25mm) machined from the mid-section of the plate. The results obtained were in agreement were those previously reported for the T8771 heat treated condition i.e 10-12 MPa$\sqrt{m}$(5), and were slightly lower than the desired level. The failure mechanism was observed to be predominantly brittle intergranular fracture. It has been shown however that the S-L toughness can be significantly improved by a secondary ageing treatment. The increase in toughness is associated with an increase in the proportion of dimpled intergranular fracture at the expense of brittle intergranular fracture. Two test pieces were aged for 5 minutes at 210°C in an air circulating oven, and then quenched in cold water. The time taken for the specimen to achieve the required temperature was ~30 minutes. This treatment resulted in an increase in toughness of ~50% which, although lower than the toughness values previously reported, are approaching acceptable levels. It would seem therefore that aluminium lithium alloys are capable of achieving high toughness in the S-L orientation, suggesting that poor toughness is not an inherent problem with this family of alloys, but arises because of a lack of understanding of metallurgical control. Further work has suggested that the toughness may be reverted back to pre re-ageing values on exposure to moderate temperatures for some period of time. This area of work will require further study.

Fatigue Crack Growth

Constant amplitude fatigue crack growth rates were determined in accordance with ASTM E647 (1990), for each of the plates at two nominal values of stress ratio (R = 0.1 and 0.5) over the ΔK range 5-30 MPa$\sqrt{m}$. For the 8090 plates, compact tension specimens were used of full plate thickness, machined from the L-T and T-L orientations. Test were carried out in laboratory air at a frequency of 5Hz using a servo-hydraulic fatigue machine fitted with a 25kN load cell. The applied loads were continually monitored by computer and were corrected automatically if the measured values differed by more than 0.1kN from the loads demanded. The crack length was determined using a compliance technique, with a clip gauge mounted at the mouth of the notch at a distance of ~0.25W (where W = test piece width)

The fatigue crack growth rate curves for the 25mm and 37.5mm 8090 plate are shown in Figures 5(a) and 5(b). For the high R value, the crack growth rates for the L-T and T-L orientations are similar and comparable for the two thicknesses of plate over the ΔK range tested, and are higher than the crack growth rates for the lower R value. The rates are also comparable to the high R value data obtained for the 12.5mm plate. The crack growth rates obtained at the low R value showed differing behaviour. For the 25mm plate, the general trend was continued with the slower crack growth rate being observed in the T-L direction. Both orientations exhibited the characteristic constant growth rate plateau over the ΔK range 10-15 MPa$\sqrt{m}$, however the plateaus occurred at rates of 10^{-4} mm/cycle for the L-T direction, and $2x10^{-5}$ mm/cycle for the T-L direction. This is in contrast to the data obtained for the 12.5mm plate where the plateau was observed at 10^{-4} mm/cycle for both directions. The 37.5mm plate again showed differing behaviour with the plateaus for both directions being at $2x10^{-5}$ mm/cycle in the ΔK range 10-13 MPa$\sqrt{m}$, the L-T direction showing faster crack growth rates outside this ΔK range.

Inspection of the fatigue fracture surfaces showed some interesting features. For the 8090 alloy, at all plate thicknesses and stress ratios, two distinct fracture modes were observed to occur and these are shown in Figure 6. The first mode was macroscopically flat, and normal to the direction of the applied load, and had a clean grey appearance. The second type of fracture mode was rough and facetted, and for tests conducted at the low R value, much darker in colour, showing evidence of fretting. When observed under oblique lighting, the rough fracture appeared as bright facets. For the high R value the facets were larger and brighter than those at low R, and showed little evidence of fretting. Other workers have observed this transition(7-9) and have shown that the rough fracture surface is comprised of shear facets. The other interesting feature to note is that the transition in fracture mode does not occur evenly across the specimen thickness, but initiates at the centre and fans outwards towards the edges as the crack length increases. This behaviour was observed for all the 8090 plates in both orientations.

The 2090 plate exhibited fatigue crack growth behaviour similar to the 8090 plates, showing a transition from relatively smooth fracture at low ΔK values to highly facetted rough fracture with a large amount of fretting at values of above ΔK=8 MPa$\sqrt{m}$ for R=0.1 and above ~7 MPa$\sqrt{m}$ at R=0.5. However for any given ΔK, the fracture surface at the centre of the plate appear to be more coarse and rough for the 2090 compared to the 8090 12.5mm plate (Figure 7). Again, in similarity with the 8090 alloy, the transition in fracture mode occurred initially at the specimen centre and fanned outwards towards the edges. A microsection taken perpendicular to the crack growth direction shows the formation of asperities at the specimen centre with an included angle of ~50°. These have been shown to be comprised of a pair of shear band facets which form due to planar slip and the intensity of the crystallographic texture(10). At the edges of the specimen, where the texture is less intense, the large shear band facets are less abundant.

from the loading line. The polynomial expression given in the ASTM standard for this position of the clip gauge was used to relate the compliance to the fatigue crack length. Between 20 and 25 data points were recorded for each fatigue test. At each data point, a record was made of the load/displacement data over a 2 cycle period. This was done dynamically without interruption of the test. Estimates of the crack closure loads were obtained for each data point by determining the point of deviation from linearity of the load/displacement plots and these were used to calculate an effective ΔK for the specimen using the equation:-

$$\Delta K_{(effective)} = U \times \Delta K_{(nominal)}$$

where: $U = (P_{max} - P_{closure}) \div (P_{max} - P_{min})$

Fatigue crack growth rate curves were plotted against both ΔK(nom) and $\Delta K_{(eff)}$.

Difficulties were experienced in obtaining straight cracks perpendicular to the applied load when using compact tension test pieces to measure the FCGR in the 2090 alloy. Single edge notch (SENT) specimens were therefore used. As with the 8090 alloys, the crack growth rates were measured at R=0.1 and R=0.5, under constant amplitude loading. The crack length was measured using a pulsed DCPD system, the crack length being recorded after every 0.3mm crack extension. The stress intensity factor was calculated from an expression given by C.M. Ward-Close for a single edge notch specimen with bending restrained(6). No smoothing of the crack growth data was done during crack growth rate calculations, and no estimates of crack closure loads were obtained for this specimen geometry.

The fatigue crack growth rate curves for the 12.5mm 8090 plate are shown in Figure 4(a). As expected, the higher R value produced a faster crack growth rate, compared to the low R value, at a given ΔK for both the L-T and T-L orientations. At both R values the L-T direction had the faster crack growth rate compared to the T-L direction, at values of ΔK values of less than 11.5 MPa√m and 9 MPa√m for high and low R respectively. Above these values, the growth rates were comparable. The other interesting feature to note is the plateau of a near constant crack growth rate of 10^{-4} mm/cycle between ΔK values of 10-15MPa√m at an R value of 0.1.

The fatigue crack growth rate curves for the 12.5mm 2090 plate are shown in Figure 4(b). As with the 8090 plate, the higher R value produced a faster crack growth rate for any given ΔK and orientation, the effect being more prominent at the higher ΔK range. The L-T direction had the faster crack growth rate compared to the T-L direction, at values of ΔK of greater than 6 MPa√m. Plateaus of a near constant crack growth rates of $1x10^{-5}$ and $8x10^{-6}$ mm/cycle occurred for the L-T and T-L directions between ΔK values of 8-13MPa√m and 8-20MPa√m respectively. In comparison with the 8090 plate, the 2090 alloy showed superior fatigue crack growth resistance at ΔK values of greater than 5 MPa√m.

The formation of the shear facets would be expected to lead to a significant increase in the level of roughness induced crack closure, and this was indeed evident from the load displacement data for the low R value. The high R value of 0.5 was chosen to provide fatigue crack growth free from crack closure effects, as demonstrated by previous workers$^{(7)}$. Inspection of the load/displacement data showed this to be the case. Figure 8 shows how the parameter U changes as a function of ΔK for the 25mm 8090 plate, and is characteristic of all plate thicknesses and orientations. The specimen was fatigued at a constant alternating load range and R value, starting at a ΔK of 10 MPa√m, with the initial fracture being of the flat tensile mode. As the shear mode fracture develops, U decreased sharply, reaching a minimum at a ΔK of ~15 MPa√m. The range over which U decreased corresponded to the region of constant crack growth rate on the da/dN vs ΔK curves thus indicating that the ΔK values within this range were modified by crack closure to a much narrower range of somewhere between 10 and 11 MPa√m. As the value of ΔK increased from 15 MPa√m, U also increased reflecting a decrease in the crack closure load. This trend observed for U as a function of ΔK is in agreement with the models for roughness induced crack closure.

The fatigue crack growth rate curves for 8090-T8771 25 and 37.5mm thick plate, plotted as a function of $\Delta K_{(eff)}$, are given in Figure 9. By plotting the data as a function of $\Delta K_{(eff)}$ the effects of crack closure are removed, and the low R value data should be superimposed on the high R value data. The results obtained were in broad agreement with this model. Another interesting point concerns the plateau region of the curve. Whilst the severity of the plateau was reduced, an inflexion of the curve, indicating a deceleration in crack growth rate was still evident thus indicating that the plateau was not solely controlled by crack closure mechanisms. Microsections taken from fatigued specimens clearly showed the shear mode fracture mechanism, however also associated with the shear facets was a high degree of secondary cracking and crack branching (Figure 10). Such features act so as to shield the crack tip from the full effects of the applied ΔK range and are not accounted for in the crack closure model, therefore the persistence of the plateau in the $\Delta K_{(eff)}$ plots is understandable.

The reasons for the change in fracture mode from flat tensile to shear mode are as yet unclear, although several workers$^{(7,11,12)}$ have speculated on possible mechanisms including the effects of texture and environment. The crack lengths at which the transition occurred at the centre of the specimens were measured for each of the plates, and the corresponding $\Delta K_{(nom)}$ and $\Delta K_{(eff)}$ were determined. The results are shown in Table 9. The results indicate that the transition occurs at different ΔK values at the high R and low R values for both directions, the lower value being for the high R. Similarly, no correlation existed between $K_{(max)}$ at transition and the R values. However, when compared as $\Delta K_{(eff)}$ reasonable agreement was obtained between the high and low R values, suggesting that $\Delta K_{(eff)}$ is the controlling parameter. A number of other parameters are controlled by the $\Delta K_{(eff)}$ term, including reverse plastic zone size, crack growth rate, and CTOD. The transition in fracture mode however, varies through the thickness of the specimen, and some rationale is required to explain this effect. Arguments based on the reverse plastic zone size appear to be illogical since, as has been shown, the yield stress is lower at the surface of the plate compared to the centre, and hence the reverse plastic zone size is larger in this region. If the transition is related to the reverse plastic zone size, i.e. transition occurs when the reverse plastic zone size reaches a critical value, then the transition should occur at the edges of the specimen, and converge towards the centre. It seems more likely that variation in transition across the specimen is related to the variation in crystallographic texture, with the regions of greater textural intensity, i.e. the centre of the plate, being prone to change in fracture mode at lower values of $\Delta K_{(eff)}$. Further work would be required to support this hypothesis.

Summary

In summary therefore, it has been shown that:

i) both the 8090 and 2090 alloys are capable of achieving high strengths in the L and T directions, but suffer from a high degree of anisotropy. The 8090-T8771 also showed through thickness variations in tensile properties.

ii) The measured fracture toughness values of the 8090 plate decreased with increasing plate thickness, and barely achieved the desired minimum values for medium strength plate. The toughness in the S-L orientation was low but could be improved by a short ageing treatment. The toughness of the 2090 plate was low than the 8090 plate of the same thickness in the L-T direction, but better in the T-L direction. The S-L toughness was not determined.

iii) The fatigue crack growth rates for both 8090 (all thicknesses) and 2090, under constant amplitude loading over the ΔK range 5-30 MPa$\sqrt{m}$, were dependent on orientation and stress ratio (R) with the faster rates being observed in the L-T direction and at high R for any given ΔK value.

iv) A plateau of near constant crack growth rate at ΔK values of between 8 and 15 MPa$\sqrt{m}$ was observed in all cases. This is attributed to a combination of crack closure and crack tip shielding mechanisms due to a change in fracture mode from flat tensile to crystallographic shear. The transition appeared to be controlled by the stress parameter $\Delta K_{(eff)}$, and was influenced by the through thickness variation in texture. Better fatigue performance was observed for the 2090 plate compared to the 8090 plate of the same thickness. This was because the increased grain size and propensity for planar slip in the 2090 alloy led to an increased fatigue fracture surface roughness, and hence an increase in crack tip shielding.

References

1.	W. T'Hart L. Schra D. McDarmaid M. Peters	Mechanical Properties and Fracture Toughness of 8090-T651 Plate and 2091 and 8090 Sheet. AGARD-CP-444-P-5 August 1989.
2.	S. Fox H.M. Flower D.S. McDarmaid	Mechanical Anisotropy in Al-Li Based Alloy Sheet. Int. Conf. "Aluminium alloys - their physical and mechanical properties", University of Virginia,June 1986. Eds. E.A Stark Jr. and T.H. Sanders Jr., Publ EMAS Cradely Heath, England.
3.	S.J. Harris B. Noble A. Dodd	The Effects of Texture on the Tensile and Fatigue Properties of 8090 Plate Alloys. 5th Int. Aluminium-Lithium Conf., Williamsburg, Virginia. March 1989.
4.	C.J. Peel B. Evans D.S. McDarmaid	The Current Status of the United Kingdom Lightweight Lithium Containing Aluminium Alloys. 3rd Int. Aluminium-Lithium Conf., Oxford, July 1985
5.	S.P. Lynch	Fracture of 8090 Aluminium-Lithium Alloy Plate Short Transverse Fracture Toughness. RAE Technical Report TR90035 July 1990.
6.	C.M Ward-Close	Stress Intensity Factors for a Single-Edge Notch Tension Test Piece With Clamped Ends. RAE Technical Report TR84048 May 1984.
7.	R.M.J. Kemp R.N. Wilson P.J. Gregson	The Effects of Frequency and R-Ratio on Fatigue Crack Growth Behaviour in Al-Li-Cu-Mg Alloy (8090) Plate. Fatigue Fract. Engng Mater. Struct. Vol 15, No. 3, pp 291-308 1992.
8.	D.S. McDarmaid	Fatigue and Fatigue Crack Growth Behaviour of Medium and High Strength Al-Li-Cu-Mg-Zr Alloy Plate. RAE Technical Report TR85016 Feb. 1985.
9.	M. Peters K. Welpmann D.S. McDarmaid W.T.G. t'Hart	Fatigue Properties of Al-Li Alloys AGARD-CP-444-P-6 August 1989.
10.	P.S. Pao L.A. Cooley M.A. Imam G.R. Yoder	Fatigue Crack Growth in 2090 Al-Li Alloy. Scripta Met. Vol. 23, pp 1455-1460, 1989.

11. J.M. Newman, P.J. Gregson, P.D. Pitcher, P.J. Forsyth — The Effect of Grain Structure on Fatigue Crack Growth in Al-Li Alloys. 5th Int. Aluminium-Lithium Conf., Williamsburg, Virginia. March 1989.

12. R.S. Piascik, R.P. Gangloff — Environmental Fatigue of an Al-Li-Cu Alloy: Part 1. Intrinsic Crack Propagation Kinetics in Hydrogenous Environments. Met. Trans A. Vol 22A pp 2415-2428 Oct. 1991.

	Li	Cu	Mg	Zr	Fe	Na	Al
8090 (12.5mm)	2.42	1.14	0.67	0.12	0.05	<0.01	Rem
8090 (25mm)	2.21	1.07	0.61	0.10	0.05	<0.01	Rem
8090 (37.5mm)	2.69	1.23	0.66	0.12	0.05	<0.01	Rem
8090 min	2.20	1.0	0.6	0.04	-	-	Rem
8090 max	2.60	1.6	1.3	0.16	-	-	Rem
2090 (12.5mm)	2.11	2.47	-	0.08	0.03	<0.01	Rem
2090 min	1.90	2.40	-	0.08	-	-	Rem
2090 max	2.60	3.00	0.25	0.15	0.12	-	Rem

TABLE 1

COMPOSITIONS OF THE ALUMINIUM-LITHIUM PLATES (Wt %)

Material	Treatment	Temp °C	Time (Hours)
8090-T8771 (All Thicknesses)	Solution	530	0.25
	7% Plastic Stretch		
	Age	170	32
2090-T8E41	Solution	549	0.25
	6% Plastic Stretch		
	Age	163	24

TABLE 2

MECHANICAL AND HEAT TREATMENT PROCEDURES FOR THE ALUMINIUM-LITHIUM PLATES

Plate	Position	Grain Size L x T x S (μm)	Main Texture Component	Intensity (No. x Random)
8090				
12.5	½t ¼t	33 x 15 x 8	{110} <112> {110} <112>	16.3 13.4
25	½t ¼t	53 x 45 x 10	{110} <112> {110} <112>	14.7 7.6
37.5	Surface ½t ¼t	40 x 33 x 9 67 x 53 x 14	{110} <112> {110} <112>	15.1 6.9
2090				
12.5	½t	300 x 200 x 18 (90 x 30 x 18)	{110} <112>	22.8
	¼t		{110} <112>	8.0

Table 3

Grain Size and Texture of Aluminium-Lithium Alloy Plates

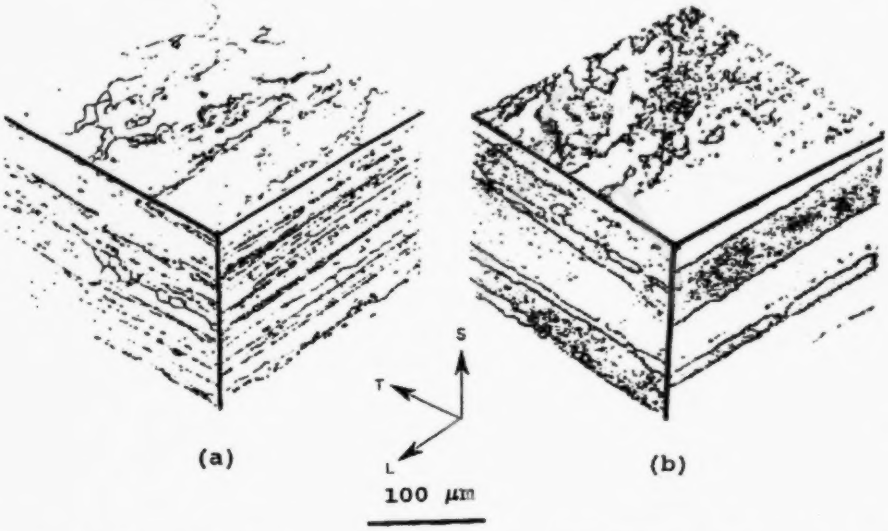

(a) (b)

Figure 1: Composite microstructures of (a) 8090-T8771 and (b) 2090-T8E41 plate (12.5mm thick).

DEFENCE
RESEARCH
AGENCY

ANGLE TO RD	Rp 0.1 MPa	Rp 0.2 MPa	Rp 0.5 MPa	Rm MPa	Elong %	E GPa
0	490	507	527	572	4.8	75.5
10	467	491	505	542	5.3	76.6
20	433	460	478	516	7.4	75.8
30	405	433	474	521	9.3	75.8
40	392	417	449	509	9.5	72.7
50	367	379	404	479	12.4	74.5
60	366	378	408	492	9.4	73.4
70	375	391	430	519	9.8	73.5
80	415	437	470	536	10.5	75.7
90	456	482	497	549	8.6	73.8
L *	-	410		460	5	-
T *	-	390	-	450	5	-

(* Specified minima for Lital A)

TABLE 4

8090-T8771 (12.5mm Plate) TENSILE DATA

ANGLE TO RD	Rp 0.1 MPa	Rp 0.2 MPa	Rp 0.5 MPa	Rm MPa	Elong %	E GPa
0	543	555	569	589	8.7	75.9
10	528	540	551	573	4.4	76.7
20	513	529	542	560	5.5	75.1
30	490	516	542	568	5.9	75.4
40	466	482	500	528	8.8	73.1
50	440	455	476	505	9.1	74.3
60	436	451	481	532	7.0	74.9
70	459	477	512	559	7.5	74.4
80	505	524	544	572	5.3	76.1
90	530	548	559	583	6.8	75.2

TABLE 5

2090-T8E41 (12.5mm Plate) TENSILE DATA

Orientation	D	Rp 0.1 MPa	Rp 0.2 MPa	Rp 0.5 MPa	Rm MPa	El %	E GPa
L	¼t	415	426	438	479	7.1	75.1
	½t	480	496	506	537	4.9	78.0
	¾t	429	444	456	500	6.1	75.9
	*	-	410	-	460	5	-
T	¼t	364	380	402	483	10.8	77.5
	½t	456	480	491	533	7.8	79.5
	¾t	370	389	408	474	9.5	76.4
	*	-	390	-	450	5	-

* Specified Minimum Values

(D is the depth of the tensile specimen central axis from the plate surface)

TABLE 6

8090-T8771 (25mm Plate) THROUGH THICKNESS TENSILE DATA

Orientation	D	Rp 0.1 MPa	Rp 0.2 MPa	Rp 0.5 MPa	Rm MPa	El %	E GPa
L	$^1/_6$t	431	446	463	506	6.3	76.5
	½t	509	523	537	556	3.5	75.9
	$^5/_6$t	437	453	472	511	5.5	76.0
	*	-	410	-	460	5	-
T	$^1/_6$t	370	386	411	487	9.4	76.4
	½t	464	497	521	557	6.3	76.3
	$^5/_6$t	374	388	414	489	9.5	76.2
	*	-	390	-	450	5	-
S	-	350	378	430	509	2.7	78.0
	*	-	360	-	420	2.5	-

* Specified Minimum Values

(D is the depth of the tensile specimen central axis from the plate surface)

TABLE 7

8090-T8771 (37.5mm Plate) THROUGH THICKNESS TENSILE DATA

DEFENCE
RESEARCH
AGENCY

Material	Plate Thickness mm	Orien- tation	Specimen Thickness mm	K_Q MPa $m^{1/2}$	K_{1C} MPa $m^{1/2}$
8090-T8771	12.5	L-T	12.5	32.9	-
				33.6	-
		T-L		-	22.2
				-	22.7
				22.3	-
2090-T8E41	12.5	L-T	12.5	-	30.7
				25.5	-
				29.6	-
		T-L		30.6	-
				26.2	-
8090-T8771	25	L-T	25	31.9	-
				31.3	-
		T-L		24.3	-
				24.4	-
8090-T8771	37.5	L-T	37.5	29.9	-
				28.0	-
		T-L		26.6	-
				27.9	-
		L-T	25	-	28.3
			12.5	-	26.1
		S-L	12.5	9.8	-
				12.4	-
				-	17.7*
				-	16.1*
LITAL A**	-	L-T	-	-	30
	-	T-L	-	-	25
	-	S-L	-	-	15

(* Specimens re-aged for 5 mins at 210°C)
(** Specified Minimum Values)

TABLE 8

PLANE STRAIN FRACTURE TOUGHNESS RESULTS
(Tests conducted at 20°C)

DEFENCE
RESEARCH
AGENCY

Plate Thickness mm	Orientation	R value	ΔK MPa$\sqrt{m}$	$K_{(max)}$ MPa$\sqrt{m}$	$\Delta K_{(eff)}$ MPa$\sqrt{m}$
12.5	L-T	0.1	12.1	13.4	11.2
		0.5	11.6	23.2	11.6
	T-L	0.1	10.4	11.6	ND
		0.5	9.7	19.4	9.7
25	L-T	0.1	11.9	13.2	9.8
		0.5	10.4	20.8	10.4
	T-L	0.1	10.4	11.6	7.8
		0.5	8.5	9.4	8.5
37.5	L-T	0.1	11.3	12.5	7.8
		0.5	8.6	17.2	8.6
	T-L	0.1	11.5	12.8	8.2
		0.5	9.3	18.6	9.3

TABLE 9

8090-T8771 PLATE FATIGUE FRACTURE MODE TRANSITION DATA

DEFENCE
RESEARCH
AGENCY

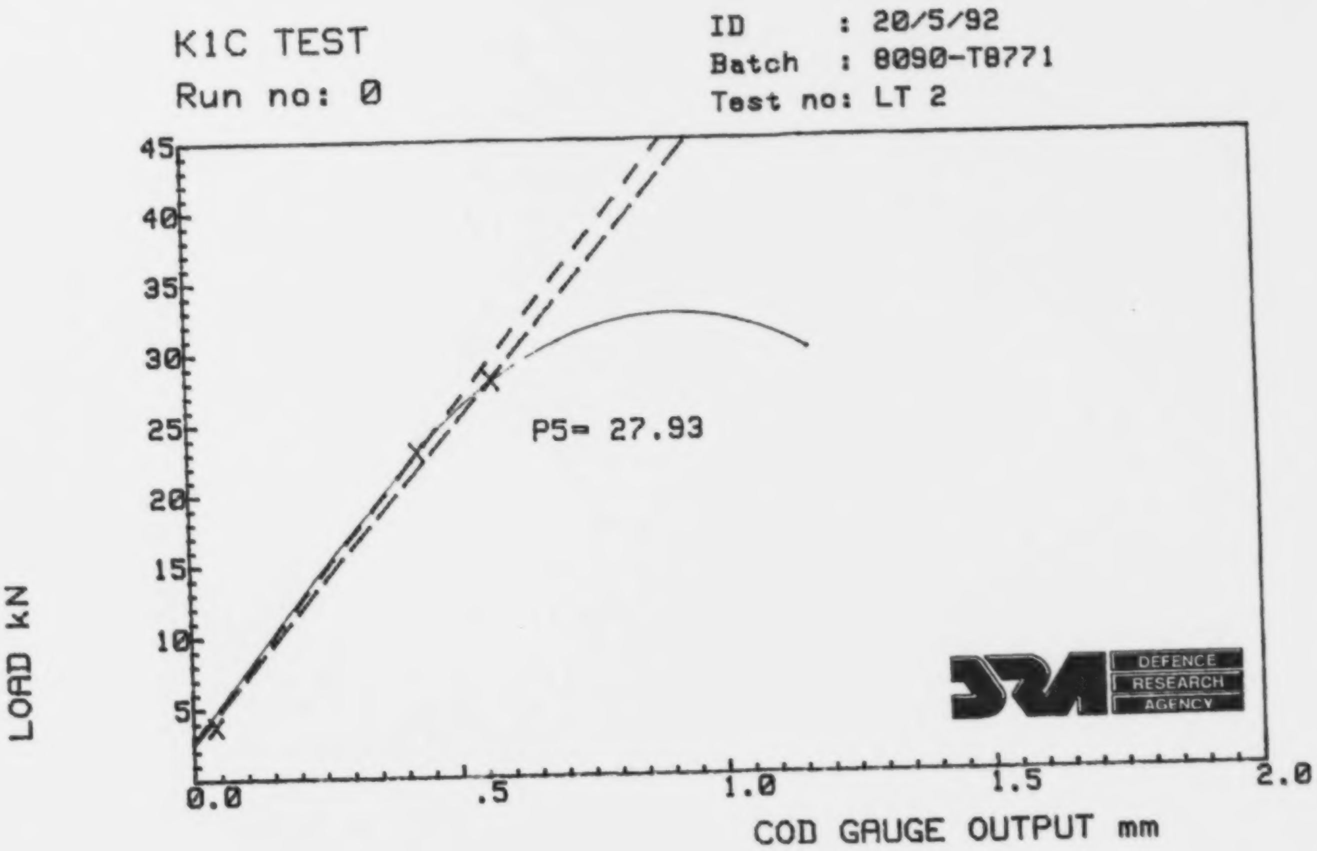

Figure 2: Load/displacement graph for 8090-T8771 37.5mm plate (L-T) fracture toughness (K_{1c}) test.

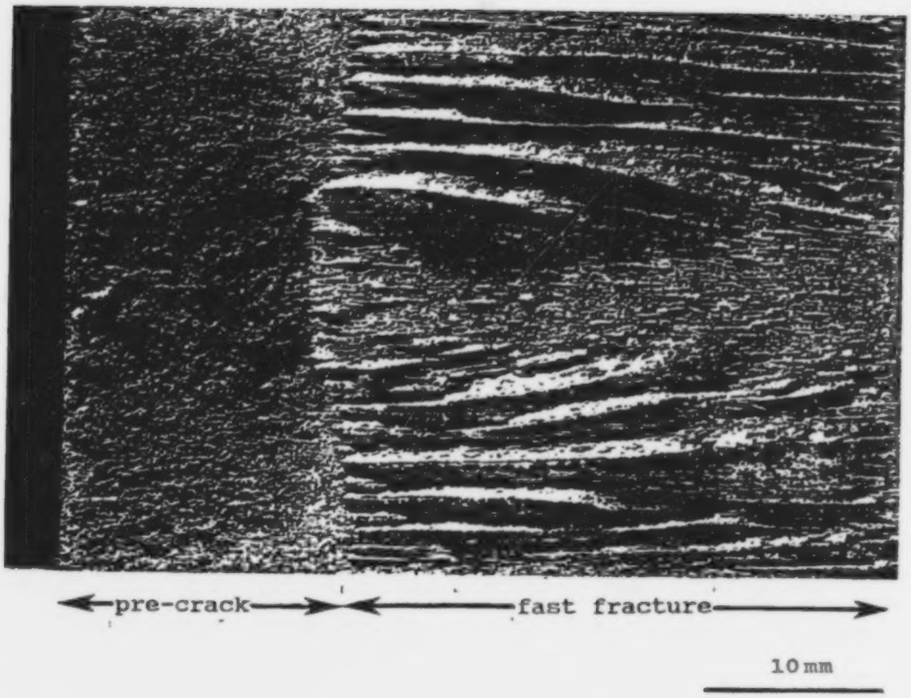
pre-crack
fast fracture
10 mm

Figure 3: View of fatigue pre-crack and final fracture surface of 8090-T8771 37.5mm plate (L-T) fracture toughness (K_{1c}) test. x3

DEFENCE
RESEARCH
AGENCY

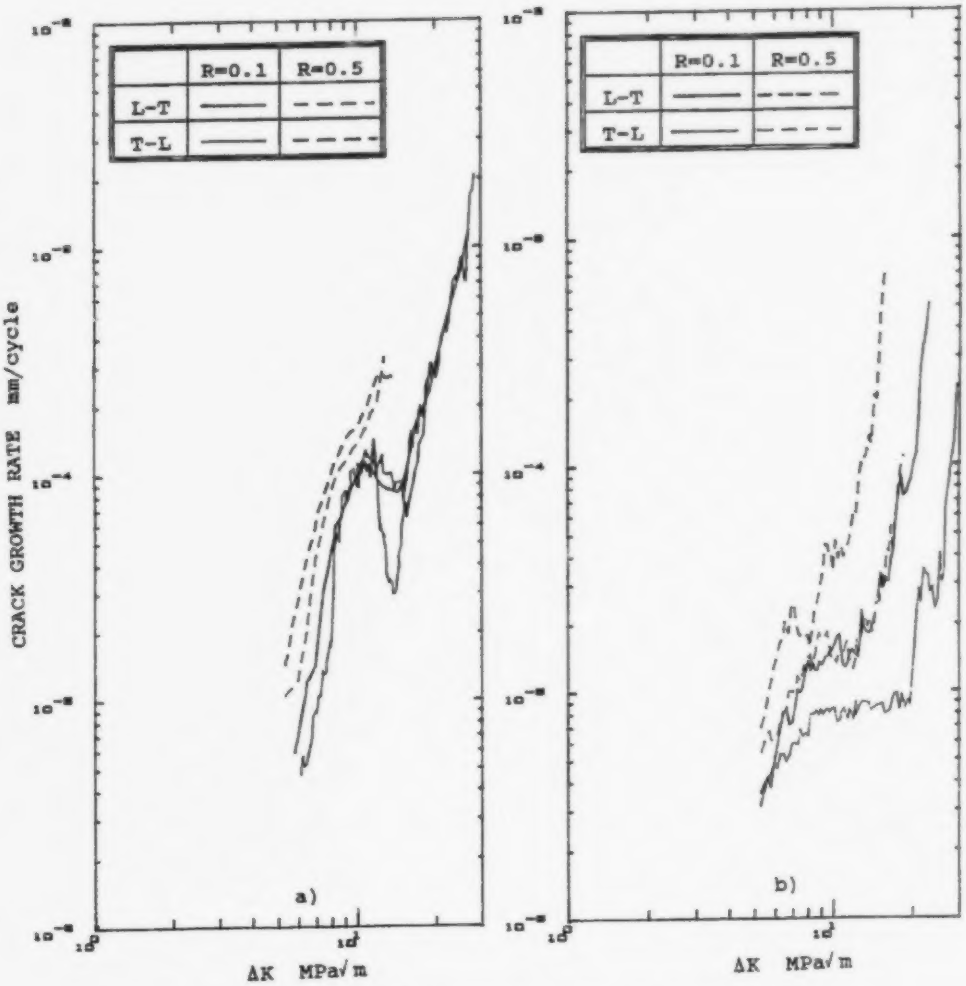

Figure 4: Effect of test orientation and stress ratio on the fatigue crack growth rate of (a) 8090-T8771 and (b) 2090-T8E41 12.5mm plate.

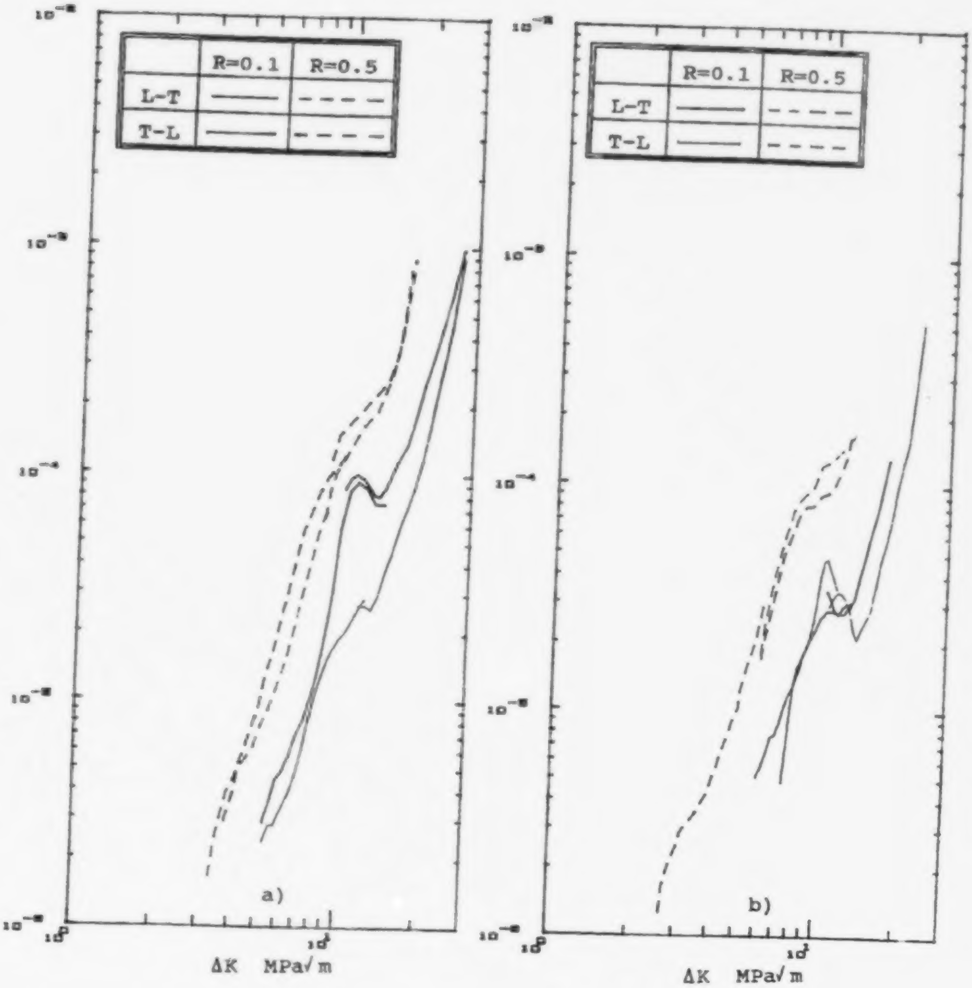

Figure 5: Effect of test orientation and stress ratio on the fatigue crack growth rate of 8090-T8771 (a) 25mm plate and (b) 37.5mm plate.

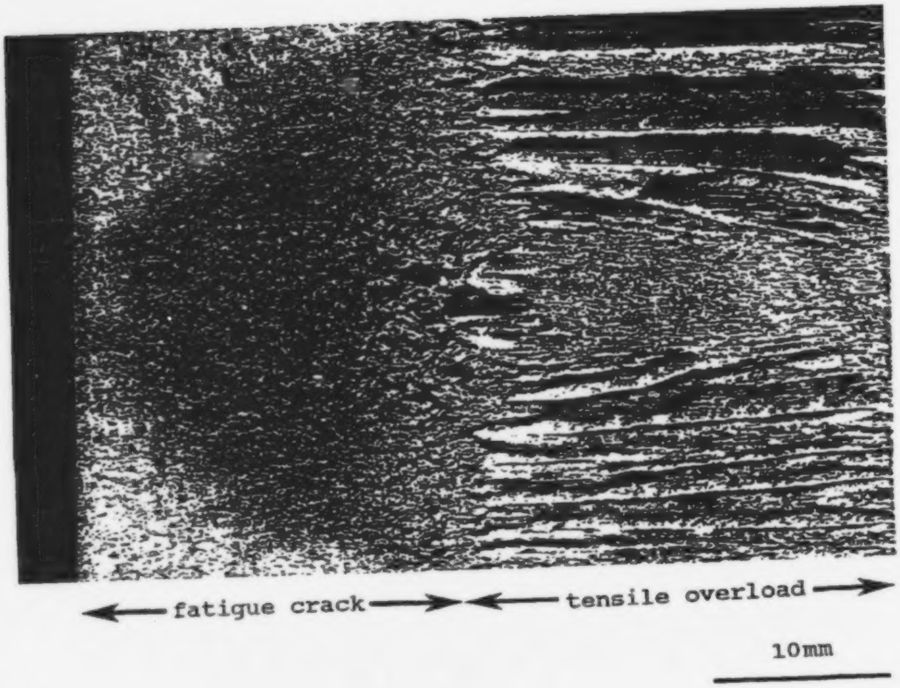
fatigue crack
tensile overload
10mm

Figure 6: View of fatigue crack in 8090-T8771 37.5mm plate showing the variation in fracture mode through the specimen thickness. (L-T, R=0.1) x3

DEFENCE RESEARCH AGENCY

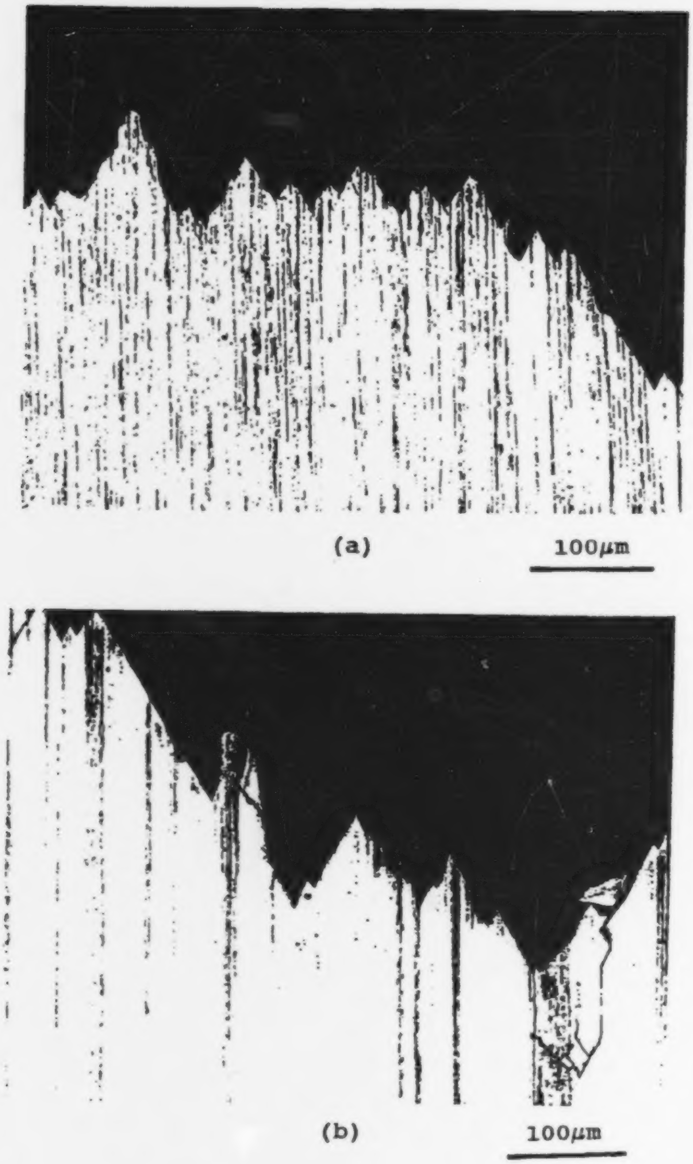

Figure 7: Micrographs showing shear facets developed during fatigue of (a) 8090-T8771 and (b) 2090-T8E41 12.5mm plate. L-T, R=0.1, ΔK=15 MPa√m. x200

DEFENCE
RESEARCH
AGENCY

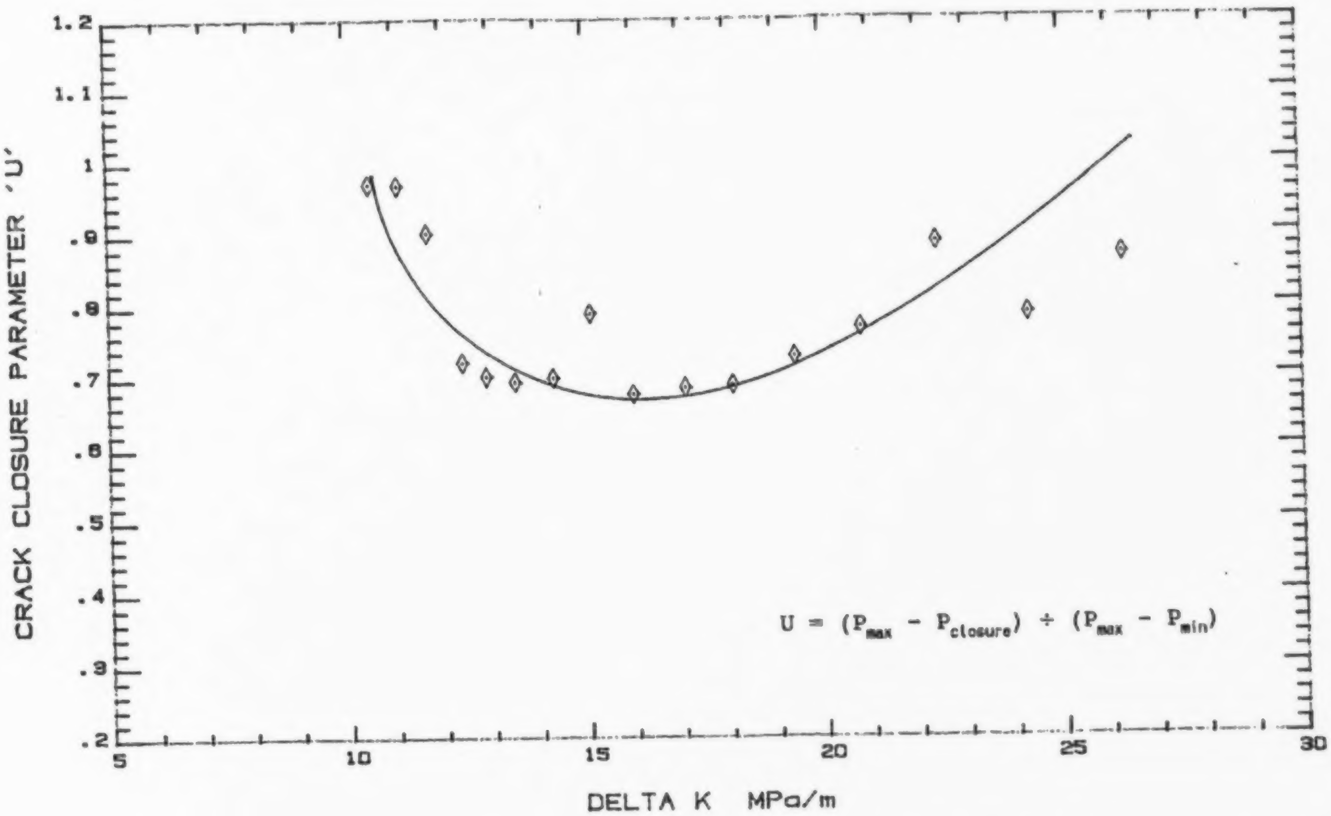

Figure 8: Variation of crack closure parameter "U" as a function of ΔK.
8090-T8771 (25mm Plate) L-T oriention. Stress Ratio R=0.1.

DEFENCE
RESEARCH
AGENCY

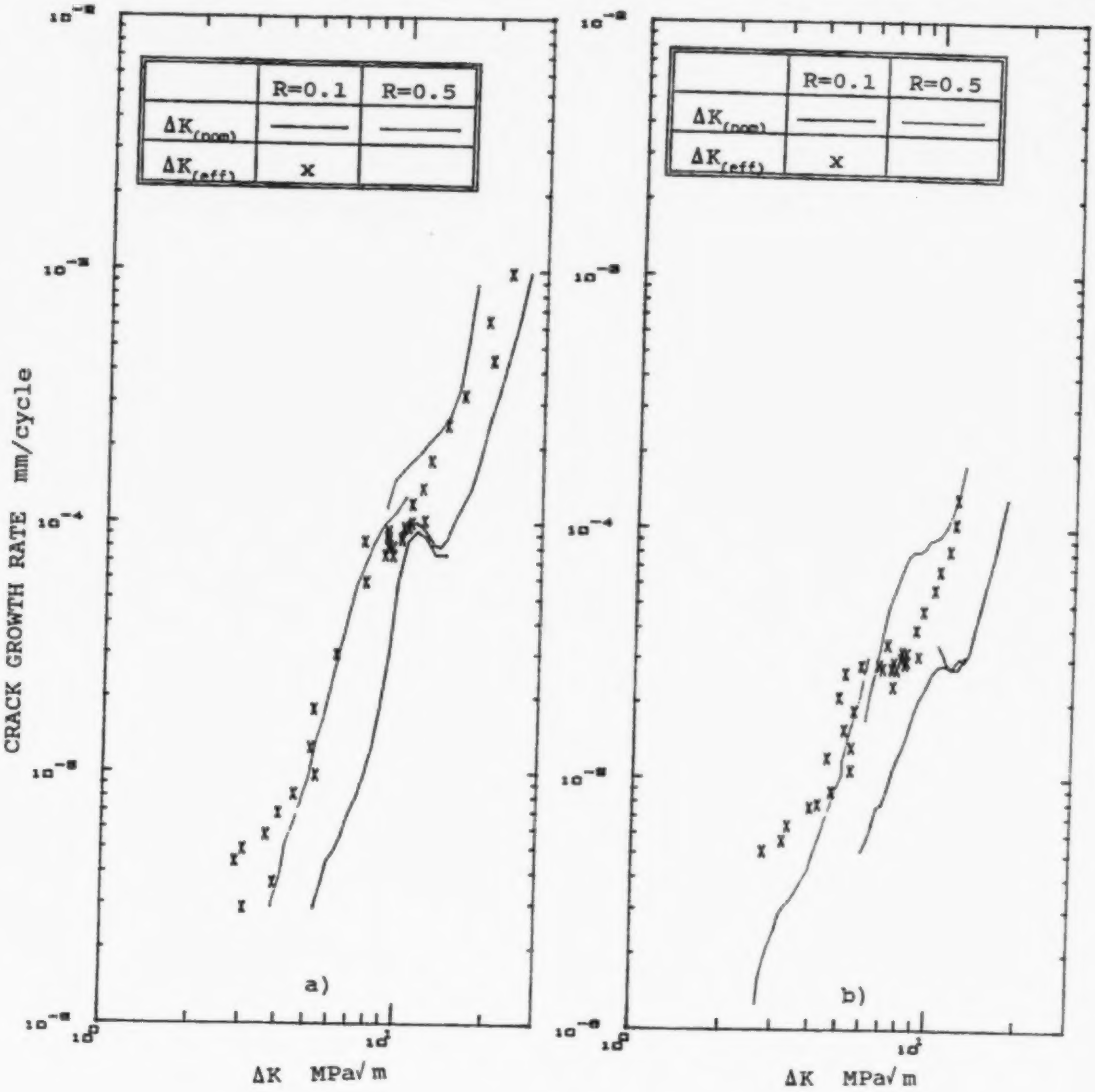

Figure 9: Effect of plotting fatigue crack growth rate against $\Delta K_{(nominal)}$ and $\Delta K_{(effective)}$ for 8090-T8771 (a) 25mm plate and (b) 37.5mm plate (L-T orientation).

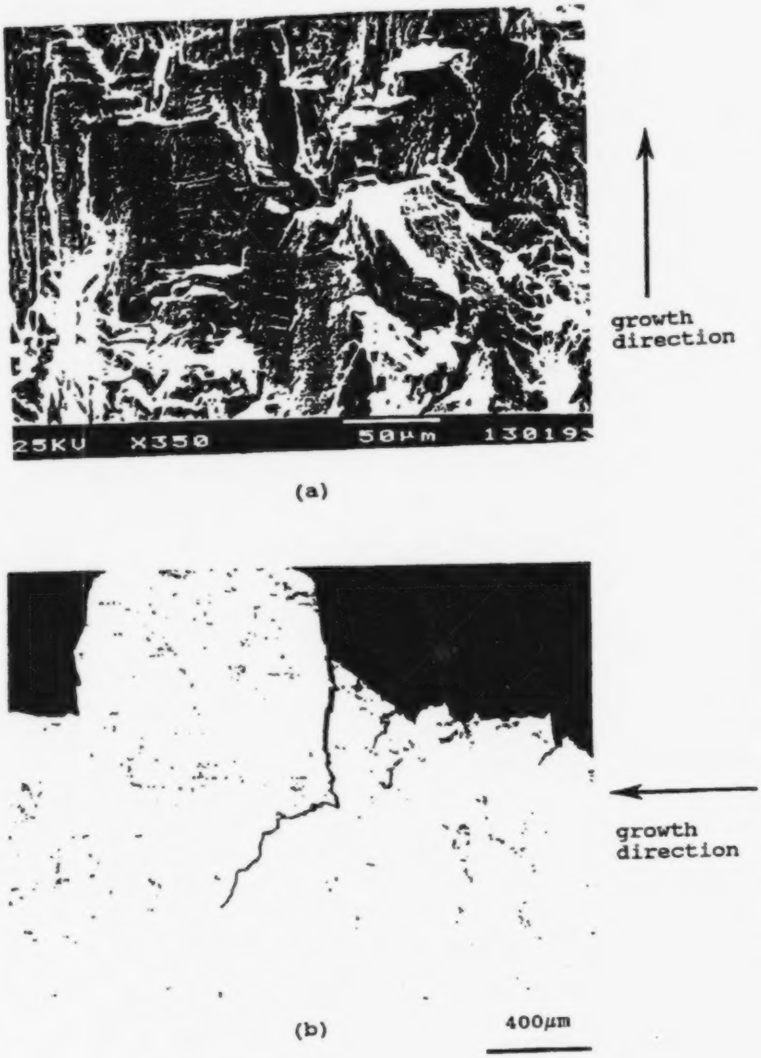
25KU X350 50µm 13019
growth direction
(a)
growth direction
(b)
400µm

Figure 10: (a) Scanning electron micrograph of fatigue crack in 8090-T8771 plate (37.5mm) showing secondary cracking. L-T orientation, R=0.1, $\Delta K= 15$ MPa$\sqrt{m}$.
(b) Micrograph of fatigue crack in 8090-T8771 plate (37.5mm). Same parameters as (a).

DEFENCE
RESEARCH
AGENCY

141644

12.

"The Effects of Orientation on Fatigue Crack Growth and Fracture in 8090 Aluminum-Lithium Plate"

X. Wu, W. Wallace, M.D. Raizenne, and A.K. Koul

IAR/NRC, Ottawa, Ont.

THE EFFECTS OF ORIENTATION ON FATIGUE CRACK GROWTH AND FRACTURE IN 8090 ALUMINUM-LITHIUM PLATE

X.J. Wu, W. Wallace, M.D. Raizenne and A.K. Koul

Abstract

A series of fatigue crack growth rate (FCGR) tests is carried out to determine FCGR in 8090 aluminum-lithium plate as a function of stress intensity range and specimen orientation. The directionality of fatigue crack growth is related to the strong texture (preferred orientation) in this alloy. Based on the previous restricted slip reversibility (RSR) model [1], a mathematical model is developed for transgranular fatigue crack growth in highly textured materials. In the model, the effect of texture on the FCGR is related to a geometric factor $\cos^2\phi$, where ϕ defines the angle between the load axis and the normal of the favourable slip plane. The effect of orientation on FCGR is shown to be a combination of the effects of the material's anisotropic mechanical properties and the variation of angle ϕ with specimen orientation. The model further predicts that fatigue crack growth rate will be slower in many textured materials than texture free materials because $\phi > 0$ and $\cos^2\phi < 1$.

I. INTRODUCTION

The development of aluminum-lithium alloys has been motivated primarily by their potential for use in the next-generation of aerospace structures. Interest lies in their high modulus-to-weight ratio and superior performance, as compared with traditional high strength aluminum alloys.

It is now well known that aluminum-lithium alloys exhibit uncommonly good resistance to the growth of fatigue cracks and show extremely marked anisotropy in their mechanical properties and fracture behavior [2-10]. Such performance is believed to be the consequence of strong textures developed during mill processing and the highly planar slip behavior of these alloys. Localized slip planarity promotes macroscopic crack deflection and leads to an unusual fracture mode with an extraordinary surface roughness comprised of well-defined slip band facets. Some researchers have suggested that the superior fatigue crack growth resistance of aluminum-lithium alloys is particularly related to some extrinsic shielding mechanism (viz. roughness-induced crack closure) [6,7]. Rarely have discussions been made on the intrinsic toughening effects induced by the presence of strong textures in aluminum-lithium alloys. Especially, quantitative assessment of the texture effect has not been provided.

The purposes of the present study are

- To examine the orientation dependence of fatigue crack growth in 8090 Al-Li alloy, through a series of FCGR tests. The variations of FCGR as a function of specimen orientation would reflect the effect of texture on the FCGRs in this alloy.
- To extend the RSR model [1] to transgranular fatigue crack growth in Al-Li alloys, taking account the effect of crystallographic texture (preferred orientation) on the kinetics of partially reversible slip which promote the crack growth.

II. EXPERIMENTAL DETAILS

Materials

The material studied was 8090-T8771 Al-Li alloy, in the form of 12.5 mm plate. The nominal composition of the alloy is given in Table 1. Its average mechanical properties in longitudinal (L) direction are listed in Table 2 [11]. Four compact tension (CT) specimens, Fig. 1, were cut from the original plate (20 × 20") such that the loading direction was a) parallel to the rolling direction (LT specimen), b) inclined at 15° (L+15° specimen), c) inclined at 30° (L+30° specimen) and d) inclined at 45° to the rolling direction (L+45° specimen). The CT specimens used conformed to ASTM E-647 specifications.

Table 1 Nominal Alloy Composition

Element (wt. %)						
Li	Cu	Mg	Zr	Fe	Si	Al
2.37	1.13	0.74	0.11	0.05	0.03	Bal.

Table 2 Mechanical Properties [11]

Orientation	Y. S. (MPa)	UTS (MPa)	Elongation (%)
L	471	546	5.6

Instrumentation

FCGR testing was performed on a MTS 810 testing system at the SML-IAR, NRC. Measurements of crack opening displacement (COD) were obtained using a clip-on gage (MTS 632.02c-20) placed between knife edges mounted on the front face of the specimen on either side of the machined notch. A travelling microscope was used to measure crack length on either side of the specimen. The traversing stage of the microscope was readable to 0.01 mm accuracy.

Test Conditions and Procedures

All the four CT specimens were precracked in fatigue at a maximum load of 8 kN and a minimum load of -0.0125 kN at a frequency of 20 Hz. The precrack length $a_o > 1.4$ mm. Constant amplitude FCGR tests were conducted using the following test conditions:

test frequency	$f = 20$ Hz,
maximum load	$P_{max} = 8$ kN,
stress ratio	$R = P_{min}/P_{max} = K_{min}/K_{max} = 0.1$,
environment	laboratory air,
wave form	sine wave,
test temperature	RT.

The maximum load was chosen to yield ΔK values in the range of 10 - 30 MPa$\sqrt{m}$. At these ΔK values, the size of the plastic zone ahead of the crack tip was presumed to be small compared to the crack length such that linear elastic fracture mechanics (LEFM) could be applied in accordance with ASTM E-647 specifications.

At selected cycle intervals, fatigue cycling was stopped, then the load vs COD relation was recorded and, at the maximum load, crack length was measured. This test sequence was repeated until the specimen completely fractured.

III. EXPERIMENTAL RESULTS

It was observed that crystallographic crack growth occurred in all specimens, exhibiting meandering crack path profiles. In the LT and L+15° specimens, the macroscopic crack appearred to propagate along the direction normal to the rolling direction but the catastrophic fracture occurs diagonally. In the L+30° specimen the fatigue crack deflected about 20° and in the L+45° specimen the fatigue crack deflected nearly 10° from the notch direction. The catastrophic fracture was observed to take off at 30° to 45° with respect to the notch direction. Pictures of the broken specimens are shown in Fig. 2. It appears that the L-T plane is the plane of microstructural symmetry in 8090 Al-Li plate.

Compliance data for the LT, L+15°, L+30° and L+45° specimens are plotted against the crack geometry parameter a/W as shown in Fig. 3, where the projected crack length (projection on the notch direction) is used for *a* and CEB represents the normalized compliance (CEB = B×E×COD/P, where B is the specimen width, E is the elastic modulus, COD is the crack mouth opening displacement and P is the load). It can be seen from Fig. 3 that the normalized compliance only varies slightly with specimen orientation.

It was observed that catastrophic fracture occurred at different crack lengths in different specimens. Crack length vs number of cycles data for the four specimen are shown in Fig.4. Since the final crack length can be related to the fracture toughness, the results indicate that fracture toughness, K_{Ic}, is also a function of specimen orientation. The K_{Ic} values for the four tested orientations are calculated, using the last data points as the critical crack lengths, and are listed in Table 3 where comparisons with results from other sources are also given whenever data are available. The reference data [13] were obtained from fatigue crack growth rate curves for 35mm 8090 plate, and calculated from the last data point shown (i.e. highest ΔK). Statistically significant data will have to be generated to determine whether the results in Table 3 represent a general trend.

Table 3 Variation of Fracture Toughness with Specimen Orientation

specimen orientation	K_{IC} (MPa$\sqrt{m}$)	K_{IC} (MPa$\sqrt{m}$) with reference
L-T	29	30 [12], 20 [13]
L+15°	30	
L+30°	22	
L+45°	26	10 [13]

Since, in all the specimens, the macroscopic crack deflection is less than 30° with respect to the notch direction, it is appropriate to use the projected crack length to calculate the stress intensity factor ΔK [14]. The fatigue crack growth rate, da/dN, is calculated from the crack length vs number of cycles relation using the secant method, i.e.,

$$\frac{\Delta a}{\Delta N} = \frac{a_{i+1} - a_i}{N_{i+1} - N_i} \tag{1}$$

at $a = (a_{i+1} + a_i)/2$. da/dN vs ΔK relations for LT, L+15°, L+30° and L+45° specimen orientations are shown in Fig. 5, and all data are compared in Fig. 6. From Figs. 4 and 6 it can be concluded that the L-T orientation exhibits the best fatigue crack growth resistance and the fatigue crack growth resistance is increasingly reduced with an increase in the inclined angle up to 30° with respect to the L-T orientation. Then, the fatigue crack growth resistance is regained a little as the inclined angle increased to 45°.

Fractographic examination of the fracture surfaces was made using SEM and optical fractography techniques. Fig. 7 (a)-(d) shows the typical fracture surface morphology observed for Stage II crack growth in the four specimen where the fracture surface in all cases is comprised of intersecting slip band facets. These intersecting slip band facets have a rather smooth, brittle appearance. However, in all specimens there were often pockets of ductile dimpled rupture, which sometimes appeared as complete transgranular regions, and sometimes as narrow bands along the apex of two intersecting slip band facets, as shown in Fig. 7 (e). In the pre-cracking region, the fracture surfaces were observed to consists of a mixture of slip band facets and brittle fracture surfaces, as shown in Fig. 7 (f). Under high magnifications, fine striations could be observed on those brittle surfaces, Fig. 7 (g). The brittle mode of crack growth formed a flat fracture surface. This mode of fracture was found to be predominate during precracking. The same mode of fracture was even observed in the early stage of crack growth (up to a ΔK value of ~ 16 MPa$\sqrt{}$m) in the L+30° and L+45° specimens. The reasons for the occurrence of such an unexpected mode of fracture are not clear. The fracture mode in the over-load region was found to be faceted brittle fracture, Fig. 7 (h). It is interesting to note that no evidence of ductile tearing could be found in this region.

Crack closure was also examined under the K-increasing conditions in these four tests following the ASTM recommended procedure [15]. As shown in Fig. 8, for all the specimens, the COD vs P relation exhibits a good linear behavior over the entire load range. The only evidence of crack closure was found at extremely low loads of generally less than 1 kN, where it can be seen in Fig. 8 that the P versus COD plots do not pass through the origin. Also, the fracture surfaces all contained regions of black discolouration which was possibly caused by oxidation due to surface rubbing. The blackening was only seen in the rougher regions of the fatigue fractures and not in the pre-cracked region or overload region.

IV. DISCUSSION

Crystallographic Texture and Fatigue Crack Growth Paths in 8090 Plate

It has been found by several workers [13,16,17] that the strong texture in the centre of a 8090 Al-Li alloy plate is {110} <112> (the "brass" type), Fig. 9. Taking the the rolling direction as the [112] pole, the slip band facets can be identified as $(1\bar{1}1)$ planes and their conjugate, $(\bar{1}11)$ planes. The pair of (111) and $(\bar{1}11)$ planes intersect at an angle of

$$\Phi = \angle([1\bar{1}1], [\bar{1}11]) = \cos^{-1}\left(\frac{1}{3}\right) = 70.56^\circ.$$

In the L-T specimen, the crystallographic crack growth would take place along the [110] direction which makes an angle of

$$\theta = \angle([110], [11\bar{1}]) = \cos^{-1}\sqrt{\frac{2}{3}} = 35.26^\circ$$

with respect to the notch direction (in this case the long transverse (T) direction). Suppose the [112] grains (grains with [112] pole in the rolling direction) and the $[\bar{1}12]$ grains are evenly distributed along T direction, the crystallographic crack path may meander symmetrically about the T-axis, hence the macroscopic crack lies along the T-axis . However, this may not always be the case, Hull has observed macroscopic crack deflection of nearly 45° in a 8090 LT specimen [10]. This deviation is suspected to be due to grain orientation and distribution that favours slip along one definite direction passing through several similarly oriented grains which results in asymmetrical crack growth. From Fig. 9, the angle of intersection between slip band facets in the LT specimen width direction can be calculated as 2×(90° - 35.26°) = 109.48°, which agrees with the measured angle, Fig. 10 (a). The angle of intersection between slip band facets in the thickness direction is found to be the projection of angle Φ on the $(1\bar{1}1)$ plane (T plane) which equals to Φ cos 35.26° = 57.6°, which is the value observed experimentally. In the L+15° specimen, the same slip systems are believed to operate such that crystallographic crack growth follows a similar path as in LT specimen and the same asperity angles would be expected as shown in Fig. 10 (b). But in this case the macroscopic crack should deflect 15° with respect to the notch direction, as observed in Fig. 2 (b) and illustrated in Fig. 9 (c). In the L+30° specimen, slip may operate alternatively along [011] and $[10\bar{1}]$ directions in [112] grains or [110] direction in $[\bar{1}12]$ grains, making the in-plane angle of intersection between slip band facets to be either 54.74° or 70.52°, as observed in the crack profile of Fig. 10 (c). In the L+45° specimen, crystallographic crack growth may proceed alternatively along [011] and $[10\bar{1}]$ directions such that the macroscopic crack lies along [110] direction about which the lattice structure is in symmetry. In this case it is expected that the macroscopic crack would deflect at an angle of 45° - 35.26° = 9.74° from the original notch direction. The in-plane angle of intersection between slip band facets is predicted to be 70.52°, the same as observed in Fig. 10 (d). Table 4 summarize the favourable slip system(s) and the crystallographic crack growth direction θ (with respect to the macroscopic crack).

Table 4 Favourable Slip Systems & Crystallographic Directions

specimen orientation β	favourable slip systems	crystallographic angle θ
0° (L-T)	[110] {111}	35.26°
15° (L+15°)	[110] {111}	35.26°
30° (L+30°)	[011], $[10\bar{1}]$, [110] {111}	54.74° and 70.52°
45° (L+45°)	[011], $[10\bar{1}]$ {111}	54.74°

The FCGR Model

It is well-recognized that transgranular fatigue cracks propagate by alternating slip within the plastic zone ahead of the crack tip [18-22]. Slip, i.e. dislocation glide, occurs in definite crystallographic directions and along definite crystallographic planes, usually the closely packed planes. The preferred slip system is thus defined by the preferred direction and the preferred plane. Slip bands in a face centred cubic (f.c.c.) system, such as an Al-Li-Cu alloy during fatigue, are anticipated to form along the {111} plane. In f.c.c. polycrystalline materials with strong textures, the <111> pole is often displaced from the stress axis, and as a consequence, slip occurs on the preferred slip planes that are inclined at an angle ϕ with respect to the load axis and hence crack growth proceeds along these inclined crystallographic planes. A three dimensional view and a two dimensional view of such a deformation and fracture mechanism are shown schematically in Fig. 11 and Fig. 12 respectively. According to the concept of restricted slip reversibility [1], the net fatigue crack growth rate represents the difference between the distances travelled by dislocations within the plastic zone during forward slip and slip reversal in one load cycle. In the RSR model, the FCGR has been found to be equal to the product of the net plastic strain ahead of the crack tip and the plastic zone size, and this is expressed by the relationship [1]

$$\frac{da}{dN} = (\gamma_f - \gamma_r)\, r_p \cos\theta . \tag{2}$$

where γ_f and γ_r are the plastic strains associated with the forward slip and slip reversal respectively, r_p is the plastic zone size and θ is the preferred slip direction.

The accumulation of plastic strain during dislocation glide is governed by the rate equation [23]

$$\dot{\gamma}(r,\theta) = \dot{\gamma}_o \exp\left[-\frac{\Delta G^* - V(\tau - H\gamma - \tau_o)}{kT}\right] \qquad (3)$$

where $\dot{\gamma}_o$ is a pre-exponential factor, ΔG^* is the activation energy, V is the activation volume, H is the work hardening coefficient, τ_o is the initial internal stress, $k = 1.38\times10^{-23}$ JK^{-1} is the Boltzmann constant, T is the absolute temperature and τ is the shear stress resolved on the slip plane (Figs. 11 and 12). For a crack with the surface inclined at an angle ϕ to the load axis, the linear elastic crack-tip stress field is expressed as (Appendix A)

$$\sigma_{ij} = \frac{K}{\sqrt{2\pi r}} f_{ij}(\theta)\cos^2\phi .$$

and the shear stress τ along the θ-direction (the slip direction) is (Appendix A)

$$\tau = \frac{K}{2\sqrt{2\pi r}} \sin\theta\cos\frac{\theta}{2}\cos^2\phi \qquad (4)$$

Using equation (3), the average plastic strain rate within the plastic zone can be computed through the summation of local strain rates $\dot{\gamma}$ (r,θ) over the length of plastic zone along the crystallographic direction θ:

$$(\dot{\gamma})_{average} = \frac{1}{r_p}\int_b^{r_p} \dot{\gamma}(r,\theta)\,dr$$

where b is the Burgers vector, the smallest dislocation-free zone size.

Upon substituting the stress expression (4) into equation (3) and using the mean value theorem for integral [24], the average crack-tip strain rate can be represented by

$$\dot{\gamma} = \dot{\gamma}_o \exp\{-\frac{\Delta G^* - [\alpha(\theta) K\cos^2\phi - VH\gamma - V\tau_o]}{kT}\}. \qquad (5)$$

where

$$\alpha(\theta) = \frac{V}{\sqrt{2\pi L}}\frac{1}{2}\sin\theta\cos\frac{\theta}{2} \qquad (b<r_m<r_p)$$

is the work factor and r_m is the mean-value distance defined by the mean-value theorem. Since the stress decreases rapidly away from the crack tip, the plastic strain rate is mainly influenced by thermally activated glide that occurs within a short distance of the crack tip. The mean-value distance r_m depends largely on the microstructure and defect density near the crack tip and is less relevant to the actual length of the entire plastic zone over which the average is taken. Therefore, $\alpha(\theta)$ can be considered, for the first order of approximation, as a material constant which is independent of the plastic zone size and the stress intensity factor.

It will be recognized that forward slip occurs during rising load in a fatigue cycle and slip reversal occurs during the decreasing part of the load cycle. The mechanisms controlling the forward slip and the slip reversal processes are the same in mechanical fatigue, but these mechanisms will be different in corrosion fatigue where for example the oxide debris formation on fresh metal surface may affect the slip reversal. For general mechanisms of restricted slip reversal, under triangular wave form loading, the forward and reverse plastic strain (γ_f and γ_r) can be calculated by integrating equation (5) over the rising and decreasing parts of the load cycle as shown in the Appendix B. The net plastic strain (γ_f - γ_r) can then be obtained as:

$$\gamma_f-\gamma_r = \ln\left[\frac{\left(\dfrac{V_f H\dot{\gamma}_{of}}{2f\alpha_f \Delta K\cos^2\phi}\right)^{\frac{kT}{V_f H}}\exp\left(-\dfrac{\Delta G_f^* + V_f\tau_{of}}{V_f H}\right)}{\left(\dfrac{V_r H\dot{\gamma}_{or}}{2f\alpha_r \Delta K\cos^2\phi}\right)^{\frac{kT}{V_r H}}\exp\left(-\dfrac{\Delta G_r^* + V_r\tau_{or}}{V_r H}\right)}\right] + \left(\frac{\alpha_f}{V_f H}-\frac{\alpha_r}{V_r H}\right)\frac{\Delta K\cos^2\phi}{1-R}. \tag{6}$$

Within the constraints of small scale yielding, the plastic zone size, $r_p \cos\theta$, can be approximated by [25]

$$r_x = r_p\cos\theta = \frac{1}{3\pi}\left(\frac{\Delta K}{2\sigma_y}\right)^2. \tag{7}$$

Substituting equations (6) for (γ_f - γ_r) and equation (7) for $r_p\cos\theta$ into equation (2), the fatigue crack growth rate can be expressed as:

$$\frac{da}{dN} = \frac{(\alpha_f V_r-\alpha_r V_f)\cos^2\phi}{12\pi V_f V_r H(1-R)}(\Delta K-\Delta K_{th})\left(\frac{\Delta K}{\sigma_y}\right)^2, \tag{8}$$

where

$$\Delta K_{th} = \frac{(1-R)HV_f V_r}{(\alpha_f V_r - \alpha_r V_f)\cos^2\phi} \cdot \left[\frac{1}{H}\left(\tau_{of} - \tau_{or} + \frac{\Delta G_f^*}{V_f} - \frac{\Delta G_r^*}{V_r}\right) - \ln \frac{\left(\dfrac{V_f H\dot{\gamma}_{of}}{2f\alpha_f \Delta K\cos^2\phi}\right)^{\frac{kT}{V_f H}}}{\left(\dfrac{V_r H\dot{\gamma}_{or}}{2f\alpha_r \Delta K\cos^2\phi}\right)^{\frac{kT}{V_r H}}} \right]. \tag{9}$$

Equation (9) defines the fatigue threshold condition in terms of a complex function of temperature, frequency, and stress ratio. The ΔK_{th} is a microstructure – environment sensitive variable because it is controlled by activation energies, activation volumes and work factors.

In mechanical fatigue, where microstructure is stable and where environmental effects are absent, α_f and α_r are of the same order of magnitude, and both forward slip and slip reversal occur by the same mechanism so that $\Delta G_f^* = \Delta G_r^*$, $V_f = V_r = V$, $\tau_{of} = \tau_{or}$ and $\dot{\gamma}_{of} = \dot{\gamma}_{or}$, and as a result, the ΔK_{th} term in equation (7) vanishes to zero because $kT/VH << 1$ [1]. Hence, in highly textured materials, the FCGR under pure mechanical fatigue conditions is given by

$$\frac{da}{dN} = \frac{(\alpha_f - \alpha_r)\cos^2\phi}{12\pi VH\sigma_y^2(1-R)}(\Delta K)^3. \tag{10}$$

Equation (10) is similar to the Paris relationship [26] with a physically defined proportional factor and the power law exponent of 3.

It has been shown previously that FCGR model based on restricted slip reversal (RSR) concepts provides a physical description for crack growth processes that result in transgranular fracture [1]. The model also provides a physical basis for striation formation during fatigue crack growth, a feature that has been verified through numerous experimental observations. The fatigue crack growth rate in the previous model was also shown to be dependent on microstructural and environmental quantities such as activation volumes and work factors, material properties such as yield stress and work hardening coefficient as well as test conditions (ΔK and R). The model took the same form as the Paris equation with the power law exponent of 3, where

$$\frac{da}{dN} = \frac{(\alpha_f - \alpha_r)\,(\Delta K)^3}{12\pi V H \sigma_y^2 (1-R)}. \tag{11}$$

Upon comparing equations (10) and (11), it becomes evident that the proportional constant in the present FCGR model incorporates a geometric factor $\cos^2\phi$ to account for texture effects, and specifically for the fact that the crack faces being produced are often not normal to the loading direction. In the case of texture free material, $\phi = 0$, and equation (10) reduces to equation (11). Equation (10) predicts that if a material is produced in a texture free or a highly textured condition, the textured material will usually reveal a lower FCGR than the texture free material because ϕ will be greater than zero and therefore $\cos^2\phi < 1$. This assumes that texture will not affect yield strength, work hardening coefficient and mean slip distance α_f and α_r. If this is not the case, which is usual, then the variation in these parameters need to be taken into account, as indicated by equation (10).

Taking the {110} <112> texture for consideration, the load axis can be expressed with the crystallographic coordinate (Fig. 9) as $[1,1,\sqrt{2}\tan(54.74^\circ+\beta)]$, where β is the angle between the load axis and the rolling direction and 54.74° is the angle between the rolling direction and the <110> direction. Thus,

$$\cos\phi = \frac{1}{\sqrt{3}}\sin(\beta+54.74) \tag{12}$$

Substituting equation (12) for $\cos\phi$ in equation (10), the fatigue crack growth rate in materials with {110} <112> texture will be expressed as a function of stress intensity range ΔK and loading direction β in the form of

$$\frac{da}{dN} = \frac{(\alpha_f - \alpha_r)\sin^2(\beta+54.74)}{36\pi V H \sigma_y^2 (1-R)}(\Delta K)^3. \tag{13}$$

Comparison with Experiments

Fig. 13 shows the comparison of FCGRs for a number of conventional aluminum alloys [9,27-29] and aluminum-lithium alloys, 2090-T8E41 [9] and 8090-T8771 (in the present study). Mechanical properties of these alloys are given in Table 5. Compensated for $(1-R)H\sigma_y^2$ (the work hardening coefficient, H, is estimated by [UTS - Y.S.]/El.), the FCGR data of conventional aluminum alloys are represented by one regression line (the upper solid line) and aluminum-lithium alloys are represented by another regression line (the lower solid line), both with the slope of 3 in the log-log scale. To understand the importance of the geometric factor $\cos^2\phi$ on FCGR of Al-Li alloys, rough estimates of proportional constant variables $(\alpha_f - \alpha_r)/V$ are obtained by fitting equation (11) to the data for conventional aluminum alloys, Fig. 13. In the case of conventional aluminum alloys $(\alpha_f - \alpha_r)/V = 0.697\ \mathrm{m}^{-1/2}$. Using this $(\alpha_f - \alpha_r)/V$ value for substitution in equation (13), the predicted FCGR curve (the dashed line) falls very close to the experimentally observed FCGR in the case of 2090-T8E41 and 8090-T8771 L-T specimen ($\beta = 0$), Fig. 13. These calculations clearly indicate that relative to conventional aluminum alloys, 90 percent of the total reduction in compensated FCGR for aluminum-lithium alloys are accounted for merely by the texture dependent geometric factor $\cos^2\phi$. These calculations further suggest that the superior FCGR resistance of Al-Li alloys, such as 2090-T8E41 and 8090-T8771, can be attributed to the presence of strong textures as well as extrinsic shielding or roughness induced crack closure effects. The later did not appear to be significant for the tests carried out in the present study.

In Fig. 13, the predicted FCGRs for Al-Li alloys are marginally higher than the experimentally observed values by a factor of about 1.5. It is not clear whether this discrepancy would be eliminated if exact values of proportional constant variables, i.e., $(\alpha_f - \alpha_r)/V$, for Al-Li alloys are used in equation (10) or whether this small error is related to FCGR retardation due to roughness induced crack closure effects.

Table 5 Mechanical Properties of Aluminum Alloys

Alloys	Y.S. (MPa)	UTS (MPa)	El. (%)
2024-T351	355	465	15
2219-T851	352	455	10
7075-T651	483	531	8
7475-T761	428	490	8
8090-T8771	471	546	5.6
2090-T8E41	555	592	6

For 8090 Al-Li alloy, a simple single crystal model [30] is used to predict the yield strength along the tested directions. The model is based on the Schmid law [31] and assumes that the critical resolved shear stress, τ_{CRSS}, is constant for all the primary slip systems such that

$$\sigma_y = \frac{\tau_{CRSS}}{m}$$

where m is the Schmid factor which takes its maximum on the preferred slip system. The predicted values of yield strength are listed in Table 6.

Substituting $(\alpha_f - \alpha_r)/V = 0.697\ (\mathrm{MPa})^{-1}\mathrm{m}^{-1/2}$ (the norminal value for age-hardenable Al-base alloys), yield strength values in Table 6 into equation (13) and assuming a constant work hardening coefficient, $H = 1339.3$ MPa, the fatigue crack growth rate in 8090 Al-Li plate along various orientations can be calculated using equation (13). The comparison of the prediction of equation (13) with experimental data is shown in Fig. 14 (the line for L+30° coincides with that for L+45°) and a very good agreement is observed. It should be noted that the proportional constant $(\alpha_f - \alpha_r)/V$ is a function of the crystallographic direction θ which may take different angles for different specimen orientations, Table 4. Considering slip always occurs along favourable directions, this angular effect is considered to be less significant than the $\cos^2\phi$ dependency. Also, the work hardening coefficient may vary with orientation as discussed previously. These effects are not included in the analysis leading to Fig. 14.

Table 6 Predicted Yield Strength

Orientation	L	L+15°	L+30°	L+45°
m [29]	0.4	0.466	0.495	0.5
Y.S. (MPa)	471*	404.3	380.6	376.8

* the value is given in Table 2.

V. CONCLUSIONS

i) Fatigue crack growth behavior of 8090 Al-Li alloy has been related to the {110}<112> texture in this alloy. With a strong preferred orientation, the polycrystalline material behaves more or less like a single crystal.

ii) A transgranular fatigue crack growth rate model for highly textured material is developed using the restricted slip reversibility and linear elastic fracture mechanics concepts, the model provides a physical description for transgranular fatigue crack growth involving highly planar slip in Al-Li alloys. For mechanical fatigue, the model takes the form of the Paris equation with the power-law exponent of 3. The effect of texture (preferred orientation) on FCGR has been related to a geometric factor $\cos^2\phi$ for the favourable slip system. With {110}<112> texture, the fatigue crack growth rate in 8090 Al-Li plate is expressed in an explicit function of stress intensity range and the orientation angle β.

iii) The model predicts that FCGR would be slower in textured materials than in texture free materials because the geometric factor for the preferred orientation is less than unity. The quantitative analysis shows that the reduction in FCGR of aluminum-lithium alloys, 2090-T8E41 and 8090-T8771, as compared with conventional aluminum alloys, can be accounted for by texture effects, their higher yield strengths and their work hardening coefficients.

iv) Extrinsic shielding in the form of roughness induced crack closure may not always be the primary reason for superior FCGR resistance of Al-Li alloys.

VI. FUTURE STUDIES

The four FCGR tests along the previous orientations should be repeated. It is recommended that further tests on L+30° and L+45° specimens be run at a lower load to avoid any "overload" effect. Load shedding technique should also be employed to examine the *K* dependence of fracture mode. Investigations should also be extended to examine the single-overload effect and the crack closure effect on fatigue crack growth in 8090 Al-Li alloy. Particular interests of future studies are:

1. The influence of single overload on crack growth mode, macroscopic crack deflection and crack growth retardation should be examined.

2. The manifestation of crack closure in load shedding tests and its effect on the fatigue threshold of aluminum-lithium alloys should be examined.

3. Environmental interactions with the reversible planar slip that affects the rate of fatigue crack growth in aluminum-lithium alloys should be studied.

Acknowledgement

The experimental part of this work was done during an assignment at SML-IAR when the first author, X.J. Wu, was a graduate student at University of Ottawa. The financial assistance then provided to him by Prof. A.S. Krausz from his NSERC grant is gratefully acknowledged.

The work was carried out under Structures and Materials Laboratory Program 3G3: Aerospace Structures, Structural Dynamics and Acoustics, Project JGQ00: Application of Aluminum-Lithium Alloys to Aircraft Structures. The test material was provided by Dr. Jack Morrison of Defence Research Establishment Pacific. Special thanks from the first author goes to Dave Chow and Raymond Dainty for assisting him in using SEM and optical micrography instruments.

REFERENCES

1. X.J. Wu, A.K. Koul, A.S. Krausz, "A Transgranular Fatigue Crack Growth Model Based On Restricted Slip Reversibility", LTR-ST-1831, NRC, 1991.
2. E.J. Coyne, T.H. Sanders, E.A. Starke, Jr., in *Aluminum-Lithium Alloys* (edited by T.H. Sanders and E.A. Starke, Jr.), TMS-AIME, Warrendale, PA, 1981, pp. 293-305.
3. S.J. Harris, B. Noble, K. Dinsdale, in *Aluminum-Lithium Alloys* (edited by T.H. Sanders and E.A. Starke, Jr.), TMS-AIME, Warrendale, PA, 1981, pp. 219-233.
4. P.E. Bretz, L.N. MUeller, A.K. Vasudevan, in *Aluminum-Lithium Alloys II Conf., AIME.*, Monterey, California, pp. 543-559, 1983.
5. M. Peters, K. Welpman, W. Zink, T.H. Sanders Jr., in *Aluminum-Lithium Alloys III Conf. Inst. Metals*, Oxford, U.K., pp. 237-246, 1985.
6. K.T. Venkateswara Rao, W. Yu, R.O. Ritchie, *Metallurgical Transactions*, **19A**, pp. 563-568, 1988.
7. K.T. Venkateswara Rao, W. Yu, R.O. Ritchie, *Aluminum-Lithium Alloys: Design, Development and Application Update*, ASM Int., pp. 173-186, 1987.
8. K.T. Venkateswara Rao, R.S. Piascik, R.P. Gangloff, R.O. Ritchie, in *Aluminum-Lithium Alloys*, Vol. II, 5th Int. Al-Li Conf., Williamsburg, VA, pp. 955-971, 1989.
9. G.R. Yoder, P.S. Pao, M.A. Imam, L.A. Cooley, in *Aluminum-Lithium Alloys*, Vol.II, 5th Int. Al-Li Conf., Williamsburg, VA, pp. 1033-1041, 1989.
10. D.A. Hull, "Fatigue Testing of High Strength Aluminum-Lithium Alloys", Contract Report No. A0005-PR-002, Engineering Material Research Ltd, 1991.
11. Supplied Data Sheet, Serial No. 0143639, Aluminum Supply Ltd., Totteridge, London, Nov. 4, 1990.
12. D. McCammond, S.A. Meguid, A.N. Sinclair, J.K. Spelt, R.D. Venter, M. Gabbani and M. Mummi, "A Critical Review of Aluminum Lithium Technology and Its Impact on Aircraft Structural Design, Manufacture and Maintenance", Part II, NAE-CR-4, NRC No. 31068, 1989.
13. S. J. Harris, B. Noble and A. Dodd, in *Aluminum-Lithium Alloys*, Vol.II, 5th Int. Al-Li Conf., Williamsburg, VA, pp. 1033-1041, 1989.
14. K.S. Chan and J.H. Fitzgerald, *Eng. Fract. Mech.* **40**, 251 (1991).
15. "Test Plan and Instructions for E24.04.04 Round Robin on Crack Opening Load Measurement", ASTM E-24, 1991.
16. M. Peters, K. Welpmann and T.H. Sanders Jr., Proc. 3rd Conf. on R & D for Transport, E.M.R.S., Strasboutg, 1985.
17. S. Fox, H.M. Flower and D.S. McDarmaid, Int. Conf. on "Aluminum Alloys - Physical and Mechanical Properties", University of Virginia, EMAS, Warley, U.K., 1986, pp. 939-950.
18. C. Laird and G.C. Smith, *Phil. Mag.* **7**, 847 (1962).
19. P. Newmann, *Acta Metall.* **22**, 1155 (1974).
20. R.M.N. Pellox, *ASM Trans. Quart.* **62**, 1 (1969).

21. F.A. McClintock, in *Fracture*, Vol 3 (edited by H. Liebowitz), p. 47. Academic Press (1971).
22. C. Fong and D. Tromans, *Metall. Trans.* **19**A, 2753 (1988).
23. A.S. Krausz, H. Eyring, *Deformation kinetics*, Wiley Interscience, 1975.
24. V.I. Smirnov, *A Course of Higher Mathematics*, Vol. I, Pergamon Press, 1964.
25. G.R. Irwin, *Handbuch der physik*, Springer-Verlag, Berlin, 1958, p. 551.
26. P.C. Paris, in *Fatigue Thresholds*, Vol. I (edited by J. Backlund, A.F. Blom and C.J. Beevers), Engineering Materials Advisory Service, 1982, p.3.
27. J. Gallagher (editor), *Damage Tolerant Design Handbook*, Metals and Ceramics Information Center, Columbus, Ohio, 1983, p. 7.5-120.
28. J.M. Cox, D.E. Pettit, S.L. Langenbeck, in *Fatigue at Low Temperature*, ASTM STP 857, p. 241 (1985).
29. A.J. McEvily, in *Fatigue Mechanisms: Advances in Quantitative Measurement of Physical Damage*, ASTM STP 811, p. 283 (1983).
30. M. Peters, K. Welpmann and T.H. Sanders, Jr., in *Advanced Materials Reseach and Developments for Transport*, VII, Strasbourg, France, 1985, p. 63.
31. E. Schmid, *Z. Elektrochem.*, **37**, 447 (1931).

APPENDIX A

In linear elastic fracture mechanics, a crack problem can be, by the principle of superposition, decomposed into (I) the stress problem of an uncracked body with the prescribed stress and displacement boundaries (denoted as S_σ and S_u respectively) and (II) the stress problem of the cracked body with a distribution of stress, σ_n, along the crack surfaces which is opposite in sign and equal to the resolved stress on the assumed crack plane in problem I, as shown in Fig. 15. The crack-tip stress field is then obtained by solving problem II, which can be expressed in a generalized form as

$$\sigma_{ij} = \frac{K}{\sqrt{2\pi r}} f_{ij}(\theta)$$

where

$$K = Y\sigma_n\sqrt{\pi a}$$

is the stress intensity factor and Y is the shape factor.

If the crack plane is inclined to the stress axis at an angle ϕ, as shown in Fig. 12 (b), the resolved stress on the crack plane will be given by dividing the resolved load, $P\cos\phi$, by the area of the inclined plane, $A/\cos\phi$ (A is the area of the plane normal to the stress axis), and this yields

$$\sigma_n = \frac{P}{A}\cos^2\phi = \sigma\cos^2\phi$$

Accordingly, the crack tip stress fields for such a crack configuration is expressed as

$$\sigma_{ij} = \frac{K}{\sqrt{2\pi r}} f_{ij}(\theta)\cos^2\phi .$$

APPENDIX B

Assume that the fatigue loading is a triangular wave form (Fig. 16). Over the rising load cycle period, the variation of the stress intensity factor as a function of time is described by:

$$K = K_{\min} + \frac{\Delta K t}{t_R} = \left(\frac{R}{1-R} + \frac{t}{t_R}\right)\Delta K, \qquad 0 < t < t_R\,,$$

where $R = K_{\min}/K_{\max}$, $\Delta K = K_{\max} - K_{\min}$.

Then the integration of the plastic strain rate (equation 4) over the rising load cycle for the forward slip process will lead to:

$$\int_0^{\gamma_f} \exp\left(\frac{V_f H\gamma}{kT}\right) d\gamma = \dot{\gamma}_{of} \exp\left(-\frac{\Delta G_f^* + V_f \tau_{of}}{kT}\right) \int_0^{t_R} \exp\left(\frac{\alpha_f \cos^2\theta\, K}{kT}\right) dt$$
$$= \dot{\gamma}_o \exp\left(-\frac{\Delta G_f^* + V_f \tau_{of}}{kT}\right) \int_0^{t_R} \exp\left[\frac{\alpha_f \cos^2\theta\, \Delta K}{kT}\left(\frac{R}{1-R} + \frac{t}{t_R}\right)\right] dt$$

and the result is

$$\frac{kT}{V_f H}\left[\exp\left(\frac{V_f H\gamma_f}{kT}\right) - 1\right] = \frac{\dot{\gamma}_{of}\, kT}{2 f \alpha_f \Delta K \cos^2\phi} \exp\left(-\frac{\Delta G_f^* + V_f \tau_{of}}{kT}\right)$$
$$\exp\left(\frac{\alpha_f \cos^2\theta\, R\Delta K}{(1-R)\, kT}\right)\left[\exp\left(\frac{\alpha_f \cos^2\theta\, \Delta K}{kT}\right) - 1\right]. \qquad \text{(B1)}$$

where the test frequency $f = 1/2t_R$, as shown in Fig. 16.

Over the decreasing load cycle, the variation of the stress intensity factor as a function of time is described by:

$$K = K_{\max} - \frac{\Delta K}{t_R}(t - t_R) = \left(\frac{2-R}{1-R} - \frac{t}{t_R}\right)\Delta K, \qquad t_R < t < 2t_R\,.$$

Then the integration of the plastic strain rate (equation 4) over the decreasing load cycle for the slip reversal process will lead to:

and the result is

$$\int_0^{\gamma_r} \exp\left(\frac{V_r H\gamma}{kT}\right) d\gamma = \dot{\gamma}_{or} \exp\left(-\frac{\Delta G_r^* + V_r \tau_{or}}{kT}\right) \int_{t_R}^{2t_R} \exp\left(\frac{\alpha_r \cos^2\theta\, K}{kT}\right) dt$$

$$= \dot{\gamma}_{or} \exp\left(-\frac{\Delta G_r^* + V_r \tau_{or}}{kT}\right) \int_{t_R}^{2t_R} \exp\left[\frac{\alpha_r \cos^2\theta\, \Delta K}{kT}\left(\frac{2-R}{1-R} - \frac{t}{t_R}\right)\right] dt$$

$$\frac{kT}{V_r H}\left[\exp\left(\frac{V_r H\gamma_r}{kT}\right) - 1\right] = \frac{\dot{\gamma}_{or}\, kT}{2 f \alpha_r \Delta K \cos^2\phi} \exp\left(-\frac{\Delta G_r^* + V_r \tau_{or}}{kT}\right)$$
$$\exp\left(\frac{\alpha_r \cos^2\theta\, R\Delta K}{(1-R)\, kT}\right)\left[\exp\left(\frac{\alpha_r \cos^2\theta\, \Delta K}{kT}\right) - 1\right]. \qquad \text{(B2)}$$

At low temperatures (T<0.3T_m , T_m is the absolute melting temperature), the condition:

$$\exp\left(\frac{VH\gamma}{kT}\right) > 1, \quad \exp\left(\frac{\alpha\, \Delta K \cos^2\phi}{kT}\right) > 1$$

is often satisfied [1]. Then the forward slip plastic strain in equation (A1) can be approximated by:

$$\gamma_f = \frac{kT}{V_f H} \ln\left[\frac{V_f H \dot{\gamma}_{of}}{2 f \alpha_f \Delta K \cos^2\phi} \exp\left(-\frac{\Delta G_f^* + V_f \tau_{of}}{kT}\right)\right] + \frac{\alpha_f \cos^2\theta\, \Delta K}{(1-R)\, V_f H}. \qquad \text{(B3)}$$

(B4)

and the reverse slip plastic strain can be approximated by

$$\gamma_r = \frac{kT}{V_r H} \ln\left[\frac{V_r H \dot{\gamma}_{or}}{2 f \alpha_r \Delta K \cos^2\phi} \exp\left(-\frac{\Delta G_r^* + V_r \tau_{or}}{kT}\right)\right] + \frac{\alpha_r \cos^2\theta\, \Delta K}{(1-R)\, V_r H}.$$

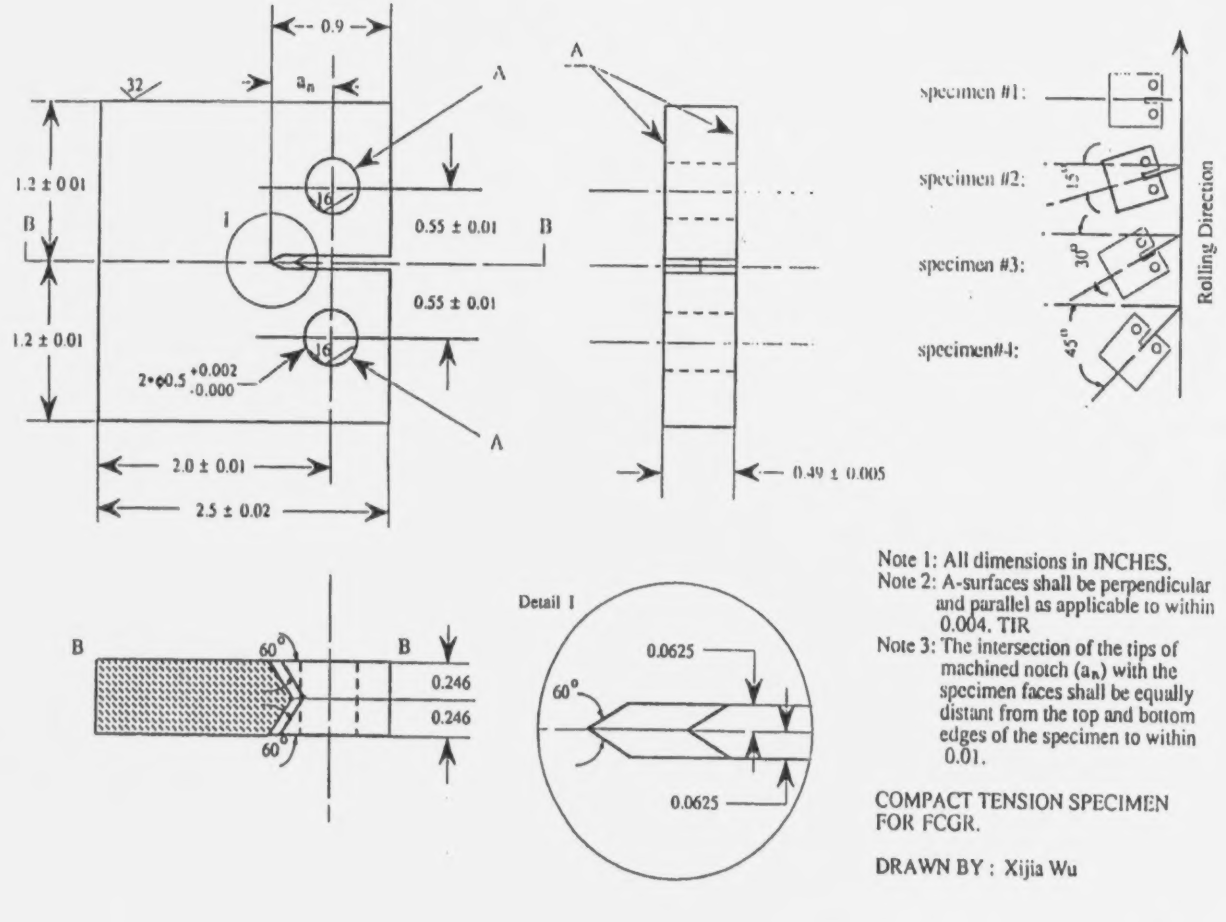
0.9
a_n
32
A
1.2 ± 0.01
B
I
16
0.55 ± 0.01
B
0.55 ± 0.01
1.2 ± 0.01
2•φ0.5 +0.002 -0.000
16
A
2.0 ± 0.01
2.5 ± 0.02
A
0.49 ± 0.005
specimen #1:
specimen #2:
15°
specimen #3:
30°
specimen#4:
45°
Rolling Direction
B
60°
B
0.246
0.246
60°
Detail I
0.0625
60°
0.0625

Note 1: All dimensions in INCHES.
Note 2: A-surfaces shall be perpendicular and parallel as applicable to within 0.004. TIR
Note 3: The intersection of the tips of machined notch (a_n) with the specimen faces shall be equally distant from the top and bottom edges of the specimen to within 0.01.

COMPACT TENSION SPECIMEN
FOR FCGR.

DRAWN BY : Xijia Wu

Fig. 1 Dimensions of the C(T) specimen and their orientation with respect to the rolling direction.

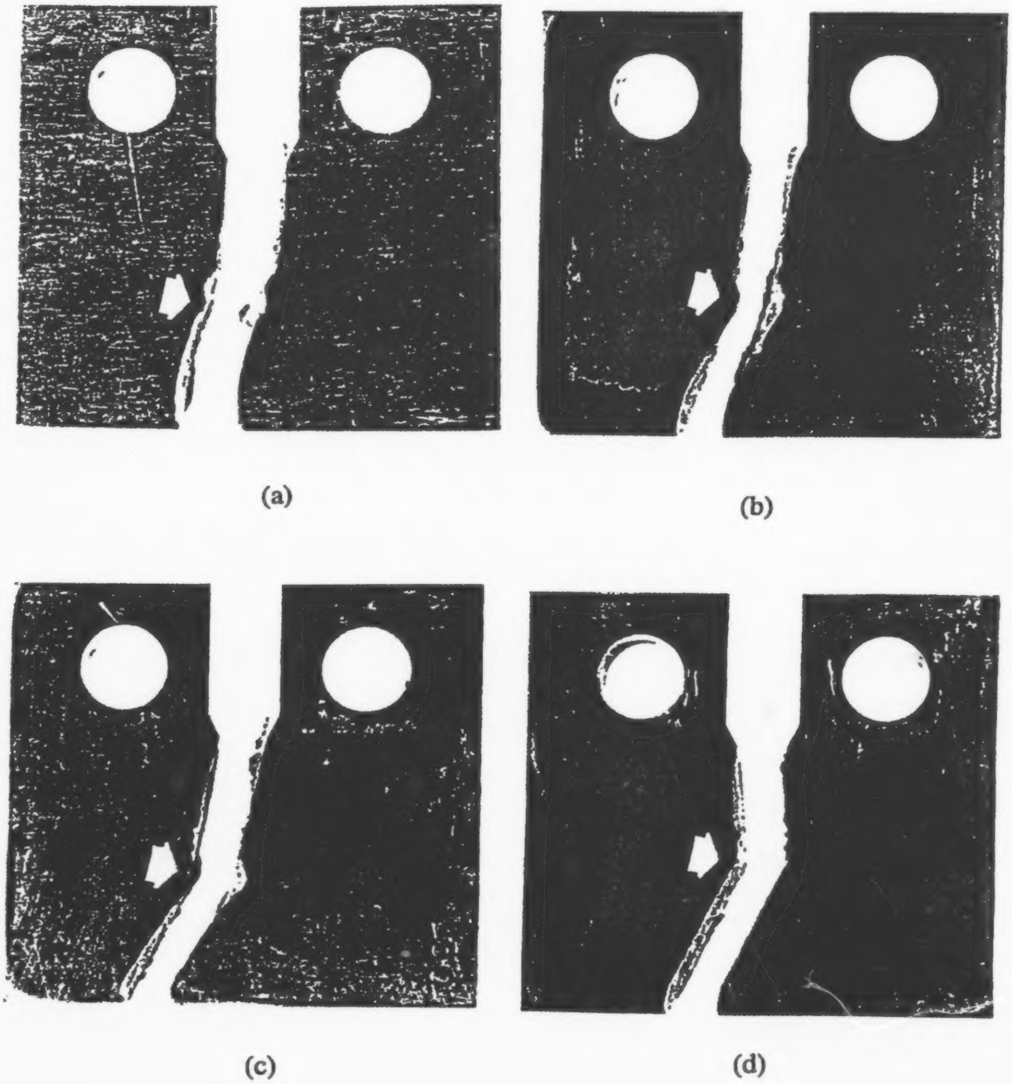

(a)

(b)

(c)

(d)

Fig. 2. Pictures of broken specimens: a) LT; b) L+15°; c) L+30° and d) L+45° specimen. Arrows indicate the onset of abrupt fracture.

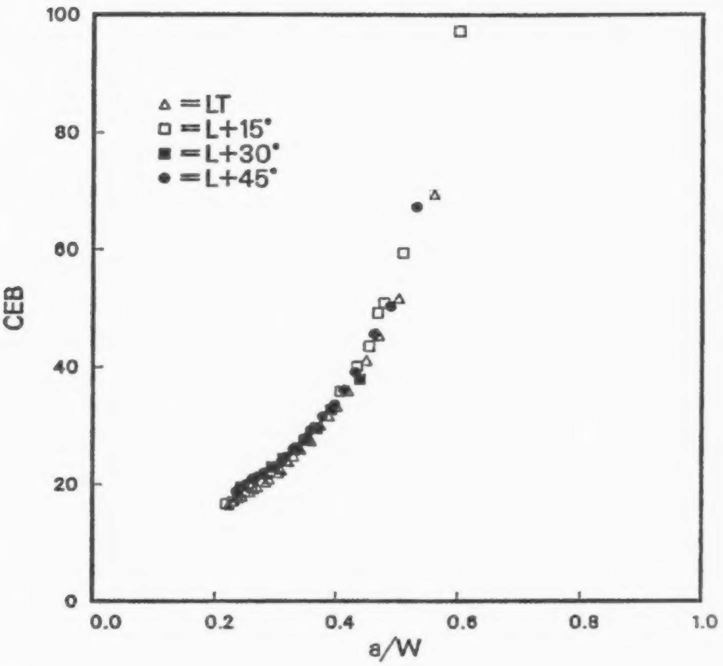

Fig. 3 Compliance vs a/W relations

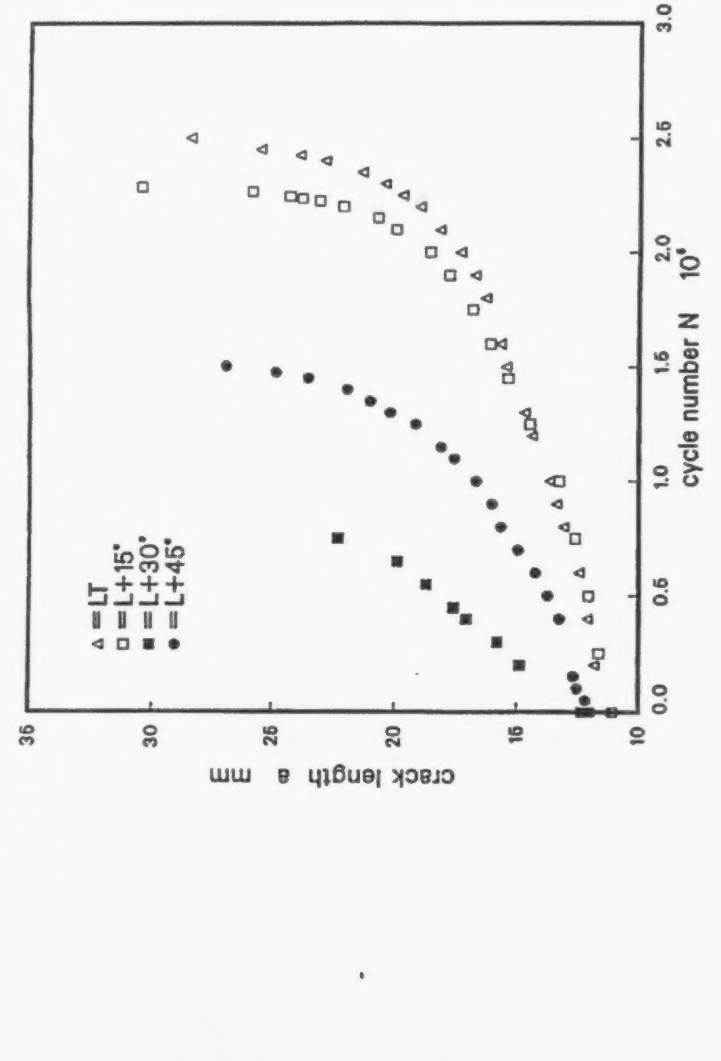

Fig. 4 Crack length vs cycle number relations.

Fig. 5 fatigue crack growth rate in a) LT; b) L+15°; c) L+30°; and d) L+45° specimen.

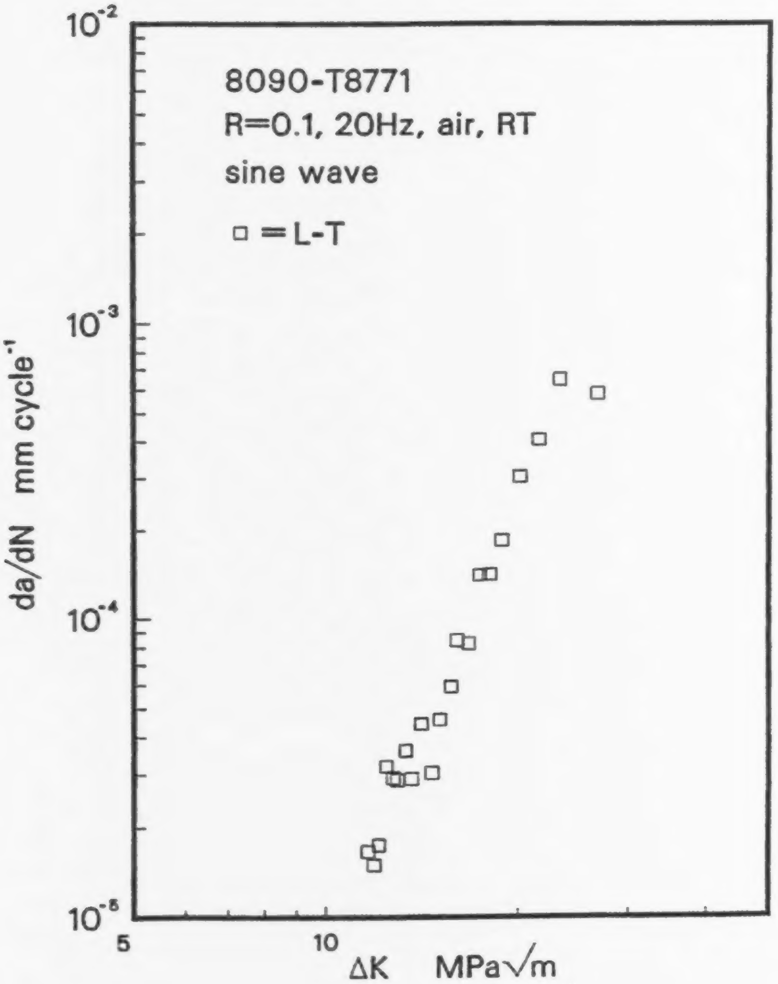

Fig. 5a

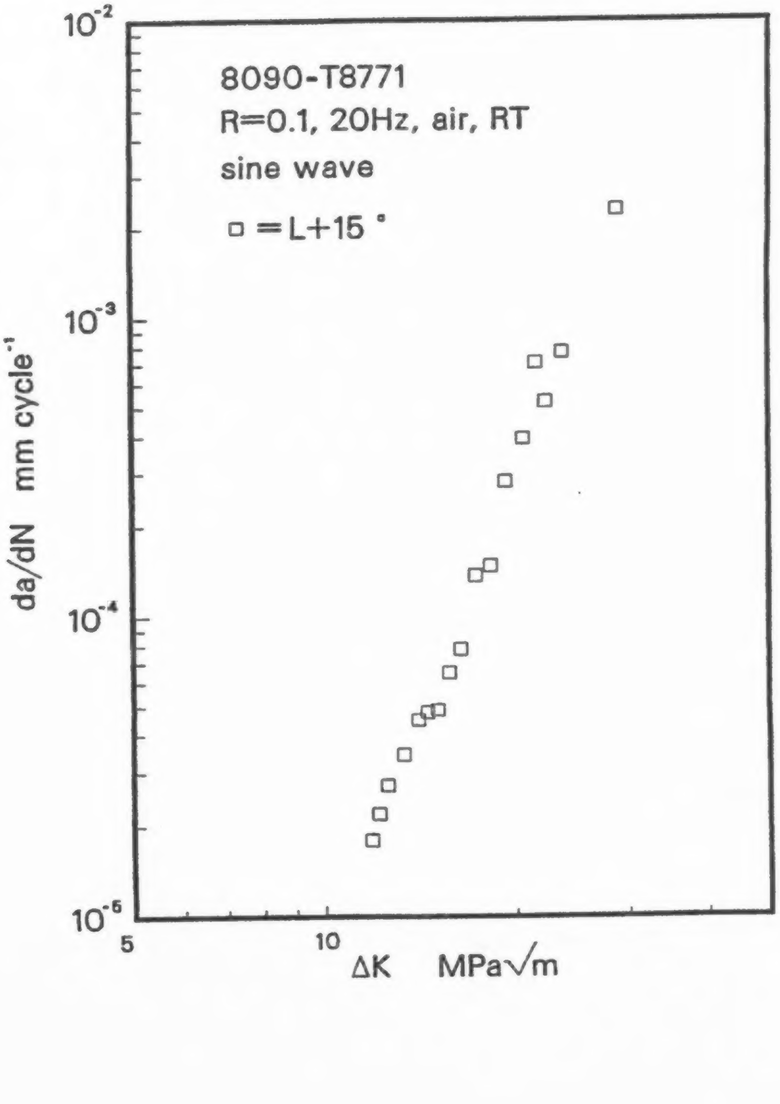
8090-T8771
R=0.1, 20Hz, air, RT
sine wave
□ = L+15 °
da/dN mm cycle^{-1}
10^{-2}
10^{-3}
10^{-4}
10^{-5}
5
10
ΔK MPa√m

Fig. 5b

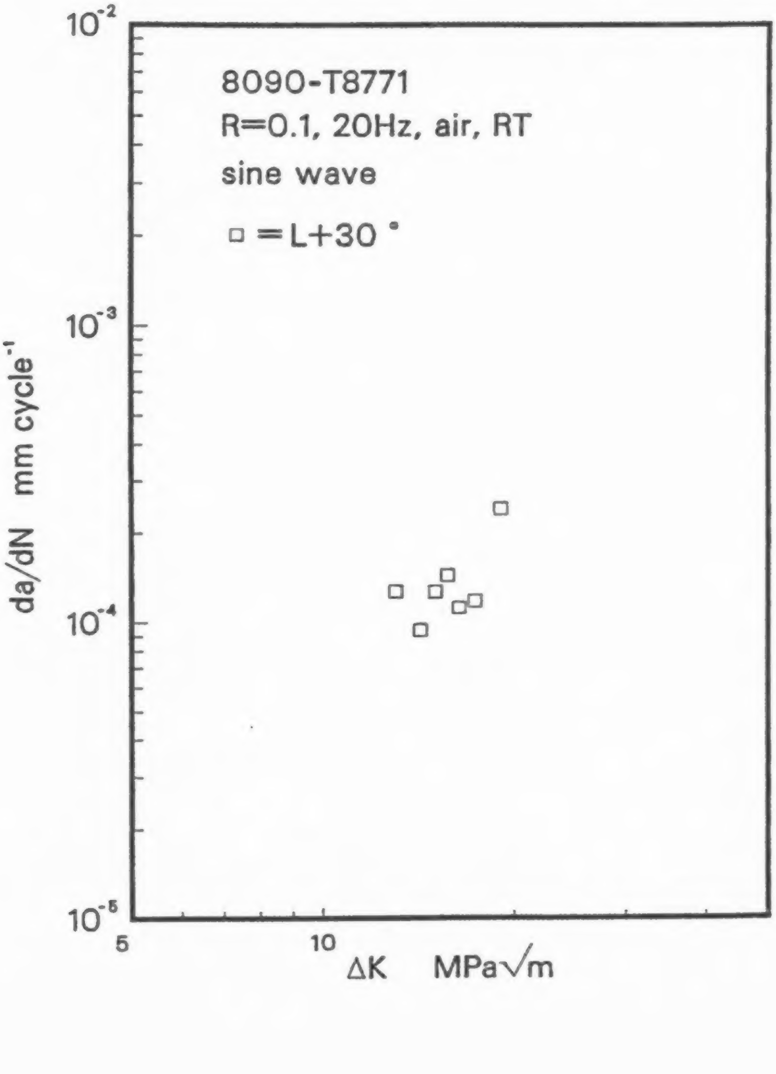
8090-T8771
R=0.1, 20Hz, air, RT
sine wave
□ = L+30 °
10^{-2}
10^{-3}
10^{-4}
10^{-5}
da/dN mm cycle^{-1}
5
10
ΔK MPa√m

Fig. 5c

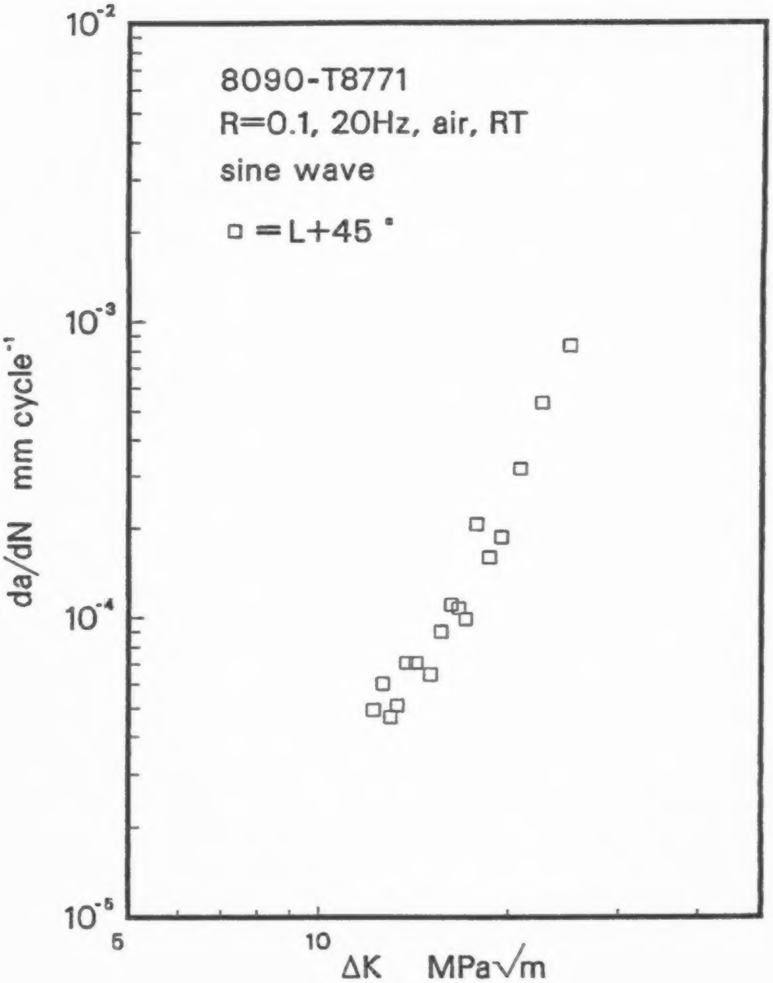
8090-T8771
R=0.1, 20Hz, air, RT
sine wave
□ =L+45 °
10^{-2}
10^{-3}
10^{-4}
10^{-5}
da/dN mm cycle^{-1}
5
10
ΔK MPa√m

Fig.5d

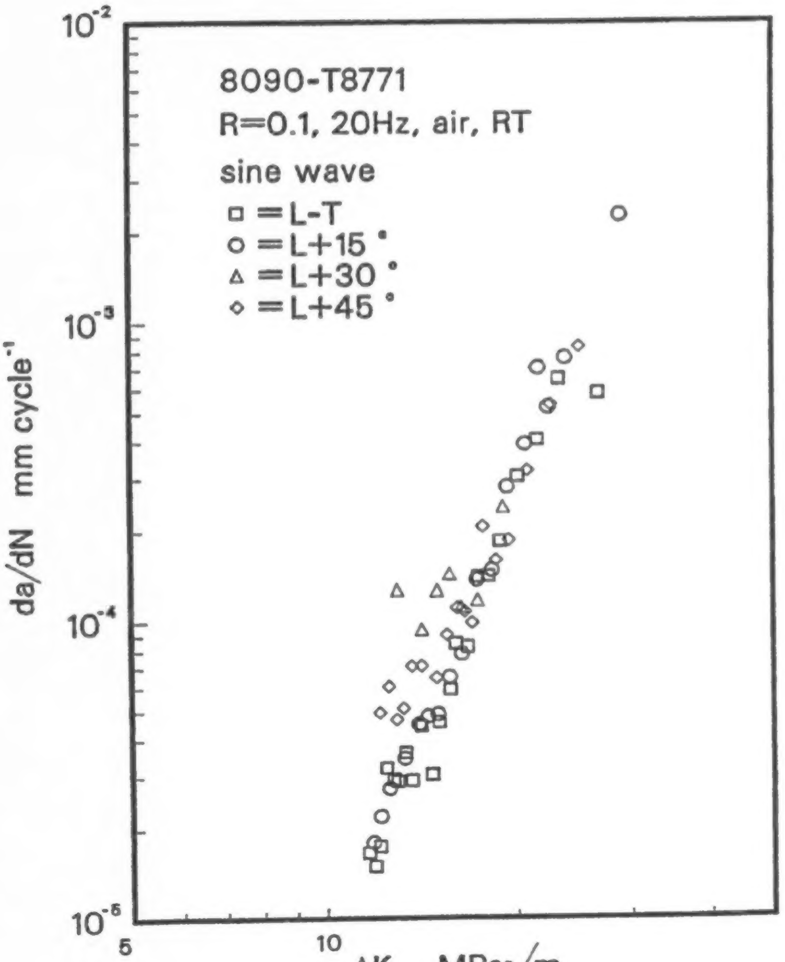

Fig. 6 Comparison of da/dN along different orientations.

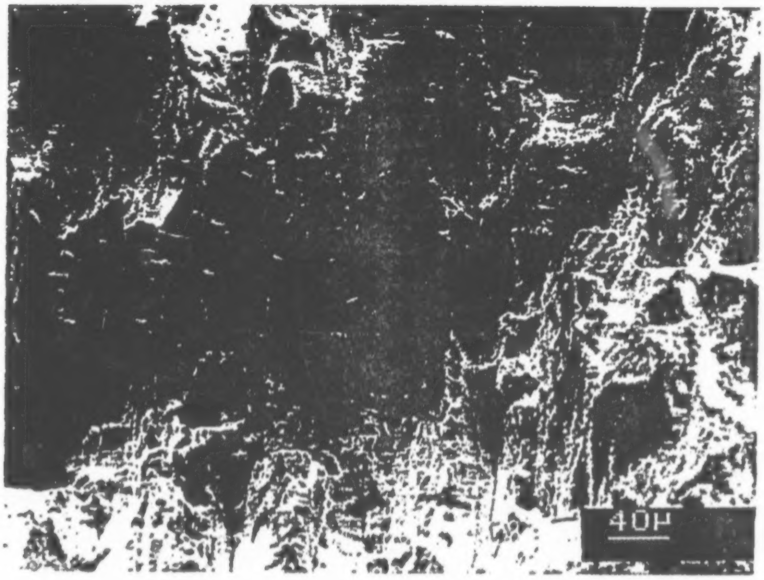

(a)

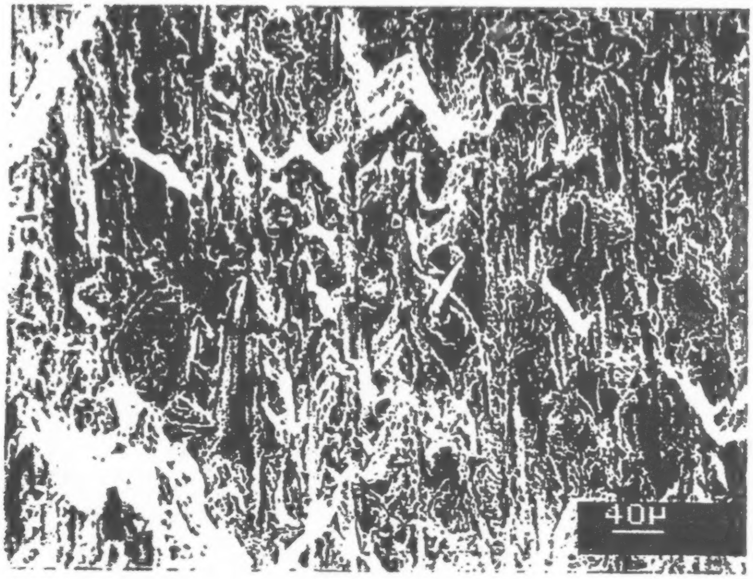

(b)

Fig. 7. Fracture surface morphology for a) LT; b) L+15°;

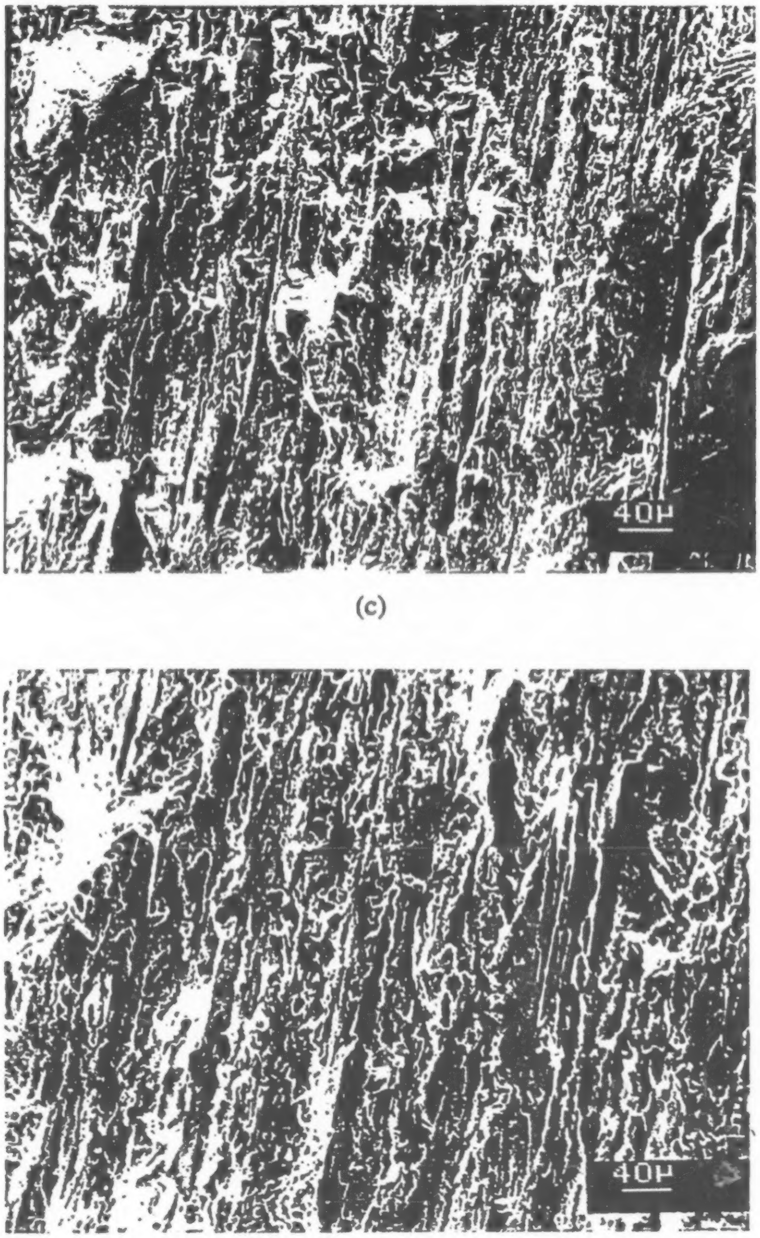

(c)

(d)

Fig. 7. c) L+30°; d) L+45° specimen at crack length a = 17 mm;

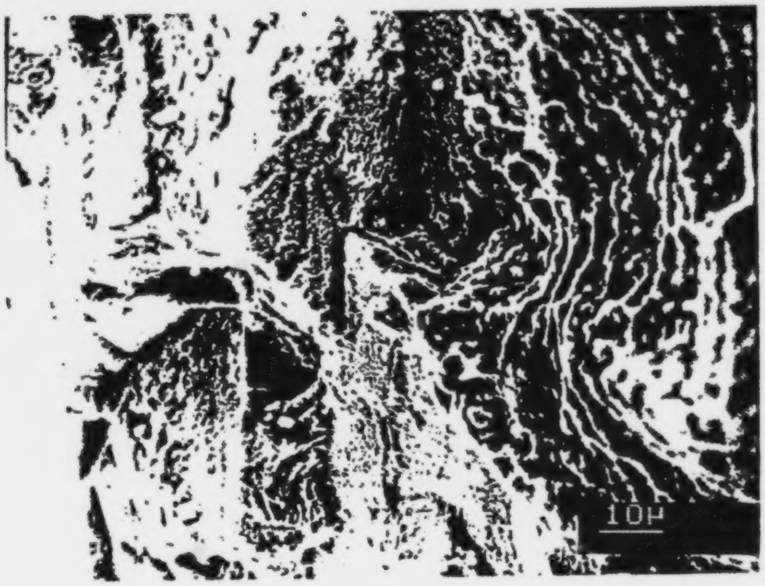

Fig. 7. e) centre of LT specimen at approximately 3 mm from starter notch;

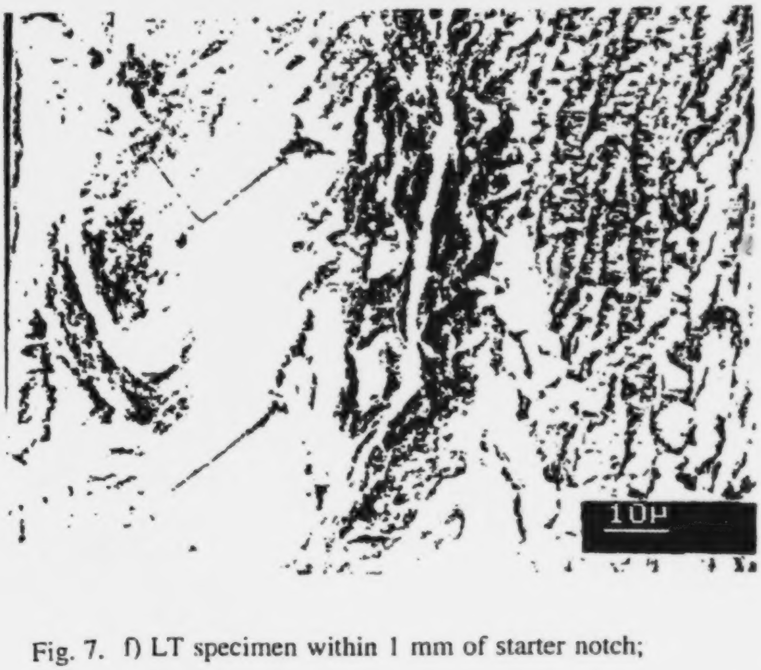

Fig. 7. f) LT specimen within 1 mm of starter notch;

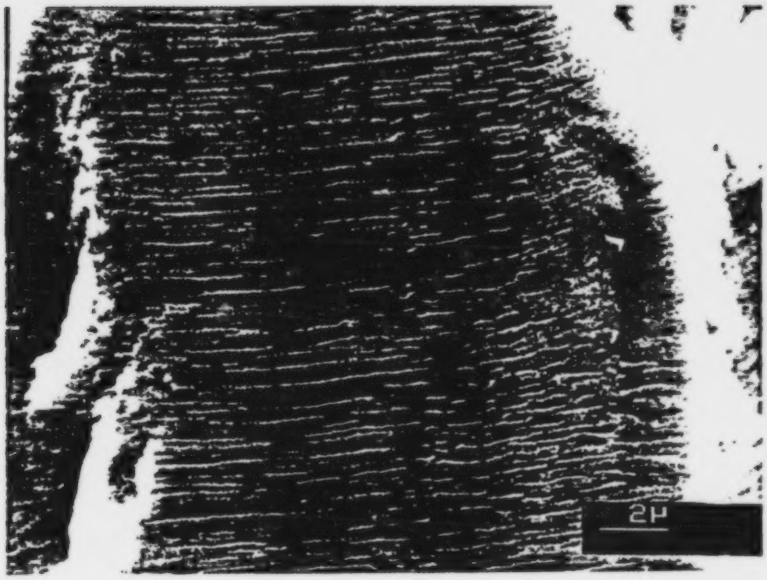

Fig. 7. g) L+45° specimen showing striations in the flat pre-crack region;

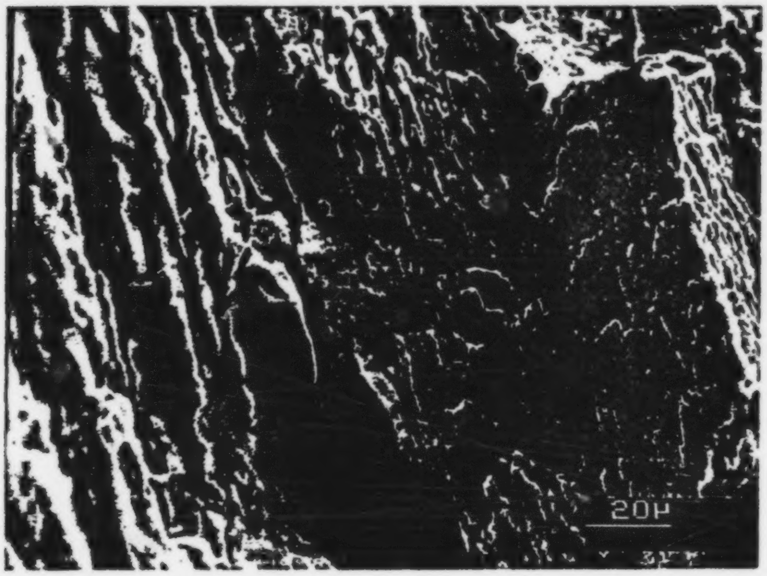

Fig. 7. h) LT specimen, the overload region.

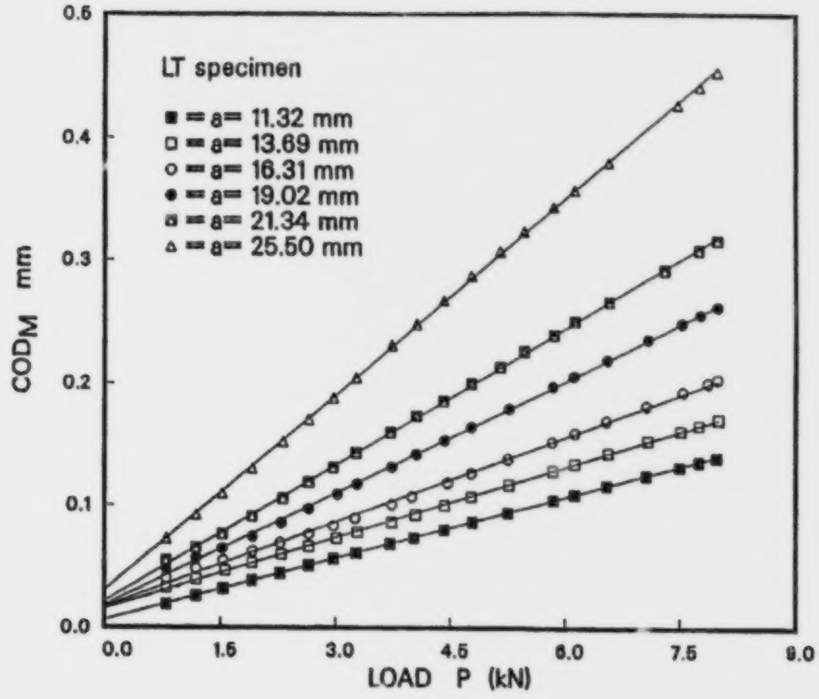

Fig. 8. Crack opening displacement (COD) vs load (P) relations for a) LT,

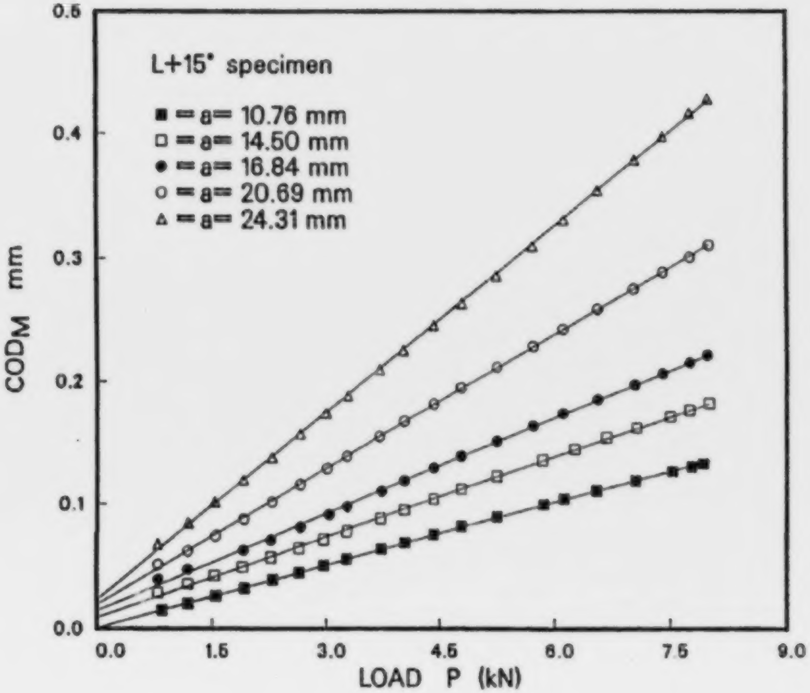
L+15° specimen
■ = a= 10.76 mm
□ = a= 14.50 mm
● = a= 16.84 mm
○ = a= 20.69 mm
△ = a= 24.31 mm
COD$_M$ mm
0.0
0.1
0.2
0.3
0.4
0.5
LOAD P (kN)
0.0
1.5
3.0
4.5
6.0
7.5
9.0

Fig. 8. b) L+15°,

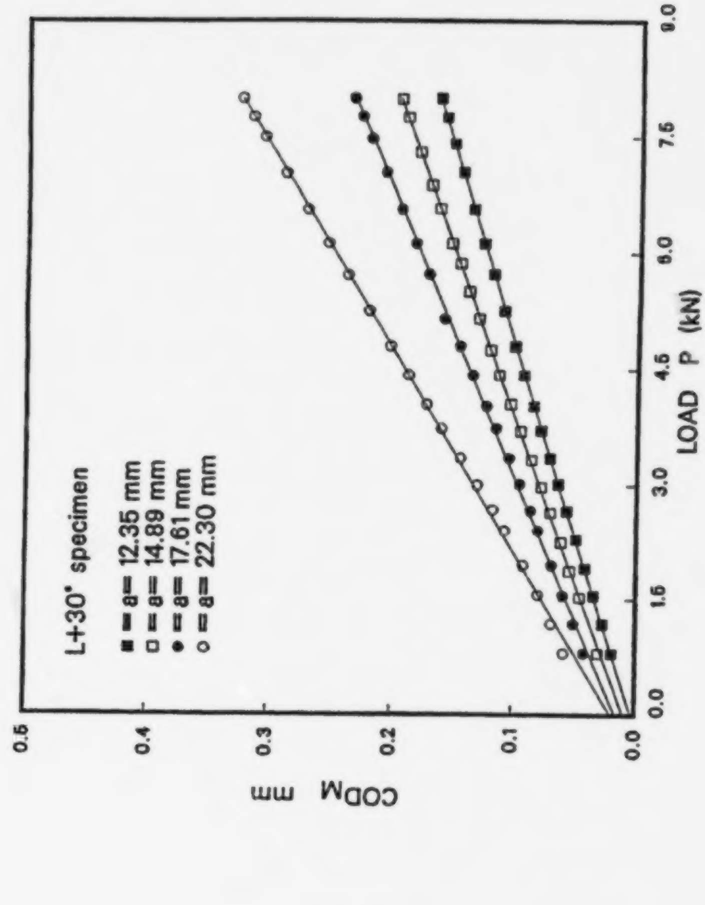
L+30° specimen
■ = a= 12.35 mm
□ = a= 14.89 mm
● = a= 17.61 mm
○ = a= 22.30 mm
CODM mm
0.0
0.1
0.2
0.3
0.4
0.5
LOAD P (kN)
0.0
1.5
3.0
4.5
6.0
7.5
9.0

Fig. 8. c) L+30°,

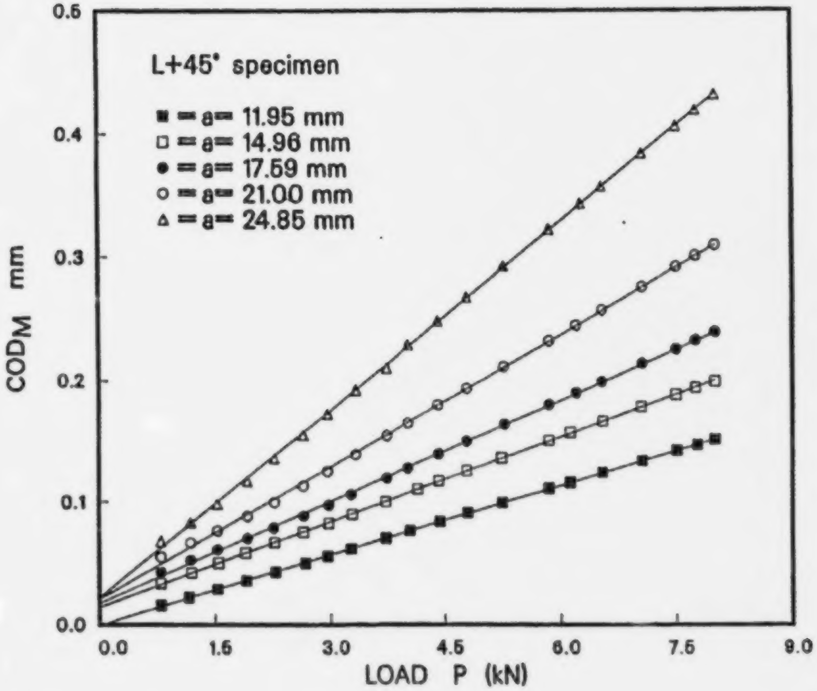

Fig. 8. d) L+45° specimen.

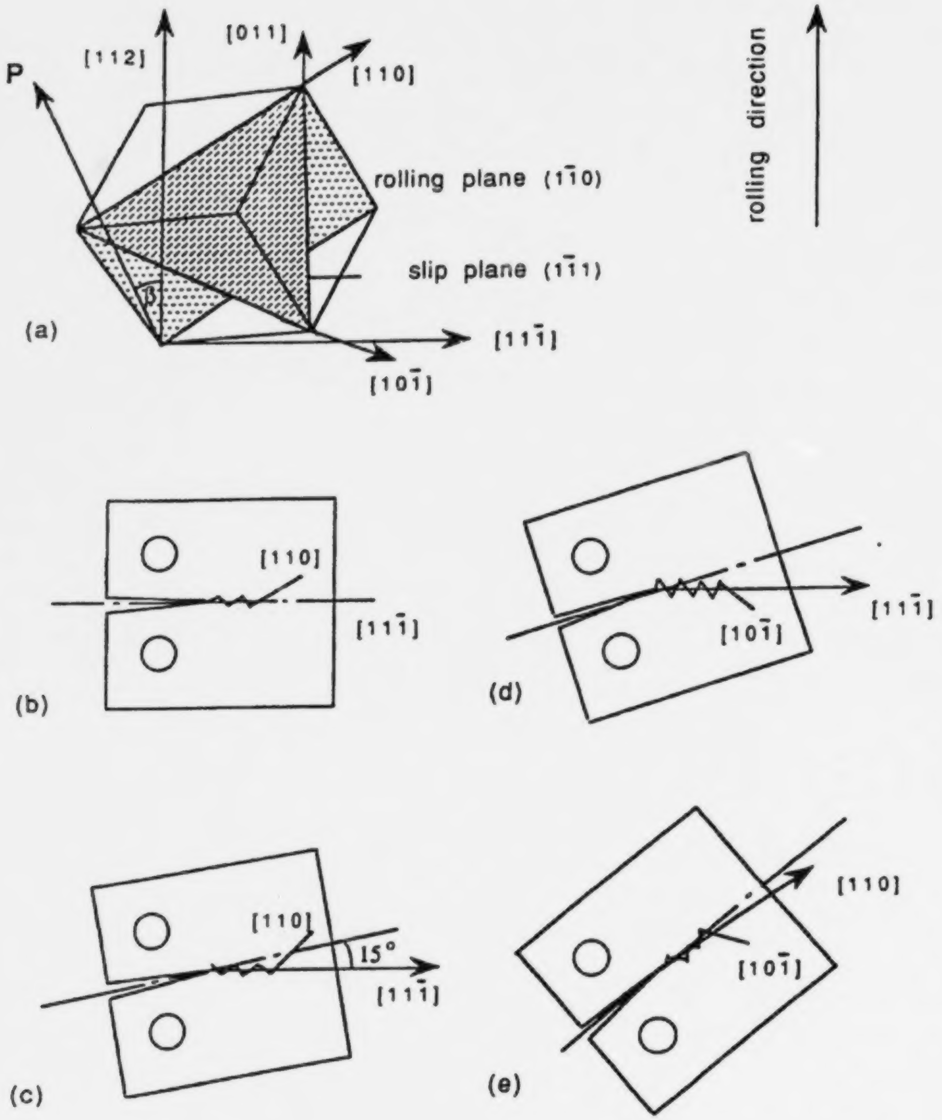
P
[112]
[011]
[110]
rolling plane (1$\bar{1}$0)
slip plane (1$\bar{1}$1)
β
(a)
[11$\bar{1}$]
[10$\bar{1}$]
rolling direction
[110]
[11$\bar{1}$]
(b)
[11$\bar{1}$]
[10$\bar{1}$]
(d)
[110]
15°
[11$\bar{1}$]
(c)
[110]
[10$\bar{1}$]
(e)

Fig. 9. The rolling texture and geometry of fatigue crack growth in 8090 Al-Li plate: a) {110}<112> texture, P indicates the loading direction and β is the angle between the load axis and the rolling direction; schematic of crack growth path in b) LT, c) L+15°, d) L+30°, e) L+45° specimen.

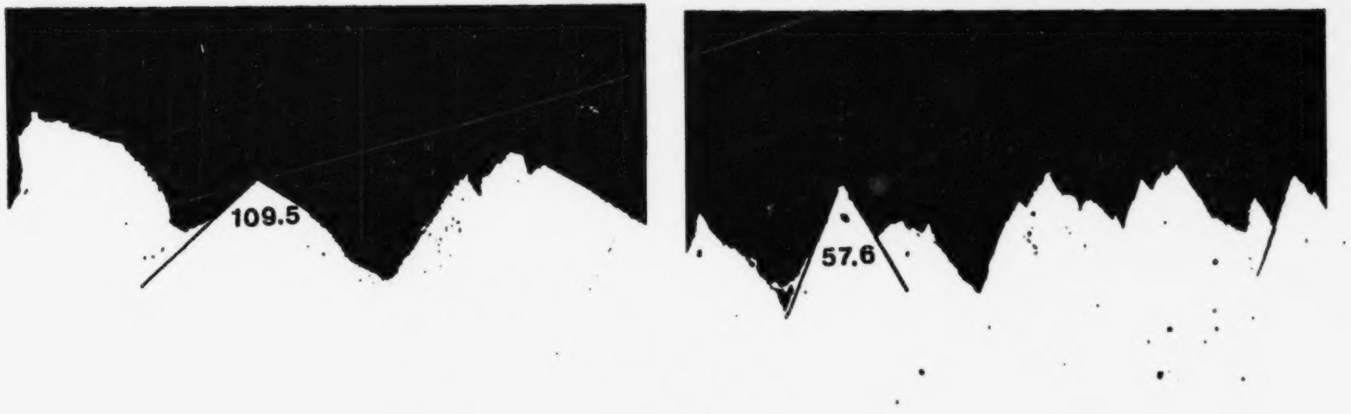

propagating direction (a) thickness direction

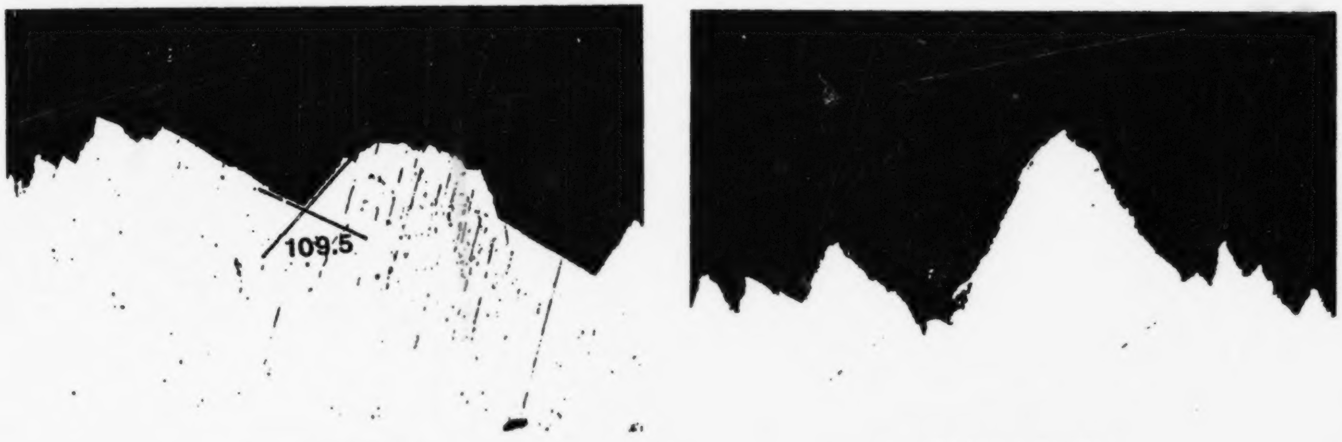

propagating direction (b) thickness direction

Fig. 10. Fatigue crack profiles in a) LT, b) L+15°, c) L+30°, d) L+45° specimen.

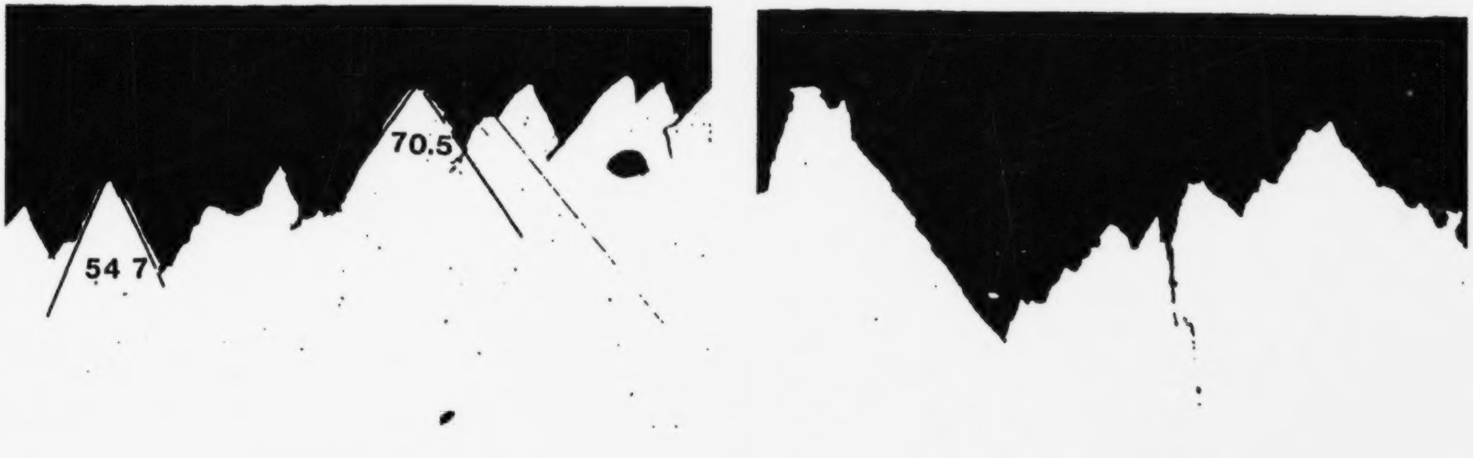

propagating direction

thickness direction

(c)

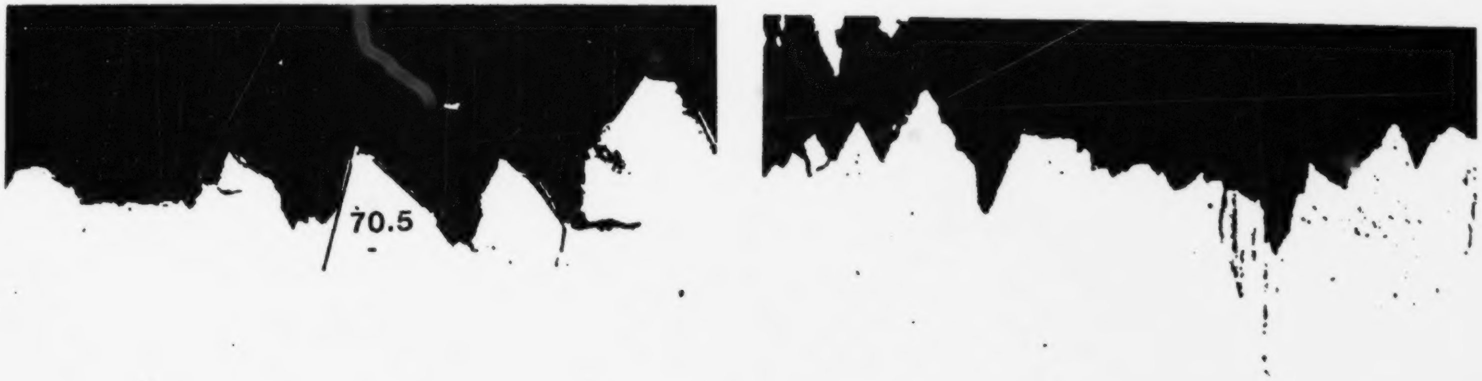

propagating direction

thickness direction

(d)

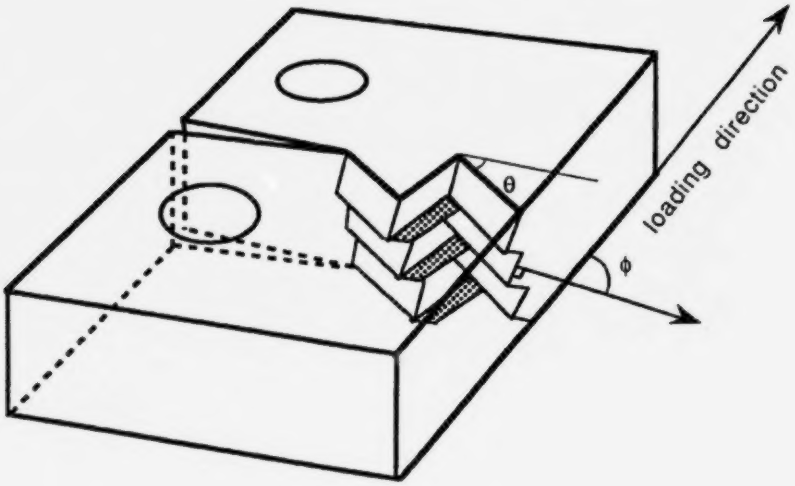
θ
φ
loading direction

Fig. 11. (a) A three dimensional view of fatigue crack growth mode in highly textured materials.

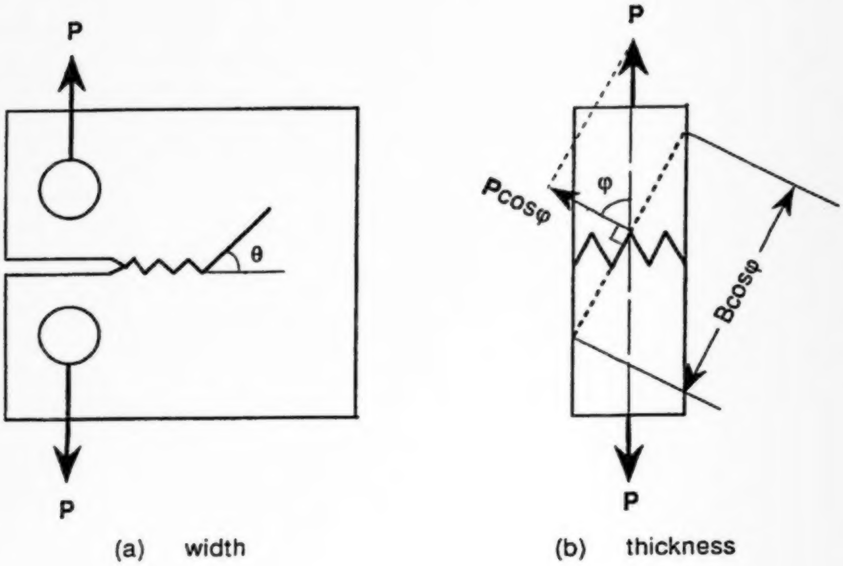
P
θ
P
(a) width
P
φ
Pcosφ
Bcosφ
P
(b) thickness

Fig. 12. Schematic diagram of fatigue crack profile for Al-Li alloys, a) specimen width direction and b) specimen thickness direction.

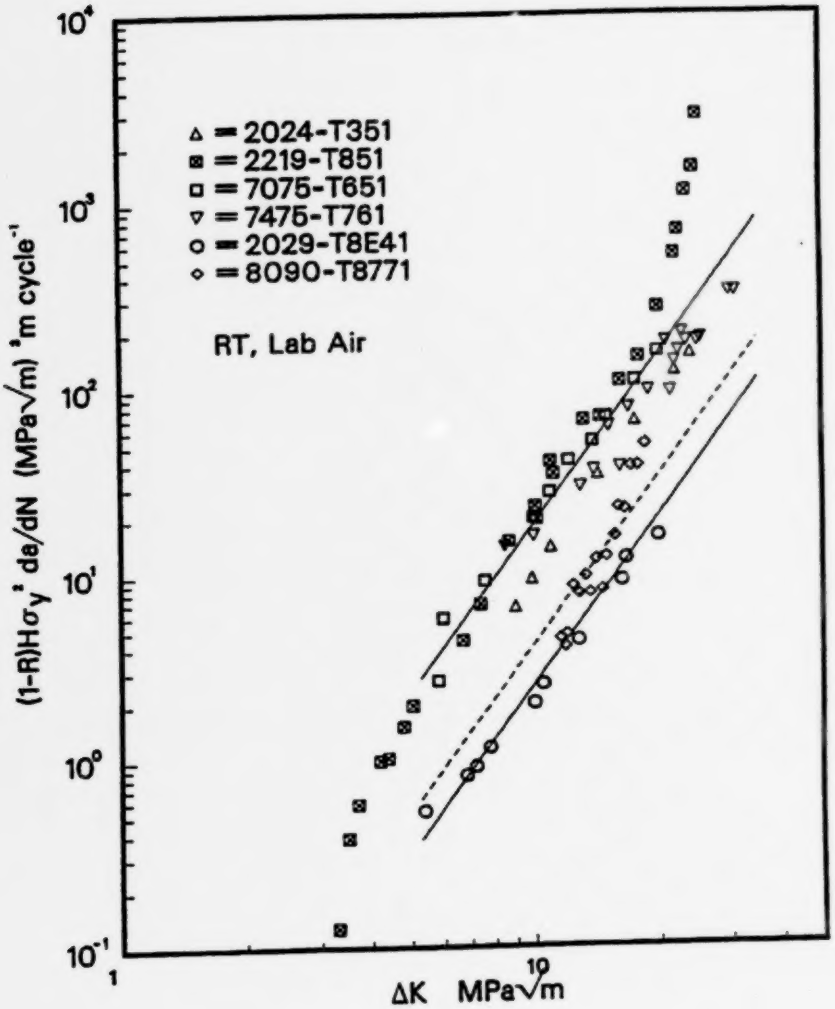

Fig. 13. Comparison of fatigue crack growth rates in conventional aluminum alloys, 2024-T351 [27], 2219-T851 [28], 7075-T651 [9] and 7475-T761 [29], and aluminum-lithium alloys, 2090-T8E41 [9] and 8090-T8771.

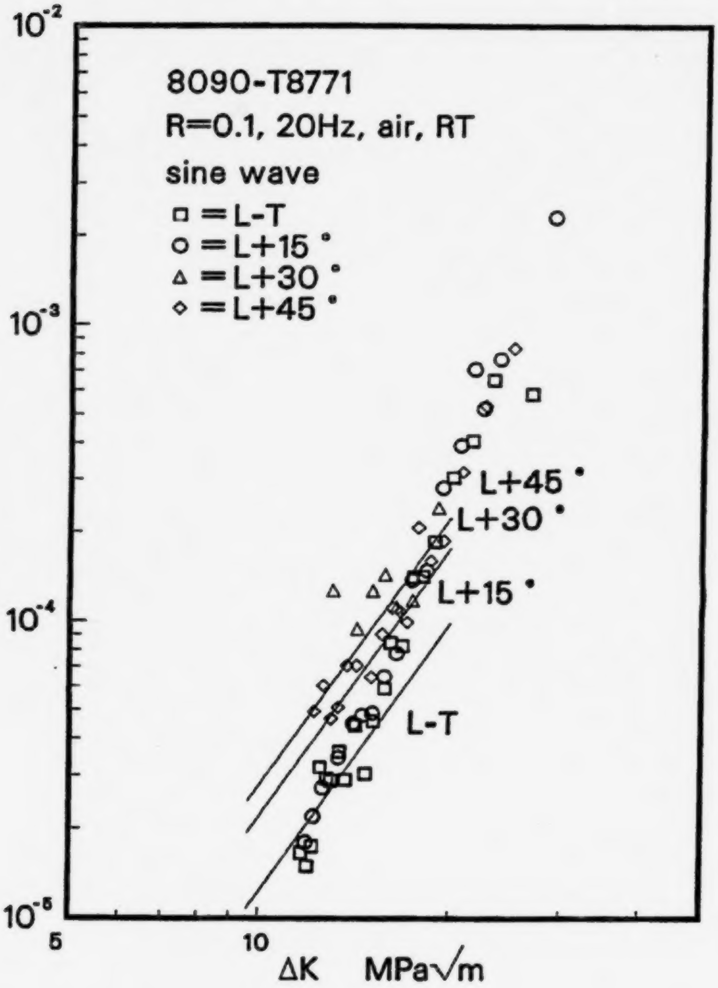

Fig. 14. Orientation dependence of fatigue crack growth rate in 8090 Al-Li alloy. The symbols represent test data. The solid lines are descriptions made from equation (13).

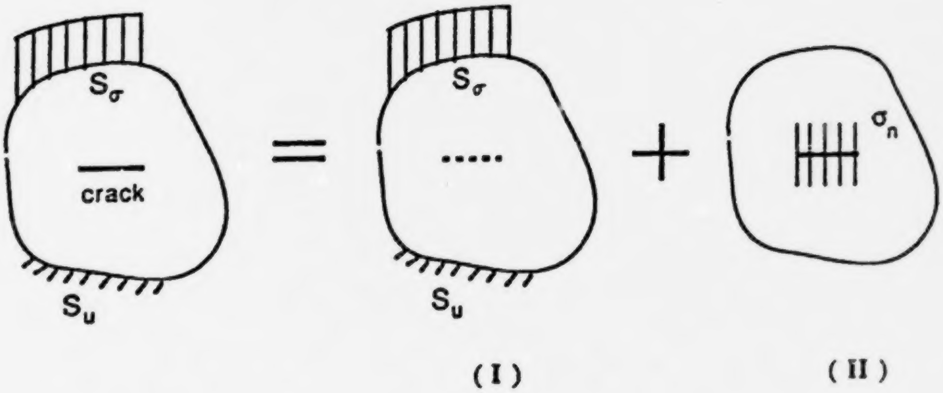
S_σ
crack
S_u
=
S_σ
S_u
+
σ_n
(I)
(II)

Fig. 15. Decomposition of a crack problem into problems I and II.

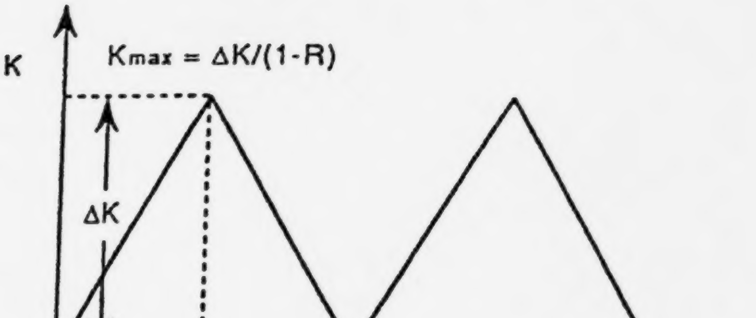

Fig. 16. Schematic of triangular loading profile in fatigue. R is the stress ratio. The frequency $f = 1/2t_R$.

141645

13.

"Directionality of Strength and Toughness in Aluminum-Lithium Plate"

J. Morrison and Z. Zhai

DREP Victoria, B.C.

K.J. KarisAllen

DREA, Halifax, N.S.

DIRECTIONALITY OF STRENGTH AND TOUGHNESS IN ALUMINUM-LITHIUM PLATE

Jack Morrison and Zhen Hua Zhai
Defence Research Establishment Pacific, FMO Victoria, B.C., V0S 1B0

Ken KarisAllen
Defence Research Establishment Atlantic, FMO Halifax, N.S., B3K 2X0

ABSTRACT

The high stiffness and low density of lithium-containing aluminum alloys make them prime candidates for a number of civil and defence aircraft applications, notably in the fuselage of the EH101 helicopter. The Defence Research Establishment Pacific is evaluating various aluminum-lithium alloys in a variety of product forms. This paper describes a study of the variation of strength and toughness with specimen orientation relative to the rolling direction in aluminum-lithium plate. Differences in tensile properties through the plate thickness have also been examined. Fracture toughness has been measured in the short-transverse loading direction as well as in directions within the rolling plane. Comparisons have been made with conventional aerospace aluminum alloys as part of an assessment of the damage tolerance implications of aluminum-lithium exploitation.

INTRODUCTION

Over the past decade a major effort has been made by various aluminum producers to develop and commercialize new lithium-bearing aluminum alloys for weight reduction in aerospace structures (1-3). At a given strength level, alloys containing lithium have lower density and increased stiffness relative to conventional aerospace aluminum. Alloys of interest include 8090 (Al-Li-Cu-Mg) and 2090 (Al-Li-Cu). They have been manufactured in a variety of product forms, and have been shown to be relatively easy to process for aircraft structural applications. It is well recognized, however, that the strong crystallographic texture developed during processing of these alloys and the complex precipitation resulting from their heat treatment yields a material with some unusual properties (4). In particular the aluminum-lithium alloys tend to be more anisotropic than the conventional 2000 and 7000 series alloys (5). For example, their tensile strength is reported to show a distinct minimum at approximately 55° to the rolling direction in aluminum-lithium sheet, and the short-transverse fracture toughness is known to be lower in aluminum-lithium plate than in equivalent strength conventional aerospace alloys (6-8).

During the past few years, the Defence Research Establishment Pacific (DREP) has been investigating commercial aluminum-lithium alloys in a variety of product forms from various sources in anticipation of their future utilization in defence equipment. This paper describes an investigation of the strength and toughness of both 8090 and 2090 nominally 13-15 mm thick plate. Variations in strength were measured with respect to specimen orientation relative to the rolling direction, and also to specimen location through the plate thickness. The orientation dependence of fracture toughness has also been determined. In addition, short-transverse fracture toughness has been measured using chevron-notched short bar specimens, which is the only standardized technique available for this measurement (9). Canadian interest in aluminum-lithium currently centres on its use in the EH101 helicopter, which the Canadian Forces have ordered for both anti-submarine and search-and-rescue roles. Virtually all of the aluminum structure to be used in the fuselage will be fabricated from lithium-containing sheet, forgings, and extrusions (10).

EXPERIMENTAL PROCEDURE

Materials

The aluminum-lithium plates studied in this investigation were purchased in 1989 and are listed in Table I(a) together with the test certificate chemical composition (specified ranges in the case of 2090). In addition, Table 1(b) shows the mechanical property data provided by the manufacturers (Alcan for 8090 and Alcoa for 2090). It should be recognized that, although the data trends generated in this work are expected to be broadly typical of the behaviour of these alloys, given the developmental nature of aluminum - lithium technology, differences can be expected between product of different vintages. It is believed that more recent 8090 product will be somewhat more isotropic than the earlier material because of processing improvements. Likewise for most applications 2090 plate has been superseded by alternative alloys such as 2091. It should also be noted that the two aluminum-lithium plates have significantly different strengths, and would therefore not normally be considered for the same structural component. The comparisons presented in this paper are therefore intended primarily to explore generic similarities in mechanical behaviour. Also included in this study for comparison were 13 mm thick 2024-T351 and 7075-T651 plates, conventional aerospace alloys of roughly equivalent strength levels to the two lithium-containing plates.

The heat treatments for these plates were:

8090-T8771: solution treated at 530°C, 7% stretch, artificially aged 32 hours at 170°C.

2090-T8E41: solution treated at 550°C, water quenched, 6% stretch, artificially aged 24 hours at 165°C (this was an experimental temper since registered as T81).

2024-T351: solution treated, stress relieved by stretching, naturally aged.

7075-T651: solution treated, stress relieved by stretching, artificially aged.

Typical composite microstructures of both the 8090 and 2090 alloys are shown in Figure 1. The plates have the characteristic directionality of aluminum-lithium. The unrecrystallized 8090 microstructure consists of relatively uniform flat elongated grains, whereas the 2090 has bands of coarse unrecrystallized grains, sometimes separating regions of finer grains, particularly towards the plate centre. Both plates have a pronounced (110)<112> texture, which has been reported to be more variable through the plate thickness in the 2090 alloy (11).

Table I(a) - Chemical Composition (wt %).

Material	Li	Cu	Mg	Fe	Si	Zr	Na
8090-T8771 12.5 mm plate	2.35	1.2	0.64	0.05	0.03	0.11	0.0005
2090-T8E41 15 mm plate	1.9 - 2.6	2.4 - 3.0	≤0.25	≤0.12	≤0.10	0.08 - 0.15	-

Table I(b) - Mechanical Properties.

Material		0.2% Proof Stress MPa	UTS MPa	Elongation %	Toughness K_Q MPa$\sqrt{m}$
8090-T8771	Longitudinal	508	555	5	31 (L-T)
12.5 mm plate	Transverse	479	548	8	28 (T-L)
2090-T8E41	Longitudinal	559	595	5	-
15 mm plate	Transverse	586	617	7	-

Tensile Tests

Duplicate rectangular tensile specimens nominally either 6 or 13 mm thick with a 13 mm wide by 25 mm gauge length were cut from the as-received plates with their long axis orientated at 30° intervals clockwise starting at the rolling direction and ending up at the L+150° position. These six orientations were also used as the loading directions in the fracture toughness tests. For each orientation, 6 mm thick tensile specimens were machined from one surface of the plate, and also from the mid-thickness (Figure 2). The 13 mm thick specimens (actually 15 mm for the thicker 2090 plate) were machined from the full plate thickness. Finally, 13 mm by 6 mm 2024 and 7075 specimens taken from the top half of the plates were alsoprepared, but only from the longitudinal and transverse orientations. All of the tensile specimens were tested using standard procedures under ambient conditions.

Fracture Toughness Tests

Duplicate full thickness compact specimens with W = 51 mm were machined from the two aluminum-lithium plates in the same six loading orientations used in the tensile tests. The intended crack plane and crack extension directions were, of course, orthogonal to the loading direction (Figure 3). Compact specimens of the same dimensions were also machined in the L-T and T-L orientations from the 2024 and 7075 alloy plates. Integral knife edges were machined into the specimens to accommodate a clip gauge. These specimens had a through thickness machined notch 23 mm long (nominal a/W = 0.45 before precracking). They were all fatigue precracked to a/W = 0.5 in accordance with ASTM Standard E399 at an R ratio of 0.1 and frequency of 10 Hz, then side grooved 10% of the thickness on each side prior to toughness testing. The side grooving (not currently included in the ASTM Standard) was done to try to ensure that, as far as possible, the crack would remain in its intended fracture plane. It was recognized that the directionality of aluminum-lithium would tend to cause cracks to deviate, and make it difficult to obtain a meaningful toughness estimate. The precracking and final fracture tests were carried out in an automated servo-hydraulic test system. Toughness, K_Q, was estimated either from maximum load or from the load corresponding to a 5% change in compliance as appropriate using the standard K expressions of ASTM Standard E399, with the net thickness modification of ASTM Standard E813. Based on the test certificate data the minimum specimen thickness required for a valid K_{Ic} measurement in the aluminum-lithium was approximately 9 mm, and somewhat less for 7075-T651. It was, however, recognized that plate thickness would be insufficient for a valid measurement in 2024-T351.

Chevron-notched short bar specimens were also employed for toughness determination in the same 6 orientations, using the procedure of ASTM Standard E1304. These specimens had a nominal 13 mm square cross section and W/B = 2. As is shown in Figure 4, it was possible to orient the specimens with the fracture plane running either through the plate thickness (analogous to the compact specimen orientations), or in the plane of the plate at the centreline (short-transverse orientations). In either case it should be borne in mind that the short bar specimen will sample proportionately more of the plate mid-thickness than the compact specimen. The minimum specimen thickness requirement for chevron-notched specimen testing is nominally half that of a compact specimen, so that, in principle, even 2024 can provide valid data. One difficulty encountered was that, because of machining difficulties, the chevron slot maximum width had to be relaxed from the required 0.37 mm to 0.48 mm. This may, on occasion result in spurious load peaks prior to initiation of crack extension because of the reduced constraint at the root of the groove. For this reason at least four specimens of each material and orientation were tested, using the same computer controlled machine employed for the compact specimen tests. A schematic of the testing fixture is shown in Figure 5. Although periodic compliance measurements were made during these tests, the toughness estimates, designated K_{vM} were based on maximum load per Annex A of ASTM E1304. The tests were all performed under ambient conditions.

RESULTS

Tensile Tests

Figure 6(a) and 6(b) show the variation of tensile yield and ultimate strengths with orientation and through- thickness location in the 8090 and 2090 plate respectively. It can be seen that both materials are strongest in the longitudinal and transverse directions, and, as expected, weakest at 60° and 120° to the rolling direction. The two plates are symmetrical in properties, so that the 30°and 150°orientations also give similar results. Overall the yield strength of 8090 is more orientation dependent than 2090, with a variation of up to 25%. Tensile strengths are more uniform in both alloys. Except in the softest orientations, the plates are significantly stronger in the centre than the outside. This is in contrast to conventional heat-treatable aluminum alloy plate, which usually has lower strength in the centre (12). The equivalence of full thickness data to that from the half section indicates, not surprisingly, that through thickness properties are symmetrical about the plate centre.

Table 2 summarizes the longitudinal and transverse results in comparison with the 2024 and 7075 alloys. It is noteworthy that there is not much difference in strength variability at these two orientations for the four materials. The high strength 2090 is equivalent to 7075, while the medium strength 8090 is intermediate between 2024 and 7075. The aluminum - lithium alloys have lower work hardening capacities (low yield/ultimate ratios at a given strength). Tensile elongation follows roughly inversely the strength variations (Figure 7).

Tensile specimen fracture appearance follows a characteristic pattern in both alloys. Figure 8 shows the broken full thickness specimens. In the stronger longitudinal and transverse directions, specimens tend to fail either in a simple 45° shear (longitudinal), or by extensive splintering along the specimen gauge length (transverse). In both cases, the deformation is highly localized, with little apparent plasticity. Moving from the longitudinal orientation towards the transverse there is a trend to a more uniform distribution of deformation, accompanied by rumpling of the surface, and a reduction of cross sectional area. Not surprisingly, the most plasticity is apparent in the softest 60° and 120° specimen orientations. The softer orientations also frequently have fracture surfaces containing relatively short delaminations. The smaller fractured specimens taken from the surface and centre of the plates show similar trends, but without the delaminations or splitting, presumably because of the reduced constraint. As a result of these irregular fractures, tensile elongations tend to be more variable than usual and more difficult to measure.

Table 2 - Summary of Tensile Properties.

Alloy	orientation	yield strength (MPa)	UTS (MPa)	Elongation (%)
2024-T351	Long.	395	490	18
	Trans.	355	490	15
7075- T651	Long.	535	575	12
	Trans.	510	580	12
8090-T8771	Long.	480	540	9
	Trans.	450	525	12
2090-T8E41	Long.	521	539	8
	Trans.	544	574	6

Fracture Toughness

Typical compact specimen load-displacement curves for aluminum-lithium plate are shown in Figure 9. The 2024 alloy showed slow stable tearing through a load maximum in both T-L and L-T orientations. The other three materials behaved similarly in the L-T orientations, but the T-L specimens fractured in a relatively unstable manner with much less deformation, particularly in 7075 and 8090. The remaining orientations generally showed stable crack extension during fracture.

The fractured aluminum-lithium specimens showed a number of unusual features (Figure 10). The appearance of the precrack varied dramatically with orientation, particularly in 8090 alloy. T-L and L-T oriented specimens had a very rough surface which was assumed to be blackened by fretting debris resulting from the extensive closure stress observed during fatigue cracking. In the L+30° L+150° loading directions the fatigue cracks were smooth and thumbnail shaped except at the surface, but tended to grow at an angle to the intended fracture plane. At the surface, presumably because of the reduced constraint, there was further evidence of fretting. The L+60° and L+120° specimens were also smooth, but in addition contained delaminations parallel to the plate surface where there were further indications of local fretting, again because of the local relaxation of constraint, resulting in mismatched fracture surfaces. Fractured 2090 specimens had generally smooth fatigue cracks, with some surface roughness in T-L and L-T orientations. Notwithstanding the 20% total sidegrooving introduced after precracking, most of the aluminum-lithium specimens showed some tendency for cracks to deviate from the intended fracture plane, most notable in the L-T orientation. The K_Q values obtained from the compact specimens in general did not meet the requirement of ASTM Standard E399 that $P_{max}/P_Q \leq 1.1$.

Although specimen fracture behaviour was quite reproducible, the through-thickness - notched short bar specimens did not, in general, produce reliable fracture toughness estimates. The cracks tended to break out of the fracture plane, leaving either a conical fracture surface or fracture of one of the specimen loading arms. For reasons that are not very clear, 8090 short bar specimens gave mostly lower toughness estimates than the corresponding compact specimens, while in the other alloys they tended to yield high toughness values. Only in the T-L orientation did compact and short bar specimens agree, this, of course being the direction in which cracks showed the least tendency to diverge.

The load-displacement curves from the short-transverse specimens were of the crack jump type, but highly reproducible except for the occasional spurious load peak prior to the onset of crack extension (Figure 11). These specimens all fractured cleanly in the desired plane, producing very flat fractures with clear indications of the rolling direction (Figure 12). Figure 13 shows the fracture toughness of both 8090 and 2090 as a function of orientation for both compact specimens and short-transverse short bar specimens. The trends are similar for both in-plane and short-transverse loading, but 8090 is more anisotropic than 2090. Figure 14 shows that the ratio $K_{vM}(ST)/K_Q$ for each alloy is between 0.5 and 0.6 and is insensitive to orientation.

Figure 15 shows the toughness/strength ratio for 8090-T8771 and 2090-T8E41 expressed as $(K/\sigma_y)^2$ which has dimensions of length, and is related to the plastic zone size at the tip of a crack, and is also the parameter which scales the size requirements of specimens for toughness tests. The 8090 alloy is again noticeably more anisotropic than 2090, but also more inherently plastic. Aluminum-lithium is roughly comparable to the equivalent strength conventional alloy.

Finally, Table 4 summarizes the fracture toughness data for the T-L and L-T orientations for all four alloys tested. The designation K_{QvM} for the short-transverse tests refers to a chevron-notched short bar test using maximum load for toughness calculation. The compact specimen K_Q results indicate that the two lithium containing alloys have comparable through-thickness toughness to equivalent strength conventional alloys, and the 8090 results agree reasonably well with the manufacturer's data (Table 1). On the other hand, the aluminum-lithium alloys have only 50-60% of the short transverse toughness of the comparable strength conventional material.

Table 4 - Fracture Toughness Summary.

alloy	K_Q MPa$\sqrt{m}$ L-T	T-L	K_{QvM} MPa$\sqrt{m}$ S-T	S-L
2024-T351	35	30	33	30
7075-T651	28	23	26	22
8090-T8771	36	28	19	14
2090-T8E41	23	21	13	12

CONCLUSIONS

a). Although the differences between longitudinal and transverse yield strengths and fracture toughnesses in aluminum-lithium are, if anything, less than in the 2024 and 7075 alloys, both 2090 and 8090 alloys are distinctly weaker in orientations close to 60° from the rolling direction. The 8090-T8771 alloy showed the greatest anisotropy of both strength and toughness.

b). As expected, mechanical properties were symmetrical with respect to orientation, but, in contrast to observations made elsewhere on conventional alloys, the aluminum-lithium is stronger at the plate centre than close to the surface.

c). The aluminum-lithium alloys had similar fracture toughness to conventional aerospace aluminum alloys of the same strength level in notch orientations normal to the plate surface.
d) The ASTM E1304 chevron-notched short bar fracture toughness procedure provided consistent and reproducible short-transverse toughness values for all of the alloys studied, even in this relatively thin plate. 2024 and 7075 were found to have the same short-transverse toughness as for in-plane loaded specimens. The relatively low short-transverse toughness of the aluminum-lithium alloys was confirmed, being of the order of 50% to 60% of that from through-thickness notches.

e). Although the orientation dependence of elongation to fracture shows a roughly inverse relationship to yield strength, fracture toughness does not. Generally speaking orientations close to T-L show lower toughness than elsewhere. In this orientation the pronounced grain directionality is presumably exerting a greater influence on the fracture behaviour than are the crystallographic and slip related processes which would normally control the deformation.

REFERENCES

1. R.J.H. Wanhill, "Status and Prospects for Aluminium-Lithium Alloys in Aircraft Structures", Fatigue of Metallic Materials, Mirko Klesnil and Petr Lukas, Eds., Elsevier, 1992, 43-82.

2. E.A. Starke, and W.E. Quist, "The Microstructure and Properties of Aluminum-Lithium Alloys", New Light Alloys, AGARD Conference Proceedings No. 444, Advisory Group for Aerospace Research and Development, Neuilly-sur-Seine, 1989, 4-1 - 4-23.

3. R. Grimes, "Current Status of Aluminium-Lithium Based Alloys, Metals and Materials, August 1992, 436-437.

4. W.G.J. 't Hart, L. Schra, D.S. McDarmaid, and M. Peters, "Mechanical Properties and Fracture Toughness of 8090-T651 Plate and 2091 and 8090 Sheet", New Light Alloys, AGARD Conference Proceedings No. 444, Advisory Group for Aerospace Research and Development, Neuilly-sur-Seine, 1989, 5-1 - 5-17.

5. O. Engler and K. Lücke, "Influence of the Precipitation State on the Cold Rolling Texture in 8090 Al-Li Material", Materials Science and Engineering, Vol. A148, 1991, 15-23.

6. N. Eswara Prasad and G. Malakondaiah, "Anisotropy of Mechanical Properties in Quaternary Al-Li-Cu–Mg Alloys", Bull. Mater. Sci., Vol. 15, No. 4, August 1992, 297-310.

7. S.P Lynch, "Fracture of 8090 Al-Li Plate, I. Short Transverse Fracture Toughness", Materials Science and Engineering, Vol. A136, 1991, 25-43.

8. S.P. Lynch, R. Byrnes, and R.B. Nethercott, A. Bragianos, and A. Crosky, "Effects of Double Ageing Treatments on Fracture Toughness of an 8090 Al-Li Alloy Plate", Sixth International Conference on Aluminium-Lithium, Garmisch-Partenkirchen, October 1991.

9. J. Morrison, and K.J. KarisAllen, "Specimens Size and Orientation Effects in Chevron-Notch Fracture Testing of Aluminum Alloy Plate", Chevron-Notch Fracture Test Experience: Metals and Non-Metals", ASTM STP 1172, K.R. Brown and F.I. Baratta, Eds., American Society for Testing and Materials, Philadelphia, 1992, 43-53.

10. A.F.Smith, "Uses and Properties of Al-Li on the new EH101 Helicopter", New Light Alloys, AGARD Conference Proceedings No. 444, Advisory Group for Aerospace Research and Development, Neuilly-sur-Seine, 1989, 19-1 - 19-19.

11. M.W. Squibb, Defence Research Agency, Farnborough, UK, Private Communication, April 1993.

12. Brown, K.R., "The Use of the Chevron-Notched Short Bar Specimen for Plain - Strain Toughness Determination in Aluminum Alloys", Chevron-Notched Specimen Testing and Stress Analysis, ASTM STP 855, American Society for Testing and Materials, Philadelphia, 1984, 237-254.

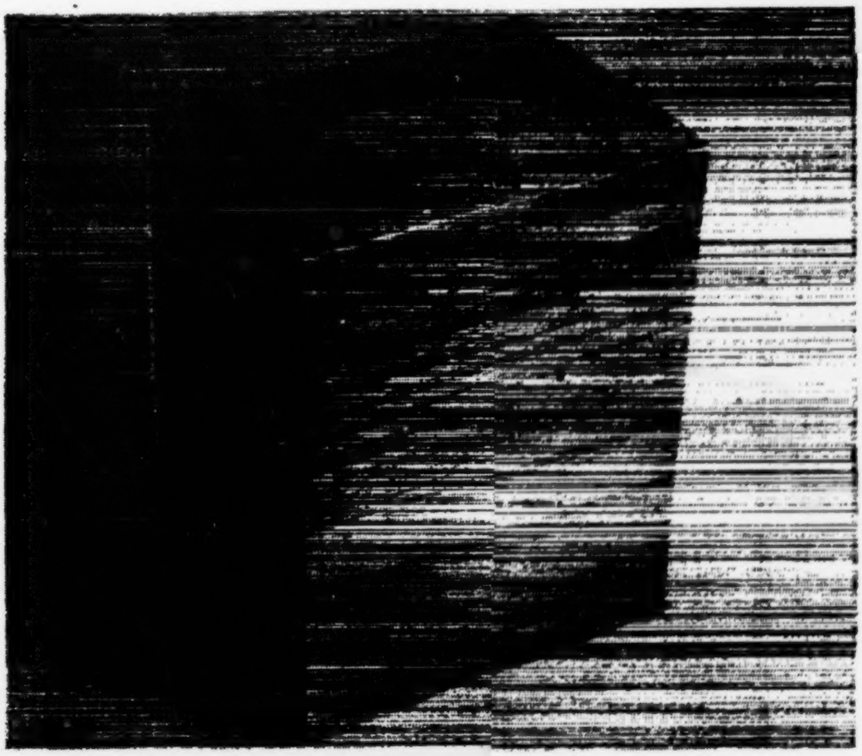

2090-T8E41

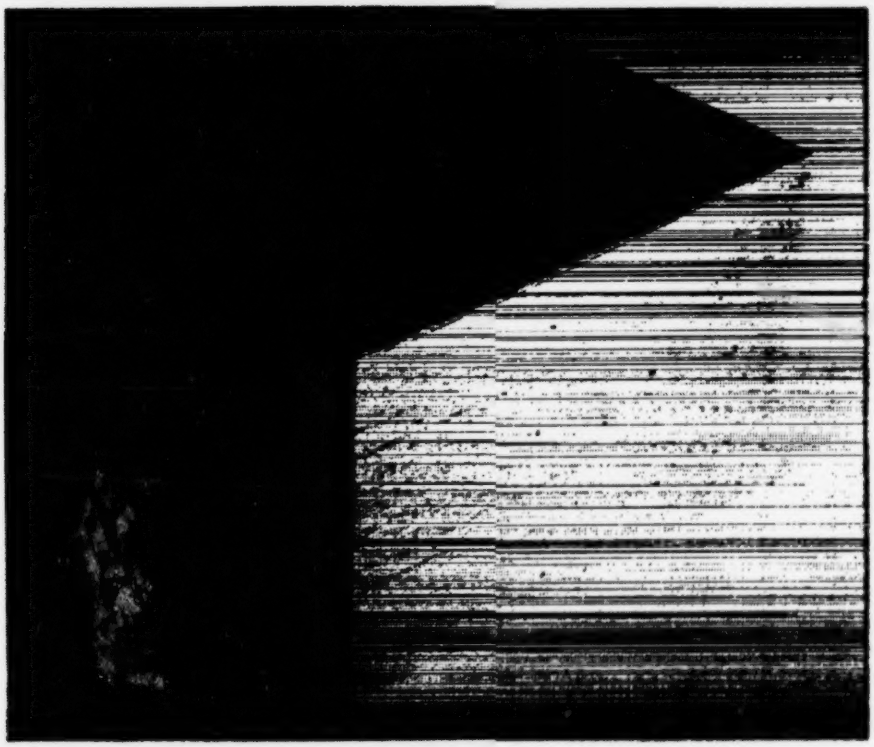

8090-T8771

Figure 1. Typical microstructures of the [illegible]

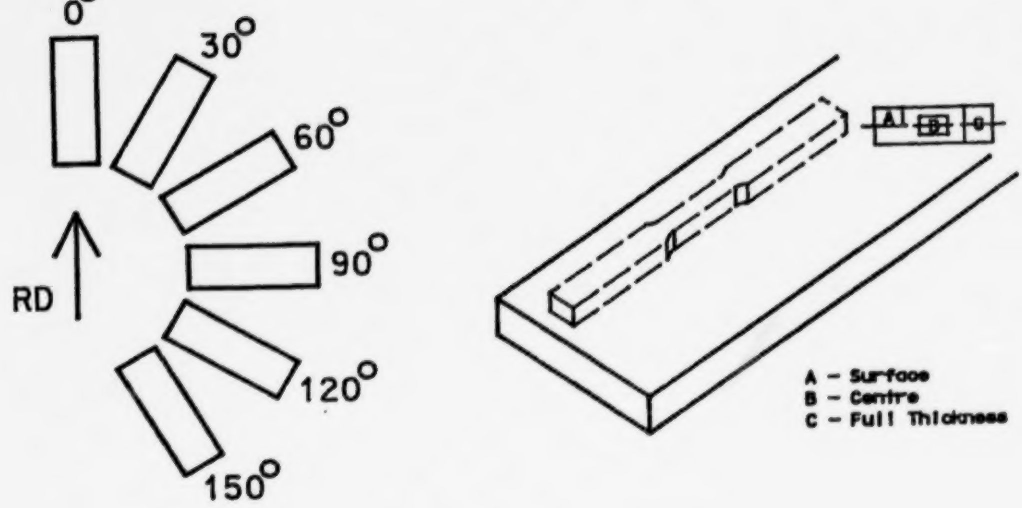
0°
30°
60°
90°
120°
150°
RD
A
B
C
A - Surface
B - Centre
C - Full Thickness

Figure 2 - Orientations and plate positions for tensile test specimens.

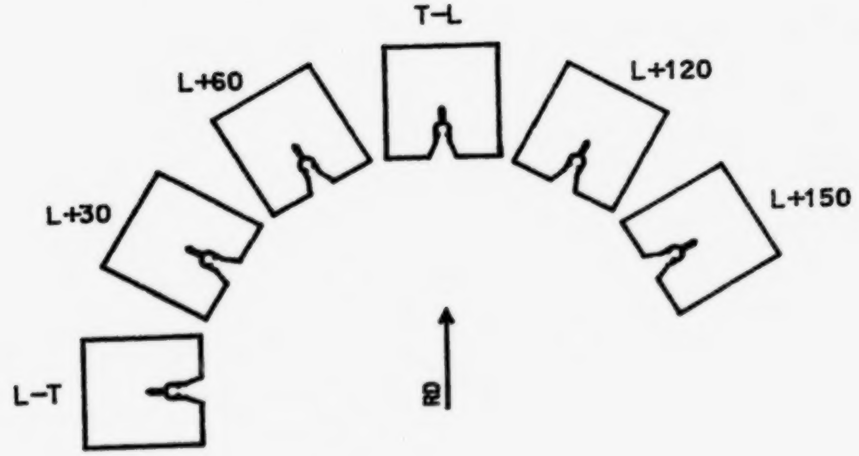
T-L
L+60
L+120
L+30
L+150
L-T
RD

Figure 3 - Compact fracture toughness specimen orientations.

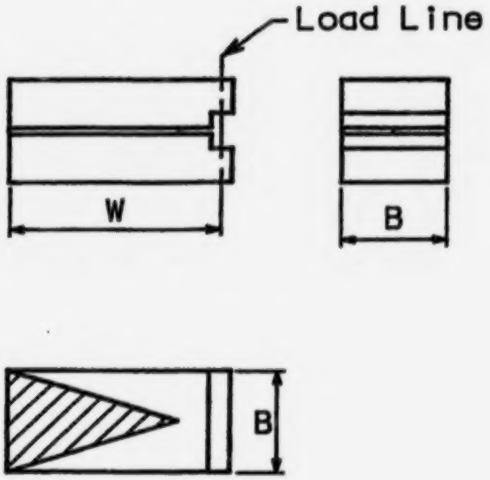
Load Line
W
B
B

Figure 4 - Chevron-notched short bar geometry.

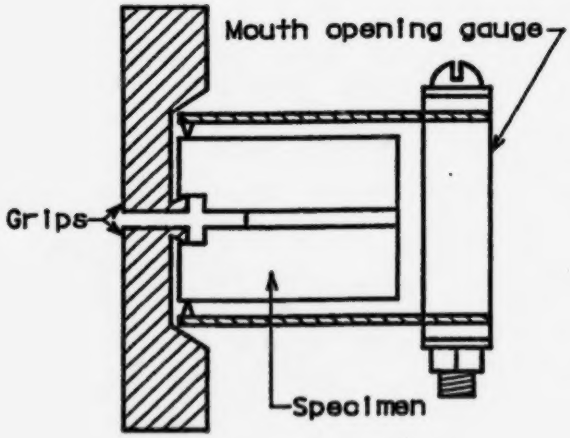
Mouth opening gauge
Grips
Specimen

Figure 5 - Chevron-notched short bar testing arrangement.

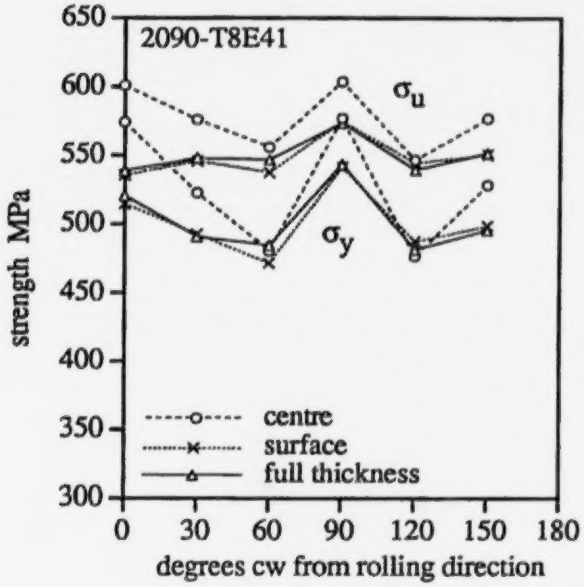

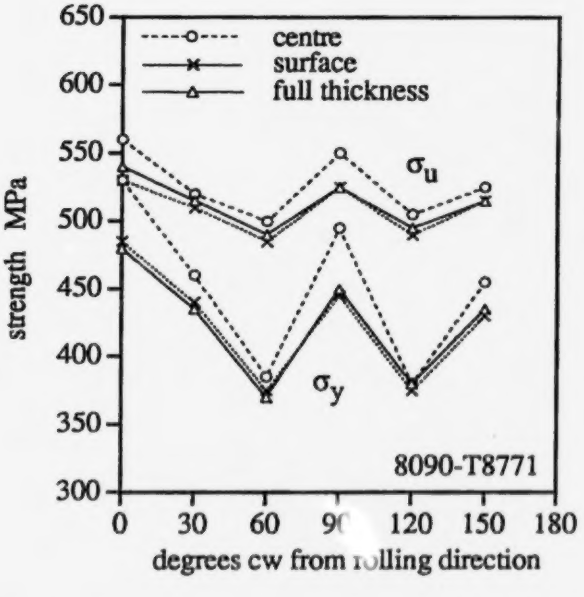

Figure 6 - Effect of orientation and through-thickness location on tensile strength.

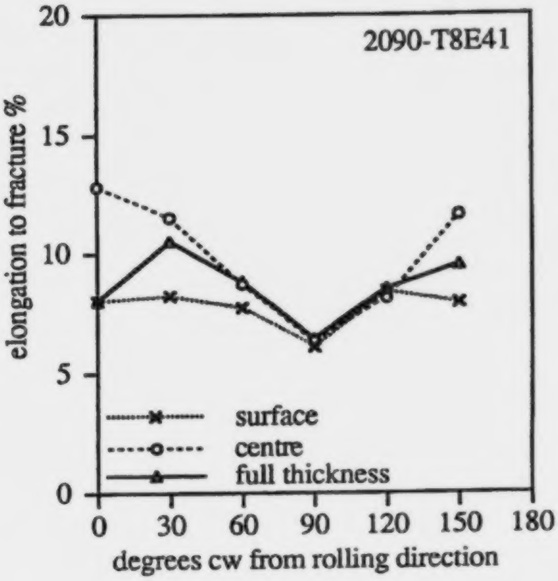

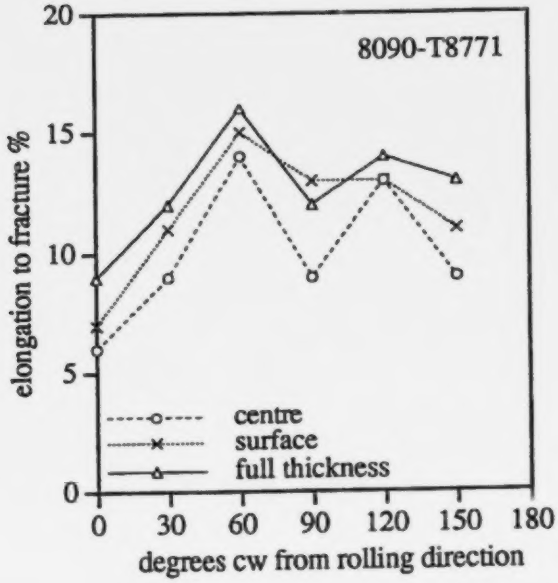

Figure 7 - Orientation dependence of tensile elongation.

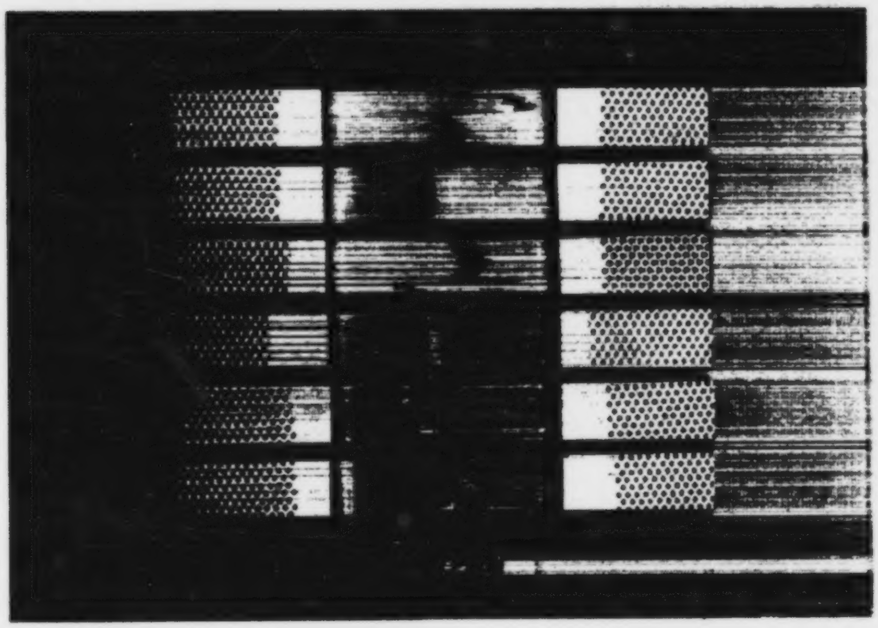

8090-T8771

Bottom is longitudinal, then 30°, 60°, transverse, 120°, and 150° cw from rolling direction

Figure 8 - Broken full thickness tensile specimens.

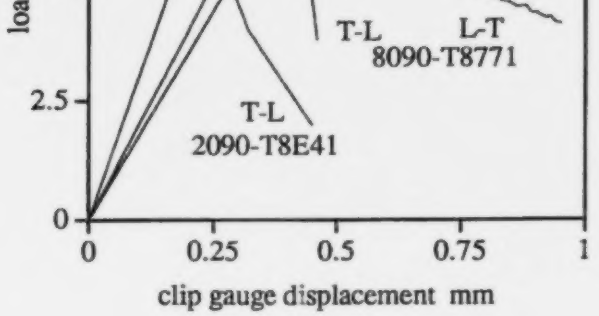

Figure 9 - Load-displacement curves from compact specimen tests.

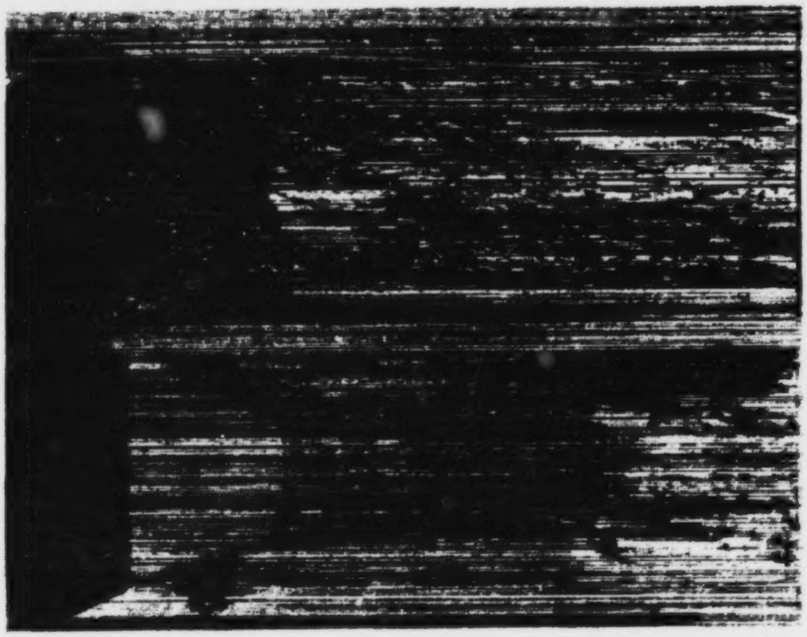

Top is L-T, bottom is L+60°

Figure 10 - Fracture surfaces of 8090 aluminum-lithium compact specimens.

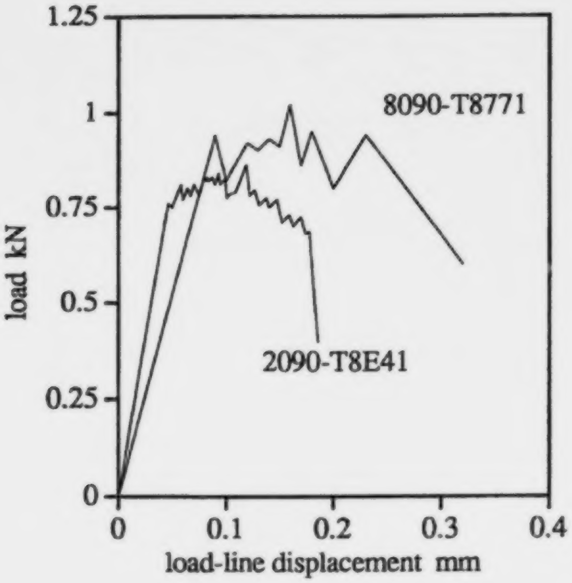

Fig. 11 - Load-displacement curves from short-transverse fracture tests (S-L orientation).

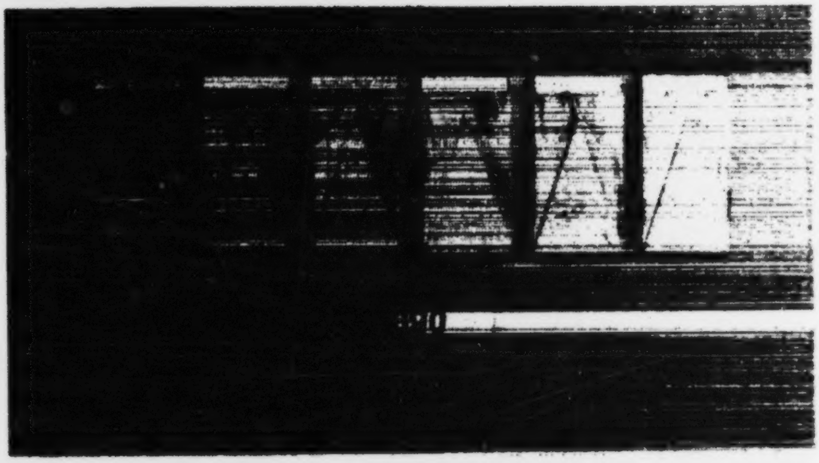

8090-T8771

Figure 12 - Fracture surfaces of short-transverse short bar specimens.

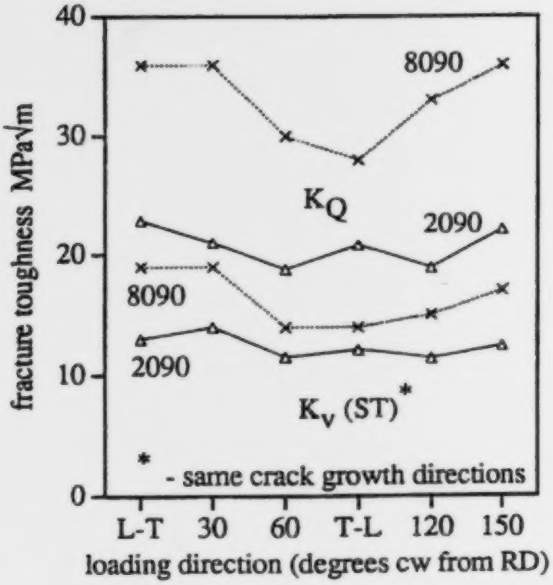

Figure 13 - Orientation dependence of toughness.

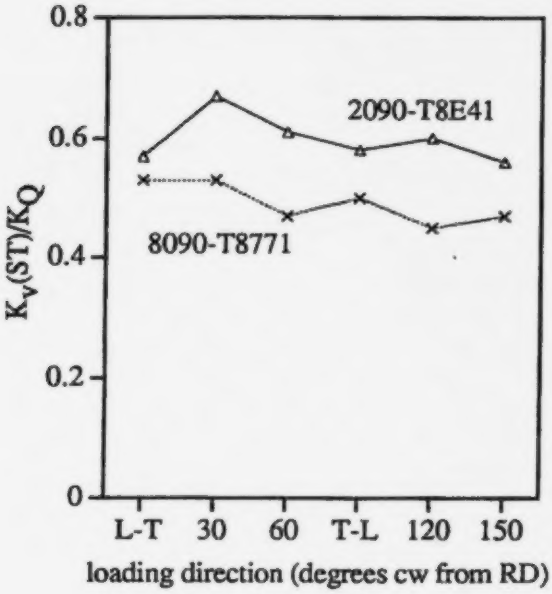

Figure 14 - Orientation dependence of $K_V(ST)/K_Q$.

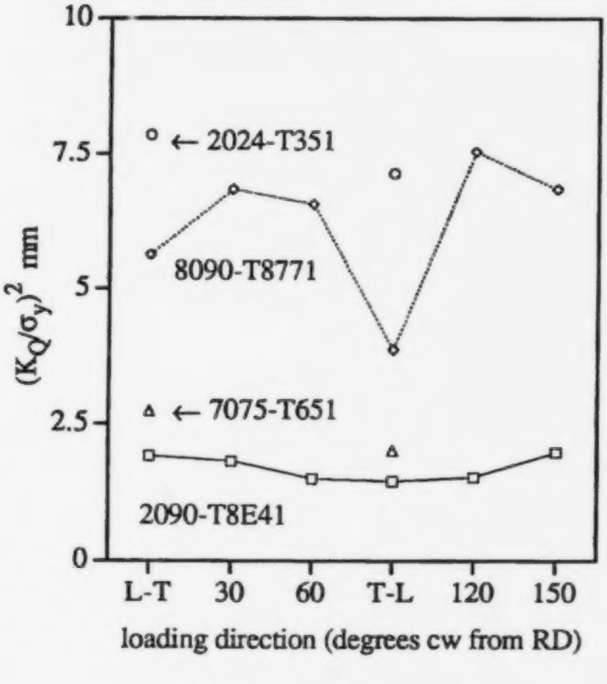

Figure 15 - Toughness/strength ratios.

141646

14.

"Constant Amplitude Fatigue Crack Growth in Aluminum-Lithium"

Z. Zhai and J. Morrison

DREP.Victoria, B.C.

Constant Amplitude Fatigue Crack Growth in Aluminum-Lithium

Zhen Hua Zhai and Jack Morrison

Defence Research Establishment Paciific
Victoria, B.C.

INTRODUCTION

A number of studies ~~(1-5)~~ of the constant load amplitude fatigue crack growth behaviour of aluminum-lithium alloys have indicated an improvement over conventional alloys. Important contributions to the reduction in crack extension rates include roughness induced crack closure, deviations from the intended crack plane, and non-planar propagation of the crack. All of these effects reduce the effective stress intensity at the crack tip. The anisotropy of mechanical properties and the strong texture found in these alloys, which has been argued to promote inhomogenous plastic deformation and planar slip also results in a variability of crack growth behaviour with the orientation of the fracture plane ~~(6-7)~~.

This paper describes a detailed study of the orientation dependence of fatigue crack growth in aluminum-lithium plate compared to conventional aerospace alloys. The materials studied were the same 8090, 2090, 2024, and 7075 plates described in ~~the previous~~ paper 3 ~~(8)~~. Likewise the same six compact specimen orientations were employed for the aluminum-lithium tests (fig. 1), plus the L-T and T-L orientations for the 2024 and 7075 specimens.

EXPERIMENTAL PROCEDURES

The constant amplitude fatigue crack propagation tests were conducted in accordance with ASTM Standard E647 using 50 mm wide full plate thickness compact specimens. There is a marked tendency of fatigue cracks in the aluminum-lithium alloys to deviate from the intended crack plane. It was decided that, for the purposes of this study, the crack growth rates would be measured as far as possible solely in the direction of interest. Therefore, in order to keep the fatigue cracks extending normal to the applied load, the specimens were sidegrooved 10% of thickness on each side. In this way it was hoped that a well defined stress intensity and stress ratio could be maintained. Given the known directionality of properties in the aluminum-lithium alloys (9), it was recognized that this procedure might not reflect the behaviour of cracks in real structures. The alternative procedure would be to allow the fatigue cracking to proceed in whatever direction it deviated towards, and modify the stress intensity accordingly to account for the out of plane loading.

The tests were carried out under ambient conditions (about 35% relative humidity) in a servohydraulic testing machine controlled by a 386 model computer running the Instron program, "Advanced Fatigue Crack Propagation". Crack length was monitored automatically using unloading compliance determined from a clip gauge placed on the specimen load line. The initial notch length was approximately 12 mm. Very little load shedding was employed, precracking being carried out at a load close to the start ΔK for the test, which resulted in an initial crack extension rate of about 10^{-5} mm/cycle. The tests were conducted using a triangular waveform at a frequency of 10 Hz, and at two load ratios ($R = 0.1$ and 0.5). Data were collected at crack length increments of 0.6 mm. On completion of the test, an optical examination was made of the fractured specimen. Crack growth rates were calculated using unsmoothed point-to-point averaging. A detailed fractographic study of these specimens using scanning electron microscopy is described in the following paper (10).

RESULTS AND ANALYSIS

a) 2024-T351 and 7075-T651

Figures 2 and 3 show da/dN versus ΔK curves for the 2024-T351 and 7075-T651 specimens from the two orientations at each of the two R ratios. It can be seen that, as has often been observed (11), the stiffer 7075 alloy generally has a higher crack growth rate at a given ΔK. Likewise the end of the threshold and onset of power law crack growth occurs at a higher da/dN in the 7000 series alloy, indicative of the stronger influence of closure in this alloy. There is only a small orientation dependence in T-L and L-T. Increasing the R ratio results in a small increase in the separation of the 7075 and 2024 curves at low and intermediate ΔK. In the linear Stage II region of these curves, the slope is approximately 3 for alloy 7075, and about 3.5 for 2024 alloy.

In figs. 4 and 5 the above data are replotted to show more clearly the retardation of crack growth rates at low stress ratios. The difference found in the threshold region decreases approaching the linear stage 2, but there is still a persistent separation thereafter. The irregular crack growth rates at low stress intensity levels are largely eliminated by increasing the stress ratio.

A small but systematic trend with orientation was observed (fig. 6) by plotting the number of cycles as a function of the stress intensity range, starting at the same load and crack length at an arbitrary zero cycles. This effect may be related to the lower fracture toughness in the T-L orientations, and seems reproducible, although there were not many suitable specimens for comparison with the same initial crack lengths and ΔK values, the final precracking being carried out so as to give a desired crack growth rate. Interestingly enough, increasing the load ratio appears to decrease the apparent orientation effect, pointing to an orientation dependent closure as one contributor.

In both the 2024-T351 and 7075-T651 specimens, the fatigue cracks grew across the specimen within the side grooves and normal to the applied load without significant deviation. The fatigue cracks were smooth (fig. 7).

b) 8090-T877

Figures 8 and 9 show da/dN versus ΔK curves for the 8090-T8771 specimens from the six orientations at each of the two R ratios. A pronounced orientation dependence is observed, both in crack growth rate and fracture appearance.

In the L-T and T-L orientations, the fatigue fracture surfaces observed on the 8090 alloy specimens are much rougher than in 2024-T351 and 7075-T651 (figure 10a). In the remaining 8090 orientations (fig. 11), the cracks start off smooth (fig. 10b), but increasingly roughen from the edges inwards as the crack extends. This may be the result of the fact that ΔK is increasing as the crack grows. It is assumed that the dark rough surfaces result from fretting as a result of crack closure. Only in the L-T orientation did the crack remain perpendicular to the applied loading direction, otherwise the cracks grew out of the intended fracture plane despite the constraint provided by the side-grooves. There is, however, a restraining effect of the side grooves near the surface. For example, in the L+30 orientation viewed end-on in the crack growth direction, the fatigue fracture surface bulges up in a thumbnail shape across the specimen thickness. In the T-L orientation, the crack grew markedly away from the intended plane. At $R = 0.1$, it deviated at an angle of about 52° at a very early stage of growth, and remained at that angle until unstable rupture occurred (fig. 10b), whereas at $R = 0.5$, the crack only deviated in this manner after zig-zagging several times, leaving behind a laminated, saw-toothed surface (figure 10c).

In figure 11, the 8090 specimens are arranged with the same surface of the plate uppermost. The deviation of the crack from its intended plane is not random. In the L+30 and

L+150 orientations (with the intended crack plane at 60° either side of the rolling direction) , the cracks tilted about 5° towards the rolling direction, changing the crack growth planes to ±55° from the rolling direction, which has been reported to be the softest tensile orientation. This is obviously the same orientation towards which the T-L samples deviated. It has also been determined elsewhere (12) that the texture in the centre of 8090 plate is {110}<112>, so that the ±55° directions correspond to [110] slip directions. For the most part these specimens had smooth fracture appearances.

In the L+60 and L+120 orientations (crack growth nominally at ±30° to the rolling direction), the cracks deviated about five degrees away rather than towards the rolling direction, growing for most of the test at ±65° to the rolling direction. As part of this process there was also a tendency for the crack to step completely out of the intended plane. This may reflect the fact that although the crack would prefer to grow at the larger angle, once it has left the groove the relaxed constraint prevents it from doing so. At a high stress intensity near the end of the test, the cracks further deviated towards the ±55° orientations. These specimens initially generated smooth fracture surfaces, but as the cracks deviated and the cyclic stress intensity increased, the smooth region was gradually squeezed into a triangle at the specimen centre. This suggests that a change in fatigue mechanism occurs above some minimum ΔK.

Given the normal scatter expected in the da/dN vs. ΔK plots, with the exception of the T-L specimens, there is little orientation dependence indicated in figs. 8 and 9, and the overall trends are similar. The T-L curves show the strong effect of the large deviation in fracture plane on crack growth retardation, but the smaller deviations described above for the other orientations tend to result in similar curves, which cannot be ranked systematically. Not surprisingly there is a strong stress ratio effect on the shape of these curves, with the higher R ratio reducing the observed closure effect (figure 12). The crack growth rates at $R=0.5$ are markedly higher than at $R=0.1$, and the effect is stronger than in the conventional alloys. The stress ratio effect is also less marked in the T-L compared to the other orientations. It is interesting to note that the low propagation rate T-L orientation also has the lowest measured fracture toughness.

c) 2090-T8E41

Figures 13 and 14 show da/dN versus ΔK curves for the 2090-T8E41 specimens from the six orientations at each of the two R ratios.

It has been reported (11) that in the centre of 2090-T8E41 plate, the texture is the same as that found in the 8090-T8771 plate, namely {110}<112>, but is much less intense near the surface. This may be why the fracture surfaces of 2090-T8E41 specimens differ from those of 8090-T8771 (figures 15 and 16). In 8090-T8771, the crack in T-L orientation grew out of the original plane across virtually the entire thickness, whereas in 2090-T8E41 the deviation occurs mainly in the centre, and the deviation is not as severe (figure 15a). During most of the growth, the crack centre meandered along a path inclined at less than 45 degrees from the intended fracture plane. Only at a very late stage did the crack approach 55° from the rolling direction. In 8090 the L-T orientated crack managed to stay on the intended plane, but in 2090, at $R = 0.1$, the L-T fracture surface also grew out of plane, although not as far as in the T-L orientation. The general appearance of cracks growing in the remaining 4 orientations is similar in 2090 to 8090. However, in contrast to 8090, the fracture surfaces of the L+30 and L+150 alloy 2090 specimens are rough (fig. 15b), and again the edges have a strong tendency to stay within the side grooves. In 2090 specimens the fracture surfaces in the L+60 and L+120 orientations are the smoothest. The overall appearances are shown in Figure 16.

The variations in texture may also explain the apparent increase in da/dN darta scatter in 2090 alloy seen in figs. 13 and 14 (excluding L-T and T-L). Other than in the L-T and T-L specimens, the trends are similar to those in 8090. In 2090 there is an indication that, at growth rates below 10^{-4} mm/cycle, the L+60 and L+120 specimens show higher gowth rates at a given ΔK. This trend is not apparant in the 8090 results. The dependence of crack growth rate on stress ratio in 2090 seems somewhat smaller than in the 2024, 7075 and 8090 (figure 17).

Figures 18 and 19 show crack growth data from the orientations with the fastest crack growth rates for each alloy respectively at each stress ratio. The lithium containing alloys have similar crack growth rates, and their strong stress ratio effect compared to the conventional alloys is apparent. 2090 (and 8090 at R=0.5) appears to undergo faster crack growth than 2024 at low ΔK, otherwise the aluminum-lithium alloys are more fatigue crack groowth resistant than the 2024 or 7075 alloys.

A more detailed analysis of data repeatability at the different orientations would be needed to conclusively evaluate the orientation effects. Likewise there is a need to evaluate the crack growth behaviour in specific directions, notably at ±35° and ±55° to the rolling direction. The orientation and R ratio effects indicated in the above data are also being subjected to a crack closure analysis based on ΔK_{eff}.

CONCLUSIONS

1. In 2024-T351 and 7075-T651 plates, the T-L orientation yields faster crack growth rates than L-T. An increasing R ratio reduces this effect.

2. Fatigue crack propagation in 2090-T8E41 and 8090-T8771 plates is orientation dependent. The T-L orientation is the most resistant.

3. Strong closure effects are seen in aluminum-lithium alloys. The R ratio has no effect on orientation dependence in 2090 and 8090 alloys, but markedly affects the rate of crack propagation.

4. 2090 and 8090 both show superior resistance to crack propagation to 7075-T651 plate even in the weakest orientations. At low stress intensity ranges and high stress ratios, aluminum - lithium is slightly less resistant than alloy 2024.

REFERENCES

1. R.J.H. Wanhill, "Status and Prospects for Aluminium-Lithium Alloys in Aircraft Structures", *Fatigue of Metallic Materials*, Elsevier, 1992, pp. 43-82.

2. Venkateswara Rao, K.T., Yu W., and Ritchie, R.O., "Fatigue Crack Propagation in Aluminum-Lithium Alloy 2090: Part I. Long Crack Behaviour", Metallurgical Transactions A, **19A**, (1988), pp. 549-561.

3. Peters, M., Welpmann, K., McDairmaid, D.S., 't Hart, W.G.J., "Fatigue Properties of Al-Li Alloys", *New Light Alloys*, Proceedings No. 44, Advisory Group for Aerospace Research and Development, (1089), pp. 6-1 - 6-18.

4. Venkateswara Rao, K.T., Bucci, R.J., Jata, K.V., and Ritchie, R.O., "A Comparison of Fatigue Crack Propagation Behaviour in Sheet and Plate Aluminum-Lithium Alloys, Materials Sci. and Engineering, **A141**, (1991), pp. 39-48.

5. Peters, M., Welpmann, K., Zink, W., and Sanders, T.H. Jr., "Fatigue Behaviour of Al-Li-Cu - Mg Alloys,*Aluminuum Alloys III*, The Institute of Metals, (1986), pp. 239-246.

6. Bréchet, T., and Louchet, F., "Fatigue of Al-Li Alloys: Mechanical Properties, Microstructure (TEM and SEM) and Strain Localization", J. Materials Sci., **25** (1990), pp. 3053-3060.

7. Jata, K.V., and Starke, E.A. Jr., "Fatigue Crack Growth and Fracture Toughness Behaviour of an Al-Li-Cu Alloy", Metallurgical Transactions A, **17A**, (1986), pp. 1011-1026.

8. Morrison, J., Zhai, Z., and KarisAllen K.J., "Directionality of Strength and Toughness In ALuminum-Lithium Plate", Proc. Workshop *Research and Development on Aluminum-Lithium Alloys, (efence Research Establishment Pacific*, *(1993)*, pp. 287-304.

9. N. Eswara Prasad and G. Malakondaiah, "Anisotropy of Mechanical Properties in Quaternary Al-Li-Cu–Mg Alloys", Bull. Mater. Sci., **15**, No. 4, (1992), pp. 297-310.

10. Hull, D.A., "A Fractographic Study of Selected Aluminum-Lithium Alloys", Proc. Workshop *Research and Development on Aluminum-Lithium Alloys, (efence Research Establishment Pacific, (1993)*, pp.?????,.

11. Paris, P.C., "Twenty Years of Reflection on Questions involving Fatigue Crack Growth, Part I: Historical Observations and Perspectives", *Fatigue Thresholds Vol. 1*, EMAS Publications, (1981), pp. 3-10.

12. Squibb, M.W., and Wilson, R.N., "The Fatigue and Fracture Behaviour of Aluminum - Lithium Plate - UK Study", Proc. Workshop *Research and Development on Aluminum-Lithium Alloys, Defence Research Establishment Pacific*, *(1993)*, pp.215-240.

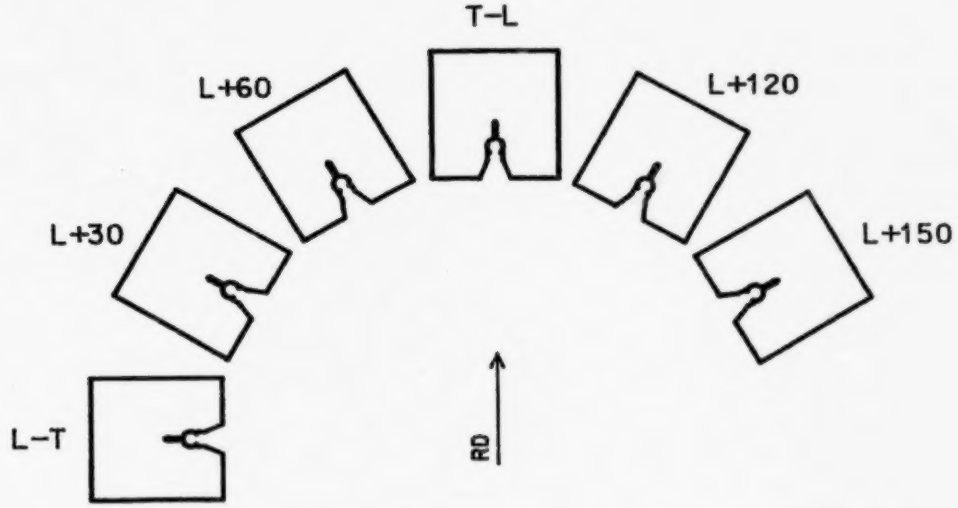
T–L
L+60
L+120
L+30
L+150
L–T
RD

Figure 1. Aluminum-lithium specimen orientations.

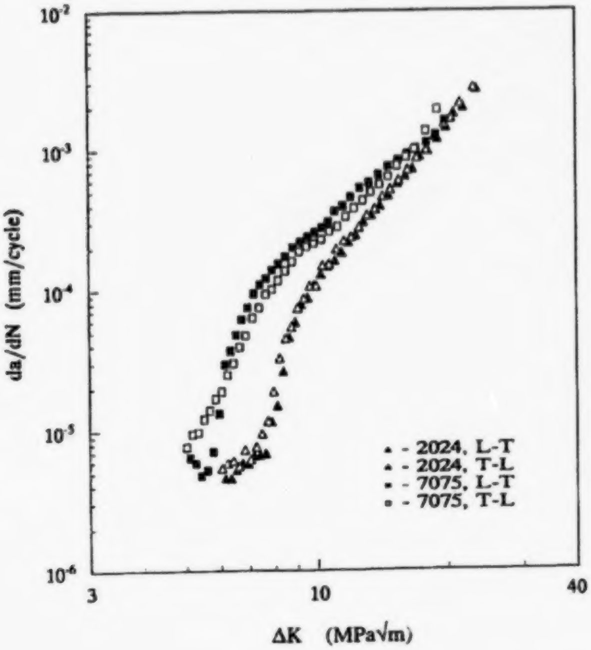

Figure 2. Fatigue crack growth rate versus stress intensity factor range for 2024-T351 and 7075-T651 plates. R = 0.1.

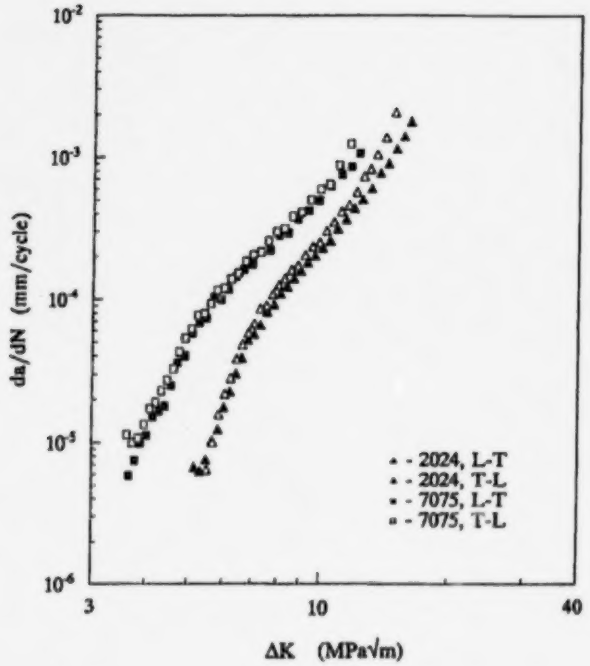

Figure 3. Crack growth rate versus stress intensity range for 2024 and 7075 at R = 0.5.

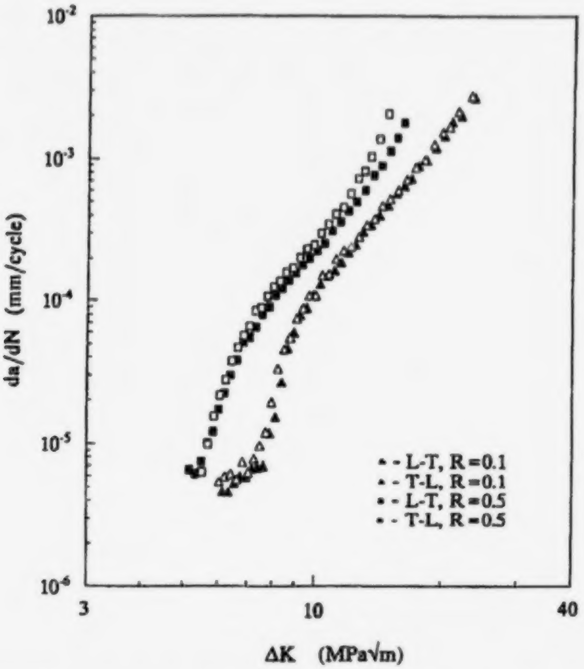

Figure 4. The effect of R ratio on crack growth in 2024.

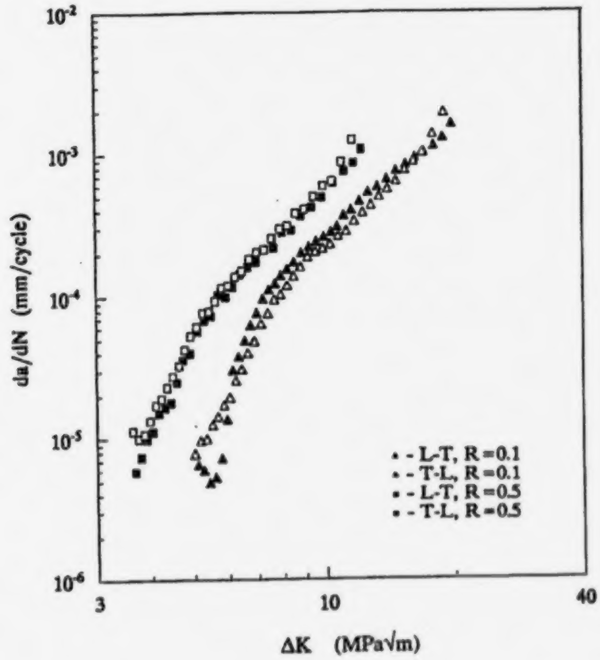

Figure 5. The effect of R ratio on crack growth in 7075.

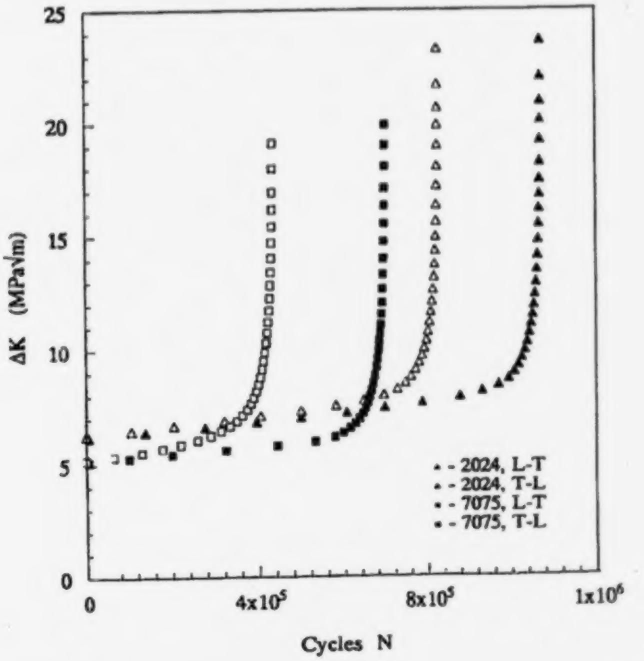

Figure 6. Crack length in ΔK as a function of elapsed cycles in 2024 and 7075 at R = 0.1. Initial crack length nominally 15 mms.

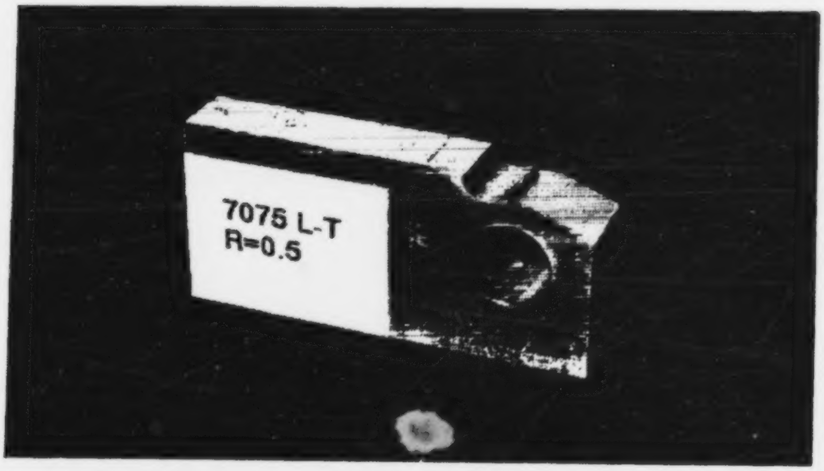

Figure 7. Fracture surface in the L-T orientation in 7075.

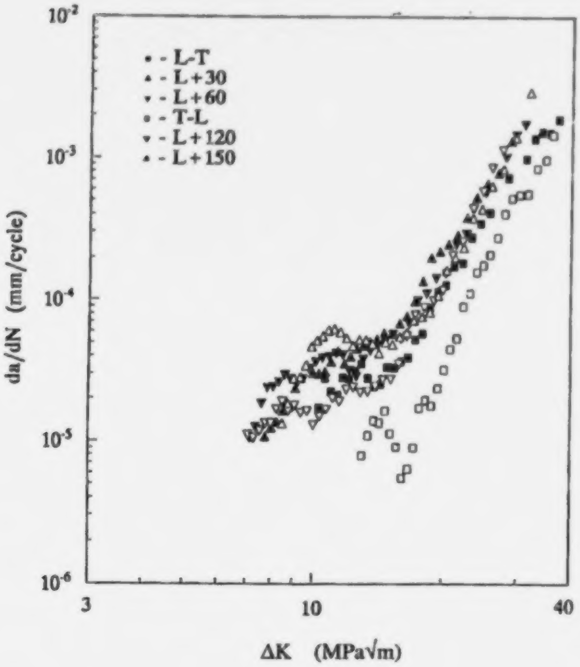

Figure 8. Fatigue crack growth rate versus stress intensity factor range for 8090-T8771 plate at R = 0.1.

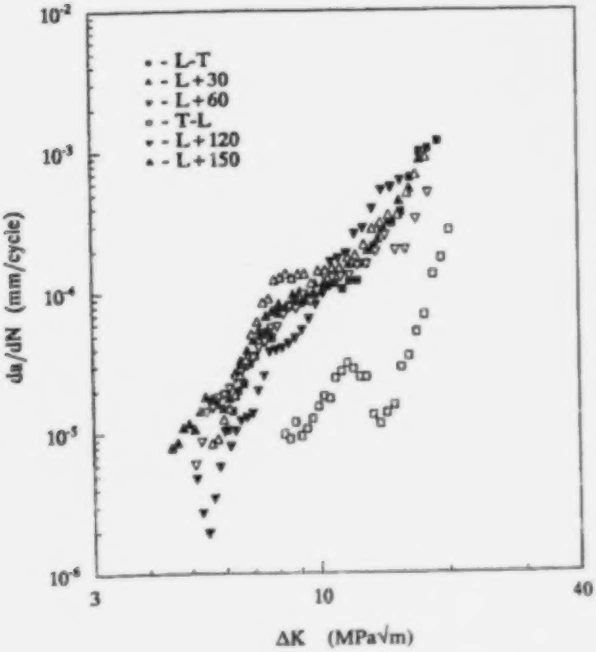

Figure 9. Crack growth rate versus stress intensity factor range for 8090 at R = 0.5.

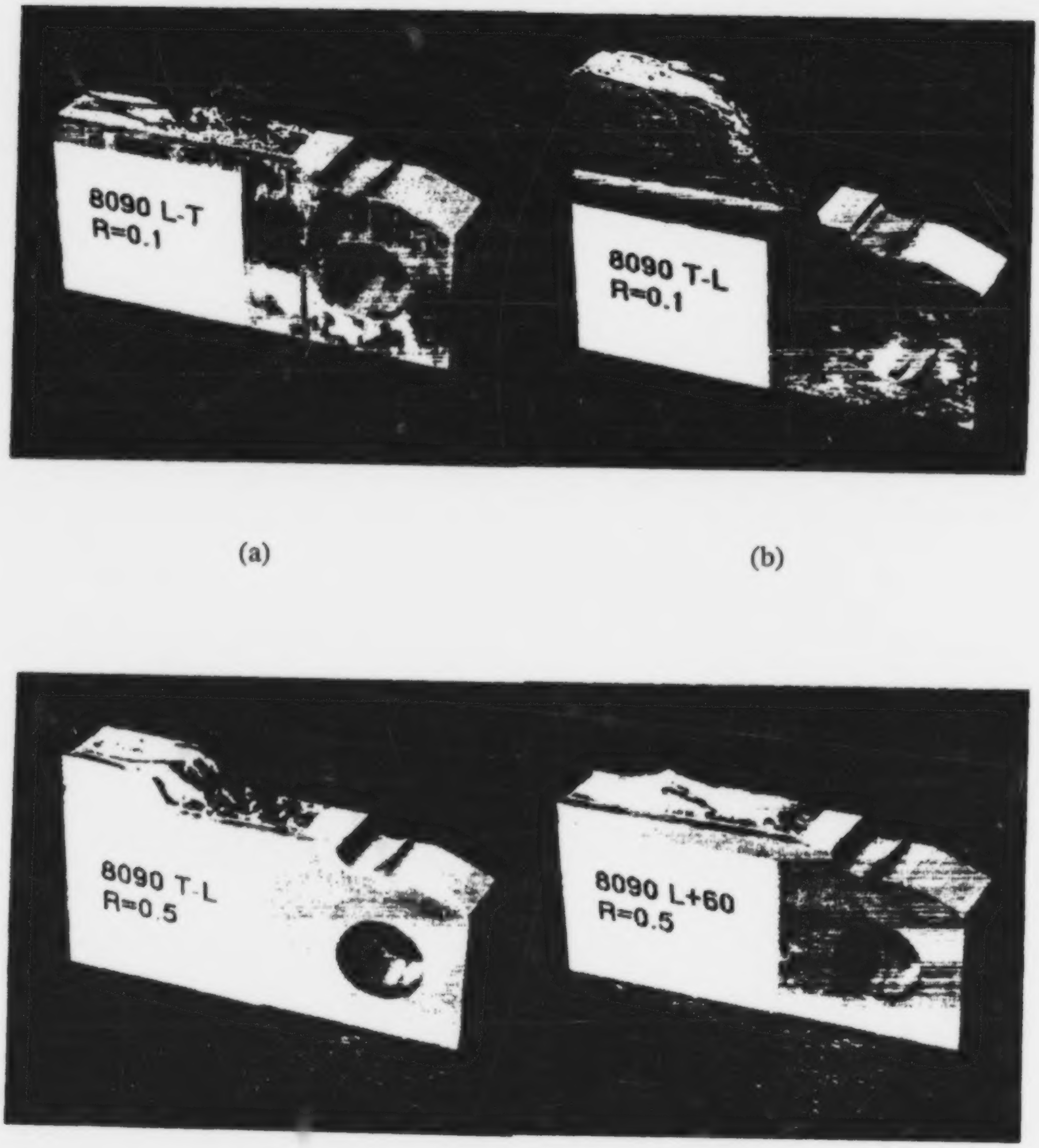
8090 L-T
R=0.1
8090 T-L
R=0.1
8090 T-L
R=0.5
8090 L+60
R=0.5

(a) (b)

(c) (d)

Figure 10. Fracture surfaces of 8090 plate.

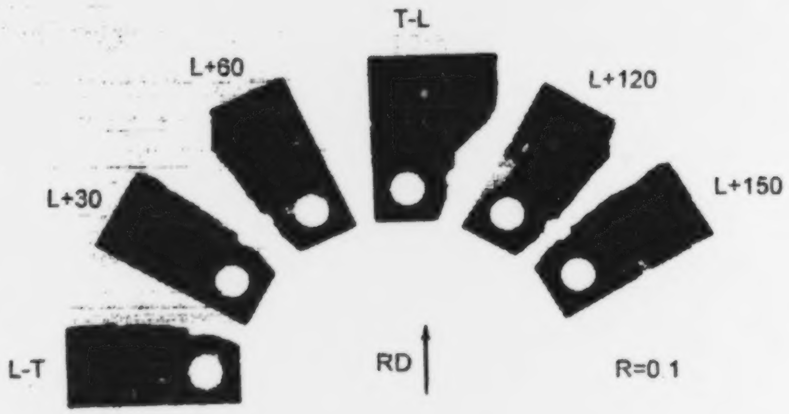
T-L
L+60
L+120
L+30
L+150
L-T
RD
R=0.1

(a)

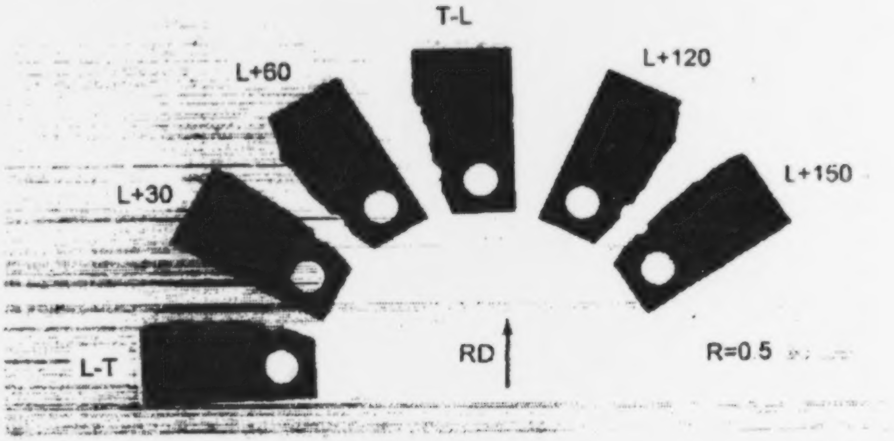
T-L
L+60
L+120
L+30
L+150
L-T
RD
R=0.5

(b)

Figure 11. Profiles of broken 8090 specimens.

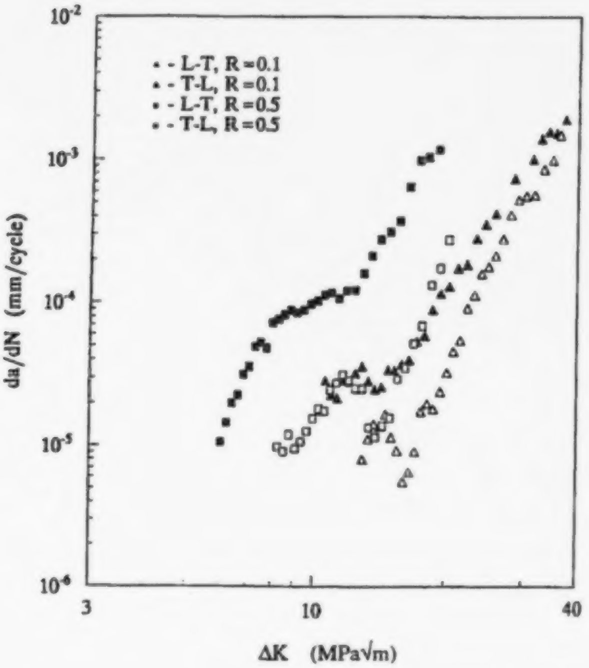

Figure 12. The effect of R ratio on crack growth in 8090.

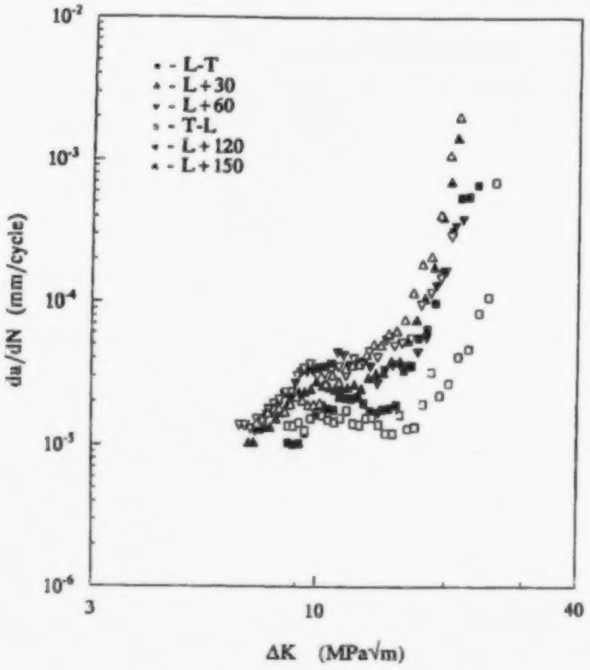

Figure 13. Fatigue crack growth rate versus stress intensity factor range for 2090-T8E41 plate at R = 0.1.

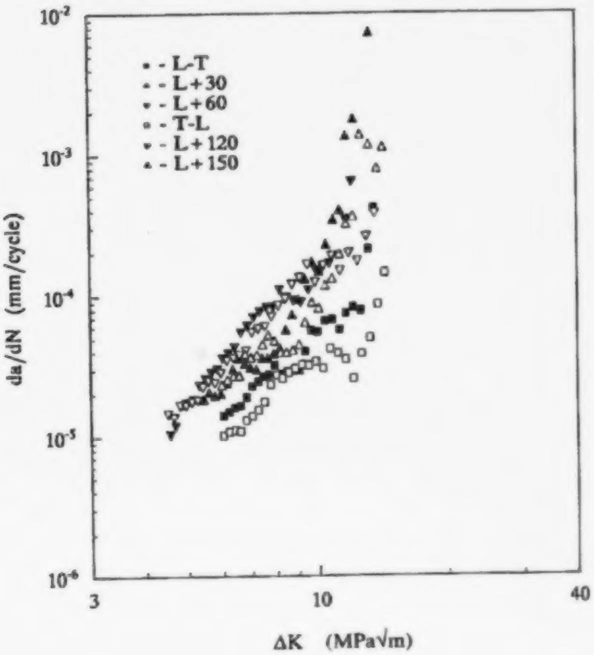

Figure 14. Crack growth rate versus stress intensity factor range for 2090 at R = 0.5.

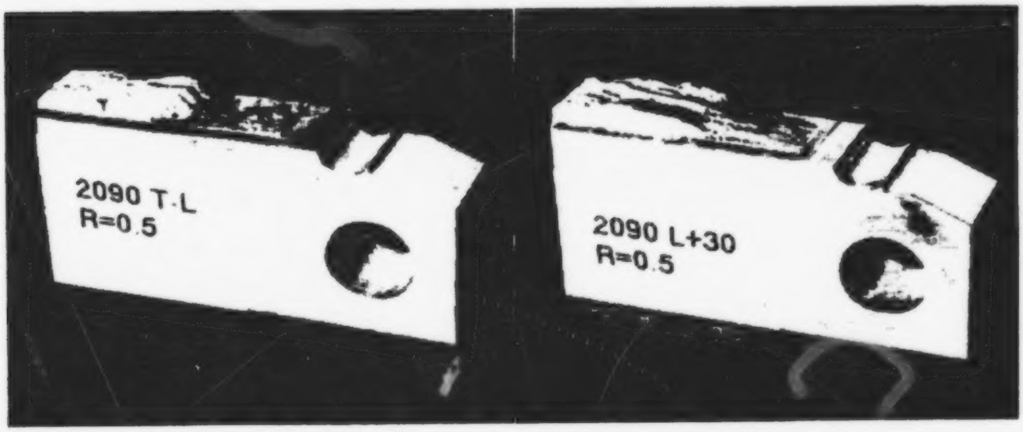
2090 T-L
R=0.5
2090 L+30
R=0.5

(a) (b)

Figure 15. Fracture surfaces of 2090 plate.

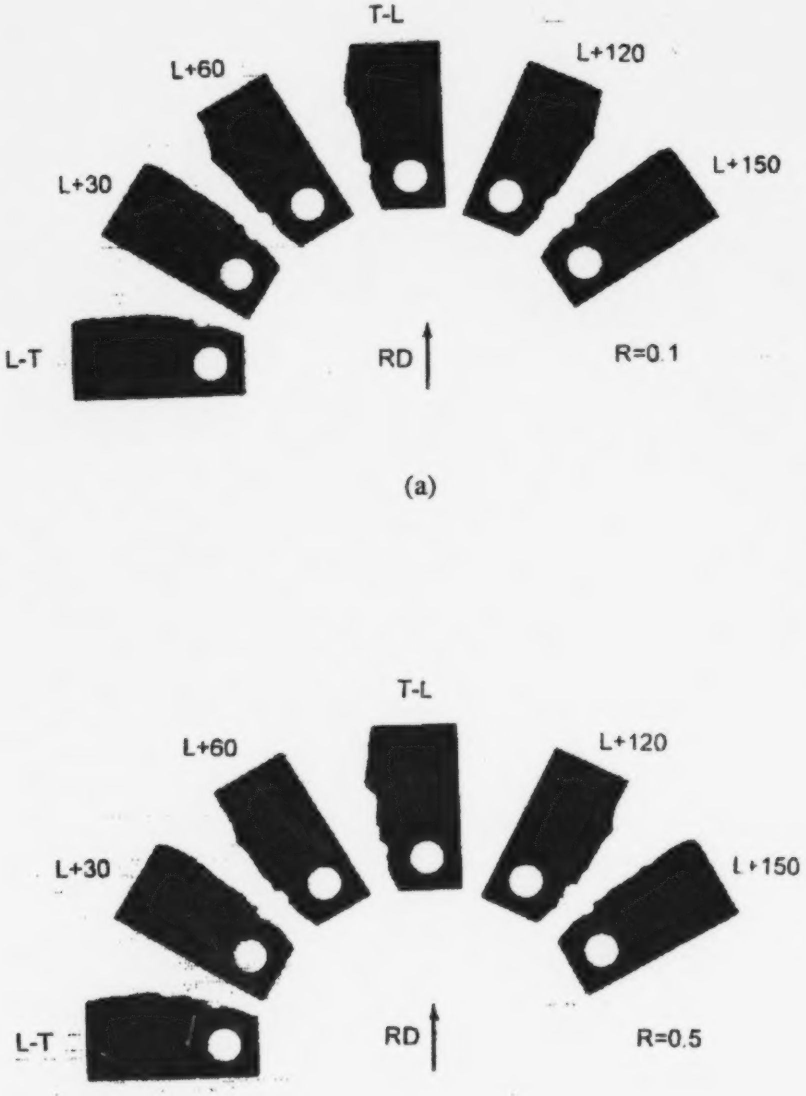
T-L
L+60
L+120
L+30
L+150
L-T
RD
R=0.1
T-L
L+60
L+120
L+30
L+150
L-T
RD
R=0.5

(a)

(b)

Figure 16. Profiles of broken 2090 specimens.

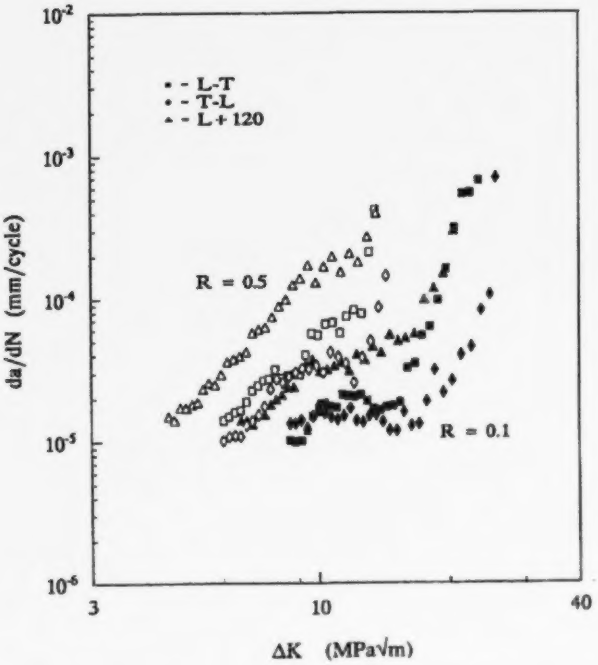

Figure 17. The effect of R ratio on crack growth in 2090. Solid symbols denote R = 0.1; open symbols R = 0.5.

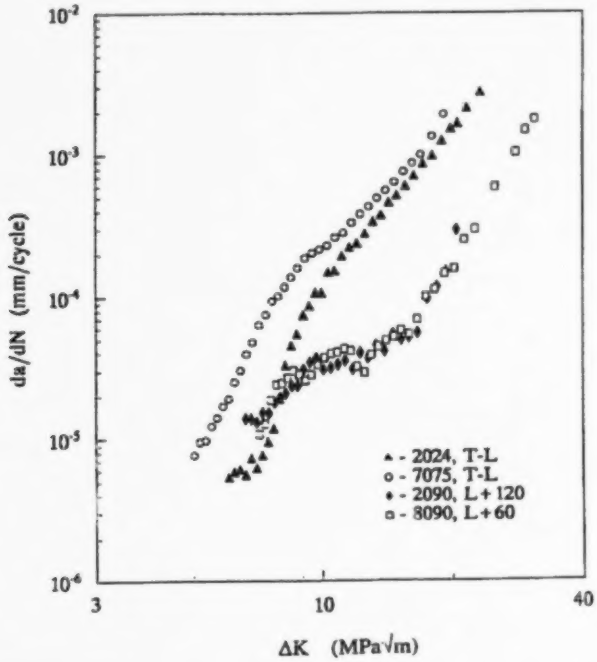

Figure 18. Comparison of crack growth rates in orientations of least resistance. R = 0.1.

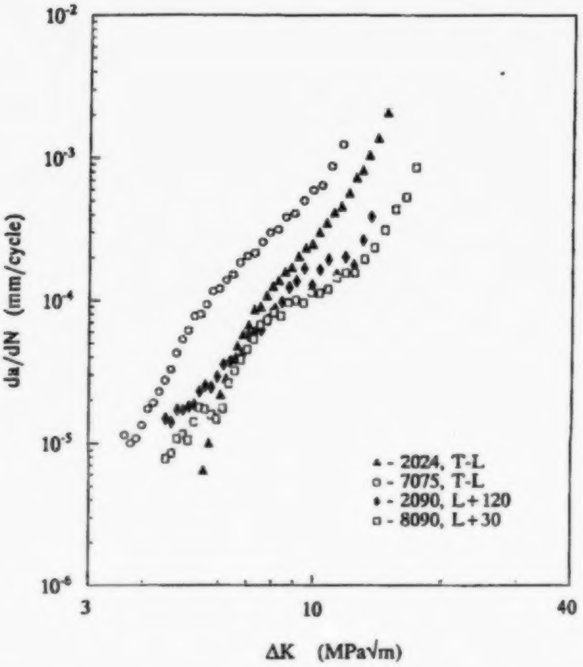

Figure 19. Comparison of crack growth rates in orientations of least resistance. R = 0.5.

141647

15.

"A Fractographic Study of Selected Aluminum-Lithium Alloys"

D. A. Hull

Engineering Material Research, Downsview, Ont.

A FRACTOGRAPHIC STUDY OF SELECTED ALUMINUM-LITHIUM ALLOYS.

BY

D.A. HULL [1]

The effect of Aluminum-Lithium 2090-T8E41 and 8090-T8771 plate orientation on constant amplitude fatigue crack growth rates (FCGR) has been investigated by the Defense Research Establishment Pacific~~, (DREP) of Victoria, B.C~~. Side grooved, compact tension specimens, W = 51 mm, 8090 B = 12.5 mm, and 2090 B = 14.7 mm were evaluated with a 10 Hz constant amplitude triangular waveform at ambient temperature and humidity. The DREP FCGR results are presented in these proceedings ~~(1)~~. In this study, a Scanning Electron Microscope (SEM) was used to inspect the DREP Al-Li compact tension specimen fracture surfaces. Metallographic and texture analysis results are presented prior to the fractographic results.

METALLOGRAPHY AND TEXTURE RESULTS.

Al-Li 2090 and 8090 grain structures are compared to a conventional damage tolerant Al-Cu 2024-T351 alloy in Figure 1. These samples were removed from the plate's mid-thickness location and were etched with Kellor's reagent. The parallel elongated grain structure in both the Al-Li plate L and T directions is clearly evident.

The high degree of preferred crystal orientation frequently found in Al-Li plate alloys has been shown (2-4) to significantly effect material behaviour. DREP Al-Li plate texture (5) was analyzed at the surface and mid-thickness locations. Stereographic plots of Al-Li 8090 and 2090 (111) planes are shown at the top and bottom of the Figure 2 respectively. The rolling, L, and transverse, T, directions are located on the vertical and horizontal axes respectively. The 8090 texture at the middle of the plate shows a higher degree of crystal orientation than at the surface. The 2090 mid-thickness texture is similar to the 8090 texture. However the 2090 surface texture is significantly different. This result suggests a 2090 through-the-thickness variation in texture exists. The different 2090 surface texture may be the result of limited recrystallization at the surface (6).

---

[1] Engineering Material Research, Downsview, Ontario
M3J 2S1

The DREP compact tension specimens orientations relative to the plate transverse and rolling axes are shown in Figure 3. Off-axis specimen orientations were at ± 30 and ± 60 degrees to the transverse direction. Both alloys exhibited significant amounts of out-of-plane macroscopic crack branching. The 8090 crack branching directions for each specimen orientation are shown schematically in the figure.

In the following fracture surface photomicrographs the crack propagation direction is indicated by the upper left hand corner arrow and the scale is located at the lower right side.

8090-T8771 RESULTS.

In Figure 4, 8090 fracture surfaces for T-L and L-T crack extension directions in Figure 4a and 4b respectively are compared to the same 2090 directions in Figure 4c and 4d. The machined starter notch is shown on the left of each photograph and the vertical arrow indicates the onset of unstable crack growth. In Figure 4a, the 8090 T-L direction exhibits 50-55 degrees of crack branching relative to the rolling direction with fracture occurring on the T-L direction.- see Figure 4a inset. The black region at the fracture surface center is composed of a powder believed to be wear and corrosion products. In Figure 4b, 8090 FCG remained in the L-T plane. Increasing surface roughness occurred in the specimen interior before spreading to the specimen sides.

In comparison to the 8090 surfaces, the 2024 fracture surfaces in Figure 4c-d appear macroscopically smooth. However the 2024 L-T surface exhibits more facets that makes it more reflective than its L-T surface.

In Figure 5 the 8090 L-T surface is shown in more detail. The "A" marker at a crack length of 19.0 mm in Figure 5a is shown at greater magnification in Figures 5b and c. A secondary crack lying along a grain boundary is present at the center of Figure 5b, and in more detail on the right of Figure 5c. On the left the "fissures" at 45 degrees to the main crack growth direction are believed to be formed by a combination of slip and tensile fracture. At this crack length slip directions within individual grains do not usually extend into adjacent grains.

In Figure 6a, marker "A" is located at a 8090 L-T crack length of 24.0 mm at the beginning of a region of increasing center thickness surface roughness. Figure 6b reveals the surface roughness to be composed of crystallographic facets that extend across grain boundaries. Progressively larger facets are formed that rise vertically from the fracture plane.

The fracture surface for a 30 degree specimen orientation relative to the transverse direction is illustrated in Figure 7a. The "A" and "B" markers identify the magnified regions presented in Figure 7b and 7c respectively. At a crack length of 19.0 mm, Figure 7b appears similar to the 8090 L-T surface of Figure 5b. Few crystallographic facets were observed on this fracture surface. At a 28.0 mm crack length in Figure 7c, the surface is composed of patches of fatigue crack striations, tearing and secondary cracks normal to the main crack growth direction.

The specimen orientation of 60 degrees relative to the transverse direction is presented in Figure 8. Markers "A" and "B" are located at 15.0 mm and 19.0 mm crack lengths respectively. Figure 8b depicts the specimen center thickness where a secondary crack is inclined to the main crack propagation direction and is beside a facet. Marker "B"'s region in Figure 8c shows secondary cracks that formed along grain boundaries.

The same 60 degree specimen orientation in Figure 9a reveals the "A" and "B" marker locations at a crack length of 34.0 mm in Figure 9b and 9c respectively. The center region at "A" shows extensive secondary cracking normal and parallel to the primary crack direction. Inclined facets are frequently formed at the trailing edge of these secondary cracks. Near the specimen surface at marker "B", secondary cracking along grain boundaries is more frequent. Cracking proceeds along each grain at different elevations or steps.

The specimen T-L orientation i.e, the rolling direction, is shown in Figures 10-13 and illustrates many of the features previously observed. In Figure 10, marker "A" is located at a horizontal crack length of 21.0 mm. Intersecting slip planes, secondary cracking and cyrstallographic cracking are evident in Figure 10b and c. At a marker "A" crack length of 28.0 mm in Figure 11, extensive grain boundary delaminations are noted in Figure 11b. Surface rubbing produced the black wear particles that are illustrated in Figure 11c.

Metallographic through-the-thickness sections of T-L fracture surfaces are presented in Figure 12. The crack growth direction is into the page for Figure 12a and b. Figure 12a shows the center thickness fracture surface is produced by a combination of long range slip and cracking along grain boundaries. Near the specimen sides, i.e., the free surface, secondary cracking along grain boundaries occurs less frequently and fracture occurs by the linkup of long range slip.

The region of T-L unstable crack growth is illustrated in Figure 13. Fracture follows grain boundaries in Figure 13b with intermediate regions of shear and tensile dimples are evident in Figure 13c.

2090-T8E41 RESULTS.

The progressive changes in the 2090 L-T fracture surface are illustrated in Figures 14 and 15. Figure 14a shows markers "A", "B" and "C" at crack lengths of 16.0, 22.0, and 30.0 mm respectively. A center thickness triangular shaped region of increased surface roughness is defined by the black wear debris clinging to this surface. Figure 14b shows that secondary cracking occurs less frequently than for the 8090 L-T surface. Tearing and fine patches of "brittle" striations were frequently observed. Views of the fracture surfaces at markers "B" and "C" are presented in Figure 15a and b respectively. A transition to a crystallographic mode of FCG is illustrated in these photographs. Higher magnification views of the latter surface are shown in Figure 15c and d. The region of unstable crack growth is shown in Figure 16. Fracture has not proceeded along grain boundaries to the same degree as noted for the 8090 material.

Marker "A" is located at a crack length of 20.0 mm on the 2090 T-L fracture surface in Figure 17a. The change in the center thickness surface roughness is more abrupt than was observed for the L-T orientation. Figure 17b depicts this change in more detail. A narrow band of planar steps separates the rough and relatively smoother surfaces. The latter surface is shown in greater detail in Figure 17c.

Marker "A" at a crack length of 23.0 mm in Figure 18a is shown at higher magnification in Figure 18b. Secondary cracking along grain boundaries allows crack extension to occur at different elevations.

Misalignment of mating fracture surfaces produces wear particles by abrasion as illustrated in figure 18c. Examples of this wear type are presented in Figures 19a and b. The region of unstable crack growth shown by Marker "B" in Figure 18a is presented in greater detail in Figure 19c and d. Secondary cracking along grain boundaries occurs more frequently than was observed for the L-T orientation.

DISCUSSION.

Inspection of the fracture surfaces has provided insight into Al-Li crack extension mechanisms. Additional work will attempt to correlate the observed fractographic features with DREP's crack growth rate data.

ACKNOWLEGEMENT.

This research was supported by the Defense Research Establishment Pacific's Material Research Department.

REFERENCES.

(1) Z, Zhai, Morrison, J., "Constant Amplitude Fatigue Growth in Aluminum-Lithium", Defense Research Establishment Pacific,

(2) Venkateswara Rao, K.T., Yu, W., Ritchie, R.O.,"Cryogenic Toughness of Commercial Aluminum-Lithium Alloys: Role of Delamination Toughening", Metallurgical Transaction A, Vol. 20A, 1989, pp. 485-497.

(3) Wu, X. J., Wallace, W., Raizenne, M. D., Koul, A. K., "The Effects of Orientation on Fatigue Crack Growth and Fracture in 8090 Aluminum-Lithium Plate," Institute of Aerospace Research, Report LTR ST 1912, National Research Council, 1993, pp. 1-45.

(4) Morrison, J.,"Directionality of Strength and Toughness in Aluminum-Lithium Plate and Extrusion", Defense Research Establishment Pacific,

(5) "Pole Figure and Orientation Distribution Function Analysis of Four Al-Li Alloy Specimens", Lambda Research Inc., Report 0625-001, April 1993.

(6) Pao, P.S., Cooley, L.A., Imam, M.A., Yoder, G.R., "Fatigue-Crack Growth in 2090 Al-Li Alloy", Scripta Metallurgica, Vol. 23, 1989, pp. 1455-1460.

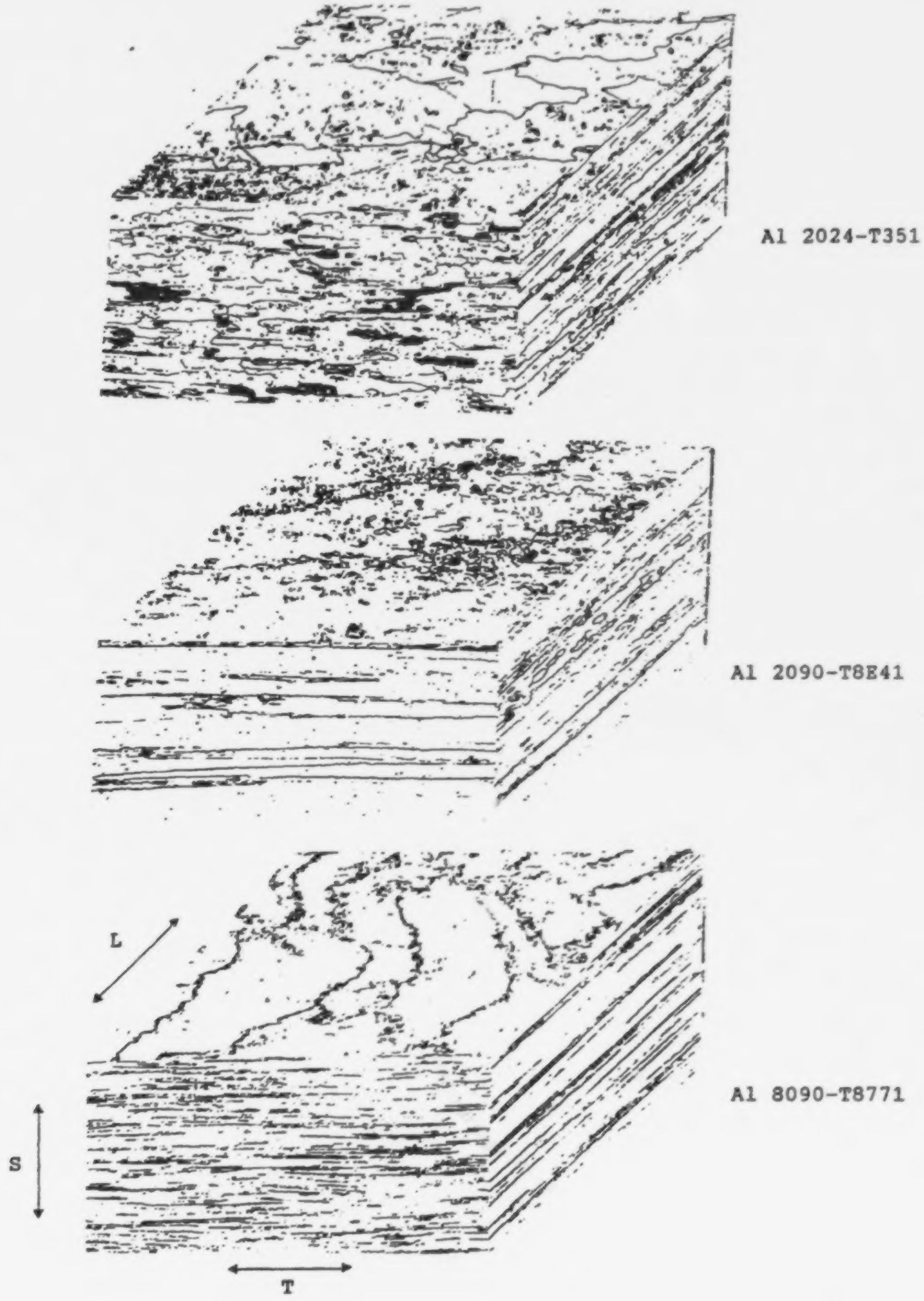
Al 2024-T351
Al 2090-T8E41
Al 8090-T8771
L
S
T

Figure 1.
Grain structure of Al 2024-T351, 2090-T8E41 and 8090-T8771 alloys.

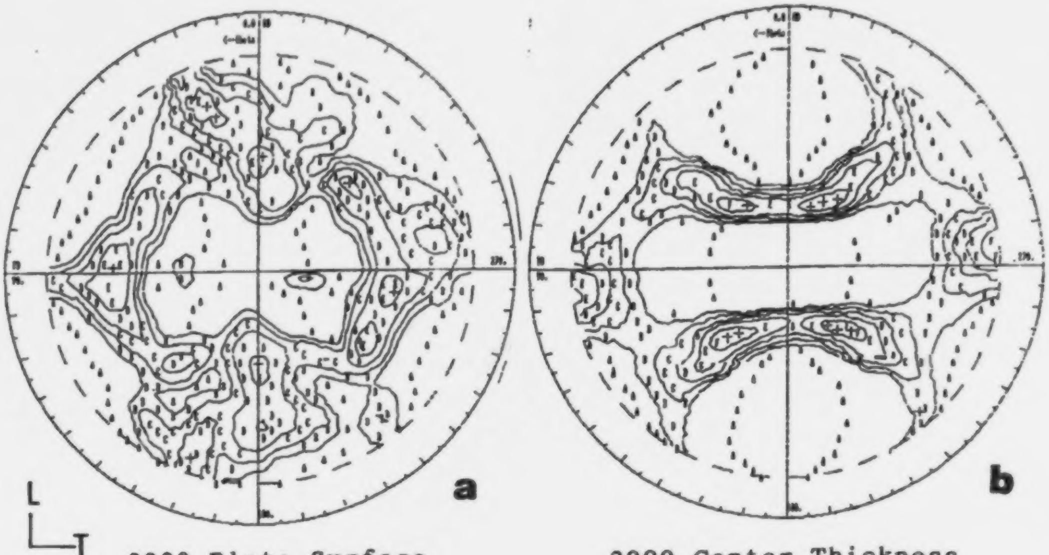

2090 Plate Surface

2090 Center Thickness

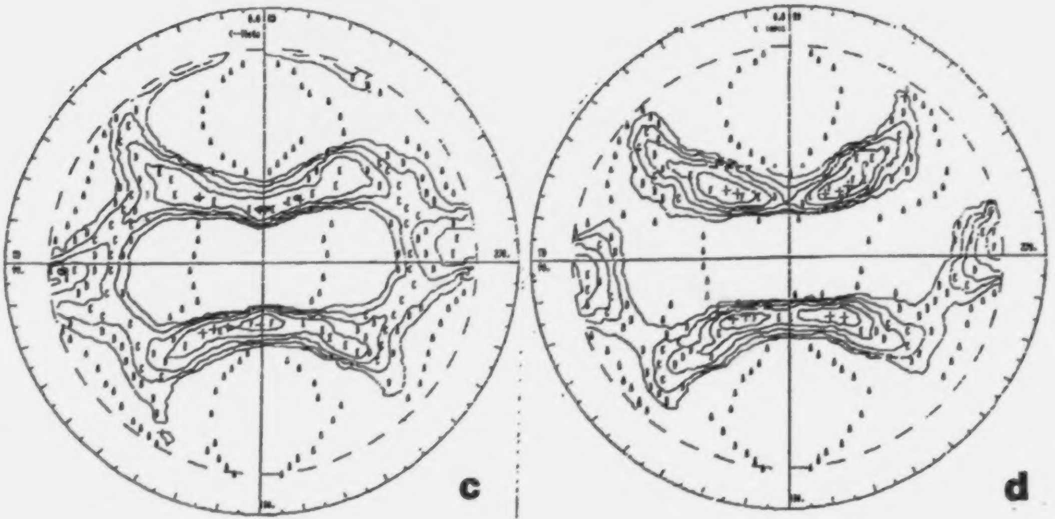

8090 Plate Surface

8090 Center Thickness

Figure 2.
Al-Li 2090-T8E41 and <111> plane pole figures
for the plate surface and center thickness positions.

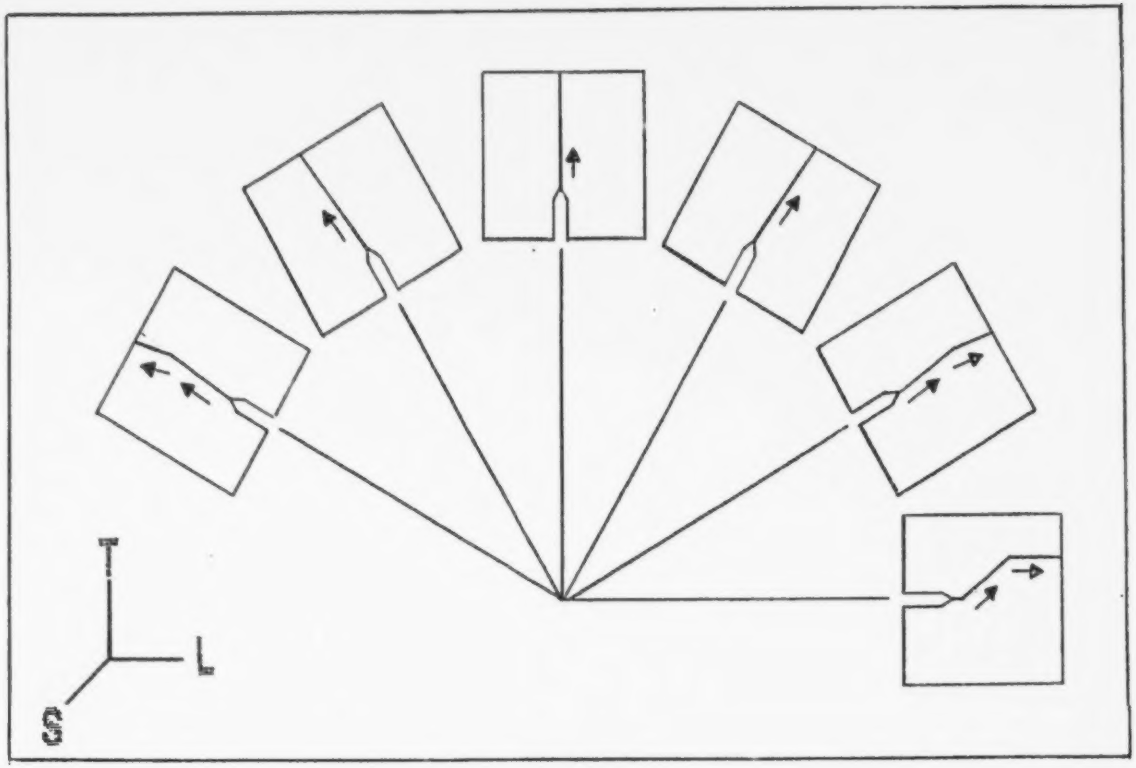

Figure 3.
Compact tension specimen orientation and direction of 8090-T8771 crack path deviation.

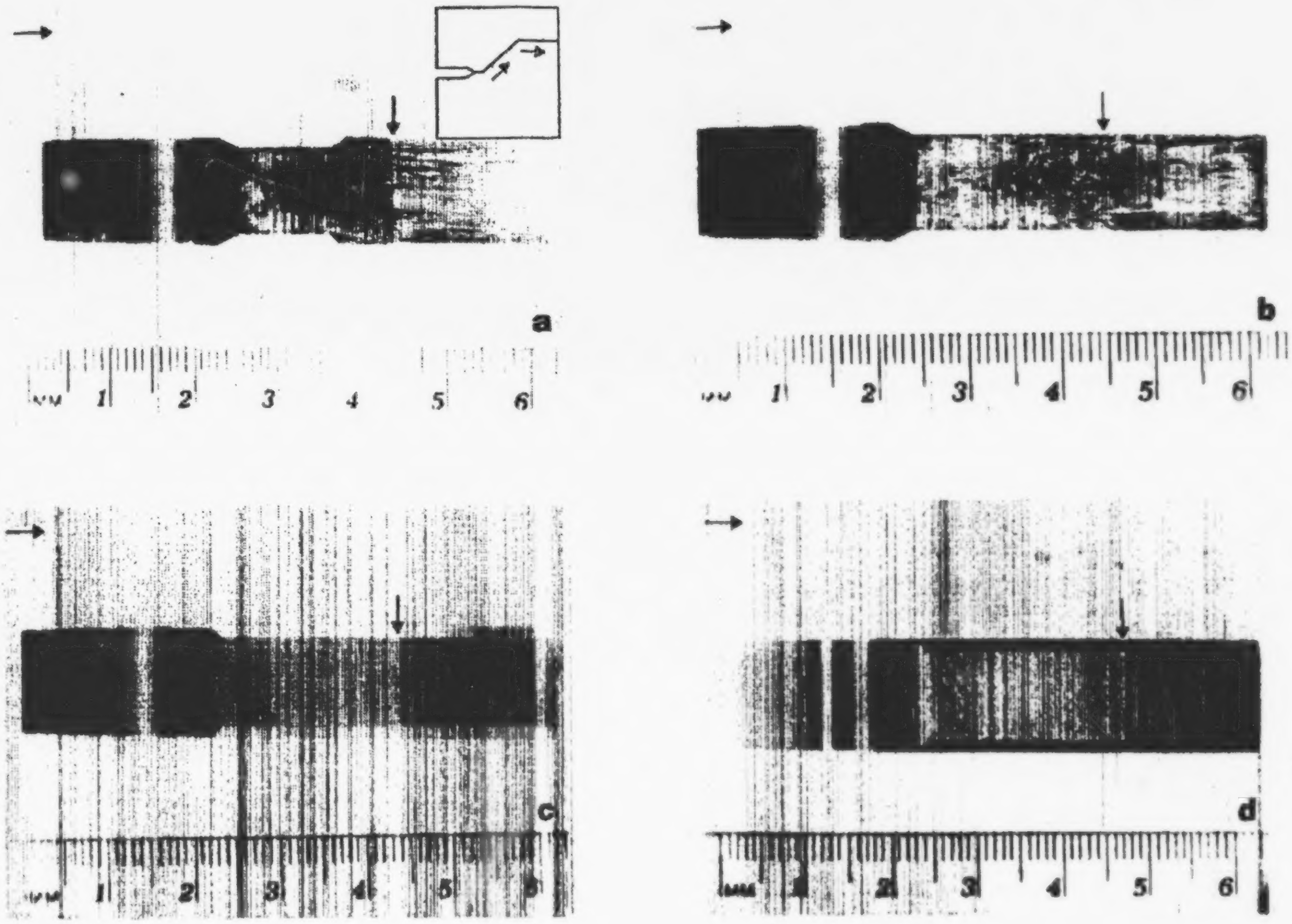

Figure 4.
Comparison of 8090-T8771 and 2024-T351 compact tension fracture surfaces. Al-Li 8090 T-L and L-T fracture surfaces are presented in (a) and (b) respectively. Al 2024-T351 T-L and L-T specimen fracture surfaces are shown in (c) and (d).

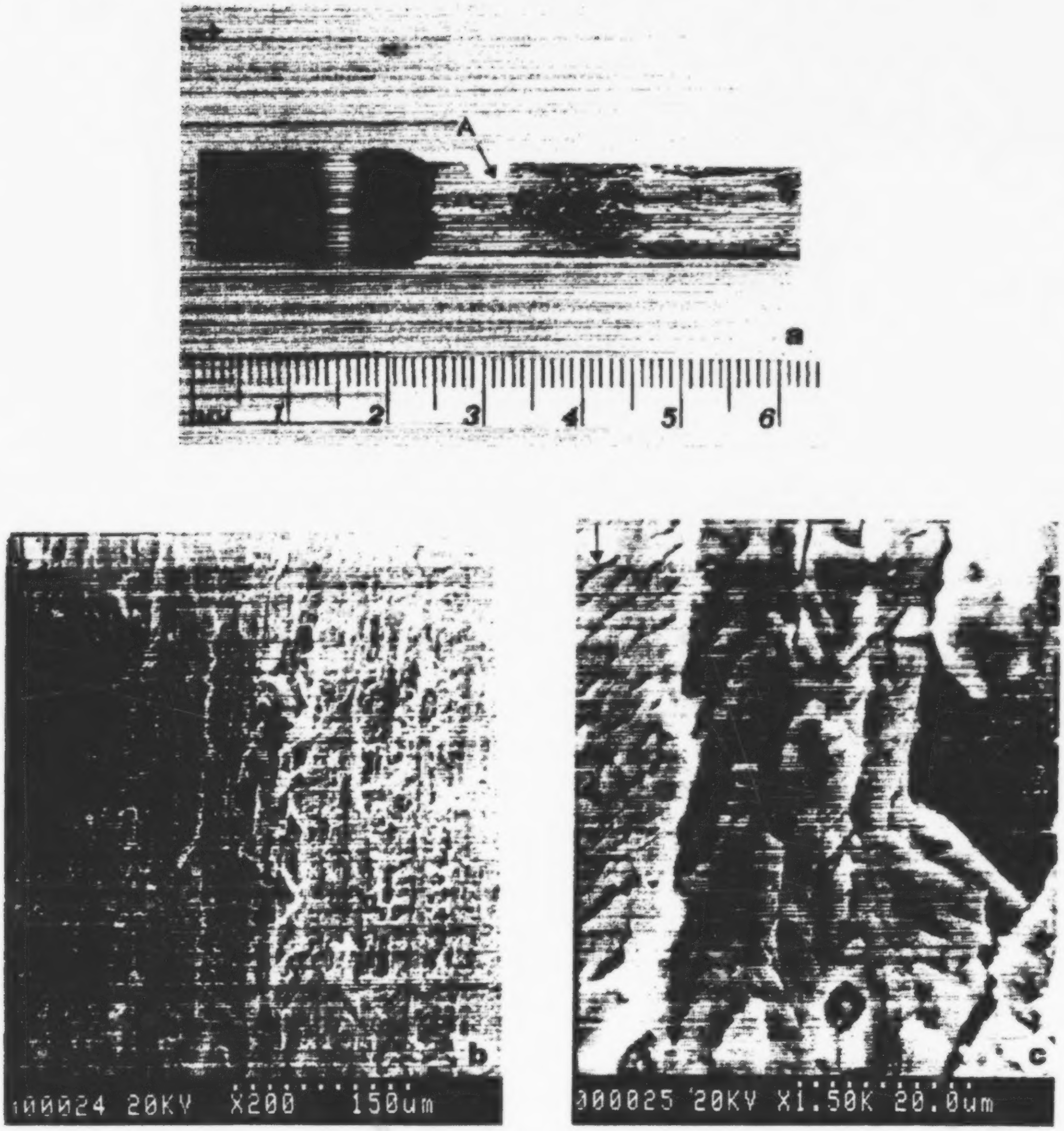
A
a
1
2
3
4
5
6
b
000024 20KV X200 150um
c
000025 20KV X1.50K 20.0um

Figure 5.
8090-T8771 L-T fracture surface is shown in (a). Marker "A" at a crack length of 19.0 mm is presented in greater detail in (b) and (c).

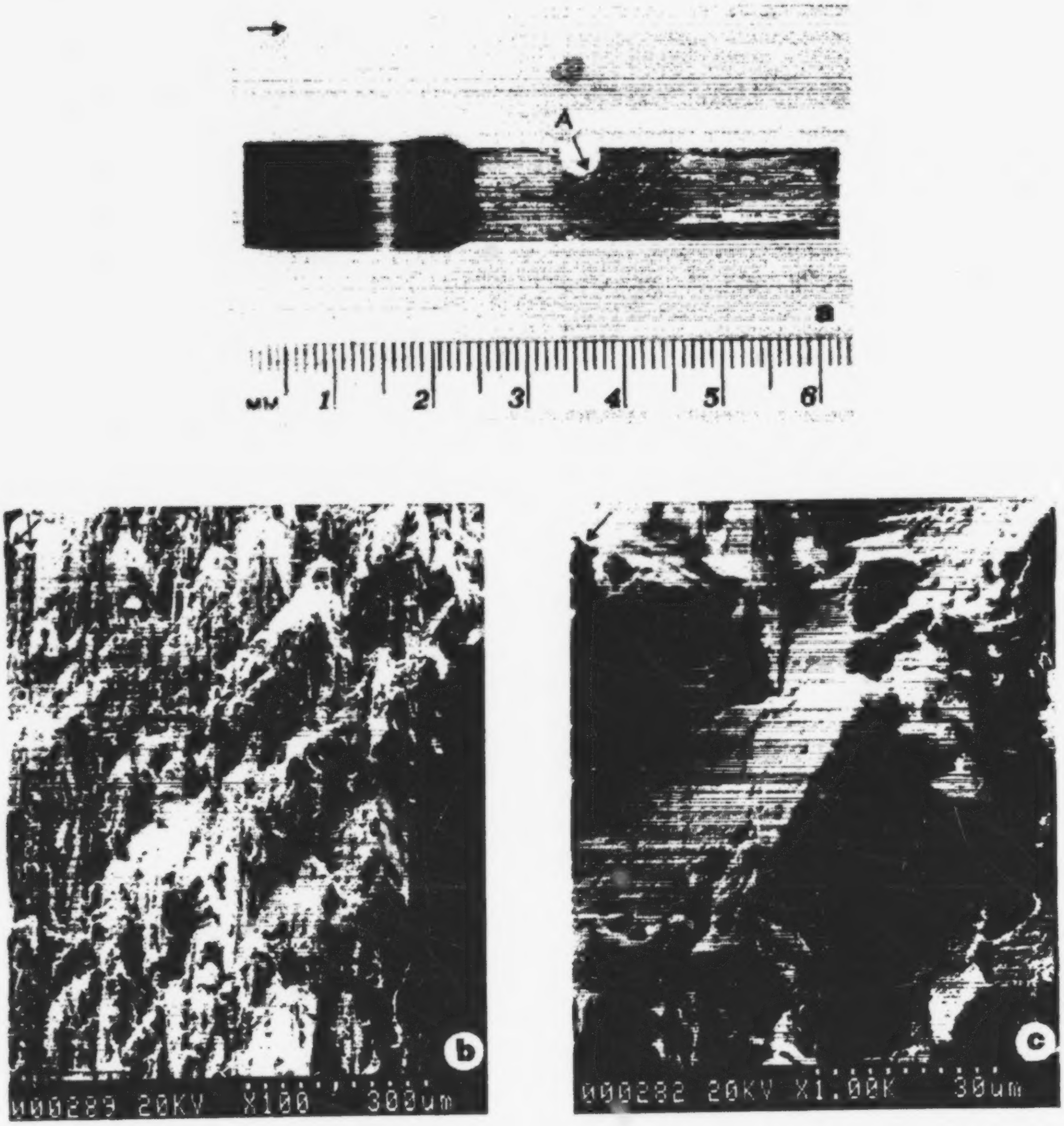
A
a
mm 1 2 3 4 5 6
b
W00289 20KV X100 300um
c
W00282 20KV X1.00K 30um

Figure 6.
8090-T8771 macroscopic surface roughness at marker "A" (crack length = 24.0 mm) in (a) is shown at higher magnification in (b) and (c).
Crack extension along crystallographic planes produces the geometric features that extend across grain boundaries.

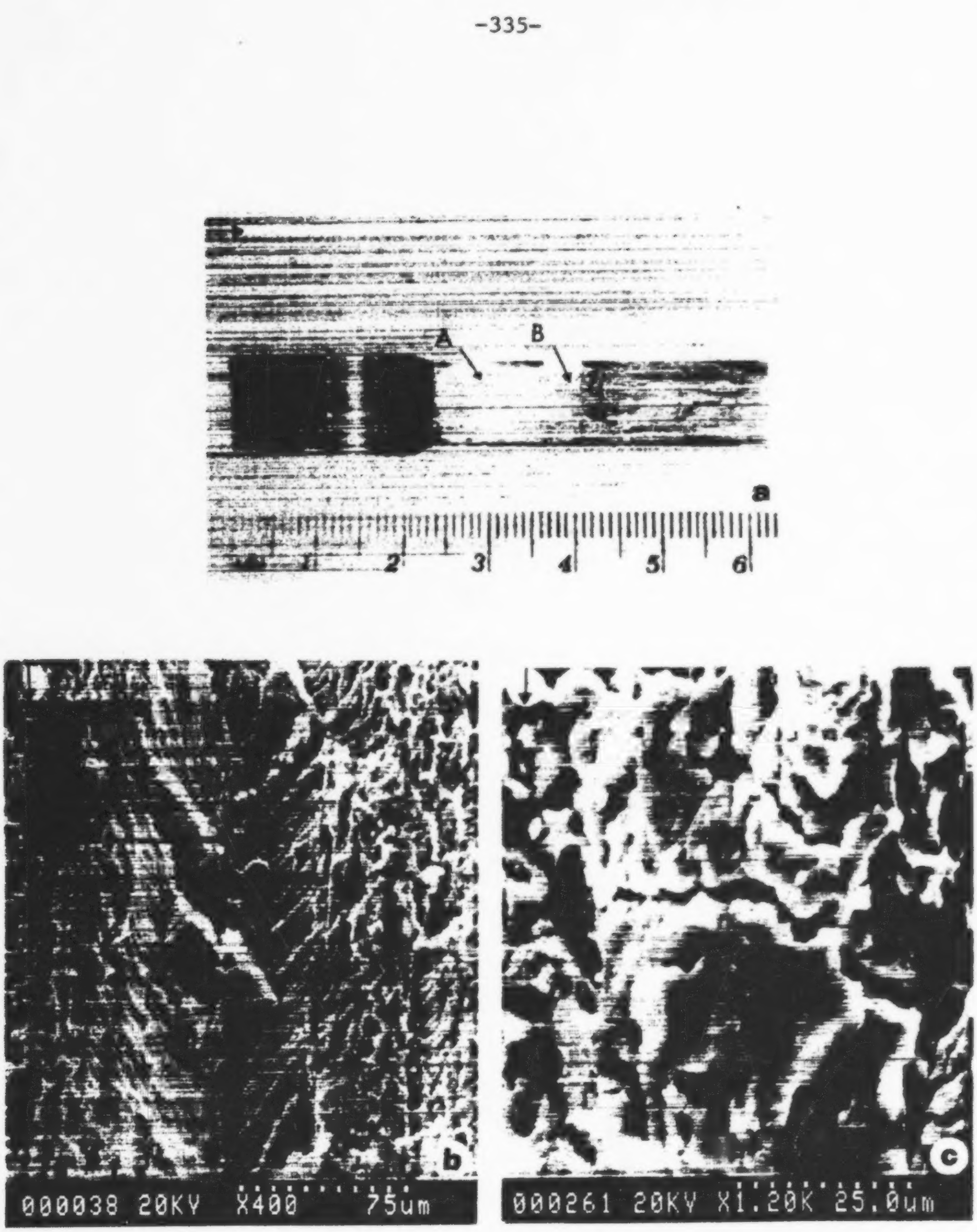
A
B
a
1
2
3
4
5
6
b
000038 20KV X400 75um
c
000261 20KV X1.20K 25.0um

Figure 7.
8090-T8771 fracture surface at 30 degrees to the transverse direction. Detailed views at markers "A" and "B" in (a) are shown in (b) and (c) respectively. Crystallographic cracking at a crack length of 19.0mm was not frequently observed in (b). Secondary cracks perpendicular to the crack growth direction are evident in (c) at a crack length of 28.0 mm.

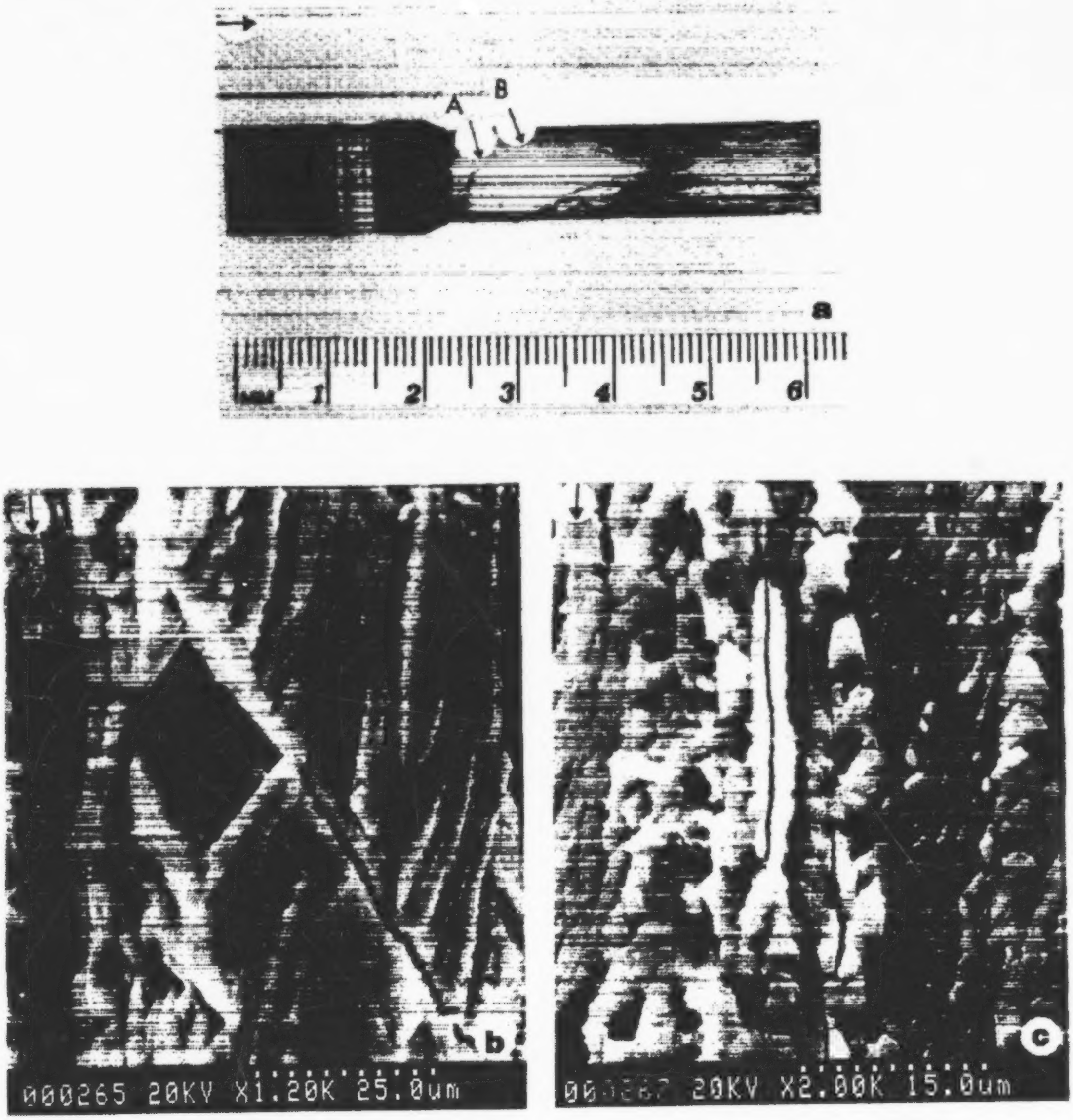
A
B
1
2
3
4
5
6
a
b
000265 20KV X1.20K 25.0um
c
20KV X2.00K 15.0um

Figure 8.
8090-T8771 fracture surface at 60 degrees to the transverse direction. In (b), facet formation at a secondary crack is shown at at a crack length of 15.0mm for marker "A". Secondary cracks parallel to the crack growth direction were observed near the specimen free surface in (c) for marker "B" at 19.0mm crack length.

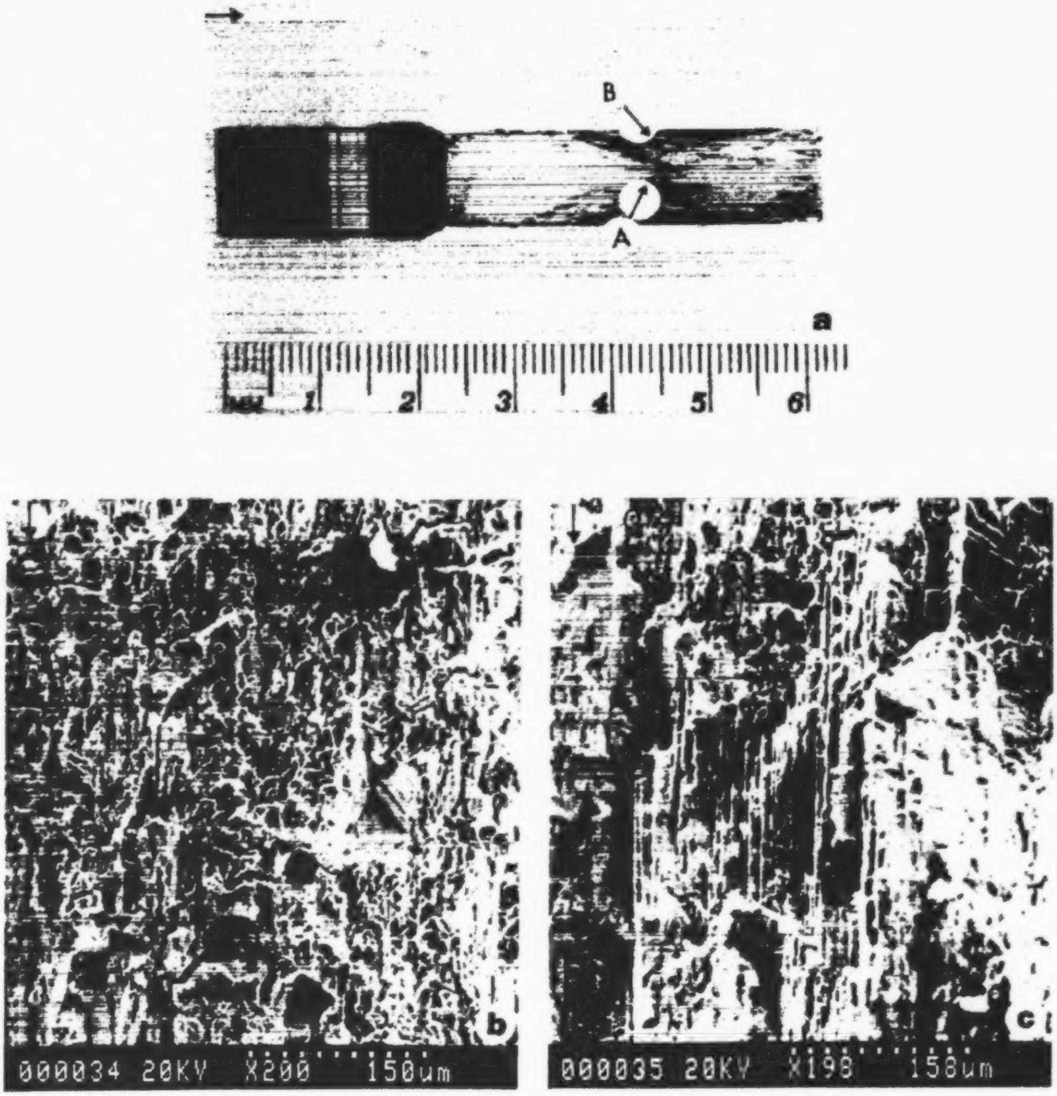
B
A
a
1
2
3
4
5
6
b
000034 20KV X200 150um
c
000035 20KV X198 158um

Figure 9.
Another view of the 8090-T8771 60 degree orientation at a 34.0 mm crack length. Marker A shows extensive secondary cracking occurred at the specimen interior in (b). Cracking along grain boundaries that occurred nearer to the surface is illustrated in (c).

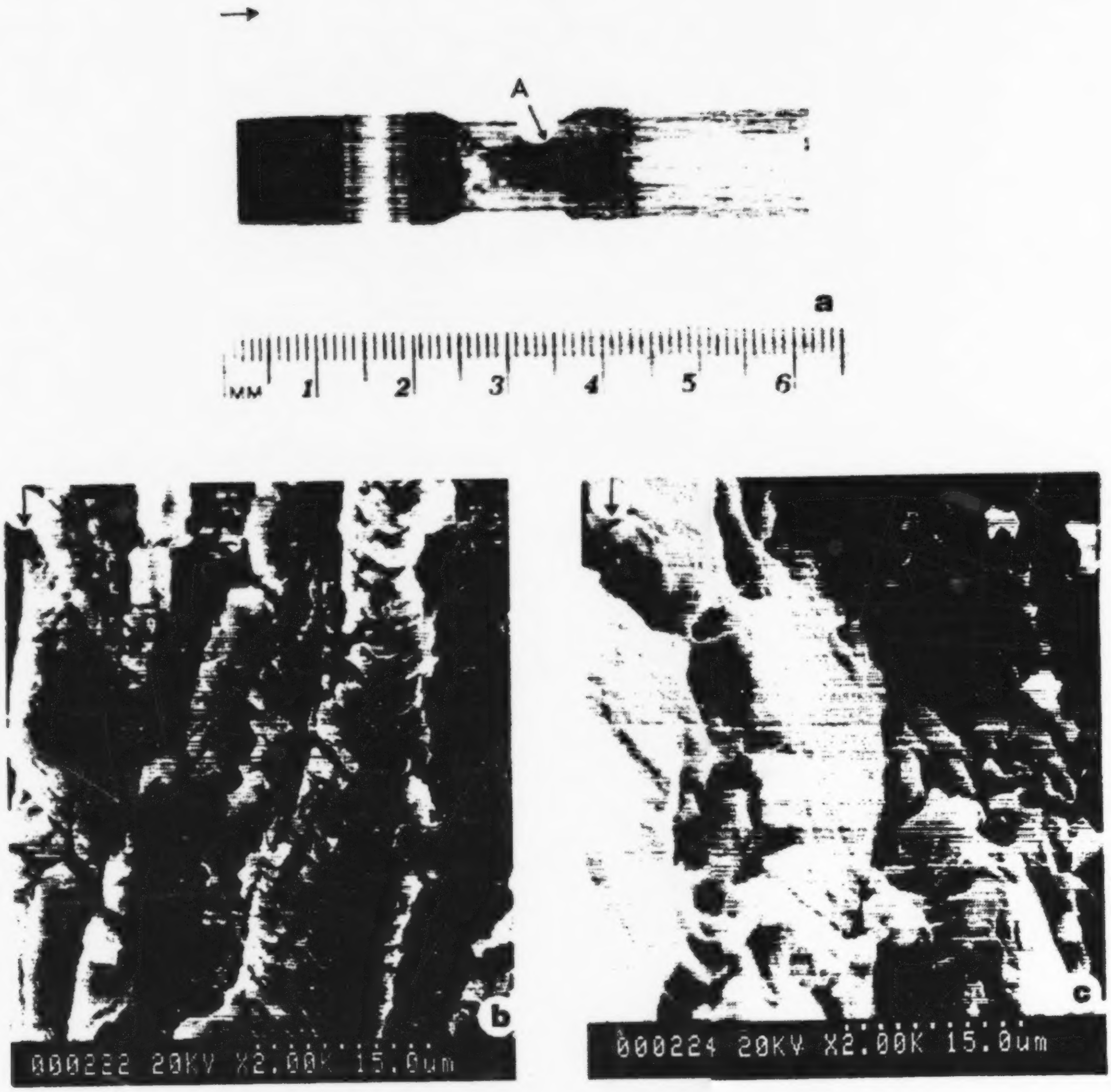
A
a
MM 1 2 3 4 5 6
b
000222 20KV X2.00K 15.0um
c
000224 20KV X2.00K 15.0um

Figure 10.
8090-T8771 L-T fracture surface shows intersecting secondary cracks followed favourable crystallographic directions for the elongated grain shown in (b). Fine dimples are found on the inclined facet shown in (c).

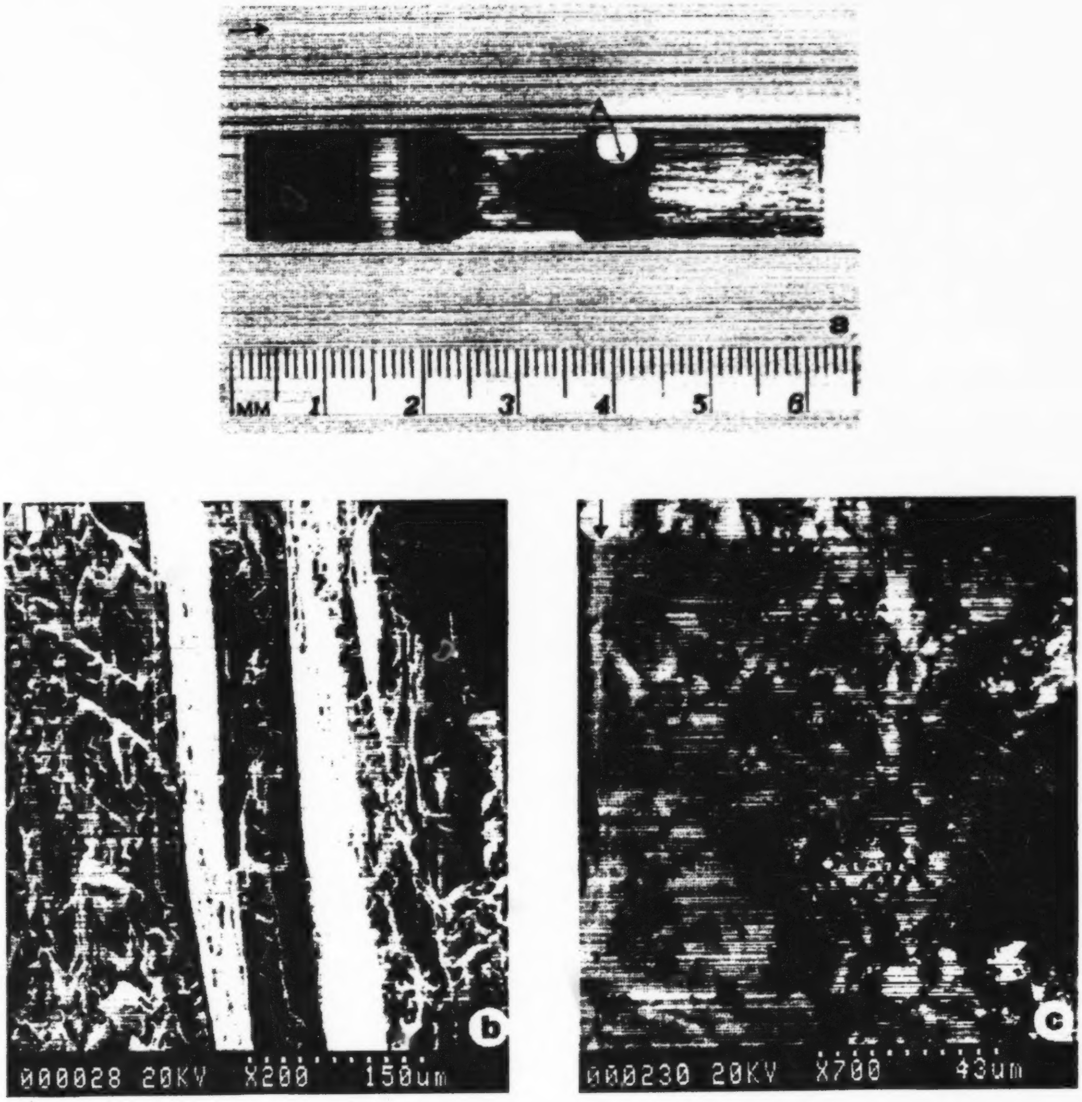
a
MM 1 2 3 4 5 6
b
000028 20KV X200 150um
c
000230 20KV X700 43um

Figure 11.
8090-T8771 L-T fracture surface near final fracture. Secondary cracking along grain boundaries is believed to produce the steps shown in (b). Black powder suspected to be wear and corrosion products are illustrated in (c).

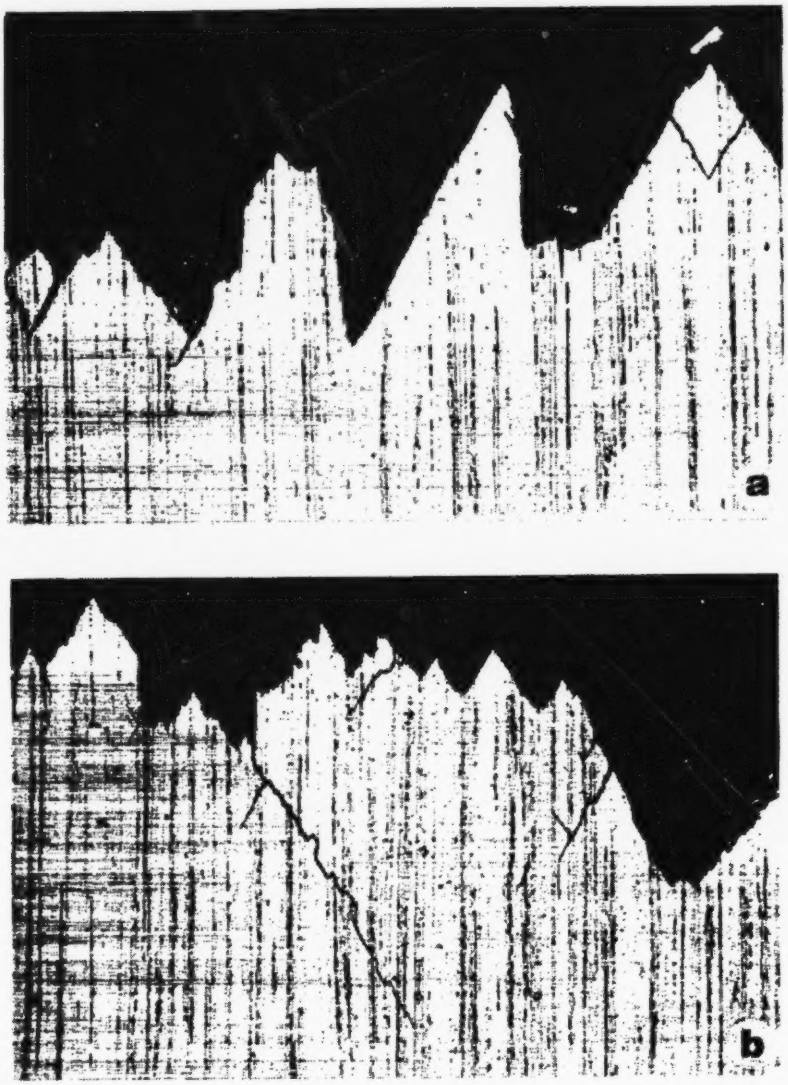

Figure 12.
Through-the-thickness metallographic samples taken from 8090-T8771 T-L fracture surfaces at the center thickness in (a) reveals cracking occurs by slip plane and grain boundary cracking. Near the specimen free surface in (b), grain boundary cracking is reduced.

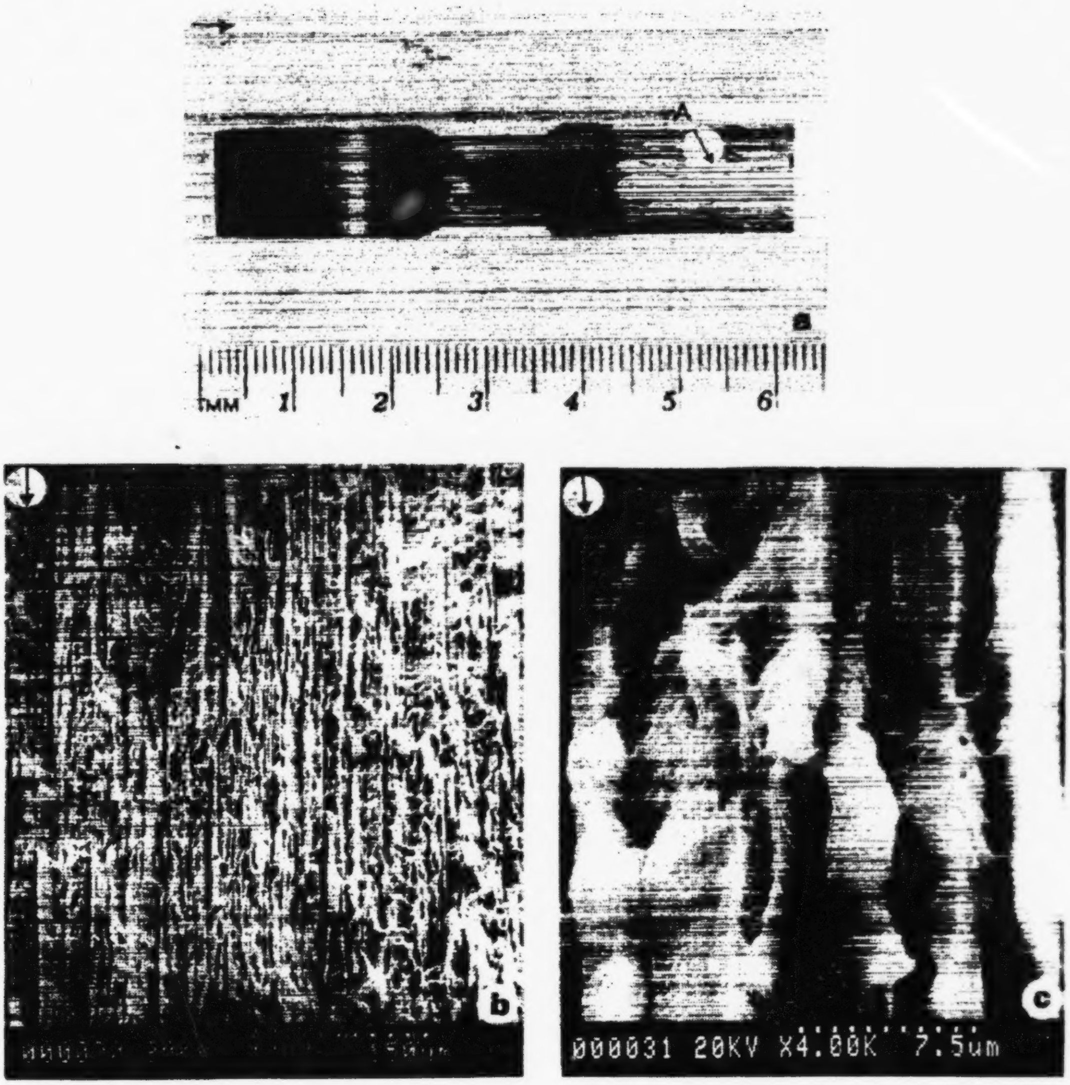
A
a
MM 1 2 3 4 5 6
b
c
000031 20KV X4.00K 7.5um

Figure 13.
8090-T8771 T-L fast fracture region at marker "A" in (a) is shown at higher magnification in (b) and (c). Grain boundaries are evident in (b). Fine dimples cover inclined intermediate regions that end in sharp ridges. These features suggest tensile failure began at the grain boundaries.

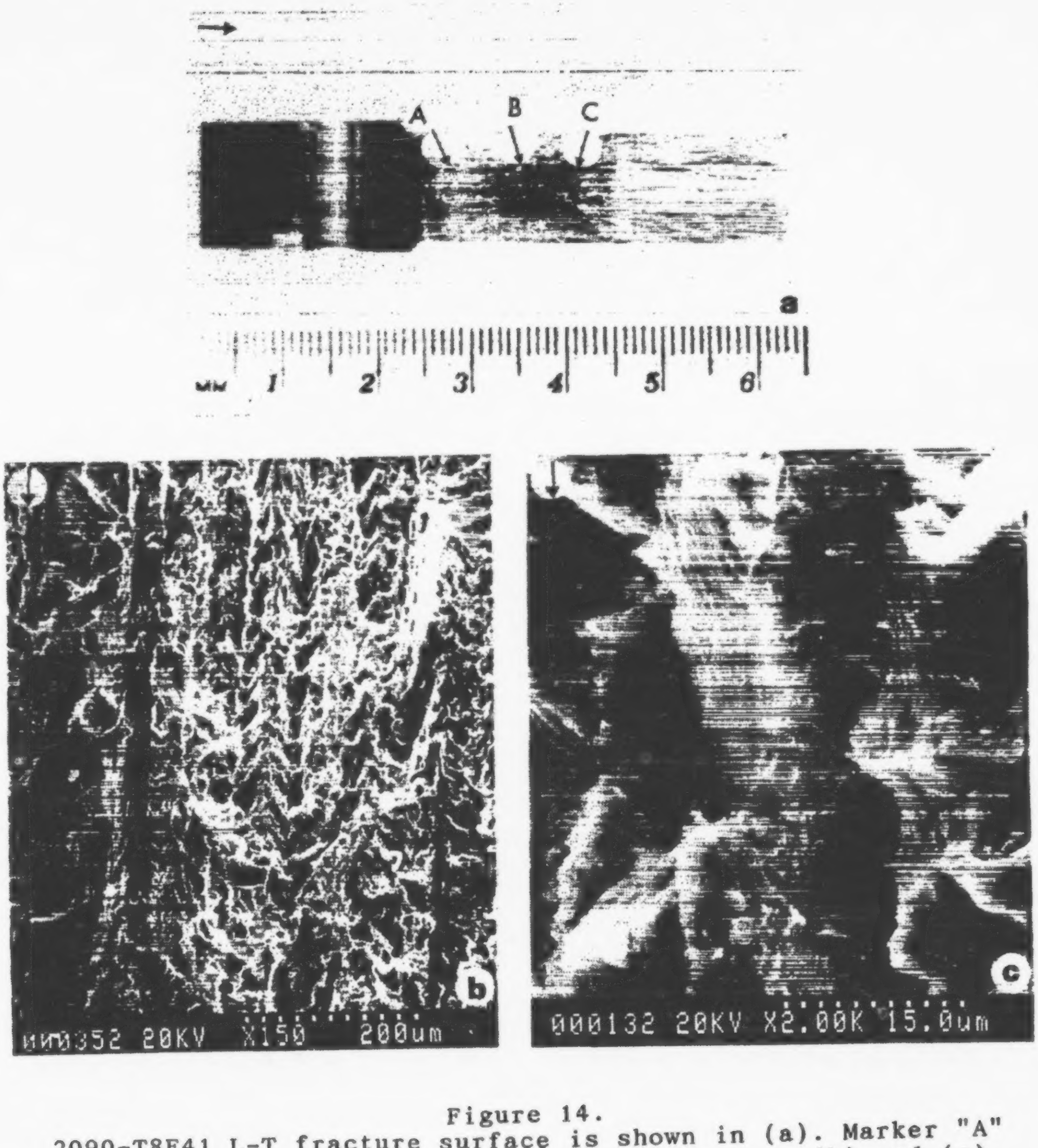
A
B
C
a
mm
1
2
3
4
5
6
b
000352 20KV X150 200um
c
000132 20KV X2.00K 15.0um

Figure 14.
2090-T8E41 L-T fracture surface is shown in (a). Marker "A" at a crack length of 16.0 mm is illustrated in (b) and (c). Tearing and fine patches of "brittle" striations are evident in (c).

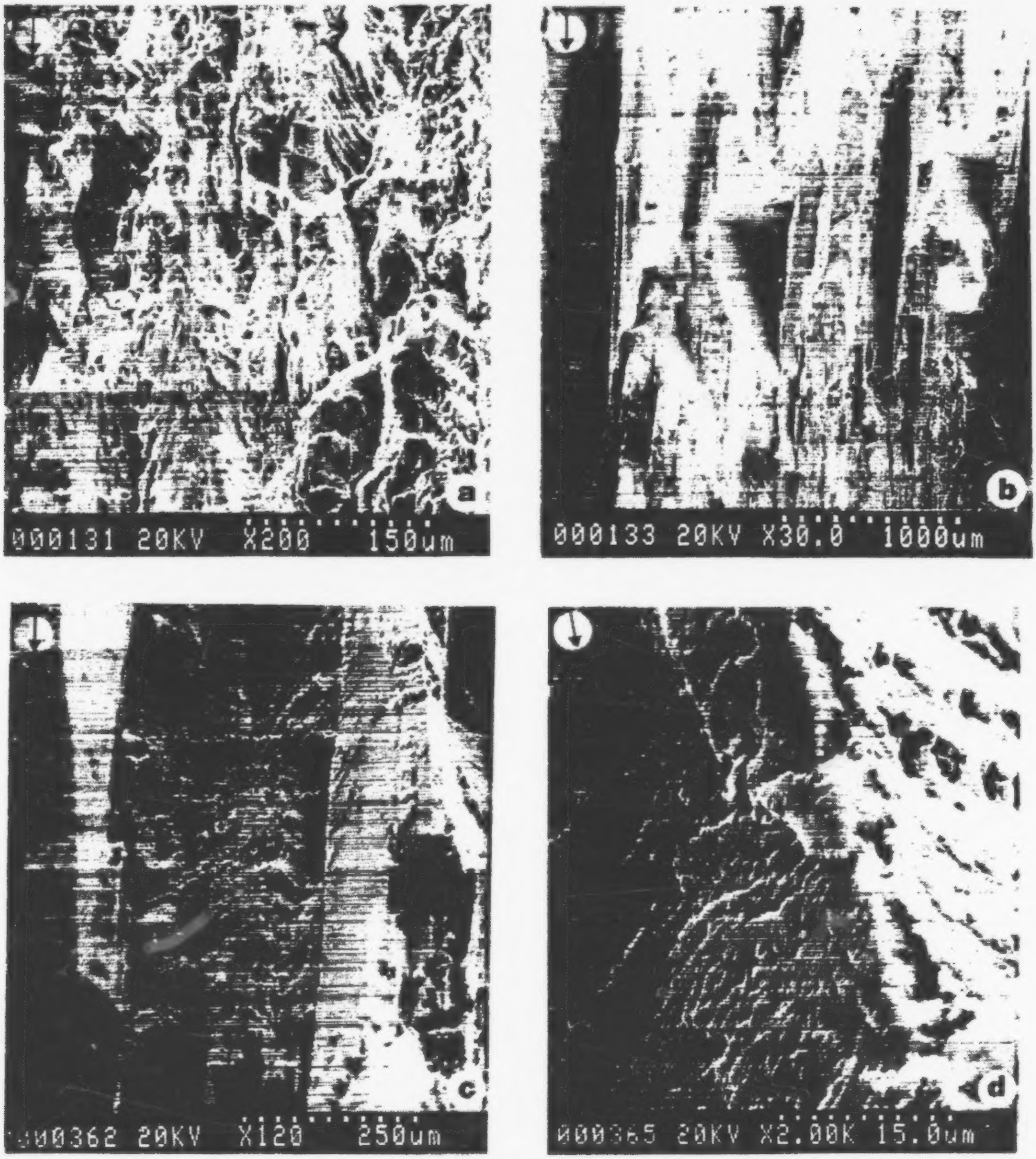
a
000131 20KV X200 150um
b
000133 20KV X30.0 1000um
c
000362 20KV X120 250um
d
000365 20KV X2.00K 15.0um

Figure 15.
2090-T8E41 L-T fracture surface in (a) and (b) are from the marker "B" (22.0 mm crack length) and "C" (30.0 mm crack length) locations respectively in Figure 15. Increased tearing and a transition to crystallographic cracking are present. Higher magnification of (b) are presented in (c) and (d).

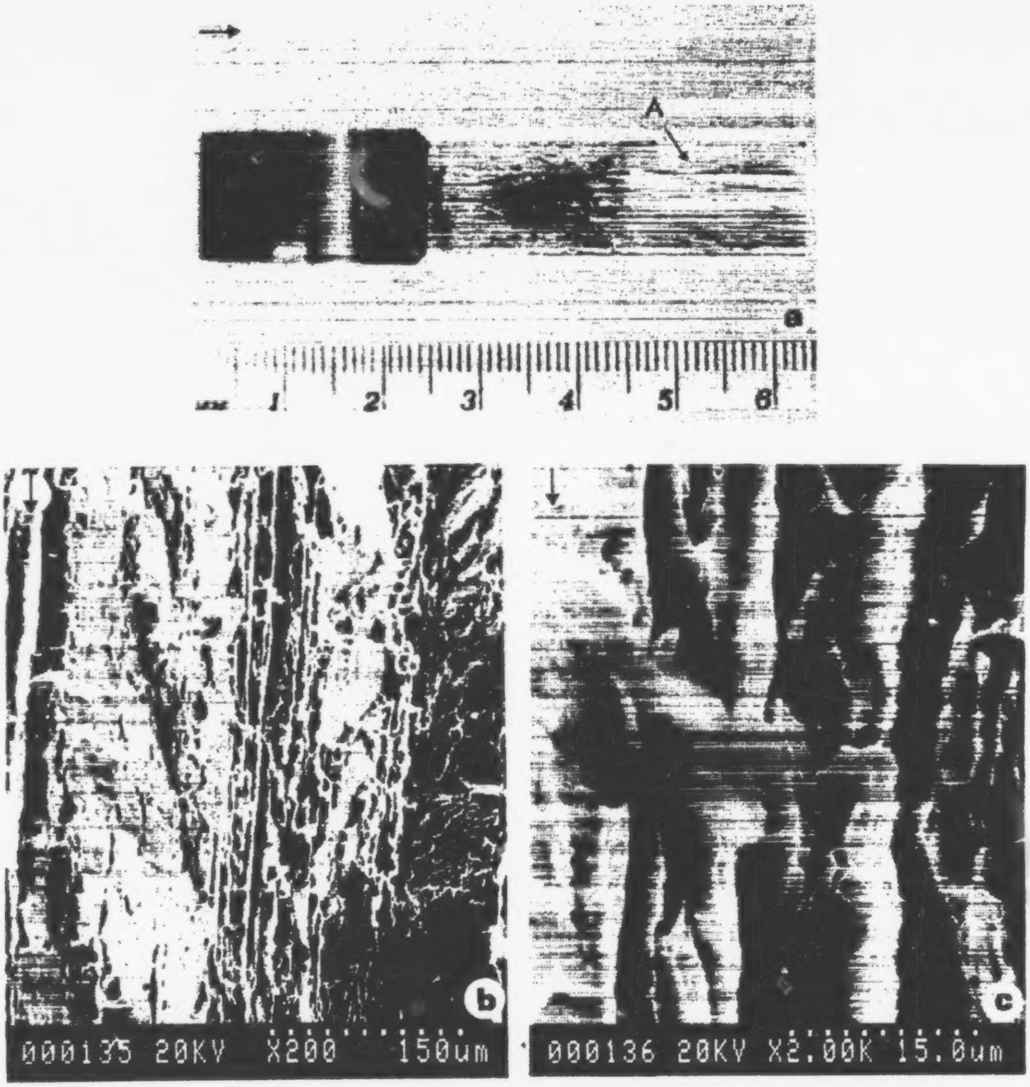
A
a
1
2
3
4
5
6
b
000135 20KV X200 150um
c
000136 20KV X2.00K 15.0um

Figure 16.
The fast fracture region of a 2090-T8E41 fracture surface is shown in (a)-(c). Fracture has not been localized at the grain boundaries to the same degree as observed for the 8090-T8771 alloy.

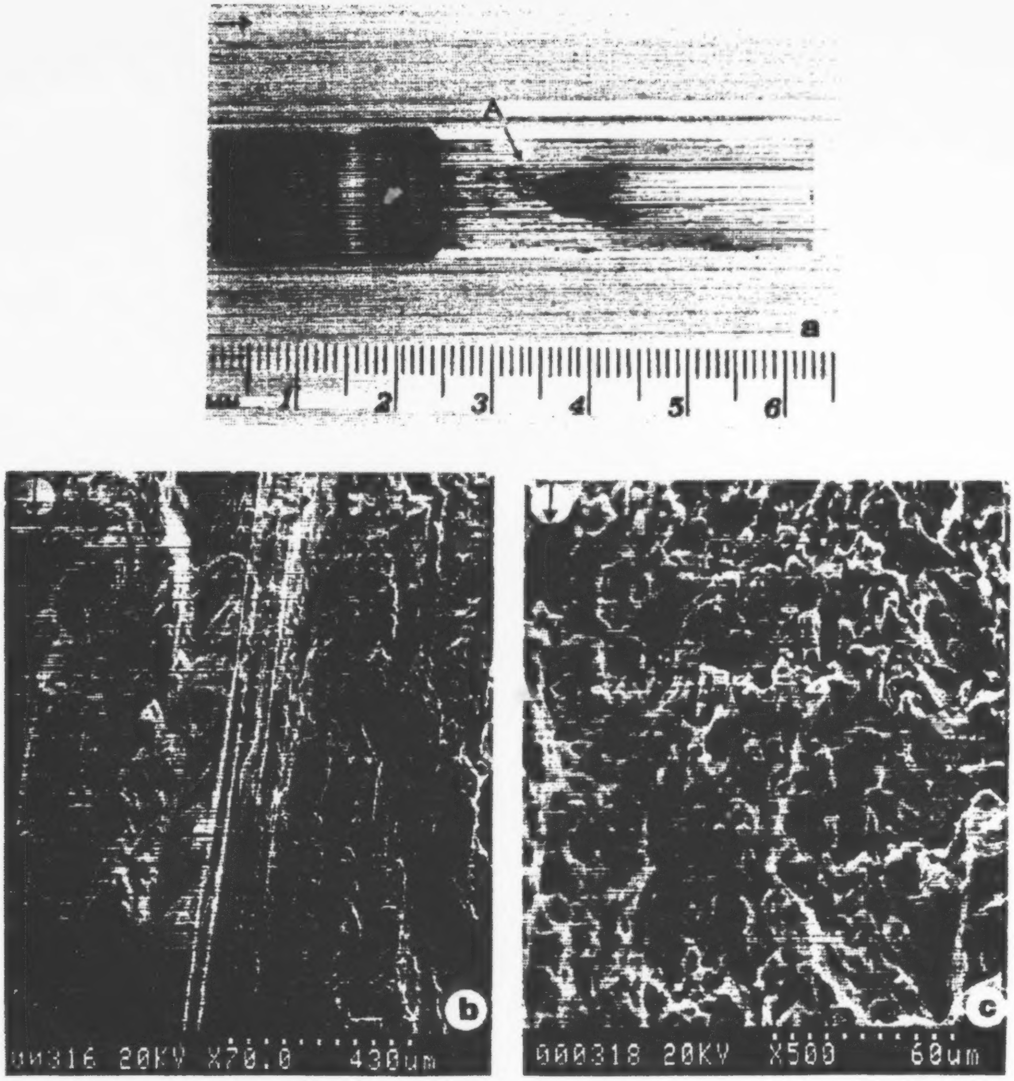
A
a
1
2
3
4
5
6
b
000316 20KV X70.0 430um
c
000318 20KV X500 60um

Figure 17.
Marker "A" on a 2090-T8E41 T-L crack length of 20.0 mm is shown in greater detail in (b). A sharp transition in surface roughness is evident. A view of the macroscopically smooth surface on the right of (b) is detailed in (c).

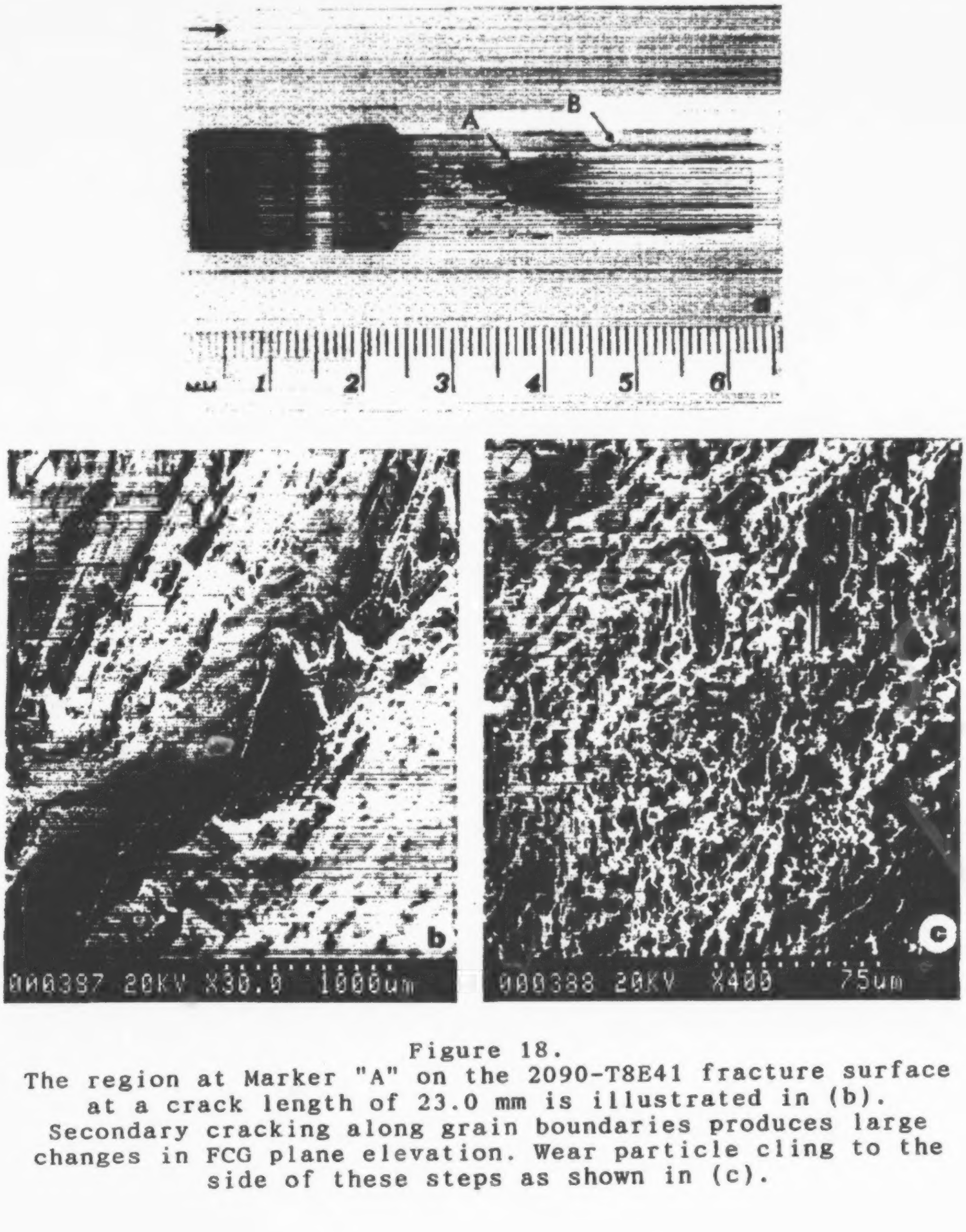
A
B
a
mm 1 2 3 4 5 6
b
000387 20KV X30.0 1000um
c
000388 20KV X400 75um

Figure 18.
The region at Marker "A" on the 2090-T8E41 fracture surface at a crack length of 23.0 mm is illustrated in (b). Secondary cracking along grain boundaries produces large changes in FCG plane elevation. Wear particle cling to the side of these steps as shown in (c).

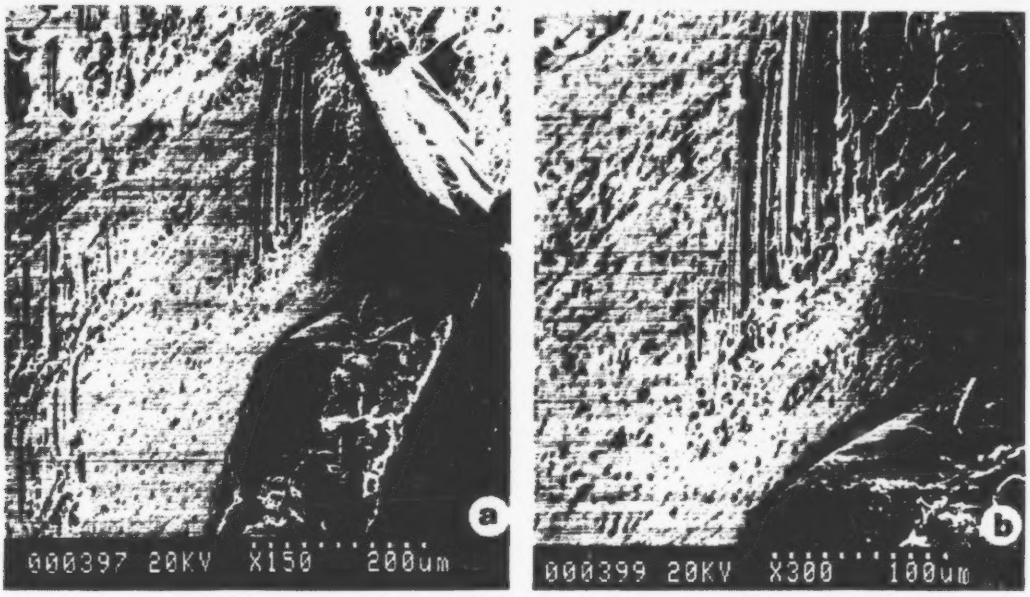
a
000397 20KV X150 200um
b
000399 20KV X300 100um

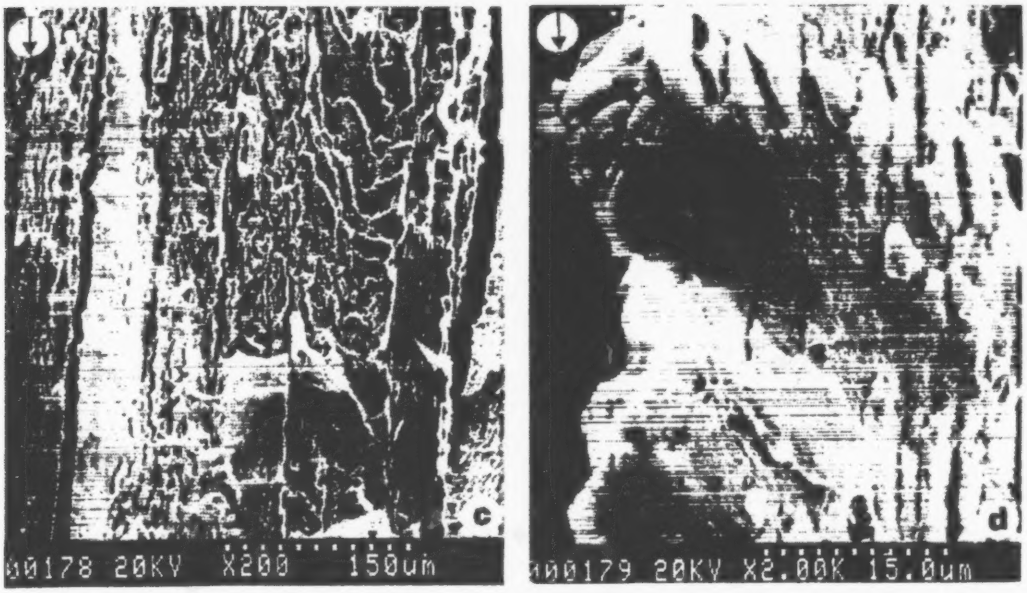
c
00178 20KV X200 150um
d
000179 20KV X2.00K 15.0um

Figure 19.
Misalignment of mating fracture surfaces produce wear particles by abrasion as presented in (a) and (b).
The fast fracture region at marker "B" in Figure 19 is shown in greater detail in (c) and (d).

141648

16.

"Fatigue Crack Investigation of 2090 and 8090 Aluminum-Lithium Alloys"

D.A. Hull

Engineering Material Research, Toronto,

M.D. Raizenne

IAR / NRC, Ottawa, Ont.

FATIGUE CRACK GROWTH OF
2090 AND 8090 ALUMINUM-LITHIUM ALLOYS.

BY

D.A. HULL (1)
M.D. RAIZENNE (2)

DU

Constant and variable amplitude fatigue crack growth rates in two Aluminum-Lithium alloys, 2090-T8E41 and 8090-T8771 were compared with an aluminum-copper 2024-T351 alloy. The damage tolerant, aerospace grade 2024-T351 was chosen to provide baseline data.

T-L compact tension specimens, W = 50.8 mm and B = 11.2 mm were machined from 2024 and 8090 12.5 mm thick plate and from 2090 14.75 mm thick plate. Specimen geometry met the requirements of the ASTM Standard Test Method for the Measurement of Fatigue Crack Growth Rates, (E647-92). A chevron fatigue crack starter notch facilitated pre-cracking.

The specimens were evaluated on a computer controlled, servo-hydraulic 165 kN load frame. Crack mouth opening displacement was measured with a MTS clip gauge. Clip gauge knife edges were attached to the specimens with screws. Travelling microscopes that were used to measure surface crack lengths, had a reading accuracy of 0.01 mm. All experiments were conducted at ambient temperature and relative humidity.

A compliance method of determining crack length was used. Compliance calibration curves were determined from a minimum of two specimens. A Weibull curve was fit to specimen compliance and optical measurements of the crack length's horizontal component. Curves were constructed for each alloy. Correlation coefficients

---

(1) Engineering Material Research, Downsview Ontario
M3J 2S1

(2) Institute of Aerospace Research, National Research Council, Ottawa, Canada, K1A 0R6

greater than 97% indicated a satisfactory "goodness of fit" had been attained. A 2024 compliance versus crack length curve is shown in Figure 1.

Three load sequences were employed to reveal material behaviour. These sequences included, ΔK decreasing and increasing, single block overload and a modified version of FALSTAFF. A 10 Hz triangular waveform was used for all of the sequences. The ΔK decreasing threshold and ΔK increasing experiments were conducted in accordance to E647-92 recommmendations. The single block overload consisted of 990 constant amplitude cycles followed by ten 10% overload cycles.

The Fighter Aircraft Loading STAndard For Fatigue (FALSTAFF)(1) simulates the loads experienced by a fighter aircraft's lower wing skin near the wing root over 200 flights. Freedom of movement in the specimen clevis grip pins required FALSTAFF compressive loads to be set to zero. Consequently a modified FALSTAFF Tension (FALSTAFFT) only sequence was used.

Specimen fracture surfaces were inspected with a Scanning Electron Microscope and metallographic surfaces were prepared to determine grain structure.

RESULTS

Typical 2024, 2090 and 8090 ΔK applied decreasing and increasing crack growth rate (FCGR) data is presented in Figure 2. More scatter in the 8090 FCGR was observed relative to the two other alloys. In terms of decreasing FCGR at constant ΔK the alloys are ranked in the order of 2024, 2090 and 8090. Consequently, the 8090 alloy has the lowest FCGR for the ΔK applied data presented.

Comparison of 2024 single block overload and constant amplitude FCGR in Figure 3 does not reveal a significant difference. However, a similar 2090 comparison in Figure 4 reveals a noticeable reduction in FCGR. A period of constant FCGR creates a plateau in the da/dN versus ΔK plot. Limited 8090 single block overload data was not available for comparison. Single block overload crack length versus cycles for the 2024 and 2090 alloys are shown in Figure 5.

FALSTAFFT crack length versus cycles are presented in Figure 6.

Metallographic samples for the 2024-T351, 2090-T8E41 and 8090-T8771 materials were prepared from the plate mid-section and etched with Kellor's reagent to reveal grain structure.- See Figure 7. Grain recrystallization in the Al-Li alloys is inhibited by the presence of Zr (2) that leads to the large pancake shaped grains in the Al-Li alloys. The aligned Al-Li grain boundaries are visible in both the T-S and L-S planes.

Fracture surface features for the single block overload and FALSTAFFT surfaces are presented in the following figures. The arrow at the top left corner of each figure shows the local crack direction. Magnification and a scale are found at the lower right corner of the figure.

Single block overload 2024 fracture surfaces are illustrated in Figure 8. The photographs were taken at a crack length of 12.0 mm. An overview of the surface is shown in Figure 8(a) where the horizontal crack arrest lines were created during application of the ten 10% overloads. The vertical lines delineate the elongated grain boundaries.
Figures 8(b) and (c) show detailed views of a crack arrest boundary. It is believed that the torn region has occurred during local crack tip deflection around the overload plastic zone. Figure 9 illustrates the 2024 surface appearance at a crack length of 31.0 mm. The wider spacing of the overload fatigue crack striations are adjacent to regions of constant amplitude FCG in Figures 9(b) and (c). Local crack tip deflection around the plastic overload zone is reduced at higher ΔK values.

Views of a 2090 single block overload fracture surface at a 19.0 mm crack length are shown in Figure 10. The regular spacing of the horizontal crack arrest fronts occur every 1000 cycles. Inspection of Figure 10(b) and (c) reveal the "brittle" striations are less distinct than the 2024 striations. A secondary crack has formed at a grain boundary triple point as illustrated in Figure 11. Decreasing crack front arrest line spacing indicates the local crack front slowed down as the tip of the new grain was encountered. The crack front changed direction from approximately 270 to 240 degrees as it crossed into the new grain.

Al 8090-T8771 single block overload crack arrest lines in Figure 12 appear similar to the 2090 fracture surfaces. These photographs were taken at a crack length of 19.0 mm. Surfaces were smoother and cyrstallographic types of crack extension were reduced. Figure 13 illustrates the increasing 8090 fracture surface roughness at a crack length of 22.0 mm. Crystallographic features are frequently bracketed by grain boundaries which limited cyrstallographic feature height. A ridge and region of rubbing contact are shown in Figure 13(a) and these features are presented in greater detail in Figure 13(b) and (c) respectively. Lines believed to correspond to single block overload arrest lines are shown on the side of the ridge. The rubbed region is coated with wear particles and is representative of many areas found on the fracture surface. Macroscopically, the wear particles appear as a loosely adherent black powder.

An overview of FALSTAFFT fracture surface at a crack length of 22.0 mm is shown in Figure 14(a). Detailed views in Figure 14(b) and(c), allows inspection of the striation structure. Secondary cracks that are normal to the primary crack front direction are believed to result from crack deflection at overloads.

In Figure 15, tensile fracture zones were noted near the final fracture on 2090 FALSTAFFT surfaces. The light coloured regions define areas of unstable crack growth that occurred with the changing load magnitude. Fatigue striations are observed to precede regions of ductile tearing and dimpling in Figures 15(b) and (c).

Patches of fatigue striations were noted on two locations of a fast fracture surface in Figure 16. It is believed that reductions in FALSTAFFT load magnitude caused the stress intensity to decrease below the threshold for unstable crack growth for a period of 20-30 load cycles. In Figure 16(b) vertical grain boundary delaminations on the fast fracture surfaces are contrasted with the horizontal secondary crack on the fatigue surface.

Long range secondary cracking that followed grain boundaries was observed on the 8090 fracture surfaces. One of these cracks is presented in Figure 17(a)-(c). Typical FALSTAFFT fracture surface features are shown in Figure 17(d).

CONCLUSIONS

Different FCGR and mode of fracture were observed for the 2090 and 8090 materials when they were evaluated with variable amplitude loading. The 2090 alloy exhibited increasing regions of unstable crack growth during FALSTAFFT evaluation prior to final fracture. Variable amplitude loading resulted in local crack tip deflections and a reduction in crystallographic features found on the fracture surfaces.

ACKNOWLEGEMENT

The first author gratefully acknowledges that this research was supported by the National Research Council of Canada.

REFERENCES.

(1) "FALSTAFF, Description of a Fighter Aircraft Loading Standard for Fatigue Evaluation," Joint publication of Flugzeugwerke Emmen, Switzerland; Laboratorium fur Betriebsfestigkeit (LBF), Germany; National Aerospace Laboratory (NLR), The Netherlands; and Industrie-Anlagen-Betriebsgesellschaft mbH (IABG), West Germany, 1976.

(2) Smith, A.F., "Aluminum-Lithium Alloys for Helicopter Structures," Metals and Materials, August 1987, pp 439-444.

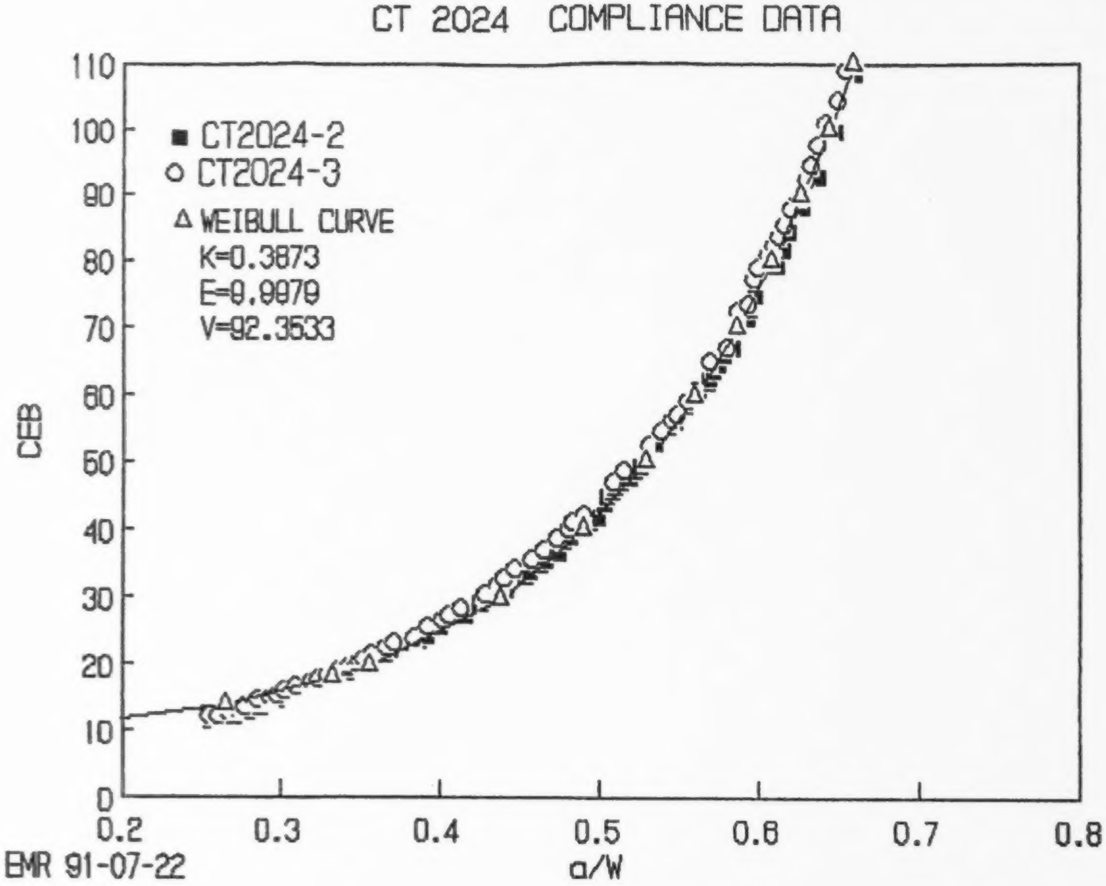

Figure 1.
Al 2024-T351 non-dimensional compliance versus crack length.

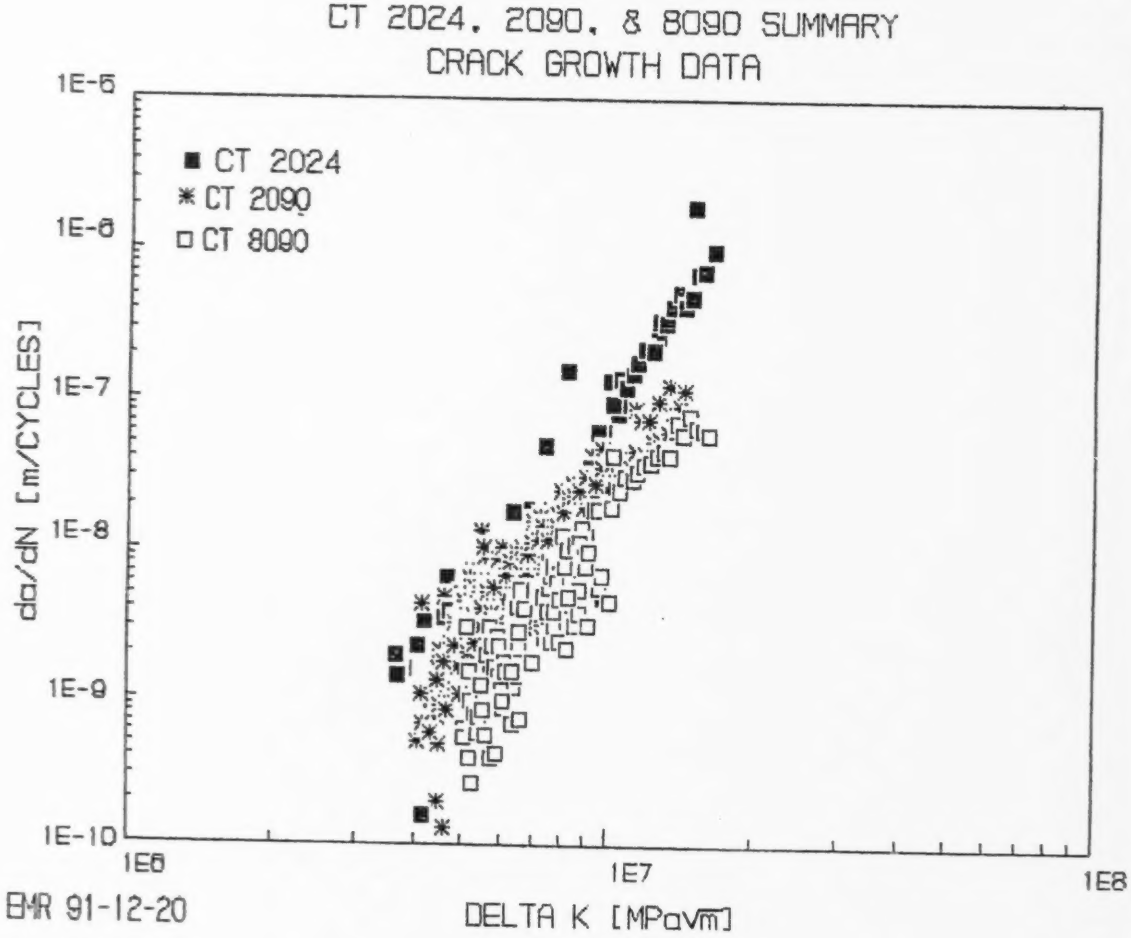

Figure 2.
Al 2024-T351, 2090-T8E41 and 8090-T8771 FCG obtained for ΔK applied decreasing and increasing conditions.

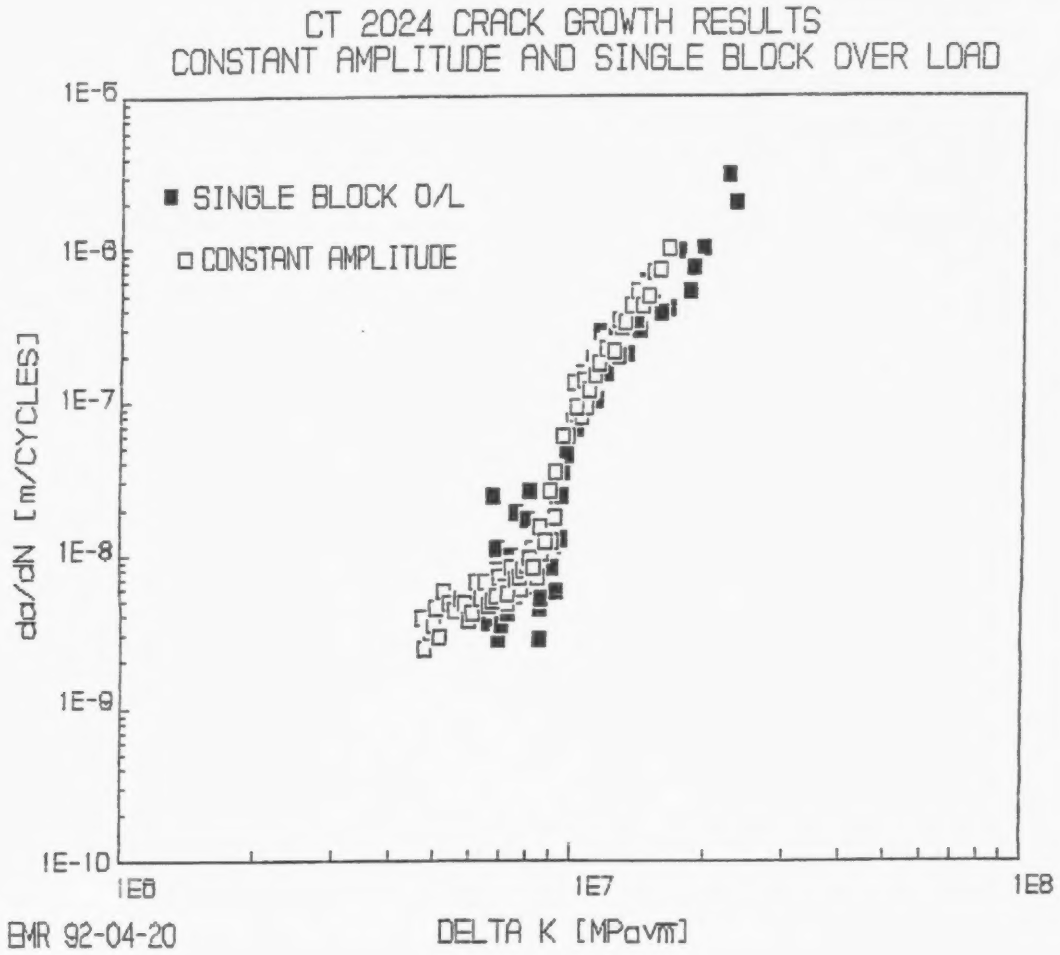

Figure 3.
A comparison of Al 2024-T351 ΔK constant amplitude and single block overload FCG suggests the 10% overload cycles did not effect FCG.

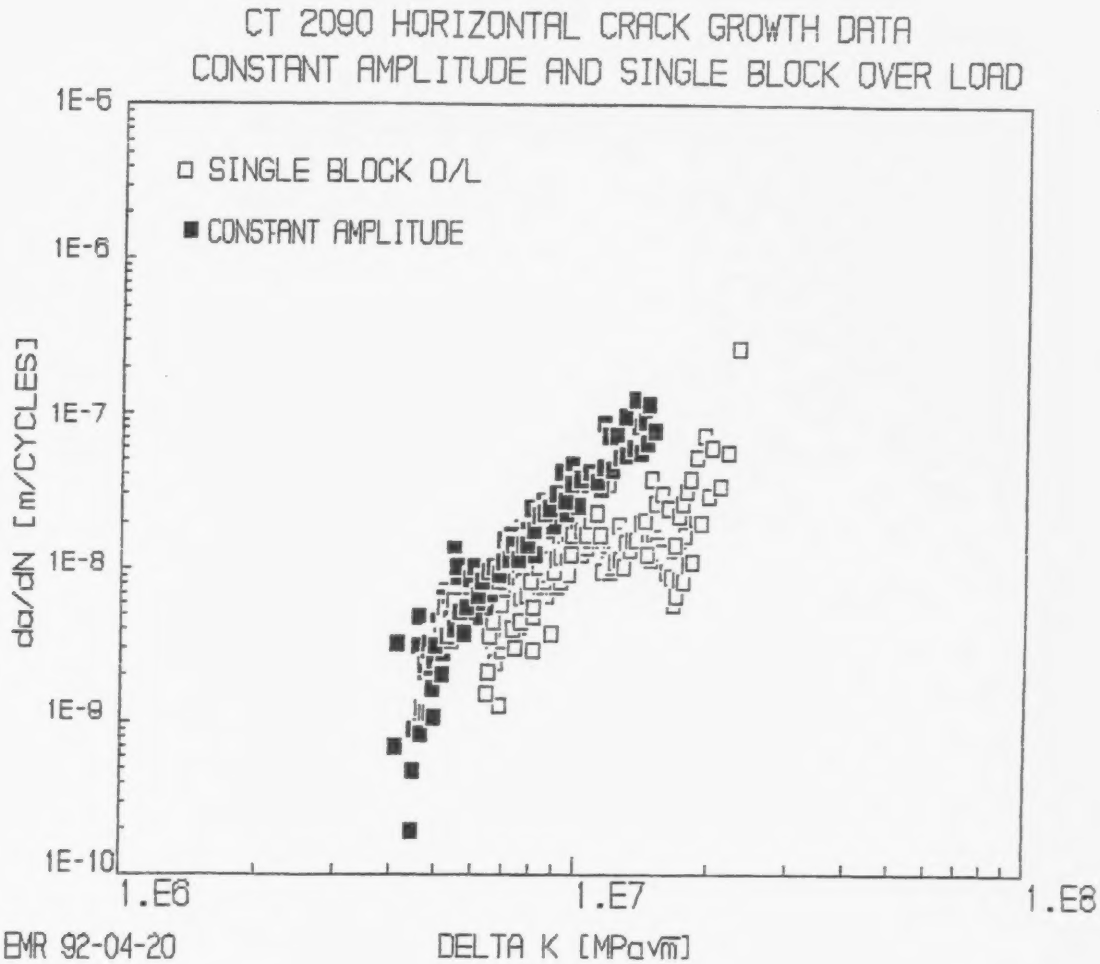

Figure 4.
Al 2090-T8E41 single block overload FCG shows a significant reduction relative to constant amplitude data.

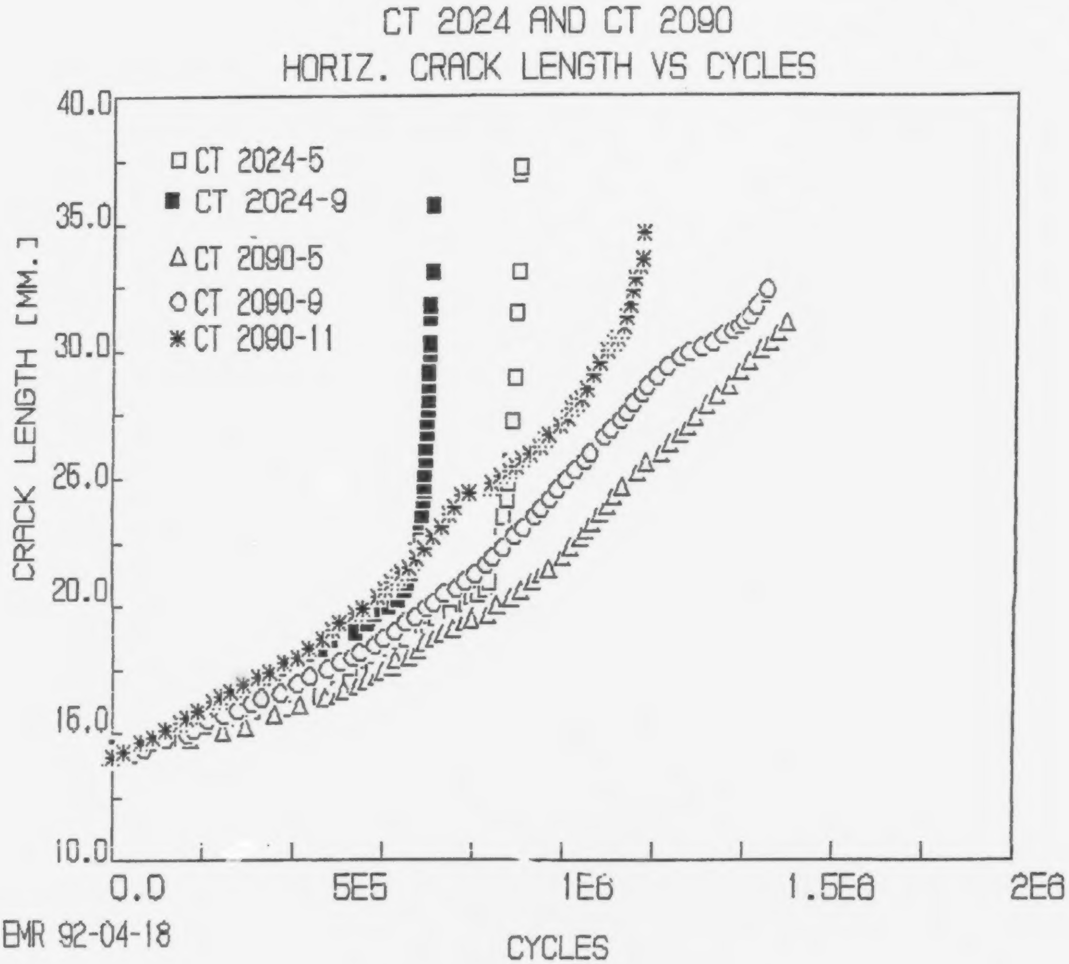

Figure 5.
Al 2024-T351 and 2090-T8E41 single block overload crack length versus cycles are compared.

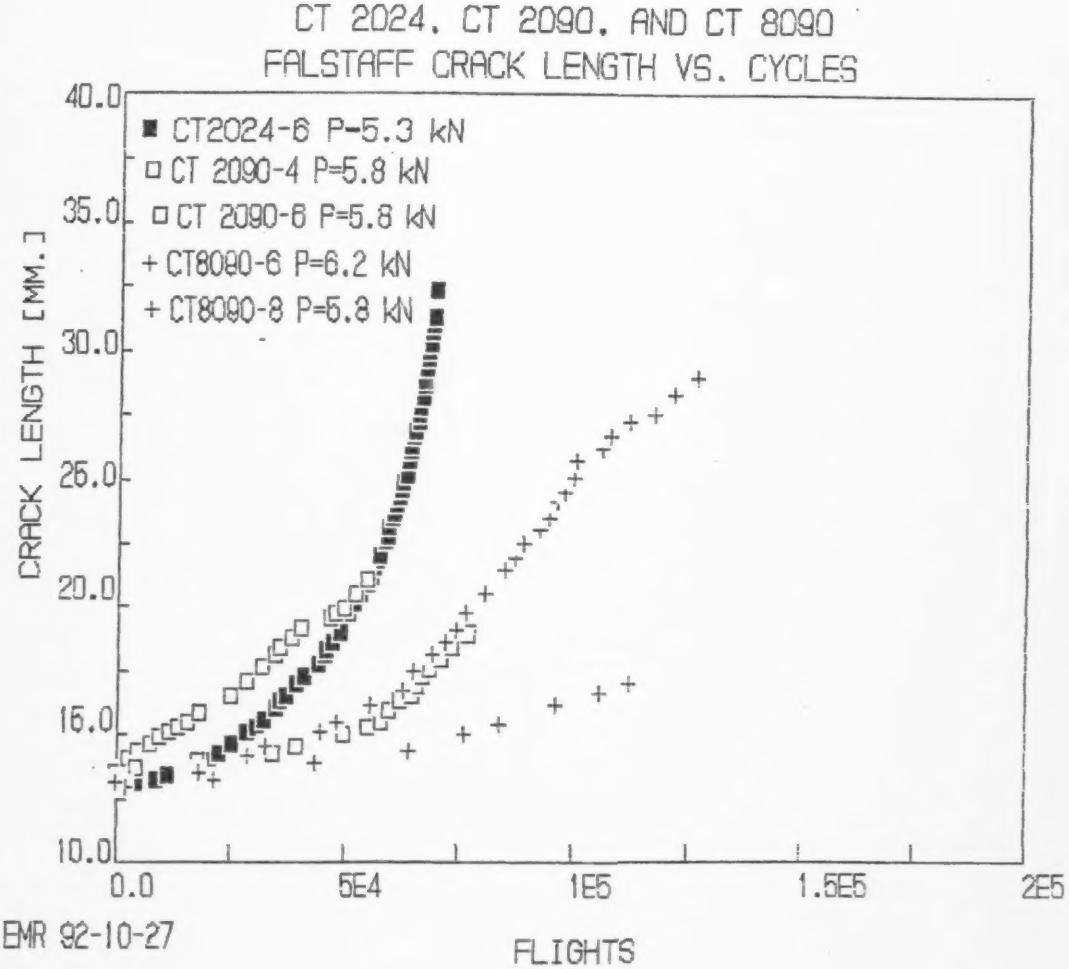

Figure 6.
FALSTAFFT crack length versus cycle data are compared.

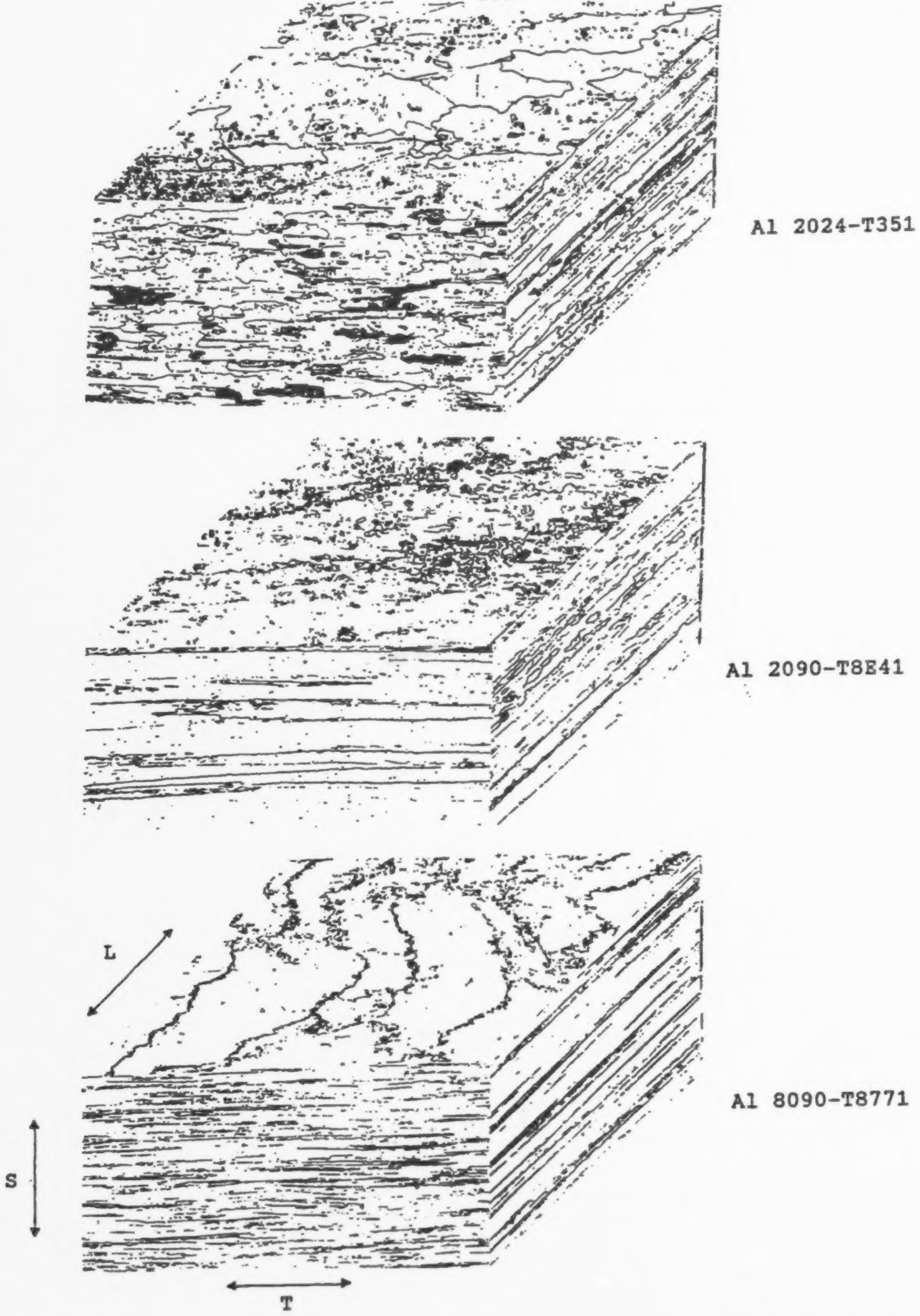
Al 2024-T351
Al 2090-T8E41
L
Al 8090-T8771
S
T

Figure 7.
Metallographic samples were prepared for each alloy and etched with Kellor's reagent to reveal grain structure.

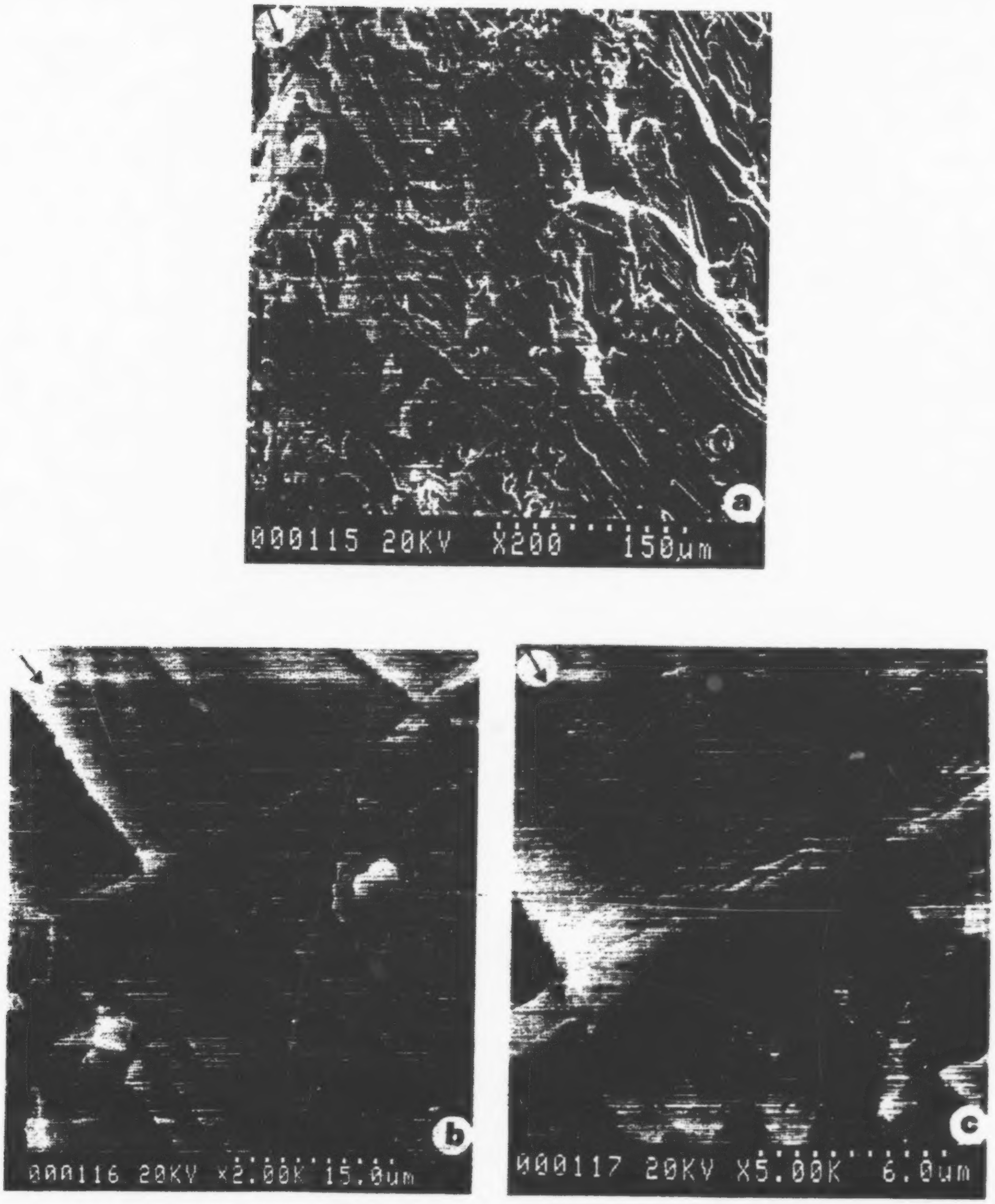
a
000115 20KV X200 150μm
b
000116 20KV x2.00K 15.0um
c
000117 20KV X5.00K 6.0um

Figure 8.
An overview of the 2024-T351 overload surface at a crack length of 12.0 is shown in (a). Detailed views of the fatigue striations are shown in (b) and (c).

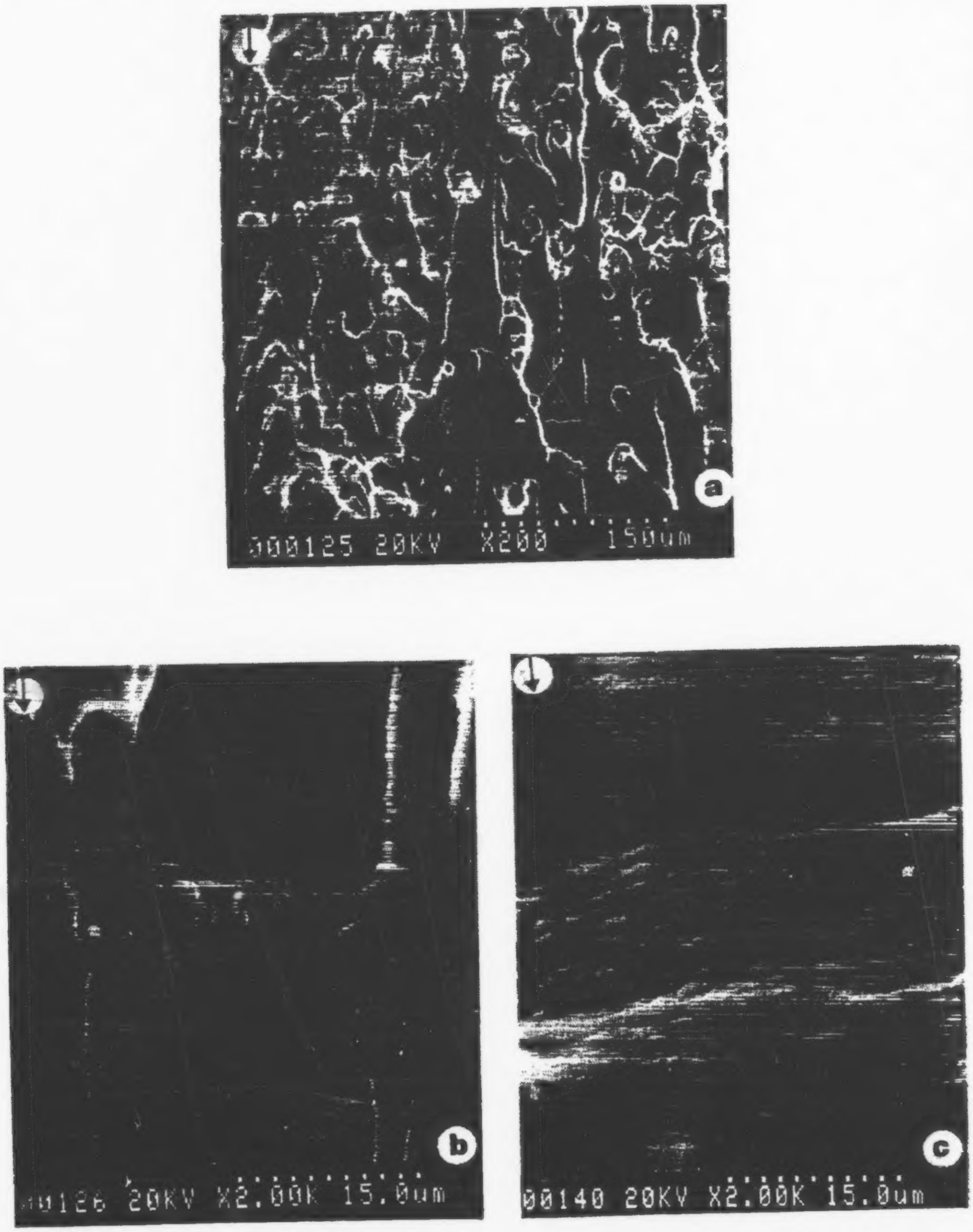
000125 20KV X200 150um
a
0126 20KV X2.00K 15.0um
b
00140 20KV X2.00K 15.0um
c

Figure 9.
Al-Cu 2024-T351 single block overload spacing at a crack length of 31.0 mm. A narrow band that defines the individual overload striations is shown at increasing magnifications in (a)-(c). The overload band appears tilted relative to the plane of the constant amplitude direction.

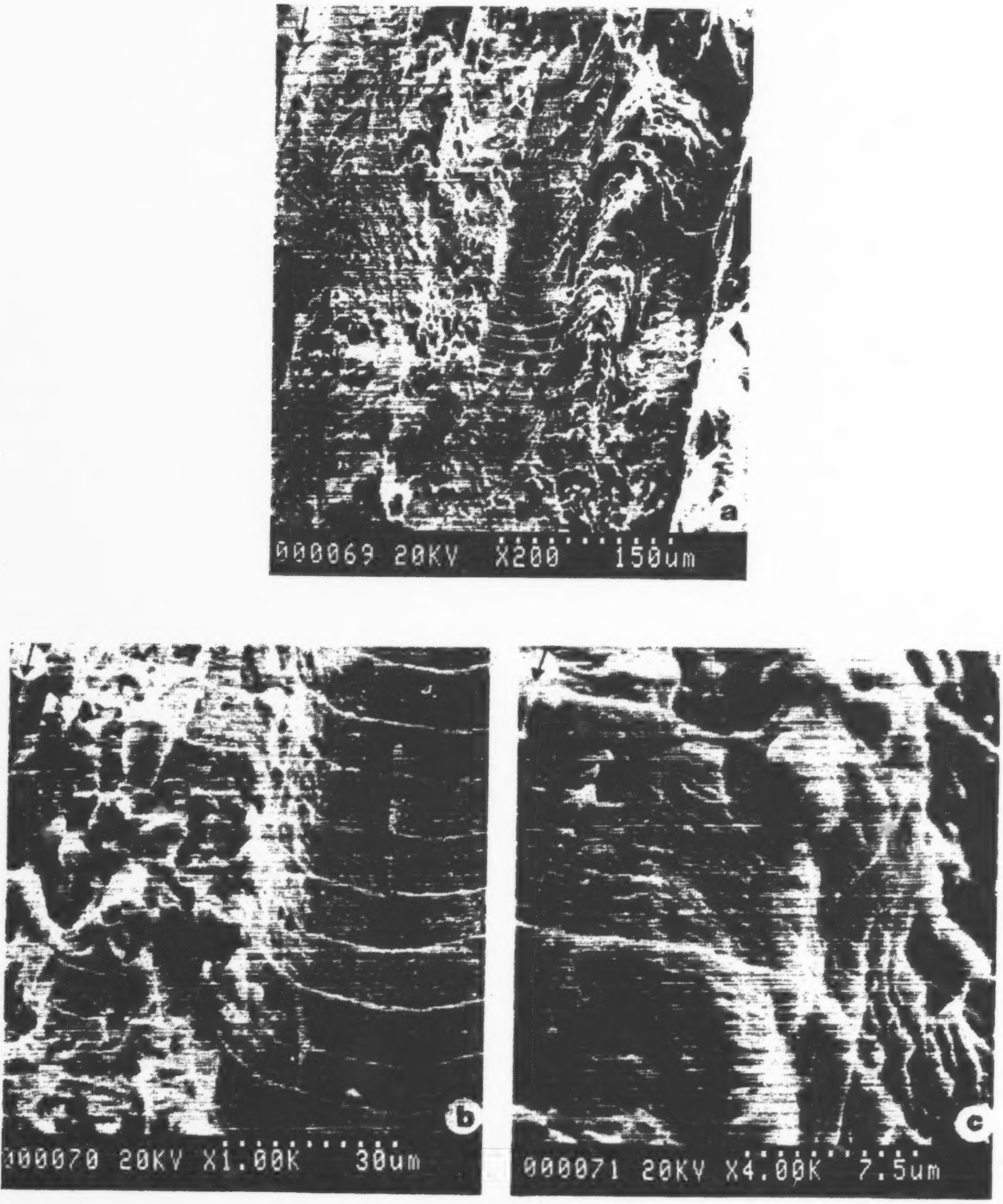
a
000069 20KV X200 150um
b
000070 20KV X1.00K 30um
c
000071 20KV X4.00K 7.5um

Figure 10.
Al-Li 2090-T8E41 single block overloads are shown at a crack length of 19.0 mm. Local changes in crack direction across grains are easily detected. Striations have a "brittle" appearance.

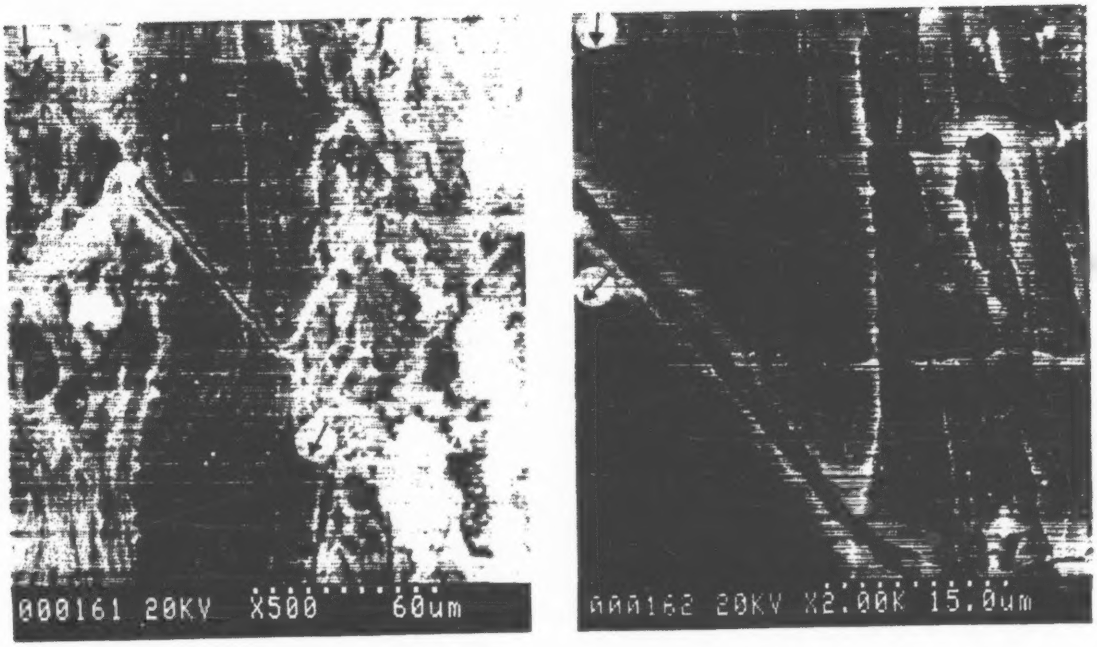
000161 20KV X500 60um
000162 20KV X2.00K 15.0um

Figure 11.
An overview of secondary crack formation at a grain boundary triple point on the 2090-T8E41 fracture surface in (a) is shown in greater detail in (b).

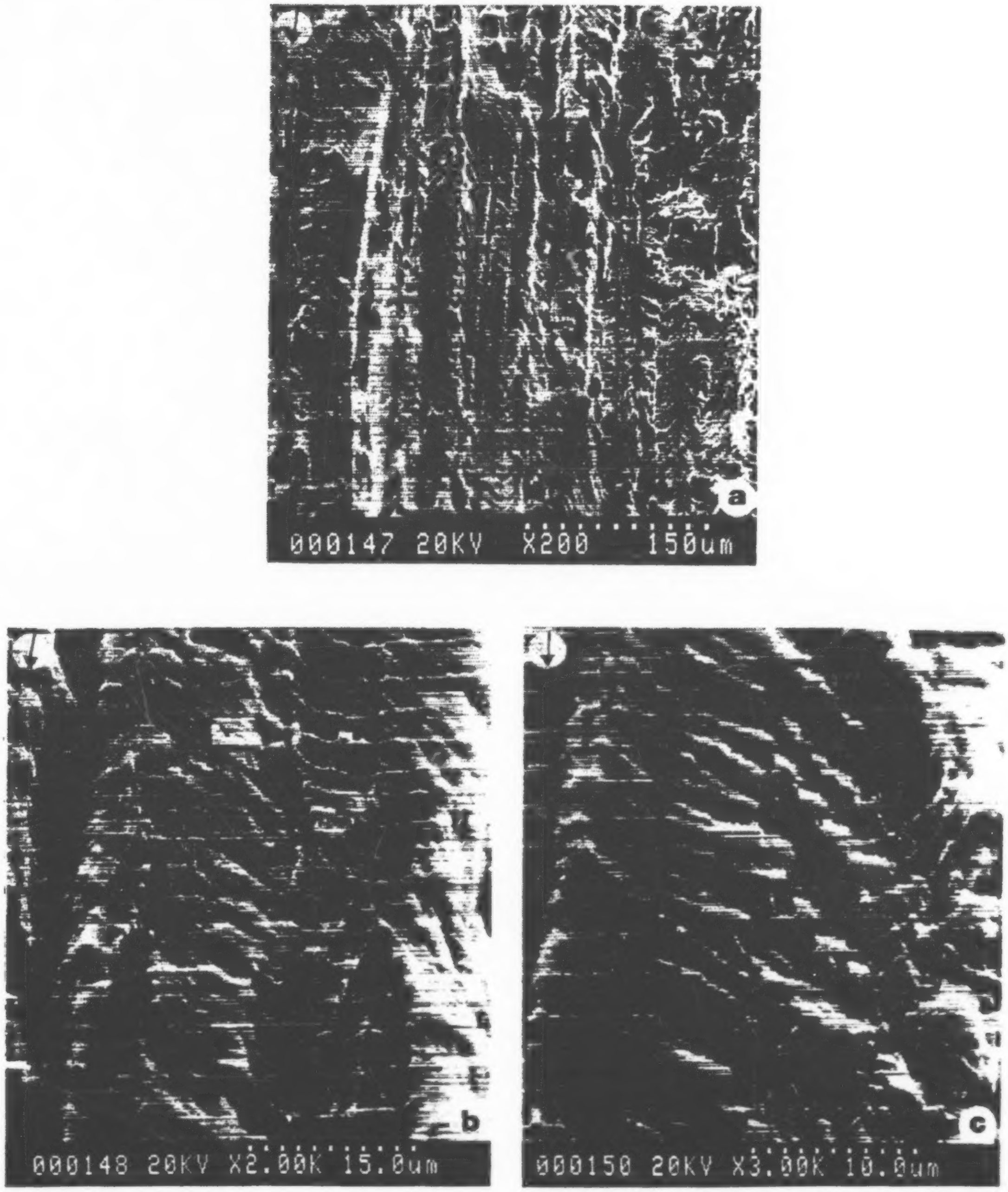
a
000147 20KV X200 150um
b
000148 20KV X2.00K 15.0um
c
000150 20KV X3.00K 10.0um

Figure 12.
Views of the 8090-T8771 single block overload fracture surface at a crack length of 17.0 mm are shown at increasing magnifications in (a)-(c). Elongated grain boundaries are clearly visible.

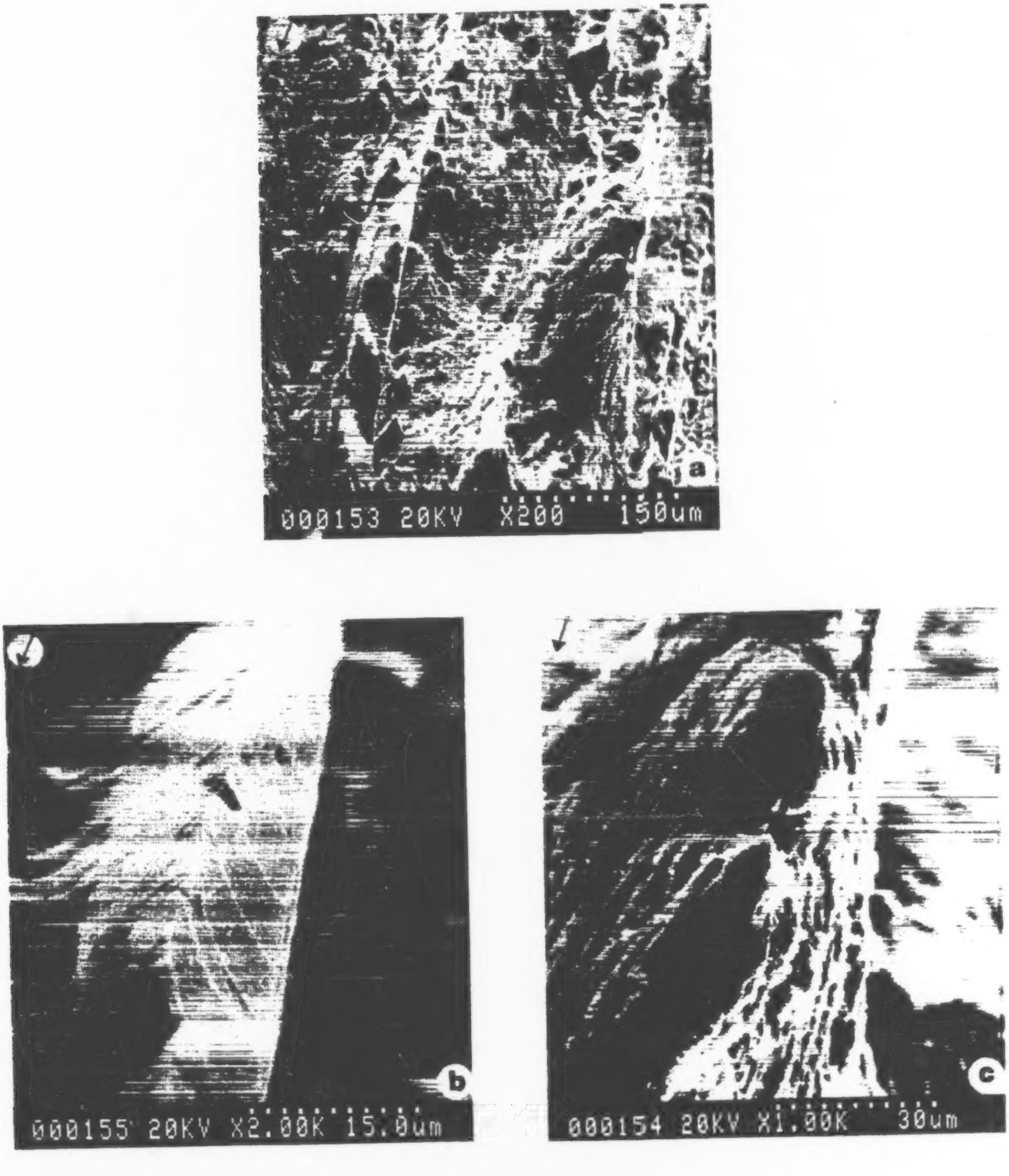
a
000153 20KV X200 150um
b
000155 20KV X2.00K 15.0um
c
000154 20KV X1.00K 30um

Figure 13.
Al-Li 8090-T8771 single block overload surface at 22.0 mm crack length shows increasing surface roughness in (a). Cyrstallographic features are bracketed by grain boundaries. Arrest lines are clearly visible on the sides of the ridge in (b). Wear particles coat a region of rubbed material in (c).

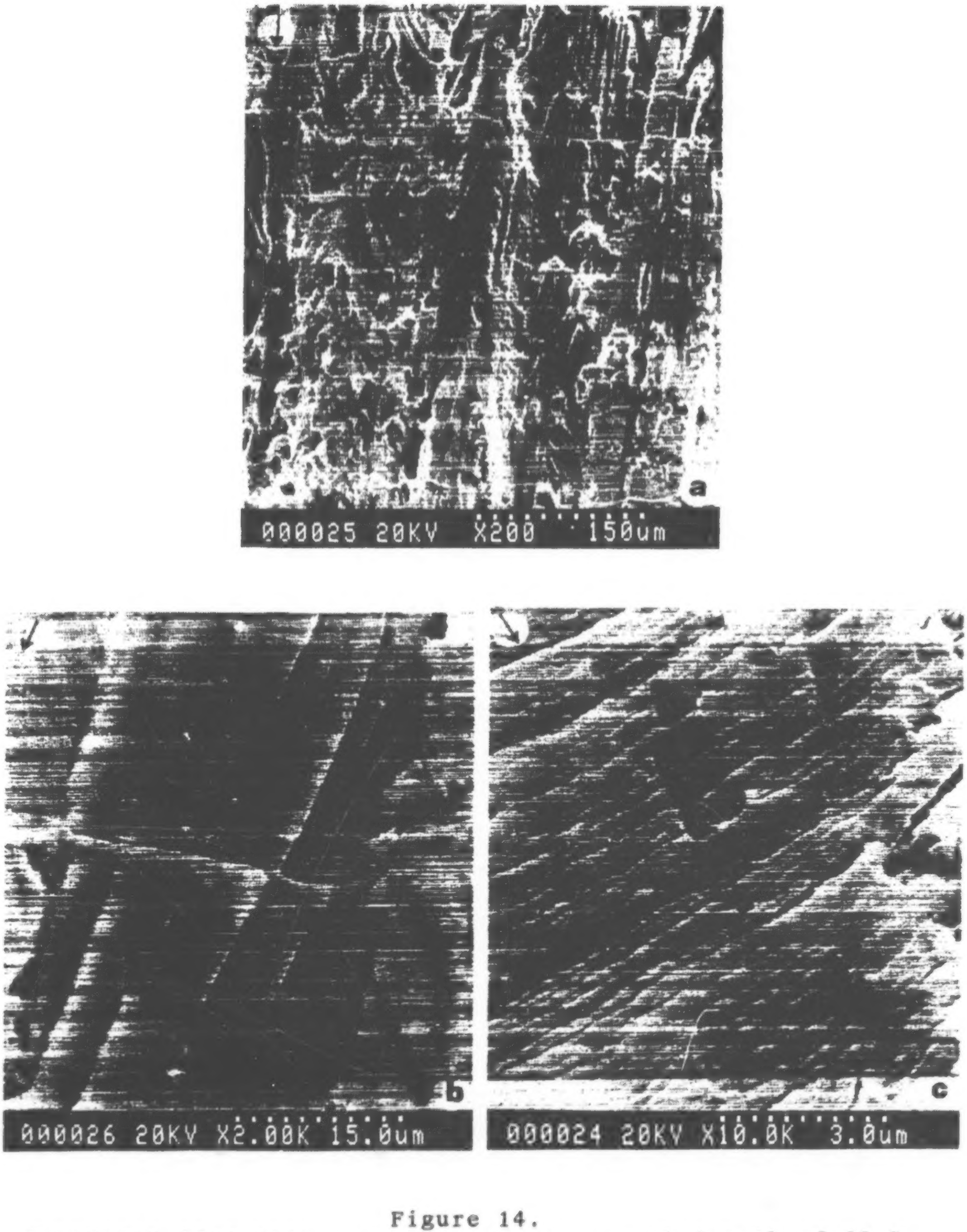
a
000025 20KV X200 150um
b
000026 20KV X2.00K 15.0um
c
000024 20KV X10.0K 3.0um

Figure 14.
FALSTAFFT 2024-T351 crack growth at a crack length of 22.0 mm is shown in (a). Higher magnification of (a) is shown in (b). The secondary cracks that formed along slip planes at fatigue striations are shown in (c).

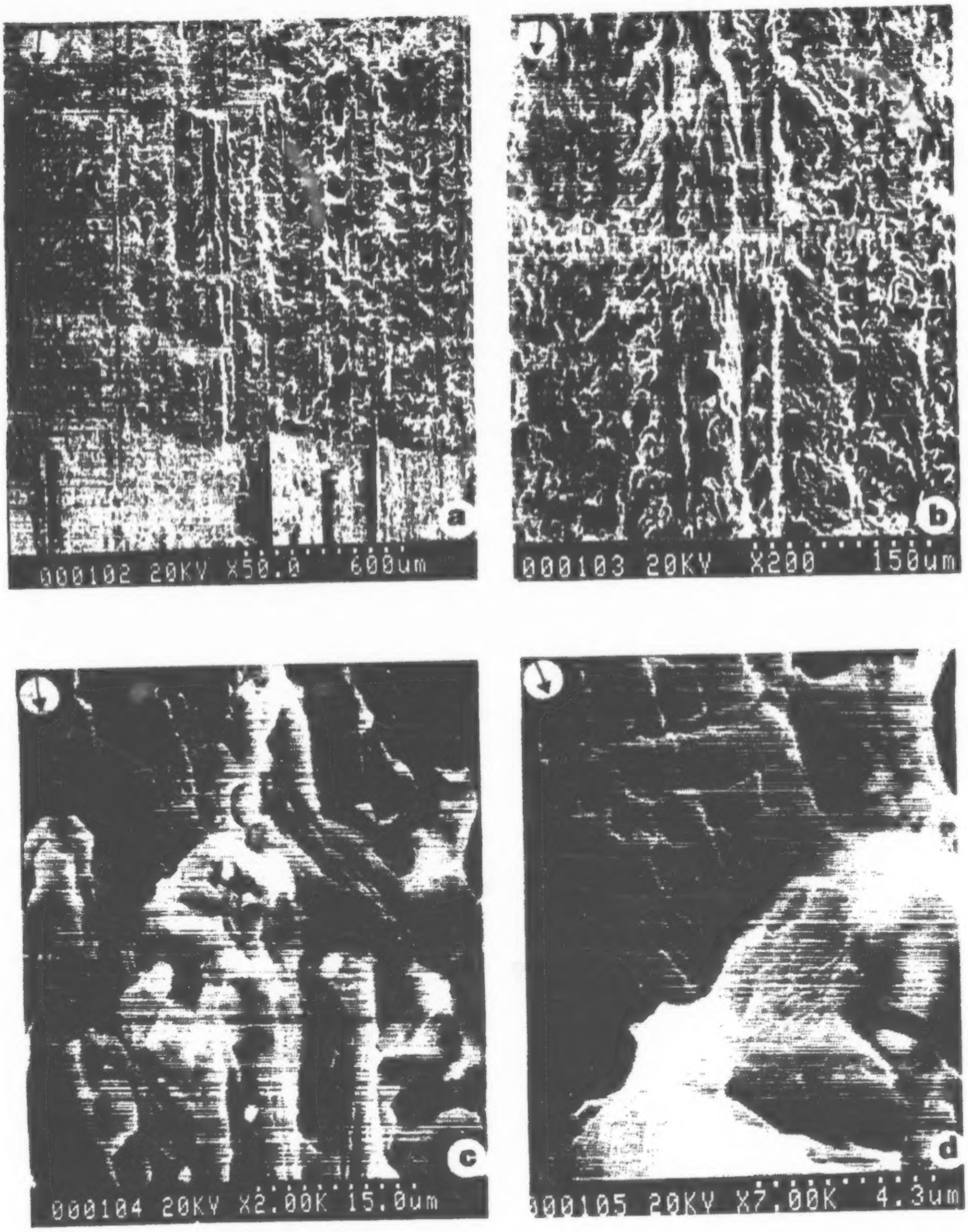
a
000102 20KV X50.0 600um
b
000103 20KV X200 150um
c
000104 20KV X2.00K 15.0um
d
000105 20KV X7.00K 4.3um

Figure 15.
Zones of tensile fracture were found on the 2090-T8E41 near final fracture. Light coloured regions represent unstable crack growth that occurred with FALSTAFFT's changing load magnitude in (a) and (b). Increasing magnification of these regions are shown in (c) and (d).

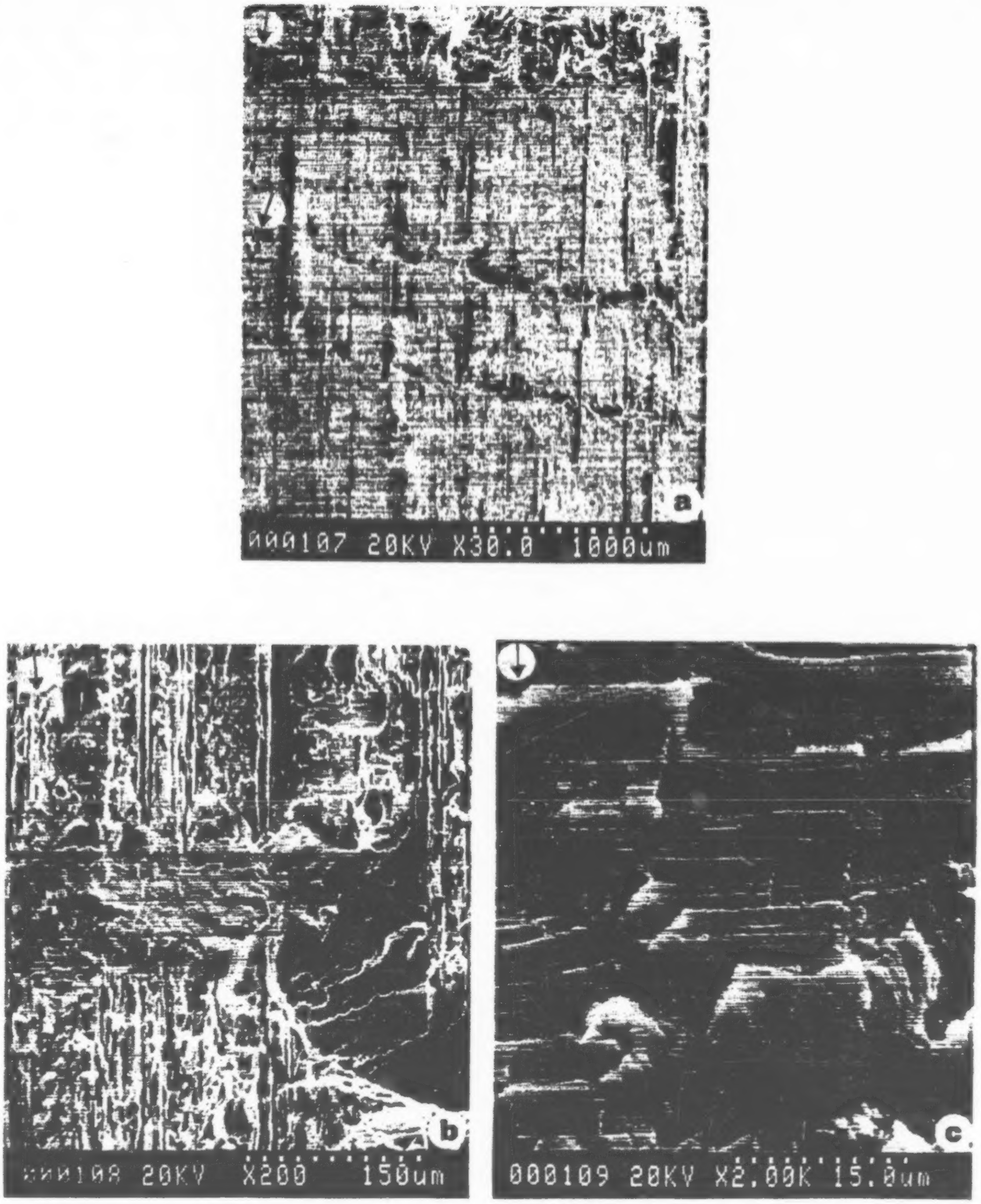
a
000107 20KV X30.0 1000um
b
000108 20KV X200 150um
c
000109 20KV X2.00K 15.0um

Figure 16.
Dark coloured zones of fatigue crack striations were found on the 2090-T8E41 during predominantly unstable crack growth in (a). Details of one of these zones is shown in (b) and (c). In (b), vertical grain boundary delaminations on the fast fracture surface are in contrast with the horizontal secondary cracks that are visible on the fatigue striation patch.

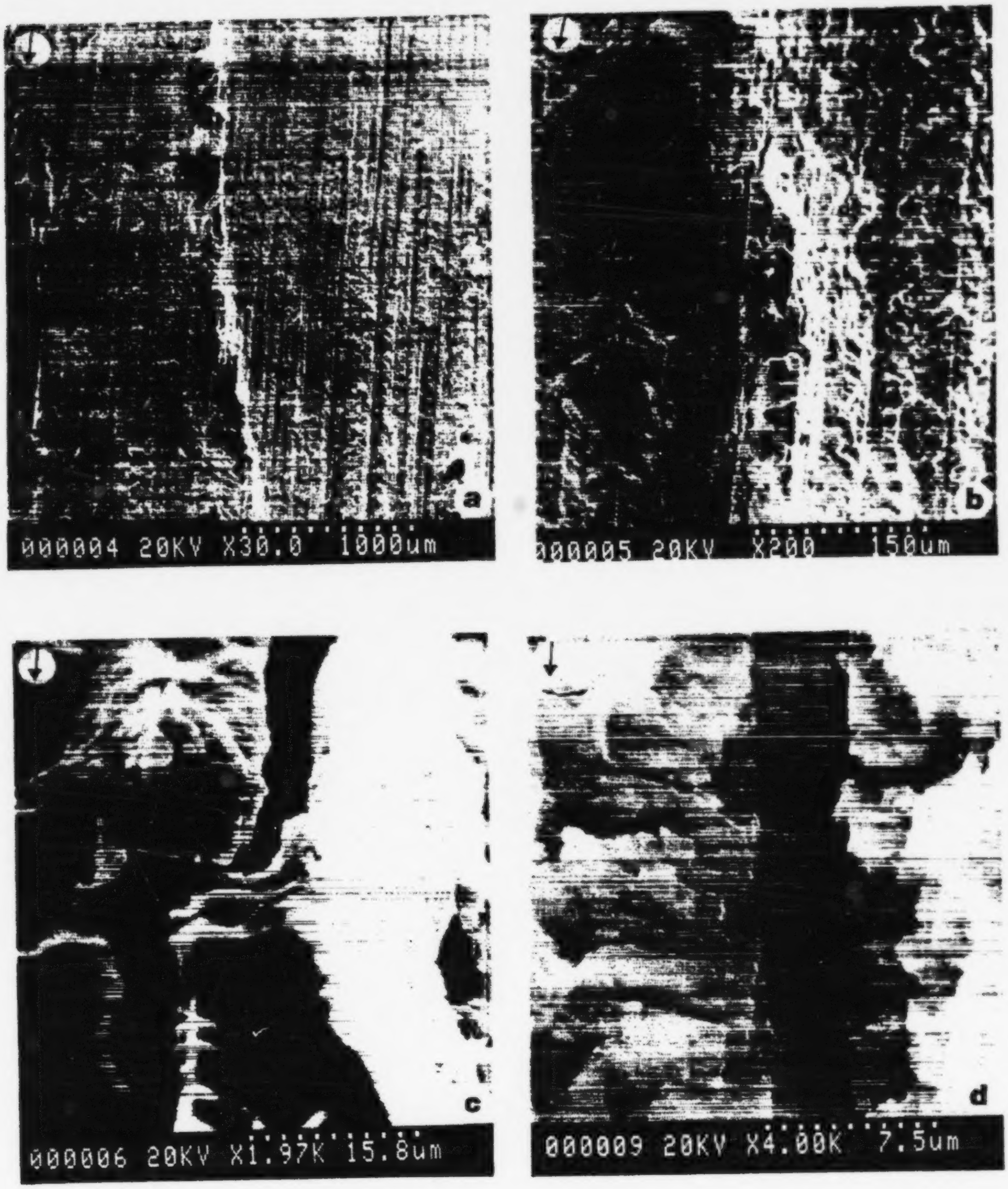
a
000004 20KV X30.0 1000um
b
000005 20KV X200 150um
c
000006 20KV X1.97K 15.8um
d
000009 20KV X4.00K 7.5um

Figure 17.
An overview of Al 8090-T8771's FALSTAFFT fracture surface is illustrated in (a). Long range secondary cracks appear to follow grain boundaries in (b) and (c). A typical FALSTAFFT fracture surface is presented in (d).

DISTRIBUTION

REPORT NUMBER:	DREP Report 93-1
TITLE:	Research and Development on Aluminum-Lithium Alloys
AUTHOR:	J. Morrison (editor)
DATED:	November 1993
SECURITY GRADING:	UNCLASSIFIED

All Workshop Attendees

DSIS Report Collection

DREA - Dr R.S. Hollingshead
 - Mr K. KarisAllen
DRES - D/Defence Technologies Divison
DREV - D/Armaments Division
DREO - Chief

CRAD - DGRD Ops
 - DRDM
 - DRDL

CRC - Dr D.G. Zimcik

MTL/CANMET - Chief

Alcan Kingston - Dr D. Lloyd

ARL, Melbourne, Australia - Dr S. Lynch
MRL, Melbourne, Australia - Dr D. Saunders

DSE, Auckland, New Zealand - Mr G. Wakefield

DRA Holton Heath, UK - Dr R. Jones
DRA Farnborough, UK - Dr R.N. Wilson

ARO, Research Triangle Park, USA - Dr A. Crowson
NAWC, USA - Dr G. London

DREP - Mr A.J. Russell
 - Library

DOCUMENT CONTROL DATA

(Security classification of title, body of abstract and indexing annotation must be entered when the overall document is classified)

1 **ORIGINATOR** (the name and address of the organization preparing the document. Organizations for whom the document was prepared, e.g. Establishment sponsoring a contractor's report, or tasking agency, are entered in section 8.)

Defence Research Establishment Pacific
FMO Victoria, BC
VOS 1B0

2. **SECURITY CLASSIFICATION** (overall security classification of the document including special warning terms if applicable)

UNCLASSIFIED

3 **TITLE** (the complete document title as indicated on the title page. Its classification should be indicated by the appropriate abbreviation (S,C or U) in parentheses after the title.)

Research and Development on Aluminum-Lithium Alloys

4 **AUTHORS** (Last name, first name, middle initial)

Morrison, John (editor)

5 **DATE OF PUBLICATION** (month and year of publication of document)

November 1993

6a. **NO. OF PAGES** (total containing information. Include Annexes, Appendices, etc.)

378

6b. **NO. OF REFS** (total cited in document)

–

7 **DESCRIPTIVE NOTES** (the category of the document, e.g. technical report, technical note or memorandum. If appropriate, enter the type of report, e.g. interim, progress, summary, annual or final. Give the inclusive dates when a specific reporting period is covered.)

DREP Report - Workshop Proceedings

8. **SPONSORING ACTIVITY** (the name of the department project office or laboratory sponsoring the research and development. Include the address.)

DREP

9a **PROJECT OR GRANT NO** (if appropriate, the applicable research and development project or grant number under which the document was written. Please specify whether project or grant)

9b. **CONTRACT NO.** (if appropriate, the applicable number under which the document was written)

10a **ORIGINATOR'S DOCUMENT NUMBER** (the official document number by which the document is identified by the originating activity. This number must be unique to this document.)

DREP Report 93-1

10b. **OTHER DOCUMENT NOS.** (Any other numbers which may be assigned this document either by the originator or by the sponsor)

11. **DOCUMENT AVAILABILITY** (any limitations on further dissemination of the document, other than those imposed by security classification)

(X) Unlimited distribution
( ) Distribution limited to defence departments and defence contractors; further distribution only as approved
( ) Distribution limited to defence departments and Canadian defence contractors; further distribution only as approved
( ) Distribution limited to government departments and agencies; further distribution only as approved
( ) Distribution limited to defence departments; further distribution only as approved
( ) Other (please specify):

12 **DOCUMENT ANNOUNCEMENT** (any limitation to the bibliographic announcement of this document. This will normally correspond to the Document Availability (11). However, where further distribution (beyond the audience specified in 11) is possible, a wider announcement audience may be selected.)

13. **ABSTRACT** (a brief and factual summary of the document. It may also appear elsewhere in the body of the document itself It is highly desirable that the abstract of classified documents be unclassified. Each paragraph of the abstract shall begin with an indication of the security classification of the information in the paragraph (unless the document itself is unclassified) represented as (S), (C), or (U) It is not necessary to include here abstracts in both offical languages unless the text is bilingual).

//The high stiffness and low density of lithium-containing aluminum alloys makes them prime candidates for a number of commercial and defence aircraft applications. It is well recognized that the strong crystallographic texture developed during the processing of these alloys, and the complex precipitation resulting from their heat treatment yields a material with some unusual properties. For several years Canadian government laboratories have had programs on aluminum-lithium alloysdealing with both long term research and development to characterize these materials, and the quality assurance issues and life cycle management implications arising from their exploitation in defence systems. This workshop was inrended to provide a review of the activities undertaken to date, and to foster an increasing coordination of the overall effort to maximize the technical support provided to the Canadian Forces. //

La haute rigidité et la densité faible d'alliages d'aluminium contenant du lithium les apprêtent aux applications pour des aéronefs commerciaux et de défense. La forte texture cristallographique qui se produit au cours du traitement de ces alliages ainsi que la précipitation complexe résultant du traitement thermique de ceux-ci produit un matériau aux propriétés peu communes. Depuis quelques années les laboratoires du gouvernement canadien ont des programmes qui portent sur les alliages aluminium-lithium : la recherche à long terme aussi bien que le développement pour caractériser ces matériaux, ainsi que les questions d'assurance de qualité et les implications de gestion de cycle de vie provenant de l'exploitation de ces matériaux dans les systèmes de défense. Le but de cet atelier fut de résumer les activités initiées à date et d'encourager la coordination croissante de l'effort global de maximiser les soutiens techniques fournis aux Forces canadiennes.

14. **KEYWORDS, DESCRIPTORS or IDENTIFIERS** (technically meaningful terms or short phrases that characterize a document and could be helpful in cataloguing the document. They should be selected so that no security classification is required. Identifiers, such as equipment model designation, trade name, military project code name, geographic location may also be included. If possible keywords should be selected from a published thesaurus. e.g. Thesaurus of Engineering and Scientific Terms (TEST) and that thesaurus-identified. If it is not possible to select indexing terms which are Unclassified, the classification of each should be indicated as with the title.)

aluminum-lithium
microstructure
mechanical properties
corrosion
fatigue
fracture
alloy selection